Physics of Atomic Nuclei, Vol. 67, No. 5, 2004, pp. 1003–1009. Translated from Yadernaya Fizika, Vol. 67, No. 5, 2004, pp. 1025–1032.

ELEMENTARY PARTICLES AND FIELDS
Theory

T-Odd Correlation in $K^+ \to \pi^0 l^+ \nu\gamma$ Decays beyond the Standard Model

V. V. Braguta, A. A. Likhoded, and A. E. Chalov

Institute for High Energy Physics, Protvino, Moscow oblast, 142284 Russia

Received March 19, 2003; in final form, September 12, 2003

Abstract—The T-odd correlation $\xi = \mathbf{q}\cdot[\mathbf{p}_\pi \times \mathbf{p}_l]/m_K^3$ in the decays $K^+ \to \pi^0 l^+ \nu\gamma$ ($l = e, \mu$) is investigated as a function of the parameters of the effective Lagrangian. It is shown that the T-odd correlation offers a good indicator of new physics in the vector and pseudovector sectors of the model under consideration. In the scalar and pseudoscalar sectors, investigation of the T-odd correlation gives no way to improve the current limits on the parameters of various extensions of the Standard Model.

1. INTRODUCTION

At present, considerable attention is being given to experimentally studying T invariance, which is one of the fundamental symmetries in contemporary physics. Of particular interest are measurements of quantities that are suppressed in the Standard Model, since effects of new physics may manifest themselves in such quantities. By way of example, we can mention the transverse polarization of the muon in the decays $K^+ \to \pi^0\mu\nu$ and $K^+ \to \mu\nu\gamma$ [1, 2]. In these processes, the muon has no transverse polarization in the Standard Model at the tree level. In the Standard Model, the transverse polarization of the muon is suppressed because it is due to final-state electromagnetic interactions. The Standard Model prediction for the transverse polarization of a lepton is as small as 5×10^{-6} in the decay $K^+ \to \pi^0\mu^+\nu$ [3, 4] and amounts to 6×10^{-4} in the decay $K^+ \to \mu^+\nu\gamma$ [5, 6]. In some extensions of the Standard Model, a nonzero polarization is generated at the tree level [7, 8].

The transverse polarization of the muon in the decay $K^+ \to \pi^0\mu^+\nu$ was measured recently in the KEK–E246 experiment [1]:

$$P_T = (-1.12 \pm 2.17(\text{stat.}) \pm 0.90(\text{syst.}))\times10^{-3}. \quad (1)$$

Unfortunately, we cannot present a similar result for the decay $K^+ \to \mu^+\nu\gamma$ because data processing has not yet been completed. The expected value of the polarization is estimated at 1.5×10^{-2} [2].

In studying CP violation, proper attention is also being given to the T-odd correlation $\xi = \mathbf{q}\cdot[\mathbf{p}_\pi \times \mathbf{p}_l]/m_K^3$ in $K^+ \to \pi^0 l^+\nu\gamma$ decays. In the differential distribution of the decay width in ξ, a nonzero asymmetry with respect to $\xi = 0$ would be signal of T violation. As in the case of the transverse polarization of the muon, the T-odd correlation is generated by final-state electromagnetic interactions within the Standard Model and is therefore zero at the tree level. Within the Standard Model, this effect was previously considered in [9]. It would be of interest to compare the Standard Model value of the asymmetry with its values obtained in various extensions of the Standard Model, and we address precisely this issue here.

Additionally, this study is motivated by the plans to study the T-odd correlation in the future OKA experiment [10], where it is natural to expect up to about 10^6–10^7 events of the decay $K^+ \to \pi^0 e^+\nu_e\gamma$ and up to about 10^5–10^6 events of the decay $K^+ \to \pi^0\mu^+\nu_\mu\gamma$.

The present article is organized as follows. In Section 2, we introduce a model-independent Lagrangian, express the asymmetry in terms of this Lagrangian, and discuss the Standard Model contribution to the asymmetry. Further, we consider the $SU(2)_L \times SU(2)_R \times U(1)$ left–right symmetric model in Section 3 and scalar models in Section 4. The results of our study are discussed in the Conclusion.

2. MODEL-INDEPENDENT APPROACH TO STUDYING THE T-ODD CORRELATION

The model-independent Lagrangian for four-fermion interactions can be represented in the form

$$\begin{aligned} L = \frac{G_F}{\sqrt{2}}\sin\theta_C(&\bar s\gamma^\alpha(1-\gamma_5)u\bar\nu\gamma_\alpha(1-\gamma_5)l \\ &+ g_s\bar s u\bar\nu(1+\gamma_5)l + g_p\bar s\gamma_5 u\bar\nu(1+\gamma_5)l \\ &+ g_v\bar s\gamma^\alpha u\bar\nu\gamma_\alpha(1-\gamma_5)l + g_a\bar s\gamma^\alpha\gamma_5 u\bar\nu\gamma_\alpha(1-\gamma_5)l), \end{aligned} \quad (2)$$

where G_F is the Fermi constant; θ_C is the Cabibbo angle; and g_s, g_p, g_v, and g_a are, respectively, the

1063-7788/04/6705-1003$26.00

scalar, the pseudoscalar, the vector, and the axial-vector coupling constant. With the aid of the Lagrangian in (2), we can express the matrix element for the decay $K(p) \to \pi^0(p')l(p_l)\nu(p_\nu)\gamma(q)$ as

$$T = \frac{G_\mathrm{F}}{\sqrt{2}} V_{us}^* e\epsilon_\alpha^* \Big(((1+g_v)V^{\alpha\beta} - (1-g_a)A^{\alpha\beta})\bar\nu(1+\gamma_5)\gamma_\beta l + (1+g_v)F_\beta \bar\nu(1+\gamma_5)\gamma^\beta \Big(\frac{p^\alpha}{pq} - \frac{p_l^\alpha}{p_l q} - \frac{\hat q\gamma^\alpha}{2(p_l q)}\Big) l + (g_s F_s^\alpha + g_p F_p^\alpha)\bar\nu(1+\gamma_5) l + g_s f \bar\nu(1+\gamma_5)\Big(\frac{p^\alpha}{pq} - \frac{p_l^\alpha}{p_l q} - \frac{\hat q\gamma^\alpha}{2(p_l q)}\Big) l \Big), \tag{3}$$

where V_{us} is an element of the Cabibbo–Kobayashi–Maskawa matrix; ϵ_α is the photon polarization vector; and the tensors $V^{\alpha\beta}$, $A^{\alpha\beta}$, F^β, F_s^α, F_p^α, and f are given by

$$V^{\alpha\beta} + \frac{p^\alpha}{pq}F^\beta = i\int d^4x e^{iqx}\langle \pi^0(p')|TJ^\alpha(x)(\bar s\gamma^\beta u)(0)|K(p)\rangle, \tag{4}$$

$$A^{\alpha\beta} = i\int d^4x e^{iqx}\langle \pi^0(p')|TJ^\alpha(x)(\bar s\gamma^\beta\gamma_5 u)(0)|K(p)\rangle,$$

$$F_s^\alpha + \frac{p^\alpha}{pq}f = i\int d^4x e^{iqx}\langle \pi^0(p')|TJ^\alpha(x)(\bar s u)(0)|K(p)\rangle,$$

$$F_p^\alpha = i\int d^4x e^{iqx}\langle \pi^0(p')|TJ^\alpha(x)(\bar s\gamma_5 u)(0)|K(p)\rangle,$$

$$F^\beta = \langle \pi^0(p')|(\bar s\gamma^\beta u)(0)|K(p)\rangle,$$

$$f = \langle \pi^0(p')|(\bar s u)(0)|K(p)\rangle,$$

J^α being the electromagnetic current. By means of Ward identities [11], we can show that the tensors in (4) satisfy the relations

$$q_\alpha V^{\alpha\beta} = 0, \quad q_\alpha A^{\alpha\beta} = 0, \quad q_\alpha F_s^\alpha = 0, \quad q_\alpha F_p^\alpha = 0. \tag{5}$$

Taking these relations into account, we can introduce the following parametrization:

$$V_{\alpha\beta} = V_1\Big(g_{\alpha\beta} - \frac{W_\alpha q_\beta}{qW}\Big) + V_2\Big(p'_\alpha q_\beta - \frac{p'q}{qW}W_\alpha q_\beta\Big) + V_3\Big(p'_\alpha W_\beta - \frac{p'q}{qW}W_\alpha W_\beta\Big) + V_4\Big(p'_\alpha p'_\beta - \frac{p'q}{qW}W_\alpha p'_\beta\Big), \tag{6}$$

$$A_{\alpha\beta} = i\epsilon_{\alpha\beta\rho\sigma}(A_1 p'^\rho q^\sigma + A_2 q^\rho W^\sigma) + i\epsilon_{\alpha\lambda\rho\sigma}p'^\lambda q^\rho W^\sigma(A_3 W_\beta + A_4 p'_\beta),$$

$$F^\beta = C_1 p'_\beta + C_2(p-p')^\beta,$$

$$F_s^\alpha = S\left(p^\alpha - \frac{pq}{p'q}p'^\alpha\right),$$

$$F_p^\alpha = iP\epsilon^{\alpha\lambda\rho\sigma}p_\lambda p'_\rho q_\sigma,$$

$$W = p_l + p_\nu.$$

In the calculations, we use the expressions obtained for the form factors V_i, A_i, and C_i within chiral perturbation theory to order p^4 [11]. The form factors S and f can be related to the known expressions for V_i and C_i by using Ward identities. The derivation of the respective relations is given in the Appendix along with the derivation of an expression for the form factor P.

In seeking possible CP-odd effects, we are interested in the distribution of the $K^+(p) \to \pi^0(p')l^+(p_l)\nu(p_\nu)\gamma(q)$ partial decay width with respect to the kinematical variable $\xi = \mathbf{q}\cdot[\mathbf{p}_\pi \times \mathbf{p}_l]/m_K^3$ in the K^+-meson rest frame,

$$\rho(\xi) = \frac{d\Gamma}{d\xi}. \tag{7}$$

Obviously, the function $\rho(\xi)$ can be represented in the form

$$\rho = f_\mathrm{even}(\xi) + f_\mathrm{odd}(\xi),$$

where $f_\mathrm{even}(\xi)$ and $f_\mathrm{odd}(\xi)$ are, respectively, an even and an odd function of ξ. The function $f_\mathrm{odd}(\xi)$ can be written as

$$f_\mathrm{odd} = g(\xi^2)\xi. \tag{8}$$

After integration of the function $\rho(\xi)$ over the entire range of ξ, only the function $f_\mathrm{even}(\xi)$ makes a nonzero contribution to the total width.

To analyze data on $K^+ \to \pi^0 l^+\nu_l\gamma$ decays, it is convenient to introduce the quantity

$$A_\xi = \frac{N_+ - N_-}{N_+ + N_-}, \tag{9}$$

where N_+ (N_-) is the number of events in which $\xi > 0$ ($\xi < 0$). Obviously, the numerator of A_ξ depends only on $f_\mathrm{odd}(\xi)$.

Since the form factors V_i, A_i, and C_i are real-valued, the distribution $\rho(\xi)$ in the tree approximation

of the Standard Model is symmetric with respect to the straight line $\xi = 0$; that is, the number of $K^+ \to \pi^0 l^+ \nu_l \gamma$ events for $\xi > 0$ is equal to that for $\xi < 0$; therefore, $A_\xi = 0$. This can be explained as follows: in the tree approximation of the Standard Model, the form factors V_i, A_i, and C_i are real-valued; the square of the matrix element for the decay processes in question is expressed in terms of only the scalar products of final-particle momenta; and there are no contributions linear in ξ. For this reason, $\rho(\xi)$ is an even function of the variable ξ.

Within the Standard Model, ξ-odd terms are due to final-state electromagnetic interaction, which gives rise to imaginary parts in some form factors; in turn, they generate a nonzero contribution to the function $f_{\rm odd}(\xi)$ and to the asymmetry A_ξ. The contribution of the final-state interactions was considered in [9] in the one-loop approximation. The calculations on the basis of the unitarity relations for the S-matrix yield

$$A_\xi = 1.14 \times 10^{-4}\ (K^+ \to \pi^0 \mu^+ \nu_\mu \gamma), \qquad (10)$$
$$A_\xi = -0.59 \times 10^{-4}\ (K^+ \to \pi^0 e^+ \nu_e \gamma).$$

This result indicates that the value of A_ξ can be used in searches for new physics since the Standard Model contribution to the asymmetry of $K^+ \to \pi^0 l^+ \nu_l \gamma$ decays is strongly suppressed.

We now consider the asymmetry A_ξ of the matrix element for $K^+ \to \pi^0 l^+ \nu \gamma$ decays as given by the Lagrangian in (2). In the K^+-meson rest frame, the square of the decay amplitude (3) can be represented in the form

$$|T|^2 = |T_{\rm even}|^2 + ({\rm Im}(g_v)C_v + {\rm Im}(g_a)C_a \qquad (11)$$
$$+ {\rm Im}(g_s)C_s + {\rm Im}(g_p)C_p)m_K^4 \xi,$$

where $|T_{\rm even}|^2$ is the ξ-even contribution to the square of the matrix element; the last term is an odd contribution; and C_a, C_v, C_s, and C_p are kinematical factors that depend only on the scalar products of the momenta of the particles involved in the decay process being considered. We do not present here the expressions for C_a, C_v, C_s, and C_p because they are rather cumbersome. From (11), it can be seen that the asymmetry does not vanish if the imaginary parts of the parameters of the Lagrangian in (2) are different from zero.

It should be noted that one can derive a relation between the kinematical factors C_a and C_v from expression (3) for the matrix element in question. Assuming that, in the model under consideration, ${\rm Im}(g_v) = -{\rm Im}(g_a)$ and ${\rm Im}(g_s) = {\rm Im}(g_p) = 0$, we conclude that the asymmetry A_ξ vanishes because the matrix element (3) differs from the matrix element within the Standard Model only by a common phase factor; that is, $C_v - C_a = 0$ in this model. Since the kinematical factors C_v and C_a are independent of the structure of a model, the equality $C_v = C_a$ must be valid in any model.

Upon integrating expression (11) over the phase space, one can obtain the asymmetry A_ξ. Here, we perform this integration numerically over the photon energy region $E_\gamma > 30$ MeV and the region $\theta_{\gamma l} > 20^\circ$ of lepton–photon opening angles in the kaon rest frame, these kinematical cuts being typical of the current and planned kaon experiments. As a result, we obtain

$$A_\xi = -(2.9 \times 10^{-6}{\rm Im}(g_s) + 3.7 \times 10^{-5}{\rm Im}(g_p) \qquad (12)$$
$$+ 3.0 \times 10^{-3}{\rm Im}(g_v + g_a))$$

for $K^+ \to \pi^0 e^+ \nu_e \gamma$ and

$$A_\xi = -(3.6 \times 10^{-3}{\rm Im}(g_s) + 1.2 \times 10^{-2}{\rm Im}(g_p)$$
$$+ 1.0 \times 10^{-2}{\rm Im}(g_v + g_a))$$

for $K^+ \to \pi^0 \mu^+ \nu_\mu \gamma$.

It should be noted that, in the asymmetry of the decay $K^+ \to \pi^0 e^+ \nu_e \gamma$, the contributions of the parameters ${\rm Im}(g_s)$ and ${\rm Im}(g_p)$ are strongly suppressed in relation to the analogous contributions for the decay involving a muon in the final state. This is because the kinematical coefficients of these parameters are proportional to the final-lepton mass.

3. $SU(2)_L \times SU(2)_R \times U(1)$ MODELS

In this section, we consider extensions of the Standard Model that are based on $SU(2)_L \times SU(2)_R \times U(1)$ symmetry [12]. In such models, each fermion generation furnishes both an $SU(2)_L$ and an $SU(2)_R$ doublet. Fermion masses are generated via the Higgs mechanism. Therefore, one must introduce at least one Higgs multiplet. We introduce a $\Phi(2,2,0)$ Higgs multiplet,

$$\Phi = \begin{pmatrix} \phi_1^0 & \phi_1^+ \\ \phi_2^- & \phi_2^0 \end{pmatrix}. \qquad (13)$$

The vacuum expectation values in this multiplet can be written as

$$\Phi = \begin{pmatrix} k & 0 \\ 0 & k' \end{pmatrix}. \qquad (14)$$

In general, the vacuum expectation values k and k' are complex. Additional Higgs multiplets are required for ensuring the breakdown of $SU(2)_L \times SU(2)_R \times U(1)$ symmetry to $U(1)$. The most straightforward

way for such symmetry breaking is to introduce two doublets $\delta_L(2,1,1)$ and $\delta_R(1,2,1)$,

$$\delta_L = \begin{pmatrix} \delta_L^+ \\ \delta_L^0 \end{pmatrix}, \quad \delta_R = \begin{pmatrix} \delta_R^+ \\ \delta_R^0 \end{pmatrix}. \tag{15}$$

For a large mass scale M_R to be generated, it is necessary that the vacuum expectation value $\langle\delta_R^0\rangle = v_R$ be considerably greater than k, k', and $\langle\delta_L^0\rangle = v_L$.

Another possible scenario of a spontaneous breakdown of $SU(2)_L \times SU(2)_R \times U(1)$ symmetry involves the triplets $\Delta_L(1,3,2)$ and $\Delta_R(3,1,2)$,

$$\Delta_{L,R} = \begin{pmatrix} \Delta^+/\sqrt{2} & \Delta^{++} \\ \Delta^0 & -\Delta^+/\sqrt{2} \end{pmatrix}_{L,R}, \tag{16}$$

whose vacuum expectation values are

$$\Delta_{L,R} = \begin{pmatrix} 0 & 0 \\ v_{L,R} & 0 \end{pmatrix}. \tag{17}$$

In just the same way as in the model involving two Higgs doublets, fulfillment of the condition $v_R \gg k, k', v_L$ is necessary for the generation of a large mass scale. Sometimes, it is required that the Lagrangian of the gauge theory under study be invariant under the transformations

$$\Psi_L \leftrightarrow \Psi_R, \quad \delta_R \leftrightarrow \delta_L, \quad \Delta_R \leftrightarrow \Delta_L, \quad \Phi \leftrightarrow \Phi^+. \tag{18}$$

This implies, in particular, that the fermion couplings to the $SU(2)_L$ and $SU(2)_R$ bosons are equal.

In the models under study, CP violation is due to the Cabibbo–Kobayashi–Maskawa matrices, which appear both in the left (K^L) and in the right (K^R) sector of the theory. The effects of CP violation are much richer in this theory than in the Standard Model because the analog of the Cabibbo–Kobayashi–Maskawa matrix in the right sector involves $N(N+1)/2$ CP-odd phases, where N is the number of generations. Here, we neglect neutrino masses and, hence, lepton mixing angles, assuming that the lepton mixing matrices are diagonal. Depending on the parameters of the model, there are two mechanisms of CP violation. The first is spontaneous CP violation occurring if the vacuum expectation values k, k', v_R, and v_L are complex and if the Yukawa couplings to fermions (elements of the matrix Φ) are real. In the case of CP violation through the second mechanism, the Yukawa couplings are complex, while the vacuum expectation values are real. The latter mechanism is realized in the Standard Model. In general, either mechanism or both of them can be operative.

Irrespective of the content of the Higgs sector responsible for symmetry breaking, the interaction between quarks and charged gauge bosons can be represented in the form [13]

$$L = \frac{g_L}{\sqrt{2}} W_L^\mu \bar{U} \gamma_\mu K^L P_L D + \frac{g_R}{\sqrt{2}} W_R^\mu \bar{U} \gamma_\mu K^R P_R D + \text{h.c.}, \tag{19}$$

where g_R and g_L are the coupling constants in, respectively, the right and the left sector of the model under study; $U^T = (u, c, t)$ and $D^T = (d, s, b)$ are physical quark states; and $P_{L,R} = (1 \mp \gamma_5)/2$. The states W_R and W_L are not physical, but they can be reduced to physical states by means of the unitary transformation

$$\begin{pmatrix} W_L \\ W_R \end{pmatrix} = \begin{pmatrix} \cos\eta & -\sin\eta \\ e^{i\omega}\sin\eta & e^{i\omega}\cos\eta \end{pmatrix} \begin{pmatrix} W_1 \\ W_2 \end{pmatrix}, \tag{20}$$

where η is the mixing angle and ω is a phase. In what follows, the phase factor is included in the matrix K^R. With the aid of (19) and (20), the effective Lagrangian for the process $s \to u\mu\nu_\mu$ can be recast into the form

$$L = -\frac{G_F}{\sqrt{2}} \frac{g_R}{g_L} (K_{su}^R)^* \xi (\bar{s}(1-\gamma_5)\gamma_\alpha u)(\bar{\nu}(1+\gamma_5)\gamma^\alpha l). \tag{21}$$

Comparing this expression with the Lagrangian in (2), we find that the parameters g_a and g_v of the Lagrangian under consideration are given by

$$g_v = g_a = -\frac{g_R}{g_L} \frac{(K_{su}^R)^*}{\sin\theta_c} \eta. \tag{22}$$

In the following, we assume that the input Lagrangian of the model is invariant under the transformations in (18), this leading to the relation $g_R = g_L$. We also assume that the mixing matrices K^R and K^L satisfy the relation $|(K^R)_{ij}| = |(K^L)_{ij}|$. This relation holds if the vacuum expectation values of the Higgs fields are real; that is, CP violation is due to the complex-valuedness of the Yukawa couplings. In this case, $K^L = K^R$ [14]. The equality $|(K^R)_{ij}| = |(K^L)_{ij}|$ also holds in models featuring a spontaneous violation of CP symmetry. In this case, the matrix of Yukawa couplings is real and symmetric, while the vacuum expectation values are complex, which leads to the relation $K^L = (K^R)^*$ [15]. With the aid of the above relation, the matrix K^R can be represented in the form

$$K^R = e^{i\gamma} \begin{pmatrix} e^{-i\delta_2}\cos\theta_C & e^{-i\delta_1}\sin\theta_C \\ -e^{-i\delta_1}\sin\theta_C & e^{i\delta_2}\cos\theta_C \end{pmatrix}. \tag{23}$$

Given the explicit form of the matrix K^R, the imaginary parts of g_a and g_v can be written as

$$\mathrm{Im}(g_a) = \mathrm{Im}(g_v) = -\eta \sin(\gamma - \delta_1). \quad (24)$$

Experimental data obtained at low energies make it possible [16] to set the following constraints on the parameters of the model: $M_R > 715$ GeV and $\eta < 0.013$. Taking into account these constraints and the relation $|\mathrm{Im}(g_a)| = |\mathrm{Im}(g_v)| < \eta$, we obtain upper bounds on A_ξ:

$$|A_\xi| < 2.6 \times 10^{-4} \quad (K^+ \to \pi^0\mu^+\nu_\mu\gamma), \quad (25)$$
$$|A_\xi| < 0.8 \times 10^{-4} \quad (K^+ \to \pi^0 e^+\nu_e\gamma).$$

Such values of the asymmetry can be observed experimentally only upon accumulating up to about 10^7 events of the decay $K^+ \to \pi^0\mu^+\nu_\mu\gamma$ and up to about 10^8 events of the decay $K^+ \to \pi^0 e^+\nu_e\gamma$.

4. MODELS INVOLVING SCALAR INTERACTION

In this section, we consider models where $\mathrm{Im}(g_a) = \mathrm{Im}(g_v) = 0$. In this case, a nonzero asymmetry is entirely due to nonvanishing values of the parameters $\mathrm{Im}(g_s)$ and $\mathrm{Im}(g_p)$. This feature is characteristic of some leptoquark and multi-Higgs models [7, 8, 17].

It should be noted that the decay $K^+ \to \pi^0 e^+\nu_e\gamma$ is inappropriate for studying such models. This can be explained by the fact that the kinematical factors C_s and C_p in (11) are proportional to the lepton mass; therefore, both scalar and pseudoscalar contributions to the asymmetry are strongly suppressed. Moreover, the fact that, in the multi-Higgs models, Yukawa couplings are proportional to the fermion mass leads to an additional suppression of the asymmetry there.

Of the two decays under study, only $K^+ \to \pi^0\mu^+\nu_\mu\gamma$ is of interest in connection with the models being considered. In order to set a limit on the asymmetry of this decay, we first consider the decay $K^+ \to \pi^0\mu^+\nu_\mu$. A model-independent analysis of the transverse polarization of the muon in this decay [7] allows one to conclude that this physical quantity is not sensitive to variations in the coupling constants g_v, g_a, and g_p.

A limit on $\mathrm{Im}(g_s)$ can be obtained from an analysis of the matrix element for the decay $K(p)^+ \to \pi^0(p')\mu^+(p_\mu)\nu_\mu(p_\nu)$:

$$M = \frac{G_\mathrm{F}}{2}\sin\theta_\mathrm{C}(f_+(p+p')^\lambda \quad (26)$$
$$+ f_-(p-p')^\lambda)\bar{u}(p_\nu)(1+\gamma_5)\gamma_\lambda v(p_\mu).$$

The value of $\mathrm{Im}(\chi) = \mathrm{Im}(f_-/f_+)$ can be extracted from the data on the transverse polarization that were obtained in the KEK–E246 experiment [1]. The result is

$$\mathrm{Im}(\chi) = (-0.28 \pm 0.69(\mathrm{stat.}) \quad (27)$$
$$\pm 0.30(\mathrm{sys.})) \times 10^{-2}.$$

Making use of the effective Lagrangian (2), we find that $\mathrm{Im}(\chi)$ and $\mathrm{Im}(g_s)$ are related by the equation

$$\mathrm{Im}(\chi) = \mathrm{Im}(g_s)\frac{m_K^2}{m_\mu m_s}. \quad (28)$$

From (27) and (28), we can readily obtain the constraint $|\mathrm{Im}(g_s)| < 6.7 \times 10^{-4}$. To set a limit on the constant $\mathrm{Im}(g_p)$, we assume that $\mathrm{Im}(g_p) \sim -\mathrm{Im}(g_s)$. This relation is valid in any model if the u-quark mass is neglected. Within this approach, it is not necessary to consider the internal structure of the models under consideration. Making use of the above constraints on the model parameters, we obtain the following bound on the asymmetry A_ξ in the decay $K^+ \to \pi^0\mu^+\nu_\mu\gamma$:

$$|A_\xi| < 6.0 \times 10^{-6}. \quad (29)$$

This indicates that, for this asymmetry to be observed experimentally, it is necessary to accumulate not less than 10^{10} events.

5. CONCLUSION

For the models specified by the effective Lagrangian (2), the asymmetry A_ξ of $K^+ \to \pi^0 l^+\nu\gamma$ decays has been evaluated within chiral perturbation theory to order p^4.

It has been shown that the scalar and pseudoscalar sectors make a nonzero contribution to the asymmetry A_ξ. However, the contribution of the scalar interaction to the asymmetry of the decay $K^+ \to \pi^0 e^+\nu_e\gamma$ is strongly suppressed because the kinematical factors responsible for the dependence of A_ξ on $\mathrm{Im}(g_s)$ and $\mathrm{Im}(g_p)$ are proportional to the lepton mass. In the case of a final-state muon, the asymmetry depends rather strongly on the scalar interaction. Nevertheless, the contribution of the scalar interaction to the asymmetry can hardly be observed because data obtained from the KEK–E246 experiment lead to stringent constraints on the respective coupling constant. To observe an asymmetry as small as

$$|A_\xi| < 6.0 \times 10^{-6},$$

which is two orders of magnitude smaller than the Standard Model contribution to the correlation, one needs some 10^{10} events of the decay.

The KEK–E246 experiment provides rather stringent constraints only on the scalar and pseudoscalar coupling constants, but it furnishes no information

about the vector or pseudovector interactions. Limits on the parameters of these interactions could be obtained in the planned OKA experiment. Our results reveal that the asymmetry A_ξ is highly sensitive to the parameters of the vector and pseudovector interactions in the effective Lagrangian. The respective effects can be sought in the K^+-meson decays producing an electron or a muon in the final state. With allowance for the constraints on the parameters of the $SU(2)_L \times SU(2)_R \times U(1)$ model, we have found that the asymmetry A_ξ can be constrained as

$$|A_\xi| < 2.6 \times 10^{-4}, \quad K^+ \to \pi^0 \mu^+ \nu_\mu \gamma,$$
$$|A_\xi| < 0.8 \times 10^{-4}, \quad K^+ \to \pi^0 e^+ \nu_e \gamma,$$

where the limits are somewhat greater than the respective Standard Model contributions to the T-odd correlation.

Our results give sufficient grounds to believe that the planned OKA experiment would open new possibilities for studying the vector and pseudovector sectors of the model under consideration, provided that the statistical level will be enhanced by an order of magnitude. In this case, the asymmetry A_ξ would offer an efficient indicator of new physics.

ACKNOWLEDGMENTS

We are grateful to V.V. Kiselev, A.K. Likhoded, and V.F. Obraztsov for stimulating discussions and enlightening comments.

This work was supported in part by the Russian Foundation for Basic Research (project no. 01-02-16585), the Ministry for Higher Education of the Russian Federation (grant no. E02-3.1-96), and the CRDF (grant no. MO-011-0).

APPENDIX

Within chiral perturbation theory, we consider the QCD Lagrangian involving external sources [18]; that is,

$$L = L_{\rm QCD} + \bar{q}\gamma_\mu(v^\mu + \gamma_5 a^\mu)q - \bar{q}(s - i\gamma_5 p)q, \tag{A.1}$$

where $L_{\rm QCD}$ is the massless QCD Lagrangian; $q^T = (u, d, s)$ are quark fields; and v_μ, a_μ, s, and p are 3×3 Hermitian matrices. It is straightforward to show that the Lagrangian in (A.1) is invariant under the local $SU(3)_L \times SU(3)_R$ transformations

$$q_L \to g_L q_L, \quad q_R \to g_R q_R, \tag{A.2}$$
$$s + ip \to g_R(s + ip)g_L^+,$$
$$l_\mu = g_L l_\mu g_L^+ + i g_L \partial_\mu g_L^+,$$
$$r_\mu = g_R r_\mu g_R^+ + i g_R \partial_\mu g_R^+,$$
$$l_\mu = v_\mu - a_\mu, \quad r_\mu = v_\mu + a_\mu.$$

The effective Lagrangian of chiral perturbation theory is constructed on the basis of the symmetry in (A.2) as an expansion in powers of external momenta; that is,

$$L_{\rm eff} = L_2 + L_4 + \ldots, \tag{A.3}$$

where L_2 and L_4 are $O(p^2)$ and $O(p^4)$ terms, respectively. Note that L_2 is invariant under the transformations in (A.2), whereas the invariance of L_4 is violated by a chiral anomaly [11, 18]. At the same time, the effective Lagrangian is invariant under the transformations

$$v_\mu \pm a_\mu \to g(v_\mu \pm a_\mu)g^+ + ig\partial_\mu g^+, \tag{A.4}$$
$$s + ip \to g(s + ip)g^+,$$
$$g \in SU(3).$$

The generating functional is also invariant under the transformations in (A.4):

$$Z[v', a', s', p'] = Z[v, a, s, p]. \tag{A.5}$$

In chiral perturbation theory, Ward identities are derived from this invariance by employing the transformation $g = 1 + i\alpha + O(\alpha^2) \in SU(3)$. This yields [11]

$$\left\langle \alpha \partial_\mu \frac{\delta Z}{\delta v_\mu} \right\rangle = i \left\langle \sum_{I=v,a,s,p} [\alpha, I] \frac{\delta Z}{\delta I} \right\rangle, \tag{A.6}$$

where the angular brackets $\langle\,\rangle$ imply an evaluation of the respective trace.

Let us consider the matrix element $\langle 0|T a_\mu^3(x) a_\nu^{4+5i}(y) V_\alpha^{4-5i}(z) V_\beta^{\rm em}(w)|0\rangle$, where $a_\mu^3(x)$ and $a_\nu^{4+5i}(y)$ are the axial-vector currents corresponding to the π^0 and K^+ mesons, respectively; $V^{4-5i}(z)$ is the vector current for the $\bar{s} \to \bar{u}$ transition; and $V_\beta^{\rm em}(w)$ is the electromagnetic current. The divergence ∂_z^α of this matrix element can be calculated by using the Ward identities. For this purpose, we must substitute $\lambda^4 - i\lambda^5$ for α into (A.6) and then apply, to Eq. (A.6), the linear operator

$$\hat{A} = \frac{\delta}{\delta a_\mu^3(x)} \frac{\delta}{\delta a_\nu^{4+5i}(y)} \frac{\delta}{\delta V_\alpha^{\rm em}(z)}. \tag{A.7}$$

The functional derivatives here must be evaluated at $v_\mu = a_\mu = p = 0$ and $s = M$, where M is the quark mass matrix. The resulting expression can be represented in the form

$$\partial_z^\alpha \langle 0|T a_\mu^3(x) a_\nu^{4+5i}(y) V_\alpha^{4-5i}(z) V_\beta^{\rm em}(w)|0\rangle \tag{A.8}$$
$$= i(m_u - m_s)\langle 0|T a_\mu^3(x) a_\nu^{4+5i}(y) s^{4-5i}(z) V_\beta^{\rm em}(w)|0\rangle$$
$$+ \langle 0|T a_\mu^3(x) a_\nu^{4+5i}(y) V_\beta^{4-5i}(z)|0\rangle \delta(w - z)$$
$$+ \langle 0|T a_\nu^{4+5i}(y) a_\mu^{4-5i}(z) V_\beta^{\rm em}(w)|0\rangle \delta(z - x)$$

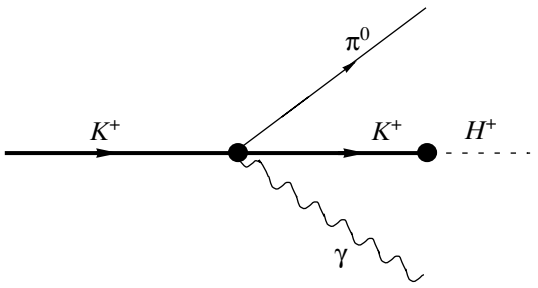

Feynman diagram contributing to the form factor P.

$$-\frac{1}{2}\langle 0|Ta_\mu^3(x)a_\nu^3(z)V_\beta^{\rm em}(w)|0\rangle\delta(z-y)$$
$$-\frac{\sqrt{3}}{2}\langle 0|Ta_\mu^3(x)a_\nu^8(z)V_\beta^{\rm em}(w)|0\rangle\delta(z-y).$$

Using reduction formulas, we can express the matrix element for the $K^+\to\pi^0$ transition in terms of the vacuum expectation values from formula (A.8). The last three terms in (A.8) do not contribute to the ultimate expression because they do not involve π^0 and K^+ pole terms simultaneously. In view of this, expression (A.8) can be recast into the form

$$\partial_\nu^y\langle\pi^0|TV_\mu^{\rm em}(x)V_\nu^{4-5i}(y)|K^+\rangle \qquad (A.9)$$
$$=\langle\pi^0|V_\mu^{4-5i}(y)|K^+\rangle\delta(x-y)$$
$$+i(m_u-m_s)\langle\pi^0|TV_\mu^{\rm em}(x)S^{4-5i}(y)|K^+\rangle.$$

In terms of the notation in (4), the required relation between the scalar and the vector form factor has the form

$$V^{\mu\nu}W_\nu+\left(F^\mu-\frac{F^\nu q_\nu}{pq}p^\mu\right)=(m_u-m_s)F_s^\mu. \qquad (A.10)$$

The expression for f can be derived in a similar way,

$$F^\nu(p_\nu-p'_\nu)=(m_u-m_s)f. \qquad (A.11)$$

A nonzero contribution to the form factor P is entirely due to the anomalous terms in the effective Lagrangian of chiral perturbation theory. The anomalous term contributing to P has the form [1]

$$L_{\rm anom}(\Phi^3\gamma)=-i\frac{e\sqrt{2}}{4\pi^2f_\pi^3}\epsilon^{\mu\nu\rho\sigma}A_\sigma\langle Q\partial_\mu\Phi\partial_\nu\Phi\partial_\rho\Phi\rangle, \qquad (A.12)$$

where Φ is the matrix of the pseudoscalar-meson octet, $Q=1/3\times{\rm diag}(2,-1,-1)$, and $f_\pi=93.2$ MeV. The Feynman diagram making a nonzero contribution to the form factor P is shown in the figure. The respective expression for the form factor has the form

$$P=\frac{\sqrt{2}}{4\pi^2f_\pi^2}\frac{1}{W^2-M_K^2}\frac{M_K^2}{m_s+m_u}, \qquad (A.13)$$

where $W=p-p'-q$.

REFERENCES

1. M. Abe *et al.* (KEK–E246 Collab.), hep-ex/0211049.
2. Yu. G. Kudenko, Yad. Fiz. **65**, 269 (2002) [Phys. At. Nucl. **65**, 244 (2002)]; hep-ex/0103007.
3. A. R. Zhitnitskiĭ, Yad. Fiz. **31**, 1024 (1980) [Sov. J. Nucl. Phys. **31**, 529 (1980)].
4. V. P. Efrosinin, I. B. Khriplovich, G. G. Kirilin, and Y. G. Kudenko, Phys. Lett. B **493**, 293 (2000); hep-ph/0008199.
5. V. V. Braguta, A. E. Chalov, and A. A. Likhoded, Phys. Rev. D **66**, 034012 (2002); hep-ph/0205203.
6. R. N. Rogalev, Phys. Lett. B **521**, 243 (2001); hep-ph/0105187.
7. G. Belanger and C. Q. Geng, Phys. Rev. D **44**, 2789 (1991).
8. C. H. Chen, C. Q. Geng, and C. C. Lih, Phys. Rev. D **56**, 6856 (1997); hep-ph/9709447.
9. V. V. Braguta, A. A. Likhoded, and A. E. Chalov, Phys. Rev. D **65**, 054038 (2002); hep-ph/0106147.
10. V. F. Obraztsov and L. G. Landsberg, Nucl. Phys. B (Proc. Suppl.) **99**, 257 (2001); hep-ex/0011033.
11. J. Bijnens, G. Ecker, and J. Gasser, Nucl. Phys. B **396**, 81 (1993); hep-ph/9209261.
12. J. C. Pati and A. Salam, Phys. Rev. D **10**, 275 (1974); R. N. Mohapatra and J. C. Pati, Phys. Rev. D **11**, 566 (1975); G. Senjonovic and R. N. Mohapatra, Phys. Rev. D **12**, 1502 (1975);
13. P. Langacker and S. Uma Sankar, Phys. Rev. D **40**, 1569 (1989).
14. A. Masiero, R. N. Mohapatra, and R. D. Peccei, Nucl. Phys. B **192**, 66 (1981).
15. J. M. Frere, J. Galand, A. Le Yaouanc, *et al.*, Phys. Rev. D **46**, 337 (1992); G. Barenboim, J. Bernabeu, and M. Raidal, Nucl. Phys. B **478**, 527 (1996); hep-ph/9608450.
16. M. Czakon, J. Gluza, and M. Zralek, Phys. Lett. B **458**, 355 (1999); hep-ph/9904216.
17. H. Y. Cheng, Phys. Rev. D **42**, 2329 (1990); **26**, 143 (1982); Y. Grossman, Nucl. Phys. B **426**, 355 (1994); hep-ph/9401311; H. Y. Cheng, Int. J. Mod. Phys. A **7**, 1059 (1992); J. F. Nieves, Nucl. Phys. B **189**, 182 (1981).
18. A. Pich, Rep. Prog. Phys. **58**, 563 (1995); hep-ph/9502366.

Translated by R. Rogalyov

Physics of Atomic Nuclei, Vol. 67, No. 5, 2004, pp. 1010–1018. From Yadernaya Fizika, Vol. 67, No. 5, 2004, pp. 1033–1041.

ELEMENTARY PARTICLES AND FIELDS
Theory

Off-Peak Inclusive J/ψ and Associated $J/\psi + c + \bar{c}$ and $J/\psi + \eta_c$ Production in e^+e^- Annihilation at BELLE*

S. P. Baranov**

Lebedev Institute of Physics, Russian Academy of Sciences, Leninskiĭ pr. 53, Moscow, 119991 Russia

Received February 21, 2003

Abstract—We consider the inclusive and associated production of J/ψ mesons under BELLE conditions. In the framework of QCD perturbation theory and nonrelativistic bound-state formalism, the different production mechanisms are analyzed in detail. The calculations are compared with recent experimental data, and significant disagreement is found in a few cases. For these channels, the predictions of a nonperturbative model are also explored. We find that the J/ψ polarization has a strong dependence on the production dynamics, so that it may serve as a sensitive indicator in future experimental studies.

1. INTRODUCTION

Investigation of the J/ψ production mechanisms in hadron–hadron and electron–hadron collisions has been an intensively discussed subject in high-energy physics over the last decade. A complementary topic is the production of J/ψ particles (as well as other quarkonia states) in e^+e^- annihilation. In comparison with other reactions, the latter case shows at least two interesting features. First, the theoretical calculations are not subject to the uncertainties coming from the parton distributions in the initial beams. Hence, attention can be focused on the J/ψ formation mechanism on its own. In particular, this provides much better conditions for the inspection of basic theoretical inputs, such as the applicability of the perturbation approach and the nonrelativistic heavy-quark bound-state formalism. Another remarkable feature of the e^+e^- annihilation processes is that the production of two heavy-quark pairs (say, the associated production of J/ψ and D mesons) is not suppressed in comparison with the production of a single quark pair (say, the inclusive J/ψ production).

In the present paper, we give theoretical predictions on the inclusive and associated production of J/ψ mesons and compare them with the data [1, 2] collected recently by the BELLE Collaboration at KEK. The collaboration reports the measurement of a number of cross sections: the inclusive production of J/ψ mesons, the associated production of J/ψ and D mesons, and the associated production of J/ψ and η_c mesons. The measurements have been carried out at the invariant beam energy $\sqrt{s} = 10.6$ GeV.

The outline of the paper is as follows. In Section 2, we explain the theoretical framework which is based on the standard perturbation theory and nonrelativistic bound-state formalism. Here, we also discuss the main sources of theoretical uncertainties. The numerical results are displayed in Section 3. The conclusions are summarized in Section 4. The technical details and the explicit expressions for the matrix elements used in calculations are collected in the Appendix.

2. THEORETICAL BACKGROUNDS

At the quark level, the processes of interest may be interpreted as

$$e^+ + e^- \to \gamma^* \to J/\psi + g + g, \qquad (1)$$

$$e^+ + e^- \to \gamma^* \to J/\psi + c + \bar{c}, \qquad (2)$$

$$e^+ + e^- \to \gamma^* \to J/\psi + \eta_c. \qquad (3)$$

The presence of the final-state gluons in reaction (1) is motivated by the necessity to get rid of the energy excess (as $\sqrt{s} > m_\psi$), where at least two gluons are needed to meet the color and charge parity conservation. The production of unbound charmed quarks in reaction (2) is assumed to be followed by fragmentation, which results in the formation of charmed hadrons. The fragmentation probabilities may be regarded as model parameters, or they can be taken from independent experimental measurements. On the contrary, in the case of reaction (3), the formation of the hadronic final state is already completed at the quark level, and no fragmentation is needed. The corresponding Feynman diagrams are displayed in

*This article was submitted by the author in English.

** e-mail: baranov@sci.lebedev.ru

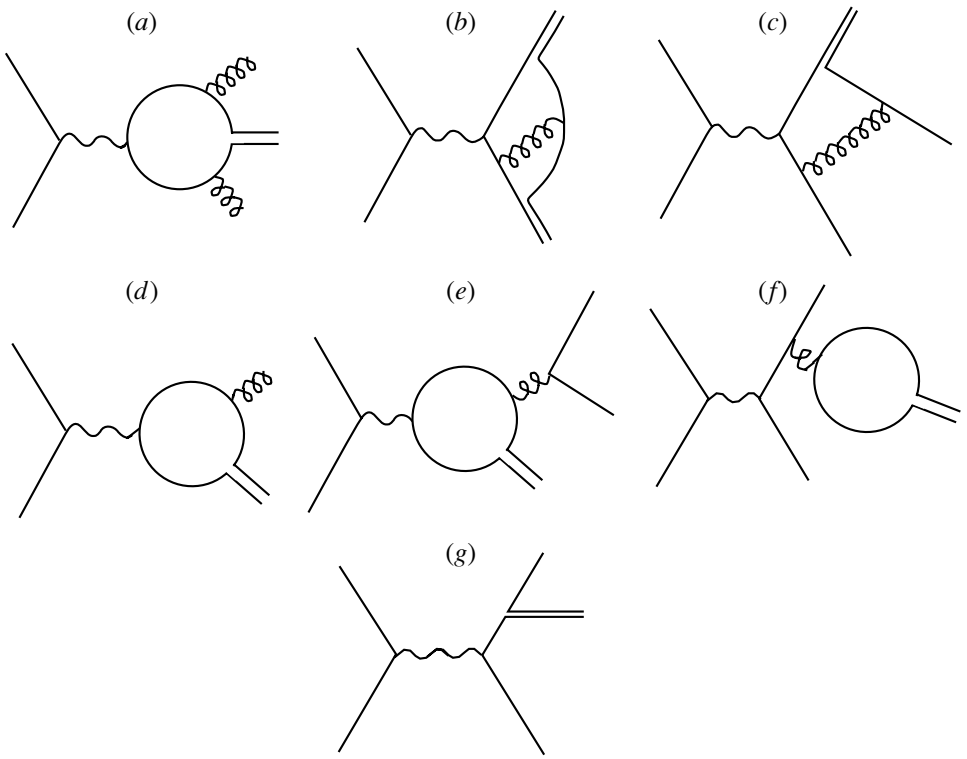

Fig. 1. Feynman diagrams representing the production of J/ψ particles via the color-singlet (a–c) and color-octet (a–f) mechanisms. Diagram (g) represents the nonperturbative model with pointlike ψcc coupling (see the text).

Fig. 1. The full gauge-invariant set comprises six diagrams of the type (a) for reaction (1), four diagrams of the type (b) for reaction (3), and four diagrams of the type (c) for reaction (2).

The evaluation of the relevant matrix elements (see Appendix) has been performed in accord with the standard Feynman rules. To guarantee the proper spin and angular orbital momentum structure of the quarkonium states under consideration, the color-singlet spin projection operators [3] have been introduced in the amplitudes of the processes (1)–(3). The gauge invariance of the matrix elements has been explicitly tested by substituting the virtual photon momentum for its polarization vector.

The most important theoretical uncertainties refer to the value of the meson wave function $\Psi_\psi(0)$ and to the choice of the renormalization scale μ^2 in the running coupling constant $\alpha_s(\mu^2)$. One can also consider the production of P-wave states (followed by their radiative decay $\chi_c \to \psi\gamma$) and take into account the hypothetical color-octet contributions. Now we will discuss these uncertainties in more detail.

The value of the J/ψ-meson wave function is thought to be known [4] from the experimentally measured leptonic decay with $\Gamma_{l\bar{l}}$:

$$|\Psi_\psi(0)|^2 = \Gamma_{l\bar{l}} \frac{m_\psi^2}{16\pi\alpha^2 e_c^2} \left(1 - \frac{16\alpha_s}{3\pi}\right).$$

Here, the effect of including or neglecting strong radiative corrections (the second term in the above formula) approaches a factor of 2. This brings the largest theoretical uncertainty. In calculations, we accept the choice with radiative corrections, $|\Psi_\psi(0)|^2 = 0.07\ \mathrm{GeV}^3$, and ascribe the same value to the wave function of the η_c meson.

Although the possible definitions of the renormalization scale μ may be formally very different (say, $\sqrt{s}/2$ or m_ψ, or the two-body invariant mass of J/ψ meson with a coproduced particle, etc.), they lead to rather close numerical values of μ. Typically, in the kinematic conditions under study, they range from 3 to 5 GeV, and so the variations in the strong coupling constant do not exceed 15% (producing an effect for the cross section of about 30%). In calculations, we set $\alpha_s = \mathrm{const} = 0.25$.

As far as the contributions from P waves are concerned, they only can be important for the process (2). In general, the production of P waves is suppressed in comparison with that of S waves by the inequality $|\Psi'_P(0)|^2/m_\psi^2 \ll |\Psi_S(0)|^2$, although this suppression is partly compensated by the large number of spin degrees of freedom in the χ_c family. Besides the effect of the wave function, the contributions from P-wave states to the processes (1) and (3) are subject to an additional suppression owing to the radiation of extra

gluons (which is required by the color and charge parity conservation). When estimating the contributions from χ_c states, we take $|\Psi'_\chi(0)|^2 = 0.006$ GeV^5, as is predicted by the potential model [5].

Last, we discuss the hypothetical color-octet production channels which are represented by Feynman diagrams shown in Figs. 1*d*–1*f*. Using the standard spectroscopic notation for the $c\bar{c}$ states, we write

$$e^+ + e^-\gamma^* \to {}^3P_J^8 + g, \quad (4)$$

$$e^+ + e^-\gamma^* \to {}^3S_1^8 + q + \bar{q}, \quad (5)$$

$$e^+ + e^-\gamma^* \to {}^3P_J^8 + q + \bar{q}. \quad (6)$$

The color-octet production scheme [6] implies that the $c\bar{c}$ quark pair is perturbatively created in a hard subprocess as an octet color state and subsequently evolves into a physical quarkonium state via emitting soft (nonperturbative) gluons, which may be interpreted as a series of classical color-dipole transitions: ${}^3P_J^8 \to J/\psi + g$, ${}^3S_1^8 \to J/\psi + g + g$. The nonperturbative transition probabilities are regarded as free parameters, which are assumed to obey a definite hierarchy in powers of v, the relative velocity of the quarks in the bound system under study. This freedom is commonly used to estimate the color-octet parameters by adjusting them to experimental data. Only the diagrams of Fig. 1*d*, which contribute to the subprocess (4), may be expected to be of any importance in the present kinematic conditions. In comparison with all other production channels (both color-singlet and color-octet), these diagrams are of formally leading order in α_s, which partly compensates the suppression by powers of v. In our numerical estimates, we use the nonperturbative matrix elements taken from [7] and set the light-quark mass equal to 300 MeV.

As an alternative to the nonrelativistic treatment of bound states, we also consider a nonperturbative model proposed in [8]. This model does not rely on the concept of the quarkonium wave function; instead, a pointlike charmed quark–meson interaction is introduced in the form $\mathcal{L}_{\psi cc} = g_{\psi cc}\bar{c}\gamma_\mu c\epsilon_\psi^\mu$, with ϵ_ψ being the J/ψ-meson polarization vector. The interaction strength is regulated by the coupling constant α_ψ, which has been set by the authors of [8] as high as $\alpha_\psi = g_{\psi cc}^2/(4\pi) = 1/4$. The relevant Feynman diagram is displayed in Fig. 1*g*.

3. RESULTS AND DISCUSSION

We start the discussion by recalling the experimental results reported by BELLE: $\sigma^{\exp}(e^+e^- \to J/\psi X) = 1.47 \pm 0.1 \pm 0.11$ pb [1], $\sigma^{\exp}(e^+e^- \to J/\psi D^{*+}X) = 0.53^{+0.19}_{-0.15} \pm 0.14$ pb [2], $\sigma^{\exp}(e^+e^- \to J/\psi D^0 X) = 0.87^{+0.32}_{-0.28} \pm 0.20$ pb [2], and $\sigma^{\exp}(e^+e^- \to J/\psi\eta_c)\mathrm{Br}(\eta_c \to \geq 4 \text{ charged}) = 0.033^{+0.007}_{-0.006} \pm 0.009$ pb [2].

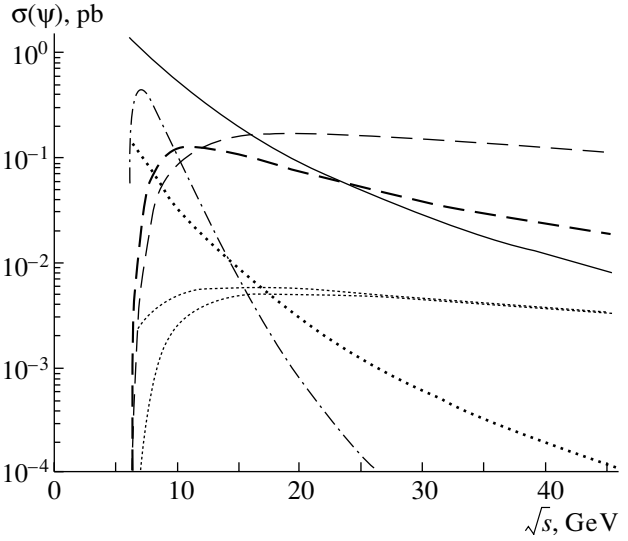

Fig. 2. The energy dependence of the cross sections corresponding to different production mechanisms: (solid curve) color-singlet $J/\psi + g + g$ channel (1); (dash-dotted curve) color-singlet $J/\psi + \eta_c$ channel (3); (thick dashed curve) color-singlet $J/\psi + c + \bar{c}$ channel (2); (thick dotted curve) color-octet ${}^3P_J^8 + g$ channel (4); (upper and lower thin dotted curves) color-octet ${}^3S_1^8 + q + \bar{q}$ and ${}^3S_1^8 + c + \bar{c}$ channels (5); (thin dashed curve) predictions of the nonperturbative model of [8] for the $J/\psi + c + \bar{c}$ channel, rescaled by a factor of 10^{-2}.

According to the Lund model [9], $c\bar{c}$ fragmentation produces charmed mesons at the rate 0.26 per event for D^{*+} and 0.59 per event for D^0, where both numbers include feed-down from higher states (in particular, $D^{*+} \to D^0\pi^+$). Assuming that these rates apply to $c\bar{c}$ fragmentation in $e^+e^- \to J/\psi c\bar{c}$, the authors calculate [2] $\sigma^{\exp}(e^+e^- \to J/\psi c\bar{c}) = 0.87^{+0.21}_{-0.19} \pm 0.17$ pb. Subtracting this number from the inclusive J/ψ cross section, one obtains $\sigma^{\exp}(e^+e^- \to J/\psi gg) \approx 0.60$ pb.

Our theoretical predictions are based on the following parameter settings: charmed-quark mass $m_c = m_\psi/2 = 1.55$ GeV; light-quark mass $m_q = 300$ MeV; color-singlet wave functions $|\Psi_\psi(0)|^2 = |\Psi_\eta(0)|^2 = 0.07$ GeV^3, $|\Psi'_\chi(0)|^2 = 0.006$ GeV^5 [5]; color-octet wave functions $|\Psi_{[{}^3S_1^8]}(0)|^2 = 0.7 \times 10^{-3}$ GeV^3, $|\Psi'_{[{}^3P_0^8]}(0)|^2 = 0.6 \times 10^{-3}$ GeV^5 [7]; strong coupling constant $\alpha_s = 0.25$; prompt ψcc coupling constant $\alpha_\psi = 1/4$ [8].

The results of our calculations are summarized in the table and in Figs. 2–4. The table presents

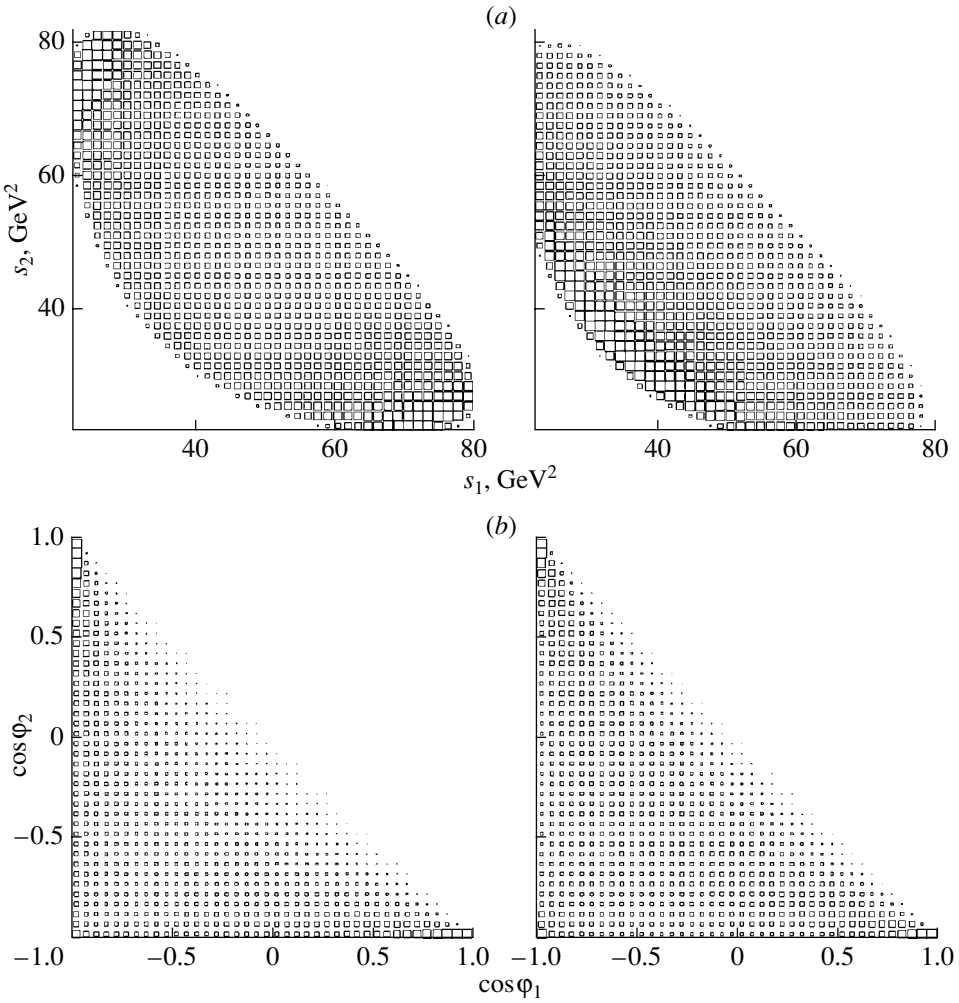

Fig. 3. (a) Double differential distribution $d^2\sigma/ds_1 ds_2$ on the two-body invariant masses $s_1 = (p_\psi + p_c)^2$ and $s_2 = (p_\psi + p_{\bar{c}})^2$. Left panel, predictions of the standard perturbation theory; right panel, predictions of the nonperturbative model of [8]. (b) Double differential angular distribution $d^2\sigma/d\cos\varphi_1 d\cos\varphi_2$, with φ_1 and φ_2 being the angles between the momentum of the J/ψ meson and the momenta of the accompanying charmed quarks measured in the e^-e^+ c.m. system. Left panel, predictions of the standard perturbation theory; right panel, predictions of the nonperturbative model [8].

the theoretical predictions for the different production mechanisms considered at $\sqrt{s} = 10.6$ GeV. The energy behavior of the production cross sections is displayed in Fig. 2. The estimated size of the non-charm-associated production cross section $\sigma(\psi gg)$ is in reasonable agreement with its experimental value. We also agree with the analyses of the color-singlet contributions presented by other authors [10, 11]. The contributions from the color-octet mechanisms are not important at the considered energies. This statement is supported by the experimental measurements. In particular, the collaboration points out [1] that "the color-octet $J/\psi g$ signal predicted in [6] is not observed."

The results on the associated production of J/ψ and η_c mesons are rather inconclusive, because the probability for η_c decay to yield a total charged multiplicity greater than four is unknown. The sum of the measured [12] branching fractions amounts to not too large a quantity, $\mathrm{Br}(\pi^+\pi^+\pi^-\pi^-) + \mathrm{Br}(\pi^+\pi^-K^+K^-) + \mathrm{Br}(K^+K^+K^-K^-) = 1.2\% + 2.1\% + 2.0\% = 5.3\%$, although the list of the decay channels is, of course, incomplete. One can, however, hardly expect the overall branching ratio $\mathrm{Br}(\eta_c \to \geq 4\,\text{charged})$ to be as large as 40%, which is necessary to make the theoretical and experimental numbers compatible with each other.

A serious discrepancy is seen in the associate production of J/ψ and open charm states. The theoretical estimates lie below the data by a significant factor, thus indicating an unresolved problem. In contrast, the predictions of nonperturbative approach of [8] lie

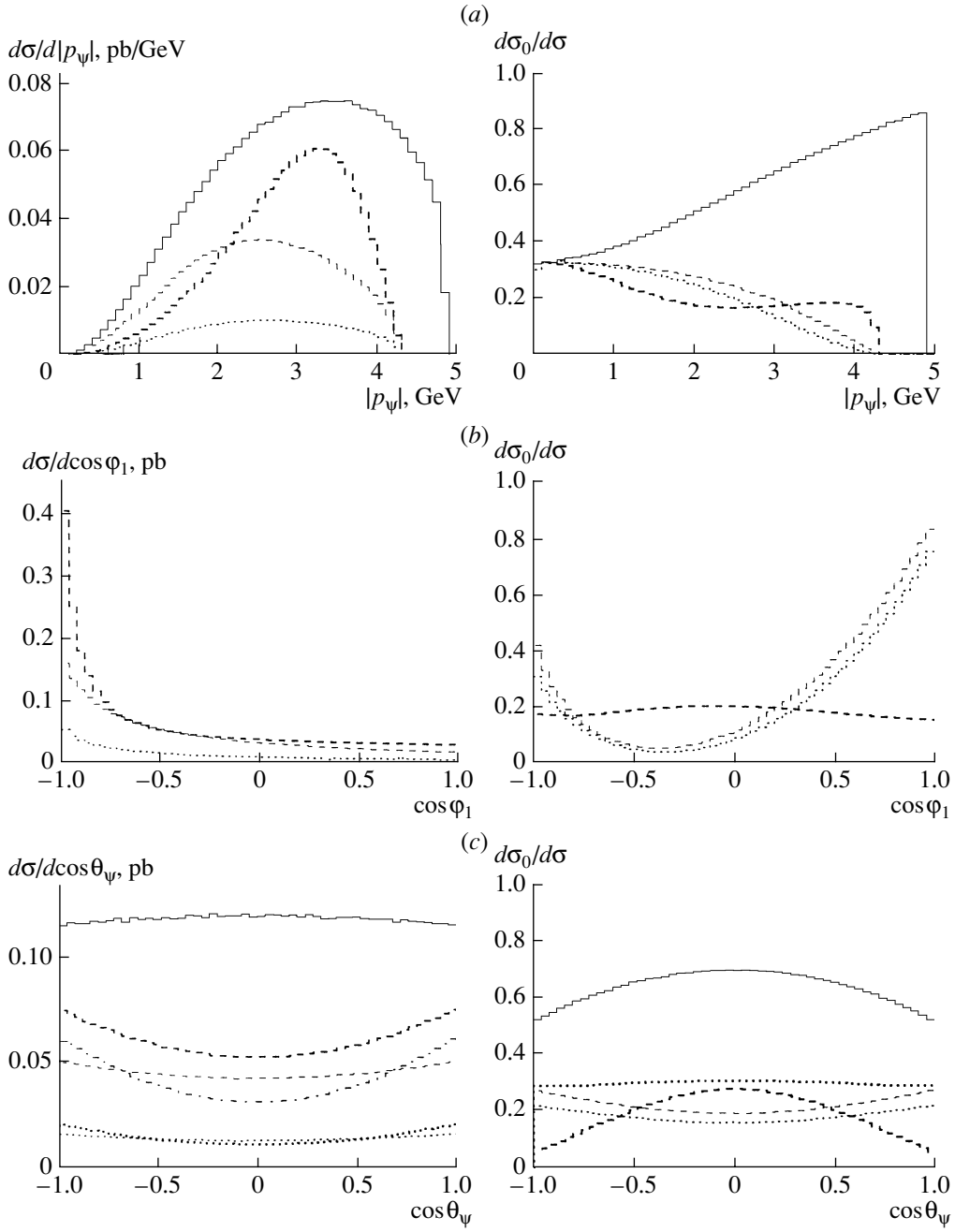

Fig. 4. (*a*) The differential cross section $d\sigma/d|p_\psi|$ and the fraction of longitudinally polarized J/ψ mesons as functions of the J/ψ absolute momentum $|p_\psi|$ measured in the e^-e^+ c.m. system. (*b*) The differential cross section $d\sigma/d\cos\varphi_1$ and the fraction of longitudinally polarized J/ψ mesons as functions of the angle between the momentum of the J/ψ meson and the momentum of the accompanying charmed quark measured in the e^-e^+ c.m. system. (*c*) The differential cross section $d\sigma/d\cos\theta_\psi$ and the fraction of longitudinally polarized J/ψ mesons as functions of the angle between the momentum of J/ψ meson and the momentum of the initial electron measured in the e^-e^+ c.m. system. Notation of the curves is the same as in Fig. 2. For ease of presentation, the contributions from subprocesses (1), (5) and the model [8] are shown rescaled by the factors 1/2, 10, and 10^{-2}, respectively.

above the data by one order of magnitude. The size of the latter contribution on its own is not indicative because it is determined by the artificial coupling constant α_ψ, but the difference in the production dynamics is clearly seen in the energy dependence of the corresponding cross sections, as is shown in Fig. 2.

Important information of the production dynamics can also be obtained from the differential cross sec-

tions and interparticle correlations. Shown in Fig. 3 are the double differential distribution $d^2\sigma/ds_1 ds_2$ on the two-body invariant masses $s_1 = (p_\psi + p_c)^2$ and $s_2 = (p_\psi + p_{\bar{c}})^2$, and the double differential angular distribution $d^2\sigma/d\cos\varphi_1 d\cos\varphi_2$, with φ_1 and φ_2 being the angles between the momentum of the J/ψ meson and the momenta of the accompanying charmed quarks measured in the e^+e^- c.m. system.

According to the standard perturbation theory (Fig. 3*a*, left panel), the production events tend to concentrate in the upper left and lower right corners of the Dalitz plot, where one of the invariant masses s_1 or s_2 is large and the other one is small. On the contrary, in the nonperturbative approach of [8] (Fig. 3*a*, right panel), the events are mostly concentrated near the lower left boundary of the phase space. The distributions on the angles φ_1 and φ_2 (Fig. 3*b*) are rather similar in both cases. However, these angular observables may be useful in discriminating some other production models. In particular, in the fragmentation approach of [13], the production of $J/\psi + c + \bar{c}$ states in the kinematic area $\varphi_1 < 0, \varphi_2 < 0$ is strongly suppressed if not forbidden completely.

The double differential distributions $d^2\sigma/dE_\psi d\cos\theta_\psi$ has been considered earlier in [6] for the processes (2) and (4) and in [14] for the processes (1) and (2). The shape of the J/ψ angular distribution at the endpoint of the energy spectrum was considered in [6] as a signal of the hypothetical color-octet subprocess (4).[1)] For completion, we show in Fig. 4 the distribution of the J/ψ total momentum $d\sigma/d|p_\psi|$, the distribution of the angle between the momentum of J/ψ meson and the momentum of the accompanying charmed quark $d\sigma/d\cos\varphi_1$, and the distribution of the angle between the momentum of the J/ψ meson and the momentum of the initial electron $d\sigma/d\cos\theta_\psi$ for all the mentioned subprocesses (1)–(6).

In addition to that, we find it extremely instructive to consider the J/ψ spin alignment, as it is known to be a sensitive probe of the production dynamics [15]. Polarization of J/ψ mesons can be accessed by measuring the angular distribution of positive or negative leptons appearing in the decay $J/\psi \to l^+l^-$:

$$d\Gamma_{ll}/d\cos\theta_l \sim 1 + \alpha\cos^2\theta_l \qquad (7)$$

(where θ_l is the angle between the lepton 3-momentum in the J/ψ rest frame and the J/ψ direction in the c.m. frame of the colliding beams). The parameter α is connected with the fraction of longitudinally polarized J/ψ mesons $h_0 = \sigma_{\text{hel}=0}/\sigma_{\text{incl}}$ by the identity $\alpha = (1 - 3h_0)/(1 + h_0)$. In addition to the results presented in [15], we show the behavior of the variable h_0 as a function of $|p_\psi|$, φ_1, and θ_ψ. One can see that the J/ψ polarization depends distinctively on the production channel.

[1)] As we have mentioned already, this signal was not found at BELLE.

J/ψ production channels and their partial contributions to $\sigma^{\text{theor}}_{J/\psi}$ at $\sqrt{s} = 10.6$ GeV (the parameter settings are explained in the text)

Subprocess	Diagram	Cross section, pb
Color-singlet channels		
$J/\psi + g + g$	a	0.476
$J/\psi + \eta_c$	b	0.083
$J/\psi + c + \overline{c}$	c	0.120
$\chi_c + c + \overline{c}$	c	0.018
Color-octet channels		
${}^1S_0^8 + g$	d	0.006
${}^3P_J^8 + g$	d	0.028
${}^3P_J^8 + q + \overline{q}$	e	0.002
${}^3S_1^8 + q + \overline{q}$	f	0.005
${}^3S_1^8 + g + \overline{g}$	a	0.006
${}^3P_J^8 + c + \overline{c}$	$c + e$	0.001
${}^3S_1^8 + c + \overline{c}$	$c + f$	0.003

4. CONCLUSION

We have considered the inclusive and associated production of J/ψ mesons under conditions of the BELLE experiment at KEK. In the framework of QCD perturbation theory and nonrelativistic bound state formalism, the different contributing mechanisms were analyzed in detail. The theoretical calculations were compared with experimental data.

The estimated size of the non-charm-associated production cross section $\sigma(\psi gg)$ is found to be in reasonable agreement with its measured value. Experimental data show no need for color-octet contributions, and the peculiar color-octet signal predicted in the literature is not observed. This accords with our theoretical estimates, which show that the color-octet contributions are of only minor importance under present conditions.

On the contrary, a serious discrepancy is seen in the associated production of J/ψ and open-charm mesons. This may be taken as an indication that the production of J/ψ particles in this channel is probably dominated by other, nonperturbative, mechanisms. In

order to discriminate between the possible models, a more detailed analysis of the event kinematics is required. The measurement of the interparticle correlations and J/ψ polarization properties may shed more light on the production dynamics.

APPENDIX

We list the analytic expressions for the matrix elements and differential cross sections of all considered processes. We start with the matrix elements of the process (1). The corresponding Feynman diagram is displayed in Fig. 1*a*. Let q_1, q_2, k_1, k_2, and p_ψ be the 4-momenta of the incoming electron, incoming positron, outgoing gluons, and the outgoing J/ψ meson, respectively; ϵ_1, ϵ_2 and ϵ_ψ the gluons and the J/ψ meson polarization vectors; m_c the charmed-quark mass; $q_1+q_2=q$; and s the invariant energy squared, $s=(q_1+q_2)^2$. Let also p_c and $p_{\bar c}$ be the momenta of the charmed quark and charmed antiquark which constitute the J/ψ meson: $p_c+p_{\bar c}=p_\psi$, $2m_c=m_\psi$. We also introduce the projection operators $J(S,L)$ [3] which guarantee the proper spin and orbital angular momentum of the quarkonium state under consideration:

$$J(\eta_c)\equiv J(S=0,L=0) \tag{A.1}$$
$$=\gamma_5(\hat p_c+m_c)/m_\psi^{1/2},$$
$$J(\psi)\equiv J(S=1,L=0) \tag{A.2}$$
$$=\hat\epsilon_\psi(\hat p_c+m_c)/m_\psi^{1/2},$$
$$J(\chi_c)\equiv J(S=1,L=1) \tag{A.3}$$
$$=(\hat p_{\bar c}-m_c)\hat\epsilon_S(\hat p_c+m_c)/m_\psi^{3/2}.$$

States with various projections of the spin momentum onto the quantization axis are represented by the polarization vector ϵ_S. In calculations, the polarization vector $\epsilon(S_z)$ was defined as an explicit 4-vector. In the frame where the z axis is oriented along the quarkonium momentum vector, $p_\psi=(0,0,|p_\psi|,E_\psi)$, the polarization vector reads

$$\epsilon(\pm1)=(1,\pm i,0,0)/\sqrt{2}, \tag{A.4}$$
$$\epsilon(0)=(0,0,E_\psi,|p_\psi|)/m_\psi.$$

Then, for the matrix elements of the process (1), we have

$$\mathcal{M}_1(\psi gg)=\bar u(q_2)\gamma_\mu u(q_1) \tag{A.5}$$
$$\times\,\mathrm{tr}\{\hat\epsilon_1(\hat p_c+\hat k_1+m_c)\gamma_\mu(-\hat p_{\bar c}-\hat k_2+m_c)$$
$$\times\,\hat\epsilon_2 J(\psi)\}s^{-1}[2(p_ck_1)]^{-1}[2(p_{\bar c}k_2)]^{-1},$$
$$\mathcal{M}_2(\psi gg)=\bar u(q_2)\gamma_\mu u(q_1) \tag{A.6}$$
$$\times\,\mathrm{tr}\{\hat\epsilon_1(\hat p_c+\hat k_1+m_c)\hat\epsilon_2(-\hat p_{\bar c}+\hat q+m_c)$$
$$\times\,\gamma_\mu J(\psi)\}s^{-1}[2(p_ck_1)]^{-1}[s-2(p_{\bar c}q)]^{-1},$$
$$\mathcal{M}_3(\psi gg)=\bar u(q_2)\gamma_\mu u(q_1) \tag{A.7}$$
$$\times\,\mathrm{tr}\{\gamma_\mu(\hat p_c-\hat q+m_c)\hat\epsilon_1(-\hat p_{\bar c}-\hat k_2+m_c)$$
$$\times\,\hat\epsilon_2 J(\psi)\}s^{-1}[s-2(p_cq)]^{-1}[2(p_{\bar c}k_2)]^{-1}.$$

Expressions for the matrix elements of the other three diagrams $\mathcal{M}_i$, $i=4,5,6$, can be obtained from the above formulas by the replacement $p_c\leftrightarrow p_{\bar c}$, $m_c\to -m_c$.

The differential cross section has the form

$$d\sigma(\psi gg)=\frac{\alpha_s^2\alpha^2e_c^2}{4s^2}|\Psi_\psi(0)|^2\frac{2}{3}\frac{1}{4} \tag{A.8}$$
$$\times\sum_{\text{spin}}\sum_{i=1}^{6}|\mathcal{M}_i(\psi gg)|^2ds_1ds_2d\cos(\theta)d\phi,$$

where we have explicitly shown the color factor 2/3, e_c is the electric charge of the charmed quark, $s_1=(p_\psi+k_1)^2$, $s_2=(p_\psi+k_2)^2$, and θ and ϕ are the azimuthal and polar angles of the J/ψ meson in the e^+e^- c.m. system.

Now we turn to the process (2) shown in Fig. 1*c*. In addition to the definitions which we have already made, let p_1 and p_2 be the 4-momenta of the unbound charmed quark and charmed antiquark accompanying the J/ψ meson. Then, we have for the matrix elements

$$\mathcal{M}_1(\psi c\bar c)=\bar u(q_2)\gamma_\mu u(q_1)\bar u(p_1) \tag{A.9}$$
$$\times\,\gamma_\mu(\hat p_1-\hat q+m_c)\gamma_\nu J(\psi)\gamma_\nu u(p_2)$$
$$\times\,s^{-1}[s-2(p_1q)]^{-1}[2m_c^2+2(p_{\bar c}p_2)]^{-1},$$
$$\mathcal{M}_2(\psi c\bar c)=\bar u(q_2)\gamma_\mu u(q_1)\bar u(p_1) \tag{A.10}$$
$$\times\,\gamma_\nu(\hat q-\hat p_c+m_c)\gamma_\mu J(\psi)\gamma_\nu u(p_2)$$
$$\times\,s^{-1}[s-2(p_cq)]^{-1}[2m_c^2+2(p_{\bar c}p_2)]^{-1}.$$

Expressions for the matrix elements of the other two diagrams can, again, be obtained from the present formulas by replacing the quarks with antiquarks and vice versa: $p_c\leftrightarrow p_{\bar c}$, $p_1\leftrightarrow p_2$, $m_c\to -m_c$.

Then, the differential cross section is

$$d\sigma(\psi c\bar c)=\frac{\alpha_s^2\alpha^2e_c^2}{4s^2}|\Psi_\psi(0)|^2\frac{16}{9}\frac{1}{4} \tag{A.11}$$
$$\times\sum_{\text{spin}}\sum_{i=1}^{4}|\mathcal{M}_i(\psi c\bar c)|^2ds_1ds_2d\cos(\theta)d\phi$$

with the explicitly shown color factor 16/9, $s_1=(p_\psi+p_1)^2$, $s_2=(p_\psi+p_2)^2$, and θ and ϕ being the azimuthal and polar angles of the J/ψ meson in the e^+e^- c.m. system. For the production of P waves, the factor $|\Psi_\psi(0)|^2$ must be replaced by $|\Psi'_\chi(0)|^2/m_\chi^2$ together with using the spin projection operator (10) in the expressions for $\mathcal{M}_1$–$\mathcal{M}_4$.

Now consider the process (3) shown in Fig. 1*b*. Let p_{c1} and $p_{\bar{c}1}$ be the 4-momenta of the charmed quark and antiquark forming the J/ψ meson, and p_{c2} and $p_{\bar{c}2}$ be the momenta of the charmed quark and antiquark forming the coproduced η_c meson. Then,

$$\mathcal{M}_1(\psi\eta_c) = \bar{u}(q_2)\gamma_\mu u(q_1) \quad \text{(A.12)}$$
$$\times \mathrm{tr}\{J(\psi)\gamma_\nu J(\eta_c)\gamma_\nu(\hat{q} - \hat{p}_{c1} + m_c)\gamma_\mu\}$$
$$\times s^{-1}[s - 2(p_{c1}q)]^{-1}[2m_c^2 + 2(p_{\bar{c}1}p_{\bar{c}2})]^{-1},$$
$$\mathcal{M}_2(\psi\eta_c) = \bar{u}(q_2)\gamma_\mu u(q_1) \quad \text{(A.13)}$$
$$\times \mathrm{tr}\{J(\psi)\gamma_\nu J(\eta_c)\gamma_\mu(\hat{p}_{c2} - \hat{q} + m_c)\gamma_\nu\}$$
$$\times s^{-1}[s - 2(p_{c2}q)]^{-1}[2m_c^2 + 2(p_{\bar{c}1}p_{\bar{c}2})]^{-1}.$$

Expressions for the matrix elements of the other two diagrams can be obtained from the symmetry relation between the charmed quarks and antiquarks: $p_{c1} \leftrightarrow p_{\bar{c}1}$, $p_{c2} \leftrightarrow p_{\bar{c}2}$, $m_c \to -m_c$.

The differential cross section reads

$$d\sigma(\psi\eta_c) = \frac{8\pi^3\alpha_s^2\alpha^2 e_c^2}{s^2}|\Psi_\psi(0)|^2|\Psi_\eta(0)|^2 \quad \text{(A.14)}$$
$$\times \sqrt{s(s-4m_\psi^2)}\frac{16}{9}\frac{1}{4}\sum_{\text{spin}}\sum_{i=1}^{4}|\mathcal{M}_i(\psi\eta)|^2 d\cos(\theta)$$

with 16/9 being the color factor and θ being the azimuthal angle of the J/ψ meson in the e^+e^- c.m. system.

For the color-octet subprocesses (4)–(6) shown in Figs. 1*d*–1*f*, we have

$$\mathcal{M}_1({}^3P_J^8 g) = \bar{u}(q_2)\gamma_\mu u(q_1) \quad \text{(A.15)}$$
$$\times \mathrm{tr}\{\hat{\epsilon}_g(\hat{q} - \hat{p}_{\bar{c}} + m_c)\gamma_\mu J(\chi_c)\}$$
$$\times s^{-1}[s - 2(p_{\bar{c}}q)]^{-1},$$
$$\mathcal{M}_1({}^3S_1^8 q\bar{q}) = \bar{u}(q_2)\gamma_\mu u(q_1) \quad \text{(A.16)}$$
$$\times \mathrm{tr}\{\gamma_\nu(\hat{q} - \hat{p}_{\bar{c}} + m_c)\gamma_\mu J(\chi_c)\}\bar{u}(p_1)\gamma_\nu u(p_2)$$
$$\times s^{-1}[s - 2(p_{\bar{c}}q)]^{-1}[(p_1 + p_2)^2]^{-1},$$
$$\mathcal{M}_1({}^3P_J^8 q\bar{q}) = \bar{u}(q_2)\gamma_\mu u(q_1)\bar{u}(p_1) \quad \text{(A.17)}$$
$$\times \gamma_\nu(\hat{q} - \hat{p}_2 + m_q)\gamma_\mu u(p_2)\mathrm{tr}\{\gamma_\nu J(\psi)\}$$
$$\times s^{-1}[s - 2(p_2q)]^{-1}m_\psi^{-2},$$

where p_1, p_2, m_q, and e_q are the 4-momenta, the mass, and the electric charge of the coproduced quarks q and $\bar{q}$. Expressions for the other matrix elements (one additional diagram for each subprocess) can be obtained by the usual permutation of quarks and antiquarks.

The differential cross sections read

$$d\sigma(\psi g) = \frac{2\pi^2\alpha_s\alpha^2 e_c^2}{m_\psi^2 s^2}|\Psi'_{{}^3P_J^8}(0)|^2 \quad \text{(A.18)}$$
$$\times (s - m_\psi^2)2\frac{1}{4}\sum_{\text{spin}}\sum_{i=1}^{2}|\mathcal{M}_i({}^3P_J^8 g)|^2 d\cos(\theta),$$

$$d\sigma(\psi q\bar{q}) = \frac{\alpha_s^2\alpha^2}{4s^2}\frac{1}{4}\sum_{\text{spin}}\sum_{i=1}^{2}[e_q^2|\Psi_{[{}^3S_1^8]}(0)|^2 \quad \text{(A.19)}$$
$$\times |\mathcal{M}_i({}^3S_1^8 q\bar{q})|^2 + e_c^2|\Psi'_{[{}^3P_J^8]}(0)|^2$$
$$\times |\mathcal{M}_i({}^3P_J^8 q\bar{q})|^2/m_\psi^2]ds_1 ds_2 d\cos(\theta)d\phi,$$

with $\Psi_{[{}^3S_1^8]}(0)$ and $\Psi'_{[{}^3P_J^8]}(0)$ being the fictitious color-octet wave functions, which are connected to the nonperturbative transition matrix elements:

$$\langle 0|\mathcal{O}({}^3S_1^8 \to J/\psi)|0\rangle = \frac{9}{2\pi}|\mathcal{R}_{[{}^3S_1^8]}(0)|^2$$
$$= \frac{9}{2\pi}4\pi|\Psi_{[{}^3S_1^8]}(0)|^2,$$

$$\langle 0|\mathcal{O}({}^3P_J^8 \to J/\psi)|0\rangle = \frac{9}{2\pi}|\mathcal{R}'_{[{}^3P_J^8]}(0)|^2$$
$$= \frac{9}{2\pi}2\pi|\Psi'_{[{}^3P_J^8]}(0)|^2.$$

For the sake of uniformity, we consistently use the notation in terms of $\Psi(0)$ and $\Psi'(0)$ for both color-singlet and color-octet contributions.

Finally, in the nonperturbative approach of [8], the process (2) is represented by the Feynman diagram shown in Fig. 1*g*. The matrix element is given by

$$\mathcal{M}_1(\psi c\bar{c}) = \bar{u}(q_2)\gamma_\mu u(q_1)\bar{u}(p_1) \quad \text{(A.20)}$$
$$\times \hat{\epsilon}_\psi(\hat{q} - \hat{p}_2 + m_c)u(p_2)s^{-1}[s - 2(p_2q)]^{-1}$$

(where the diagram with quark–antiquark permutation has to be added also), and the differential cross section is

$$d\sigma(\psi c\bar{c}) = \frac{\alpha_\psi\alpha^2 e_c^2}{16\pi s^2}\frac{1}{4} \quad \text{(A.21)}$$
$$\times \sum_{\text{spin}}\sum_{i=1}^{2}|\mathcal{M}_i(\psi c\bar{c})|^2 ds_1 ds_2 d\cos(\theta)d\phi.$$

Here, $\alpha_\psi = g_{\psi cc}^2/(4\pi)$ stands for the nonperturbative ψcc coupling constant.

REFERENCES

1. K. Abe *et al.* (The BELLE Collab.), Phys. Rev. Lett. **88**, 052001 (2002).
2. K. Abe *et al.* (The BELLE Collab.), Belle Preprint 2002-13; KEK Preprint 2102-27; hep-ex/0205704.
3. C.-H. Chang, Nucl. Phys. B **172**, 425 (1980); R. Baier and R. Rückl, Phys. Lett. B **102**, 364 (1981); E. L. Berger and D. Jones, Phys. Rev. D **23**, 1521 (1981); H. Krasemann, Z. Phys. C **7**, 189 (1979); G. Guberina, J. Kühn, R. Peccei, and R. Rückl, Nucl. Phys. B **174**, 317 (1980).

4. R. Barbieri, R. Gatto, and E. Remiddi, Phys. Lett. B **106**, 497 (1981).
5. E. J. Eichten and C. Quigg, Phys. Rev. D **52**, 1726 (1995).
6. E. Braaten and Y.-Q. Chen, Phys. Rev. Lett. **76**, 730 (1996); F. Yuan, C.-F. Qiao, and K.-T. Chao, Phys. Rev. D **56**, 321 (1997).
7. P. Cho and A. K. Leibovich, Phys. Rev. D **53**, 150 (1996); **53**, 6203 (1996).
8. G. L. Kane, J. P. Leveille, and D. M. Scott, Phys. Lett. B **85B**, 115 (1979).
9. T. Sjöstrand, Comput. Phys. Commun. **82**, 74 (1994).
10. V. V. Kiselev, A. K. Likhoded, and M. V. Shevlyagin, Phys. Lett. B **332**, 411 (1994).
11. J. H. Kühn and H. Schneider, Phys. Rev. D **24**, 2996 (1981); Z. Phys. C **11**, 253 (1981); L. Clavelli, Phys. Rev. D **26**, 1610 (1982); V. M. Driesen, J. H. Kühn, and E. Mirkes, Phys. Rev. D **49**, 3197 (1994).
12. K. Hagiwara *et al.* (Particle Data Group), Phys. Rev. D **66**, 010001 (2002).
13. A. B. Kaidalov, hep-ph/0301246.
14. P. Cho and A. K. Leibovich, Phys. Rev. D **54**, 6690 (1996).
15. S. Baek, P. Ko, J. Lee, and H. S. Song, J. Korean Phys. Soc. **33**, 97 (1998).

Physics of Atomic Nuclei, Vol. 67, No. 5, 2004, pp. 1019–1026. From Yadernaya Fizika, Vol. 67, No. 5, 2004, pp. 1042–1049.

ELEMENTARY PARTICLES AND FIELDS
Theory

$SU(2) \times SU(2)$ Chiral Quark Model with Nonlocal Interaction*

A. E. Dorokhov, **A. E. Radzhabov**, and **M. K. Volkov**

Joint Institute for Nuclear Research, Dubna, Moscow oblast, 141980 Russia

Received January 4, 2003; in final form, August 18, 2003

Abstract—Masses and interactions of light mesons are described in the framework of the model with the chiral invariant $SU(2) \times SU(2)$ four-quark interaction. The nonlocal kernel of the interaction is chosen in the form that ensures the absence of ultraviolet divergences in the Feynman diagrams and poles in the quark propagator. Within this model, we demonstrate that, in the chiral limit, the pion mass equals zero and the Goldberger–Treiman relation is fulfilled. The sigma-meson mass and the widths of strong decays $\sigma \to \pi\pi$, $\rho \to \pi\pi$ are estimated. © *2004 MAIK "Nauka/Interperiodica".*

1. INTRODUCTION

Chiral symmetry is one of the basic symmetries of hadron interactions [1]. The phenomenological Lagrangians successfully describing interactions of light baryons and mesons were constructed forty years ago [2]. At that time, the Nambu–Jona-Lasinio (NJL) model was proposed, where the authors attempted to explain the origin of the nucleon mass by spontaneous breaking of chiral symmetry [3].

In 1976, this model was used for construction of the chiral-symmetric four-quark interaction that, after bosonization, leads to the phenomenological meson Lagrangians obtained earlier [4]. This model was developed in [5, 6] and, after that, was widely utilized by many authors [7]. The quark NJL model can be successfully used to obtain not only the phenomenological Lagrangians but also the mass spectrum of mesons, the relations between the strong coupling constants in the scalar–pseudoscalar and vector–axial-vector sectors. In this model, it is also possible to describe the breaking of the $SU(3)$ symmetry taking into account the mass difference of strange and u, d quarks. This explains the inequality of the weak decay constants f_π and f_K and the differences of the strange- and nonstrange-meson masses. Including the gluon anomalies in the consideration allows us to solve the $U_A(1)$ problem and to describe the mass difference of the η, η' mesons [6].

However, the NJL models have some defects. They contain ultraviolet (UV) divergences and do not provide quark confinement. Usually, UV divergences are removed by using the cutoff parameter Λ taken at an energy scale of the order of 1 GeV. The physical meaning of this cutoff is connected with the separation of the energy–momentum region, where spontaneous breaking of the chiral symmetry and bosonization of quarks take place. Unfortunately, this procedure is not unique and can be realized in different ways. However, it is worth noting that, as a rule, the different schemes of UV cutoff lead to close results.

Right after the discovery of the nontrivial classical solutions in QCD, instantons [8], it was recognized that they might be important in hadron physics. Indeed, it was shown, in particular, that the instanton-induced nonlocal quark–quark interaction provides a mechanism explaining the spontaneous breaking of chiral symmetry [9] and the $U_A(1)$ problem [10]. Later on, within the realistic instanton liquid model of QCD vacuum [11], the main features of the spectrum of light mesons and baryons were described [12]. The instanton-induced quark–quark interaction, being nonlocal, naturally regularizes the UV divergences in an analytical form. So, in the instanton model, the UV cutoff results from the internal nonlocal structure of the nonperturbative QCD vacuum. At the same time, the model does not explain the quark confinement. This problem becomes essential in the description of hadrons with masses exceeding the sum of constituent quark masses.

There are many works devoted to the construction of nonlocal quark models providing quark confinement [13–20]. In these models, the dynamical quark mass depends on momentum. One of the models of this kind is considered here. The nonlocal four-quark interaction is taken in a separable form motivated by the instanton model. However, a more general space–spin–flavor structure of the quark interaction is allowed than follows from the quark zero-mode arguments. Namely, the four-fermion couplings in different channels are fixed directly from the meson mass

*This article was submitted by the authors in English.

**e-mail: dorokhov@thsun1.jinr.ru
***e-mail: aradzh@thsun1.jinr.ru
****e-mail: volkov@thsun1.jinr.ru

spectrum. Further, we use one of the simplest ansätze for the nonlocal kernel, which allows us to obtain the dynamically generated quark propagator without poles. Our model is close to the model [17]. However, our choice of the nonlocal kernel is motivated by the existence of the nonlocal quark condensate in QCD.

The paper is organized as follows. In Section 2, we consider a nonlocal four-quark interaction and, after bosonization, derive the gap equation for dynamical quark mass. The nonlocal kernel is defined in Section 3. In Section 4, the masses and couplings of the scalar and pseudoscalar mesons are obtained and the main parameters of the model are fixed. The verification of the Goldberger–Treiman relation is given. In Section 5, calculations of the ρ-meson coupling constant, g_ρ, and the decay width $\rho \to \pi\pi$ are given. The axial-vector meson, a_1, and the π–a_1 mixing are also considered. The last section is devoted to the discussion of our results.

2. $SU(2) \times SU(2)$ QUARK MODEL WITH NONLOCAL INTERACTION

The $SU(2) \times SU(2)$ symmetric action with the nonlocal four-quark interaction has the form

$$\mathcal{S}(\bar{q},q) = \int d^4x \Biggl\{ \bar{q}(x)(i\hat{\partial}_x - m_c)q(x) + \frac{G_\pi}{2}(J_\sigma(x)J_\sigma(x) + J^a_\pi(x)J^a_\pi(x)) - \frac{G_\rho}{2}J^{\mu a}_\rho(x)J^{\mu a}_\rho(x) - \frac{G_{a_1}}{2}J^{\mu a}_{a_1}(x)J^{\mu a}_{a_1}(x) \Biggr\}, \quad (1)$$

where $\bar{q}(x) = (\bar{u}(x), \bar{d}(x))$ are the u and d quark fields; m_c is the diagonal matrix of the current quark masses; and G_π, G_ρ, and G_{a_1} are the coupling constants of the scalar–pseudoscalar, vector, and axial-vector quark currents, respectively. The nonlocal quark currents $J_I(x)$ are expressed as

$$J_I(x) = \int\int d^4x_1 d^4x_2 f(x_1)f(x_2) \times \bar{q}(x - x_1)\Gamma_I q(x + x_2), \quad (2)$$

where the nonlocal function $f(x)$ normalized by $f(0) = 1$ characterizes the space dependence of the quark condensate. In (2), the matrices Γ_I are defined as

$$\Gamma_\sigma = 1, \quad \Gamma^a_\pi = i\gamma^5\tau^a,$$
$$\Gamma^{\mu a}_\rho = \gamma^\mu\tau^a, \quad \Gamma^{\mu a}_{a_1} = \gamma^5\gamma^\mu\tau^a,$$

where τ^a are the Pauli matrices and γ^μ and γ^5 are the Dirac matrices.

In this article, we mainly consider the strong interactions. The electroweak fields may be introduced by gauging the quark field by the Schwinger phase factors (see, e.g., [17, 21, 22]). This method is used in derivation of the Goldberger–Treiman relation.

After bosonization, the action becomes

$$\mathcal{S}(q,\bar{q},\sigma,\pi,\rho,a) = \int d^4x \Biggl\{ -\frac{1}{2G_\pi} \times \left(\tilde{\sigma}(x)^2 + \pi^a(x)^2\right) + \frac{1}{2G_\rho}(\rho^{\mu a}(x))^2 + \frac{1}{2G_{a_1}}(a_1^{\mu a}(x))^2 + \bar{q}(x)(i\hat{\partial}_x - m_c)q(x) + \int\int d^4x_1 d^4x_2 f(x - x_1)f(x_2 - x) \times \bar{q}(x_1)(\tilde{\sigma}(x) + \pi^a(x)i\gamma^5\tau^a + \rho^{\mu a}(x)\gamma^\mu\tau^a + a_1^{\mu a}(x)\gamma^5\gamma^\mu\tau^a)q(x_2) \Biggr\}, \quad (3)$$

where $\tilde{\sigma}$, π, ρ, and a_1 are the σ-, π-, ρ-, and a_1-meson fields, respectively. The field $\tilde{\sigma}$ has a nonzero vacuum expectation value $\langle\tilde{\sigma}\rangle_0 = \sigma_0 \neq 0$. In order to obtain a physical scalar field with zero vacuum expectation value, it is necessary to shift the scalar field as $\tilde{\sigma} = \sigma + \sigma_0$. This leads to the appearance of the nonlocal quark mass $m(p^2)$ instead of the current quark mass m_c:

$$m(p^2) = m_c + m_{\rm dyn}(p^2) = m_c - \sigma_0 f^2(p^2) = m_c + (m_q - m_c)f^2(p^2), \quad (4)$$

where m_q is a dimensional parameter, which plays the role of the constituent quark mass. These relations result from the solution of the gap equation

$$m(p^2) = m_c + iG_\pi \frac{2N_c}{(2\pi)^4} f^2(p^2) \times \int d^4k f(k^2)^2 {\rm Tr}\,[S(k)] \quad (5)$$

that one derives from the action, Eq. (3), by using

$$\left\langle \frac{\delta\mathcal{S}}{\delta\sigma} \right\rangle_0 = 0. \quad (6)$$

N_c is the number of quark colors. In the leading order of the $1/N_c$ expansion, the quark propagator $S(p)$ with dynamical mass is given by

$$S(p) = (\hat{p} - m(p^2))^{-1}. \quad (7)$$

3. DYNAMICAL QUARK MASS

Let us recall that, in the instanton model, the nonlocal function $f(p^2)$, defining the kernel of the nonlocal four-quark interaction, is expressed in terms of the profile function of the quark zero mode. In [17],

taking the same separable form of the kernel, the function $f(p^2)$ was chosen in the Gaussian form. This choice also removes UV divergences, but in addition provides the quark confinement. Here, we follow a different ideology. Namely, similar to [13], we demand absence of pole singularities in the scalar part of the quark propagator[1)]

$$\frac{m(p^2)}{m^2(p^2)+p^2} \equiv \frac{1}{2}Q(p^2). \tag{8}$$

Note that the left side of (8) coincides with the nonlocal quark condensate if the quark propagator is taken in the form (7) [23]. The function $Q(p^2)$ is considered as an entire function in the complex p^2 plane, decreasing in the Euclidean domain at $p^2 \to \infty$. In particular, in this work, the Gaussian function is used:

$$Q(p^2) = \frac{1}{\mu}\exp\left(-\frac{p^2}{\Lambda^2}\right), \tag{9}$$

where μ and Λ are arbitrary parameters. At each p, Eq. (8) has the following solutions:

$$m_{\pm}(p^2) = Q^{-1}(p^2)\left(1 \pm \sqrt{1-p^2Q^2(p^2)}\right). \tag{10}$$

Then, three different situations occur:

(i) There is some region of real p^2 where $p^2Q^2(p^2) > 1$. This situation leads to the appearance of complex values of the quark mass. We do not consider this case further.

(ii) The relation $p^2Q^2(p^2) < 1$ is fulfilled in the whole domain of real p^2. Then, from two possible solutions, we can use only the solution $m_-(p^2)$ which decreases at $p^2 \to \infty$:

$$m(p^2) = m_-(p^2) \tag{11}$$
$$= Q^{-1}(p^2)\left(1 - \sqrt{1-p^2Q^2(p^2)}\right).$$

(iii) The function $p^2Q^2(p^2)$ equals 1 at a single real point p_0^2. In this case, the continuous mass function is

$$m(p^2) = Q^{-1}(p^2)$$
$$\times \left(1 - \mathrm{sgn}(p^2-p_0^2)\sqrt{1-p^2Q^2(p^2)}\right).$$

The last case is defined by conditions

$$p^2Q^2(p^2)|_{p^2=p_0^2} = 1, \quad (p^2Q^2(p^2))'|_{p^2=p_0^2} = 0, \tag{12}$$

which constrains the model parameters m_q and Λ as

$$p_0^2 = \frac{\Lambda^2}{2}, \quad \mu^2 = \frac{\Lambda^2}{2e}, \quad m_q = 2\mu, \tag{13}$$

where e is the base of exponent. As a result, only one parameter remains free. This is due to equivalence of the third case to the choice of normalization condition $m(p^2 = p_0^2) = \sqrt{p_0^2}$.

If the current quark mass m_c is nonzero, Eqs. (9) and (10) are modified as follows:

$$\frac{m_{\mathrm{dyn}}(p^2)}{m^2(p)+p^2} = \frac{1}{2}Q(p^2),$$

$$m_{\mathrm{dyn}\pm}(p^2) = Q^{-1}(p^2) - m_c \tag{14}$$
$$\pm\sqrt{(Q^{-1}(p^2)-m_c)^2 - (p^2+m_c^2)},$$

and Eq. (13) becomes

$$p_0^2 = \frac{\Lambda^2}{2}\epsilon, \quad \epsilon = \left(1 - \frac{m_c^2}{\Lambda^2} - \frac{m_c}{\Lambda}\sqrt{2+\frac{m_c^2}{\Lambda^2}}\right), \tag{15}$$

$$\mu^2 = \Lambda^2\exp(-\epsilon)\left(1-\frac{\epsilon}{2}\right), \tag{16}$$

$$m_q = \mu\left(1+\sqrt{1-2\frac{m_c}{\mu}}\right).$$

We checked that, in the second case, the model with Gaussian nonlocality (9) predicts σ-meson mass and decay widths $\sigma \to \pi\pi$, $\rho \to \pi\pi$ that are in disagreement with experiment. The third case allows us to construct the scheme where not only the main low-energy theorems are fulfilled, but also better agreement with experimental data is achieved. Therefore, the present work is devoted to investigation of this case.

4. PSEUDOSCALAR AND SCALAR MESONS

Let us consider the scalar and pseudoscalar mesons. The meson propagators are given by

$$D_{\sigma,\pi}(p^2) = \frac{1}{-G_\pi^{-1} + \Pi_{\sigma,\pi}(p^2)} = \frac{g_{\sigma,\pi}^2(p^2)}{p^2 - M_{\sigma,\pi}^2}, \tag{17}$$

where $M_{\sigma,\pi}$ are the meson masses, $g_{\sigma,\pi}(p^2)$ are the functions describing renormalization of the meson fields, and $\Pi_{\sigma,\pi}(p^2)$ are the polarization operators (see Fig. 1) defined by

$$\Pi_{\sigma,\pi}(p^2) = i\frac{2N_c}{(2\pi)^4} \tag{18}$$
$$\times \int d^4k f^2(k_-^2)f^2(k_+^2)\mathrm{tr}\left[S(k_-)\Gamma_{\sigma,\pi}S(k_+)\Gamma_{\sigma,\pi}\right],$$

where $k_+ = k + p/2$, $k_- = k - p/2$. The meson masses $M_{\sigma,\pi}$ are found from the position of the pole in the meson propagator

$$\Pi_{\sigma,\pi}(M_{\sigma,\pi}^2) = G_\pi^{-1}, \tag{19}$$

[1)] In this section, we use the Euclidean metric.

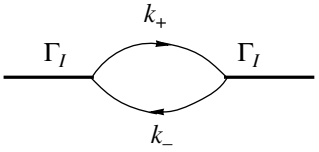

Fig. 1. Meson polarization operator. The thick lines are mesons. All loops in Figs. 1, 3–6 consist of constituent quarks (thin lines).

and the constants $g_{\sigma,\pi}(M^2_{\sigma,\pi})$ are given on the meson mass shell by (see also Fig. 2)

$$g^{-2}_{\sigma,\pi}(M^2_{\sigma,\pi}) = \frac{d\Pi_{\sigma,\pi}(p^2)}{dp^2}|_{p^2=M^2_{\sigma,\pi}}. \qquad (20)$$

In the chiral limit, the pion constant $g_\pi(0)$ is given by [24]

$$g^{-2}_\pi(0) = \frac{N_c}{4\pi^2 m_q^2} \qquad (21)$$
$$\times \int\limits_0^\infty duu \frac{m^2(u) - um(u)m'(u) + u^2 m'^2(u)}{(u+m^2(u))^2}.$$

4.1. Pion Mass

Describing the pion properties, we can consider only the lowest order of the expansion in small p^2. Indeed, in our model, $M^2_\pi \ll m_q^2, \Lambda^2$ (see numerical estimates of m_q, Λ in Section 4.3 below). In this approximation, one gets

$$M^2_\pi = g^2_\pi(0)\left(\frac{1}{G_\pi} - \frac{N_c}{2\pi^2}\int\limits_0^\infty duu\frac{f^4(u)}{u+m^2(u)}\right). \qquad (22)$$

On the other hand, the constant G_π is defined by the gap equation ($m_q \equiv m(0)$)

$$\frac{1}{G_\pi} = \frac{1}{m_q - m_c}\frac{N_c}{2\pi^2}\int\limits_0^\infty duu\frac{f^2(u)m(u)}{u+m^2(u)} \qquad (23)$$
$$= \frac{N_c}{2\pi^2}\int\limits_0^\infty duu\frac{f^4(u)}{u+m^2(u)} + m_c\frac{1}{m_q^2}\frac{N_c}{2\pi^2}$$
$$\times \int\limits_0^\infty duu\frac{m_{\rm dyn}(u)}{u+m^2_{\rm dyn}(u)} + O(m_c^2).$$

As a result, the pion mass equals

$$M^2_\pi = -2m_c\frac{g^2_\pi(0)}{m_q^2} \qquad (24)$$

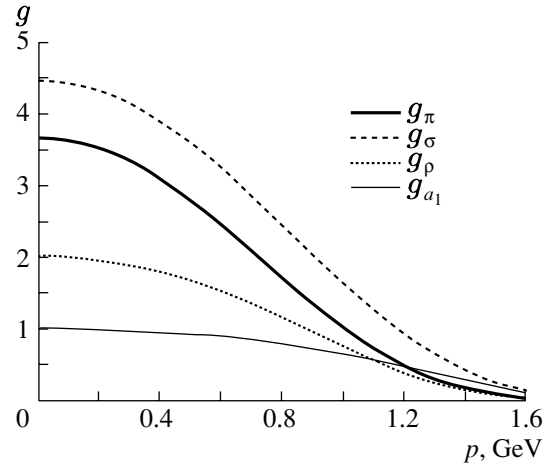

Fig. 2. Momentum dependence of the meson strong coupling constants.

$$\times\left(-\frac{N_c}{4\pi^2}\int\limits_0^\infty duu\frac{m_{\rm dyn}(u)}{u+m^2_{\rm dyn}(u)}\right) + O(m_c^2).$$

It is worth noting that the expression in the parentheses represents the quark condensate in the chiral limit $m_c = 0$. Hence, the Gell-Mann–Oakes–Renner relation is reproduced:

$$M^2_\pi \approx -2\frac{g^2_\pi}{m_q^2}m_c\langle\bar{q}q\rangle_0. \qquad (25)$$

4.2. Goldberger–Treiman Relation

For description of the decay $\pi \to \mu\nu$, the external weak field must be introduced. We use the method consisting in the replacement of the quark fields in the interaction part of the Lagrangian by the quark fields with Schwinger factors depending on the external weak field. This procedure ensures the gauge invariance of the interaction with respect to the weak field. The amplitude of the process $\pi \to \mu\nu$ has the form

$$A^\mu_{(\pi\to\mu\nu)}(p) = ip^\mu F_\pi, \qquad (26)$$

where F_π is the weak pion decay constant, $F_\pi = 93$ MeV [25]. The diagrams *1–3* of Fig. 3 give the following contributions:

$$F^{(1)}_\pi = \frac{N_c}{p^2}g_\pi \qquad (27)$$
$$\times\int\frac{d^4k}{(2\pi)^4}f(k^2_+)f(k^2_-){\rm tr}[i\gamma^5 S(k_-)\hat{p}\gamma^5 S(k_+)],$$

$$F^{(2)}_\pi = i\frac{N_c}{p^2}g_\pi\int\frac{d^4k}{(2\pi)^4}{\rm tr}[S(k)]f(k^2)(f((k+p)^2)$$
$$+ f((k-p)^2) - 2f(k^2)),$$

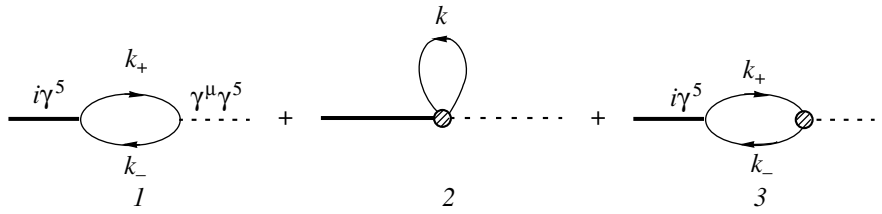

Fig. 3. Weak pion decay. Dashed lines denote a weak external field. Circles are nonlocal vertices.

$$F_\pi^{(3)} = \frac{m_q N_c}{p^2} g_\pi \int \frac{d^4k}{(2\pi)^4} f(k_+^2) f(k_-^2)$$
$$\times \mathrm{tr}[i\gamma^5 S(k_-)\gamma^5 S(k_+)](f(k_+^2) - f(k_-^2))^2,$$

which in the chiral limit at $p^2 = 0$ are reduced to

$$F_\pi^{(1)} = \frac{g_\pi}{m_q}\frac{N_c}{8\pi^2}\int_0^\infty duu\frac{m(u)(2m(u) - um'(u))}{(u + m^2(u))^2},$$

$$F_\pi^{(2)} + F_\pi^{(3)} = \frac{g_\pi}{m_q}\frac{N_c}{8\pi^2}$$
$$\times \int_0^\infty duu\frac{um'^2(u) - 2m(u)m'(u) - um(u)m''(u)}{u + m^2(u)}.$$

Summing all terms, integrating by parts the term with m'', and using (21), one obtains the Goldberger–Treiman relation:

$$F_\pi = F_\pi^{(1)} + F_\pi^{(2)} + F_\pi^{(3)} = \frac{g_\pi}{m_q}\frac{N_c}{4\pi^2}$$
$$\times \int_0^\infty duu\frac{m^2(u) - um(u)m'(u) + u^2m'^2(u)}{(u + m^2(u))^2},$$

$$F_\pi = \frac{m_q}{g_\pi}. \qquad (28)$$

4.3. Numerical Estimates

First, let us consider the chiral limit $m_c = 0$. Three model parameters m_q, Λ, and G_π are defined from (5), (13), and (28):

$$\Lambda = 406\ \mathrm{MeV}, \quad G_\pi = 63\ \mathrm{GeV}^{-2}, \quad m_q = 348\ \mathrm{MeV} \qquad (29)$$

(in this case $g_\pi(0) = 3.7$). If $m_c \neq 0$, by using also Eq. (25) with $M_\pi = 140$ MeV, one obtains very similar numbers

$$\Lambda = 400\ \mathrm{MeV}, \quad G_\pi = 61\ \mathrm{GeV}^{-2}, \qquad (30)$$
$$m_q = 346\ \mathrm{MeV}, m_c = 14.5\ \mathrm{MeV}$$

(in this case $g_\pi(M_\pi) = 3.6$).

4.4. Sigma Meson

By using the parameters (30), we get $M_\sigma = 450$ MeV and $g_\sigma(M_\sigma) = 3.8$. The amplitude of the decay $\sigma \to \pi\pi$, described by the diagram in Fig. 4, is equal to $A_{(\sigma\to\pi^+\pi^-)} = 1.5$ GeV. Then, the total decay width is $\Gamma_{(\sigma\to\pi\pi)} = 120$ MeV. Comparing these results with experimental data, one finds that M_σ is in satisfactory agreement with experiment; however, the calculated decay width is smaller than the experimental one [25].

5. VECTOR AND AXIAL-VECTOR MESONS

The propagators of the vector and axial-vector mesons have transversal and longitudinal parts:

$$D^{\mu\nu}_{\rho,a_1} = T^{\mu\nu}D^T_{\rho,a_1} + L^{\mu\nu}D^L_{\rho,a_1}, \qquad (31)$$

where $T^{\mu\nu} = g^{\mu\nu} - p^\mu p^\nu/p^2$, $L^{\mu\nu} = p^\mu p^\nu/p^2$, and

$$D^T_{\rho,a_1} = \frac{1}{G^{-1}_{\rho,a_1} + \Pi^T_{\rho,a_1}(p^2)} = \frac{g^2_{\rho,a_1}(p^2)}{M^2_{\rho,a_1} - p^2}, \qquad (32)$$
$$D^L_{\rho,a_1} = \frac{1}{G^{-1}_{\rho,a_1} + \Pi^L_{\rho,a_1}(p^2)}.$$

Here, Π^T_{ρ,a_1} and Π^L_{ρ,a_1} are the transversal and longitudinal parts of the polarization operator $\Pi^{\mu\nu}_{\rho,a_1}(p^2)$:

$$\Pi^{\mu\nu}_{\rho,a_1}(p^2) = i\frac{2N_c}{(2\pi)^4}$$
$$\times \int d^4k f^2(k_-^2) f^2(k_+^2)\mathrm{Tr}\left[S(k_-)\Gamma_{\rho,a_1}S(k_+)\Gamma_{\rho,a_1}\right].$$

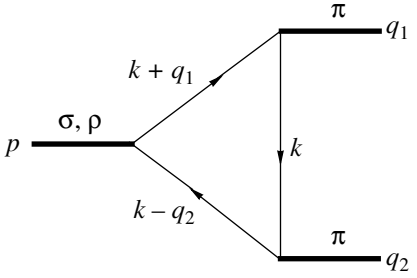

Fig. 4. Decays $\sigma \to \pi\pi$, $\rho \to \pi\pi$.

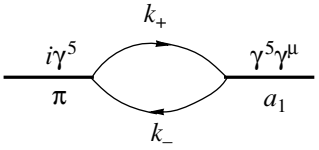

Fig. 5. Transition loop describing π–a_1 mixing.

The constants G_{ρ,a_1} are fixed by physical meson masses,

$$G^{-1}_{\rho,a_1} = -\Pi^T_{\rho,a_1}(M_{\rho,a_1}),$$

and numerically equal to $G_\rho = 6.44$ GeV^{-2}, $G_{a_1} = 0.739$ GeV^{-2}. Note that there is no pole in the longitudinal part of the vector-meson propagators.

The constants $g_{\rho,a_1}(M^2_{\rho,a_1})$ are equal to

$$g^{-2}_{\rho,a_1}(M^2_{\rho,a_1}) = -\frac{d\Pi^T_{\rho,a_1}(p^2)}{dp^2}|_{p^2=M^2_{\rho,a_1}}. \qquad (33)$$

5.1. ρ Meson and Decay $\rho \to \pi\pi$

From Eq. (33), we obtain $g_\rho(M_\rho) = 1.2$. The decay $\rho \to \pi\pi$ is described by a triangle diagram similar to the diagram in Fig. 4. The amplitude for the process is

$$A^\mu_{(\rho\to\pi\pi)} = g_{(\rho\to\pi\pi)}q^\mu, \qquad (34)$$

where $q = q_1 - q_2$. We obtain $g_{(\rho\to\pi\pi)} = 5.6$ and the decay width $\Gamma_{(\rho\to\pi\pi)} = 130$ MeV, which is in qualitative agreement with the experimental value 149.2 ± 0.7 MeV [25].

5.2. Axial-Vector Meson and π–a_1 Mixing

For the a_1-meson constant, we obtain $g_a(M_{a_1}) = 0.5$. The longitudinal component of the a_1-meson field is mixed with the pion, as is illustrated in Fig. 5. The amplitude describing this mixing is

$$A^\mu_{(\pi\to a_1)}(p^2) = iC_{(\pi\to a_1)}p^\mu. \qquad (35)$$

The value of the constant $C_{(\pi\to a_1)}$ is 80 MeV. The additional renormalization of the pion field is described by the ratio (see Fig. 6)

$$\frac{C^2_{(\pi\to a_1)}}{g^2_{a_1}(0)(G^{-1}_{a_1} + \Pi^L_{a_1}(0))} \approx C^2_{(\pi\to a_1)}G_{a_1} \approx 0.005. \qquad (36)$$

As one can see, this ratio is small and the effect of the π–a_1 mixing can be neglected.

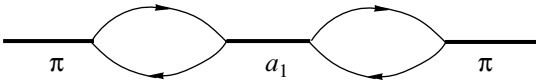

Fig. 6. Diagram describing additional renormalization of the pion field.

6. DISCUSSION AND CONCLUSION

In this work, we have considered one of the possibilities of construction of the nonlocal chiral quark model providing absence of UV divergences and quark confinement. These features of the model are specified by the nonlocal kernel, which appeared in the four-quark interaction. Such a structure of the four-quark interaction can be motivated by the instanton model [22, 24]. A similar model was considered in [17], where the nonlocal form factor was chosen in the Gaussian form that exponentially decreases in the Euclidean domain of momenta. Recently, in [23], it was demonstrated that the functions defining the nonlocal kernel are related to the nonlocal quark condensate. From this point of view, it looks more natural to require that, not a form factor, but a scalar part of the quark propagator $m(p^2)/(p^2 + m^2(p^2))$ should be an entire function. Let us note that this idea is close to the method proposed in [13], where the confinement is provided by demanding the absence of poles in the quark propagator.

As has been shown in [23], assuming that $m(p^2)/(p^2 + m^2(p^2))$ is a decreasing function of p^2 in the Euclidean region leads to three different possibilities for the dynamical quark mass $m(p^2)$ at different values of the parameters m_q and Λ (see Section 3). One of them has complex-valued masses on the real axis, and we did not consider it. The second possibility is connected with such a choice of parameters when the function $p^2Q^2(p^2) < 1$ in the whole domain of real p^2. Then, the solution $m_-(p^2)$ can be used, where the mass function has a zero at zero quark virtuality. In this case, the main requirements of chiral models are fulfilled. However, in this version of the model, the mass of the sigma meson and the strong decay widths of the σ and ρ mesons are in disagreement with experimental data.

Therefore, in the present work, we studied the third possibility, when the function $p^2Q^2(p^2) = 1$ at some point $p^2 = p_0^2$. In this case, $m(p^2)$ is the combination of the solutions $m_+(p^2)$, $m_-(p^2)$. This mass function is nonzero at $p^2 = 0$ and drops monotonically with increasing p^2. In this case, one can predict a scalar meson mass and decay width $\rho \to \pi\pi$ which are closer to experimental values. However, the decay width $\sigma \to \pi\pi$ remains too small.

It is useful to compare some results obtained in this model with analogous results obtained in the framework of the local NJL model [6]. Let us start with the π–a_1 mixing. In the local NJL model, the amplitude describing the π–a_1 mixing equals $A^{\mu\mathrm{NJL}}_{(\pi\to a_1)} = i\sqrt{6}mp^\mu$, where $m = 280$ MeV is the constituent quark mass. Therefore, the coefficient $C^{\mathrm{NJL}}_{(\pi\to a_1)}$ in the NJL model equals 680 MeV. This value is one order of magnitude larger than that in the present model. As a result, it leads to the noticeable additional renormalization of the pion field in the local NJL model $\tilde{g}^{\mathrm{NJL}}_\pi = g^{\mathrm{NJL}}_\pi Z^{1/2}_{\mathrm{NJL}}$, where $Z_{\mathrm{NJL}} = \left(1 - 6m^2/M^2_{a_1}\right)^{-1} \approx 1.4$, while in the present model $Z = 1.004$. Therefore, in the local NJL model, the π–a_1 mixing plays a more important role.

Let us compare also the amplitude of the decay width $\sigma \to \pi\pi$ in these models. In the local NJL model, this amplitude equals $A^{\mathrm{NJL}}_{(\sigma\to\pi^+\pi^-)} = 4mg = 2.8$ GeV (here, $g = 2.5$). This amplitude is twice as large as that in the present model. However, after taking into account π–a_1 mixing, this amplitude takes the form $A^{\mathrm{NJL}}_{(\sigma\to\pi^+\pi^-)} = 4mgZ^{-1}_{\mathrm{NJL}} = 2$ GeV. This leads to a noticeable decrease in the decay width, which becomes smaller than experimental data.

The failure of the models to describe the σ meson is expectable. Similar problems appeared in the QCD sum rule method. In the scalar channel with vacuum quantum numbers, the corrections from different sources may be valuable. Indeed, it was shown recently that the $1/N_c$ corrections in this channel are rather big [26], and thus we cannot trust the results of the model in this case.

In conclusion, let us summarize the main results of this work. The pseudoscalar, scalar, vector, and axial-vector sectors of the model have been considered. It was shown that the low-energy theorems are fulfilled. The masses and strong coupling constants of the mesons were calculated. The strong coupling constants of the mesons were shown to decrease noticeably with increasing p^2 in the physical domain (see Fig. 2). The π–a_1 mixing was considered, and it was found that this mixing could be neglected. Among satisfactory predictions of the model, there are the decay width $\rho \to \pi\pi$ and the mass of the σ meson. However, the width of decay $\sigma \to \pi\pi$ is significantly below the experimental value [25].

In the future, we plan to describe the electromagnetic interactions in the framework of this model, verify the vector meson dominance, calculate the electromagnetic pion radius, and consider the processes $\pi^0 \to \gamma\gamma$, $\gamma^* \to \gamma\pi$ (here γ^* is a virtual photon), the polarizability of the pion, and the $\pi\pi$ scattering length.

ACKNOWLEDGMENTS

We thank D. Blaschke, G.V. Efimov, S.B. Gerasimov, and S.N. Nedelko for fruitful discussions.

This work was supported in part by the Russian Foundation for Basic Research (project nos. 02-02-16194 and 03-02-17291), INTAS (project no. 00-00-366), and the Heisenberg–Landau program.

REFERENCES

1. V. De Alfaro, S. Fubini, G. Furlan, and C. Rossetti, *Currents in Hadron Physics* (Elsevier, New York, 1973).
2. S. Weinberg, Phys. Rev. Lett. **18**, 188 (1967); J. Wess and B. Zumino, Phys. Rev. **163**, 1727 (1967); S. Gasiorowicz and D. A. Geffen, Rev. Mod. Phys. **41**, 531 (1969).
3. Y. Nambu and G. Jona-Lasinio, Phys. Rev. **122**, 345 (1961).
4. T. Eguchi, Phys. Rev. D **14**, 2755 (1976); K. Kikkawa, Prog. Theor. Phys. **56**, 947 (1976).
5. M. K. Volkov and D. Ebert, Yad. Fiz. **36**, 1265 (1982) [Sov. J. Nucl. Phys. **36**, 736 (1982)]; D. Ebert and M. K. Volkov, Z. Phys. C **16**, 205 (1983); M. K. Volkov, Ann. Phys. (N.Y.) **157**, 282 (1984); D. Ebert and H. Reinhardt, Nucl. Phys. B **271**, 188 (1986); D. Ebert, H. Reinhardt, and M. K. Volkov, Prog. Part. Nucl. Phys. **33**, 1 (1994).
6. M. K. Volkov, Fiz. Élem. Chastits At. Yadra **17**, 433 (1986) [Sov. J. Part. Nucl. **17**, 186 (1986)].
7. T. Kunihiro and T. Hatsuda, Prog. Theor. Phys. **71**, 71 (1984); Phys. Rep. **247**, 221 (1994); U. G. Meissner, Phys. Rep. **161**, 213 (1988); U. Vogl and W. Weise, Prog. Part. Nucl. Phys. **27**, 195 (1991); S. P. Klevansky, Rev. Mod. Phys. **64**, 649 (1992).
8. A. A. Belavin, A. M. Polyakov, A. S. Shvarts, and Y. S. Tyupkin, Phys. Lett. B **59**, 85 (1975).
9. C. G. Callan, R. F. Dashen, and D. J. Gross, Phys. Rev. D **17**, 2717 (1978).
10. G. 't Hooft, Phys. Rev. Lett. **37**, 8 (1976).
11. E. V. Shuryak, Nucl. Phys. B **203**, 93 (1982).
12. A. E. Dorokhov and N. I. Kochelev, Sov. J. Nucl. Phys. **52**, 135 (1990); A. E. Dorokhov, Y. A. Zubov, and N. I. Kochelev, Fiz. Élem. Chastits At. Yadra **23**, 214 (1992) [Sov. J. Part. Nucl. **23**, 522 (1992)].
13. G. V. Efimov and M. A. Ivanov, Fiz. Élem. Chastits At. Yadra **20**, 1129 (1989) [Sov. J. Part. Nucl. **20**, 479 (1989)]; G. V. Efimov and M. A. Ivanov, *The Quark Confinement Model of Hadrons* (IOP, Bristol, 1993); G. V. Efimov and S. N. Nedelko, Phys. Rev. D **51**, 176 (1995).
14. F. Gross and J. Milana, Phys. Rev. D **45**, 969 (1992).
15. M. Buballa and S. Krewald, Phys. Lett. B **294**, 19 (1992).
16. C. D. Roberts and A. G. Williams, Prog. Part. Nucl. Phys. **33**, 477 (1994); C. J. Burden, L. Qian, C. D. Roberts, *et al.*, Phys. Rev. C **55**, 2649 (1997); nucl-th/9605027.

17. R. D. Bowler and M. C. Birse, Nucl. Phys. A **582**, 655 (1995); R. S. Plant and M. C. Birse, Nucl. Phys. A **628**, 607 (1998).
18. C. M. Shakin and W. D. Sun, Phys. Rev. C **54**, 1414 (1996); L. S. Celenza, B. Huang, H. S. Wang, and C. M. Shakin, Phys. Rev. C **60**, 025202 (1999).
19. K. Langfeld and M. Rho, Nucl. Phys. A **596**, 451 (1996).
20. D. Blaschke, Y. L. Kalinovsky, and P. C. Tandy, in *Proceedings of the XI International Conference on Problems of Quantum Field Theory, Dubna, 1998*, p. 454; hep-ph/9811476; D. Blaschke, G. Burau, Y. L. Kalinovsky, *et al.*, Int. J. Mod. Phys. A **16**, 2267 (2001); nucl-th/0002024.
21. H. Ito, W. W. Buck, and F. Gross, Phys. Rev. C **43**, 2483 (1991); **45**, 1918 (1992).
22. I. V. Anikin, A. E. Dorokhov, and L. Tomio, Phys. Part. Nucl. **31**, 509 (2000); A. E. Dorokhov and W. Broniowski, Eur. Phys. J. C **32**, 79 (2003).
23. A. E. Dorokhov and W. Broniowski, Phys. Rev. D **65**, 094007 (2002); hep-ph/0110056.
24. D. Diakonov and V. Y. Petrov, Nucl. Phys. B **245**, 259 (1984); **272**, 457 (1986).
25. K. Hagiwara *et al.*, Phys. Rev. D **66**, 010001 (2002).
26. R. S. Plant and M. C. Birse, Nucl. Phys. A **703**, 717 (2002).

Physics of Atomic Nuclei, Vol. 67, No. 5, 2004, pp. 1027–1034. From Yadernaya Fizika, Vol. 67, No. 5, 2004, pp. 1050–1058.

ELEMENTARY PARTICLES AND FIELDS
Theory

New Spectral Representation and Evaluation of f_π and the Quark Condensate $\langle\bar{q}q\rangle$ in the Terms of String Tension*

Yu. A. Simonov

Institute of Theoretical and Experimental Physics,
Bol'shaya Cheremushkinskaya ul. 25, Moscow, 117259 Russia

Received October 14, 2003

Abstract—New spectral representations for f_π and chiral condensate are derived in QCD and used for calculations in the large-N_c limit. Both quantities are expressed in this limit through string tension σ and gluon correlation length T_g without fitting parameters. As a result, one obtains $\langle\bar{q}q\rangle = -N_c\sigma^2 T_g a_1$, $f_\pi = \sqrt{N_c}\sigma T_g a_2$, with $a_1 = 0.0823$, $a_2 = 0.30$. Taking $\sigma = 0.18$ GeV^2 and $T_g = 1$ GeV^{-1}, as known from analytic and lattice calculations, this yields $\langle\bar{q}q\rangle(\mu = 2\text{ GeV}) = -(0.225\text{ GeV})^3$, $f_\pi = 0.094$ GeV, which is close to the standard values. © *2004 MAIK "Nauka/Interperiodica".*

1. INTRODUCTION

Chiral symmetry breaking (CSB) is known to occur in QCD at large N_c if confinement is preserved in this limit [1]. Lattice calculations for $N_c = 2, 3$ indicate that confinement and CSB coexist in the confinement phase at $T \le T_c$ and disappear simultaneously above T_c [2]. At larger N_c, it was found on the lattice that the $1/N_c$ corrections to all observables studied are not large [3], suggesting that a smooth limit at large N_c is possible.

In the framework of the field correlator method (FCM) [4], the dynamics of confinement and deconfinement is associated with the set of field correlators $D^{(n)}_{\mu_1\nu_1,\dots,\mu_n\nu_n}(x_1,\dots,x_n) = \langle F_{\mu_1\nu_1}(x_1)\dots F_{\mu_n\nu_n}(x_n)\rangle$,[1)] of which the lowest one, $D^{(2)}(x_1,x_2) \equiv D^{(2)}(x_1 - x_2)$, plays the dominant role [5]. Moreover, $D^{(2)}(x)$ was calculated on the lattice [6] and its confining part, $D(x)$, was shown to disappear exactly above T_c [7].

In [8, 9], CSB was also found as a consequence of confinement, and in [9, 10] the effective chiral Lagrangian (ECL) was derived from the $4q$ interaction term using $D(x)$ as a kernel.

The resulting ECL in [9, 10] has a general structure which can be reduced to the expressions derived in the framework of the instanton model [11] or the NJL model [12], when the corresponding kernels are introduced there.

In the case of confinement, the effective quark mass operator $M(x)$ in QCD obtained in [9, 10] contains the effect of the scalar confining string connecting the quark to the nearest antiquark. Moreover, all invariant quark Green's functions can be expressed at large N_c through the string spectrum, as was done in [10] in the PS channel.

The phenomenon of CSB was shown in [9, 10] as occurring due to the spontaneous creation of the scalar string (similar to the creation of the scalar condensate in nonconfining models [12, 13]), which generates CSB and chiral Nambu–Goldstone (NG) fields {see Eqs. (50)–(54) in [9] and Eqs. (21)–(24) in [10]}.

Since confinement is present in our formalism (in the form of $M(x)$), one can ask the question how confinement fits in the chiral picture of the NG spectrum, and, in particular, how CSB modifies the lowest PS states computed in FCM (or in any quark model) taking into account confinement and disregarding CSB. Two such lowest states, $\pi^{(0)}$ and its first radial excitation $\pi^{(1)}$ with masses $m(\pi^{(0)}) \equiv m_0 \cong 0.4$ GeV and $m(\pi^{(1)}) \equiv m_1 \cong 1.35$ GeV, have been computed in FCM (see Appendix 3). It was shown in [10] that the ECL obtained there with account of confinement has a remarkable property: the PS spectrum of confinement transforms due to CSB in such a way that $\pi^{(0)}$ becomes a NG pion with the mass satisfying the Gell-Mann–Oakes–Renner (GOR) relation [13], while the first radial excitation shifts only slightly.

In deriving that property, it was essential that all basic quantities in the ECL and, in particular, the pion self-energy operator can be expressed as a spectral

*This article was submitted by the author in English.

[1)]Parallel transporters are omitted here for simplicity.

decomposition in the confinement (stringlike) spectrum states, which is possible in the large-N_c limit.

In this paper, we follow this line to obtain a more fundamental relation, namely, to calculate the quark condensate $\langle\bar{q}q\rangle$ and the pion decay constant f_π using new spectral representations for these quantities. Since in the latter all masses and coupling constants are expressed via $D(x)$, i.e., via the string tension σ and the gluon correlation length T_g, we have an expression for $\langle\bar{q}q\rangle$ and f_π in terms of σ and T_g. The most important role in the spectral representations is played by the lowest PS meson $\pi^{(0)}$—the "to-be pion"—which is the quark model analog of the pion with mass m_0 shifted by the hyperfine interaction from the ρ-meson mass. In Appendix 3, we derive the mass m_0 and the corresponding wave function in the framework of FCM in terms of σ and α_s.

Having established the connection of $\langle\bar{q}q\rangle$ and f_π with σ, T_g [$\langle\bar{q}q\rangle = -N_c\sigma^2 T_g a_1$, $f_\pi = \sqrt{N_c}\sigma T_g a_2$, with $a_1 = 0.0823$, $a_2 = 0.30$ (explained in the text below)], it is easy to understand that, at the deconfinement transition when σ vanishes at $T = T_c$, also $\langle\bar{q}q\rangle$ and f_π vanish in agreement with lattice data [2].

Some specification with respect to the notion of "magnetic confinement" [14] is needed at this point, since the magnetic counterpart of $D(x)$ and the corresponding spatial string tension stay nonzero above T_c. This topic will be studied elsewhere.

The paper is organized as follows. In the next section, the ECL is written together with the appropriate expressions for $\langle\bar{q}q\rangle$ and f_π. In Section 3, the spectral representations for these quantities are derived, with coefficients depending on eigenfunctions of the $\bar{q}q$ system in the PS channel. Section 4 is devoted to the discussion of results in comparison to lattice data and to the concluding remarks. Four appendices are included in the paper, containing, respectively, the evaluation of $M(0)$, derivation of spectral representation, explicit calculation of eigenvalues and eigenfunctions in the pseudoscalar spectrum, and the contribution of the small-distance region.

2. THE EFFECTIVE CHIRAL LAGRANGIAN

The quadratic part of the ECL for pions was derived in [10] and has the form

$$W^{(2)}(\phi) = \frac{N_c}{2}\int \phi_a(k)\phi_a(-k)\bar{N}(k)\frac{d^4k}{(2\pi)^4}, \quad (1)$$

where the notation of [10] has been used, $\phi_a = 2\pi_a/f_\pi$, and

$$\bar{N}(k) = \frac{1}{4}\left[G^{(MM)}(k) + \mathrm{tr}(\Lambda M_S)\right] \quad (2)$$
$$= (m_\pi^2 + k^2)\frac{f_\pi^2}{4N_c} + O(k^4),$$

$$G^{(MM)}(k) \equiv -\int \mathrm{tr}(\Lambda(y,x)\gamma_5 M_S(x) \quad (3)$$
$$\times \Lambda(x,y)\gamma_5 M_S(y))e^{ik(x-y)}d^4(x-y),$$

$$\Lambda(x,y) = (\hat{\partial} + m + M_S)^{-1}_{x,y}. \quad (4)$$

Here and below, the trace is taken over flavor and Lorentz indices.

As was shown in [10], the two terms in the square brackets in (2) cancel for $k^2 = m = 0$, and one obtains the GOR relation for the pion mass [13]:

$$mN_c\mathrm{tr}\Lambda \equiv m|\langle\bar{\psi}\psi\rangle_{\mathrm{M}}| \quad (5)$$
$$= \frac{1}{2}(m_u + m_d)|\langle\bar{u}u + \bar{d}d\rangle| = m_\pi^2 f_\pi^2.$$

To calculate the quark condensate, defined in the Minkowskian spacetime, one can write $\langle\bar{\psi}\psi\rangle_{\mathrm{M}} = -N_c\mathrm{tr}\Lambda$ and use the identical transformation

$$\mathrm{tr}\Lambda_{xx} = \mathrm{tr}\left\langle\frac{1}{(M_S + m + \hat{\partial})}(M_S + m - \hat{\partial})\frac{1}{(M_S + m - \hat{\partial})}\right\rangle \quad (6)$$
$$= \int\langle\mathrm{tr}(\gamma_5\Lambda(x,y)\gamma_5(M_S + m)\Lambda(y,x))\rangle d^4y \equiv -\int G^{(M)}(x,y)d^4y \equiv -G^{(M)}(k=0).$$

Hence $\mathrm{tr}\Lambda_{xx}$ reduces to the zero-momentum component of the $q\bar{q}$ Green's function in the PS channel, which differs from (3) only by vertex operators.

To define f_π, one needs the first term in the k^2 expansion of $G^{(MM)}(k)$ (3) [cf. Eq. (2)], so that one has

$$G^{(MM)}(k) - G^{(MM)}(0) = \frac{k^2 f_\pi^2}{N_c} + O(k^4). \quad (7)$$

As was argued in [10], both $G^{(MM)}(k)$ and $G^{(M)}(k)$ have spectral representations in the large-N_c limit, with the same set of poles $m_n, n = 0, 1, 2, \ldots, m_0 \equiv m(\pi^{(0)})$,

$$G^{(MM)}(k) = -\sum_{n=0}^{\infty}\frac{(c_n^{(M)})^2}{k^2 + m_n^2}, \quad (8)$$

$$G^{(M)}(k) = -\sum_{n=0}^{\infty} \frac{c_n c_n^{(M)}}{k^2 + m_n^2}.$$

In the next section, we shall determine the coefficients $c_n, c_n^{(M)}$, and m_n for the lowest states, and now we define $\langle\bar{q}q\rangle$ and f_π in terms of spectral sums (8). From (6) and (7), one has

$$\langle\bar{\psi}\psi\rangle_{\rm M} = -2N_c \sum_{n=0}^{\infty} \frac{c_n c_n^{(M)}}{m_n^2}, \qquad (9)$$

$$f_\pi^2 = 2N_c \sum_{n=0}^{\infty} \frac{(c_n^{(M)})^2}{m_n^4}.$$

The coefficients c_n and $c_n^{(M)}$ differ by the presence of the vertex operator $M_S \equiv M(0)$ in the latter, which is a constant computed in Appendix 1; therefore, one has $c_n^{(M)} = M(0)c_n$, and, limiting oneself to the first term in the sum (9), one obtains

$$|\langle\bar{\psi}\psi\rangle_{\rm M}| \geq m_0^2 f_\pi^2 \frac{c_n}{c_n^{(M)}} = \frac{m_0^2 f_\pi^2}{M(0)}. \qquad (10)$$

Inserting $M(0) = 148$ MeV from Appendix 1 and $|\bar{\psi}\psi| = (225\ \text{MeV})^3$, $f_\pi = 94$ MeV, one obtains $m_0 \cong 437$ MeV, which is close to the value $m_0 = 400$ MeV calculated in Appendix 3. On the other hand, the sum (9) for $\langle\bar{\psi}\psi\rangle$ converges more slowly than that for f_π, and therefore one has inequality in (10) due to the presence of higher terms in $\langle\bar{\psi}\psi\rangle$.

3. CALCULATION OF $\langle\bar{q}q\rangle$ AND f_π

The integration region in the spacetime integrals in (3), (6) can be split into two parts: $|x-y| > T_g$ and $|x-y| \leq T_g$. In the first (long-distance) region, the relativistic local potential-type dynamics sets in at spacetime distances exceeding T_g [15, 16] and the result can be expressed in terms of the spectrum, as will be done below in this section. The second region can be treated in the OPE formalism [17] and is considered in Appendix 4. It is shown there that the contribution of this region is parametrically small in the parameter $\sigma T_g^2 \ll 1$. Only the long-distance contribution is calculated in this section below.

We start with the calculation of f_π, and to this end we write the $q\bar{q}$ Green's function $G^{(MM)}(k)$ in terms of c.m. and relative coordinates as follows (another derivation is given in Appendix 2):

$$-G^{(MM)}(k) = \int d^4X \qquad (11)$$

$$\times\, G^{(MM)}(\mathbf{r}_{12}=0; \mathbf{R}=0, \mathbf{r}'_{12}=0, \mathbf{R}'=\mathbf{X}, T) e^{i\mathbf{k}\cdot\mathbf{X}}$$

$$= M^2(0) \sum_n |\varphi_n(0)|^2$$

$$\times \frac{d\mathbf{P}}{(2\pi)^3} dT d\mathbf{X} e^{-E(P)T - i\mathbf{P}\cdot\mathbf{X} + i\mathbf{k}\cdot\mathbf{X}}$$

$$= M^2(0) \sum_n |\varphi_n(0)|^2 \int_0^\infty e^{-E(\mathbf{k})T} dT$$

$$= M^2(0) \sum_n \frac{|\varphi_n(0)|^2}{\sqrt{m_n^2 + \mathbf{k}^2}}.$$

Expanding (11) in $\mathbf{k}^2$ and comparing to (7), one finds f_π^2,

$$f_\pi^2 = N_c M^2(0) \sum_{n=0}^{\infty} \frac{|\varphi_n(0)|^2}{m_n^3}. \qquad (12)$$

Comparing (9) and (12), one finds

$$c_n^{(M)} = \sqrt{\frac{m_n}{2}} M(0) \varphi_n(0), \qquad (13)$$

$$c_n = \sqrt{\frac{m_n}{2}} \varphi_n(0).$$

In a similar way, one computes $\langle\bar{q}q\rangle$ from (6) and finds

$$-\langle\bar{q}q\rangle = N_c M(0) \sum_{n=0}^{\infty} \frac{|\varphi_n(0)|^2}{m_n}. \qquad (14)$$

Here, $\varphi_n(\mathbf{r})$ is the $3D$ spin-singlet wave function of the $q\bar{q}$ system, as obtained, e.g., in the relativistic Hamiltonian method of FCM [15] or else in the Bethe–Salpeter equation with the kernel not depending on relative time, as is discussed in Appendix 2.

The accuracy of the method with respect to calculation of $|\varphi_n(0)|^2$ can be checked by comparison of the predicted leptonic width with experiment, as is done in Appendix 3. Taking into account both color Coulomb and confining interaction, one has

$$|\varphi_n(0)|^2 = \mu_n \left(\sigma + \frac{4}{3}\alpha_s \left\langle \frac{1}{r^2} \right\rangle\right)/(4\pi), \qquad (15)$$

where μ_n is the constituent energy (mass) computed through σ [15]; we refer the reader to Appendix 3 for the details of calculation of m_n and $|\varphi_n(0)|^2$.

As is shown in [16] and discussed in Appendix 3, the masses m_n^2, μ_n^2 grow linearly with n in the large-N_c limit; hence, the sum (14) for $\langle\bar{q}q\rangle$ is formally diverging if the spectrum of radially excited mesons extends to infinitely large masses. In fact, the experimental spectrum can be followed up to mass values around $m_{\rm cont} \cong 2.5$ GeV, where resonances become very wide and strongly mix between themselves and

with hybrids, forming the continuum of states. Following the ideology of the QCD sum rules [17], one could replace this continuum by perturbative diagrams, which do not contribute to $\langle\bar{q}q\rangle$. Therefore, we shall keep the first three terms in the sum (14) over n (the term with $n=3$ gives a negligible contribution). As was mentioned in the beginning of this section, the relativistic potential description of $G^{(MM)}(\mathbf{r}_{12},\mathbf{R},\mathbf{r}_{12},\mathbf{R}',T)$ is possible only for time $T\gtrsim T_0$, while, for $T<T_0, T_0\sim T_g$, one should use the properties of the $\bar{q}q$ Green's function $\tilde{G}$, as given by the OPE [17]. As is discussed in Appendix 4, the region of small times and relative distances, covered by the OPE treatment, gives a contribution to $\langle\bar{q}q\rangle$ proportional to $O(\sigma^{5/2}T_0^4/T_g^2,\sigma m)$ and therefore can be disregarded for light quarks and small $T_0<T_g$. As a result, one should exclude from the integration over dT in (11) the region $(0,T_0)$, which brings about the following factor in (14) instead of $1/m_n$,

$$\frac{1}{m_n}\to\frac{e^{-m_nT_0}}{m_n}, \tag{16}$$

and in (12),

$$\frac{1}{m_n^3}\to\frac{e^{-m_nT_0}}{m_n^3}(1+m_nT_0). \tag{17}$$

Retaining for $\langle\bar{q}q\rangle$ the first three terms in the sum (14) and two terms in (12), one has

$$-\langle\bar{q}q\rangle=N_cM(0)\Big\{\frac{\varphi_0^2(0)e^{-m_0T_0}}{m_0} + \frac{\varphi_1^2(0)e^{-m_1T_0}}{m_1}+\frac{\varphi_2^2(0)e^{-m_2T_0}}{m_2}\Big\}, \tag{18}$$

$$f_\pi^2=N_cM(0)\Big\{\frac{\varphi_0^2(0)e^{-m_0T_0}}{m_0^3}(1+m_0T_0) + \frac{\varphi_1^2(0)e^{-m_1T_0}}{m_1^3}(1+m_1T_0)\Big\}. \tag{19}$$

Using (A.25), (A.27), and (A.30), one has

$$\varphi_0^2(0)=\frac{0.109\ \mathrm{GeV}^3}{4\pi}, \tag{20}$$

$$\varphi_1^2(0)=\frac{0.097\ \mathrm{GeV}^3}{4\pi},\quad \varphi_2^2(0)=\frac{0.115\ \mathrm{GeV}^3}{4\pi};$$

$$m_0=0.4\ \mathrm{GeV},\quad m_1=1.35\ \mathrm{GeV},\quad m_2=1.85\ \mathrm{GeV}.$$

For a reasonable estimate, we set $T_0=T_g=1\,\mathrm{GeV}^{-1}$ and the value $M(0)=0.148$ GeV from Appendix 1 and obtain

$$-\langle\bar{q}q\rangle=(0.195\ \mathrm{GeV})^3,\quad f_\pi=0.094\ \mathrm{GeV}. \tag{21}$$

One can check that the behavior of (18) for $\langle\bar{q}q\rangle$ at small T_0 is smooth; e.g., when changing T_0 from $T_g=1\ \mathrm{GeV}^{-1}$ to $0.5\ T_g$, the result changes by roughly 10%.

To check the sensitivity to the change of T_g, we have taken $T_g=1/1.5\ \mathrm{GeV}^{-1}$ and recalculated all quantities; e.g., from (A.7), one has $M(0)=0.12$ GeV. The resulting values are not changed much from (21),

$$-\langle\bar{q}q\rangle\left(T_g=\frac{1}{1.5}\ \mathrm{GeV}^{-1}\right)=(0.189\ \mathrm{GeV})^3, \tag{22}$$

$$f_\pi=0.076\ \mathrm{GeV}.$$

It is remarkable that f_π in (21) is very close to the value obtained from the pion decay and used in the chiral perturbation theory [18], $f_\pi=93$ MeV. At the same time, $|\langle\bar{q}q\rangle|$ is somewhat less than the standard value $(240\ \mathrm{MeV})^3$, and we discuss in the concluding section the scale dependence and comparison with existing lattice measurements.

4. DISCUSSION AND CONCLUSIONS

The quark condensate and f_π are given by Eqs. (18), (19), and (22), where all quantities can be expressed through m,σ, and T_g, since $\varphi_n^2(0)$, m_n, and $M(0)$ are expressed through these quantities, while T_0 can be taken in the region of plateau and, e.g., equal to T_g. In this way, one obtains [$m=0$, $\sigma=0.18\ \mathrm{GeV}^2$, $T_0=T_g=1\ \mathrm{GeV}^{-1}$, and Eq. (21) for $\langle\bar{q}q\rangle$]

$$f_\pi\cong 0.094\ \mathrm{GeV},\quad -\langle\bar{q}q\rangle\cong(0.20\ \mathrm{GeV})^3. \tag{23}$$

Several corrections should be added to these results. First of all, the short-distance contribution to $\langle\bar{q}q\rangle$ is of relative order $\sqrt{\sigma}T_g\sim 0.45$ and can substantially increase the result. Another essential point is the value of T_g, which increases in the presence of dynamical quarks, and can be smaller if gluelump data [19] are taken into account, $T_g=0.7\ \mathrm{GeV}^{-1}$. This influences significantly the value of $M(0)$; however, an independent check can be made, since $M(0)$ also enters the strong decay matrix element, and the value $M(0)=0.148$ GeV is reasonably close to the phenomenological value known from the $^3P_0$ model [20].

We are now in position to compare (23) with the lattice data. There, the computation was done in the quenched case for Wilson fermions [21] and also for the overlap action [22]. Before using the evaluation coefficient for $\langle\bar{q}q\rangle$, one can compare the result (23), which does not contain any scale μ or any evolution corrections, with the so-called renormalization

group invariant (RGI) lattice measurements, which yield [21]

$$-\langle\bar{q}q\rangle^{\rm RGI}_{\rm lat} = [(206 \pm 44 \pm 8 \pm 5)\ {\rm MeV}]^3. \quad (24)$$

This value is in reasonable agreement with (23). As the next step, we take the evolution coefficient for $\langle\bar{q}q\rangle$ computed in [23] ($n_f = 0$, $N_c = 3$)

$$C_s^{\overline{MS}}(\mu) = [\alpha_s(\mu)]^{-4/11}\{1 - 0.219\alpha_s - 0.1054\alpha_s^2\}. \quad (25)$$

For $\mu = 2$ GeV, taking $\alpha_s \approx 0.3$, and identifying $\langle\bar{q}q\rangle$ in (23) with $\langle\bar{q}q\rangle^{\rm RGI}$, one obtains for the long-distance contribution to the condensate

$$\langle\bar{q}q\rangle(\mu = 2\ {\rm GeV}) \cong \langle\bar{q}q\rangle^{RGI} C_s^{\overline{MS}} \cong -(225\ {\rm MeV})^3. \quad (26)$$

This value, given in the abstract of the paper, is obtained without inclusion of the coefficient used on the lattice [21] to calculate the transition from the lattice RGI result to the $\overline{MS}$ scheme; this coefficient is anyhow close to unity.

The lattice value at $\mu = 2$ GeV for Wilson quarks in [20] is

$$\langle\bar{q}q\rangle^{\overline{MS}}(\mu = 2\ {\rm GeV}) = -[242 \pm 9\ {\rm MeV})]^3 \quad (27)$$

and differs from the result [22]: $-(282(6)\ {\rm MeV})^3 \times \left(\frac{a^{-1}}{1766\ {\rm MeV}}\right)^3$. An independent estimate from the QCD sum rules yields [24]

$$\langle\bar{q}q\rangle(\mu = M_N) = -[225 \pm 9\ {\rm MeV}]^3. \quad (28)$$

As a result, one can see that our long-distance contribution to $\langle\bar{q}q\rangle$, Eq. (26), is somewhat smaller than the lattice data (27), but is certainly in the same ballpark, and the evaluation of the short-distance contribution is important to improve the accuracy of calculation.

At the same time, the resulting value f_π (23) is in good agreement with the standard value, obtained from the pion decay and used in the chiral perturbation theory [18].

The method used above can be easily applied to the case of nonzero quark mass m and the $SU(3)$ flavor group to calculate $\langle\bar{s}s\rangle$, f_K, etc., which will be published elsewhere [25].

ACKNOWLEDGMENTS

This work was supported by the Federal Program of the Russian Ministry of Industry, Science, and Technology (project no. 40.052.1.1.1112). The financial support of INTAS (grant nos. 00-110 and 00-366) is gratefully acknowledged.

APPENDIX 1

Calculation of the Vertex Mass $M(0)$

One starts with the definition of the nonlocal mass operator $M_S(u,v)$ given in [9, 10] {see, e.g., Eq. (24) in [10]}:

$$M_S(u,v) = (\gamma_\mu\Lambda(u,v)\gamma_\mu)_{\rm sc} J(u,v). \quad (A.1)$$

The mass operator enters in the gauge-invariant Green's functions [see, e.g., Eq. (3)] via the quark propagator $\Lambda(x,y)$ (4), where $M_S(z,u)$ enters at all intermediate points and also at initial and final points $(x+\bar{x})/2$ and $(y+\bar{y})/2$, where the nonlocal pion $\phi(x,\bar{x})$ is emitted. According to the prescription given in [10], we choose the set of contours $C(z)$ for all intermediate points z in the Green's function $G((x+\bar{x})/2, (y+\bar{y})/2)$, which minimizes the mass eigenvalues. One simple choice is to take the contours $C(z)$ from z along the shortest path to the x_4 axis passing through $(x+\bar{x})/2$ and $(y+\bar{y})/2$ and along x_4 axis to the origin at the point $(x+\bar{x})/2$.

When M_S is situated at the initial or final point of the $q\bar{q}$ Green's function, i.e., at the points $M_S(x,\bar{x})$ or $M_S(y,\bar{y})$, where the $q\bar{q}$ or pion is created or annihilated, then it is convenient to choose points $x, \bar{x}$ on the axis 1 with the origin at $(x+\bar{x})/2$. In this way, one obtains for $x_1 > 0, \bar{x}_1 \equiv y_1 < 0, y_4 \equiv \bar{x}_4$

$$J(x,y) = \int_0^{x_1} du \int_{y_1}^{0} dv D(u-v, x_4 - y_4). \quad (A.2)$$

It is convenient to use for D the Gaussian form,

$$D(\mathbf{x}, x_4) = D(0)e^{-(\mathbf{x}^2+x_4^2)/(4T_g^2)} = \frac{\sigma}{2\pi T_g^2} e^{-(\mathbf{x}^2+x_4^2)/(4T_g^2)}, \quad (A.3)$$

which yields

$$J(x,y) = \frac{\sigma}{\pi} e^{-(x_4-y_4)^2/(4T_g^2)}(1 - e^{-(\mathbf{x}-\mathbf{y})^2/(4T_g^2)}). \quad (A.4)$$

Now one has to estimate the scalar part of the quark Green's function $\Lambda(x,y)$ in (A.1), for which in [8] it was found that it behaves as a smeared δ function with the smearing radius equal to $1/\sqrt{\sigma}$ {see Eq. (24) in the second reference of [8]}. We simplify this form, taking

$$\Lambda(x,y) = \left(\frac{\sigma}{\pi}\right)^{3/2} e^{-(\mathbf{x}-\mathbf{y})^2\sigma}; \quad (A.5)$$

$$\int \Lambda(x,y) d(\mathbf{x}-\mathbf{y}) = 1.$$

To obtain the localized form of the vertex function

$$M_S(x) \equiv M(0) = \int M_S^{(0)}(x,y)d^4(x-y), \quad \text{(A.6)}$$

we substitute into (A.6) $J(x,y)$ from (A.4) and $\Lambda(x,y)$ from (A.5) to get finally

$$M(0) = \left[1 - \left(\frac{4T_g^2\sigma}{4T_g^2\sigma+1}\right)^{3/2}\right]\frac{2\sigma T_g}{\sqrt{\pi}} \quad \text{(A.7)}$$
$$\equiv \eta\frac{2\sigma T_g}{\sqrt{\pi}}.$$

In the limit $\sigma T_g^2 \to 0$, one obtains $M(0) \approx 2\sigma T_g/\sqrt{\pi}$, i.e., exactly the value which appears in the strong decay vertex of the string in [20]. This is not surprising, since in both cases $M(0)$ is a mass corresponding to a piece of the string with a length of the order of T_g; hence, $M(0) \sim \sigma T_g$. The factor η in (A.7) describes the attenuation due to the nonlocality of $\Lambda(x,y)$ at small $|\mathbf{x}-\mathbf{y}|$ for light quarks. For heavy quarks, this factor tends to zero, since the localization of $\Lambda(x,y)$ becomes stronger; indeed, the quark Green's function Λ for $m \to \infty$ is proportional to $\delta^{(3)}(\mathbf{x}-\mathbf{y})$ (see [8]). Effectively, for nonzero m, this can be described via replacing η in (A.7) by the factor

$$\eta \to \eta(m) = \left[1 - \left(\frac{4T_g(\sigma T_g+m)}{4T_g(\sigma T_g+m)+1}\right)^{3/2}\right]. \quad \text{(A.8)}$$

For light quarks and $\sigma = 0.18$ GeV^2, $T_g = 1$ GeV^{-1}, the factor $\eta \equiv \eta(0)$ is $\sim 1 - 0.27 = 0.73$, and from (A.7) one gets $M(0) \approx 0.148$ GeV.

APPENDIX 2

Derivation of the Spectral Representations, Eqs. (12) and (13)

Consider the $q\bar{q}$ Green's function of the type given in Eq. (6):

$$G_\Gamma(x,y) = \langle \mathrm{tr}(\Gamma\Lambda(x,y)\Gamma\Lambda(y,x))\rangle, \quad \text{(A.9)}$$

where $\Gamma = \gamma_5, \gamma_\mu, \ldots$, and the $q\bar{q}$ Green's function in the 4×4 spinor representation:

$$G^{(q\bar{q})}_{\alpha\beta,\gamma\delta}(x,\bar{x};y,\bar{y}) = \langle \Lambda_{\alpha\beta}(x,y)\Lambda_{\gamma\delta}(\bar{y},\bar{x})\rangle. \quad \text{(A.10)}$$

Following the standard procedure from [26], one can introduce the c.m. and relative coordinates, i.e.,

$$X = \frac{x+\bar{x}}{2}, \quad Y = \frac{y+\bar{y}}{2}, \quad \text{(A.11)}$$
$$r = x-\bar{x}, \quad r' = y-\bar{y},$$

and define

$$G^{(q\bar{q})}(x,\bar{x};y,\bar{y}) \quad \text{(A.12)}$$
$$= \int d^4P e^{iP(X-Y)}\frac{d\varepsilon}{2\pi}e^{-i\varepsilon r_0}G_P(\mathbf{r},\mathbf{r}',\varepsilon,\mathbf{r}'_0).$$

Here, G_P satisfies an equation

$$(E-E_2-H_1)(E_2-H_2)G_P = \beta_1\beta_2\hat{1}, \quad \text{(A.13)}$$

where $E = E_1+E_2 = P_0$, $E_1-E_2 = 2\varepsilon$, and

$$H_i = m_i\beta_i + \mathbf{p}\cdot\boldsymbol{\alpha}_i + \beta_i M_S. \quad \text{(A.14)}$$

At this point, one can exploit the property of H_i that it does not depend on relative time r_0, and therefore one can integrate in (A.12) over $d\varepsilon$ with the result [26, 27]

$$G_P\Big|_{\substack{r_0=0\\ r'_0=0}} = \beta_1\beta_2 \quad \text{(A.15)}$$
$$\times \int\limits_{-\infty}^{\infty}\frac{d\varepsilon/2\pi}{(E_1-H_1)(E_2-H_2)} = i\beta_1\beta_2\frac{1}{E-\hat{H}},$$

$$\hat{H} \equiv H_1+H_2.$$

As the result, one obtains

$$\int d^4(X-Y)G^{(q\bar{q})}(x,\bar{x};y,\bar{y})\big|_{r_0=r'_0=0} \quad \text{(A.16)}$$
$$= \left\langle \mathbf{r}\left|\frac{i\beta_1\beta_2}{\hat{H}}\right|\mathbf{r}'\right\rangle = \sum_n\langle\mathbf{r}|n\rangle\frac{i\beta_1\beta_2}{E_n}\langle n|\mathbf{r}'\rangle.$$

One can now express G_Γ, with $\Gamma = \gamma_5$, as

$$\int d^4(X-Y)G_\Gamma(x,y) = i\sum_{n=0}^{\infty}\frac{\psi_n(0)\psi_n^+(0)}{E_n}, \quad \text{(A.17)}$$

where we have defined the relativistic wave function $\psi_n(\mathbf{r}) \sim \gamma_5\langle\mathbf{r}|n\rangle$, $\psi_n^+(\mathbf{r}) \sim \beta_1\beta_2\langle n|\mathbf{r}\rangle$, satisfying the Hamiltonian equation

$$\hat{H}\psi_n(\mathbf{r}) = E_n\psi_n(\mathbf{r}). \quad \text{(A.18)}$$

As is known from dynamical calculations with the Bethe–Salpeter equation [28] with the scalar confining kernel, the dominant role in $\psi_n(\mathbf{r})$ is played by the $^1S_0$ component $\varphi_n(\mathbf{r})$ of the wave function, which satisfies the relativistic Schrödinger equation with hyperfine interaction, discussed in Appendix 3. Therefore, one can identify $\psi_n(\mathbf{r}) \to \varphi_n(\mathbf{r}), E_n \to m_n$, and Eq. (6) with the help of (A.17) goes over to Eq. (14).

APPENDIX 3

Calculation of the Masses m_n and $\varphi_n(0)$ through σ in FCM

The mass eigenvalue $\bar{m}_n$ of the spin-averaged state $(3m_n^{(\rho)} + m_n^{(\pi)})/4$ for $L = 0$ can be written as [15, 16]

$$\bar{m}_n = M_0(n) + \Delta_{\rm SE} + \Delta_{\rm C}, \tag{A.19}$$

where $M_0(n)$ is the eigenvalue of the spinless Salpeter equation, which can be written as

$$M_0(n) = 4\mu_0(n) = 4\left\langle \sqrt{\mathbf{p}^2 + m^2} \right\rangle_n. \tag{A.20}$$

For $m = 0$, $\mu_0(n)$ is expressed through $\sqrt{\sigma}$ and dimensionless coefficients $a(n)$—zeros of Airy functions [15]:

$$\mu_0(n) = \sqrt{\sigma}\left(\frac{a(n)}{3}\right)^{3/4}, \tag{A.21}$$
$$a(0) = 2.338, \qquad a(1) = 4.088.$$

Taking into account nonzero m, one finds $\mu_0(n)$ from the equation

$$1 = \frac{m^2}{\mu_0^2} + \frac{\sigma^{2/3}}{3\mu_0^{4/3}}a(n). \tag{A.22}$$

For large $m \gg \sqrt{\sigma}$, the solution of (A.22) is

$$\mu_0^2(n) \cong m^2\left[1 + \frac{a(n)}{3}\left(\frac{2\sigma\mu}{m^2(m+\mu)}\right)^{2/3}\right]. \tag{A.23}$$

The term $\Delta_{\rm SE}$ is the self-energy correction [19], which can be written as

$$\Delta_{\rm SE}(n) = -\frac{4\sigma\eta(m)}{\pi\mu_0(n)}, \tag{A.24}$$

and $\eta(m)$ is computed through m; for $m = 0$, $\eta(m = 0) = 0.9$–1.0.

Taking all contributions into account, one obtains for the light quarks $(m = 0)$

$$\bar{m}_0 = 0.652 \text{ GeV}, \tag{A.25}$$
$$\bar{m}_n^2 = \bar{m}_0^2 + \Omega_0 n, \qquad n = 0, 1, 2, \ldots,$$

where Ω_0 is computed solely through σ and is equal to $\Omega_0 \cong 1.6$ GeV^2, which is close to the experimental slope $\Omega_{\rm exp}(L = 0) = 1.64 \pm 0.11$ GeV^2 (see [16] for references and discussion).

Now we take into account the hyperfine interaction which produces the HF splitting between ρ and π states:

$$\Delta_{\rm HF} = \Delta_{\rm HF}^{\rm Pert} + \Delta_{\rm HF}^{\rm NP}, \tag{A.26}$$

$$\Delta_{\rm HF}^{\rm Pert} = \frac{8\alpha_s(\mu_{\rm HF})|R_n(0)|^2}{9\mu_0^2(n)}.$$

Here, $R_n(0) = \sqrt{4\pi}\varphi_n(0)$ is the radial meson wave function, which can also be found from the leptonic width of the ρ meson. One has

$$|R_0(0)|^2 = \mu_0(0)\left(\sigma + \frac{4}{3}\alpha_s\langle r^{-2}\rangle\right) \tag{A.27}$$
$$= \begin{cases} 0.091 \text{ GeV}^3, & \alpha_s = 0, \\ 0.109 \text{ GeV}^3, & \alpha_s = 0.3. \end{cases}$$

These values can be checked vs. the leptonic width of ρ,

$$\Gamma_{e^+e^-} = \begin{cases} 6.36 \text{ keV}, \ \alpha_s = 0, \\ 7.62 \text{ keV}, \ \alpha_s = 0.3, \end{cases}$$

while $\Gamma_{e^+e^-}^{\rm exp} = (6.85 \pm 0.11)$ keV.

Thus, one obtains $\Delta_{\rm HF}^{\rm Pert}$ from (A.26),

$$\Delta_{\rm HF}^{\rm Pert} = \begin{cases} 0.26 \text{ GeV}, \ \alpha_s = 0, \\ 0.24 \text{ GeV}, \ \alpha_s = 0.3. \end{cases}$$

The nonperturbative part $\Delta_{\rm HF}^{\rm NP}$ is expressed through the correlator $D(x)$ [20] and depends on the accepted value of $G_2 \equiv \frac{\alpha_s}{\pi}\langle F_{\mu\nu}^a F_{\mu\nu}^a\rangle$,

$$\Delta_{\rm HF}^{\rm NP} \cong 50 \text{ MeV}\left(\frac{G_2}{0.012 \text{ GeV}^4}\right). \tag{A.28}$$

We take two values of $G_2 = G_2^{\rm st} = 0.012$ GeV^4 and $G_2 = 2G_2^{\rm st}$. Thus, one obtains for the lowest mass of PS state in the $q\bar{q}$ approach (no chiral effects)

$$m_0 = \bar{m}_0 - \frac{3}{4}\Delta_{\rm HF} \tag{A.29}$$
$$= \left[0.652 - \frac{3}{4}(0.3\text{–}0.35)\right] \text{ GeV} = 0.39\text{–}0.43 \text{ GeV}.$$

As a result, we accept the following values for m_0 and m_1 [the latter is calculated in the same way using (A.25) and $\Delta_{\rm HF}(n = 1)$]:

$$m_0 = 0.4 \text{ GeV}, \quad m_1 = 1.35 \text{ GeV}. \tag{A.30}$$

APPENDIX 4

Small Distance Contribution to $\langle\bar{q}q\rangle$

To separate the small-distance contribution, we start from Eq. (6), where we take into account the nonlocal structure of $M_S(u, v)$ and set $m = 0$,

$$\mathrm{tr}\Lambda_{xx} = \int d^4u d^4y \tag{A.31}$$
$$\times \mathrm{tr}(\gamma_5\Lambda(x, y)\gamma_5 M_S(y, u)\Lambda(u, x)).$$

In the limit where one retains the most singular part—the free part of $\Lambda(x,y)$—one has

$$\Lambda(x,y) \approx \Lambda_{\text{free}}(x,y) \tag{A.32}$$
$$= \frac{1}{2\pi^2}\left(\frac{\hat{x}-\hat{y}}{(x-y)^4} + \frac{m}{2(x-y)^2}\right) + \ldots.$$

From (A.1), one can derive the behavior of $M_S(y,u)$ at small $|y-u| \le T_0, T_g$,

$$M_S(y,u) \sim \frac{\sigma}{T_g^2} c|y-u|^2 \Lambda(y,u), \tag{A.33}$$

where the coefficient c is of the order of unity.

The nonperturbative part of $\Lambda(x,y)$ is not singular (modulo logarithms) and is proportional to $\sigma^{3/2}$ [cf. Eq. (A.5)] (apart from the OPE part of Λ, which has $m\langle\bar{q}q\rangle$ and $\langle F^2\rangle$ terms and is even less singular at small x). Finally, inserting (A.33), (A.32) into (A.31) and integrating in the region $|x-y|, |y-u|, |u-x| \le T_0$, one can write the short-distance contribution to (A.31) as

$$\mathrm{tr}\Lambda_{xx}(\text{small distance } \le T_g) = O\left(\sigma m, \sigma^{5/2}\frac{T_0^4}{T_g^2}\right). \tag{A.34}$$

As can be seen from (18), the long-distance part is $O(\sigma^2 T_g)$ and is dominant at $\sigma T_g^2 \to 0, T_0 \le T_g$.

REFERENCES

1. S. Coleman and E. Witten, Phys. Rev. Lett. **45**, 100 (1980).
2. F. Karsch, AIP Conf. Proc. **602**, 323 (2001); hep-lat/0109017; Ch. Schmidt, K. Karsch, and E. Laermann, Nucl. Phys. B (Proc. Suppl.) **106**, 423 (2002).
3. M. Teper, hep-ph/0203203.
4. H. G. Dosch, Phys. Lett. B **190**, 177 (1987); Yu. A. Simonov, Nucl. Phys. B **307**, 512 (1988); for a review see A. Di Giacomo, H. G. Dosch, V. I. Shevchenko, and Yu. A. Simonov, Phys. Rep. **372**, 319 (2002); hep-ph/0007223; H. G. Dosch and Yu. A. Simonov, Phys. Lett. B **205**, 339 (1988).
5. Yu. A. Simonov, JETP Lett. **71**, 127 (2000); V. I. Shevchenko and Yu. A. Simonov, Phys. Rev. Lett. **85**, 1811 (2000).
6. A. Di Giacomo and H. Panagopoulos, Phys. Lett. B **285**, 133 (1992).
7. A. Di Giacomo, E. Meggiolaro, and H. Panagopoulos, Nucl. Phys. B **483**, 371 (1997).
8. Yu. A. Simonov, Yad. Fiz. **60**, 2262 (1997) [Phys. At. Nucl. **60**, 2069 (1997)]; hep-ph/9704301; Yu. A. Simonov and J. A. Tjon, Phys. Rev. D **62**, 014501 (2000); **62**, 094511 (2000).
9. Yu. A. Simonov, Phys. Rev. D **65**, 094018 (2002); hep-ph/0201170.
10. Yu. A. Simonov, hep-ph/0302090.
11. C. G. Callan, R. Dashen, and D. J. Gross, Phys. Rev. D **17**, 2717 (1978); **19**, 1826 (1979); Yu. A. Simonov, Phys. Lett. B **412**, 371 (1997); for a review and references see Th. Shaefer and E. V. Shuryak, Rev. Mod. Phys. **70**, 323 (1998).
12. Y. Nambu and G. Jona-Lasinio, Phys. Rev. **122**, 345 (1961); S. P. Klevansky, Rev. Mod. Phys. **64**, 649 (1992).
13. M. Gell-Mann, R. L. Oakes, and B. Renner, Phys. Rev. **175**, 2195 (1968); S. L. Glashow and S. Weinberg, Phys. Rev. Lett. **20**, 224 (1968).
14. Yu. A. Simonov, Piz'ma Zh. Éksp. Fiz. **54**, 256 (1991) [JETP Lett. **54**, 249 (1991)]; Yad. Fiz. **58**, 357 (1995) [Phys. At. Nucl. **58**, 300 (1995)].
15. A. Yu. Dubin, A. B. Kaidalov, and Yu. A. Simonov, Yad. Fiz. **56** (12), 213 (1993) [Phys. At. Nucl. **56**, 1745 (1993)]; Yu. A. Simonov, hep-ph/9911237.
16. A. M. Badalian, B. L. G. Bakker, and Yu. A. Simonov, Phys. Rev. D **66**, 034026 (2002); hep-ph/0204088; A. M. Badalian and B. L. G. Bakker, Phys. Rev. **66**, 034025 (2002); hep-ph/0202246.
17. M. A. Shifman, A. I. Vainshtein, and V. I. Zakharov, Nucl. Phys. B **147**, 385 (1979); **147**, 448 (1979).
18. M. Jamin, Phys. Lett. B **538**, 71 (2002); hep-ph/0201174.
19. Yu. A. Simonov, Nucl. Phys. B **592**, 350 (2001); M. Foster and C. Michael, Phys. Rev. D **59**, 094509 (1999); V. Bornyakov, G. Schierholz, and T. Streuer, Nucl. Phys. B (Proc. Suppl.) **106**, 676 (2002); hep-lat/0111018.
20. Yu. A. Simonov, hep-ph/0211410.
21. L. Giusti, F. Rapuano, M. Talevi, and A. Vladikas, Nucl. Phys. B **538**, 249 (1999); hep-lat/9807014.
22. R. G. Edwards, V. M. Heller, and R. Narayanan, Phys. Rev. D **59**, 094510 (1999); hep-lat/9811030; P. Hernandez, K. Jansen, and L. Lellouch, Phys. Lett. B **469**, 198 (1999); T. DeGrand (MILC Collab.), Phys. Rev. D **63**, 034503 (2001); hep-lat/0107014.
23. J. A. M. Vermaseren, S. A. Larin, and T. van Ritbergen, Phys. Lett. B **405**, 327 (1997); T. van Ritbergen, J. A. M. Vermaseren, and S. A. Larin, Phys. Lett. B **400**, 379 (1997); K. G. Chetyrkin, Phys. Lett. B **404**, 161 (1997).
24. H. G. Dosch and S. Narison, Phys. Lett. B **417**, 173 (1998); hep-ph/9709215.
25. S. M. Fedorov and Yu. A. Simonov (in preparation).
26. E. E. Salpeter and H. A. Bethe, Phys. Rev. **84**, 1232 (1951).
27. Yu. A. Simonov, Yad. Fiz. **62**, 2087 (1999) [Phys. At. Nucl. **62**, 1932 (1999)]; hep-ph/9912383.
28. P. C. Tiemeijer, PhD Thesis (Utrecht Univ., 1993); P. C. Tiemeijer and J. A. Tjon, Phys. Rev. C **48**, 896 (1993).

Physics of Atomic Nuclei, Vol. 67, No. 5, 2004, pp. 1035–1049. Translated from Yadernaya Fizika, Vol. 67, No. 5, 2004, pp. 1059–1073.

ELEMENTARY PARTICLES AND FIELDS
Theory

Integration over Moduli Space in Superstring Theory

G. S. Danilov

Petersburg Nuclear Physics Institute, Russian Academy of Sciences, Gatchina, 188350 Russia

Received October 15, 2003

Abstract—A calculation of multiloop superstring amplitudes is considered, the equivalence of popular approaches to determining these amplitudes being discussed. A calculation of poorly defined integrals over singular configurations is clarified. Amplitudes obtained by a correct method do not involve divergences in any order of perturbation theory. © *2004 MAIK "Nauka/Interperiodica".*

1. INTRODUCTION

In calculating multiloop amplitudes of the Ramond–Neveu–Schwarz superstring [1–11], the fact that supersymmetric transformations are not split—that is, fermion states are mixed to boson ones—plays an important role. An amplitude is calculated at preset reference fields of a zweibein e_m^a and a two-dimensional gravitino ϕ_m, where m is the vector index on the string world sheet and a is the vector index in the tangent space. Owing to local symmetries, including supersymmetry, the amplitude does not depend on either e_m^a or ϕ_m. Two basic approaches to calculating amplitudes rely on different descriptions of the string world sheet.

Within the supercovariant approach [7–11], which is manifestly supersymmetric on the string world sheet, the quantities e_m^a and ϕ_m have a conformally flat form—that is, $e_m^a = e\delta_m^a$ and $\phi_m = \gamma_m\iota$. Here, γ_m is the two-dimensional Dirac matrix and ι is a two-dimensional spinor. The spin structures are defined by means of supergroups of the Schottky type on a (1|1) complex supermanifold [12]. Generally, a transformation of this supergroup depends on three boson and two Grassmann (odd) complex parameters. At nonzero odd parameters, this transformation mixes bosons and fermions. Not all of such superconformal extensions of ordinary spin structures [13] can be used in superstring theory [14]. Supergroups appropriate for all of the spin structures, including the Ramond sector, were constructed in [11, 15–17]. The integration measures were calculated with the aid of the relations presented in [10, 11] and derived from the requirement that the relevant amplitude be independent of the choice of the reference zweibein and gravitino field. The group of local symmetries of a (super)string is overly wide for each of the integration measures to be unambiguously defined by these relations, apart from a factor independent of moduli. This factor is established from the requirement that the amplitude be factorized as handles move away from each other (this leads to a factorization at the poles associated with intermediate single-particle states). The respective calculation does not employ explicit super Beltrami differentials. Within the theory of a closed and oriented string, local amplitudes involving an arbitrary number of loops were calculated in [11] in an explicit form that is convenient for investigations.

In describing [1–6] a supermanifold by specifying a Riemann surface, the zweibein is chosen to be conformally flat, but the Klein group is split—that is, fermions are not mixed to bosons upon going around noncontractible cycles. Grassmann moduli are carried by the two-dimensional-gravitino field, which cannot therefore have a conformally flat form everywhere on the Riemann surface. In this case, two-dimensional supersymmetry is not manifest. Nevertheless, the amplitude must not depend on the choice of a two-dimensional-gravitino field ϕ_m. As a rule, the gravitino field ϕ_m is chosen as $\phi_m = \phi_m^{(0)}$, where

$$\phi_m^{(0)} = \sum_{s=1}^{2n-2} \lambda_s^{(m)}\phi_{sm}, \quad \gamma^m\phi_m^{(0)} = 0, \qquad (1)$$
$$\lambda_s^{(+)} \equiv \lambda_s, \quad \lambda_s^{(-)} \equiv \overline{\lambda}_s.$$

Here, $\lambda_s^{(m)}$ stands for Grassmann moduli and ϕ_{sm} depends on coordinates and, in general, on boson moduli. For the simplest choice [2] of super Beltrami differentials, the amplitude appears to be dependent on ϕ_{sm}. Under different assumptions, a two-loop amplitude was recently considered in the studies of D'Hoker and Phong [6], where the integration measures are invariant under those supersymmetric transformations for which the local parameter of a transformation is the sum of terms proportional to Grassmann moduli. Since the transformations being discussed are able to change ϕ_{sm}, the integration measures are independent of ϕ_{sm}. Additionally, the integration measures are modular forms and their

1063-7788/04/6705-1035$26.00

GSO projection vanishes. The same is expected for one-, two-, and three-point functions for massless states.

In fact, the amplitude must not depend on the gravitino field taken in the general form $\phi_m = \phi_m^{(0)} + \phi_m^{(1)}$, where $\phi_m^{(1)}$ does not depend on Grassmann moduli but depends on boson moduli and on alien Grassmann numbers (not moduli). The reduction $\phi_m \to \phi_m^{(0)}$ requires a transformation of the general form involving alien Grassmann quantities. Therefore, $\phi_m^{(0)}$ independence is not a sufficient criterion that the amplitude is calculated correctly. Indeed, local amplitudes are determined by the requirement that the integral of a local amplitude with respect to ordinary and Grassmann moduli be independent of local variations of the fields e_m^a and ϕ_m. Within the supersymmetric scheme, this was shown in [10, 11]. In the present study, we propose a similar calculation, relying on the description in [1–6]. We will see that, for different choices of boson and fermion moduli and for different e_m^a and ϕ_m, local amplitudes are related by the Jacobian of the corresponding transformation. Thereby, we establish a relationship between the schemes used in [1–6] and in [7–11], which has so far remained unclear. We will obtain a condition necessary for the super Beltrami differentials to be consistent with two-dimensional supersymmetry. This condition restricts the choice of super Beltrami differentials in schemes where supersymmetry is not manifest. Neither in [2] nor in [6] do the super Beltrami differentials satisfy the above restriction. For two- and three-loop amplitudes, one can take, for moduli, elements of a period matrix on a supermanifold. It is this choice that was made in [6]. The amplitude is then indeed represented by an integral not featuring surface terms, the local amplitude having "good" properties [6]. Nevertheless, the expression that is obtained here for the amplitude differs strongly from that proposed in [6]. The aforementioned properties of a local amplitude are caused by the fact that, for the above choice of moduli, the group of modular transformations on a supermanifold is split. This choice of moduli is possible only for the surfaces of genus 2 and 3, where the moduli and the period matrix are in one-to-one correspondence.

On a supermanifold of genus $n > 3$, the modular group is not split at any choice of moduli. Therefore, the local amplitude is not covariant under modular transformations on a Riemann surface. In the integral, the above modular symmetry is restored owing to surface terms that are always present in this case. In schemes where supersymmetry is not manifest on the string world sheet, surface terms compensate, in addition, the dependence of the local amplitude on the field of the two-dimensional gravitino. The integral must be calculated carefully because of the presence of singularities in the integrand. Indeed, we see that the integral in question with respect to boson and Grassmann variables can converge or diverge, depending on the choice of integration variables. In this case, the integration procedure must be formulated on the basis of the requirement that local symmetries of the amplitude be preserved. Within the supercovariant scheme, such a procedure was developed in [18]. The amplitudes are then obtained to be finite. Moreover, the one-, two-, and three-point amplitudes for massless states vanish. A similar procedure could also be developed in schemes where supersymmetry is not manifest.

In fact, the amplitude can be calculated by using different choices of moduli and different methods for describing supermanifolds. In order to calculate the interaction amplitude explicitly, one must express (in any case with the exception of that of hyperelliptic surfaces) 1-differentials and the period matrix in terms of the parameters of the Klein group whose transformations correspond to rounds about noncontractible cycles. In general, such expressions can be obtained in terms of the parameters of the Schottky groups rather than in terms of the parameters of nonfree groups. Therefore, local amplitudes are naturally obtained in terms of the Schottky variables, but we will see that they can also be expressed in terms of theta-like functions [2]. For local amplitudes involving an arbitrary number of loops ($n > 1$), explicit expressions, which are convenient for investigations, were given in [11] within the supercovariant scheme; however, this can hardly be accessible within the description proposed in [2–6].

2. SUPER BELTRAMI DIFFERENTIALS

Within schemes of the type in [2–6], the amplitude A_n involving n loops is given by an integral of the local amplitude $\widehat{B}_{L,L'}(\{q'_M, \overline{q}'_M\}; \{\phi\})$ with respect to boson and fermion moduli $\{q'_N, \overline{q}'_N\}$; that is,[1)]

$$\widehat{B}_{L,L'}(\{q'_M, \overline{q}'_M\}; \{\phi\}) = \int (\mathcal{D}\Omega)(d^2\Lambda_M) V \exp S_\phi, \tag{2}$$

$$A_n = \int (d^2 q'_N) \sum_{L,L'} \widehat{B}_{L,L'}(\{q'_M, \overline{q}'_M\}; \{\phi\}),$$

where summation is performed over the spin structures L and L' of right- and left-handed fields and $(\mathcal{D}\Omega)$ is the product of the differentials of matter fields and ghost fields that is multiplied by the phase space. Additionally, integration is performed with respect to the global parameters Λ_M and $\bar{\Lambda}_M$ that are dual to the

[1)] An overbar everywhere denotes complex conjugation.

corresponding moduli. Further, we have $M = (m, \alpha)$, where m numbers boson ($m = 1, \ldots, 3n-3$) moduli, while $\alpha \in \{\alpha_i\}$ numbers fermion ($i = 1, \ldots, 2n-2$) moduli. We will use the gravitino field in the form (1), so that ϕ_m is specified by its components $\phi_\pm$ and $q'_{\alpha_i} \equiv \lambda_i$. In general, the local amplitude $\widehat{B}_{L,L'}(\{q'_M, \overline{q}'_M\}; \{\phi\})$ is dependent on ϕ_m, although A_n is expected to be independent of the gravitino field ϕ_m. We denote by V the product of the interaction vertices that is integrated over the supermanifold. The supermanifold is parametrized by the coordinate $t = (z|\vartheta)$, where ϑ is the Grassmann partner of the local coordinate z. The transformation $t \to \Gamma_s(t)$ of the Klein group, where

$$t \to \Gamma_s(t): \quad z \to g_s(z; \{q_m\}), \tag{3}$$
$$\vartheta \to \pm\sqrt{\partial_z g_s(z; \{q_m\})}\vartheta, \quad \partial_z = \frac{\partial}{\partial z},$$

corresponds to the round about the noncontractible cycle s. Since we admit various choices of moduli, it is not assumed that q_m and q'_m must coincide with the Schottky moduli. In general, we have $q'_m \neq q_m = q_m(\{q'_n, \lambda_i\})$ (for example, this is so for the choice made in [6]—see Section 3.) Also, q'_m is a function of the Schottky moduli and the fermion moduli λ_i. Matter fields form the scalar supermultiplets $X^{\mathcal{N}}(t, \bar{t})$, where $\mathcal{N} = 0, \ldots, 9$. The ghosts form the $(3/2)$-superfield $B(t, \bar{t})$ and the (-1)-superfield $C(t, \bar{t})$. Further, we have[2)]

$$S_\phi = \int d^2t \Big[B(t,\bar{t})\Upsilon^{(+)}_{N\ell}(t,\bar{t};\{q'_{M\ell'}\}) - \bar{B}(t,\bar{t})\Upsilon^{(-)}_{N\ell}(t,\bar{t};\{q'_{M\ell'}\}) \Big]\Lambda_{N\ell} + S^{(\phi)}_m(X) + S^{(\phi)}_{\mathrm{gh}}(B,C;\bar{B},\bar{C}), \tag{4}$$

where $S^{(\phi)}_m(X)$ is the matter action functional, $S^{(\phi)}_{\mathrm{gh}}(B, C; \bar{B}, \bar{C})$ is the ghost action functional, and the so-called super Beltrami differentials $\Upsilon^{(\pm)}_{N\ell}(t, \bar{t}; \{q'_{M\ell'}\})$ appear owing to ghost zero modes; also, $M\ell = M\pm$, $q'_{M+} = q'_M$, $q'_{M-} = \overline{q}'_M$, $\Lambda_{M+} = \Lambda_M$, and $\Lambda_{M-} = \bar{\Lambda}_M$. Additionally, we have

$$S^{(\phi)}_{\mathrm{gh}}(B,C;\bar{B},\bar{C}) = \int \frac{d^2z}{\pi} d\vartheta d\overline{\vartheta} \Big[B\widehat{D}^{(\phi)}_+ C - \bar{B}\widehat{D}^{(\phi)}_- \bar{C} \Big], \tag{5}$$

$$S^{(\phi)}_m(X) = -2\int \frac{d^2z}{\pi} d\vartheta d\overline{\vartheta} D^{(\phi)}_+ X_{\mathcal{N}} D^{(\phi)}_- X^{\mathcal{N}},$$

where

$$D^{(\phi)}_- = D + \frac{1}{2}\phi_+ \Big[\vartheta\frac{\partial}{\partial\overline{\vartheta}} + \overline{\vartheta}\vartheta\frac{\partial}{\partial\overline{z}} \Big], \tag{6}$$
$$D^{(\phi)}_+ = \overline{D(t)} + \frac{1}{2}\phi_- \Big[\overline{\vartheta}\frac{\partial}{\partial\vartheta} - \overline{\vartheta}\vartheta\frac{\partial}{\partial z} \Big],$$
$$D(t) = \vartheta\partial_z + \partial_\vartheta, \quad \widehat{D}^{(\phi)}_- = D^{(\phi)}_- - (\overline{\partial_z}\phi_+)\overline{\vartheta}\vartheta,$$
$$\widehat{D}^{(\phi)}_+ = D^{(\phi)}_+ + (\partial_z\phi_-)\overline{\vartheta}\vartheta.$$

For the sake of simplicity, $S^{(\phi)}_m(X)$ is given under the assumption that ϕ_{sm} in (1) do not overlap one another. We write $\Upsilon^{(\pm)}_{N\ell}(t, \bar{t}; \{q'_{M\ell}\})$, which is dual to the boson modulus ($N = n$) or the fermion modulus ($N = \alpha$), as

$$\Upsilon^{(+)}_{N\ell}(t,\bar{t};\{q'\}) = \overline{\vartheta}\vartheta\frac{\partial\phi_-}{\partial q'_{N\ell}} - r^{(+)}_{M\ell'}(t,\bar{t};\{q_{M'\ell''}\})\frac{\partial q_{M\ell'}}{\partial q'_{N\ell}}, \tag{7}$$

$$\Upsilon^{(-)}_{N\ell}(t,\bar{t};\{q'\}) = \vartheta\overline{\vartheta}\frac{\partial\phi_+}{\partial q'_{N\ell}} - r^{(-)}_{M\ell'}(t,\bar{t};\{q_{M'\ell''}\})\frac{\partial q_{M\ell'}}{\partial q'_{N\ell}},$$

where $\{q'\} \equiv \{q'_{M\ell}\}$, $\{q_{M\ell}\} = \{q_M, \overline{q}_M\}$, and $\{q_M\} = \{q_m, \lambda_i\}$. We will show that $r^{(\pm)}_{N\ell}(t, \bar{t}; \{q_{M\ell}\})$ must admit the representation

$$r^{(+)}_{N\ell}(t,\bar{t};\{q_{M\ell}\}) = \widehat{D}^{(\phi)}_+ v^{(+)}_{N\ell}(t,\bar{t};\{q_{M\ell}\}), \tag{8}$$
$$r^{(-)}_{N\ell}(t,\bar{t};\{q_{M\ell}\}) = \widehat{D}^{(\phi)}_- v^{(-)}_{N\ell}(t,\bar{t};\{q_{M\ell}\}),$$

where $v^{(\pm)}_{\alpha\ell}(t, \bar{t}; \{q_{M\ell}\})$ does not have discontinuities upon rounds about any noncontractible cycle and the discontinuity $v^{(\pm)}_{n\ell}(t, \bar{t}; \{q_{M\ell}\})$ is determined by the corresponding transformation (3). Additionally, we have

$$v^{(+)}_{n\ell}(\Gamma_s(t), \overline{\Gamma_s(t)}; \{q_{M\ell}\}) = v^{(+)}_{n\ell}(t,\overline{t};\{q_{M\ell}\})\frac{\partial g_s(z;\{q_m\})}{\partial z} - \frac{\partial g_s(z;\{q_m\})}{\partial q_{n\ell}}, \tag{9}$$

where the discontinuity in question is given by the last term on the right-hand side of (9). It follows from here that $v^{(+)}_{n-}(t, \overline{t}; \{q_{M\ell}\})$ does not have discontinuities. The discontinuity of the function $v^{(-)}_{n\ell}$ is given by the complex-conjugate expression. From (8), it then immediately follow, among other things, that ($d^2t =$

[2)] Summation over dummy indices is implied everywhere in this article, with the exception of the cases of doubly repeated (L, L') or indices in the arguments of functions. The cases where this is not so are indicated explicitly unless they are obvious.

$d^2zd^2\vartheta$)

$$\int d^2t\widehat{\chi}_\alpha^{(\phi+)}(t)r_{n+}^{(+)}(t,\bar{t};\{q_{M\ell}\})=0, \qquad (10)$$
$$\int d^2t\widehat{\chi}_N^{(\phi+)}(t)r_{\alpha\ell}^{(+)}(t,\bar{t};\{q_{M\ell}\})=0,$$

where the integral is taken over the Riemann surface and the ghost zero mode $\widehat{\chi}_M^{(\phi+)}(t)$ is calculated in terms of the Green's function $\widehat{G}_{(\phi)}^{(+)}(t,t')$ by the formula

$$\widehat{\chi}_M^{(\phi+)}(t)=\int d^2t_1\widehat{\chi}_M(t_1)\overline{D(t_1)}\widehat{G}_{(\phi)}^{(+)}(t_1,t), \quad (11)$$

$$\widehat{D}_+^{(\phi)}\widehat{G}_{(\phi)}^{(+)}(t,t')=-\widehat{G}_{(\phi)}^{(+)}(t,t')[\widehat{D}_+^{(\phi)}]^T$$
$$=\delta^2(z-z')\delta^2(\vartheta-\vartheta').$$

Here, the operator $\widehat{D}_+^{(\phi)}$ acts on $(\bar{t},t)$ and the operator $[\widehat{D}_+^{(\phi)}]^T$ acts on $(\bar{t}',t')$. In general, $\widehat{G}_{(\phi)}^{(+)}(t_1,t)$ also depends on $(\bar{t}_1,\bar{t})$, while the zero mode $\widehat{\chi}_M^{(\phi+)}(t)$ of the operator $[\widehat{D}_+^{(\phi)}]^T$ transposed to the operator $\widehat{D}_+^{(\phi)}$ also depends on $\bar{t}$. At $\phi_-\equiv 0$, the function $\widehat{G}_{(\phi)}^{(+)}(t,t')$ reduces to $\widehat{G}(t,t')$, while $\widehat{\chi}_M^{(\phi+)}(t)$ reduces to $\widehat{\chi}_M(t)$, where

$$\widehat{G}(t,t')=-\widetilde{G}_b(z,z')\vartheta'+\vartheta\widetilde{G}_f(z,z'), \qquad (12)$$
$$\widehat{\chi}_m(t')=-\vartheta'\widetilde{\chi}_m(z'), \quad \widehat{\chi}_\alpha(t')=\widetilde{\chi}_\alpha(z').$$

Here, $\widetilde{G}_b(z,z')$ and $\widetilde{G}_f(z,z')$ are, respectively, 2- and (3/2)-tensors in the z' plane, while $\widetilde{\chi}_m(z')$ and $\widetilde{\chi}_\alpha(z')$ are, respectively, 2- and (3/2)-zero modes. Further, we can write

$$\widehat{G}_{(\phi)}^{(+)}(t,t')=\widehat{G}(t,t') \qquad (13)$$
$$-\int d^2\tilde{t}\widehat{G}(t,\tilde{t})[\widehat{D}_+^{(\phi)}-\bar{D}]\widehat{G}_{(\phi)}^{(+)}(\tilde{t},t'),$$

where $\widehat{D}_-^{(\phi)}$ and $D\equiv D(\tilde{t})$ are defined in (6). Since the kernel of this equation is proportional to ϕ_-, it can be solved by iterations. Owing to the presence of zero modes, both functions $\widetilde{G}_b(z,z')$ and $\widetilde{G}_f(z,z')$ have discontinuities in the z plane, this leading to discontinuities in $\widehat{G}_{(\phi)}^{(+)}(t_1,t)$. Calculating $v_{N+}^{(+)}(t,\overline{t};\{q_{M\ell}\})$ in (8) in terms of the Green's function, we can show that the first of the equations in (10) is caused by the fact that the discontinuities of the function $v_{N+}^{(+)}(t,\overline{t};\{q_{M\ell}\})$ do not involve terms proportional to ϑ. The second equation is caused by the absence of discontinuities in $r_{\alpha\ell}^{(+)}(t,\bar{t};\{q_{M\ell}\})$. The constraints in (10) are due to the fact that the relations

$$\int d^2t\widehat{\chi}_M^{(\phi+)}(t)r_{N+}^{(+)}(t,\bar{t};\{q_{M'\ell}\}) \qquad (14)$$
$$=\int\limits_s dt\widehat{\chi}_M^{(\phi+)}(t)[v_{N+}^{(+)}(t,\overline{t};\{q_{M\ell}\})]_s$$

[here, $dt=dzd\vartheta$], which follow directly from (8), cannot be satisfied only by choosing moduli. For the aforementioned discontinuities $[v_{N+}^{(+)}(t,\overline{t};\{q_{M\ell}\})]_s$ of the functions $v_{N+}^{(+)}(t,\overline{t};\{q_{M\ell}\})$ upon a round about the cycle s, the matrix whose elements (MN) are formed by the integrals in (14) with respect to t is indeed degenerate. In (14), the integral for each s is calculated along a noncontractible cycle that corresponds to the same handle and which is dual to the cycle s. We imply that summation is performed over cycles s. The analogous relations for $r_{N-}^{(-)}(t,\bar{t};\{q_{M'\ell}\})$ involve zero modes of the operator $[\widehat{D}_-^{(\phi)}]^T$. The Green's functions and zero modes in (12), which are specified in terms of the Schottky parameters, are considered in [17]. They can also be expressed in terms of vacuum correlation functions [2–6] that depend on arbitrary points (see Appendix A). In this case, $\widetilde{G}_b(z,z')$ is expressed in terms of the correlation function $G_2(z',z;\{p_m\})$, which depends on $3n-3$ points $\{p_m\}$. The function $\widetilde{G}_f(z,z')$ is expressed in terms of the correlation function $G_{3/2}(z',z;\{p_\alpha\})$, which depends on $2n-2$ points $\{p_\alpha\}$. From Eqs. (A.1) and (A.3), it follows, among other things, that the unphysical poles [2] in $\{p_m\}$ and $\{p_\alpha\}$ for the corresponding correlation functions coincide with those zeros of the determinants in (A.1) and (A.3) ($\det\widetilde{A}$ and $\det\hat{A}$, respectively) for which the positions of the points being discussed do not coincide with one another. Since the quantity $r_{\alpha\ell}^{(+)}(t,\bar{t};\{q_{M\ell}\})$ does not have discontinuities, it can be set to zero, as was done in [2–4], but the first of the equalities in (10) is not satisfied in [2–4]. In [6], both constraints in (10) do not hold (see also the next section).

As usual, that part of the contribution from $r_{M\ell}^{+}(t_1,\overline{t}_1;\{q_{M\ell}\})$ to $\hat{B}_{L,L'}(\{q_M,\overline{q}_M\};\{\phi\})$ which is orthogonal to ghost zero modes can be eliminated by a shift of the superfield C. This shift is given by an integral involving that component of the ghost Green's function which is orthogonal to the above ghost zero modes. Upon integration by parts, the remainder reduces to integrals of expressions involving only $[v_{N\ell}^{(+)}(t,\bar{t};\{q_{M\ell}\})]_s$ along noncontractible cycles. Therefore, $\widehat{B}_{L,L'}(\{q_M,\overline{q}_M\};\{\phi\})$ is independent of a particular choice of $v_{Mj}^{(\pm)}(t,\bar{t};\{q_{N\ell}\})$, and the explicit

expression for $v_{Mj}^{(\pm)}(t,\bar{t};\{q_{N\ell}\})$ is not required for calculating the amplitude.

In order to derive Eqs. (7) and (8), we proceed from an integral [19] with respect to all fields, including the zweibein field and the field of the two-dimensional gravitino. In so doing, we map [10, 11] Riemann surfaces onto the complex plane w, choosing the same Klein group $w \to K^{(n)}(w)$ for all surfaces of given genus n. For the sake of simplicity, one can choose the split group. The integral is divided by the volume of the group $\mathcal{G}$ of local symmetries of the amplitude. This group contains the transformations of two-dimensional reparametrization and two-dimensional supersymmetry; local Lorentz transformations in the tangent space; Weyl transformations; and, finally, shifts of the gravitino field by $\gamma_m\iota$. The zweibein $\tilde{e}_m^a(w,\overline{w})$ and the gravitino field $\tilde{\phi}_m(w,\overline{w})$ are expressed in terms of reference fields and the set of gauge functions $\{\Phi\}$. After that, we go over from integration with respect to $\tilde{e}_m^a(w,\overline{w})$ and $\tilde{\phi}_m(w,\overline{w})$ to integration with respect to $\{\Phi\}$ and moduli that characterize the properties of the surface. At first, we will use globally defined transformations. The Klein group will not then change and, hence, will remain the same for all surfaces of given genus. In this case, the reference fields $\{e_m^a(w,\overline{w};\{q_P,\overline{q}_P\}),\phi_m(w,\overline{w};\{q_P,\overline{q}_P\})\}$ depend on the $(3n-3|2n-2)$ complex moduli q_P that are specified apart from modular transformations. Locally, the reference fields in question can have an arbitrary form, this being convenient for deriving Ward identities (see next section). The Jacobian J of the transformation is given by the superdeterminant

$$J = \mathrm{sdet}\begin{pmatrix} \delta\tilde{e}_m^a/\delta\Phi, \partial\tilde{e}_m^a/\partial q_P, \partial\tilde{e}_m^a/\partial\overline{q}_P \\ \tilde{\delta}\phi_m/\delta\Phi, \partial\tilde{\phi}_m/\partial q_P, \partial\tilde{\phi}_m/\partial\overline{q}_P \end{pmatrix}. \quad (15)$$

As usual, the Jacobian is written as an integral with respect to the ghost fields and the global parameters Λ_P and $\bar{\Lambda}_P$, which are dual to q_P and $\overline{q}_P$. It is useful [10, 20] to combine the zweibein and the gravitino field into the superzweibein $E_M^A(f,\bar{f}) \equiv E_M^A(\{f^N\})$, where $f = (w|\hat{\theta})$ and $f^N = (f,\bar{f})$. Here, M or N numbers components (vector and spinor ones) on the string world sheet, while A numbers components in the tangent space. Denoting original f^N by f_1^N, one can find that the change of the superzweibein under the $\mathcal{G}$-group transformation specified by the set $\{\Phi\}$ of local functions is given by

$$E_M^A(\{f_1^N\}) = \frac{\partial f^{N_1}}{\partial f_1^M} E_{N_1}^B(\{f^N\}) U_B^A(\{f^N\},\{\Phi\}), \quad (16)$$

where $U_B^A(\{f^N\},\{\Phi\})$ is a local matrix and $f_1^N \equiv f_1^N(\{f^N\},\{\Phi\})$. The derivatives with respect to the Grassmann coordinates are calculated from the left. Strictly speaking, we imply, in (16), the superzweibein according to [10] rather than according to [20]. In contrast to [20], the superzweibein according to [10] retains its form under the transformations of the full group $\mathcal{G}$; therefore, it is more convenient for calculations. It does not involve an additional scalar field that is present in [20]. The final results are identical in both schemes, that in [10] and that in [20]. Although there is no fully covariant connection with respect to $\mathcal{G}$, there exist two fully covariant differential operators $\widetilde{D}$ and D_b^a, which are what is really needed in superstring theory. The first operator acts on a superscalar, while the second gives the variation of the superzweibein under an infinitesimal transformation of the group $\mathcal{G}$. In this case, we have[3)]

$$\widetilde{D} = E^M\frac{\partial}{\partial f^M}, \quad D_b^a = \rho_b\rho^a\left(\widetilde{D} - \frac{2}{s}\partial_M(sE^M)\right), \quad (17)$$

where

$$\partial_M = \frac{\partial}{\partial f^M}.$$

Here, $s = \mathrm{sdet}(E_M^A)$ and $E^M \equiv E^M(\{f^N\})$ is the spinor component in the tangent space of the inverse superzweibein E_A^M and the derivatives are calculated from the left. Upon integration with respect to $\{\Phi\}$, the amplitude is given by an integral that is similar to that in (2); that is,

$$\widetilde{B}_{L,L'}(\{q_M,\overline{q}_M\};\{e_m^a,\phi_m\}) = \int(\mathcal{D}\Omega)(d^2\Lambda_M)V\exp\widetilde{S}, \quad (18)$$

$$A_n = \int(d^2q_M)\sum_{L,L'}\widetilde{B}_{L,L'}(\{q_M,\overline{q}_M\};\{e_m^a,\phi_m\}),$$

$$\widetilde{S} = \int d^2w d^2\hat{\theta}s\Big[(\widetilde{D}\rho^0X^{\mathcal{N}})\widetilde{D}X_{\mathcal{N}} + \hat{B}_a\Big(D_b^aC^b + \rho_a\widetilde{C}\Big) + \hat{B}_a\rho_b\rho^a \times E^M(\{f^N\};\{q_{R\ell'}\})\frac{\partial E_M^b(\{f^N\};\{q_{R\ell'}\})}{\partial q_{M\ell}}\Lambda_{M\ell}\Big]. \quad (19)$$

Here, $E_A^M(\{f^N\};\{q_{R\ell}\}) = (E_a^M(\{f^N\};\{q_{R\ell}\}), E^M(\{f^N\};\{q_{R\ell}\}))$ is the inverse superzweibein and

[3)] As in [10], we use the matrices ρ^0, ρ^1, ρ^3, and $\rho^\pm = (\rho^1 \pm \rho^0)/\sqrt{2}$. In addition, we have $\rho^0 = -i\sigma_2$, $\rho^1 = \sigma_1$, and $\rho_3 = \sigma_3$, where σ_1, σ_2, and σ_3 are the Pauli matrices. For any Majorana spinor η, we define $(\hat{\eta})^\alpha = \eta_\beta(\rho^0)^\alpha_\beta$.

$\hat{B}_a$ and $(C^a, \tilde{C})$ are the (3/2) and (−1) ghost superfields. Other definitions are given in (17) and in Footnote 3. The derivatives with respect to the Grassmann moduli are calculated from the right. Upon integration with respect to $\tilde{C}$, we have $\hat{B}_a\rho^a = 0$. The last term in the bracketed expression on the right-hand side of (19) bears a resemblance to super Beltrami differentials, but the zweibein in (19) may have an arbitrary form, while the Klein group on the w plane does not depend on q_M. Therefore, q_M appears only in the reference zweibein and the gravitino field. A transition to the conformally flat zweibein is accomplished by means of the appropriate transformation $f^M \to t^M$, where f^M depends on q_m and, possibly, on Grassmann moduli. Since a local gravitational anomaly is absent for the critical superstring being considered, the above transformation changes only the last term in the bracketed expression on the right-hand side of (19) because it involves derivatives with respect to moduli—namely, this term acquires the addition $-D_b^a[v_{R\ell}^M(\{t^N\};\{q_{N\ell}\})E_M^b(\{t^N\})]\Lambda_{R\ell}$, where the operator D_b^a is given in (17) and

$$v_{R\ell}^M(\{t^N\};\{q_{N\ell}\}) \tag{20}$$
$$= \sum_P \epsilon(RP)\frac{\partial f^P(\{t^N\};\{q_{N\ell}\})}{\partial q_{R\ell}}\frac{\partial t^M}{\partial f^P}.$$

Here, $\epsilon(RP) = 1$ if both R and P are boson (fermion) components. Otherwise, we have $\epsilon(RP) = -1$. In the derivation, we use the relation

$$\sum_{M,N}\Big[\epsilon(M(N+R))E^M v_{R\ell}^N \partial_M E_N^a \tag{21}$$
$$-\epsilon(MR)E^M v_{R\ell}^N \partial_N E_M^a\Big] - \sum_M \frac{2}{s}(\partial_M s E^M)v_{R\ell}^a = 0.$$

It is sufficient to verify formula (21) for $e_m^a = e\delta_m^a$ and $\phi_m = 0$ since its right-hand side is covariant under local transformations of the group $\mathcal{G}$ (if use is made of the superzweibein according to [10]). Upon integration with respect to $\tilde{C}$ and the corresponding redefinition of fields and global parameters, one obtains expression (2) involving the quantities given by formulas (4), (7), and (8). Apart from factors, $v_{R\ell}^{(\pm)}(t,\bar{t};\{q_{M\ell}\})$ is equal to $v_{R\ell}^M(\{t^N\};\{q_{N\ell}\})$, where the vector index is $M = \pm$. In contrast to the transformations of the Klein group on the supermanifold f, the transformations $t \to \Gamma_s(t)$ (3) depend on q_m. A variation of the quantity $v_{R\ell}^M(\{t^N\};\{q_{N\ell}\})$ under this transformation is obtained directly from (20); as a result, we have formula (9). Bypassing (18) and (19), one can also derive formula (2) directly from an integral with respect to fields, including the zweibein field and the fields of two-dimensional gravitino. In this case, the derivatives with respect to $q_{M\ell}$ in the Jacobian arise because the transformation $f_1^M \to t^M$ depends on $\{q_{M\ell}\}$.

The gravitino field ϕ_m in (2) can be reduced to a given field $\hat{\phi}_m^{(0)}$ by means a local group-$\mathcal{G}$ transformation that preserves a conformally flat form of the zweibein and the Grassmann moduli independence of the transformations of the Klein group. The boson moduli then acquire Grassmann additions that depend on ϕ_m. Therefore, the dependence on ϕ_m disappears only upon integration with respect to moduli under the condition that the integral is globally invariant under the transformation being discussed. In this case, one can also go over to the supercovariant description according to [7–11, 17], reducing ϕ_m to zero. Thus, the two descriptions are equivalent.

3. LOCAL AMPLITUDE AND INTEGRATION DOMAIN

The integral in (2) with respect to fields requires a regularization ensuring that the superstring amplitude does not depend on local variations of reference fields. This integral can also be obtained by solving the Ward relations that are similar to those in [10, 11] and which were derived from the requirement $\delta_\perp A_n = 0$. Here, $\delta_\perp A_n$ is a variation of the amplitude in (18) under infinitesimal transverse variations $\delta_\perp e_m^a$ and $\delta_\perp\phi_m$ of the zweibein e_m^a and the two-dimensional-gravitino field ϕ_m. In this case, we have $e_a^m\delta_\perp e_m^a = e_a^m\varepsilon_{ab}\delta_\perp e_m^b = 0$ and $\gamma^m\phi_m = 0$, where $\varepsilon_{-+} = -\varepsilon_{+-} = 1$. The phase space in (18) depends on e_m^a and ϕ_m, but it is invariant under the above variations. Therefore, the variation $\delta_\perp A_n$ of the superstring amplitude (18) is due only to the variation of the functional in (19). Going over to the conformally flat zweibein, we obtain the relations for $\hat{B}_{L,L'}(\{q_M,\overline{q}_M\};\{\phi\})$ in (2). Since $\delta_\perp e_m^a$ and $\delta_\perp\phi_m$ are arbitrary, the relations are local in $t = (z|\vartheta)$. Further, we have

$$\widehat{B}_{L,L'}(\{q_M,\overline{q}_M\};\{\phi\}) \tag{22}$$
$$= \widehat{Z}_{L,L'}(\{q_M,\overline{q}_M\};\{\phi\})\langle V\rangle_\phi,$$

where $\langle V\rangle_\phi$ is the vacuum expectation value of V in (2) and $\widehat{Z}_{L,L'}(\{q_M,\overline{q}_M\};\{\phi\})$ is a vacuum function. For the sake of simplicity, we set $q'_m = q_m$ [see (2) and (3)]. As before, we have $\{q_\alpha\} = \{\lambda_i\}$. In (1), we set $\phi_{s-} = \pi\delta^2(z - z_{(s)})$ and $\phi_{s+} = \pi\delta^2(z - \overline{z}'_{(s)})$, assuming that all $z_{(s)}$ and $\overline{z}'_{(s)}$ differ from one another. Concurrently, the δ functions can be smoothed if this is necessary. The specified points can depend on boson moduli. In order to calculate the integral under consideration, it is sufficient to assume that $\delta_\perp e_m^a$ and

$\delta_\perp\phi_m$ are nonzero at points that are different from $z_{(s)}$ and $\bar{z}'_{(s)}$. The derivation of the required equations is similar to the derivation of equations in [10], the results being

$$\widehat{\chi}_N^{(\phi+)}(t)\frac{\partial}{\partial q_N}\ln\widehat{Z}_{L,L'}(\{\phi\}) = \langle T\rangle_\phi - \frac{\partial}{\partial q_N}\widehat{\chi}_N^{(\phi+)}(t), \tag{23}$$

$$\widehat{\chi}_N^{(\phi+)}(t)\frac{\partial}{\partial q_N}\langle V\rangle_\phi = \langle TV\rangle_\phi - \langle T\rangle_\phi\langle V\rangle_\phi;$$

$$T = -(DX^{\mathcal{N}})\partial_z X_{\mathcal{N}} + \frac{3}{2}B\partial_z F + (\partial_z B)F - \frac{1}{2}(DB)(DF), \tag{24}$$

$$\widehat{\chi}_N^{(\phi+)}(t) = -\langle B(t,\bar{t})\Lambda_N\rangle_\phi,$$

$$F(t,\bar{t}) = C(t,\bar{t}) - v_{N\ell}^{(+)}(t,\bar{t};\{q_{M\ell}\})\Lambda_{R\ell}, \tag{25}$$

along with the analogous equations for the derivatives with respect to the complex-conjugate moduli $\overline{q}_N$. Here, $\widehat{Z}_{L,L'}(\{\phi\}) \equiv \widehat{Z}_{L,L'}(\{q_M,\overline{q}_M\};\{\phi\})$ is the same as in (22), $\widehat{\chi}_N^{(\phi+)}(t)$ are given in (11), and $F(t,\bar{t})$ has discontinuities that are calculated according to (9). The derivatives with respect to $\{q_\alpha\}$ are calculated from the right. All of the derivatives with respect to the moduli are calculated under the condition that the zweibein remains conformally flat. In the presence of the gravitino, the correlation function $\langle XX\rangle_\phi$ for scalar superfields, the correlation function $\langle CB\rangle_\phi$ for ghost superfields, and the zero modes $\langle B\Lambda_{M\ell}\rangle_\phi$ are calculated in a standard way by supplementing expression (4) with the term $[X\tilde{\mathcal{X}} + B\tilde{\mathcal{C}} + \tilde{\mathcal{B}}C + \mathcal{L}_{R\ell}\Lambda_{R\ell} + \text{c.c.}]$, which contains the sources $\tilde{\mathcal{X}}$, $\tilde{\mathcal{B}}$, $\tilde{\mathcal{C}}$, and $\mathcal{L}_{R\ell}$ of the corresponding fields $(X,B,C,\Lambda_{R\ell})$. The terms that are linear in C or in the nonzero modes of the field B are removed by shifts of the fields (B,C) with the aid of that component of the Green's function $G^{(\phi+)}(t;t_1)$ which is orthogonal to $\widehat{\chi}_N^{(\phi+)}(t_1)$. As usual, the dependence on the sources is singled out in the form of an exponential of $[-\tilde{\mathcal{X}}\langle XX\rangle_\phi\tilde{\mathcal{X}} - \tilde{\mathcal{B}}\langle CB\rangle_\phi\tilde{\mathcal{C}} - \mathcal{L}_{M\ell}\langle\Lambda_{M\ell}B\rangle_\phi\tilde{\mathcal{C}}]$. By using $\langle CB\rangle_\phi$ and $\langle B\Lambda_{M\ell}\rangle_\phi$, one can calculate $\langle FB\rangle_\phi$, where $F \equiv F(t,\bar{t})$ is defined in (25). In contrast to $\langle CB\rangle_\phi$, neither $\langle FB\rangle_\phi$ nor $\langle B\Lambda_N\rangle$ depend on the choice of the function $v_{Mj}^{(\pm)}(t,\bar{t};\{q_{N\ell}\})$. For a δ-function field ϕ_-, the required correlation function $\langle FB\rangle_\phi$ involves an ambiguity, which can be removed if one first takes a smoothed field ϕ_-. If $\{\lambda_i = 0\}$, then

$$-\langle F(t)B(t')\rangle_{\phi=0} \equiv G(t,t') = -\widetilde{G}_b(z,z')\vartheta' + \vartheta G_{3/2}(z',z;\{z_{(i)}\}), \tag{26}$$

where $\{z_{(i)}\}$ is the set of points at which $\phi_- \neq 0$; for information about $G_{3/2}(z',z;\{z_{(i)}\})$, see the text after formula (14) and Appendix A. The correlation function for scalar superfields is given by the Green's function for the operator $D_-^{(\phi)}D_+^{(\phi)}$ [see (6)]. Here, the holomorphic Green's functions, as well as superscalar functions and their periods, are constructed for the operator $D_+^{(\phi)}$. For $\phi_m \equiv 0$, they are given in [1, 7, 11] in terms of the Schottky variables. In calculating T, one discards the singularity at coinciding arguments in the correlation functions in (24). Because of the superfield F, the quantity T has a discontinuity under the transformation in (3). This discontinuity is canceled by the discontinuity of the derivative $-\partial_{q_N}\hat{\chi}_N^{(\phi+)}(t)$. As a result, the right-hand side of the first equality in (23) does not have discontinuities in the z plane.

Equations (23) are analogous to the corresponding equations in [10, 11], but, there, the vacuum correlation functions and zero modes are calculated on the nonsplit supermanifold [10, 11, 17] specified by the transformations $\tilde{t} \to \tilde{\Gamma}_s(\tilde{t})$ of the super Schottky groups. Here, $\tilde{t} = (\tilde{z}|\tilde{\vartheta})$ is a coordinate on this supermanifold and the spin structures L and L' are defined on the aforementioned supergroups. Concurrently, the Schottky multiplier $\tilde{k}_s$ and two limiting points $(\tilde{u}_s|\tilde{\mu}_s)$ and $(\tilde{v}_s|\tilde{\nu}_s)$ on the supermanifold correspond to each handle. Further, (3|2) of $(\tilde{u}_s,\tilde{v}_s|\tilde{\mu}_s,\tilde{\nu}_s)$ moduli are fixed owing to $SL(2)$ symmetry and, hence, do not enter into the set of $(3n-3|2n-2)$ complex moduli $\{\tilde{q}_M\}$. The amplitude is given by an integral of the type in (2) of the local amplitude $B_{L,L'}(\{\tilde{q}_M,\overline{\tilde{q}_M}\}) \equiv B_{L,L'}$, where

$$B_{L,L'} = \widetilde{Z}_{L,L'}(\{\tilde{q}_M,\overline{\tilde{q}_M}\})\langle V\rangle, \tag{27}$$

$$\widetilde{Z}_{L,L'}(\{\tilde{q}_M,\overline{\tilde{q}_M}\}) = \det{}^{-5}[\tilde{\omega}(\{\tilde{q}_M\};L) + \overline{\tilde{\omega}(\{\tilde{q}_M\};L')}]Z_L(\{\tilde{q}_M\})\overline{Z_{L'}(\{\tilde{q}_M\})}.$$

Here, $\langle V\rangle$ is the integral of the vacuum expectation value of the product of interaction vertices over the supermanifold. Further, $\widetilde{Z}_{L,L'}(\{\tilde{q}_M,\overline{\tilde{q}_M}\})$ is a vacuum function, $Z_L(\{\tilde{q}_M\})$ being a holomorphic function of q_M. For all even spin structures, the quantities $B_{L,L'}$ were derived in [11]. Here, $\tilde{\omega}(\{\tilde{q}_M\};L)/(2\pi i)$ is the period matrix on the supermanifold. Since fermions are mixed to bosons, the matrix $\tilde{\omega}(\{\tilde{q}_M\};L)$ depends on the Grassmann moduli and on L. The substitutions $\tilde{t} \to t$ and $\tilde{q}_M \to q_M$ preserve a conformally flat zweibein, but the generating transformations $t \to \Gamma_s(t)$ of the Klein group become independent of Grassmann moduli; therefore, there appears a gravitino field. Further, we

have $\tilde{\omega}(\{\tilde{q}_M\};L)=\omega(\{q_M\};L)/(2\pi i)$—that is, the period matrix on the supermanifold coincides with the period matrix $\omega(\{q_M\};L)/(2\pi i)$ calculated for the superscalar functions of the operator $D_+^{(\phi)}$ in (5). In [6], it was referred to as "the super period matrix." We take $\tilde{t}(t)$ that is holomorphic everywhere, with the exception of poles at the points $z=z_{(i)}$, this leading to the appearance of the δ-like gravitino field that does not vanish at the points $z=z_{(i)}$. In this case, one has [12, 17]

$$\tilde{z}=z+f(z)+[1+f'(z)]\vartheta\xi(z), \qquad (28)$$

$$\tilde{\vartheta}=\sqrt{1+f'(z)}\left[\left(1+\frac{1}{2}\xi(z)\xi'(z)\right)\vartheta+\xi(z)\right],$$

$$\frac{\partial f(z)}{\partial\bar{z}}+[1+f'(z)]\xi(z)\frac{\partial\xi(z)}{\partial\bar{z}}=0,$$

where $f(z)$ and $\xi(z)$ are, respectively, a boson and a fermion function; $f'(z)=\partial_z f(z)$; and $\xi'(z)=\partial_z\xi(z)$. Owing to the last relation in (28), the zweibein remains conformally flat, as follows from (16) and from the explicit form of the superzweibein according to [10] or [20]. Upon the transformation in (28), the supertensor of rank p acquires the known factor $[D(t)\tilde{\vartheta}]^{-p}$. In addition, the ghost zero modes are transformed by the matrix $\partial q_m/\partial\tilde{q}_N$. In the same way as in [17], the modular transformation leads to $\langle FB\rangle\to\langle FB\rangle_\phi$ + an extra term that generates an addition to T. This addition is canceled by that addition to $\partial_{q_N}\widehat{\chi}_N^{(\phi+)}(t)$ which emerges from the fact that transformation (28) depends on the moduli. As a result, there arise Eqs. (23). Concurrently, Eqs. (22) and (27) are related by the Jacobian $\hat{J}$ of the transformation $(\tilde{q}_M,\overline{\tilde{q}_M})\to(q_M,\overline{q}_M)$:

$$\widehat{Z}_{L,L'}(\{q_M,\overline{q}_M\};\{\phi\})=\hat{J}\widetilde{Z}_{L,L'}(\{\tilde{q}_M,\overline{\tilde{q}_M}\}), \qquad (29)$$
$$\langle V\rangle_\phi=\langle V\rangle.$$

In order to calculate $\tilde{t}(t)$ and $\tilde{q}_M(\{q_N\})$, we use the method developed in [17] for the modular transformations. In this case, both $\tilde{t}(t)$ and $\tilde{q}_M(\{q_N\})$ are calculated in [17] by using the set of equations $\tilde{\Gamma}_s(\tilde{t}(t))=\tilde{t}(\Gamma_s(t))$. By way of example, we consider surfaces of genus 2. For the sake of definiteness, we fix $\tilde{u}_1,\tilde{v}_1,\mu_1,\nu_1$, and $\tilde{u}_2$ by the equalities $\tilde{u}_1=u_1$, $\mu_1=0$, $\tilde{v}_1=v_1$, $\nu_1=0$, and $\tilde{u}_2=u_2$. Furthermore, we define $\tilde{q}_m=q_m-\delta q_m$. We then have

$$\delta q_m=\frac{\lambda_1\lambda_2}{4}\left[\widetilde{G}_f(z_{(1)},z_{(2)})\widetilde{\chi}_m(z_{(1)})\right. \qquad (30)$$
$$-\widetilde{G}_f(z_{(2)},z_{(1)})\widetilde{\chi}_m(z_{(2)})$$
$$-\oint_2 dz\widetilde{\chi}_m(z)[P_1(z)\widetilde{G}_f(z,z_{(2)})$$
$$\left.-P_2(z)\widetilde{G}_f(z,z_{(1)})]\right],$$

$$P_i(z)=2\frac{z-v_2}{u_2-v_2}\widetilde{\chi}_{\mu_2}(z_{(i)})-2\frac{z-u_2}{u_2-v_2}\widetilde{\chi}_{\nu_2}(z_{(i)}),$$
$$\mu_2=\lambda_1\widetilde{\chi}_{\mu_2}(z_{(1)})+\lambda_2\widetilde{\chi}_{\mu_2}(z_{(2)}),$$
$$\nu_2=\lambda_1\widetilde{\chi}_{\nu_2}(z_{(1)})+\lambda_2\widetilde{\chi}_{\nu_2}(z_{(2)}).$$

Here, the functions $\widetilde{G}_b(z,z')$, $\widetilde{G}_f(z,z')$, $\widetilde{\chi}_m(z)$, and $\widetilde{\chi}_\alpha(z)$ at $\alpha=(\mu_2,\nu_2)$ are the same as in relations (12), (A.1), and (A.3). Integration is performed in the positive direction along the contour surrounding both Schottky circles of handle 2 and, for a handle of the Ramond type, the cut between the points u_2 and v_2, which exists in this case [11, 17]. Furthermore, δq_m does not have discontinuities in the $z_{(1)}$ and $z_{(2)}$ planes, this being ensured by the choice of the Green's function $\widetilde{G}_f(z,z_{(2)})$. For the above choice, $\widetilde{G}_f(z,z_{(2)})$ does not have discontinuities upon the rounds about A_1 and B_1 cycles. Moreover, $\widetilde{G}_f(z_{(s)},z_{(i)})-P_i(z)$ does not have discontinuities in the $z_{(s)}$ plane upon the rounds about A_2 and B_2 cycles. The latter follows from the fact that the discontinuity of the integral in (30) upon the round about A_2 and B_2 cycles in the $z_{(i)}$ plane arises because of the pole of the function $\widetilde{G}_f(z,z_{(i)})$ at $z=z_{(i)}$ and coincides with the discontinuity of the polynomial $-P_s(z_{(i)})$. Integrals of this type are discussed in detail in [17]. The derivation of formulas (30) is analogous to the calculation developed in [17] for modular transformations. If we use Schottky moduli, then δq_m is $(\delta v_2,\delta k_1,\delta k_2)$. If the period matrix $\omega_{rs}^{(0)}/(2\pi i)$ on a Riemann surface is used for moduli, then $q_m\to q_{ij}$, where $i\le j$, and $\widetilde{\chi}_m(z)\to\widetilde{\chi}_{ij}(z)=J_i(z)J_j(z)$. Here, $J_r(z)$ is a scalar function with periods $\omega_{rs}^{(0)}$. As above, we identify q'_m in (2) with q_m.

From (29), it is obvious that the local amplitude in (22) depends on the points $z_{(i)}$ and $\overline{z}'_{(i)}$ of the gravitino field. On the other hand, the superstring amplitude represented by an integral of the local amplitude (27) does not involve the gravitino field. In fact, the $z_{(i)}$- and $\overline{z}'_{(i)}$-dependent terms in (29) are total derivatives in moduli space, which, upon integration by parts, are canceled by the surface terms in the integral. In the integral of (27), the surface terms are caused by the fact that expression (27) is covariant [17] under modular transformations [17] on the nonsplit supermanifold [12]. In general, this supermodular transformation [17] is a globally defined holomorphic variation of the coordinate $\tilde{t}$ that is accompanied by a holomorphic variation of the moduli $\{\tilde{q}_M\}$ and the change in

the spin structure. Therefore, integration of expression (27) with respect to $\{\tilde{q}_M\}$ is performed over the fundamental region of the supermodular group—that is, the group of supermodular transformations being discussed. The boundary of the region is formed by the moduli that are related by supermodular transformations mixing fermion moduli to boson ones. In just the same way as the ordinary modular transformation [21], the supermodular transformation specifies a new basis of noncontractible cycles. Therefore, the period matrix $\tilde{\omega}(\{\tilde{q}_M\}; L)$ in (27) is varied in the same way as the matrix $\omega^{(0)}(\{q_m\})$ is varied [21] under the corresponding modular transformation on a Riemann surface. In this case, the boundary of the fundamental domain is determined by a set of conditions of the type $\mathcal{G}_i(\omega(\{q_M\}; L), \overline{\omega(\{q_M\}; L')}) = 0$, where the functions $\mathcal{G}_i$ were obtained by a superconformal extension [18] of the functions that determine the boundary in [21]. Thus, the superstring amplitude is given by the product of the integral of expression (27) and $\mathcal{O}(\{\mathcal{G}_i\})$, where

$$\mathcal{O}(\{\mathcal{G}_i\}) = \prod_i \varrho(\mathcal{G}_i), \tag{31}$$
$$\mathcal{G}_i \equiv \mathcal{G}_i(\omega(\{q_M\}; L), \overline{\omega(\{q_M\}; L')}),$$

$\omega(\{q_M\}; L') = \tilde{\omega}(\{\tilde{q}_M\}; L')$, and $\varrho(x) = 1$ for $x > 0$ and $\varrho(x) = 0$ for $x < 0$. This step function is taken in the sense that it is expanded in Grassmann parameters contained in x. It is this circumstance that obviously leads to surface terms in the integral. Otherwise, integration is performed over the fundamental domain [21] of the ordinary modular group. A shift of the integration variables that is proportional to the Grassmann parameters changes surface terms as well. As a result, the integral does not depend on the choice of integration variables. Moreover, the same integral over any other fundamental domain can be obtained by means of supermodular transformations. Therefore, the integral does not depend on the fundamental domain over which it is calculated (provided that the singularities are integrated correctly—see the next section), as it must. By applying the transformation $\tilde{q}_M \to q_M$, one obtains the integral in (2), where $q'_m = q_m$. As above, the quantity $\omega(\{q_M\}; L)/(2\pi i)$ in (31) is calculated as periods of superscalar functions for the operator $D_+^{(\phi)}$ in (5). For a δ-like gravitino field, we denote this matrix by $\omega_{rs}^{(+)}(\{q_M\}; \{z_{(i)}\}; L)/(2\pi i)$. In particular, a matrix of genus 2 is obtained to be

$$\omega_{rs}^{(+)}(\{q_M\}; \{z_{(i)}\}; L) = \omega_{rs}^{(0)}(\{q_m\}) \tag{32}$$
$$- \frac{\lambda_1\lambda_2}{2}[\partial_{z_{(1)}} J_r(z_{(1)})] R_f(z_{(1)}, z_{(2)}; L)[\partial_{z_{(2)}} J_s(z_{(2)})],$$

where, as before, $\omega_{rs}^{(0)}(\{q_m\})/(2\pi i)$ is an ordinary period matrix; $J_r(z)$ have the periods $\omega_{rs}^{(0)}(\{q_m\})$; and the Green's function $R_f(z, z'; L)$ is a (1/2)-tensor in each of the arguments, this Green's function satisfying the condition $R_f(z, z'; L) \to (z - z')^{-1}$ for $z \to z'$.

The second equality in (23) is satisfied if the known expression from [1] is used for the interaction vertices. The vacuum function in (22) has the form

$$\widehat{Z}_{L,L'}(\{q_M, \overline{q}_M\}; \{\phi\}) \tag{33}$$
$$= \frac{\Xi_L(\{q_m\}; \{z_{(i)}\})\overline{\Xi_{L'}(\{q_m\}; \{z'_{(i)}\})}}{\det^5[2\mathrm{Re}\,\omega^{(0)}(\{q_m\})]}$$
$$\times \breve{Z}_{L,L'}(\{q_M, \overline{q}_M\}; \{z_{(i)}, \overline{z}'_{(i)}\}),$$

where $\omega^{(0)}(\{q_m\})/(2\pi i)$ is identical to that in (32) and $\breve{Z}_{L,L'}(\{q_M, \overline{q}_M\}; \{z_{(i)}, \overline{z}'_{(i)}\})$ is a function such that $\breve{Z}_{L,L'}(\{q_M, \overline{q}_M\}; \{z_{(i)}, \overline{z}'_{(i)}\}) = 1$ if $\{\lambda_i = 0\}$. Here, $\breve{Z}_{L,L'}(\{q_M, \overline{q}_M\}; \{z_{(i)}, \overline{z}'_{(i)}\})$ and $\langle V\rangle_\phi$ are calculated by expanding the expression $\exp[S_m^{(\phi)}(X) + S_{\mathrm{gh}}^{(\phi)}(B, F; \bar{B}, \bar{F})]$ in powers of ϕ_m. The quantity $\langle V\rangle_\phi$ can also be calculated by using the correlation function for scalar superfields in the gravitino field ϕ_m. The result obtained in this way is then expanded in powers of ϕ_m. We can see that the supercurrent caused by ghosts is calculated in terms of the correlation function (26) rather than in terms of (B, C). An ambiguity in $G_{3/2}(z_{(j)}, z_{(s)}; \{z_{(i)}\})$ is removed by calculating this correlation function for a smoothed gravitino field. The same result can be obtained by applying the above transformation to the amplitude in (27), which does not involve the ambiguity being discussed. We note that, under the transformation in question, the initial and final moduli are related by the transformation in (30). In order to isolate each of the derivatives $\partial \ln \widehat{Z}_{L,L'}(\{\phi\})/\partial q_N$ in (23), both sides of the first equation in (23) are multiplied by an appropriate polynomial in t, and the result is integrated over noncontractible cycles. This derivation (which is omitted here) is analogous to the derivation in [10, 11, 17]. As a matter of fact, Eq. (23) is used to calculate $\Xi_L(\{q_m\}; \{z_{(i)}\})$ in (33). In this case, we have

$$\Xi_L(\{q_m\}; \{z_{(i)}\}) \tag{34}$$
$$= \Xi'_L(\{q_m\}; \{p_n\}; \{z_{(i)}\})/\det[\widetilde{\chi}_m(p_n)],$$
$$\Xi_L(\{q_m\}; \{z_{(i)}\}) = Z'_L(\{q_m\})/\det[\widetilde{\chi}_\alpha(z_{(i)})].$$

Here, $Z'_L(\{q_m\})$ was calculated in [11, 17] in terms of the Schottky parameters {in the notation used in [17],

$Z'_L(\{q_m\})$ is equal to $Z_{0(m)}Z_{0(gh)}H$, where H is calculated for zero Grassmann parameters—see (B5)–(B7) in [17]} and is independent of the localization points of the Beltrami differentials. The zero modes $\widetilde{\chi}_m(z)$ and $\widetilde{\chi}_\alpha(z)$ were determined above. Apart from a constant factor, the quantity $\Xi'_L(\{q_m\};\{p_n\};\{z_{(i)}\})$ is the product of the corresponding chiral determinants in [2], which have the localization points $\{p_n\}$ and $\{z_{(i)}\}$. Indeed, it is shown in Appendix B that $\Xi'_L(\{q_m\};\{p_n\};\{z_{(i)}\})$ obeys the same equations with respect to variations of the metric as the above product of the chiral determinants, which was obtained in [2] in terms of theta functions and functions related to them. As was mentioned above, vacuum correlation functions (in particular, see Appendix A) can also be expressed both in terms of functions that are relative to theta functions and in terms of the Schottky parameters. Thus, the local amplitude in (22) can be written in the above two forms. It differs from the amplitude in [2] by the contribution caused by ghosts and also by the presence of surface terms, which are absent in [2].

The surface terms can be eliminated from only two- and three-loop amplitudes. For this, it is necessary to make the substitution of moduli $q_r \to q'_r$ in such a way as to remove the dependence on Grassmann parameters in the period matrix $\omega(\{q_M\};L)/(2\pi i)$ on the supermanifold. We then have $\omega(\{q_M\};L)=\omega^{(0)}(\{q'_m\})$, where, as above, $\omega^{(0)}(\{q'_m\})/(2\pi i)$ is the ordinary period matrix. In particular, it follows from (32) that, for a surface of genus 2, we have

$$\sum_r \delta q'_r \frac{\partial\omega^{(0)}_{mn}(\{q'_s\})}{\partial q'_r} = \frac{1}{2}[\partial_{z_{(1)}}J_m(z_{(1)})] \times R_f(z_{(1)},z_{(2)};L)[\partial_{z_{(2)}}J_n(z_{(2)})], \qquad (35)$$
$$q_r = q'_r + \lambda_1\lambda_2\delta q'_r,$$

where q'_m, which are new boson moduli, do not involve Grassmann parameters. In the local amplitude, only the term $\lambda_1\lambda_2\overline{\lambda}_1\overline{\lambda}_2\widetilde{B}_{L,L'}$, which is proportional to $\lambda_1\lambda_2\overline{\lambda}_1\overline{\lambda}_2$, contributes to the integral. We will show that $\tilde{B}_{L,L'}$ does not depend on the localization of the gravitino field. Indeed, the quantity $\tilde{B}_{L,L'}$ can be expressed in terms of (27) by using the change of variables $\tilde{q}_m \to q'_m, (\mu_2,\nu_2)\to(\lambda_1,\lambda_2)$. The result can be written as

$$\widetilde{B}_{L,L'} = B^{(11)}_{L,L'} + \frac{\partial}{\partial q'_m}\frac{\partial}{\partial\overline{q}'_n}\left[\mathcal{K}_m(L)\overline{\mathcal{K}}_n(L')B^{(00)}_{L,L'}\right] - \frac{\partial}{\partial q'_m}\left[\mathcal{K}_m(L)B^{(01)}_{L,L'}\right] - \frac{\partial}{\partial\overline{q}'_n}\left[\overline{\mathcal{K}}_n B^{(10)}_{L,L'}\right], \qquad (36)$$

$$\mathcal{K}_m = \frac{\delta q_m - \lambda_1\lambda_2\delta q'_m}{\det[\widetilde{\chi}_\alpha(z_{(i)})]},$$

$$B_{L,L'} = B^{(00)}_{L,L'} + \mu_2\nu_2 B^{(10)}_{L,L'} + \overline{\mu}_2\overline{\nu}_2 B^{(01)}_{L,L'} + \mu_2\nu_2\overline{\mu}_2\overline{\nu}_2 B^{(11)}_{L,L'}.$$

Here, $B^{(jl)}_{L,L'}$ is independent of (μ_2,ν_2), $B_{L,L'}$ is given by (27), (μ_2,ν_2) is expressed in terms of (λ_1,λ_2) according to (30), and the relation between $\tilde{q}_m$ and q'_m can be seen from (30) and (35). In (36), only the quantity $\mathcal{K}_m$ can depend on $z_{(1)}$ and $z_{(2)}$. It can easily be seen, however, that the residue at the point $z_{(1)}\to z_{(2)}$ on the right-hand side of (35) is equal to $[\partial_{z_{(2)}}J_m(z_{(2)})][\partial_{z_{(2)}}J_n(z_{(2)})]$ and is canceled by the residue of the expression $[\partial_{q'_r}\omega^{(0)}_{mn}(\{q'_s\})]\widetilde{\chi}_r(z_{(2)})$. If we choose $\omega^{(0)}_{mn}$ for moduli, the tensor zero modes are indeed $[\partial_{z_{(2)}}J_m(z_{(2)})][\partial_{z_{(2)}}J_n(z_{(2)})]$ [see the text after Eq. (30)]. Therefore, the quantity $[\delta q'_m - \delta\hat{q}_m]$ remains finite at $z_{(1)}=z_{(2)}$. Further, the expression $[\delta q_m - \delta\hat{q}_m]$ is antisymmetric in its arguments and is a (3/2)-tensor in each of them. Therefore, the $z_{(1)}$ and the $z_{(2)}$ dependence of this expression is isolated in the form of the factor $\det[\widetilde{\chi}_\alpha(z_{(i)})]$. Thus, $\mathcal{K}_m$ does not depend on $z_{(1)}$ and $z_{(2)}$. Therefore, $\widetilde{B}_{L,L'}$ does not depend on the points $z_{(1)}$ and $z_{(2)}$ either. We denote by $\widehat{Z}^{(0)}_{L,L'}(\{q'_M,\overline{q}'_M\})$ the vacuum function in terms of the variables q'_m. By using (27), one can easily find that this vacuum function is the product of a factorized expression and an ordinary nonholomorphic factor; that is,

$$\widehat{Z}^{(0)}_{L,L'}(\{q'_M,\overline{q}'_M\}) = \frac{Z_L(\{q'_M\};\{z_{(i)}\})\overline{Z_{L'}(\{q'_M\};\{z'_{(i)}\})}}{\det{}^5[2\mathrm{Re}\,\omega^{(0)}(\{q'_m\})]}, \qquad (37)$$

$$Z_L(\{q'_M\};\{z_{(i)}\}) = \Xi_L(\{q'_m\};\{z_{(i)}\})[1-\lambda_1\lambda_2 Z^{(0)}_L(\{q'_m\})],$$

where $\Xi_L(\{q'_m\};\{z_{(i)}\})$ is defined in (33) and is calculated by means of (34). Since the modular group is now split, the amplitude in (36) has correct modular properties. In particular, the function

$$Z=\sum_L \Xi_L(\{q'_m\};\{z_{(i)}\})Z^{(0)}_L(\{q'_m\})/\det[\partial\omega_{(j)}/\partial q'_m]$$

is invariant under modular transformations. Here, $\omega_{(1)}=\omega_{11}(\{q'_r\})$, $\omega_{(2)}=\omega_{22}(\{q'_r\})$, $\omega_{(3)}=\omega_{12}(\{q'_r\})$, and $Z^{(0)}_L(\{q'_m\})$ is identical to that in (37). Furthermore, one can verify that the quantity Z is

not singular for $k_s \to 0$ or v_2. In the limit $v_2 \to u_2$, it transforms into the product of vacuum functions on a torus and, hence, vanishes. Therefore, we have $Z \equiv 0$ identically. Nevertheless, the function in (37) differs from the corresponding expression in [6]. In order to reveal this distinction, we note that $\widetilde{B}_{L,L'}$ in (36) can also be expressed in terms of (22) with the aid of the transformation in (35). In particular, we obtain

$$Z_L^{(0)}(\{q'_m\}) = 5R_f(z_{(1)}, z_{(2)}; L)\partial_{z_{(1)}}\partial_{z_{(2)}} \quad (38)$$
$$\times R_b(z_{(1)}, z_{(2)}) + \widetilde{W}_L(z_{(1)}, z_{(2)}) - \widetilde{W}_L(z_{(2)}, z_{(1)})$$
$$+ \frac{\partial\delta q'_m}{\partial q'_m} + \delta q'_m \frac{\partial}{\partial q'_m}\ln\Xi_L(\{q'_m\};\{z_{(i)}\}),$$
$$\widetilde{W}_L(z_{(1)}, z_{(2)}) = \widetilde{G}_b(z_{(2)}, z_{(1)}) \quad (39)$$
$$\times \left[\partial_z G_{3/2}(z, z_{(1)};\{z_{(i)}\})\right]_{z=z_{(2)}}$$
$$- \frac{1}{2}\left[\partial_z\chi_{(1)}(z)\right]_{z=z_{(2)}} \partial_{z_{(1)}}\widetilde{G}_b(z_{(2)}, z_{(1)}),$$

where $\Xi_L(\{q'_m\};\{z_{(i)}\})$ is defined in (34) and $R_b(z, z')$ is the scalar holomorphic Green's function. The fermion Green's function $R_f(z, z'; L)$ is the same as in (32), and $\widetilde{G}_b(z, z')$ is the same as in (12). The quantities $\delta q'_m$ are given by (35). The function $G_{3/2}(z, z_{(1)};\{z(i)\})$ is defined as $G_{3/2}(z, z';\{z(i)\}) + \chi_{(1)}(z)/(z' - z_{(1)})$ in the limit $z' \to z_{(1)}$, while $G_{3/2}(z, z';\{z(i)\})$ is the same as in (26) and (A.3). The zero modes $\chi_{(i)}(z)$ are $\chi_\alpha(z)$ in (A.3) at $\alpha = (i)$. From (38), it can be seen, among other things, that the quantity $Z_L^{(0)}(\{q'_m\})$ is expressed in terms of $\widetilde{G}_b(z_{(1)}, z_{(2)})$ rather than in terms of $G_2(z_{(2)}, z_{(1)})$—the latter takes place for the corresponding quantity in [6]. If $\omega_{mn}^{(0)}$ are chosen for moduli, then the zero modes $\widetilde{\chi}_m(p_n)$ in $\Xi_L(\{q'_m\};\{z_i\})$ [see (34)] are equal to $[\partial_{z_{(2)}}J_m(z_{(2)})][\partial_{z_{(2)}}J_n(z_{(2)})]$ [see text at the end of the paragraph after Eq. (30)]. The derivatives with respect to the moduli are calculated under the condition that the metric remains conformally flat (generally, they differ from the derivatives in [2], which were calculated by integrating the derivatives with respect to the metric). In this case, $\partial_{q'_m}\Xi_L(\{q'_m\};\{z_{(i)}\})$ is expressed in terms of the right-hand side of the first equation in (23), while the quantity $\partial_{q'_m}\delta q'_m$ is calculated within the method proposed in [11]; first, the discontinuities of the sought function $\partial_{q'_m}\delta q'_m$ are calculated with respect to the variables $z_{(1)}$ and $z_{(2)}$, whereupon the function itself is reconstructed on the basis of these discontinuities. All of the derivatives are calculated at fixed $z_{(1)}$ and $z_{(2)}$. We omit the explicit expressions for the derivatives being discussed. One can verify that expression (38) does not have a pole at $z_{(1)} = z_{(2)}$, is antisymmetric in its arguments, and is a (3/2)-tensor with respect to each of them. In order to prove that expression (38) depends on $z_{(1)}$ and $z_{(2)}$ through the factor $\det[\widetilde{\chi}_\alpha(z_{(i)})]$, it is necessary to show, in addition, that there are no poles at the points where $\det[\widetilde{\chi}_\alpha(z_{(i)})] = 0$ and $z_{(1)} \neq z_{(2)}$. This seriously complicates a direct verification [with the aid of (38)] of the $z_{(1)}$ and $z_{(2)}$ independence of (37). From (7) and (35), one can see that relations (10) do not hold for the super Beltrami differentials in [6]. In calculating $\widetilde{B}_{L,L'}$ directly from the integral with respect to fields, it should be borne in mind that correlation functions and zero modes have "correct" properties under the transformation $z \to g_s(z;\{q_r\})$ in (3). The quantities q_r expressed in terms of the new moduli q'_r acquire additional terms that are proportional to Grassmann moduli. Therefore, any given correlation function $K(z, z';\{q'_r\})$ has the form $K(z, z';\{q'_r\}) = K_0(z, z';\{q'_r\}) + \lambda_1\lambda_2\delta q'_r\partial_{q'_r}K_0(z, z';\{q'_r\})$. Here, $K_0(z, z';\{q'_r\})$ is an ordinary correlation function, which changes in a correct way under the transformation $z \to g_s(z;\{q'_r\})$. In just the same way as was done above, the derivatives in the expression being discussed are calculated by the method proposed in [11, 17]. The zero modes are calculated analogously. Additionally, it should be recalled that, now, the discontinuities of the super Beltrami differentials depend on the Grassmann moduli. Finally, the boundary of the fundamental domain in the z plane now depends on the Grassmann moduli (since $q_r = q'_r + \lambda_1\lambda_2\delta q'_r$). In the integral with respect to the coordinates of the vertices involved, surface terms therefore appear instead of the surface terms in the integral over the moduli space—the latter are absent now. Additionally, the local amplitude in (22) acquires the factor $\det[\widetilde{\chi}_\alpha(z_{(i)})]\overline{\det[\widetilde{\chi}_\alpha(z'_{(i)})]}$. The dependence on $z_{(1)}$ and $z_{(2)}$ in expression (22) for $\langle V\rangle_\phi/\det[\widetilde{\chi}_\alpha(z_{(i)})]$ disappears only upon integration with respect to the coordinates $(z_{(i)}|\vartheta_i)$ of the interaction vertices. All of the properties being discussed manifest themselves in one form or another in specifying a surface of genus 2 as a hyperelliptic surface through branch points. As in [6], expression (39) takes a simpler form if $z_{(1)}$ and $z_{(2)}$ are chosen in such a way that $R_f(z_{(1)}, z_{(2)}; L) = 0$, and, hence, $\delta q'_m = 0$.

4. INTEGRATION OF SINGULARITIES

In the general case of $n > 3$, it is impossible to choose moduli in such a way that the modular group would be split. In this case, a local amplitude does

not possess good modular properties on a Riemann surface. Even upon summation over spin structures, it has singularities in the region of degeneracy of this Riemann surface, since, in general, there are no reasons for the vanishing of the sum over the spin structures of zero-, one-, two-, and three-point functions of massless states. Indeed, the spacetime supersymmetry prescribes the vanishing of only the corresponding total amplitudes [22]. The aforesaid refers to the supercovariant local amplitude (27) as well. The same integral with respect to ordinary and Grassmann variables can be finite or divergent, depending on the choice of integration variables. This can be illustrated by the following simple example:

$$I = \int \frac{dxdyd\alpha d\beta d\bar{\alpha}d\bar{\beta}}{|z-\alpha\beta|^p}\varrho(1-|z|^2). \qquad (40)$$

Here, $z = x + iy$, α and β are Grassmann variables, p characterizes the strength of a singularity, and ϱ is a step function [see (31)]. For the sake of simplicity, we restrict the integration region by the condition $|z|^2 \leq 1$. Integrals of this type do indeed appear in (2). In particular, the integration measures in (22) and in (27) involve singularities of the type in (40) at $p = 2$ [11, 17]. Upon integration with respect to the Grassmann variables, we arrive at the integral

$$I = p^2 \int \frac{dxdy}{4|z|^{p+2}}\varrho(1-|z|^2), \qquad (41)$$

which diverges at $z = 0$ if $\mathrm{Re}p > 0$. On the other hand, we can go over in (40) to the new variable $\tilde{z} = z - \alpha\beta$. In this case, the Grassmann variables are present only in the step function $\varrho(|\tilde{z}+\alpha\beta|^2)$. Upon integration with respect to the Grassmann variables, expression (40) therefore reduces to an integral along the circle $|z|^2 = 1$, and this integral is finite for any p. Eventually, we have

$$I = -\int \frac{d\tilde{x}d\tilde{y}d\alpha d\beta d\bar{\alpha}d\bar{\beta}}{|\tilde{z}|^p}\alpha\beta\bar{\alpha}\bar{\beta} \qquad (42)$$
$$\times \left[\delta(|\tilde{z}|^2-1) + |\tilde{z}|^2\frac{d\delta(|\tilde{z}|^2-1)}{d|\tilde{z}|^2}\right] = -\frac{\pi p}{2}.$$

Thus, the integral in (40) depends on the choice of integration variables, at least if $\mathrm{Re}p > 0$ (see [18] for a more detailed discussion). It is common practice to calculate an integral over the vicinity of a singular point by using a cutoff that eliminates a small region $V_\epsilon \to 0$ containing the singular point. Specifically, the integral in (41) is calculated with the cutoff $\varrho(|z|^2 - \epsilon)$, while that in (42) is calculated with the cutoff $\varrho(|\tilde{z}|^2 - \epsilon)$. Of course, $\epsilon \to 0$ in both cases. It is obvious from the aforesaid that, by choosing appropriate variables in the vicinity of singular points, one can remove divergences even in an integral for each spin structure (L, L'). In fact, the calculation must rely on the requirement that all local symmetries of the amplitude be retained. Such a procedure was proposed in [18] within the supercovariant scheme in terms of the Schottky variables. There, the divergences in the Schottky multipliers are canceled locally in the sum over appropriate spin structures in the same way as in [7]. If only one handle is separated from the others, the divergence disappears upon summation over the spin structures of this handle, mainly because of the vanishing of the zero-, one-, two-, and three-point functions on a torus. Thus, singularities are present only if the supermanifold of genus $n > 1$ degenerates into the sum of supermanifolds of genera $n_i > 1$, not more than three interaction vertices being on each of the above degenerate supermanifolds of lower genera. Therefore, the divergences at the limiting points $\{u_s, v_s\}$ of the generating Schottky transformations are not canceled locally even in the sum over spin structures. In this case, however, the integral converges if one performs integration consecutively with respect to the variables of each handle. By way of example, we consider two degenerate handles. First, we perform integration with respect to the limiting points associated with handle 1 at fixed limiting points (u_2, v_2). This integral with respect to spin structures of handle 1 converges owing primarily to the aforementioned vanishing of zero-, one-, two-, and three-point functions on the torus. For the analogous reason, the result does not have a nonintegrable singularity with respect to the variables of handle 2. Therefore, the result of the preceding calculation can be integrated with respect to the limiting points of handle 2, this yielding a finite expression. In general, the implementation of a similar procedure leads to a finite result at each step. It can be shown that such a calculation preserves all local symmetries of the amplitude. Concurrently, the total vacuum amplitude, the constant for the dilaton–vacuum transition, and the total two- and three-point amplitudes of massless boson states vanish. We are going to discuss the details of the corresponding calculations in a forthcoming publication. A similar procedure can also be proposed within a scheme featuring the gravitino field. In this case, however, the presence of the gravitino field complicates the expressions for local amplitudes. In view of this, it is impossible in general obtain the above local amplitudes in a form that could be appropriate for calculating the respective integrals.

ACKNOWLEDGMENTS

This work was supported by the Russian Foundation for Basic Research (project nos. 00-02-16691 and NSh-1124.2003.2).

APPENDIX A

The product of the Green's functions $\widetilde{G}_b(z,z')$ and $\widetilde{G}_f(z,z')$ used in this study and the factor π are, respectively, the Green's functions $-G^{(b)}_{\rm gh}(z,z')$ and $G^{(f)}_{\rm gh}(z,z')$ used in [17] {see formulas (33) in [17]}, while $\pi\widetilde{\chi}_m(z)$ and $\pi\widetilde{\chi}_\alpha(z)$ are, respectively, $\tilde{\chi}^{(0)}_{R_s}(z)$ and $\tilde{\chi}^{(0)}_{F_s}(z)$ in [17]. The function $\widetilde{G}_b(z,z')$ and the correlation function $G_2(z',z;\{p\})$, where $\{p\}\equiv\{p_m\}$, are related by the equations

$$\widetilde{G}_b(z,z') = G_2(z',z;\{p\}) - \int\limits_s G_2(\tilde{z},z;\{p\})\frac{d\tilde{z}}{2i}P^s_m(\tilde{z})\widetilde{\chi}_m(z'), \tag{A.1}$$

$$G_2(z',z;\{p\}) = \widetilde{G}_b(z,z') - \widetilde{G}_b(z,p_j)\chi^{(j)}_2(z';\{p\}),$$

$$\chi^{(j)}_2(z;\{p\}) = \int\limits_s \chi^{(j)}_2(\tilde{z};\{p\})\frac{d\tilde{z}}{2i}P^s_m(\tilde{z}) \times \widetilde{\chi}_m(z) \equiv \widetilde{A}^{-1}_{jm}\widetilde{\chi}_m(z),$$

$$\widetilde{A}^{-1}_{jm}\widetilde{A}_{ml} = \delta_{jl}, \quad \widetilde{A}_{jm} = \widetilde{\chi}_m(p_j),$$

$$G_2(p,z;\{p\}) = 0, \quad (z'-p_j)G(z,z';\{p\}) \to \chi^{(j)}_2(z;\{p\}) \text{ for } z'\to p_j\in\{p\}; \tag{A.2}$$

$$\chi^{(j)}_2(p_l;\{p\}) = \delta_{jl}, p_l\in\{p\}; \quad P^s_m(z) \equiv \partial_{q_m}g_s(z;\{q_n\})/\partial_z g_s(z;\{q_n\}).$$

Upon the transformation $z\to g_s(z;\{q_n\})$, the function $\widetilde{G}_b(z,z')$ acquires the additional term $[\partial_{q_m}g_s(z;\{q_n\})]\widetilde{\chi}_m(z')$ [17]. In order to obtain the first equality in (A.1), the function $\widetilde{G}(z,z')$ is written as an integral of $-G_2(\tilde{z},z;\{p\})\widetilde{G}(\tilde{z},z')$ along the contour around $\tilde{z}=z$. By deforming the contour, the integral is reduced to the sum of integrals along noncontractible cycles. Upon the round about the cycle s, the function $\widetilde{G}_b(z,z')$ develops a discontinuity because $g_s(z;\{q_n\})$ lies off the fundamental region in the z plane if the point z lies within this region. The relation between the corresponding zero modes ensures the absence of poles in $\widetilde{G}(z,z')$ at the points $z=p\in\{p\}$. In the above way, one can obtain the relations

$$G_{3/2}(z',z;\{p'_\alpha\}) = \widetilde{G}_f(z,z') - \widetilde{G}_f(z,p'_\beta)\chi_\beta(z'), \tag{A.3}$$

$$\chi_\beta(z') = \hat{A}^{-1}_{\beta\beta'}\widetilde{\chi}_{\beta'}(z'), \quad \hat{A}^{-1}_{\beta\beta'}\hat{A}_{\beta'\alpha} = \delta_{\beta\alpha}, \hat{A}_{\alpha\beta} = \widetilde{\chi}_\alpha(p'_\beta).$$

The corresponding inverse relations are omitted for the sake of brevity. We present the useful relation [17]

$$\int\limits_s \frac{dz}{2i}\widetilde{\chi}_m(z)P^s_n(z) = \delta_{mn},$$

where δ_{mn} is a Kronecker delta. In this case, each integral is calculated along a contour surrounding one of the two Schottky circles for handle s. This circle is chosen in such a way that the boundary of the second circle is obtained upon applying the transformation $z\to g_s(z;\{q_n\})$ to the boundary of the first circle.

APPENDIX B

According to formulas (A.4), (33), and (34), it follows from Eqs. (23) that

$$\frac{\partial}{\partial q_m}\ln\Xi'_L(\{q_m\};\{p_n\};\{z_{(i)}\}) = \int\limits_s \frac{dz}{2i}P^s_m(z)\Big[\langle T(z)\rangle - \frac{\partial}{\partial q_n}\widetilde{\chi}_n(z) - W(z)\Big] + \widetilde{A}^{-1}_{jn}\frac{\partial}{\partial q_m}\widetilde{\chi}_n(p_j), \tag{A.5}$$

where $\langle T(z)\rangle$ is that contribution to $\langle T(t)\rangle$ which is proportional to ϑ; the matrix $\widetilde{A}_{jm}$ is given in (A.1); and $W(z)$ is the contribution of $\partial_{q_\alpha}\widehat{\chi}^{(\phi+)}_\alpha(t)$ at $\lambda_i=0$,

$$W(z) = \frac{3}{2}\sum_i\Big[\partial_{z_{(i)}}\widetilde{G}_b(z_{(i)},z) + \frac{\partial}{\partial z}\chi_{\alpha_i}(z)\Big|_{z=z_{(i)}}\widetilde{G}_b(z_{(i)},z)\Big]. \tag{A.6}$$

The zero (3/2) modes $\chi_{\alpha_i}(z)$ in (A.6) are normalized by the condition $\chi_{\alpha_i}(z_{(k)})=\delta_{ik}$. The last term in (A.5) is nothing but $\partial_{q_m}[\ln\det\widetilde{\chi}_r(p_s)]$. The quantity $\partial_{q_m}\widetilde{\chi}_n(z)$ can be represented as the integral $\int\partial_{q_m}\widetilde{\chi}_n(z')\widetilde{G}(z',z)dz'/2i$ with respect to z' along the contour going around the point z. The contour is deformed in such a way that it surrounds the Schottky circles. As a result, $\partial_{q_m}\widetilde{\chi}_n(z)$ is expressed in terms of the sum of integrals of the discontinuities of the function $\partial_{q_m}\widetilde{\chi}_n(z')\widetilde{G}(z',z)$; that is,

$$\frac{\partial\widetilde{\chi}_n(z)}{\partial q_m} = \int\limits_s\frac{dz'}{2i}\Big[P^s_m(z') \times\Big(\frac{\partial\widetilde{\chi}_n(z')}{\partial z'}\widetilde{G}(z',z) + 2\widetilde{\chi}_n(z')\frac{\partial\widetilde{G}(z',z)}{\partial z'}\Big) + P^s_m(z')\Big(\frac{\partial\widetilde{\chi}_n(z')}{\partial z'}P^s_r(z')\widetilde{\chi}_r(z)\Big) \tag{A.7}$$

$$+2\widetilde{\chi}_n(z')\frac{\partial P_r^s(z')}{\partial z'}\widetilde{\chi}_r(z)\Big)+\frac{\partial\widetilde{\chi}_n(z')}{\partial q_m}P_r^s(z')\widetilde{\chi}_r(z)\Big],$$

where the integration contours are defined in the same way as in (A.4). In (A.7), we consider that, upon the transformation in (3), the function $\widetilde{G}_b(z,z')$ acquires [17] the additional term $[\partial_{q_m}g_s(z;\{q_n\})]\widetilde{\chi}_m(z')$, while $\widetilde{\chi}_n(z)$ is a 2-tensor. Therefore, we have

$$\frac{\partial\widetilde{\chi}_n(z')}{\partial q_m}\bigg|_{z'=g_s(z)}\left[\frac{\partial g_s(z)}{\partial z}\right]^2-\frac{\partial\widetilde{\chi}_n(z)}{\partial q_m} \tag{A.8}$$
$$=-2\widetilde{\chi}_n(z)\frac{\partial P_m^s(z)}{\partial z}-P_m^s(z)\frac{\partial\widetilde{\chi}_n(z)}{\partial z},$$

where $g_s(z)\equiv g_s(z;\{q_n\})$ and $P_m^s(z)$ is given by (A.2). Upon calculating the difference $P_r^s(z')\partial_{q_m}\widetilde{\chi}_n(z')-P_m^s(z')\partial_{q_r}\widetilde{\chi}_n(z')$ on the basis of (A.2), we see that, after the substitution of formula (A.7) into the last term on the right-hand side of (A.5), the contribution of the last two terms on the right-hand side of (A.7) is canceled by the second term in the integral in (A.5). We then obtain

$$\frac{\partial}{\partial q_m}\ln\Xi'_L(\{q_m\};\{p_n\};\{z_{(i)}\}) \tag{A.9}$$
$$=\int\limits_s\frac{dz}{2i}P_m^s(z)\Bigg[\langle T(z)\rangle-W(z)$$
$$+\widetilde{A}^{-1}_{jn}\left(\frac{\partial\widetilde{\chi}_n(z)}{\partial z}\widetilde{G}(z,p_j)+2\widetilde{\chi}_n(z)\frac{\partial\widetilde{G}(z,p_j)}{\partial z}\right)\Bigg].$$

By employing the correlation function in (26) to calculate T, one can verify that, under the transformations $z\to g_s(z;\{q_m\})$, the bracketed expression on the right-hand side of (A.9) is a 2-tensor. Therefore, formula (A.9) is equivalent to the formula

$$\widetilde{\chi}_m(w)\frac{\partial}{\partial q_m}\ln\Xi'_L(\{q_m\};\{p_n\};\{z_{(i)}\}) \tag{A.10}$$
$$=\oint\limits_s\frac{dz}{2i}\Bigg[\langle T(z)\rangle-W(z)+\widetilde{A}^{-1}_{jn}\Bigg(\frac{\partial\widetilde{\chi}_n(z)}{\partial z}\widetilde{G}(z,p_j)$$
$$+2\widetilde{\chi}_n(z)\frac{\partial\widetilde{G}(z,p_j)}{\partial z}\Bigg)\Bigg]\widetilde{G}(z,w),$$

where each integration contour goes, in a positive direction, around both Schottky circles for a given handle and $w\neq p_j$ is an arbitrary point on the z plane. The integral in (A.10) is determined by the sum of the residues of the Green's function at the poles $z=w$ and $z=p_j$; that is,

$$-\widetilde{\chi}_m(w)\frac{\partial}{\partial q_m}\ln\Xi'_L(\{q_m\};\{p_n\};\{z_{(i)}\}) \tag{A.11}$$
$$=\langle T(w)\rangle_v+W(w)$$
$$-\widetilde{A}^{-1}_{jn}\left(\frac{\partial\widetilde{\chi}_n(z)}{\partial z}\widetilde{G}(z,w)+2\widetilde{\chi}_n(z)\frac{\partial\widetilde{G}(z,w)}{\partial z}\right)_{z=p_j},$$

where $\langle T(z)\rangle_v$ is the vacuum expectation value of the energy–momentum tensor according to the calculation in [2] with the correlation function $G_2(z',z)$. Furthermore, $\Xi'_L(\{q_m\};\{p_n\};\{z_{(i)}\})$ is represented by an integral with respect to matter fields and ghosts. In this integral, the correlation function for a scalar field is identified with the sum of holomorphic and antiholomorphic Green's functions (having discontinuities) for the scalar Laplacian, while the Beltrami and super Beltrami differentials associated with 2 and (3/2) zero modes have the form $\delta(z-p_i)$ and $\delta(z-z_{(i)})$. In order to calculate the derivative of the integral in question with respect to q_n, we consider the expression for the integral corresponding to the moduli $q_n+\delta q_n$, where $\delta q_n\to 0$. In this integral, we make a change of variable $z\to z+\delta z(z)$, choosing δz in such a way that $q_n+\delta q_n\to q_n$. The required quantity δz is calculated from the condition $g_s(z)+\delta q_n\partial_{q_n}g_s(z)+\delta z(z)\partial_z g_s(z)=g_s(z)+\delta z(g_s(z))$, the result being $\delta z=-\widetilde{G}(z,w_j)\widetilde{a}^{-1}_{jn}\delta q_n$, where $\widetilde{a}_{nj}=\chi_n(w_j)$. Upon the above substitution, the two-dimensional metric develops the transverse component $\partial_{\bar z}\delta z(z)=-\delta^2(z-p_j)\widetilde{a}^{-1}_{jn}\delta q_n$. A variation of the integral in question in response to a variation of the moduli reduces to the emergence of the transverse components of the metric and an additional term caused by the change in the contribution of the Beltrami and super Beltrami differentials. All terms on the right-hand side of (A.11), with the exception of the first one, are due to the change in the contribution to the integral from the Beltrami and super Beltrami differentials. The first term is nothing but the derivative taken with respect to the metric and considered in [2]. It follows that Eq. (A.11) and, hence, Eq. (A.5) are equivalent to the equations for the chiral determinants in [2].

REFERENCES

1. D. Friedan, E. Martinec, and S. Schenker, Nucl. Phys. B **271**, 93 (1986).
2. E. Verlinde and H. Verlinde, Phys. Lett. B **192**, 95 (1987); Nucl. Phys. B **288**, 357 (1987).
3. J. Atick, J. Rabin, and A. Sen, Nucl. Phys. B **299**, 279 (1988); J. Atick, G. Moore, and A. Sen, Nucl. Phys. B **308**, 1 (1988).
4. G. Moore and A. Morozov, Nucl. Phys. B **306**, 387 (1988).
5. S. Mandelstam, Phys. Lett. B **277**, 82 (1992).
6. Eric D'Hoker and D. H. Phong, Phys. Lett. B **529**, 241 (2002); Nucl. Phys. B **636**, 3 (2002); **636**, 61 (2002); **639**, 129 (2002).

7. P. Di Vecchia, K. Hornfeck, M. Frau, *et al.*, Phys. Lett. B **211**, 301 (1988).
8. J. L. Petersen, J. R. Sidenius, and A. K. Tollstén, Phys. Lett. B **213**, 30 (1988); Nucl. Phys. B **317**, 109 (1989).
9. B. E. W. Nilsson, A. K. Tollstén, and A. Wätterstam, Phys. Lett. B **222**, 399 (1989).
10. G. S. Danilov, Yad. Fiz. **52**, 1143 (1990) [Sov. J. Nucl. Phys. **52**, 727 (1990)]; Phys. Lett. B **257**, 285 (1991).
11. G. S. Danilov, Phys. Rev. D **51**, 4359 (1995); (Erratum) **52**, 6201 (1995).
12. M. A. Baranov and A. S. Shvarts, Pis'ma Zh. Éksp. Teor. Fiz. **42**, 340 (1985) [JETP Lett. **42**, 419 (1985)]; D. Friedan, in *Proceedings of the Santa Barbara Workshop on Unified String Theories*, Ed. by D. Gross and M. Green (World Sci., Singapore, 1986).
13. N. Seiberg and E. Witten, Nucl. Phys. B **276**, 272 (1986).
14. L. Hodkin, J. Phys. Grav. **6**, 333 (1989).
15. G. S. Danilov, Pis'ma Zh. Éksp. Teor. Fiz. **58**, 790 (1993) [JETP Lett. **58**, 736 (1993)].
16. G. S. Danilov, Class. Quantum Grav. **11**, 2155 (1994).
17. G. S. Danilov, Nucl. Phys. B **463**, 443 (1996).
18. G. S. Danilov, Preprint PNPI-2449 (Gatchina, 2002); hep-th/0112022.
19. A. M. Polyakov, Phys. Lett. B **103**, 207 (1981).
20. P. S. Howe, J. Phys. A **12**, 393 (1979).
21. C. L. Siegal, *Topics in Complex Function Theory* (Wiley, New York, 1973), Vol. 3.
22. E. Martinec, Phys. Lett. B **171**, 189 (1986).

Translated by A. Isaakyan

Physics of Atomic Nuclei, Vol. 67, No. 5, 2004, pp. 1050–1062. Translated from Yadernaya Fizika, Vol. 67, No. 5, 2004, pp. 1074–1086.

ELEMENTARY PARTICLES AND FIELDS
Theory

Cosmological Production of Vector Bosons and Cosmic Microwave Background Radiation

D. B. Blaschke, S. I. Vinitsky, A. A. Gusev, V. N. Pervushin, and D. V. Proskurin*

Joint Institute for Nuclear Research, Dubna, Moscow oblast, 141980 Russia

Received October 9, 2003

Abstract—An intensive cosmological production of vector W and Z bosons is considered within a cosmological model that involves a relative scale of measurement. Field-theory models are studied in which cosmic microwave background radiation and baryon matter may appear as products of the decay of such primordial bosons. © *2004 MAIK "Nauka/Interperiodica".*

1. INTRODUCTION

Is modern theory able to explain the origin of observed matter in the Universe by its cosmological production from a vacuum [1–11]? As is well known, the answer to this question is associated with the problem of particle creation in the vicinity of a cosmological singularity. Thus far, it has been common practice to assume that the number of product pairs is by far insufficient for explaining the total amount of observed matter [7].

We recall that the cosmological creation of massive particles is calculated by going over to conformal variables [7], for which the limit of zero scale factor (point of a cosmic singularity) means the vanishing of masses. Vector bosons are the only particles of the Standard Model that have a singularity at zero mass [12, 13]. In this limit, the normalization of the wave function for massive vector bosons is singular in mass [12, 13]. The absence of the massless limit in the theory of massive vector bosons is well known [14]. In calculations in the lowest order of perturbation theory, this leads to a divergence of the number of product longitudinal bosons [7, 11].

There exist two opinions concerning the removal of this singularity. In [7, 15], the divergence of the number of particles is removed by means of a standard renormalization of the gravitational constant. However, it is also indicated in the monograph of Grib *et al.* [7] that the number of product particles is determined by the imaginary part of loop Feynman diagrams; since, in quantum field theory, it is the real parts of these diagrams that are subjected to renormalizarion, this means that the above divergence of the number of particles does not belong to the class of divergences in quantum field theory that are removed by means of a conventional renormalization of physical quantities. Indeed, the physical origin of this divergence is that the problem of a cosmological creation of particles from a vacuum is treated within an idealized formulation. The point is that the quantum production of particles in a finite volume for a system featuring interaction and exchange effects may lead to a set of Bose particles having a specific statistical distribution with respect to energy such that it is able to ensure the convergence of the respective integral of the momentum distribution.

In the present study, we analyze physical conditions and models for which the number of product vector bosons may be quite sufficient for explaining the origin of matter in the Universe. Such cosmological models include conformal cosmology [16], where conformal quantities of the general theory of relativity and of the Standard Model are defined as observables [17] for which there are relative reference units of intervals.

The ensuing exposition is organized as follows. Section 2 is devoted to discussing various versions of the formulation of the Cauchy problem for the cosmological production of vector particles in field theory. In Section 3, we study possible implications of such a production in the context of validating the temperature of cosmic microwave background radiation within the Standard Model, the baryon–antibaryon asymmetry of the Universe [18, 19], and a small contribution of visible baryon matter [20] to the evolution of the Universe. In the Conclusion, we discuss the results obtained by calculating the composition of matter in the Universe within the Standard Model.

2. PROBLEM OF COSMOLOGICAL PARTICLE CREATION

2.1. Theory

Let us consider cosmological particle creation in the conformally invariant version of the general theory

*e-mail: proskur@thsun1.jinr.ru

of relativity [9, 21–24]. We have

$$S_{\rm tot}[w|F] = S_{\rm D}[w|e,Q] + S_{\rm SM}[y_h w|f,e], \quad (1)$$

where, for the action of the general theory of relativity, we take the Penrose–Chernikov–Tagirova action functional for a scalar field (dilaton) w,

$$S_{\rm D}[w|e,Q] = \int d^4x \quad (2)$$
$$\times \left[|e|w^2\left(\partial_\mu Q\partial^\mu Q - \frac{R(e)}{6}\right) + w\partial_\mu\left(|e|\partial^\mu\right)w\right],$$

in the space specified by the interval

$$ds^2 = \left(e_{\underline{\lambda}\mu}dx^\mu\right)^2 = \left(e_{\underline{0}\mu}dx^\mu\right)^2 - \left(e_{\underline{i}\mu}dx^\mu\right)^2. \quad (3)$$

Here, $e_{\underline{\lambda}\mu}$ is the Fock vierbein, $R(e)$ is the curvature, and Q is an additional field that does not interact with matter [11] and which yields the observed regime of cosmological evolution. In the Standard Model action functional featuring the set of fields f, the Higgs mass $M_{\rm Higgs}$ is replaced by the dilaton multiplied by a constant $y_h \sim 10^{-17}$, $(y_h w)$. The theory specified by the action functional (1) is invariant under conformal transformations, including scale transformations for the set of all fields $[w|F]$ with the transformation parameter Ω,

$${}^{(n)}F_\Omega = {}^{(n)}F \times (\Omega)^n, \quad w_\Omega = w/\Omega, \quad (4)$$

where (n) is a conformal weight. This invariance indicates that the action functional (1) involves an extra degree of freedom.

2.2. Absolute Variables

It is common practice to assume [24] that the action of the general theory of relativity and the Standard Model arises from the action functional (1) as a consequence of choosing the *"absolute"* variables as

$${}^{(n)}F_{(a)} = {}^{(n)}F \times (w/\varphi_0)^n, \quad w_{(a)}(x^0,x^i) = \varphi_0, \quad (5)$$

with the result that the dilaton $w(x^0,x^i)$ is replaced by the parameter φ_0 that is related to the Planck mass by the equation $\varphi_0 = M_{\rm Pl}\sqrt{3/(8\pi)}$ and which did not appear in the original action functional (1). Upon the spontaneous scale-invariance breaking associated with this, the symmetry of the action functional (1) under the transformations in (4) becomes the symmetry of the physical variables in (5), which are invariant under the same scale transformations in (4). Owing to the above spontaneous breakdown of scale invariance, the extra degree of freedom characterized by a negative probability is removed from the action functional in (1), but, instead, the dimensional *"absolute"* Planck mass parameter $M_{\rm Pl}$ appears in the equations of motion. This parameter specifies initial data concerning the emergence of the Universe in the so-called Planck era. In the theory involving such a spontaneous breakdown of symmetry, the homogeneous approximation of the metric,

$$e_{(a)\underline{0}\mu}dx^\mu = dt, \quad e_{(a)\underline{i}\mu}dx^\mu = a(t)dx_{\underline{i}}, \quad (6)$$

for the variables in (5) leads to standard cosmological models, including the inflationary model [25], where the initial data of the Planck era are considered as fundamental quantities of the equations of motion.

Within this approach, there arise problems of cosmological initial data, the horizon, time and energy, homogeneity, singularity, and the quantum wave function for the Universe, and attempts are made to solve these problems at the level of the homogeneous approximation via the inflationary expansion of absolute space [25].

In [22, 23], some arguments are adduced that indicate that, in all probability, all these problems, including the emergence of the Planck era, stem from an incorrect formulation of a spontaneous breakdown of the symmetry of (5) in eliminating degrees of freedom of negative probability from the theory specified by the action functional in (1).

We recall that, within a gauge theory, a formulation where all degrees of freedom that are characterized by a negative probability are removed prior to quantizing the theory being considered is referred to as a "fundamental method" [26–28], in contrast to a "heuristic method" [29], where all degrees of freedom are treated on equal footing. In [23], it was shown that, within relativistic string theory, these two methods lead to different spectra.[1)]

Experience gained in applying the fundamental-quantization method [26, 27] to string models [23, 31] and to non-Abelian theories [28] shows that, upon a spontaneous breakdown of the gauge symmetry of the theory being considered, there arise Goldstone modes that are associated with this symmetry breaking and which cannot be removed by any gauge transformations without significantly changing the physical content of the theory, including the spectrum of its elementary and collective excitations.[2)]

[1)] The heuristic formulation of a conformally invariant theory [30] leads to conformal anomalies and the Virasoro algebra, tachyons (particles for which the masses squared are negative) appearing in the theory; at the same time, there arises the Born–Infeld model featuring a positive energy spectrum free from tachyons if extra degrees of freedom that are characterized by a negative probability are eliminated at the level of the classical theory [31].

[2)] In the non-Abelian theory of strong interactions, the analogous Goldstone mode leads to an extra contribution to the η^0-meson mass, while averaging over the topological degeneracy of initial data may lead to zero probabilities of the production of color states of quarks and gluons [28].

In [9, 16, 21], a spontaneous breakdown of the scale invariance of the theory being considered is formulated in terms of conformal variables, the Goldstone mode corresponding to this symmetry breaking being taken into account.

2.3. Conformal Variables

The choice of "*relative*" (r) variables,

$$^{(n)}F_{(r)} = {}^{(n)}F \times (w/\varphi(x^0))^n, \qquad (7)$$
$$w_{(r)}(x^0, x^i) = \varphi(x^0),$$

leaves the dilaton zero mode as a homogeneous variable $\varphi(x^0)$ with a constant volume of three-dimensional hyperspace, $V_{(r)} = \int d^3x|\bar{e}_{(r)}| \equiv \text{const}$, [11, 21] in the reference frame specified by the embedding of a three-dimensional hyperspace into the four-dimensional manifold spanned by $e_{\underline{0}\underline{0}} = N$, $e_{\underline{i}\underline{j}} = \bar{e}_{\underline{i}\underline{j}}$, and $e_{\underline{i}\underline{0}} = N_{\underline{i}}$, where N and $N_{\underline{i}}$ are referred to as, respectively, the lapse function and the shift vector [32]. In this reference frame, an variable φ plays the role of a cosmic scale factor and an evolution parameter in the world space of the field variables $[\varphi|F]$, while the canonical momentum defined as the derivative of the Lagrangian L_{tot} for the action functional (1) with respect to the time derivative of the dilaton field $(\partial_0\varphi)$,

$$P_\varphi = \frac{\partial L_{\text{tot}}[\varphi|e_{(r)}]}{\partial(\partial_0\varphi)} \qquad (8)$$
$$= -2\partial_0\varphi \int d^3x \frac{|\bar{e}_{(r)}|}{N} \equiv -2V_{(r)}\frac{d\varphi}{d\eta},$$

is the localized energy of the Universe [23]; here, $d\eta = N_0(x^0)dx^0$ is the invariant integral for the averaged lapse function $N_0^{-1}(x^0) = \int d^3x|\bar{e}_{(r)}|N^{-1}/V_{(r)}$, while the bar over $e_{(r)}$ is, as we have seen above, denotes the spatial components of the vierbein for the constant volume $V_{(r)} = \int d^3x|\bar{e}_{(r)}|$.

In terms of the conformal variables in (7), the problems of the theory that are solved in terms of the absolute variables in (5) with the aid of inflation are solved within the exact theory by means of the zero mode of the dilaton as the evolution parameter. In particular, the evolution of φ with respect to the time interval explains the problem of the horizon as a consequence of simultaneously varying particle masses and parameters of the system of fields over the entire space. The averaging of the exact equation $\delta S_{\text{tot}}/\delta N = 0$ of the theory for the lapse function N in terms of the variables in (7) over a specific spatial volume housing measured objects yields the equation of the evolution of the Universe,

$$\varphi'^2 = \rho, \qquad (9)$$

where $\rho = \int d^3x|e|[T_0^0 - \varphi^2(R_0^0 - R/2)]$, T_0^0 and R_0^0 being the components of, respectively, the Einstein energy–momentum and the Ricci tensor.

We note that, in the exact theory specified by the action functional in (1), Eq. (9) is the analog of the Friedmann equation, which was derived in the approximation of homogeneity in the general theory of relativity. Thus, the approximation of a homogeneous universe coincides with the result obtained by averaging the exact equation $\delta S_{\text{tot}}/\delta N = 0$ over the volume. Solving Eq. (9), we arrive at an analog of the Friedmann relation between the conformal time and density, $\eta(\varphi_0, \varphi_I) = \pm\int_{\varphi_I}^{\varphi_0} d\varphi/\sqrt{\rho}$.

Within the Hamiltonian formalism, where the time derivatives of the fields are replaced by the corresponding canonical momenta $P_\varphi = -2V_{(r)}\varphi'$, Eq. (9), which describes the evolution of the Universe, has the meaning of a Hamiltonian constraint, $P_\varphi^2/(4V_{(r)}) = V_{(r)}\rho$. The Hamiltonian $V_{(r)}\rho$ as a generator of the conformal time evolution of fields can be represented as the sum of the Hamiltonian for a uniform scalar field, $V_{(r)}\rho_Q$, and the Hamiltonian for local field variables, H_{field}: $V_{(r)}\rho = V_{(r)}\rho_Q + H_{\text{field}}$, where ρ_Q is the density of the uniform scalar field.

In terms of the conformal variables in (7), the Planck mass as the "absolute" parameter of the equations of motion becomes a "random" current value of the field evolution parameter $\varphi(x^0)$. In terms of the variables in (7), both the hypothesis of the Planck era and the problem of describing evolution from the Planck era (10^{-43} s) on the basis of the inflationary model of the Universe lose physical meaning.[3)]

Within the conformal variables (7), there arises the problem of studying the quantum creation and evolution of a relativistic universe in the limit of infinitely low masses $(\varphi(\eta) \to 0)$ and indefinitely high values of the Hubble parameter $(H(\eta) \to \infty)$. The variables in (5) and those in (7) provide two different cosmologies and two different formulations of the problem of studying the origin of the Universe and matter.

2.4. Conformal Cosmology

In the approximation of homogeneity, the conformal variables in (7) correspond to directly measured quantities of observational cosmology. We recall that, in describing the cosmic evolution of the

[3)]The variables in (5) arise from (7) upon the substitution $^{(n)}F_{(r)} = {}^{(n)}F_{(a)}(\varphi/\varphi_0)^{-n}$. This transformation converts the variable φ with initial cosmological data $\varphi(\eta = 0) = \varphi_I$ and $H(\eta = 0) = H_I$ into its current value $\varphi(\eta = \eta_0) = \varphi_0$, with the result that one of the ordinary (random) values of the variable φ becomes, for the equations of motion, the absolute parameter $\varphi_0 = \sqrt{3/(8\pi)}M_{\text{Pl}}$, which is related to the Planck mass.

energy of photons emitted by atoms in a cosmic object, use is made of the conformal interval $(dx^i)^2 = dt^2/a^2(t) = d\eta^2$ of photons propagating along the light cone $ds^2 = 0$ toward an observer. The redshift of spectral lines, which is a directly measurable quantity in observational cosmology, depends on the conformal time $\eta = \eta_0 - r$ at the instant of photon emission by atoms of cosmic objects that occur at the "coordinate distance" $r = \sqrt{(x^i)^2}$ from the Earth. In terms of the conformal coordinates, we find that the volume of the Universe does not increase, while all masses, including the Planck mass, are scaled by the cosmic factor $a(\eta)$:

$$m_{(r)}(\eta) = m_0 a(\eta), \qquad (10)$$
$$[M_{\rm Pl}\sqrt{3/(8\pi)}]a(\eta) = \varphi_0 a(\eta) = \varphi(\eta).$$

In terms of the conformal time, which is associated with the observed time, the square-root regime of the evolution of the Universe in the era of primordial nucleosynthesis,

$$a(t) = \widetilde{a}(\eta) = \sqrt{1 + 2H_0(\eta - \eta_0)} \qquad (11)$$
$$= 1 - rH_0 + O(r^2),$$

means that, in the era of chemical evolution, the Universe was filled with a free uniform scalar field [see Eq. (15) below] rather than with radiation. The evolution according to Eq. (11) is prescribed by a rigid equation of state such that pressure coincides with the energy density.

In [16], it was shown that, in terms of the conformal variables, data on the dependence of the redshift on the distance to supernovae [17] and data on nucleosynthesis correspond to the same rigid equation of state associated with Eq. (11).

The identification of the conformal variables in (7) with observable quantities leads to a different picture of the evolution of the Universe [11, 16, 21] in relation to the analogous identification of the variables in (5), as is done in conventional cosmology. The temperature history of a hot universe as rewritten in terms of the conformal variables in (7) appears as the evolution of elementary-particle masses in a cold universe with a constant temperature of cosmic microwave background radiation. That the cosmic-microwave-background-radiation temperature $T_{\rm CMBR}$ is independent of the redshift z is, at first glance, in glaring contradiction with the observation [33] that $6 < T_{\rm CMBR}(z = 2.3371) < 14$ K. In this observation, the temperature was deduced from the relative population of various energy levels (their energies being denoted by E_i), which follows from Boltzmann statistics. However, the argument of the Boltzmann factors, which is equal to the ratio of the temperature to the mass, features the same dependence on the factor z in a cold universe as well [16]. Therefore, this ratio can be interpreted as the z dependence of energy levels (that is, mass) at a constant temperature. The abundances of chemical elements are determined primarily by Boltzmann factors as well, which are dependent on functions of the mass-to-temperature ratio, which are invariant under conformal transformations [34].

2.5. Initial Data of Quantum Cosmology

As a rule, quantum cosmology is defined as the homogeneous approximation of the metric,

$$ds^2_{(r)} = [(d\eta)^2 - (dx^i)^2], \quad d\eta = N_0(x^0)dx^0, \quad (12)$$

with the shift function $N_0(x^0)$ inheriting the symmetry group of the general theory of relativity in the form of invariance under reparametrizations of the coordinate time, $x^0 \to \widetilde{x}^0 = \widetilde{x}^0(x^0)$. Cosmological models featuring this symmetry group, which were first described at a mathematically rigorous level by DeWitt, Wheeler, and Misner [35, 36] in the late 1960s, do not differ in any respect from the relativistic mechanics of a particle in the special theory of relativity. There is a direct correspondence between the Minkowski space of variables in the special theory of relativity and the space of field variables in the theory being considered, where the dilaton field φ plays the role of the timelike variable of Minkowski space.

In the particular case where the uniform scalar field $Q(\eta)$ is dominant, we arrive at a simple cosmological model of the Universe [11]; that is,

$$S_{\rm univ} = V_{(r)} \int \frac{dx^0}{N_0}\left[-\left(\frac{d\varphi}{dx^0}\right)^2 + \varphi^2\left(\frac{dQ}{dx^0}\right)^2\right] \qquad (13)$$
$$= \int dx^0 \Big\{ - P_\varphi \frac{d\varphi}{dx^0} + P_Q \frac{dQ}{dx^0}$$
$$+ N_0 V_{(r)}[(P_\varphi/(2V_{(r)}))^2 - (P_Q/(2\varphi V_{(r)}))^2]\Big\},$$

where $P_Q = 2V_{(r)}\varphi^2 Q'$ and $P_\varphi = 2V_{(r)}\varphi'$ are canonical momenta. A variation of the action functional with respect to the shift function $N(x^0)$ leads to a constraint equation for these two momenta,

$$P_\varphi^2 - P_Q^2/\varphi^2 = 0 \quad \Rightarrow \quad P_\varphi = \pm P_Q/\varphi, \qquad (14)$$

its solution being

$$P_Q = 2V_{(r)}H_I\varphi_I^2 = \text{const}, \quad \varphi^2 = \varphi_I^2(1 + 2H_I\eta), \qquad (15)$$

where $\varphi_I^2 H_I = P_Q/2V_{(r)}$ is an integral of the motion. As was shown in [16], the resulting evolution law (15)

for the scale factor is compatible with the evolution of supernovae in terms of conformal variables [17].

Upon the quantization of the theory specified by the action functional in (13), the Wheeler–DeWitt equation for the wave function Ψ,

$$\left[\hat{P}_\varphi^2 - \hat{P}_Q^2/\varphi^2\right]\Psi = 0,$$

arises as the direct analogy of the Klein–Gordon equation in the quantum general theory of relativity. Like that solution to the Klein–Gordon equation for a relativistic particle which describes the creation and annihilation of positive-energy particles, the solution

$$\Psi = A^+_{\mathrm{P}_{\varphi\geq 0}}\Psi^+[P_Q|\varphi]e^{\{iP_Q(Q-Q_I)\}}\theta(\varphi-\varphi_I) + A^-_{\mathrm{P}_{\varphi\leq 0}}\Psi^-[P_Q|\varphi]e^{\{-iP_Q(Q-Q_I)\}}\theta(-\varphi)$$

to the Wheeler–DeWitt equation depends on the initial data Q_I and φ_I. In order to get rid of negative energies and to create a stable quantum system, a causal quantization is postulated in quantum field theory in such a way that positive-energy excitations move in the forward direction along the time axis, while negative-energy excitations move in the backward direction with respect to time. The analogous interpretation where the coefficient A^+ is treated as the creation operator for the Universe and where the coefficient A^- is treated as the annihilation operator for the anti-Universe solves the problem of a cosmic singularity of the Universe at positive energy, since, for positive energies, the wave function does not involve the singularity point $\varphi = 0$; this singularity appears in the negative-energy wave function, which is treated as the amplitude of the probability for the annihilation of the anti-Universe.

The quantum general theory of relativity loses the geometric interval of time and information about how the metric depends on the time interval—in particular, it loses the Hubble law describing the dependence of the scale on the time interval [see Eqs. (15)]. In [22], it was proposed to make a canonical transformation (known as the Levi-Civita transformation) from the original variables to a new world space of variables. In terms of these variables, the cosmic scale (dilaton) becomes a geometric interval of time with cosmic initial data $\varphi(\eta = 0) = \varphi_I$ and $H(\eta = 0) = H_I$ in (15), which are random values of variables fitted to experimental data.

In this case, the conformal variables in (7) naturally lead to the concept of particles [9], which has been used and is being presently used in almost all of the studies devoted to the cosmological creation of particles [7].

2.6. Definition of a Particle in Quantum Field Theory

In quantum field theory, the concept of a particle can be associated only with those field variables that are characterized by a positive probability and a positive energy. Negative energies are removed by causal quantization, according to which the creation operator at a negative energy is replaced by the annihilation operator at the respective positive energy. All of the variables that are characterized by a negative probability can be removed according to the scheme of fundamental operator quantization [26]. The results obtained by applying the operator-quantization procedure to massive vector fields in the case of the conformally flat metric (12) are given in [9, 11, 13].

In order to determine the evolution law for all fields $\mathbf{v}$, it is convenient to use the Hamiltonian form of the action functional for their Fourier components $\mathbf{v}_k^I = \int d^3x e^{i\mathbf{k}\cdot\mathbf{x}}\mathbf{v}^I(\mathbf{x})$; that is,

$$S_{\mathrm{tot}} = \int_{x_1^0}^{x_2^0} dx^0 \left\{ \sum_k \left[\mathbf{p}_k^\perp \partial_0 \mathbf{v}_k^\perp + \mathbf{p}_k^{||}\partial_0\mathbf{v}_k^{||}\right] - P_a\partial_0 a + N_0\left[\frac{P_a^2}{4V_{(r)}\varphi_0^2} - V_{(r)}\rho_{\mathrm{tot}}\right]\right\}, \quad (16)$$

where $\mathbf{p}_k^\perp$ and $\mathbf{p}_k^{||}$ are the canonical momenta for, respectively, the transverse and the longitudinal component of vector bosons and ρ_{tot} is the sum of the conformal densities of the scalar field obeying the rigid equation of state and the vector field,

$$\rho_{\mathrm{tot}}(a) = \frac{\varphi_0^2 H_0^2}{a^2} + \rho_{\mathrm{v}}(a), \quad (17)$$

$$\rho_{\mathrm{v}}(a) = V_{(r)}^{-1}(H^\perp + H^{||}), \quad (18)$$

$H^\perp$ and $H^{||}$ being the Hamiltonians for a free field,[4)]

$$H^\perp = \sum_k \frac{1}{2}\left[\mathbf{p}_k^{\perp 2} + \omega^2\mathbf{v}_k^{\perp 2}\right], \quad (19)$$

$$H^{||} = \sum_k \frac{1}{2}\left[\left(\frac{\omega(a,k)}{M_{\mathrm{v}}a}\right)^2 \mathbf{p}_k^{||2} + (M_{\mathrm{v}}a)^2\mathbf{v}_k^{||2}\right].$$

Here, the dispersion relation has the form $\omega(a,k) = \sqrt{\mathbf{k}^2 + (M_{\mathrm{v}}a)^2}$; for the sake of brevity, we have also introduced the notation $\mathbf{p}_k^{||2} \equiv \mathbf{p}_k^{||}\cdot\mathbf{p}_{-k}^{||}$.

[4)] In quantum field theory, observables that are constructed from the above field variables form the Poincaré algebra [13, 26, 28]. Therefore, such a formulation, which depends on the reference frame used, does not contradict the general theory of irreducible and unitary transformations of the relativistic group [37].

Within the reparametrization-invariant models specified by action functionals of the type in (16) with the Hamiltonians in (19), the concepts of an observable particle and of cosmological particle creation were defined in [9]. We will illustrate these definitions by considering the example of an oscillator with a variable energy. Specifically, we take its Lagrangian in the form

$$\mathcal{L} = p_{\rm v}\partial_0 {\rm v} - N_0\frac{1}{2}[p_{\rm v}^2 + \omega^2 {\rm v}^2 - \omega] + \rho_0(N_0 - 1). \tag{20}$$

The quantity $H_{\rm v} = [p_{\rm v}^2 + \omega^2 {\rm v}^2]/2$ has the meaning of a conformal Hamiltonian as a generator of the evolution of the fields v and $p_{\rm v}$ with respect to the conformal-time interval $d\eta = N_0 dx^0$, where the shift function N_0 plays the role of a Lagrange multiplier. The equation for N_0 introduces the density $\rho_0 = H_{\rm v} - \omega/2$ in accordance with its definition adopted in the general theory of relativity. In quantum field theory [3, 9], the diagonalization of precisely the conformal Hamiltonian

$$H_{\rm v} = \frac{1}{2}[p_{\rm v}^2 + \omega^2 {\rm v}^2] = \omega\left[\hat{N}_{\rm part} + \frac{1}{2}\right] \tag{21}$$

specifies both the single-particle energy $\omega = \sqrt{\mathbf{k}^2 + (M_{\rm v}a(\eta))^2}$ and the particle-number operator

$$\hat{N}_{\rm part} = \frac{1}{2\omega}[p_{\rm v}^2 + \omega^2 {\rm v}^2] - \frac{1}{2} \tag{22}$$

with the aid of the transition to the symmetric variables p and q defined as

$$p_{\rm v} = \sqrt{\omega}p = i\sqrt{\frac{\omega}{2}}(a^+ - a), \tag{23}$$
$$ {\rm v} = \sqrt{\frac{1}{\omega}}q = \sqrt{\frac{1}{2\omega}}(a^+ + a).$$

In terms of the symmetric variables p and q, the particle-number operator takes the form

$$\hat{N}_{\rm part} = \frac{1}{2}[p^2 + q^2] - \frac{1}{2} = a^+ a. \tag{24}$$

Upon going over to these variables in the Lagrangian in (20), we arrive at

$$\mathcal{L} = p\partial_0 q - pq\partial_0\Delta^\perp - N_0\omega[\hat{N}_{\rm part} + 1/2], \tag{25}$$

where $\partial_0\Delta^\perp = \partial_0\omega/(2\omega)$ and where there appears sources of cosmic particle creation in the form $pq = i[(a^+)^2 - a^2]/2$. Here, we give a derivation of these sources for transverse fields, whereas, for longitudinal fields [see Eq. (19)], the analogous diagonalization of the Hamiltonian leads to the factor $\partial_0\Delta^{||} = \partial_0\varphi/\varphi - \partial_0\omega/(2\omega)$.

In order to diagonalize the equations of motion in terms of the above new variables, it is necessary to apply, to the phase space, the rotation transformation

$$p = p_\theta\cos\theta + q_\theta\sin\theta, \quad q = q_\theta\cos\theta - p_\theta\sin\theta \tag{26}$$

and the squeezing transformation

$$p_\theta = \pi e^{-r}, \quad q_\theta = \xi e^{+r}. \tag{27}$$

As a result, the Lagrangian in (25) assumes the form

$$\mathcal{L} = \pi\partial_0\xi + \pi\xi[\partial_0 r - \partial_0\Delta\cos(2\theta)] \tag{28}$$
$$+ \frac{\pi^2}{2}e^{-2r}[\partial_0\theta - N_0\omega - \partial_0\Delta\sin(2\theta)]$$
$$+ \frac{\xi^2}{2}e^{2r}[\partial_0\theta - N_0\omega + \partial_0\Delta\sin(2\theta)].$$

The equations of motion that are obtained from this Lagrangian,

$$\xi' + \xi[r' - \Delta'\cos 2\theta] \tag{29}$$
$$+ \pi e^{-2r}[\partial_0\theta - N_0\omega - \partial_0\Delta\sin(2\theta)] = 0,$$

$$\pi' - \pi[r' - \Delta'\cos(2\theta)] \tag{30}$$
$$- \xi\cdot 2e^{2r}[\partial_0\theta - N_0\omega + \partial_0\Delta\sin(2\theta)] = 0,$$

take a diagonal form,

$$\xi' + \omega_b\pi = 0, \quad -\pi' + \omega_b\xi = 0, \tag{31}$$

if $\omega_b = e^{-2r}[\omega - \theta' - \Delta'\sin(2\theta)]$ and if the rotation parameter θ and the squeezing parameter r satisfy the equations[5)]

$$[\theta' - \omega]\sinh(2r) = -\Delta'\sin(2\theta)\cosh(2r), \tag{32}$$
$$r' = \Delta'\cos(2\theta).$$

By solving these equations, we can find, according to (24), the time dependence of the number of particles produced in cosmic evolution. The result is

$$\hat{N}_{\rm part} = \frac{\cosh(2r) - 1}{2} + \cosh(2r)\hat{N}_{\text{q-part}} \tag{33}$$
$$+ \sinh(2r)\frac{\pi^2 - \xi^2}{2},$$

where $\hat{N}_{\text{q-part}} = [\pi^2 + \xi^2 - 1]/2 = b^+ b$ is the number of quasiparticles defined as variables that diagonalize

[5)] For transverse and longitudinal bosons, these equations coincide with the equations derived in [7] for the coefficients of the Bogolyubov transformation $b = \alpha a + \beta a^+$, $\alpha' - i\omega\alpha = \Delta'\beta$, by using the Wentzel–Kramers–Brillouin method {see Eqs. (9.68) and (9.69) in [7] on page 185 in the Russian edition of this monograph}, where it is necessary to make the change of variables specified by the equations $\Delta' = \omega^{(1)}/2$, $\alpha^* = \exp[i\theta - i\int d\eta\omega]\cosh r$, and $\beta = \exp[-i\theta + i\int d\eta\omega]\sinh r$.

the equation of motion. Since the equation of motion is diagonal, the number of quasiparticles is an integral of the motion—that is, a quantum number that characterizes the quantum state of the Universe. These states include the physical vacuum $|0\rangle_{\rm sq}$ of quasiparticles (that is, the squeezed vacuum, which is labeled with the subscript "sq" in order to distinguish it from the vacuum of ordinary particles),

$$b_\varsigma|0\rangle_{\rm sq}=0\quad\left(b=\frac{1}{\sqrt{2}}[\xi+i\pi]\right). \tag{34}$$

In the squeezed-vacuum state, the number of quasiparticles is equal to zero:

$${}_{\rm sq}\langle 0|\hat{N}_{\text{q-part}}|0\rangle_{\rm sq}=0. \tag{35}$$

In this case, the expectation value of the particle-number operator (33) in the squeezed-vacuum state is

$${}_{\rm sq}\langle 0|\hat{N}_{\rm part}|0\rangle_{\rm sq}=\frac{\cosh(2r(\eta))-1}{2}=\sinh^2 r(\eta). \tag{36}$$

The time dependence of this quantity is found by solving the Bogolyubov equation (32). The origin of the Universe is defined as the conformal-time instant $\eta=0$, at which the number of particles and the number of quasiparticles are both equal to zero. The resulting set of Eqs. (32) becomes closed upon specifying the equation of state and initial data for the number of particles. In just the same way, the number of particles characterized by an arbitrary set of quantum numbers ς,

$$\mathcal{N}_\varsigma(\eta)={}_{\rm sq}\langle 0|\hat{N}_\varsigma|0\rangle_{\rm sq}=\sinh^2 r_\varsigma(\eta), \tag{37}$$

and produced from the squeezed vacuum by the time instant η can be determined by solving an equation of the type in (32).

Thus, it is the conformal quantities of the theory, such as the energy $\omega_k=\sqrt{k^2+M_{\rm v}^2a^2}$, the number $\hat{N}_{\rm part}$ of particles, and the conformal density

$$\rho_{\rm v}=\sum_k {}_{\rm sq}\langle 0|\hat{N}_{k\,\rm part}|0\rangle_{\rm sq}\omega_k/V_{(r)},$$

that are associated with observables, in just the same way as the conformal time in observational cosmology is associated with the observed time [16].

3. PHYSICAL IMPLICATIONS

3.1. Calculation of the Distribution Function

Let us consider the example where the above set of equations is solved for the evolution law (11) in the case of the rigid equation of state,

$$a(\eta)=a_I\sqrt{1+2H_I\eta}\quad(a_I^2H_I=H_0),$$

where $a_I=a(0)$ and H_I are initial data at the matter-production instant. We introduce the dimensionless variables of time and momentum (τ and x, respectively) and the coefficient $\gamma_{\rm v}$ according to the formulas

$$\tau=2\eta H_I=\frac{\eta}{\eta_I},\quad x=\frac{q}{M_I},\quad \gamma_{\rm v}=\frac{M_I}{H_I}, \tag{38}$$

where $M_I=M_{\rm v}(\eta=0)$ are initial data for the mass. In terms of these variables, the single-particle energy has the form $\omega_{\rm v}=H_I\gamma_{\rm v}\sqrt{(1+\tau)+x^2}$.

The Bogolyubov equations (32) can then be represented as

$$\left[\frac{\gamma_{\rm v}}{2}\sqrt{(1+\tau)+x^2}-\frac{d\theta_{\rm v}^{||}}{d\tau}\right]\tanh(2r_{\rm v}^{||}) \tag{39}$$
$$=-\left[\frac{1}{2(1+\tau)}-\frac{1}{4[(1+\tau)+x^2]}\right]\sin(2\theta_{\rm v}^{||}),$$

$$\frac{d}{d\tau}r_{\rm v}^{||}=\left[\frac{1}{2(1+\tau)}-\frac{1}{4[(1+\tau)+x^2]}\right]\cos(2\theta_{\rm v}^{||}),$$

$$\left[\frac{\gamma_{\rm v}}{2}\sqrt{(1+\tau)+x^2}-\frac{d}{d\tau}\theta_{\rm v}^{\perp}\right]\tanh(2r_{\rm v}^{\perp})$$
$$=-\left[\frac{1}{4[(1+\tau)+x^2]}\right]\sin(2\theta_{\rm v}^{\perp}),$$

$$\frac{d}{d\tau}r_{\rm v}^{\perp}=\left[\frac{1}{4[(1+\tau)+x^2]}\right]\cos(2\theta_{\rm v}^{\perp}).$$

We solved these equations numerically at positive values of the momentum $x=q/M_I$, considering that, for $\tau\to+0$, the asymptotic behavior of the solutions is given by $r(\tau)\to{\rm const}\cdot\tau$ and $\theta(\tau)=O(\tau)$. The distributions of longitudinal $[\mathcal{N}^{||}(x,\tau)]$ and transverse $[\mathcal{N}^{\perp}(x,\tau)]$ vector bosons are given in the figure for the initial data $H_I=M_I(\gamma_{\rm v}=1)$.

From the figure, it can be seen that, for $x>1$, the longitudinal component of the boson distribution is everywhere much greater than the transverse component, this demonstrating a more copious cosmological creation of longitudinal bosons in relation to transverse bosons. A slow decrease in the longitudinal component as a function of momentum leads to a divergence of the integral for the density of product particles [2]:

$$n_{\rm v}(\eta)=\frac{1}{2\pi^2}\int_0^\infty dqq^2\left[\mathcal{N}^{||}(q,\eta)+2\mathcal{N}^{\perp}(q,\eta)\right]\to\infty. \tag{40}$$

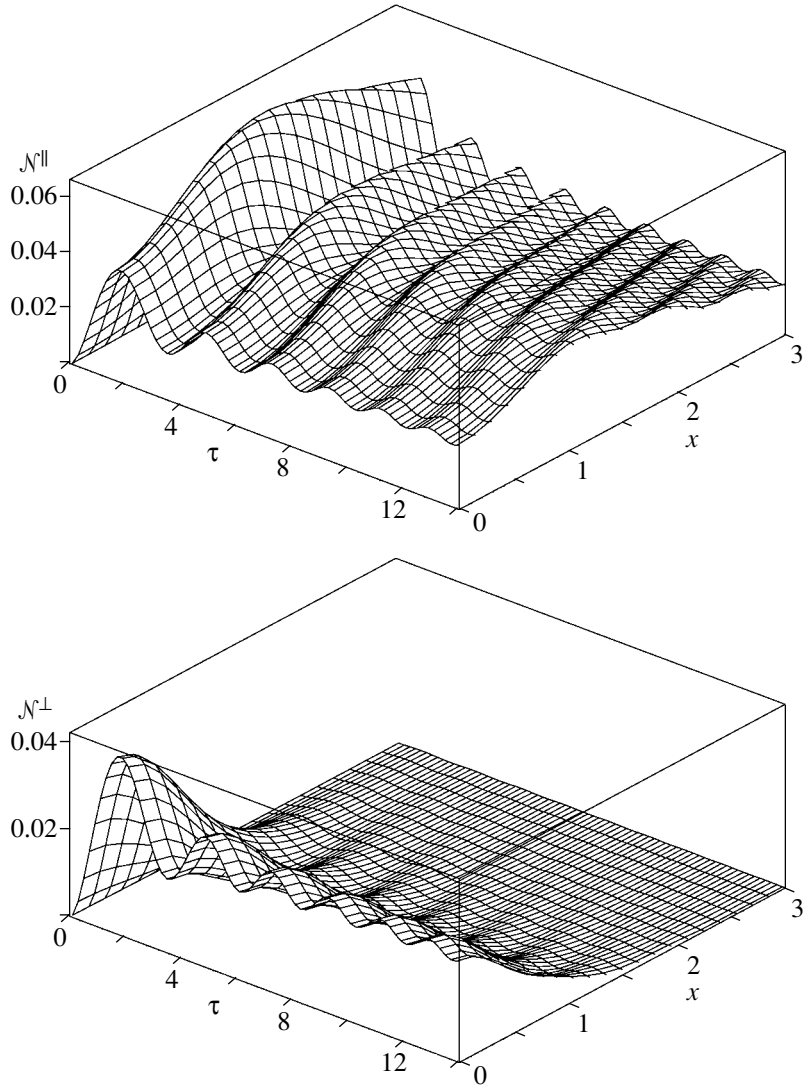

Longitudinal ($\mathcal{N}^{||}$) and transverse ($\mathcal{N}^{\perp}$) components of the boson distribution versus the dimensionless time $\tau = 2\eta H_I$ and the dimensionless momentum $x = q/M_I$ at the initial data $M_I = H_I$ ($\gamma_{\rm v} = 1$).

3.2. Thermalization of Bosons

The divergence of the integral in (40) stems from idealizing the problem of the production of a pair of particles in a finite volume for a system where there are simultaneous interactions associated with the removal of fields having a negative probability and where identical particles affect one another (so-called exchange effects). It is well known [38] that, in this case, one deals with the production of a set (rather that a pair) of particles, which acquires, owing to the aforementioned interactions, the properties of a statistical system. As a model of such a statistical system, we consider here a degenerate Bose–Einstein gas, whose distribution function has the form (we use the system of units where the Boltzmann constant is $k_{\rm B} = 1$)

$$\mathcal{F}(T_{\rm v}, q, M_{\rm v}(\eta), \eta) \qquad (41)$$
$$= \left\{\exp\left[\frac{\omega_{\rm v}(\eta) - M_{\rm v}(\eta)}{T_{\rm v}}\right] - 1\right\}^{-1},$$

where $T_{\rm v}$ is the boson temperature. We set apart the problem of theoretically validating such a statistical system and its thermodynamic exchange, only assuming fulfillment of specific conditions ensuring its existence. In particular, we can introduce the notion of the temperature $T_{\rm v}$ only in an equilibrium system. A thermal equilibrium is thought to be stable if the time within which the vector-boson temperature $T_{\rm v}$ is established, that is, the relaxation time [39]

$$\eta_{\rm rel} = [n(T_{\rm v})\sigma_{\rm scat}]^{-1} \qquad (42)$$

[as expressed in terms of their density $n(T_{\rm v})$ and the scattering cross section $\sigma_{\rm scat} \sim 1/M_I^2$], does not exceed the time of vector-boson-density formation

owing to cosmological creation, the latter time being controlled by the primordial Hubble parameter, $\eta_\mathrm{v} = 1/H_I$. From (42), it follows that the particle-number density is proportional to the product of the Hubble parameter and the mass squared (this product being an integral of the motion in the present example); that is,

$$n(T_\mathrm{v}) = n(T_\mathrm{v}, \eta_\mathrm{v}) \simeq C_H H_I M_I^2, \qquad (43)$$

where C_H is a constant. The expression for the density $n(T_\mathrm{v}, \eta)$ in Eq. (43) assumes the form

$$n_\mathrm{v}(T_\mathrm{v}, \eta) = \frac{1}{2\pi^2}\int\limits_0^\infty dqq^2\mathcal{F}\left(T_\mathrm{v}, q, M(\eta), \eta\right) \qquad (44)$$
$$\times\left[\mathcal{N}^{||}(q,\eta) + 2\mathcal{N}^{\perp}(q,\eta)\right].$$

Here, the probability of the production of a longitudinal and a transverse boson with a specific momentum in an ensemble featuring exchange interaction is given (in accordance with the multiplication law for probabilities) by the product of two probabilities, the probability of their cosmological creation, $\mathcal{N}^{||,\perp}$, and the probability of a single-particle state of vector bosons obeying the Bose–Einstein distribution in (41).

A dominant contribution to the integral in (44) from the region of high momenta (in the above idealized analysis disregarding the Boltzmann factor, this resulted in a divergence) implies the relativistic temperature dependence of the density,

$$n(T_\mathrm{v}, \eta_\mathrm{v}) = C_T T_\mathrm{v}^3, \qquad (45)$$

where C_T is a coefficient. A numerical calculation of the integral in (44) for the values $T_\mathrm{v} = M_I = H_I$, which follow from the assumption about the choice of initial data ($C_T = C_H$), reveals that this integral is weakly dependent on time in the region $\eta \geq \eta_\mathrm{v} = H_I^{-1}$ and, for the constant C_T, yields the value

$$C_T = \frac{n_\mathrm{v}}{T_\mathrm{v}^3} = \frac{1}{2\pi^2}\left\{[1.877]^{||} + 2[0.277]^{\perp} = 2.431\right\}, \qquad (46)$$

where the contributions of longitudinal and transverse bosons are labeled with the superscripts || and $\perp$, respectively.

On the other hand, the lifetime η_L of product bosons in the early Universe in dimensionless units, $\tau_L = \eta_L/\eta_I$, where $\eta_I = (2H_I)^{-1}$, can be estimated by using the equation of state $a^2(\eta) = a_I^2(1+\tau_L)$ and the W-boson lifetime within the Standard Model. Specifically, we have

$$1 + \tau_L = \frac{2H_I \sin^2\theta_{(\mathrm{W})}}{\alpha_\mathrm{QED} M_W(\eta_L)} = \frac{2\sin^2\theta_{(\mathrm{W})}}{\alpha_\mathrm{QED}\gamma_\mathrm{v}\sqrt{1+\tau_L}}, \qquad (47)$$

where $\theta_{(\mathrm{W})}$ is the Weinberg angle, $\alpha_\mathrm{QED} = 1/137$ is the fine-structure constant, and $\gamma_\mathrm{v} = M_I/H_I \geq 1$.

From the solution to Eq. (47),

$$1 + \tau_L = \left(\frac{2\sin^2\theta_{(\mathrm{W})}}{\gamma_\mathrm{v}\alpha_\mathrm{QED}}\right)^{2/3} \simeq \frac{16}{\gamma_\mathrm{v}^{2/3}}, \qquad (48)$$

it follows that, at $\gamma_\mathrm{v} = 1$, the lifetime of product bosons is an order of magnitude longer than the Universe relaxation time:

$$\tau_L = \frac{\eta_L}{\eta_I} \simeq \frac{16}{\gamma_\mathrm{v}^{2/3}} - 1 = 15. \qquad (49)$$

Therefore, we can introduce the notion of the vector-boson temperature T_v, which is inherited by the final vector-boson-decay products (photons). According to currently prevalent concepts, these photons form cosmic microwave background radiation in the Universe. Indeed, suppose that one photon comes from the annihilation of the products of $W^\pm$-boson decay and that the other comes from Z bosons. In view of the fact that the volume of the Universe is constant within the evolution model being considered, it is then natural to expect that the photon density coincides with the boson density [11]:

$$n_\gamma = T_\gamma^3 \frac{1}{\pi^2}\{2.404\} \simeq n_\mathrm{v}. \qquad (50)$$

On the basis of (43), (45), (46), and (50), we can estimate the temperature T_γ of cosmic microwave background radiation arising upon the annihilation and decay of W^+ and Z bosons. This yields

$$T_\gamma \simeq \left[\frac{2.431}{2.404\cdot 2}\right]^{1/3} T_\mathrm{v} = 0.8T_\mathrm{v}, \qquad (51)$$

where the vector-boson temperature $T_\mathrm{v} = [H_I M_I^2]^{1/3}$ is an invariant quantity within the model being considered. This invariant can be estimated at

$$T_\mathrm{v} = [H_I M_I^2]^{1/3} = [H_0 M_W^2]^{1/3} \qquad (52)$$
$$= 2.73/0.8\ K = 3.41\ \mathrm{K},$$

which is a value that is astonishingly close to the observed temperature of cosmic microwave background radiation. In the present case, this directly follows, as is seen from the above analysis of our numerical calculations, from the dominance of longitudinal vector bosons with high momenta and from the fact that the relaxation time is equal to the inverse Hubble parameter. The inclusion of physical processes, like the heating of photons owing to electron–positron annihilation [40], amounts to multiplying the photon temperature (51) by $(11/4)^{1/3} = 1.4$; therefore, we have

$$T_\gamma(e^+e^-) \simeq (11/4)^{1/3}\cdot 0.8T_\mathrm{v} = 2.77\ \mathrm{K}. \qquad (53)$$

We note that, in other models [41], the fluctuations of the product-particle density are related to primary fluctuations of cosmic microwave background radiation [42].

3.3. Inverse Effect of Product Particles on the Evolution of the Universe

The equation of motion $\varphi'^2(\eta) = \rho_{\rm tot}(\eta)$, with the Hubble parameter defined as $H = \varphi'/\varphi$, means that, at any instant of time, the energy density in the Universe is equal to the so-called critical density; that is,

$$\rho_{\rm tot}(\eta) = H^2(\eta)\varphi^2(\eta) \equiv \rho_{\rm cr}(\eta).$$

The dominance of matter obeying the extremely rigid equation of state implies the existence of an approximate integral of the motion in the form

$$H(\eta)\varphi^2(\eta) = H_0\varphi_0^2.$$

On this basis, we can immediately find the ratio of the product-vector-boson energy, $\rho_{\rm v}(\eta_I) \sim T^4 \sim H_I^4 \sim M_I^4$, to the density of the Universe in the extremely rigid state, $\rho_{\rm tot}(\eta_I) = H_I^2\varphi_I^2$. The result is

$$\frac{\rho_{\rm v}(\eta_I)}{\rho_{\rm tot}(\eta_I)} = \frac{M_I^2}{\varphi_I^2} = \frac{M_W^2}{\varphi_0^2} = y_{\rm v}^2 = 10^{-34}. \qquad (54)$$

This value indicates that the inverse effect of product particles on the evolution of the Universe is negligible.

3.4. Baryon–Antibaryon Asymmetry of Matter in the Universe

It is well known that, because of a triangle anomaly, W- and Z-boson interaction with left-handed fermion doublets $\psi_L^{(i)}$, $i = 1, 2, ..., n_L$, leads to a nonconservation of the number of fermions of each type (i) [43, 44],

$$\partial_\mu j_{L\mu}^{(i)} = \frac{1}{32\pi^2}{\rm tr}\hat{F}^*_{\mu\nu}\hat{F}_{\mu\nu}, \qquad (55)$$

where $\hat{F}_{\mu\nu} = -iF^a_{\mu\nu}g_W\tau_a/2$ is the strength of the vector fields, $F^a_{\mu\nu} = \partial_\mu A^a_\nu - \partial_\nu A^a_\mu + g\epsilon^{abc}A^b_\mu A^c_\nu$.[6)]

Taking the integral of the equality in (55) with respect to the four-dimensional variable x, we can find a relation between the change $\Delta F^{(i)} = \int d^4x\partial_\mu j_{L\mu}^{(i)}$ in the fermion number $F^{(i)} = \int d^3x j_0^{(i)}$ and the Chern–Simons functional $N_{\rm CS} = \frac{1}{32\pi^2}\int d^4x{\rm tr}\hat{F}^*_{\mu\nu}\hat{F}_{\mu\nu}$ [19]:

$$\Delta F^{(i)} = N_{\rm CS} \neq 0, \quad i = 1, 2, ..., n_L. \qquad (56)$$

The equality in (56) is considered as a selection rule—that is, the fermion number changes identically for all fermion types: $N_{\rm CS} = \Delta L^e = \Delta L^\mu = \Delta L^\tau = \Delta B/3$; at the same time, the change in the baryon charge B and the change in the lepton charge $L = L^e + L^\mu + L^\tau$ are related to each other in such a way that $B - L$ is conserved, while $B + L$ is not invariant. Upon taking the sum of the equalities in (56) over all doublets, we obtain $\Delta(B + L) = 12N_{\rm CS}$.

We can evaluate the expectation value of the Chern–Simons functional (56) (in the lowest order of perturbation theory in the coupling constant) in the Bogolyubov vacuum $b|0\rangle_{\rm sq} = 0$. Specifically, we have

$$N_{\rm CS} = N_W + N_Z$$
$$\equiv -\sum_{{\rm v}=W,Z}\int_0^{\eta_{L_{\rm v}}} d\eta \int \frac{d^3x}{32\pi^2}{}_{\rm sq}\langle 0|{\rm tr}\hat{F}^{\rm v}_{\mu\nu}{}^*\hat{F}^{\rm v}_{\mu\nu}|0\rangle_{\rm sq},$$

where η_{L_W} and η_{L_Z} are the W- and the Z-boson lifetime, respectively, and N_W and N_Z are the contributions of primordial W and Z bosons, respectively. The integral over the conformal spacetime bounded by three-dimensional hypersurfaces $\eta = 0$ and $\eta = \eta_L$ is given by

$$N_{\rm v} = -\beta_{\rm v}\frac{V_0}{2}\int_0^{\eta_{L_{\rm v}}} d\eta \int_0^\infty dk|k|^3\sin(2\theta_{\rm v})\sinh(2r_{\rm v}),$$

where ${\rm v} = W, Z$;

$$\beta_W = \frac{4\alpha_{\rm QED}}{\sin^2\theta_{\rm (W)}}; \quad \beta_Z = \frac{\alpha_{\rm QED}}{\sin^2\theta_{\rm (W)}\cos^2\theta_{\rm (W)}};$$

and $\theta_{\rm v}$ and $r_{\rm v}$ are specified by relevant solutions to the Bogolyubov equations. Upon a numerical calculation of this integral, we can estimate the expectation value of the Chern–Simons functional in the state of primordial bosons. At the vector-boson-lifetime values of $\tau_{L_W} = 15$ and $\tau_{L_Z} = 30$, this yields the following result at $n_\gamma \simeq n_{\rm v}$:

$$\frac{N_{\rm CS}}{V_{(r)}} = \frac{N_W + N_Z}{V_{(r)}} \qquad (57)$$
$$= \frac{\alpha_{\rm QED}}{\sin^2\theta_{\rm (W)}}T^3\left(4\cdot 1.44 + \frac{2.41}{\cos^2\theta_{\rm (W)}}\right) = 1.2n_\gamma.$$

On this basis, the violation of the fermion-number density in the cosmological model being considered can be estimated as [16]

$$\frac{\Delta F^{(i)}}{V_{(r)}} = \frac{N_{\rm CS}}{V_{(r)}} = 1.2n_\gamma, \qquad (58)$$

[6)] In each of the three generations of leptons (e, μ, τ) and color quarks, we have four fermion doublets—in all, there are $n_L = 12$ of them. Each of 12 fermion doublets interacts with the triplet of non-Abelian fields $A^1 = (W^{(-)} + W^{(+)})/\sqrt{2}$, $A^2 = i(W^{(-)} - W^{(+)})/\sqrt{2}$, and $A^3 = Z/\cos\theta_{\rm (W)}$, the corresponding coupling constant being $g = e/\sin\theta_{\rm (W)}$.

where $n_\gamma = 2.402T^3/\pi^2$ is the number density of photons forming cosmic microwave background radiation.

According to Sakharov [18], this violation of the fermion number is frozen by CP nonconservation, this leading to the baryon-number density

$$n_\mathrm{b} = X_{CP}\frac{\Delta F^{(i)}}{V_{(r)}} \simeq X_{CP} n_\gamma, \qquad (59)$$

where the factor X_{CP} is determined by the superweak interaction of d and s quarks ($d + s \to s + d$), which is responsible for CP violation experimentally observed in K-meson decays [45].

From the ratio of the number of baryons to the number of photons, one can deduce an estimate of the superweak-interaction coupling constant: $X_{CP} \sim 10^{-9}$. Thus, the evolution of the Universe, primary vector bosons, and the aforementioned superweak interaction [45] (it is responsible for CP violation and is characterized by a coupling-constant value of $X_{CP} \sim 10^{-9}$) lead to baryon–antibaryon asymmetry of the Universe, the respective baryon density being

$$\rho_\mathrm{b}(\eta = \eta_L) \simeq 10^{-9} \times 10^{-34}\rho_\mathrm{cr}(\eta = \eta_L). \qquad (60)$$

In order to assess the further evolution of the baryon density, one can take here the W-boson lifetime for η_L.

Upon the decay of the vector bosons in question, their temperature is inherited by cosmic microwave background radiation. The subsequent evolution of matter in a stationary cold universe is an exact replica of the well-known scenario of a hot universe [34], since this evolution is governed by conformally invariant mass-to-temperature ratios (m/T).

Formulas (47), (54), and (60) make it possible to assess the ratio of the present-day values of the baryon density and the density of the scalar field Q, which plays the role of primordial quintessence in the model being considered. We have

$$\Omega_\mathrm{b}(\eta_0) = \frac{\rho_\mathrm{b}(\eta_0)}{\rho_\mathrm{cr}(\eta_0)} = \left[\frac{\varphi_0}{\varphi_L}\right]^3 = \left[\frac{\varphi_0}{\varphi_I}\right]^3\left[\frac{\varphi_I}{\varphi_L}\right]^3, \quad (61)$$

where we have considered that the baryon density increases in proportion to the mass and that the density of the primordial quintessence Q decreases in inverse proportion to the mass squared. We recall that the ratio $[\varphi_0/\varphi_I]^3$ is approximately equal to 10^{43} and that the ratio $[\varphi_I/\varphi_L]^3$ is determined by the boson lifetime in (48) and by the equation of state $\varphi(\eta) \sim \sqrt{\eta}$. On this basis, we can estimate $\Omega_\mathrm{b}(\eta_0)$ at

$$\Omega_\mathrm{b}(\eta_0) = \left[\frac{\varphi_0}{\varphi_L}\right]^3 \times 10^{-43} \qquad (62)$$

$$\sim 10^{43}\left[\frac{\eta_I}{\eta_L}\right]^{3/2} \times 10^{-43} \sim \left[\frac{\alpha_\mathrm{QED}}{\sin^2\theta_{(\mathrm{W})}}\right] \sim 0.03,$$

which is compatible with observational data (see [20]).

Thus, the general theory of relativity and the Standard Model, which are supplemented with a free scalar field (Q) and which are considered as the result of a spontaneous breakdown of the scale symmetry of a conformally invariant theory in a specific reference frame with the initial data $\varphi_I = 10^4$ GeV and $H_I = 2.7$ K, do not contradict the following scenario of the evolution of the Universe within conformal cosmology [16]:

$\eta \sim 10^{-12}$ s, creation of vector bosons from a "vacuum";

$10^{-12} < \eta < 10^{-11}$–$10^{-10}$ s, formation of baryon–antibaryon asymmetry;

$\eta \sim 10^{-10}$ s, decay of vector bosons;

$10^{-10} < \eta < 10^{11}$ s, primordial chemical evolution of matter;

$\eta \sim 10^{11}$ s, recombination or separation of cosmic microwave background radiation;

$\eta > 10^{17}$ s, terrestrial experiments and evolution of supernovae.

4. CONCLUSION

Within the conformal formulation of the general theory of relativity and the Standard Model, we have investigated conditions under which the origin of matter can be explained by its cosmological creation from a vacuum. We have presented some arguments in support of the statement that the number of product vector-boson pairs is sufficient for explaining the total amount of observed matter and its content, provided that the Universe is considered as a conventional physical object that is characterized by a finite volume and a finite lifetime and which is described by a conformally invariant version of the general theory of relativity and the Standard Model featuring scale-invariant equations where all masses, including the Planck mass, are replaced by the dilaton variable and where the spatial volume is replaced by a constant. In this case, the energy of the entire Universe in the field space of events is described by analogy with the description of the energy of a relativistic quantum particle in Minkowski space: one of the variables (dilaton in the case being considered) becomes an evolution parameter, while the corresponding canonically conjugate momentum assumes the role of energy [22, 23]. This means that measured quantities are identified with conformal variables that are used in observational cosmology and in quantum field theory in calculating cosmological particle creation from a vacuum [6, 7, 9, 22]. Within the errors of

observation, this identification of conformal variables with observables is compatible with data on the chemical evolution of matter and data on supernovae, provided that cosmic evolution proceeds via the regime dominated by the density of a free scalar field Q [11, 16].

Thus, the identification of conformal coordinates and variables used in observational cosmology and in quantum field theory with measured quantities is a first condition under which the origin of matter can be explained by its cosmological creation from a vacuum. This is possible within a conformally invariant unified theory, where the Planck mass, which is an absolute quantity in the general theory of relativity, becomes an ordinary present-day value of the dilaton and where the Planck era loses its absolute meaning.

The construction of a stable vacuum of perturbation theory by eliminating (through the choice of gauge-invariant variables) unphysical fields whose quantization leads to a negative normalization of the wave function in this reference frame is a second condition.

Finally, the elimination of divergences in summing the probabilities of product particles over their momenta by thermalizing these particles in the region where the Boltzmann H-theorem is applicable is a third condition.

Under these conditions, it has been found in the present study that, in describing the creation of vector bosons from a vacuum in terms of conformal variables, one arrives at the temperature $(M_W^2 H_0)^{1/3} \sim 2.7$ K of cosmic microwave background radiation as an integral of the motion of the Universe and at the baryon–antibaryon asymmetry of the Universe with the superweak-interaction coupling constant $X_{CP} = n_\mathrm{b}/n_\gamma$ and the baryon density of $\Omega_\mathrm{b} = \alpha_\mathrm{QED}/\sin^2\theta_{(\mathrm{W})} \sim 0.03$, these results being in satisfactory agreement with the corresponding observed values and being compatible with the most recent data on supernovae and nucleosynthesis.

ACKNOWLEDGMENTS

We are grateful to B.A. Arbuzov, B.M. Barbashov, A.V. Efremov, V.B. Priezzhev, and P. Flin for stimulating discussions. We are also indebted to the participants of the seminar held at the Shternberg State Astronomical Institute and dedicated to the memory of A.L. Zel'manov, especially to M.V. Sazhin and A.A. Starobinsky, for discussions on the problem of choosing the units of measurements in cosmology and on the cosmological creation of massive bosons.

REFERENCES

1. É. A. Tagirov and N. A. Chernikov, Preprint No. 2-3777, OIYaI (Joint Institute for Nuclear Research, Dubna, 1968); K. A. Bronnikov and É. A. Tagirov, Preprint No. 2-4151, OIYaI (Joint Institute for Nuclear Research, Dubna, 1968).
2. G. L. Parker, Phys. Rev. Lett. **21**, 562 (1968); Phys. Rev. **183**, 1057 (1969); Phys. Rev. D **3**, 346 (1971).
3. A. A. Grib and S. G. Mamaev, Yad. Fiz. **10**, 1276 (1969) [Sov. J. Nucl. Phys. **10**, 722 (1970)].
4. R. U. Sexl and H. K. Urbantke, Phys. Rev. **179**, 1247 (1969).
5. Ya. B. Zel'dovich, Pis'ma Zh. Éksp. Teor. Fiz. **12**, 443 (1970) [JETP Lett. **12**, 307 (1970)].
6. Ya. B. Zel'dovich and A. A. Starobinskiĭ, Zh. Éksp. Teor. Fiz. **61**, 2161 (1971) [Sov. Phys. JETP **34**, 1159 (1971)].
7. A. A. Grib, S. G. Mamaev, and V. M. Mostepanenko, *Quantum Effects in Strong External Fields* (Énergoatomizdat, Moscow, 1988).
8. A. A. Starobinsky, Phys. Lett. B **91**, 99 (1980).
9. V. N. Pervushin and V. I. Smirichinski, J. Phys. A **32**, 6191 (1999).
10. L. A. Kofman, A. D. Linde, and A. A. Starobinsky, Phys. Rev. Lett. **73**, 3195 (1994); Phys. Rev. D **56**, 3258 (1997).
11. V. N. Pervushin, D. V. Proskurin, and A. A. Gusev, Grav. Cosmol. **8**, 181 (2002).
12. H. Wentzel, *Quantum Theory of Fields* (translated from German, *Einfürung in die Quantentheorie der Wellenfelder*) (Intersci., New York, 1949; OGIZ-GITTL, Moscow, 1947).
13. H.-P. Pavel and V. N. Pervushin, Int. J. Mod. Phys. A **14**, 2285 (1999).
14. V. I. Ogievetskiĭ and I. V. Polubarinov, Zh. Éksp. Teor. Fiz. **41**, 246 (1961) [Sov. Phys. JETP **14**, 246 (1962)]; A. A. Slavnov and L. D. Faddeev, Teor. Mat. Fiz. **3**, 18 (1970).
15. A. A. Starobinsky, Pis'ma Zh. Éksp. Teor. Fiz. **73**, 415 (2001) [JETP Lett. **73**, 371 (2001)].
16. D. Behnke, D. B. Blaschke, V. N. Pervushin, and D. Proskurin, Phys. Lett. B **530**, 20 (2002).
17. A. G. Riess *et al.*, Astron. J. **116**, 1009 (1998); S. Perlmutter *et al.*, Astrophys. J. **517**, 565 (1999); A. G. Riess *et al.*, Astrophys. J. **560**, 49 (2001).
18. A. D. Sakharov, Pis'ma Zh. Éksp. Teor. Fiz. **5**, 24 (1967) [JETP Lett. **5**, 17 (1967)].
19. M. E. Shaposhnikov, Nucl. Phys. B **287**, 757 (1987); V. A. Matveev *et al.,* Usp. Fiz. Nauk **156**, 253 (1988); V. A. Rubakov and M. E. Shaposhnikov, Usp. Fiz. Nauk **166**, 493 (1996).
20. M. Fukugita, C. J. Hogan, and P. J. E. Peebles, Astrophys. J. **503**, 518 (1998).
21. M. Pawlowski, V. V. Papoyan, V. N. Pervushin, and V. I. Smirichinski, Phys. Lett. B **444**, 293 (1998).
22. M. Pawlowski and V. N. Pervushin, Int. J. Mod. Phys. A **16**, 1715 (2001); V. N. Pervushin and D. V. Proskurin, Grav. Cosmol. **7**, 89 (2001).

23. B. M. Barbashov, V. N. Pervushin, and D. V. Proskurin, Teor. Mat. Fiz. **132**, 181 (2002).
24. R. Kallosh, L. Kofman, A. Linde, and A. Van Proeyen, Class. Quantum Grav. **17**, 4269 (2000).
25. A. D. Linde, *Elementary Particle Physics and Inflationary Cosmology* (Nauka, Moscow, 1990).
26. J. Schwinger, Phys. Rev. **127**, 324 (1962).
27. I. V. Polubarinov, Fiz. Élem. Chastits At. Yadra **34**, 739 (2003) [Phys. Part. Nucl. **34**, 377 (2003)].
28. Nguyen Suan Han and V. N. Pervushin, Mod. Phys. Lett. A **2**, 367 (1987); V. N. Pervushin, Phys. Part. Nucl. **34**, 348 (2003); L. D. Lantsman and V. N. Pervushin, Yad. Fiz. **66**, 1426 (2003) [Phys. At. Nucl. **66**, 1384 (2003)].
29. L. D. Faddeev and V. N. Popov, Phys. Lett. B **25B**, 29 (1967).
30. A. M. Polyakov, Phys. Lett. B **103B**, 207 (1981).
31. B. M. Barbashov and N. A. Chernikov, Preprint No. P2-7852, OIYaI (Joint Institute for Nuclear Research, Dubna, 1974).
32. A. L. Zel'manov, Dokl. Akad. Nauk SSSR **227**, 78 (1976); Yu. S. Vladimirov, *Reference Frames in Gravitation Theory* (Énergoizdat, Moscow, 1982).
33. R. Srianand, P. Petitjean, and C. Ledoux, Nature **408**, 931 (2000).
34. S. Weinberg, *The First Three Minutes: A Modern View of the Origin of the Universe* (Basic Books, New York, 1977).
35. J. A. Wheeler, *Batelle Recontres*, in *Lectures in Mathematics and Physics*, Ed. by C. DeWitt and J. A. Wheeler (Benjamin, New York, 1968); B. S. DeWitt, Phys. Rev. **160**, 1113 (1967).
36. C. Misner, Phys. Rev. **186**, 1319 (1969).
37. S. Schweber, *An Introduction to Relativistic Quantum Field Theory* (Row, Peterson and Co., Evanston, 1961; Izd. Inostr. Lit., 1963).
38. L. D. Landau and E. M. Lifshitz, *Statistical Physics* (Nauka, Moscow, 1976; Pergamon, Oxford, 1980), Part 1.
39. J. Bernstein, *Kinetic Theory in the Expanding Universe* (Cambridge Univ. Press, Cambridge, 1985).
40. E. W. Kolb and M. S. Turner, *The Early Universe* (Addison-Wesley, Reading, 1993).
41. J. C. Niemeyer, Phys. Rev. D **63**, 123502 (2001).
42. J. R. Bond *et al.* (MaxiBoom Collab.), in *Proceedings of IAU Symposium 201 (PASP), Manchester, England, 7–11 Aug. 2000*; CITA-2000-65.
43. S. Adler, Phys. Rev. **177**, 2426 (1969); J. S. Bell and R. Jackiw, Nuovo Cimento A **60**, 47 (1969); W. A. Bardeen, Phys. Rev. **184**, 1848 (1969).
44. G. 't Hooft, Phys. Rev. Lett. **37**, 8 (1976); Phys. Rev. D **14**, 3432 (1976).
45. L. B. Okun, *Leptons and Quarks* (Nauka, Moscow, 1981; North-Holland, Amsterdam, 1982).

Translated by A. Isaakyan

Physics of Atomic Nuclei, Vol. 67, No. 5, 2004, pp. 1063–1064. Translated from Yadernaya Fizika, Vol. 67, No. 5, 2004, pp. 1087–1088.

FUTURE PUBLICATIONS

Independent Production of π^- Mesons in pp Interactions

A. I. Golokhvastov

It is shown that experimental data on the multiparticle production of π^- mesons in pp interactions at $\sqrt{s} \leq 30$ GeV do not involve significant indications of the existence of any correlations between π^- mesons, apart from those that are associated with momentum conservation and with interference. The multiplicity distributions in rapidity intervals, the forward–backward correlation, and the two-particle rapidity and transverse-momentum correlations do not contradict the independent production of π^- mesons. No constraints on the multiplicity distributions of particles follow from the independent production of these particles.

Isotopic Dependence of the Shape of Se Nuclei in the Representation of Collective Models

O. I. Davidovskaya, I. E. Kashuba, and Yu. V. Porodzinsky†

The energy structure of low-lying excited states in the nuclei of even selenium isotopes is considered on the basis of a soft-nucleus model. The nuclei are treated as nonaxial rotors, longitudinal and transverse vibrations of their surface being taken into account in the approximation of a quadrupole deformation featuring an admixture of an octupole deformation. The parameters of a phenomenological collective model for the ^{72,74,76,78,80,82}Se nuclei are found both in the case of β vibrations (longitudinal vibrations) and in the presence of additional γ vibrations (transverse vibrations) of the nuclear surface.

Proton Structure Functions over the Entire Kinematical Region

A. A. Petrukhin and D. A. Timashkov

A new approach to describing inelastic charged-lepton scattering on a proton is proposed. The approach is based on combining the results obtained by theoretically studying the limiting cases of this process. The proton structure function is obtained in an analytic form that involves virtually no free parameters and which is in good agreement with experimental data over the entire kinematical region.

Diffractive Splitting of Tritons by Incident Protons

V. K. Tartakovsky, A. V. Fursaev, and B. I. Sidorenko

General expressions that are obtained in the present study for the differential cross sections describing the two- and three-body diffractive dissociation of tritons that is induced by intermediate-energy incident protons are used to calculate the energy distributions of neutrons and protons originating from this process and of scattered protons. The results are basically in satisfactory (but sometimes only qualitative) agreement with data from relevant coincidence experiments.

Double-Differential Cross Sections for Neutron Emission from Pb, W, Zr, Cu, and Al Nuclei Bombarded by 0.8-, 1.0-, and 1.6-GeV Protons

Yu. V. Trebukhovsky, Yu. E. Titarenko, V. F. Batyaev, E. I. Karpikhin, R. D. Mulambetov, S. V. Mulambetova, G. N. Smirnov, K. A. Lipatov, A. B. Koldobsky, V. M. Zhivun, Yu. V. Nekrasov, V. S. Barashenkov, H. Kumavat, S. G. Mashnik, and R. E. Prael

The results are presented of experiments that are aimed at determining the double-differential cross sections for the production of secondary neutrons from Pb, W, Zr, Cu, and Al targets exposed to protons of energy 0.8, 1.0, and 1.6 GeV. The spectra of neutrons at angles of 15°, 30°, 60°, 90°, 120°, and 150° are measured by means of a time-of-flight spectrometer in a beam extracted from the U-10 synchrotron installed at the Institute of Theoretical and Experimental Physics (ITEP, Moscow). Product neutrons were recorded by 5MAB-1F6BC501A/5L liquid scintillation detectors and NE110 solid-state scintillators. Experimental data

1063-7788/04/6705-1063$26.00

obtained in this way are compared with the results of simulations performed with the aid of high-energy transport codes CEM97, LAHET, and CASCADE.

Radiative Decays of the ϕ Meson and Nature of Light Scalar Resonances

N. N. Achasov

We show, on gauge-invariance grounds, that a new threshold phenomenon is discovered in the radiative decays $\phi \to \gamma a_0 \to \gamma\pi^0\eta$ and $\phi \to \gamma f_0 \to \gamma\pi^0\pi^0$. This enables us to conclude that the production of light scalar mesons $a_0(980)$ and $f_0(980)$ in these decays is caused by four-quark transitions, resulting in strong restrictions on the large-N_c expansions of the decay amplitudes. The analysis shows that these constraints give new pieces of evidence in favor of the four-quark nature of the $a_0(980)$ and $f_0(980)$ mesons.

Doorway States for One-Nucleon Transfer Reactions and Nuclear Correlation Energy

B. L. Birbrair and V. I. Ryazanov

Correlation effects are found to make a dominant contribution to nuclear binding energies. This result is obtained within a simple renormalizable model for multiparticle forces between nucleons.

Single-Spin Asymmetry of Inclusive γ Production in $p_\uparrow p$ Interactions at 200 GeV/c

Yu. V. Kharlov, D. A. Morozov, S. B. Nurushev, and A. N. Vasiliev

From the data of the Fermilab polarization experiment E704, the analyzing power A_N^γ of inclusively produced photons was extracted. It is small, on the order of 2 to 4%. The analyzing power of "leading" photons (fastest in $\pi^0 \to \gamma\gamma$ decay) is twice as high as A_N^γ under the assumption of a specific model for the x_F dependence of A_N^γ. A Monte Carlo simulation is performed in order to see effects at a higher statistical level than in the E704 experiment. This simulation showed that the process of inclusive photons may be used as a basis for future polarimetry at polarized colliders. An example of one local photon polarimeter at RHIC is discussed.

Physics of Atomic Nuclei, Vol. 67, No. 5, 2004, pp. 875–881. Translated from Yadernaya Fizika, Vol. 67, No. 5, 2004, pp. 899–905.

NUCLEI
Experiment

Investigation of the Excitation of Metastable States of ^{197}Pt and ^{197}Hg in (γ, n) and $(d, 2n)$ Reactions

V. A. Zheltonozhsky[1)], V. M. Mazur[2)], and Z. M. Bigan[2)]

Received November 28, 2002; in final form, June 19, 2003

Abstract—The isomeric ratios of the ^{197m,g}Pt and ^{197m,g}Hg yields in the respective (γ, n) reactions are measured for the first time in the energy range 8–17 MeV. The isomeric ratios σ_m/σ_g for ^{197m,g}Hg in the $(d, 2n)$ reaction are measured in the energy range 8–50 MeV. The experimental data are compared with the results of theoretical calculations. The effect of the structure of low-lying states and of the yrast line on the behavior of σ_m/σ_g is revealed. © *2004 MAIK "Nauka/Interperiodica".*

Nuclei of $A \sim 190$, which include those of platinum and mercury isotopes, lie between strongly deformed nuclei of rare-earth elements and the region of spherical nuclei in the vicinity of $A = 208$. Analyzing the entire body of data on the spectra of low-energy excitations, one can find that the shape of these nuclei undergoes rather complicated variations. The quadrupole moment of platinum isotopes changes sign, which, despite the fact that this quadrupole moment is 2 to 2.5 times less than that of nuclides from the rare-earth region (that is, the shape of platinum nuclei is close to spherical), is indicative of a transition to an oblate shape [1]. Mercury isotopes also seem to have an oblate shape. To a considerable extent, the spectrum of low-energy excitations of these nuclei is formed by the $3p1/2$, $2f5/2$, $3p3/2$, and $1i13/2$ single-particle (hole) states. It is the last one of these that is responsible for the existence of the $J^\pi = 13/2^+$ isomeric level. Investigation of processes leading to the population of metastable states in the aforementioned isotopes and of the energy dependence of their isomeric ratios can shed additional light on the nontrivial nature of the nuclei within this mass region.

Although the excitation of a giant dipole resonance (GDR) was systematically investigated for a wide range of nuclei [2, 3], its properties for platinum and mercury isotopes have not yet received adequate study.

No systematic research into the decay of a giant $E1$ resonance via the (γ, n) channel with the excitation of isomeric states has so far been performed for the ^{197}Pt and ^{197}Hg nuclei. To date, there have been only a few studies in which the isomeric yield ratio $d = Y_m/Y_g$ [that is, the ratio of the yield of the isomeric level (Y_m) to that of the ground-state level (Y_g)] in $(\gamma, n)^m$ reactions on targets of natural isotopic composition was measured at the same energy for the bremsstrahlung-spectrum endpoint energy of $E_\gamma^{\max} = 30$ MeV [4, 5].

The comprehensive survey of the results obtained by studying the isomeric cross-section ratios σ_m/σ_g for the ^{197}Hg nucleus in reactions induced by various particles is given in [6]. The isomeric ratios in the respective $(d, 2n)$ reaction at energies in the range 7–20 MeV were explored there most thoroughly. The measurements reported in [6] were performed with a NaI(Tl) spectrometer; therefore, it was very difficult to single out the contribution of K_X radiation from Au ($E_{K\beta1'} = 78$ keV) and Hg ($E_{K\beta1'} = 80$ keV) and the contribution of the 77-keV γ transition. For the respective $(d, 2n)$ reaction, we measured σ_m/σ_g in the energy range where such measurements have already been performed and at higher energies. For the ^{197}Hg and ^{197}Pt nuclei, the (γ, n) reaction was studied in the range 8–17 MeV.

DESCRIPTION OF THE EXPERIMENT

The isomeric ratio σ_m/σ_g for ^{197m,g}Hg in the $(d, 2n)$ reaction was measured at the U-240 cyclotron installed at the Institute for Nuclear Research (Kiev, National Academy of Sciences of Ukraine). The deuteron energy was varied by means of aluminum foils. The measurements were performed with a semiconductor spectrometer equipped with a Ge detector of volume 100 cm^3 and resolution 1.1 keV at the 412-keV γ line. Foils from natural Au 50 mg/cm^2 thick were irradiated. The yield of ^{197m,g}Hg was

[1)]Institute for Nuclear Research, National Academy of Sciences of Ukraine, pr. Nauki 47, Kiev, 03680 Ukraine.
e-mail: zhelton@kinr.kiev.ua
[2)]Institute for Electron Physics, National Academy of Sciences of Ukraine, Uzhgorod, Ukraine.

1063-7788/04/6705-0875$26.00

determined by K_α emission from Au and Hg and by 77- and 134-keV γ transitions (Fig. 1). The σ_m/σ_g values were calculated by using the relations given below. Figure 2 and Table 1 display our data.

We studied the reactions $^{198}\mathrm{Pt}(\gamma,n)^{197m,g}\mathrm{Pt}$ and $^{198}\mathrm{Hg}(\gamma,n)^{197}\mathrm{Hg}$ in a bremsstrahlung-photon beam extracted from the M-30 microtron installed at the Institute for Electron Physics (Uzhgorod, National Academy of Sciences of Ukraine). The reaction yields were measured in the energy range 8–17 MeV. The threshold for the (γ,n) reaction was 7.8 MeV and 8.3 MeV for the ^{198}Pt and ^{198}Hg isotopes, respectively. For targets, we employed samples from natural mercury (HgO) of weight 4 g pressed into thin-walled Capron containers 30 mm in diameter and 0.5-mm-thick metallic-platinum plates of dimension 20×20 mm^2. The induced activity of the irradiated samples was measured by using the semiconductor spectrometer with the detector of volume 100 cm^3. The procedure of our measurement was described in more detail in [7].

Nuclei of ^{197}Pt and ^{197}Hg from the relevant (γ,n) and $(d,2n)$ reactions are unstable. Figure 1 shows the diagrams of their decays and their quantum features [8, 9]. In both cases, the ^{197}Au isotope appears to be the product of these decays. Since the ground states of the isotopes under study are unstable, we calculated the isomeric yield ratio by the formula [10]

$$d = Y_m/Y_g \qquad (1)$$
$$= \frac{\lambda_g-\lambda_m}{\left\{\left(c\frac{N_g}{N_m}\frac{\varphi_m}{\varphi_g}(\lambda_g-\lambda_m)-p\lambda_m\right)\frac{\lambda_g}{\lambda_m}\frac{f_m(t)}{f_g(t)}\right\}+p\lambda_g},$$

where

$$f_{m,g} = [1-\exp(-\lambda_{m,g}t_{\mathrm{irr}})]\exp(-\lambda_{m,g}t_{\mathrm{cool}}) \times [1-\exp(-\lambda_{m,g}t_{\mathrm{meas}})],$$
$$\varphi_{m,g} = \xi_{m,g}\kappa_{m,g}\alpha_{m,g}.$$

Table 1. Isomeric ratios σ_m/σ_g for ^{197m,g}Hg in the $(d,2n)$ reaction

E_d, MeV	σ_m/σ_g	E_d, MeV	σ_m/σ_g
8.0	0.40(4)	35.0	1.61(16)
13.0	0.60(6)	39.3	1.59(16)
15.7	0.74(7)	44.9	0.85(8)
25.0	0.53(5)	50.0	0.73(7)
30.6	1.06(10)		

Note: The accuracy in determining the energy is $\Delta E_d \approx 0.3$ MeV.

Here, $\xi_{m,g}$ is the detector photoefficiency in recording the γ lines from the decay of, respectively, the isomeric (m) and the ground (g) state; $\kappa_{m,g}$ are the corrections for the self-absorption of the corresponding lines; $\alpha_{m,g}$ are the intensities of the γ lines corresponding to the decays of, respectively, the isomeric and the ground state; $\lambda_{m,g}$ are the decay constants for the corresponding states; $N_{m,g}$ are the numbers of pulses in the corresponding photopeaks; t_{irr}, t_{cool}, and t_{meas} are the irradiation time, the time of cooling, and the time of measurements; c is a correction for pulses that were missed and for overlapping pulses; and p is the branching fraction.

Figure 3 and Table 2 present the measured values of the isomeric yield ratio $d = Y_m/Y_g$. The relative statistical uncertainty was 1 to 2% and 0.2% at $E_\gamma^{\max}$ of 9 to 10 MeV and 16 MeV, respectively. With allowance for the accuracy in measuring the efficiency of the semiconductor spectrometer, the uncertainty in determining d for the respective (γ,n) reactions does not exceed 5%.

DISCUSSION OF THE RESULTS

From the data on the isomer yield in the vicinity of the threshold, it was found that the threshold for the reaction $^{198}\mathrm{Pt}(\gamma,n)^{197m,g}\mathrm{Pt}$ is 8.90 ± 0.15 MeV; it is 0.9 MeV greater than the energy threshold of the $(\gamma,n)^m$ reaction for this nucleus (7.6 ± 0.4 MeV). Accordingly, the threshold for the reaction $^{198}\mathrm{Hg}(\gamma,n)^{197m}\mathrm{Hg}$ is 9.70 ± 0.15 MeV, which is 1.1 MeV greater than the calculated energy of the $(\gamma,n)^m$ threshold [11].

The existence of so appreciable a threshold for the population of the metastable state is caused by a relatively large spin difference ΔJ between the ground state of the parent nucleus and the isomeric level of the product nucleus. For the metastable state to be populated by a γ-ray cascade, there must be at least five dipole transitions or fast neutrons (of energy about 1 MeV) that are able to change the angular momentum of the daughter nucleus.

Above the $(\gamma,n)^m$ threshold, the isomeric ratio of the yields increases dramatically and approaches a plateau at 16 to 17 MeV, reaching the sizable values of $d = 0.171\pm 0.010$ and $d = 0.104\pm 0.006$ at $E_\gamma^{\max} = 16$ MeV for ^{197}Pt and ^{197}Hg, respectively.

The points in Fig. 4 represent the cross sections σ_m for the excitation of the isomeric states in the reactions $^{198}\mathrm{Pt}(\gamma,n)^{197m}\mathrm{Pt}$ and $^{198}\mathrm{Hg}(\gamma,n)^{197}\mathrm{Hg}$. The cross sections were calculated from the yields with the aid of the Penfold–Leiss inverse matrix [12, 13] with a step of $\Delta E = 1$ MeV. The solid curves in

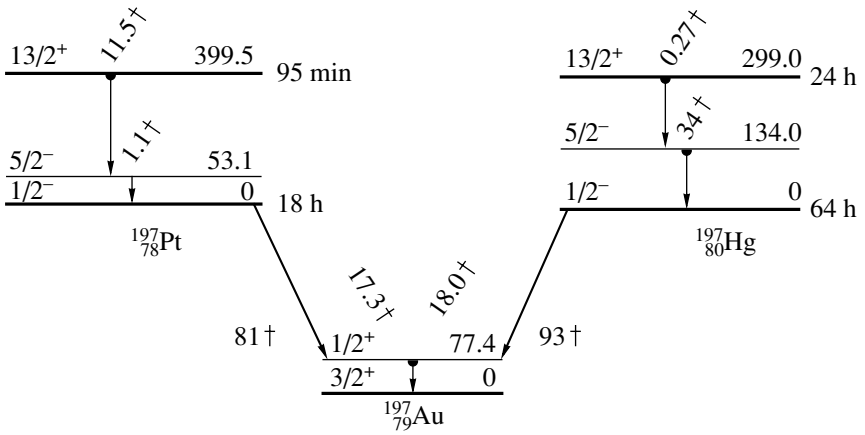

Fig. 1. Diagram of decays of the ^{197}Pt and ^{197}Hg isobars (the energies of the levels are given in keV).

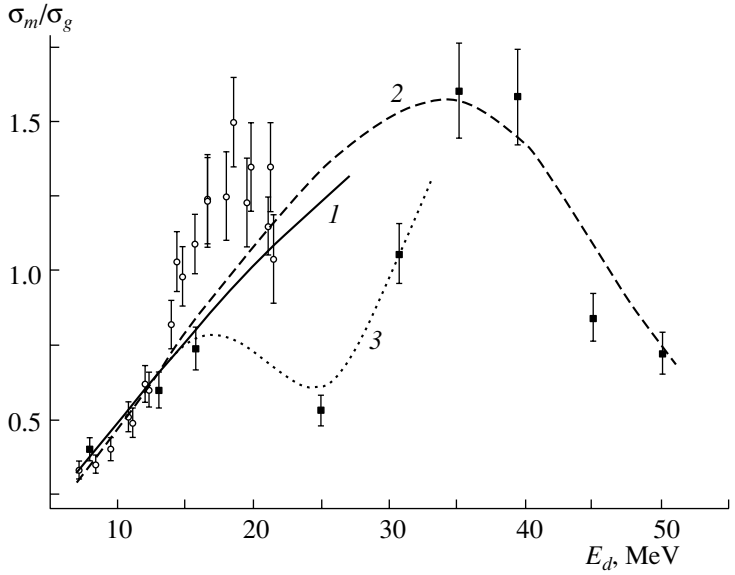

Fig. 2. Energy dependence of σ_m/σ_g for the $(d, 2n)$ reaction on ^{197}Au. The curves represent the results of the calculations on the basis of (*1*) the STAPRE code, (*2*) the cascade–evaporation model, and (*3*) the STAPRE code taking preequilibrium into account. Points correspond to experimental data (■) obtained in the present study and (○) borrowed from [6].

Fig. 4 show the results obtained by approximating the cross section σ_m by the Lorentzian distribution

$$\sigma_m(E) = \frac{\sigma_0 E^2 \Gamma_0^2}{(E^2 - E_0^2)^2 + E^2\Gamma_0^2},$$

where the cross-section value σ_0 at the maximum of $\sigma_m(E)$, the energy E_0 at this point, and the resonance half-width Γ_0 are used as adjustable parameters, their fitted values being given in Table 3, along with those of the parameters σ_1, E_1, and Γ_1 of the Lorentzian distributions corresponding to the total photoneutron cross sections σ_n used to estimate the isomeric ratios [2, 3].

A comparison of the features of the cross sections σ_m and σ_n shows that the σ_m values are considerably smaller than the σ_n values and that the maxima of the former are somewhat shifted to higher energies.

We have calculated the isomeric ratios within the statistical cascade–evaporation model (CEM) [14, 15]. The scheme of the calculations was the following. A dipole photon of energy E is absorbed by the nucleus. A neutron of orbital angular momentum l and energy ε escapes from the product compound nucleus of spin–parity (J_c, π_c), which goes over to a state of spin–parity (J_f, π_f).

The reduced probability of the emission of such a neutron from the compound nucleus is calculated by the formula

$$P(J_c, \pi_c; J_f, \pi_f) \qquad (2)$$

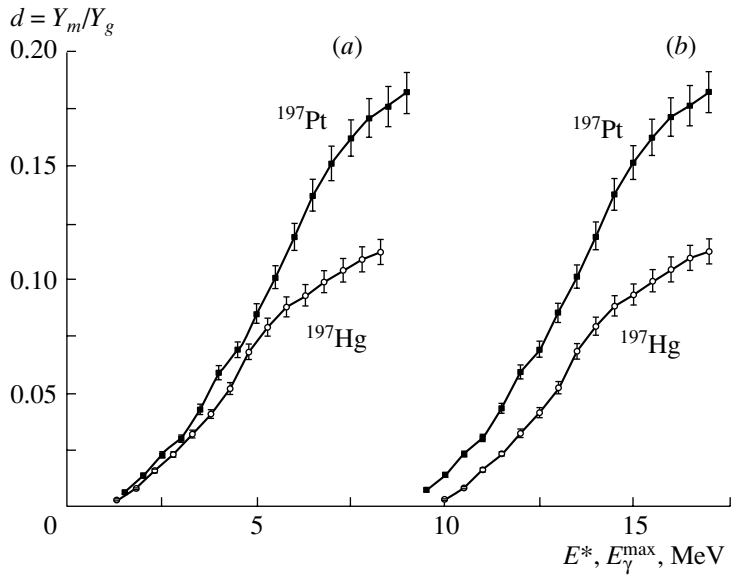

Fig. 3. Isomeric ratios of the yields in the (γ, n) reactions for (■) ^{197}Pt and (○) ^{197}Hg versus the excitation energy (*a*) E^* of the residual nucleus and versus the endpoint energy (*b*) $E_\gamma^{\max}$ of the bremsstrahlung spectrum.

$$= B\rho(J_f) \sum_{S=|J_f-s|}^{J_f+s} \sum_{l=|J_c-S|}^{J_c+S} T_l(\varepsilon)\omega_l(\pi_c, \pi_f),$$

where B is a constant, s is the spin of the emitted particle, $T_l(\varepsilon)$ is the barrier-penetrability factor [16], and $\omega_l(\pi_c, \pi_f) = [1 + (-1)^l \pi_c \pi_f]/2$ is the coefficient used to take into account the parity of the states. For the energy ε of the neutron, we took its mean energy ε_n. The level density was calculated on the basis of the Fermi gas model [17–19], which yields

$$\rho(U, J) = \rho(U)\rho(J) \qquad (3)$$
$$= \rho(U)\exp[-(J+1/2)^2/2\sigma^2],$$

where $\rho(U)$ and $\rho(J)$ are, respectively, the energy- and the spin-dependent part in the expression for the level density and σ is the spin-cutoff parameter, which, according to [18], can be calculated by the formula $\sigma^2 = 0.0889\sqrt{aU}A^{2/3}$ (here, a is the level-density parameter; A is the mass number; and U is the excitation energy, by which we mean the effective excitation energy [14]).

The product daughter nucleus of spin–parity (J_f, π_f) is deexcited by a cascade of dipole γ transitions, the last of these populating either the isomeric or the ground state. The mean transition energy is given by

$$E = 4\sqrt{U/a - \sigma/a^2}. \qquad (4)$$

Consistent calculations do not lead to perfect agreement with experimental data. For photons of energy in the range 14–16 MeV, reasonable agreement is attained by setting the spin-cutoff parameter to $\sigma = 3.4$ for ^{198}Pt and to $\sigma = 3.0$ for ^{198}Hg.

From the cross sections σ_m obtained for the reactions $^{198}\mathrm{Pt}(\gamma, n)^{197m}\mathrm{Pt}$ and $^{198}\mathrm{Hg}(\gamma, n)^{197m}\mathrm{Hg}$, we calculated the isomeric cross-section ratios $R =$

Table 2. Isomeric ratios of the ^{197m,g}Pt and ^{197m,g}Hg yields in the (γ, n) reactions

E_γ, MeV	$d = Y_m/Y_g$	
	^{197m,g}Pt	^{197m,g}Hg
9.5	0.007	–
10.0	0.014	0.003
10.5	0.023	0.008
11.0	0.03	0.016
11.5	0.043	0.023
12.0	0.059	0.032
12.5	0.069	0.041
13.0	0.085	0.052
13.5	0.101	0.068
14.0	0.119	0.079
14.5	0.137	0.088
15.0	0.151	0.093
15.5	0.162	0.099
16.0	0.171	0.104
16.5	0.176	0.109
17.0	0.182	0.112

Table 3. Parameters of the Lorentzian functions used to approximate the cross sections σ_m

Nucleus	σ_m			σ_n		
	E_0, MeV	σ_0, mb	Γ_0, MeV	E_1, MeV	σ_1, mb	Γ_1, MeV
^{198}Pt	13.96 ± 0.05	114.3 ± 4.7	2.72 ± 0.14	13.58	514	4.45
^{198}Hg	14.0 ± 0.07	71.95 ± 4.2	3.45 ± 0.28	13.72	541	4.61

$\sigma_m/(\sigma_m + \sigma_g) = \sigma_m/\sigma_n$. In the region of the cross-section maximum, they are 0.15 ± 0.02 and 0.11 ± 0.01 at $E_\gamma = 13$ MeV and 0.23 ± 0.02 and 0.14 ± 0.015 at $E_\gamma = 14$ MeV.

It is evident from the measured values of d (Fig. 3) and the calculated values of R that the isomeric ratios for ^{197}Hg are almost 1.5 times less than those for ^{197m,g}Pt. We note that a similar trend is also observed in the respective (n,γ) reactions induced by thermal neutrons—that is, $R = 0.057 \pm 0.007$ and $R = 0.034 \pm 0.003$ for ^{197}Pt and ^{197}Hg, respectively. It is impossible to explain this difference if (γ, n) and (n,γ) reactions are described in terms of statistical processes. However, an analysis of the diagrams of ^{197}Pt and ^{197}Hg levels revealed that a $13/2^-$ state is excited in ^{197}Hg at 1381 keV and that this state decays to the ground state via a cascade of $E2$ transitions, bypassing the $13/2^+$ isomeric state. There is no such state in the ^{197}Pt nucleus. The role of this state can be assessed under the assumption that the $I = I_m$ high-spin state, which decays to the ground $(1/2^-)$ state, occurs at the same energy as the $13/2^+$ isomer. The role of energy can be taken into account through the mean energy and the number of cascade transitions required for populating these states. By using formula (4), it was found that $R_{\text{rel}} = R(\text{Pt})/R(\text{Hg})$ varies from 0.8 to 0.5 as the excitation energy E^* of the residual nucleus varies from 3 to 8 MeV. This is in good agreement with the experimental values for (n,γ) and (γ, n) reactions, where R_{rel} varies from 0.73 to 0.60 if E^* varies from 3 to 6.5 MeV.

Figure 3*a* shows the isomeric ratios of the yields versus E^*. It follows from this figure that the R_{rel} value also tends to 0.5 at high excitation energies. In the vicinity of the threshold, the values of the isomeric ratios of the ^{197}Pt and ^{197}Hg yields are close to each other. Obviously, this is because the $13/2^+$ isomeric states cannot be populated via cascade transitions if the energy of the residual nucleus is below 2 to 3 MeV. Semidirect processes involving the emission of fast neutrons having an energy of 1 to 2 MeV are most probably observed at such energies. Naturally, the role of $13/2^-$ states (1381 keV) appears to be insignificant for such processes.

Thus, it should be noted that different energies of excited positive- and negative-parity states of high orbital angular momentum $(I > 5/2)$ in the nuclei being considered can lead to a drastic change in the population of the isomers. It is of crucial importance to obtain additional information about the structure of excited states in the energy region around 1.5 MeV, and the existence of new high-spin states can exert a significant effect on theoretical calculations of isomeric ratios.

The ratios σ_m/σ_g for $(d, 2n)$ reactions were calculated on the basis of the STAPRE code [20]. If only the statistical channel is considered in the same manner as above for (γ, n) reactions, σ_m/σ_g is described properly over the region extending up to 15 MeV, the spin-cutoff parameter being here $\sigma \approx 3.5$ (Fig. 2). At the same time, a minimum observed

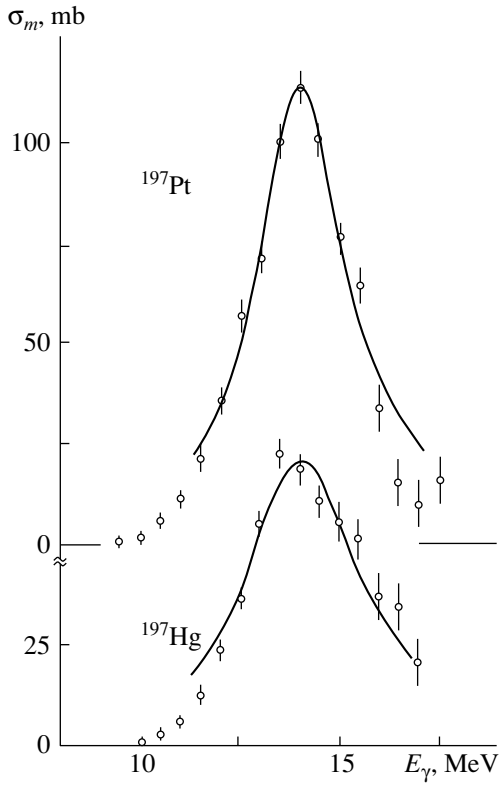

Fig. 4. Cross sections for isomeric-state excitation in (γ, n) reactions for ^{197}Pt and ^{197}Hg nuclei.

at $E_d \sim 25$ MeV and a reduction in σ_m/σ_g with increasing energy cannot be described within this approach. In order to explain this dependence of σ_m/σ_g, it is necessary to consider the influence of factors that are disregarded in the statistical approach. In our opinion, the inclusion of the yrast line is of greatest importance, this being equivalent to changing Q of the reaction, especially for isomeric states.

The relation between the contributions of statistical (primarily $E1$) and collective $E2$ transitions accompanying the deexcitation of high-spin states in the vicinity of the yrast line and the possible interpretation of a bypass of the yrast trap were studied by many authors. In our calculations, we used the cascade–evaporation model developed in [21]. Only equilibrium processes are considered within this model; however, a coefficient f that is usually referred to as the "bypass fraction" and which is used in various codes under this name is introduced in order to take into account the role of the yrast line. The coefficient f indicates that some fraction of γ deexcitation can go over from the cascade that populates the high-spin isomer to the low-spin one. In general, the bypass fraction is thought to correlate with the magnitude of configuration mixing since the spins of the isomeric states are associated with single-particle states and since, in the vicinity of the yrast line, nuclear spins are determined by collective rotational motion. But in the present case, f can characterize a transition of collective motion to single-particle motion and vice versa. It is clear that the problem of obtaining such data is of interest in itself; moreover, the value of f may be indicative of the existence of yrast traps having a preset spin.

Figure 2 shows the isomeric ratios σ_m/σ_g calculated on the basis of the cascade–evaporation model with allowance for the coefficient f. It is evident that good agreement with experimental data is achieved everywhere, with the exception of the region around 25 MeV. A minimum observed in this region can also be associated with the opening of the preequilibrium channel. Figure 2 also shows σ_m/σ_g calculated with allowance for preequilibrium but without the coefficient f. Evidently, it is precisely preequilibrium that can cause the minimum observed in σ_m/σ_g. It also follows from our calculations that a combination of the equilibrium and the preequilibrium channel describes the experimental value only if the coefficient f is taken into account. However, it should be noted that a nonmonotonic behavior of σ_m/σ_g may also be due to the influence of the competition between particle channels on the statistical γ cascade in the vicinity of the yrast line. This influence results in that, within the evaporation model, the multiplicity of the γ cascade may decrease with increasing angular momentum introduced in the nucleus, in which case the energy dependence of σ_m/σ_g becomes nonmonotonic. In order to obtain deeper insight into all of these processes, we need experimental data on the behavior of σ_m/σ_g for various incident particles over a broader energy range.

ACKNOWLEDGMENTS

This work was supported by INTAS (grant no. 2000-00463).

REFERENCES

1. A. M. Goryachev and G. N. Zalesnyĭ, Yad. Fiz. **27**, 1479 (1978) [Sov. J. Nucl. Phys. **27**, 779 (1978)]; Vopr. Teor. Yad. Fiz., No. 10, 115 (1986).
2. A. V. Varlamov, V. V. Varlamov, P. S. Rudenko, and M. E. Stepanov, Report INDC(NDS)-394 (IAEA, Vienna, 1999).
3. G. M. Gurevich, L. E. Lazareva, V. M. Mazur, *et al.*, Nucl. Phys. A **351**, 257 (1981).
4. M. G. Davydov, V. G. Machera, and A. V. Trukhov, At. Énerg. **62**, 236 (1987).
5. Yu. P. Gangrskiĭ, A. P. Tonchev, and N. P. Balabanov, Fiz. Élem. Chastits At. Yadra **27**, 1403 (1996) [Phys. Part. Nucl. **27**, 428 (1996)].
6. R. Vandenbosch and J. R. Huizenga, Phys. Rev. **120**, 1313 (1960).
7. V. M. Mazur, I. V. Sokolyuk, and Z. M. Bigan, Yad. Fiz. **54**, 895 (1991) [Sov. J. Nucl. Phys. **54**, 541 (1991)].
8. *Diagrams of Radionuclide Decays,* Publ. 38 MKRZ (Énergoizdat, Moscow, 1987) [in Russian].
9. E. Browne and R. B. Firestone, *Table of Radioactive Isotopes* (New York, 1986).
10. R. Vanska and R. Rieppo, Nucl. Instrum. Methods Phys. Res. **179**, 525 (1981).
11. P. Mohr, C. Hutter, K. Vogt, *et al.*, Eur. Phys. J. A **7**, 45 (2000).
12. A. S. Penfold and L. E. Leiss, Phys. Rev. **114**, 1332 (1959).
13. O. V. Bogdankevich and F. N. Nikolaev, *Operation with Bremsstrahlung Beams* (Atomizdat, Moscow, 1964) [in Russian].
14. L. Ya. Arifov, B. S. Mazitov, and V. G. Ulanov, Yad. Fiz. **34**, 1028 (1981) [Sov. J. Nucl. Phys. **34**, 572 (1981)].
15. Z. M. Bigan, B. M. Mazur, and Z. Z. Torich, Preprint No. 85-15, KIYaI (Kiev Institute for Nuclear Research, Kiev, 1985).
16. U. S. Emmerich, in *Fast Neutron Physics,* Ed. by J. B. Marion and J. L. Fowler (Interscience, New York, 1960–1963; Gosatomizdat, Moscow, 1966), Vol. 2; G. M. Marchuk and V. E. Kolesov, *Employing Numerical Methods to Calculate Neutron Cross Sections* (Atomizdat, Moscow, 1970).
17. H. Bethe, Phys. Rev. **50**, 332 (1936).

18. A. V. Malyshev, *Energy-Level Density and Structure of Nuclei* (Atomizdat, Moscow, 1969) [in Russian].
19. A. V. Ignatyuk, *Statistical Properties of Excited Nuclei* (Énergoatomizdat, Moscow, 1983) [in Russian].
20. M. Uhl and B. Strohmaier, Report IRK 76/10, Institut für Radiumforschung und Kernphysik (Vienna, 1976); M. Avrigeanu and V. Avrigeanu, Report NP-88-1995, Institute of Physics and Nuclear Engineering (Bucharest, 1995).
21. E. A. Bogila and V. M. Kolomiets, Ukr. Fiz. Zh. **32** (12), 7 (1987).

Translated by E. Kozlovsky

Physics of Atomic Nuclei, Vol. 67, No. 5, 2004, pp. 882–889. Translated from Yadernaya Fizika, Vol. 67, No. 5, 2004, pp. 906–913.

NUCLEI
Experiment

Excitation of Discrete Levels in ^{54}Fe and ^{56}Fe Nuclei by Means of (e, e') Reactions

V. V. Denyak*, V. M. Khvastunov, V. P. Likhachev[1)], A. A. Nemashkalo, S. P. Paschuk[2)], and H. R. Schelin[2)]

Kharkov Institute for Physics and Technology, ul. Akademicheskaya 1, Kharkov, 61108 Ukraine

Received March 13, 2003

Abstract—The excitation of discrete levels in ^{54}Fe and ^{56}Fe nuclei by means of (e, e') reactions is studied at excitation energies of up to 8 MeV over the momentum-transfer range between 0.6 and 1.7 fm^{-1}. An unconventional procedure of multipole analysis is used in experimental-data processing. Data on the reduced probability of transitions and their multipolarity are obtained for 12 low-lying levels of ^{54}Fe and 10 levels of ^{56}Fe. Five levels in ^{54}Fe and three levels in ^{56}Fe are observed for the first time in (e, e') reactions. There is no information about two of them in the present-day database on discrete levels.

INTRODUCTION

This article reports on the results of an investigation into static and dynamical properties of the excitation of discrete levels in ^{54}Fe and ^{56}Fe nuclei by means of (e, e') reactions at an incident-electron energy of about 225 MeV. The range of the excitation energies under study is between 0 and 8 MeV. Similar studies were performed in [1–7].

Analysis of those studies indicates that the results obtained previously contain a number of contradictions. For example, Peterson *et al.* [2] observed 2^+ states at about 3.5 and 5.0 MeV in ^{56}Fe, but Bellicard and Barreau [1] did not find these states. At the same time, 3^- and 4^+ states at 3.1 and 5.05 MeV, respectively, were observed in [1], but they were absent in [2]. In ^{54}Fe, 2^+ and 3^- states were identified equally well by two experimental groups ([1] and [5, 6], respectively), but totally different results were obtained there for 4^+ states. The 4.1- and 7.2-MeV levels observed in [1] were not identified in [5, 6], while the 2.5-MeV level unnoticed in [1] was studied thoroughly in [5, 6].

Analysis of those studies did not reveal any drawbacks in the experimental procedures used there. It is the method used in [1–7] to assess the position of a particular excitation level that can be subjected to question. The point is that a discrete level was separated directly in the spectrum of scattered electrons in those studies. The momentum-transfer dependence of the form factor for an individual level was then used to determine the multipolarity of the respective transition and its reduced probability. The theoretical form factor for a specific multipolarity was fitted to the experimental values of the form factor for each excitation state that was singled out in the way outlined above. The form factor corresponding to a single multipolarity and complying best of all with the experimental data was chosen on the basis of four to five fits, whereby the spin and the parity were determined for the excited nuclear state in question.

If the energy resolution does not allow one to separate excited levels directly in the spectrum of scattered electrons, they are interpreted as a single level within this approach. The multipolarity assigned to this level corresponds to the strongest level among those that were not separated in energy. Usually, this multipolarity is of a lower order, since higher multipoles manifest themselves at higher momentum transfers—that is, at smaller cross sections for (e, e') reactions. Thus, levels of high multipolarity are unintentionally removed upon data processing. This tendency must be the most pronounced if measurements are performed at low momentum transfers, as was the case in [1–7].

We used a different approach in this study. The measured range of excitation energies was broken down into bins of width about 0.2 MeV. The form factor was plotted versus momentum transfer for each bin. The theoretical dependence represented as the sum of form factors corresponding to multipole orders of 2 to 6 was fitted to the experimental values

[1)]University of São Paulo, 05315-970 São Paulo, SP, Brazil.
[2)]Federal Center of Technological Education, CEFET-PR, Curitiba, PR, CEP 80230-901, Brazil.
*e-mail: denyak@kipt.kharkov.ua

obtained for the form factor. As a result, we found the contribution of each multipolarity to the spectrum of scattered electrons as a function of nuclear excitation energy. We identified excited levels by this spectrum and determined their quantum numbers. The range of momentum transfers was extended toward higher values up to 1.7 fm^{-1}. This made it possible to investigate states of high multipolarity more precisely.

EXPERIMENTAL PROCEDURE AND DATA PROCESSING

The experiment was performed in an electron beam from the LUE-300 linear electron accelerator at the Kharkov Institute for Physics and Technology. A detailed description of the basic parts of the setup can be found in [8].

The application of an energy-compression system [9] made it possible to reduce the energy spread of the beam to 0.33%. In our case, this corresponded to 0.7–0.8 MeV.

A system for recording charged particles that is based on a 30-channel two-layer proportional chamber and a Cherenkov detector was used as a multichannel detector. The system of coincidences between signals from the two layers of the chamber and the Cherenkov detector was used to suppress the background. Loads on the recording system did not exceed one pulse per accelerator spill. The time resolution was about 25 ns, while the dead time was 200 ns.

The targets were disks from isotopically enriched iron (99.7% for a ^{56}Fe target; 94.6% ^{54}Fe and 5.1% ^{56}Fe for a ^{54}Fe target). The target thickness was 0.411 and 0.349 $\mathrm{g/cm}^2$ for ^{56}Fe and ^{54}Fe, respectively. The nonuniformity of the disk thicknesses did not exceed 1%.

Fourteen spectra of scattered electrons for each of the isotopes under study were obtained from the measurements. The spectra covered the excitation-energy range $\varepsilon = 0$–8 MeV. They were measured at scattering angles in the range $\theta = 30°$–$90°$, which corresponds to the momentum-transfer range $q' = 0.6$–$1.7\ \mathrm{fm}^{-1}$.

Elastic and quasielastic scattering on ^{12}C was measured concurrently with the spectra of scattering on ^{54}Fe and ^{56}Fe. Since scattering on ^{12}C has received adequate study, it was used to obtain absolute values of the detection efficiency in measuring the spectra for ^{54}Fe and ^{56}Fe.

A precise value of the incident-electron energy was calculated by using the position of the elastic-scattering peak for the ^{12}C nucleus. In doing this, allowances were made for the energy losses by target-atom ionization and for the shift of the elastic peak due to the kinematics of the collisions in question. The incident-electron-energy value refined in this way was $E_e = 226.0 \pm 0.1$ MeV.

The relative efficiency of the electron-counter channels was determined from the quasielastic continuum in the spectrum of scattering on ^{12}C.

The absolute detection efficiency was determined as the ratio of the experimental and theoretical values of the form factor for elastic scattering on ^{12}C. The theoretical form factor was calculated on the basis of the shell model by using a Gaussian distribution of the charge in the proton, this model producing results that comply well with experimental data. The parameters of the distribution were taken from [10].

After introducing corrections for the efficiency and energy calibration, the spectra of electrons scattered on ^{54}Fe and ^{56}Fe were subjected to the procedure of radiation unfolding. In doing this, the corrections for Schwinger radiation, radiative losses, and losses caused by interaction with atomic electrons were taken into account in accordance with the calculations from [11].

The elastic peak was approximated by a Gaussian function and was subtracted from the radiation-unfolded spectra. The half-width of the peak and its position and amplitude were used as adjustable parameters. The spectrum obtained upon subtraction was linearly interpolated within an interval of width about 0.2 MeV.

For a scattering angle of $\theta = 50°$, Fig. 1 shows an example of the spectrum obtained for ^{54}Fe after radiation unfolding, subtraction, and interpolation.

The spectra obtained by interpolation were used to plot the form factors from the 0.2-MeV bins versus momentum transfer for each value of the excitation energy. The resulting form factors were analyzed within the Helm phenomenological model [12]. The parameters of the ground-state charge distribution were determined from data on elastic scattering. All calculations were performed with allowance for the Coulomb distortion of the incident-electron wave (that is, within the improved Born approximation). The experimental form factor was represented as the sum of the theoretical ones corresponding to the multipole orders of $\lambda = 2, 3, 4, 5, 6$. The reduced probabilities for each multipolarity were used in this procedure as adjustable parameters. Figure 2 shows an example of this fit for ^{54}Fe. The $\lambda = 1$ multipole was not used in data processing since, in our experiment, the range of the momentum transfers did not cover the region of the $E1$-multipole maximum.

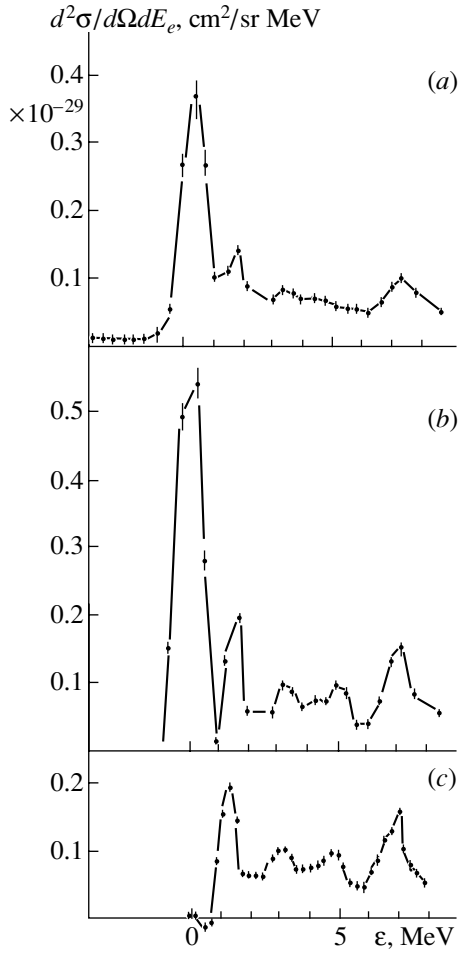

Fig. 1. Differential cross section for electron scattering on ^{54}Fe as a function of excitation energy at a scattering angle of $\theta = 50°$: (*a*) data measured in the experiment, (*b*) results obtained by radiation unfolding, and (*c*) results obtained after elastic-peak subtraction and interpolation.

RESULTS AND DISCUSSION

From an analysis of multipolarities, we obtained the dependence of the reduced transition probabilities on the nuclear excitation energy for each multipolarity (Figs. 3, 4). The resulting structure of excited states appeared to be richer than in previous studies, especially for transitions of multipolarity above $E2$. Tables 1 and 2 list our data along with the results known to date. In order to determine the reduced probability for an individual level, we constructed least squares fits to our experimental data in terms of Gaussian functions. The position, the amplitude, and the half-width of the peaks were adjustable parameters in this case. The half-width of the peaks was varied in the range 0.35–0.45 MeV, which corresponds to the energy resolution of the experiment.

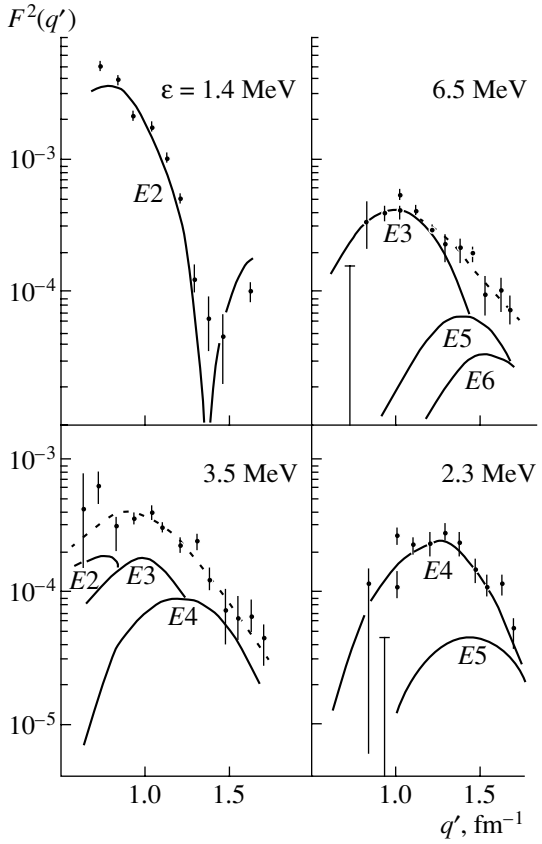

Fig. 2. Squared form factor for the ^{54}Fe nucleus as a function of momentum transfer for individual energy bins. The solid curves represent the theoretical form factors for individual multipolarities, while the dashed curves correspond to the sum of the theoretical form factors.

States of the ^{56}Fe Nucleus

We identified four states at 0.8, 2.4, 3.4, and 4.9 MeV in the $E2$-strength distribution. In the relevant (e, e') reaction, the ^{56}Fe nucleus was previously studied in [1–4, 7]. In [1, 2], the excitation of the nucleus was studied up to 6 MeV. Only 2^+ states were investigated in [3, 4, 7], those at $\varepsilon = 0.846$ MeV in [3, 4] and at $\varepsilon < 3$ MeV in [7]. The 3.4- and 4.9-MeV excited states were observed in [2], but they were not found in [1]. The reason behind this discrepancy was that 3^- and 4^+ states were identified in this energy region in [1]. The authors of [1] were unable to separate two 2^+ states from the background of intense states characterized by higher multipolarities and close excitation energies because the resolution there was poorer than in [2] and because their procedure for data processing was based on isolating a level in the primary spectrum with a subsequent determination of its multipolarity. Our procedure involving the partition into bins allowed us to observe these levels despite the fact that the energy resolution in our experiment was identical to that in [1]. By and

Table 1. Energy positions, transition multipolarities, and reduced transition probabilities for excited levels in the ^{56}Fe nucleus

E_{lev}, MeV	$B(E\lambda)$, fm$^{2\lambda}$ e^2	q', fm^{-1}	Reference
	$E2$		
0.8 ± 0.1	706 ± 49	0.6–1.7	Our study
0.85 ± 0.1	720 ± 70	0.6–1.1	[1]
0.88 ± 0.2	945 ± 45	0.6–2.4	[3]
0.85 ± 0.05	1250 ± 270	0.25–1.07	[2]
0.85 ± 0.1	678 ± 48	0.7–2.1	[4]
2.4 ± 0.2	35 ± 8	0.6–1.7	Our study
2.7 ± 0.1	112 ± 17	0.8–1.1	[1]
2.65 ± 0.05	37 ± 10	0.4–0.6	[2]
2.96 ± 0.05	21 ± 11	0.4–0.6	[2]
3.4 ± 0.1	47 ± 10	0.6–1.7	Our study
3.37 ± 0.05	41 ± 10	0.4–0.6	[2]
3.60 ± 0.05	17 ± 7	0.4–0.6	[2]
3.80 ± 0.05	10 ± 5	0.4–0.6	[2]
4.9 ± 0.1	127 ± 21	0.6–1.7	Our study
4.73 ± 0.05	19 ± 9	0.4–0.6	[2]
5.23 ± 0.05	36 ± 18	0.4–0.6	[2]
	$E3$		
3.0 ± 0.1	2170 ± 350	0.6–1.7	Our study
3.1 ± 0.1	3600 ± 300	0.8–1.1	[1]
4.5 ± 0.1	8040 ± 665	0.6–1.7	our study
4.45 ± 0.1	10370 ± 930	0.8–1.1	[1]
4.51 ± 0.05	16600 ± 4200	0.4–0.6	[2]
7.2 ± 0.2	5570 ± 470	0.6–1.7	Our study
	$E4$		
3.2 ± 0.1	$(131 \pm 13) \times 10^3$	0.6–1.7	Our study
5.1 ± 0.1	$(172 \pm 17) \times 10^3$	0.6–1.7	Our study
5.05 ± 0.1	$(110 \pm 17) \times 10^3$	0.9–1.1	[1]
6.6 ± 0.2	$(102 \pm 19) \times 10^3$	0.6–1.7	Our study
	$E5$		
2.6 ± 0.2	$(89 \pm 36) \times 10^4$	0.6–1.7	Our study

Table 2. Energy positions, transition multipolarities, and reduced transition probabilities for excited levels in the ^{54}Fe nucleus

E_{lev}, MeV	$B(E\lambda)$, fm$^{2\lambda}e^2$	q', fm^{-1}	Reference
	$E2$		
1.4 ± 0.1	769 ± 54	0.6–1.7	Our study
1.4 ± 0.1	533 ± 24	0.64–1.16	[1]
1.41 ± 0.05	600 ± 23	0.21–0.86	[6]
1.41 ± 0.05	$\sim 720 \pm 40$	0.72–1.73	[5]
1.4 ± 0.1	532 ± 32	$\sim$0.7–2.0	[4]
3.1 ± 0.1	143 ± 16	0.6–1.7	Our study
2.9 ± 0.1	225 ± 19	0.64–1.08	[1]
2.96 ± 0.05	175 ± 19	0.40–0.86	[6]
3.16 ± 0.05	48 ± 17	0.50–0.86	[6]
5.1 ± 0.1	66 ± 13	0.6–1.7	Our study
7.1 ± 0.2	56 ± 22	0.6–1.7	Our study
	$E3$		
3.5 ± 0.2	1730 ± 280	0.6–1.7	Our study
4.8 ± 0.1	2520 ± 430	0.6–1.7	Our study
4.85 ± 0.1	4390 ± 280	0.64–1.16	[1]
4.79 ± 0.05	6800 ± 1000	0.40–0.86	[6]
4.79 ± 0.05	$\sim 9400 \pm 700$	0.64–1.73	[5]
4.85 ± 0.1	4563 ± 410	$\sim$0.7–2.0	[4]
6.5 ± 0.2	3810 ± 440	0.6–1.7	Our study
6.4 ± 0.1	6110 ± 335	0.76–1.08	[1]
6.30 ± 0.05	11800 ± 1600	0.40–0.86	[6]
7.4 ± 0.2	4070 ± 610	0.6–1.7	Our study
	$E4$		
2.35 ± 0.1	$(66 \pm 9) \times 10^3$	0.6–1.7	Our study
2.54 ± 0.05	$(136 \pm 6) \times 10^3$	0.70–1.72	[6]
2.54 ± 0.05	$\sim(110 \pm 7) \times 10^3$	0.89–1.73	[5]
4.3 ± 0.1	$(95 \pm 8) \times 10^3$	0.6–1.7	Our study
4.1 ± 0.1	$(89 \pm 8) \times 10^3$	0.87–1.17	[1]
5.1 ± 0.1	$(93 \pm 12) \times 10^3$	0.6–1.7	Our study
7.0 ± 0.1	$(57 \pm 12) \times 10^3$	0.6–1.7	Our study
7.2 ± 0.1	$(173 \pm 20) \times 10^3$	0.76–1.08	[1]
	$E5$		
2.7 ± 0.1	$(1.6 \pm 0.2) \times 10^6$	0.6–1.7	Our study

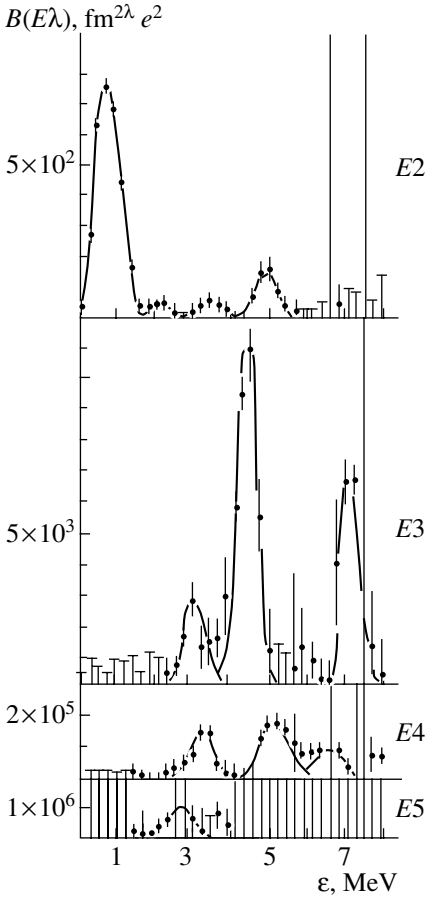

Fig. 3. Reduced probability of the excitation of the ^{56}Fe nucleus for various multipolarities of transitions as a function of excitation energy.

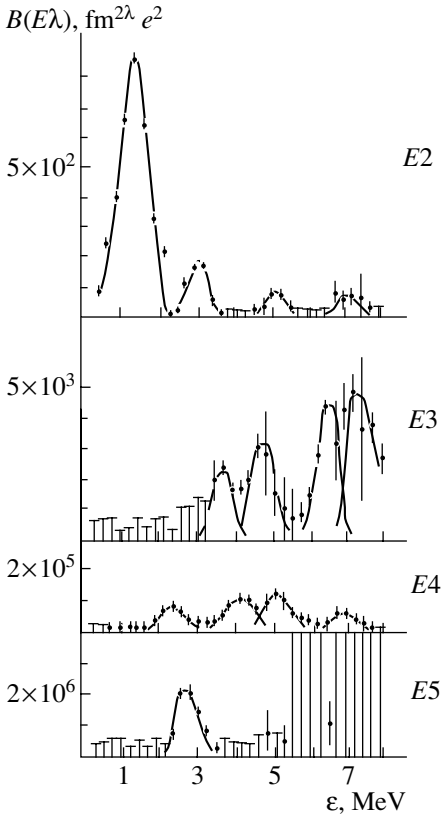

Fig. 4. As in Fig. 3, but for the ^{54}Fe nucleus.

large, the reduced probability $B(E2)$ that we obtained for all levels is in good agreement with previous results (see Table 1). The observed distinction is most probably associated with the use of different models in this and previous studies in describing the form factor.

Two $E3$ states at 3.1 and 4.5 MeV were observed in [1], while only the 4.5-MeV state was observed in [2]. Moreover, the 3.1-MeV state was not found in a more recent study characterized by a higher energy resolution; this can obviously be explained by a poor statistical accuracy of the experiment reported in [2]. It follows from [1] that the intensity of the 3.1-MeV level is one-third as great as that of the 4.5-MeV level. The $B(E3)$ value obtained in [2] for the 4.5-MeV level was determined to within 4000 fm$^{2\lambda}e^2$; thus, the uncertainty of this reduced probability is approximately equal to the $B(E3)$ value for the 3.1-MeV level. Probably, this is the reason why the 3.1-MeV level was not observed in [2]. We found both these states and a 7.2-MeV state in addition. The reduced probability of the 3.1- and 4.5-MeV levels is in agreement with the results presented in [1, 2]. The 7.2-MeV state was not observed previously in the relevant (e, e') reaction. However, the ENSDF database[3)] of excited levels in nuclei indicates that there is a 3^- state at 7.48 MeV in this energy region; in addition, there are many levels of unknown spin and parity. This state could not be found in [1, 2], because the region of excitation energies studied there was below 7 MeV.

Only one $E4$ state at 5.05 MeV was observed in [1], but no $E4$ state was found in [2], probably, because of a rather low momentum transfer. We identified three $E4$ states at $\varepsilon = 3.2$, 5.1, and 6.6 MeV. The $B(E4)$ value for the 5.1-MeV state is close to that obtained in [1]. Probably, the 3.2-MeV state corresponds to the known level at 3.12 MeV (from the ENSDF database). This state could not be found in [1], since it merges with the $E3$ state at 3.1 MeV. There are no known 4^+ levels in the energy range corresponding to the 6.6-MeV state; however, there are many levels there for which the spin and parity have yet to be determined. The excitation-energy region up to 6 MeV was studied in [1]; therefore, the 6.6-MeV state could not be found there.

[3)] "Evaluated Nuclear Structure Data File" (ENSDF) is a database that is maintained at the Brookhaven National Laboratory (www.nndc.bnl.gov).

States of the ^{54}Fe Nucleus

For the most part, two peaks are observed in the $E2$-strength distribution; they can be associated with the excitation of the previously observed states at 1.4 and 3.1 MeV. The reduced probability $B(E2)$ for the former is in fairly good agreement with the previous results, although the procedures used to obtain these data differ considerably in all of these studies. The $B(E2)$ value that we obtained for the state in the vicinity of 3.1 MeV is somewhat lower, which is caused by additional $E3$ and $E5$ transitions found in this region of the excitation energies. The levels at 5.1 and 7.1 MeV were not observed previously in the relevant (e, e') reaction; probably, they could not be separated from the 4.8-MeV $E3$ and 7.2-MeV $E4$ levels in the primary spectra. While the level at 5.1 MeV is isolated quite reliably, the data that we obtained on the $E2$-strength distribution in the region around 7.1 MeV are most likely a piece of evidence that there may exist a state there, since the reduced probability found for this state is only 2.5 times greater than its uncertainty. According to the database maintained at the Brookhaven National Laboratory, there are, however, 2^+ levels in this energy region, at 5.08 and 7.11 MeV; in addition, there are a number of levels there whose spin and parity have not yet been identified.

Previously, only two states, those at 4.8 and 6.4 MeV, were found in the $E3$-strength distribution in the excitation-energy region extending up to 8 MeV. In addition to them, our analysis revealed two more states, at 3.5 and 7.4 MeV. The separation of these states from the background of the intense 3.0- to 3.2-MeV $E2$ transitions and the 7.2-MeV $E4$ transition became possible only owing to the application of our bin-by-bin fitting procedure instead of attempts at separating peaks in the primary spectrum. The total value of $B(E3)$ for the two highest states at 6.5 and 7.4 MeV is in good agreement with previous data, but the width of this summed peak is evidently larger than our experimental resolution. There is a 3^- state at 7.49 MeV in the energy region subjected to analysis here (see ENSDF). The state at 4.8 MeV appeared to be weaker in our study than in the previous studies; this is because of the additional 5.1-MeV $E4$ transition that we observed in this energy region.

Two $E4$ states were identified at 4.1 MeV and 7.2 MeV in [1]. No states at 4.1 MeV and 7.2 MeV were observed in [5, 6], but a 2.54-MeV state, which remained unnoticed previously, was revealed and investigated in detail (up to 1.7 fm^{-1}). Probably, this state was not found in [1], because, in the case of low momentum transfers, it was not seen in the primary spectra against the background of the highly intense $E2$ states at 1.4 and 2.9 MeV. It is incomprehensible why the 4.1- and 7.2-MeV states were not observed in [5]. Our analysis revealed four states at 2.35, 4.3, 5.1, and 7.0 MeV. It is evident from Table 2 that $B(E4)$ appeared to be in good agreement only for one state, that at 4.3 MeV. The $B(E4)$ value obtained in our study for the lowest of the $E4$ states is considerably less than that in [5, 6], because we identified an additional $E5$ state at 2.7 MeV in this region. The 5.1-MeV state has already been mentioned in discussing $E3$ transitions. The discrepancy between the values of the reduced probability for the 7.0-MeV state is explained by the 7.2-MeV $E2$ and 7.4-MeV $E3$ states identified in our study. The 5.1-MeV state was not observed previously in the relevant (e, e') reaction. However, there is a 4^+ state at 4.95 MeV in this energy region (see ENSDF); in addition, there are many levels whose spin and parity have yet to be identified, as in the case of the newly revealed $E3$ states. This state could not be observed in [1] because of an insufficient energy resolution (the 5.1-MeV state merges with the 4.85-MeV $E3$ state).

New States

Several states identified in our study were not observed previously in the (e, e') reactions; moreover, there are no levels corresponding to these states in the database maintained at the Brookhaven National Laboratory.

For ^{54}Fe, these are the $E3$ state at 3.5 MeV and the $E5$ state at 2.7 MeV. The values of the reduced probabilities of these states are more than three times as great as the experimental uncertainty. Thus, we can say that these states do indeed exist at a confidence level exceeding 99%. The $E3$ state at 3.5 MeV could correspond to the known state at 3.34 MeV (see ENSDF), but this level has a positive parity in the database. There is only one high-spin level in the vicinity of the $E5$ state revealed in our study: this is the 6^+ level at 2.95 MeV (see ENSDF). We could not find any $E6$ state. In our opinion, it is unlikely that the known 6^+ level manifested itself as an $E5$ state in our data because of an imperfection of the experimental procedure or data processing. First and foremost, it is evident from Fig. 2 that the momentum-transfer range overlaps the maximum of the $E6$ transition. Therefore, the actual $E6$ strength must not be absorbed by $E5$ in fitting the theoretical form factors to the experimental data in the range of high momentum transfers q'. It is more likely that the whole cross-section fraction that was not described by the theoretical $E2$–$E5$ form factors is accumulated in the form factor corresponding to $E6$ transitions. In addition, an adequate description of all levels observed

previously gives every reason to believe that the data-processing procedure used in our study does not lead to a redistribution of the reduced probability between different multipoles.

The reduced probability for the 2.6-MeV $E5$ state in ^{56}Fe is only 2.5 times greater than its uncertainty; therefore, we cannot say that this $E5$ state was identified. Our result can be considered only as a piece of evidence that there is a level in this energy region.

CONCLUSION

Thus, we have obtained information about the reduced probability and the multipolarity of transitions for 12 low-lying states of the ^{54}Fe nucleus and 10 states of the ^{56}Fe nucleus. The bin-by-bin fitting procedure applied to the scattered-electron spectrum instead of a conventionally used analysis of individual peaks has permitted us to remove the contradictions that arose in comparing the results of previous studies. Five levels in the ^{54}Fe nucleus and three levels in the ^{56}Fe nucleus were identified for the first time in the relevant (e, e') reactions; there is no information about two of them in the present-day database of discrete levels. For the most part, the reduced transition probabilities agree with the results of previous studies; in the cases where this is not so, the discrepancy can be explained by the existence of transitions of a different multipolarity.

REFERENCES

1. J. Bellicard and P. Barreau, Nucl. Phys. **36**, 476 (1962).
2. R. J. Peterson, Horst Theissen, and W. J. Alston, Nucl. Phys. A **153**, 610 (1970).
3. J. Heisenberg, J. S. McCarthy, and I. Sick, Nucl. Phys. A **164**, 353 (1971).
4. A. S. Litvinenko, N. G. Shevchenko, A. Yu. Buki, *et al.,* Ukr. Fiz. Zh. **17**, 1197 (1972).
5. Phan Xuan Ho, J. Bellicard, Ph. Leconte, and I. Sick, Nucl. Phys. A **210**, 189 (1973).
6. C. de Vries, *Electron Scattering Activities at IKO Amsterdam, Duffusion d'Electrons a Energie Intermediair,* Recontres de Saclay, 1975, p. 485.
7. G. Hartung, A. Richter, E. Spamer, *et al.*, Phys. Lett. B **221**, 109 (1989).
8. N. G. Afanas'ev *et al.,* Yad. Fiz. **5**, 318 (1966) [Sov. J. Nucl. Phys. **5**, 223 (1966)]; N. G. Shevchenko, Doctoral Dissertation in Physics and Mathematics (Kharkov, 1980).
9. N. G. Afanas'ev, A. Yu. Buki, Yu. V. Vladimirov, *et al.,* Zh. Tekh. Fiz. **54**, 518 (1984).
10. G. R. Bishop, L'Onde Electrique **42** (424), 298 (1962).
11. M. Sasao and Y. Torizuka, Phys. Rev. C **15**, 217 (1977).
12. R. Helm, Phys. Rev. **104**, 1466 (1956).

Translated by E. Kozlovsky

Physics of Atomic Nuclei, Vol. 67, No. 5, 2004, pp. 890–900. Translated from Yadernaya Fizika, Vol. 67, No. 5, 2004, pp. 914–924.

NUCLEI
Experiment

Neutron Emission from the Reaction ^{232}Th$(n, xn'f)$

G. N. Lovchikova, A. M. Trufanov, M. I. Svirin*, and V. A. Vinogradov

Institute of Physics and Power Engineering, pl. Bondarenko 1, Obninsk, Kaluga oblast, 249020 Russia

Received June 5, 2003

Abstract—The energy distributions of neutrons accompanying the fission of ^{232}Th are measured by the time-of-flight technique at the bombarding-neutron energies of $E_n = 14.6$ and 17.7 MeV. The data obtained in this way are compared with the results of previous investigations. An excess of soft neutrons that was observed in the experimental spectra of neutrons from ^{238}U fission at $E_n = 13.2$, 14.7, 16.0, and 17.7 MeV in relation to the results of the calculations based on the model of two sources is also present in the spectra for ^{232}Th. The discrepancy between the results of the calculations and experimental data disappears as soon as one assumes the presence of a third source that is related to neutron emission from nonaccelerated fragments. © *2004 MAIK "Nauka/Interperiodica"*.

INTRODUCTION

Systematic experimental and theoretical (computational) investigations of the emission of secondary neutrons from $(n, xn'f)$ fission reactions revealed changes in the shape of the spectra of prompt fission neutrons upon going over from bombarding-neutron energies of $E_n = 2.9$ and 5.0 MeV to higher energies in the region $E_n > 13$ MeV [1–8]. In experiments devoted precisely to studying the spectra of prompt fission neutrons, a relative method of measurements was implemented consistently and was shown to be an efficient tool for overcoming various difficulties that arise in solving the problem being considered (suppression of the instability associated with long-term measurements of the spectra of prompt fission neutrons, determination of the detection efficiency for secondary neutrons, etc.). For this purpose, measurements for the induced fission of the nuclide being studied and measurements for spontaneous ^{252}Cf fission, which had received quite a comprehensive study, were performed simultaneously under conditions that were as close as possible. The features of prompt neutrons from the latter fission process have the status of neutron references [9, 10]. For the ^{252}Cf nucleus, the shape of the spectra of prompt fission neutrons, $N_{\mathrm{Cf}}(E) = \mu_0(E)N_{\mathrm{M}}(E, T_{\mathrm{Cf}})$ with $T_{\mathrm{Cf}} = 1.42$ MeV, is rather close to that of a Maxwell distribution $N_{\mathrm{M}}(E, T_{\mathrm{Cf}})$. Modest deviations from it are taken into account quite correctly by means of a correction shape function $\mu_0(E)$.

At the energies of $E_n = 2.9$ MeV [2–5] and 5.0 MeV [8] [which are below the emission-fission threshold—that is, the threshold for $(n, n'f)$ reactions], prompt fission neutrons originate from fully accelerated excited fragments produced in the fission of the compound nucleus A (target nucleus plus one neutron). In this case, the measured ratios $R_i(E, E_n) = N_i(E, E_n)/N_{\mathrm{Cf}}(E)$ of the prompt-fission-neutron spectra $N_i(E, E_n)$, $i = {}^{232}$Th, ^{235,238}U, ^{237}Np, which are being studied, to the analogous spectrum for the spontaneous fission of ^{252}Cf change nearly in direct proportion to the energy E. This implies that the shape of the prompt-fission-neutron spectra $N_i(E, E_n)$ themselves is close to that of a Maxwell distribution $N_{\mathrm{M}}(E, T_i)$. The slope of the dependence $R_i(E, E_n)$ is determined by the temperature difference $T_{\mathrm{Cf}} - T_i$ between the spectrum of prompt fission neutrons for ^{252}Cf and the analogous spectrum for the isotope under study. The smaller this difference, the more accurate the linear approximation in question.

With increasing excitation energy

$$E^* \geq \sum_{i=1}^{x} B_n^{A+1-i} + B_f^{A-x}$$

(where B_n is the neutron binding energy and B_f is the height of the fission barrier, these quantities being taken at the mass-number values indicated in the superscripts), the emission here becomes a multiparticle process, while fission appears to be energetically feasible upon the emission of one ($x = 1$) or several ($x = 2$, 3, ...) prefission neutrons. Thus, we see that, in emission fission, there are two sources of secondary neutrons: these are fully accelerated fission fragments for postfission neutrons and excited fissile

*e-mail: svirin@ippe.obninsk.ru

nuclei, which emit prefission neutrons prior to undergoing disintegration.

Spectra measured by the same method in two energy regions, below the emission-fission threshold at $E_n = 2.9$ MeV [2–5] and 5.0 MeV [8] and well above this threshold at $E_n = 13.2$ MeV [8], 14.7 MeV [2–5], and 16.0 and 17.7 MeV [6], make it possible to compare the "pure" spectra of prompt fission neutrons from fully accelerated fragments with spectra that receive contributions both from pre- and from postfission neutrons. The shape of the distributions $R(E, E_n)$ at $E_n = 2.9$ and 5.0 MeV is close to that of a linear function and serves as a reference shape, against which effects associated with the emission of prefission neutrons at $E_n > 13$ MeV manifest themselves most clearly. The reason responsible for one of such effects was understood immediately [1–3]—it is associated with the fact that the spectrum of preequilibrium neutrons is cut off at the threshold for the fission of the residual nucleus A − 1 formed upon the emission of the first neutron. This effect manifests itself as a maximum in the distribution $R(E, E_n)$ against the background of the nearly linear dependence of the postfission component, the position of this maximum being given by

$$E = E_{\max} = E_n - B_f^{A-1}. \quad (1)$$

The maximum in question would not have been observed if neutron emission had been determined by the equilibrium mechanism, in which case the evaporation spectrum is soft, the yield of neutrons being low, a few orders of magnitude less than that of preequilibrium neutrons in the vicinity of the above maximum.

Under the assumption of two sources of prompt fission neutrons, the distributions $R(E, E_n)$ for $E_n >$ 13 MeV were calculated within the statistical approach, the contribution of nonequilibrium neutrons being taken into account on the basis of the exciton model of preequilibrium decay [2, 3, 5, 7, 8]. The results of those calculations comply with experimental data only at neutron energies in the region $E \geq$ 2 MeV. In response to variations in the bombarding-neutron energy, a maximum at high energies in the distribution $R(E, E_n)$ is shifted along the energy (E) scale according to (1), this being consistent with the qualitative interpretation of features associated with a nonequilibrium emission of prefission neutrons.

At low energies ($E < 2$ MeV), there is an anomalously high yield of soft neutrons in experimental distributions in relation to the results of the calculations. The softness of the spectrum of anomalous neutrons (they are anomalous in the sense that their spectrum is not reproduced theoretically within the traditional approach based on the model of two sources of prompt fission neutrons) makes it possible to observe them against the background of the spectrum that features pre- and postfission neutrons and which is harder. By including in the calculation a third source that is associated with the system of fragments prior to their separation (that is, fragments that have already been formed, but which are still in contact—nonaccelerated fragments [7, 8]), it is possible to explain the low-energy anomaly and to remove the discrepancy between experimental data and the results of the calculations, as was done for ^{238}U at $E_n =$ 13.2 MeV [8] and 14.7, 16.0, and 17.7 MeV [7].

With the aim of additionally confirming the existence of special features observed in the shape of the spectra of prompt fission neutrons for $E_n >$ 13 MeV and testing the model description outlined above, neutron emission from the fission reaction ^{232}Th$(n, xn'f)$ at $E_n = 14.6$ and 17.7 MeV was investigated in the experiment reported in the present article. From the practical point of view, these data are of importance for the FENDL library (for thermonuclear facilities) and for the Russian library BROND-3.

EXPERIMENTAL PROCEDURE

Our experiment was conducted in a continuous neutron beam from the KG-2.5 cascade generator installed at the Institute of Physics and Power Engineering (Obninsk). Neutrons of energy $E_n =$ 14.6 and 17.7 MeV were obtained in the reaction T$(d, n)^4$He on solid-state TTi targets. The spectra of fission neutrons were measured by a time-of-flight spectrometer over the secondary-neutron-energy range 0.25–13 MeV. The spectrometer included a detector of fission fragments (multilayer ionization chamber), a shielded neutron detector, and electronics that ensured the accumulation and preliminary sorting of experimental information. The measurements were performed over a flight base of length 1.7 m at an angle of 90° with respect to the primary-neutron beam. In measuring the spectrum of prompt neutrons with the aid of a four-section multilayer ionization chamber, the same methodological approach as in [2, 3] was employed in the present experiment. Three sections of the chamber contained the ^{232}Th isotope being studied, 12 layers in each section. Fissile-substance layers 2 mg/cm^2 in thickness and 100 mm in diameter were deposited onto the two sides of an aluminum foil 0.05 mm thick. The total weight of the isotope under study was 5.65 g. The fourth, "monitoring," section consisted of two single-sided layers of the same nuclide, each containing ^{252}Cf nuclei uniformly distributed over its thickness. Each section of the chamber was connected to an individual time channel, and signals from the ionization fission

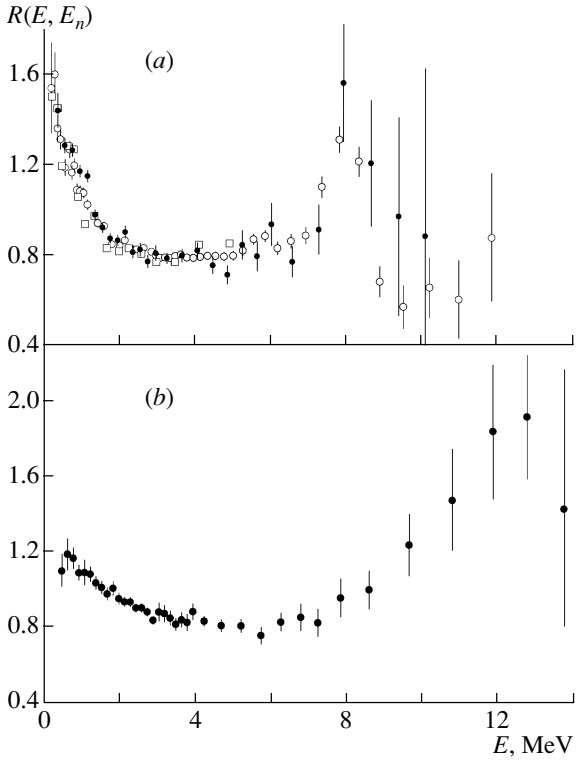

Fig. 1. Experimental ratios $R(E, E_n)$ of the spectra of fission neutrons from the $^{232}\mathrm{Th} + n$ reaction to the spectrum of neutrons from the spontaneous fission of $^{252}\mathrm{Cf}$ at the primary-neutron energies of $E_n =$ (open boxes) 14.3 MeV [11], (closed circles) 14.6 MeV (our study), and (open circles) 14.7 MeV [3] in Fig. 1*a* and at $E_n =$ 17.7 MeV (our study) in Fig. 1*b*.

chamber were used to fix the time instants of fission events. A more detailed description of the ionization chamber containing $^{232}\mathrm{Th}$ layers was given in [2, 3].

The neutron detector consisted of a stilbene crystal of diameter 63 mm and height 39 m and a FEU-30 multiplier phototube. At a primary neutron energy of $E_n \approx 18$ MeV, the shielding of the neutron detector from background radiation presents a serious problem. In our experiment, the very possibility of detecting the effect depended on the quality of the shielding. In view of this, the question of whether the background from scattered neutrons and photons can be suppressed was thoroughly explored by selecting the geometry of the shielding and by combining its individual components, as well as by choosing a shielding material.

A primary treatment of the instrumental spectra of neutrons was begun by summing the results obtained from individual measurements of the effect plus background for each section of the chamber. In order to obtain a pure effect, the magnitude of the background was determined by its average value over some time-scale interval behind the position of a gamma peak. In summing the neutron spectra from the individual sections, we took into account the distinctions between the lengths of the flight base for each channel of fission-event detection. The minimum neutron energy that could be recorded was determined by the detector threshold $E_{\mathrm{thr}} = 250$ keV. Information obtained at secondary-neutron energies in excess of $E = 350$ keV could be considered to be reliable. The upper boundary of the outgoing-neutron-energy range over which the spectra of prompt fission neutrons were measured was determined primarily by the statistics of counts and by the background conditions of the experiment. The characteristic numbers of counts for fission events and for accompanying neutrons per minute (n_f and n_n, respectively) were $n_f \approx 3 \times 10^4$ and $n_n \approx 5$. The number of neutrons recorded over the total time of the measurements was 7×10^4. The statistical error of the time-spectrum points changed from 1.5% at $E \approx 1$ MeV to 30% at a neutron energy close to the upper boundary. The total error in the ultimate results of the measurements was somewhat larger because of errors in various corrections that were introduced during data processing.

EXPERIMENTAL RESULTS

As in [6–8], the results of the present experiment are given in Fig. 1 in the form of the directly measured ratios of the spectra of prompt fission neutrons, $N(E, E_n)$, for $^{232}\mathrm{Th}$ fission induced by neutrons of energy $E_n = 14.6$ and 17.7 MeV to the spectrum of neutrons, $N_{\mathrm{Cf}}(E)$, from the spontaneous fission of $^{252}\mathrm{Cf}$:

$$R(E, E_n) = N(E, E_n)/N_{\mathrm{Cf}}(E). \qquad (2)$$

Data processing was performed in such a way that both spectra were normalized as

$$\int_0^\infty N(E, E_n)dE = \int_0^\infty N_{\mathrm{Cf}}(E)dE = 1$$

with allowance for the contribution from neutrons of energy below the detection threshold, $\mathrm{E} \le E_{\mathrm{thr}} =$ 0.25 MeV. This correction does not introduce significant uncertainties in experimental results—specifically, in the mean energy and the mean number of fission neutrons ($\bar{E}$ and $\bar{\nu}$, respectively)—since the fraction of undetected neutrons is small, so that it is straightforward to extrapolate the ratio in question to $E = 0$.

In Fig. 1*a*, the ratio $R(E, E_n)$ that we obtained at $E_n = 14.6$ MeV is contrasted against the results of earlier measurements at $E_n = 14.7$ MeV [3]. Within the errors (which are much greater in the present measurements than in [3]), the results of the two

experiments are in satisfactory agreement with each other. Also given here are the data for ^{232}Th at $E_n =$ 14.3 MeV that were obtained by Vasil'ev *et al.* [11] over a narrower range of secondary-neutron energies (0.25–5 MeV). It can be seen that the distributions $R(E, E_n)$ obtained in the aforementioned three experiments have similar shapes. That the shapes of the distributions obtained in the different experiments are consistent, this being so even in the low-energy region E < 2 MeV, where an anomalously high yield of soft neutrons was observed, gives every reason to believe that this effect does indeed exist.

From Figs. 1*a* and 1*b*, it can be seen that the ratios $R(E, E_n)$ obtained at the primary-neutron energies of $E_n = 14.6$ (14.7) and $E_n = 17.7$ MeV are similar. In the high-energy section, both distributions exhibit a maximum that is associated with the cutoff of the spectrum of preequilibrium neutrons at the threshold for the fission of the residual nucleus of mass number $A - 1$ (^{232}Th). The position of the maximum in the distributions is given by relation (1). At $E_n =$ 17.7 MeV, the maximum in the high-energy part of the distribution $R(E, E_n)$ is shifted toward higher secondary-neutron energies E in relation to the position of the maximum at $E_n = 14.6$ (14.7) MeV. According to (1), the magnitude of this shift corresponds to the difference of the two primary-neutron energies. It should be borne in mind that, because of a low yield of prompt fission neutrons at high energies E and because of the background conditions of the experiment, it is very difficult to measure the shape of the distribution $R(E, E_n)$ in the vicinity of the maximum, and the higher the value of E_n, the more serious the difficulties involved in such measurements. For the above energies of primary neutrons, the experimental values of the mean energy and the mean multiplicity of secondary neutrons accompanying the fission of ^{232}Th are given in Table 1.

In the low-energy section, the distribution $R(E, E_n)$ exhibits a rise for $E < 2$ MeV. Within the traditional concept of two neutron sources in the emission-fission process, this rise must be associated with the evaporation component of prefission neutrons. It will be shown below that, for the ^{232}Th nucleus, the experimental distributions at $E_n =$ 14.6 (14.7) and 17.7 MeV feature an excess of soft neutrons in relation to the results of the calculations based on the model of two sources.

ANALYSIS OF THE SPECTRUM OF NEUTRONS ORIGINATING FROM THE EMISSION-FISSION PROCESS

The experimental energy distributions of neutrons from the reaction ^{232}Th$(n, xn'f)$ were analyzed on the basis of the same approach as that used in [7] in studying the emission of secondary neutrons accompanying ^{238}U fission over a wide range of E_n values (between 2.9 and 17.7 MeV). With allowance

Table 1. Experimental values of the mean energy and the mean multiplicity of neutrons accompanying the fission of ^{232}Th

$\bar{E}_n$, MeV	$\bar{E}_{\text{expt}}$, MeV	$\bar{\nu}_{\text{expt}}$
14.6	1.87 ± 0.04	4.06 ± 0.10
14.7 [3]	1.84 ± 0.03	3.92 ± 0.09
17.7	1.95 ± 0.04	4.33 ± 0.13

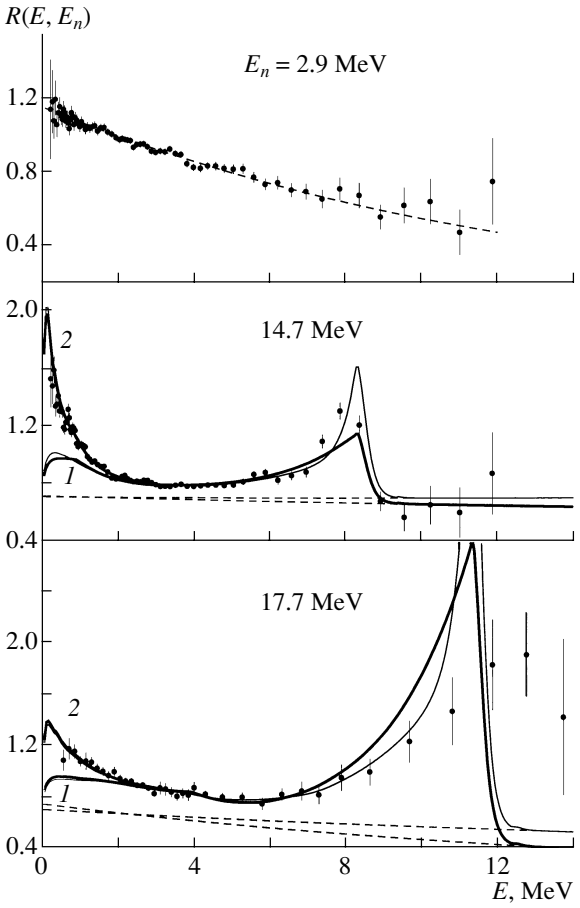

Fig. 2. Ratios $R(E, E_n)$ of the neutron spectra studied in the reaction ^{232}Th$(n, xn'f)$ to the spectrum of neutrons from the spontaneous fission of ^{252}Cf: (points) experimental data, (solid curves) results of the calculation on the basis of (3) (*1*) without and (*2*) with allowance for the contribution of neutrons from nonaccelerated fragments, (thin solid curves) description with the calculated cutoff function $f_i(E, E_n)$ (10), (thick solid curves) description based on the parametrization of $f_i(E, E_n)$ in the form of a step function with a smoothed edge, and (dashed curves) component of postfission neutrons from fully accelerated fragments.

for three sources of fission neutrons, the calculated spectrum of prompt fission neutrons can be written as

$$\frac{d\bar{\nu}(E,E_n)}{dE} = \frac{d\bar{\nu}_{\text{faf}}(E,E_n)}{dE} + \frac{d\bar{\nu}_{\text{pre}}(E,E_n)}{dE} + \frac{d\bar{\nu}_{\text{naf}}(E,E_n)}{dE}. \quad (3)$$

Here, each term is associated with one of the three neutron sources, which come into play as the energy of bombarding neutrons becomes higher. The first term in (3) corresponds to the differential yield of postfission neutrons from fully accelerated fragments. In a general form, it can be represented as a superposition of two Maxwell distributions; that is,

$$\frac{d\bar{\nu}_{\text{faf}}(E,E_n)}{dE} = \alpha \sum_{x=0}^{x_{\max}(E_n)} \bar{\nu}_{fA-x} N_{\text{M}}(E,\beta T_x) \frac{\sigma_{fA-x}}{\sigma_f}. \quad (4)$$

The mean multiplicity $\bar{\nu}_{fA-x}$ in (4) was determined for each fission chance ($x = 0, 1, 2$) by means of the systematics of $\bar{\nu}_f$ from [12] and its extrapolation to the region above the threshold for emission fission, $E_n > B_f^{A-1}$. The estimate $T_x = (2/3)\bar{E}_{fx}$ was based on the semiempirical Terrell formula [13]

$$\bar{E}_{fx} = a + b\sqrt{\bar{\nu}_{fA-x} + 1}, \quad (5)$$

where the parameters take the values of $a = 0.75$ MeV and $b = 0.65$ MeV [14], which are universal for all nuclei. The expression on the right-hand side of (4) involves the ratio σ_{fA-x}/σ_f, whose denominator is the total fission cross section

$$\sigma_f(E_n) = \sum_{x=0}^{x_{\max}(E_n)} \sigma_{fA-x}(E_n) \quad (6)$$

and whose numerator is the cross section σ_{fA-x} for the fission of the residual nucleus $A - x$ formed upon the emission of x neutrons, the latter cross section being also referred to as that for $(x+1)$th-chance fission. Experimental information can be obtained only for the total fission cross section. The partial components σ_{fA-x} for ^{232}Th are determined by decomposing the total cross section σ_f into separate chances. Here, we relied on the same method as that used in analyzing the chance structure of the cross section for ^{238}U fission [7, 15]. The constant α is introduced in order to construct a fit to experimental data and to compensate for an inevitable uncertainty in the description of $\bar{\nu}_{fA-x}$; as was indicated above, this description is based on an extrapolation of the systematics of $\bar{\nu}_f$ from [12] to the region $E_n > B_f^{A-1}$—that is, to the region of the second and third plateaus of the fission cross section. Since similar uncertainties are inherent in the use of the systematics of $T(E_n)$ from [13], the quantities T_x in (4) were varied within 3% by means of the constant β.

According to currently prevalent concepts, which have a sound experimental basis [16–19], excited fission fragments accelerated owing to their mutual Coulomb repulsion are the only source of secondary neutrons below the threshold for emission fission ($E_n < B_f^{A-1}$). In expression (3), underlying the calculation of the spectrum, there therefore remains only the first term,

$$\frac{d\bar{\nu}(E,E_n)}{dE} = \frac{d\bar{\nu}_{\text{faf}}(E,E_n)}{dE}. \quad (7)$$

Concurrently, we must set $x_{\max}(E_n) = 0$ in (4). For this case, the results of relevant experiments and of their analysis for the reaction ^{232}Th(n, f) at $E_n = 2.9$ MeV [2, 3] are given in Fig. 2. The observed shape of the distribution $R(E, E_n)$ (2) for postfission neutrons is rather close to that of a linear dependence. It is described well by the ratio of the Maxwell distribution for the ^{232}Th nucleus being studied to that for the spontaneous fission of ^{252}Cf:

$$R(E,E_n) = \frac{N_{\text{M}}(E,T)}{N_{\text{M}}(E,T_{\text{Cf}})} = (T_{\text{Cf}}/T)^{3/2} \exp\left[-\frac{T_{\text{Cf}} - T}{T_{\text{Cf}} T} E\right]. \quad (8)$$

The slope of the corresponding line is determined by the temperature difference between the neutron spectrum for californium and that for the nucleus under study (^{232}Th): $T_{\text{Cf}} = 1.42$ MeV and $T = 1.285$ MeV.

As was indicated in [20], the emission of postfission neutrons has but a small effect on the observables of the fission process—for example, on the mass–energy distributions of fission fragments. The emission of prefission neutrons at $E_n > B_f^{A-1}$ leads to more serious consequences, having a strong effect on the entire fission process. There appear new possibilities, which are often referred to as fission chances—that is, new reactions in which nuclei of lower mass and lower excitation energy undergo fission. This creates considerable difficulties for studying the energy dependence of the observables of the fission process. The emission-fission process corresponds to precisely this situation.

Distortions introduced in the shape of the postfission-neutron distribution (7) will then be determined by the quantity $d\bar{\nu}_{\text{pre}}(E,E_n)/dE$. For the energies of $E_n = 14.6$ (14.7) and 17.7 MeV, at which, in the present experiment, A (^{233}Th), $A-1$ (^{232}Th), and $A-2$ (^{231}Th) nuclei undergo fission, the differential

yield of prefission neutrons consists of three components and has the form [7]

$$\frac{d\bar{\nu}_{\rm pre}(E,E_n)}{dE} = \sum_{j=1}^{3}\frac{d\bar{\nu}_{{\rm pre}j}(E,E_n)}{dE} \qquad (9)$$
$$= N_{11}(E,E_n)\frac{\sigma_{fA-1}(E_n)}{\sigma_f(E_n)}$$
$$+ N_{12}(E,E_n)\frac{\sigma_{fA-2}(E_n)}{\sigma_f(E_n)}$$
$$+ N_{22}(E,E_n)\frac{\sigma_{fA-2}(E_n)}{\sigma_f(E_n)},$$

where

$$N_{xi}(E,E_n)$$
$$= \frac{d\sigma_{nx}(E,E_n)}{dE}f_i(E,E_n)\Big/\int\limits_E \frac{d\sigma_{nx}(E,E_n)}{dE}$$
$$\times f_i(E,E_n)dE$$

are the normalized (to unity) spectra of coincidences between first-chance neutrons ($x=1$) and events of the fission of $A-1$ ($i=1$) and $A-2$ ($i=2$) nuclei and between second-chance neutrons ($x=2$) and events of the fission of $A-2$ ($i=2$) nuclei. The "cutoff" function $f_i(E,E_n)$ is the fission probability (fissility) for the $A-i$ ($i=1,2$) nucleus as expressed in terms of the emitted-neutron energy E; that is,

$$f_i(E,E_n) = P_{fA-i}\Big(U_i \qquad (10)$$
$$= E^* - \sum_{x=1}^{i} B_n^{A-x+1} - E\Big),$$

where $E^* = E_n + B_n^A$ is the excitation energy of the primary compound nucleus of mass number A (in our case, this is ^{233}Th). At excitation energies in the region $U_i \le B_f^{A-i}$, the fission of $A-i$ nuclei is energetically impossible (effects of tunnel fission-barrier penetrability apart). The spectrum of first-chance neutrons ($x=1$) and the spectrum of first- ($x=1$) and second-chance ($x=2$) neutrons are cut off at, respectively, the energy $E = E_1 = E_n - B_f^{A-1}$ and the energy $E = E_2 = E_n - B_n^{A-1} - B_f^{A-2}$. In [7], the function $f_i(E,E_n)$ was simulated by a smoothed step function. Along with a step function, we use here a more realistic approximation obtained for the function $f_i(E,E_n)$ (10) on the basis of a calculation of the fission probabilities for $A-1$ and $A-2$ nuclei. By way of example, the cutoff function $f_1(E,E_n)$ at $E_n = 14.7$ MeV is shown in Fig. 3 for these two versions. No correction that would take into account the smearing of the upper boundary of the distributions $f_i(E,E_n)$ was introduced.

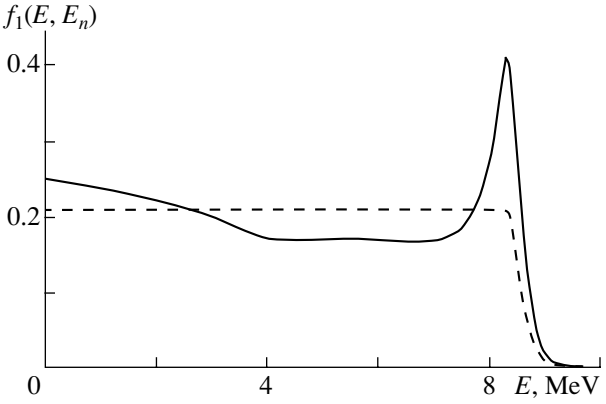

Fig. 3. Cutoff function $f_1(E,E_n)$ at $E_n = 14.7$ MeV: (solid curve) result of the calculation by formula (10) and (dashed curve) parametrization in terms of a steplike dependence.

The results obtained by describing the experimental distributions within the traditional approach of two neutron sources [in this case, $d\bar{\nu}_{\rm naf}(E,E_n)/dE = 0$ in (3)] are represented by the solid curves *1* in Fig. 2. The effect stemming from the cutoff of the hard component of first-chance (preequilibrium) neutrons at the threshold for the fission of $A-1$ nuclei (^{232}Th) and manifesting itself in the measured distributions $R(E,E_n)$ as a maximum at the neutron energy in (1) is by and large reproduced by the results of the calculations. Low statistics and unfavorable background conditions of the experiment give no way to measure, to a satisfactory precision, the shape of the distribution in the vicinity of the high-energy maximum at $E_n = 17.7$ MeV. Here, we can only state that the experimental and the calculated distributions are in qualitative agreement. Measurement of the distributions $R(E,E_n)$ for emission fission at lower primary-neutron energies in the range $E_n = 7$–10 MeV, where one can determine, to a high statistical accuracy, the shape of prefission-neutron distributions against the background of the postfission component, would make it possible to answer the question of which version of $f_1(E,E_n)$ complies with experimental data better.

In just the same way as the distributions $R(E,E_n)$ measured for ^{238}U at $E_n = 13.2$ MeV [8] and 14.7, 16.0, and 17.7 MeV [7], the experimental distributions for ^{232}Th at 14.7 MeV [3] and 17.7 MeV exhibit an anomalously high yield of soft ($E < 2$ MeV) neutrons, which is not reproduced by calculations that are based on the model of two neutron sources. At first glance, it may seem that the anomalous yield of soft neutrons has some bearing on the emission-fission process, but, in fact, this is not so. Recently, we

Table 2. Calculated values of the mean yield and the mean energy (in MeV) for various components of the spectra of neutrons from ^{232}Th fission

$E_n = 14.7$ MeV [3]				$E_n = 17.7$ MeV			
$\bar{\nu}_{\text{faf}}$	2.706	$\bar{E}_{\text{faf}}$	2.127	$\bar{\nu}_{\text{faf}}$	2.974	$\bar{E}_{\text{faf}}$	2.061
$\bar{\nu}_{\text{pre 1}}$	0.376	$\bar{E}_{\text{pre 1}}$	2.430	$\bar{\nu}_{\text{pre 1}}$	0.420	$\bar{E}_{\text{pre 1}}$	3.010
$\bar{\nu}_{\text{pre 2}}$	0.148	$\bar{E}_{\text{pre 2}}$	0.878	$\bar{\nu}_{\text{pre 2}}$	0.252	$\bar{E}_{\text{pre 2}}$	1.840
$\bar{\nu}_{\text{pre 3}}$	0.148	$\bar{E}_{\text{pre 3}}$	0.676	$\bar{\nu}_{\text{pre 3}}$	0.252	$\bar{E}_{\text{pre 3}}$	1.160
$\bar{\nu}_{\text{pre}}$	0.672	$\bar{E}_{\text{pre}}$	1.702	$\bar{\nu}_{\text{pre}}$	0.924	$\bar{E}_{\text{pre}}$	2.186
$\bar{\nu}_{\text{faf+pre}}$	3.378	$\bar{E}_{\text{faf +pre}}$	2.042	$\bar{\nu}_{\text{faf+pre}}$	3.898	$\bar{E}_{\text{faf+pre}}$	2.091
$\bar{\nu}_{\text{naf}}$	0.546	$\bar{E}_{\text{naf}}$	0.526	$\bar{\nu}_{\text{naf}}$	0.432	$\bar{E}_{\text{naf}}$	0.699
$\bar{\nu}$	3.924	$\bar{E}$	1.831	$\bar{\nu}$	4.330	$\bar{E}$	1.952

Note: Quoted in the table are the values of the mean yields and mean energies for ($\bar{\nu}_{\text{faf}}, \bar{E}_{\text{faf}}$) postfission neutrons from fully accelerated fragments, ($\bar{\nu}_{\text{pre}} = \sum_{j=1}^{3} \bar{\nu}_{\text{pre}j} = \frac{\sigma_{fA-1}}{\sigma_f} + \frac{\sigma_{fA-2}}{\sigma_f} + \frac{\sigma_{fA-2}}{\sigma_f}$, $\bar{E}_{\text{pre}} = \sum_{j=1}^{3} \bar{E}_{\text{pre}j}\bar{\nu}_{\text{pre}j}/\bar{\nu}_{\text{pre}}$) prefission neutrons and ($\bar{\nu}_{\text{pre}j}, \bar{E}_{\text{pre}j}$) their components, [$\bar{\nu}_{\text{faf+pre}} = \bar{\nu}_{\text{faf}} + \bar{\nu}_{\text{pre}}$, $\bar{E}_{\text{faf+pre}} = (\bar{E}_{\text{faf}}\bar{\nu}_{\text{faf}} + \bar{E}_{\text{pre}}\bar{\nu}_{\text{pre}})/\bar{\nu}_{\text{faf+pre}}$] the sum of post- and prefission neutrons, and ($\bar{\nu}_{\text{naf}}, \bar{E}_{\text{naf}}$) neutrons from nonaccelerated fragments; also, $\bar{\nu} = \bar{\nu}_{\text{faf}} + \bar{\nu}_{\text{pre}} + \bar{\nu}_{\text{naf}}$ and $\bar{E}$ is given by (13).

have analyzed the shape of the distribution $R(E, E_n)$ for the ^{238}U nucleus at $E_n = 7$ MeV. This analysis revealed that the shape calculated on the basis of the two-source model is in excellent agreement with experimental data over the entire range of secondary-neutron energies at which the measurements were performed ($E = 0.14$–15 MeV). The energy of 7 MeV (beginning of the second plateau of the fission cross section) is approximately 1 MeV higher than the emission-fission threshold. At the same time, the experimental distribution at $E_n = 13.2$ MeV [8] (end of the second plateau of the fission cross section) displays an excess of soft neutrons in relation to the results of the calculation within the same approach of two sources.

In order to explain the low-energy anomaly in the spectra of prompt fission neutrons for ^{238}U at $E_n \geq 13.2$ MeV [7], the model underlying the calculations was supplemented with a third source of secondary neutrons that is associated with a dinuclear system of already formed fission fragments that are not yet separated—that is, with nonaccelerated fragments. It was assumed that, in such a system, a statistical equilibrium had been established with respect to all degrees of freedom and that the lifetime of the system was sufficient for a fragment to emit A_i ($i = 1, 2$) neutrons, provided that its excitation energy satisfies the condition

$$E^*_{i0} = C(E_n + B^A_n)\frac{A_i}{A} > B^{A_i}_n. \qquad (11)$$

The coefficient C specifies that fraction of the excitation energy of the compound nucleus A which was transferred to internal degrees of freedom of already formed fragments by the instant of their separation. We bear in mind that the assumption that there exists a long-lived dinuclear system does not have a solid physical validation, but it enables us to derive, within the statistical model, a relation for calculating the spectrum of neutron emission (and to compare the results of such a calculation with experimental data). Specifically, we have

$$\frac{d\bar{\nu}_{\text{naf}}(E, E_n)}{dE} = \frac{\sigma_{fA}}{\sigma_f}\sum_{A_i} Y(A_i) \int\limits_{E^*_{i0}} G(E^*_{i0}, \langle E^*_{i0}\rangle) \times \left[\sum_{Z_j} P(A_i, Z_j) N(E, A_i, Z_j, E^*_{i0})\right] dE^*_{i0}, \qquad (12)$$

where $Y(A_i)$ is the mass distribution of fission fragments; $G(E^*_{i0}, \langle E^*_{i0}\rangle)$ is the excitation-energy distribution; $P(A_i, Z_j)$ is the charge distribution of fission fragments at fixed values of A_i (as a rule, a few isobaric nuclei correspond to them); and $N(E, A_i, Z_j, E^*_{i0})$ is the normalized (to unity) spectrum of neutrons from fragments characterized by fixed values of A_i, Z_j, and E^*_{i0} (for more details, see [7]). In describing the experimental distributions $R(E, E_n)$, the coefficient C in (11) was an adjustable parameter [note that the hardness of the spectrum in (12) and the integrated yield of neutrons are both dependent on this coefficient]. In the region $E_n \geq 13.2$ MeV, a satisfactory description of the anomalously soft component in all of the distributions

under study for the ^{238}U nucleus was attained in [7, 8] at a single value of the coefficient C ($C = 0.53$).

The solid curves in Fig. 2 represent the results obtained by analyzing the ratios $R(E, E_n)$ measured experimentally for ^{232}Th at the bombarding-neutron energies of $E_n = 14.7$ MeV [3] and 17.7 MeV (in order to avoid encumbering the figure, we did not present there the data at $E_n = 14.6$ MeV). The spectra of neutrons from nonaccelerated fragments [see Eq. (12)] were calculated for ^{232}Th with the same value of $C = 0.53$ as for ^{238}U. It can be seen that the excess of soft neutrons (those of energy in the region E < 2 MeV) in experimental distributions in relation to the description within the model of two sources (curve *1*) is faithfully reproduced by the calculation that takes into account three sources of secondary neutrons (curve *2*). The spectra of neutrons from nonaccelerated fragments originating from the fission of compound nuclei ^{233}Th are given in Fig. 4 for the primary-neutron energies of (curve *1*) 14.7 and (curve *2*) 17.7 MeV. For ^{232}Th fission, Table 2 gives the calculated values of the mean multiplicities and the mean energies of neutrons for various components of their spectrum. From Fig. 4 and from Table 2, it can be seen that the mean multiplicity of neutrons originating from nonaccelerated fragments, $\bar{\nu}_{naf}(E_n)$, is lower at the higher energy of $E_n = 17.7$ MeV than at 14.7 MeV. This apparent contradiction is clarified if we notice that the ratio σ_{fA}/σ_f, which directly appears in (12), is less at 17.7 than at 14.7 MeV. The first-chance-fission cross section σ_{fA} decreases with increasing E_n. The emission of neutrons from nonaccelerated fragments formed in the fission of $A-1$ and $A-2$ nuclei (second and third chance, respectively) is energetically impossible at the E_n values considered here. As can be seen from Table 2, the mean energy $\bar{E}_{\text{naf}}(E_n)$ for the spectrum of neutrons from nonaccelerated fragments increases with increasing E_n. The trend toward a decrease in the soft-neutron multiplicity $\bar{\nu}_{\text{naf}}(E_n)$ upon going over from $E_n = 14.7$ MeV to $E_n = 17.7$ MeV clearly manifests itself in the experimental distributions in Fig. 2 as well.

MEAN ENERGIES OF NEUTRONS IN ^{232}Th FISSION

The values of $\bar{E}(E_n)$ for the prompt-fission-neutron spectrum (3), which involves three components, are determined by the relation

$$\bar{E}(E_n) = \frac{\bar{\nu}_{\text{faf}}(E_n)\bar{E}_{\text{faf}}(E_n) + \bar{\nu}_{\text{pre}}(E_n)\bar{E}_{\text{pre}}(E_n) + \bar{\nu}_{\text{naf}}(E_n)\bar{E}_{\text{naf}}(E_n)}{\bar{\nu}_{\text{faf}}(E_n) + \bar{\nu}_{\text{pre}}(E_n) + \bar{\nu}_{\text{naf}}(E_n)}. \quad (13)$$

Below the emission-fission threshold ($E_n < B_f^{A-1}$), $\bar{\nu}_{\text{pre}}(E_n) = \bar{\nu}_{\text{naf}}(E_n) = 0$ in (13), so that the mean energy is given by

$$\bar{E}(E_n) = \bar{E}_{\text{faf}}(E_n); \quad (14)$$

that is, it is determined by the postfission component exclusively, for which there is the well-known systematics developed by Terrell [13], who proposed the parametrization of the mean energy in the form (5). In this systematics, the quantities E_n, Z, and A, which are three basic features of the nuclear-fission process that are of interest in practice, are replaced by the mean yield of neutrons from fully accelerated fragments, $\bar{\nu}_{\text{faf}}(E_n, Z, A)$, which depends on them.

Above the emission-fission threshold, a source of prefission neutrons comes into play, with the result that the mean energy for the two-component spectrum of prompt neutrons assumes the form

$$\bar{E}(E_n) = \frac{\bar{\nu}_{\text{faf}}(E_n)\bar{E}_{\text{faf}}(E_n) + \bar{\nu}_{\text{pre}}(E_n)\bar{E}_{\text{pre}}(E_n)}{\bar{\nu}_{\text{faf}}(E_n) + \bar{\nu}_{pre}(E_n)}. \quad (15)$$

The systematics proposed in [21] (see Fig. 5) relies on the ideas developed in [13] and takes into account the contribution of prefission neutrons. It combines the results obtained by theoretically calculating the spectra of fission neutrons and their mean energy with allowance for the multichance character of emission fission. This systematics contains two types of calculated curves for the mean energy: $\bar{E}(E_n)$ (15) for the two-component spectrum of neutrons accompanying the fission process (solid curve in Fig. 5) and, separately, $\bar{E}_{\text{faf}}(E_n)$ for the spectrum of neutrons belonging to the postfission component (dashed curve in Fig. 5); naturally, the two curves coincide below the $(n, n'f)$ threshold.

Experimental information about the spectra of fission neutrons was basically obtained by two methods. One of these, a more straightforward and more consistent method, employs detectors of fission fragments. A neutron is recorded in coincidence with a fission event. An implementation of this method for fast primary neutrons is a challenging task, but this eventually ensures a high quality of time and amplitude features, a low detection threshold, and a broad interval of measured energies of secondary neutrons. In the present study and in [1–4, 6, 8, 22], use was made of multilayer ionization chambers for

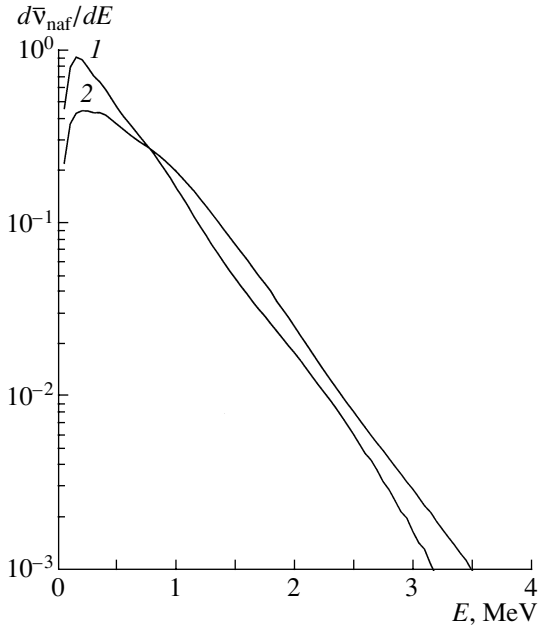

Fig. 4. Differential yield of neutrons from nonaccelerated fragments formed upon the fission of ^{233}Th compound nuclei [see Eq. (12)] at the primary-neutron energies of $E_n =$ (curve *1*) 14.7 and (curve *2*) 17.7 MeV.

fission-fragment detectors and a relative method of measurements; this made it possible to obtain reliable and high-quality experimental data on the spectra of prompt fission neutrons and on the mean energies $\bar{E}(E_n)$ (closed circles and closed boxes in Fig. 5).

The value of $\bar{E}(E_n) = 1.881$ MeV is given in Fig. 5 (closed triangle) according to measurements for the spectrum of neutrons from the fission of ^{232}Th at $E_n = 14.3$ MeV [11], these measurements being performed by the time-of-flight method with the aid of a pulsed source of primary neutrons and a fission chamber. This value differs somewhat from the mean energy presented for ^{232}Th at $E_n = 14.3$ MeV in the systematics from [21] (2.255 MeV) and borrowed from an original study of the authors of that systematics. The reason behind this discrepancy was previously discussed in [6] for ^{238}U. In [11], the spectra of fission neutrons were approximated by the distribution

$$N(E) = \alpha\frac{E}{T^2}e^{-E/T} + (1-\alpha)\frac{e^{-\omega/T_f}}{\sqrt{\pi\omega T_f}}e^{-E/T_f}\sinh\frac{2\sqrt{\omega E}}{T_f}, \quad (16)$$

where the authors of those studies associated the first term with prefission neutrons and the second term with postfission neutrons from fully accelerated fragments. According to [11], a fit to the experimental spectrum of fission neutrons for ^{232}Th leads to the following values of the parameters in (16): $T = 0.38 \pm 0.04$ MeV, $T_f = 1.17 \pm 0.02$ MeV, and $\alpha = 0.25 \pm 0.02$. The mean energy for the distribution in (16) is

$$\bar{E} = \alpha\bar{E}_{\rm I} + (1-\alpha)\bar{E}_{\rm II}, \quad (17)$$

where $\bar{E}_{\rm I} = 2T$ and $\bar{E}_{\rm II} = \omega + (3/2)T_f$ ($\omega = 0.5$ MeV). The systematics in [21] gives the value of $\bar{E}_{\rm II} = 2.255$ MeV. It is natural to associate this value with the mean energy of the postfission component and compare it with the dashed curve in Fig. 5. As to the value of $\bar{E}(E_n) = 1.881$ MeV from [11], it complies with our results in Table 1.

The systematics constructed for $\bar{E}(E_n)$ within the traditional approach of two sources of neutrons [see Eq. (15)] accompanying the fission of actinide nuclei yields mean-energy values (solid curve in Fig. 5) that lie much higher than their experimental counterparts at $E_n = 14.3$, 14.6, 14.7, and 17.7 MeV. By estimating the mean energies on the basis of an analysis of the experimental distributions of prompt fission neutrons at $E_n = 14.6$, 14.7, and 17.7 MeV with allowance for two sources according to Eq. (15) (horizontal dash *1* in Fig. 5, a value on the solid curve corresponding to it in the aforementioned systematics) and with allowance for three sources according to Eq. (13) (horizontal dash *2* in Fig. 5), one can see that only the calculation that takes into account three sources is able to reproduce experimental data. The horizontal dash *3* in Fig. 5 (a value on the dashed curve corresponds to it in the systematics) shows the level of the mean energy of the postfission component of neutrons from fully accelerated fragments.

The second method for obtaining experimental data on the basis of the spectra of fission neutrons [23–27] (open symbols in Fig. 5) employs metallic fissile targets and a pulsed source for a time reference. Here, there is no fission-fragment detector, which is present in the first method; therefore, there is no selection of events that are directly associated with a fission event. The measured distribution involves, in addition to fission neutrons, neutrons from elastic and inelastic scattering, their spectrum being concentrated within the range $0 \le E \le E_n$. At primary-neutron energies in the region $E_n \le 2$ MeV, secondary neutrons of energy in the region $E < E_{\rm min}$ ($E_{\rm min} > E_n$) are discriminated. The measured spectrum of fission neutrons lies in the energy region $E \ge E_{\rm min}$; that is, in the low-energy region $E < E_{\rm min}$, we have no experimental information that would exert a sizable effect on the sought value of the mean energy $\bar{E}(E_n)$. In view of this, it is necessary to introduce corresponding corrections in estimating the experimental values of $\bar{E}(E_n)$ on the basis of the fission-neutron spectrum. There are indirect data, including the values of $\bar{E}(E_n)$ for $E_n > 2$ MeV, which were obtained

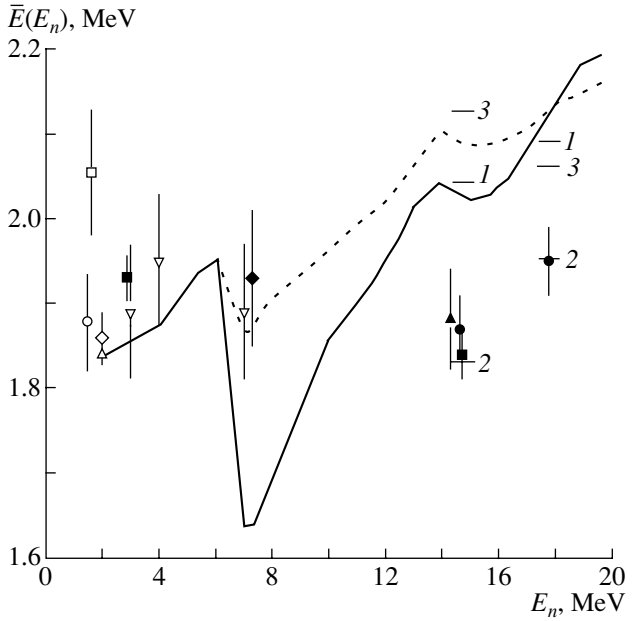

Fig. 5. Mean energies of neutrons originating from the fission of ^{232}Th target nuclei versus the primary neutron energy E_n. Points represent experimental data obtained in measurements with a fission chamber {(closed circles) our study, (closed boxes) [2, 3], (closed triangles) [11], and (closed diamonds) [22]} and in measurements with a sample {(open circles) [23], (open diamonds) [24], (open boxes) [25], (open triangles) [26], and (open inverted triangles) [27]}. The results quoted in the systematics from [21] are shown by the solid curve for the sum of pre- and postfission neutrons and by the dashed curve for postfission neutrons. Also displayed in this figure are the results of the present analysis at $E_n = 14.7$ and 17.7 MeV for (dash *1*) the case where the contribution of neutrons from nonaccelerated fragments is disregarded, (dash *2*) the case where this contribution is included, and (dash *3*) the component of postfission neutrons.

from an analysis of the total neutrons spectrum, featuring elastically and inelastically scattered neutrons as well, this analysis resorting to theoretical models and alien parameters. However, these data are hardly reliable.

That the second source of neutrons (prefission ones) comes into play is clearly manifested in a sharp reduction of the total mean energy $\bar{E}(E_n)$ (solid curve in Fig. 5) upon going over from $E_n = 6$ MeV to $E_n = 7$ MeV. In addition to the hard spectrum of postfission neutrons, there then arises the contribution from the soft spectrum of prefission neutrons, which is concentrated in the energy range $0 \le E \le E_n - B_f^{A-1}$, their integrated yield in the region around the second chance of the fission cross section being given by $\bar{\nu}_{\rm pre}(E_n) = \sigma_{fA-1}(E_n)/\sigma_f(E_n)$. A modest decrease in the mean energy for postfission neutrons (dashed curve in Fig. 5) is caused by the emergence of the second, softer, component in the postfission-neutron spectrum (4) ($x_{\max}(E_n) = 1$). Our measurements of 2001 and 2002 for the spectrum of fission neutrons for ^{238}U at $E_n = 6$ and 7 MeV confirm a decrease in the mean energy upon going over from 6 to 7 MeV.

CONCLUSIONS

(i) We have measured the energy distributions of neutrons from ^{232}Th fission induced by bombarding neutrons of energy $E_n = 14.6$ and 17.7 MeV. The data at 17.7 MeV have been obtained for the first time. Within the experimental errors, the distributions $R(E, E_n)$ measured anew at $E_n = 14.6$ MeV agree with previous data reported in [2, 3] for $E_n =$ 14.7 MeV.

(ii) The shape of the distributions $R(E, E_n)$ at $E_n = 14.6$ (14.7 [2, 3]) and 17.7 MeV has the same special features in the soft and in the hard section as those observed previously in similar measurements for ^{235}U [2, 3] and ^{237}Np [4] at $E_n = 14.7$ MeV and for ^{238}U at $E_n > 13$ MeV [2, 3, 6, 8]. The appearance of a maximum in the hard part of $R(E, E_n)$ in the vicinity of the energy $E = E_{\max} = E_n - B_f^{A-1}$ is due to the fact that the spectrum of preequilibrium neutrons is cut off at the threshold for the fission of the $A - 1$ residual nucleus formed upon the emission of the first neutron. In the low-energy section of the distributions, there is an anomalous excess of soft neutrons in relation to the results of the calculation within the traditional approach relying on the model of two sources of neutrons accompanying the emission fission of heavy nuclei.

(iii) In just the same way as in describing the spectra of neutrons from ^{238}U fission at $E_n > 13$ MeV [7, 8], good agreement between the calculated and the experimental distributions over the entire secondary-neutron-energy range subjected to measurements, including the low-energy section $E < 2$ MeV, has been attained upon taking into account, in our model calculation, the emission of neutrons from nonaccelerated fragments.

(iv) The experimental values of the mean energy of secondary neutrons in emission fission via the ^{232}Th $+ n$ reaction at $E_n = 14.6$, 14.7, and 17.7 MeV are well below the theoretical predictions based on the model of two sources [previously, similar results were obtained for $\bar{E}(E_n)$ in the ^{235}U $+ n$ and ^{237}Np $+ n$ reactions at $E_n = 14.7$ MeV and in the ^{238}U $+ n$ reaction at $E_n > 13$ MeV]. The inclusion of additional neutron emission from nonaccelerated fragments leads to agreement between the calculated and experimental values of the above mean energies.

REFERENCES

1. G. S. Boikov, V. D. Dmitriev, G. A. Kudyaev, *et al.,* At. Énergiya **69**, 23 (1990).
2. G. S. Boikov, V. D. Dmitriev, G. A. Kudyaev, *et al.*, Z. Phys. A **340**, 79 (1991).
3. G. S. Boikov, V. D. Dmitriev, G. A. Kudyaev, *et al.,* Yad. Fiz. **53**, 628 (1991) [Sov. J. Nucl. Phys. **53**, 392 (1991)].
4. G. S. Boikov, V. D. Dmitriev, M. I. Svirin, and G. N. Smirenkin, Yad. Fiz. **57**, 2126 (1994) [Phys. At. Nucl. **57**, 2047 (1994)].
5. G. S. Boikov, V. D. Dmitriev, G. A. Kudyaev, *et al.*, Ann. Nucl. Energy **21**, 585 (1994).
6. G. N. Smirenkin, G. N. Lovchikova, A. M. Trufanov, *et al.,* Yad. Fiz. **59**, 1934 (1996) [Phys. At. Nucl. **59**, 1865 (1996)].
7. M. I. Svirin, G. N. Lovchikova, A. M. Trufanov, *et al.,* Yad. Fiz. **60**, 818 (1997) [Phys. At. Nucl. **60**, 727 (1997)].
8. A. M. Trufanov, G. N. Lovchikova, M. I. Svirin, *et al.,* Yad. Fiz. **64**, 3 (2001) [Phys. At. Nucl. **64**, 1 (2001)].
9. *Nuclear Data Standards for Nuclear Measurements*, NEANDC-311 "U," INDCC (SEC)-101 (OECD, Paris, 1992).
10. W. Mannhart, IAEA-TECDOC-410 (IAEA, Vienna, 1987), p. 158.
11. Yu. A. Vasil'eva, Yu. S. Zamyatnin, E. I. Sirotinin, *et al.,* in *Physics of Nuclear Fission* (Gosatomizdat, Moscow, 1962), p. 121; Yu. A. Vasil'ev, Yu. S. Zamyatnin, Yu. I. Il'in, *et al.*, Zh. Éksp. Teor. Fiz. **38**, 671 (1960) [Sov. Phys. JETP **11**, 483 (1960)].
12. R. J. Howerton, Nucl. Sci. Eng. **62,** 438 (1977).
13. J. Terrell, Phys. Rev. **113**, 527 (1959).
14. J. Terrell, in *Proceedings of the Symposium "Physics and Chemistry of Fission," Salzburg, 1965* (IAEA, Vienna, 1965), Vol. II, p. 3.
15. M. I. Svirin, Yad. Fiz. **64**, 1660 (2001) [Phys. At. Nucl. **64**, 1581 (2001)].
16. C. Budtz-Jorgensen and H. H. Knitter, Nucl. Phys. A **490**, 307 (1988).
17. H. Marten, D. Richter, D. Seeliger, *et al.*, Nucl. Instrum. Methods Phys. Res. A **264**, 375 (1988).
18. M. V. Blinov, N. M. Kazarinov, A. N. Protopopov, *et al.,* Zh. Éksp. Teor. Fiz. **42**, 1017 (1962) [Sov. Phys. JETP **15**, 704 (1962)].
19. M. S. Samant, R. P. Anand, R. K. Choudhury, *et al.*, INDC (NDS)-251 (IAEA, Vienna, 1995), p. 95.
20. É. M. Kozulin, A. Ya. Rusanov, and G. N. Smirenkin, Yad. Fiz. **56** (2), 37 (1993) [Phys. At. Nucl. **56**, 166 (1993)].
21. I. During, H. Marten, A. Ruben, and D. Seeliger, INDC (NDS)-251/L (IAEA, Vienna, 1991), p. 159.
22. H. Marten, D. Richter, and A. Ruben, INDC (NDS)-220/L (IAEA, Vienna, 1989), p. 169.
23. A. V. Polyakov, G. N. Lovchikova, B. V. Zhuravlev, *et al.,* At. Énergiya **70**, 67 (1991).
24. M. Baba, H. Wakabayashi, M. Ishikawa, *et al.*, INDC (NDS)-220/L (IAEA, Vienna, 1989), p. 149.
25. T. Tamura *et al.*, Ann. Report of FML (Tohoku Univ., Jul. 1981).
26. N. Nakashima, Report JAERI-M, 89-143 (Tokyo, 1989), p. 30.
27. R. Batchelor *et al.*, Nucl. Phys. **65**, 236 (1965).

Translated by A. Isaakyan

Physics of Atomic Nuclei, Vol. 67, No. 5, 2004, pp. 901–910. From Yadernaya Fizika, Vol. 67, No. 5, 2004, pp. 925–934.

NUCLEI
Experiment

Method of Determination of Muon-Catalyzed Fusion Parameters in H–T Mixture*

V. M. Bystritsky and **V. V. Gerasimov**

Joint Institute for Nuclear Research, Dubna, Moscow oblast, 141980 Russia

Received August 5, 2003

Abstract—A method for measurement of the muon-catalyzed fusion (μCF) parameters in an H–T mixture is proposed. The kinetics of the μ-atomic and μ-molecular processes preceding the pt reaction in the $pt\mu$ molecule is described. Analytical expressions are obtained for the yields and time distributions of γ quanta and conversion muons formed in nuclear fusion reactions in $pt\mu$ molecules. It is shown that information on the desired parameters μCF can be found from the joint analysis of the time distributions of γ quanta and conversion muons to be obtained in experiments with the H–T mixture at three (or more) appreciably different atomic concentrations of tritium. The experiments with the H–T mixture at the meson facility PSI (Switzerland) were optimized to gain precise information about the desired μCF parameters.

1. INTRODUCTION

The investigation of the reaction between light nuclei at ultralow energies (~keV) is very important for verification of fundamental symmetries in strong interactions [1–3], the contribution of meson exchange currents [4–7] and solution of some astrophysical problems [8–10].

It is necessary to emphasize the importance of studying muon-catalyzed fusion (μCF) in an H–T mixture in order to obtain information about the characteristics of the pt reaction in the ultralow energy range (~keV).[1)]

The pt reaction is one of the least known of all processes of μCF in the mixture of hydrogen isotopes. It is very important to gain information on reaction characteristics of all muonic processes in the H–T mixture (e.g., the rate of muon transfer from $p\mu$ atom to triton, the rate of transition between hyperfine levels of $t\mu$ atoms, the rate of formation of the $pt\mu$ molecule, and the rate of nuclear synthesis in it) to interpret correctly the results of experiments in the triple mixture of hydrogen isotopes H–D–T and to describe the kinetics of all processes occurring in the mixture. From the theoretical point of view, the experiments investigating μCF processes in an H–T mixture will allow one to test an algorithm describing a three-body system of particles interacting according to the Coulomb rule.

With classical accelerators, it is practically impossible to study the pt reaction in direct collision at very low energies (~keV) because the cross sections of it and intensities of proton (triton) beams are very small [11–14].

At present, there are only two experiments [15, 16] that investigate characteristics of μCF in an H–T mixture.[2)] Only one [15] was performed with an H–T mixture, and the second [16] with triple mixture H–D–T (no doubt, exact measurements of the parameters of muon-catalyzed fusion of the pt reaction can be achieved only with the double mixture H–T).

In this paper, we give a detailed description of the kinetics of μCF for what is essential for data analysis of experimental results with an H–T mixture. An additional aim of this paper is to choose optimal conditions of the experiment for precision investigation of muonic processes in an H–T mixture.

2. KINETICS

The scheme of μ-atomic and μ-molecular processes in an H–T mixture after the negative muons

*This article was submitted by the authors in English.

** e-mail: bystvm@nusun.jinr.ru

*** e-mail: gerasimo@nusun.jinr.ru

1)In nuclear fusion reactions, in the muonic molecules of hydrogen isotopes, the astrophysical range of energies (~keV) is realized [11–14].

2)Recently, at the TRIUMF meson facility, an investigation of the processes of muonic atom ($p\mu$, $d\mu$, $t\mu$) interaction with a hydrogen lattice at a temperature of 3 K has been performed. Preliminary results of the $pt\mu$-molecule formation rate have been obtained [17, 18].

1063-7788/04/6705-0901$26.00

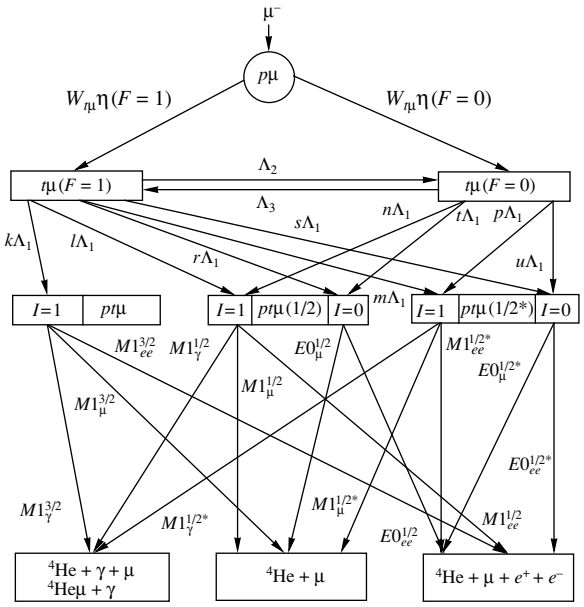

$M1_{\gamma}^{3/2} = W_{3/2}^{1}\lambda_{f,\gamma}^{pt}\,(I=1)$, $M1_{\mu}^{3/2} = W_{3/2}^{1}\lambda_{f,\mu}^{pt}\,(I=1)$, $M1_{ee}^{3/2} = W_{3/2}^{1}\lambda_{f,ee}^{pt}\,(I=1)$;
$M1_{\gamma}^{1/2} = W_{1/2}^{1}\lambda_{f,\gamma}^{pt}\,(I=1)$, $M1_{\mu}^{1/2} = W_{1/2}^{1}\lambda_{f,\mu}^{pt}\,(I=1)$, $M1_{ee}^{1/2} = W_{1/2}^{1}\lambda_{f,ee}^{pt}\,(I=1)$;
$E0_{\mu}^{1/2} = W_{1/2}^{0}\lambda_{f,\mu}^{pt}\,(I=0)$, $E0_{ee}^{1/2} = W_{1/2}^{0}\lambda_{f,ee}^{pt}\,(I=0)$;
$M1_{\gamma}^{1/2*} = W_{1/2*}^{1}\lambda_{f,\gamma}^{pt}\,(I=1)$, $M1_{\mu}^{1/2*} = W_{1/2*}^{1}\lambda_{f,\mu}^{pt}\,(I=1)$, $M1_{ee}^{1/2*} = W_{1/2*}^{1}\lambda_{f,ee}^{pt}\,(I=1)$;
$E0_{\mu}^{1/2*} = W_{1/2*}^{0}\lambda_{f,\mu}^{pt}\,(I=0)$, $E0_{ee}^{1/2*} = W_{1/2*}^{0}\lambda_{f,ee}^{pt}\,(I=0)$;
$\Lambda_1 = \varphi C_p \lambda_{p\mu}$, $\Lambda_2 = C_t\varphi\lambda_{10}$, $\Lambda_3 = C_t\varphi\lambda_{01}$.

Fig. 1. Kinetics of the muonic processes in H–T mixture.

are stopped is shown in Fig. l. As a result of the muon transfers from $p\mu$ atom to tritium nuclei,

$$p\mu + t \to t\mu + p + 183\ \text{eV}, \qquad (1)$$

$t\mu$ atoms are formed with a kinetic energy of about 45 eV (the scheme in Fig. l corresponds to a very low tritium concentration in the H–T mixture ($\leq 1\,\%$), which allows one to neglect direct capture of the muon by tritium).

The ground state of the $t\mu$ atom is split into two hyperfine structure levels with $\mathbf{F} = \mathbf{S}_t + \mathbf{S}_\mu$ being the total spin of the $t\mu$ atom ($S_t = S_\mu = 1/2$ are the spins of triton and muon, respectively) equal to $F = 1$ $[(\mathbf{S}_t\mathbf{S}_\mu) \equiv (\uparrow\uparrow)]$ and $F = 0$ $[(\mathbf{S}_t\mathbf{S}_\mu) \equiv (\uparrow\downarrow)]$. The energy of hyperfine splitting of the $t\mu$ atom is equal to 0.24 eV. The initial population of hyperfine levels is assumed statistically to be

$$\eta = 3/4 \quad (F = 1), \quad \eta = 1/4 \quad (F = 0).$$

In the collision of $t\mu$ atoms with H_2 or HT molecules,

$$t\mu + H_2 \to ((pt\mu)^+ pe)^+ + e^-, \qquad (2)$$

$$t\mu + HT \to ((pt\mu)^+ te)^+ + e^-, \qquad (3)$$

the $pt\mu$ molecule is formed by the electric dipole transition El in excited state (J, ν) (where J and ν are rotational and vibrational quantum numbers of the pt system in $pt\mu$ molecule, respectively).

Upon the collision of the $t\mu$ atom with a triton in the T_2 or HT molecule, the formation of a $tt\mu$ molecule is possible,

$$t\mu + T_2 \to ((t\mu t)^+ te)^+ + e^-, \qquad (4)$$

$$t\mu + HT \to ((t\mu t)pe)^+ + e^-, \qquad (5)$$

due to El dipole transition.

The competitive processes to the formation of a $pt\mu$ molecule are free muonic decay ($\mu \to e^- + \nu_\mu + \tilde{\nu}_e$), $tt\mu$ molecule formation [processes (4) and (5)] and the $t\mu$ atom transition between hyperfine levels:

$$t\mu(F=1) + t \xrightarrow{\lambda_{10}} t\mu(F=0) + t, \qquad (6)$$

$$t\mu(F=0) + t \xrightarrow{\lambda_{01}} t\mu(F=1) + t. \qquad (7)$$

The transition (7) is possible only when the energy of the $t\mu$ atom fulfills the condition $E_{t\mu} > \Delta E = 0.24$ eV (ΔE is the energy of hyperfine splitting of the ground state of the $t\mu$ atom). The probability of the transition of a $t\mu$ atom between hyperfine levels due to the collision of a $t\mu$ atom with a proton,

$$t\mu(F=1) + p \underset{\lambda_{01}}{\overset{\lambda_{10}}{\rightleftarrows}} t\mu(F=0) + p, \qquad (8)$$

according to [19, 20] is very small (because of the small rate of spin-flip reactions due to spin–spin interactions compared to the rate of charge-exchange reactions).

The transition of a $pt\mu$ molecule from the state with $(J\nu) = (10)$ to the ground state $(J\nu) = (00)$ proceeds very quickly ($\sim 10^{-11}$ s) and the energy difference between two states is carried out by a conversion electron.

The ground state of the $pt\mu$ molecule is split into three sublevels with total momentum $J = I + S = 3/2, 1/2, 1/2^*$ [21, 22] (see Fig. 2).

The binding energy of the ground state of the $pt\mu$ molecule (in the nonrelativistic case) equals $\varepsilon_{00} = 214$ keV.

As can be seen from Fig. 2 and Table l, the probability of the formation of a $pt\mu$ molecule in the state with total momentum J and nuclear spin $I = 1$ in the collision of a $t\mu$ atom in the orthostate with a proton is smaller than that during the collision of a $t\mu$ atom in the parastate (see Appendix A).

The populations of the states with different J, J, I, and S (S is the total spin of $pt\mu$ molecule) depend on the relations between the rate of loss of energy by the $t\mu$ atom (due to elastic and nonelastic collisions with H_2, HT, and T_2 molecules) and the rates of processes (6), (7) (λ_{10}, λ_{01}), and also on the relation between the above-mentioned rates and the rate of $pt\mu$-molecule formation.

The whole set of nuclear reactions occurring in the $pt\mu$ molecule in different states is

$$pt\mu \to \begin{cases} {}^4\mathrm{He} + \mu + \gamma \quad (19.76\ \mathrm{MeV}), & (9a)\\ {}^4\mathrm{He}\mu(1s) + \gamma \quad (19.77\ \mathrm{MeV}), & (9b)\\ {}^4\mathrm{He}\mu(2p) + \gamma, & (9c)\\ {}^4\mathrm{He}\mu(n > 2) + \gamma, & (9d)\\ {}^4\mathrm{He} + \mu \quad (19.22\ \mathrm{MeV}), & (9e)\\ {}^4\mathrm{He}\mu + e^+ + e^-, & (9f)\\ {}^4\mathrm{He}\mu + \gamma + \gamma. & (9g) \end{cases}$$

The production of 19.8-MeV γ quanta ($M1$ transition) is possible only from the state of a $pt\mu$ molecule with the total nuclear spin $I = 1$ [reactions (9a)–(9d)].

Nonradioactive transitions (9e) and (9f) proceed dominantly via the monopole $E0$ transition. The probability for the reaction channel (9g) is negligibly small.

The values of the partial rates for the different $pt\mu$ decay channels can be written as [21]

$$\lambda^{pt}_{f,i}(J) = \rho(W^0_J K^i_0 + W^1_J K^i_1), \qquad (10)$$

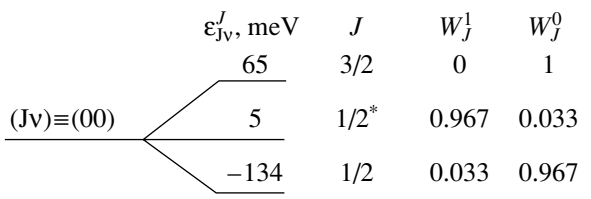

Fig. 2. Scheme of the energy sublevels of $pt\mu$-molecule ground state [21]: W^0_J and W^1_J are the probabilities that the sum of spins of proton and triton in the $pt\mu$ molecule ($\mathbf{I} = \mathbf{I}_p + \mathbf{I}_t$) in the state with angular momentum J equals 0 and 1, respectively.

where $i \equiv \gamma$, μ, e^+, e^-, 2γ; ρ is the density of the probability that the distance between the proton and triton in the $pt\mu$ molecule equals 0; and K^i_0, K^i_1 are pt reaction constants for the S wave in the nuclear states with $I = 0$ (singlet) and $I = 1$ (triplet), respectively.

For the theoretical description of the pt reaction, the resonant model of the existence of ^{4}He nuclei in excited state 0^+ near the threshold of this reaction is used. It is seen from Fig. l that transitions (6), (7) change the populations of the state of the $pt\mu$ molecule (the population of the state with $J = 3/2$ decreases; therefore, together with the $pt\mu$-molecule formation, the process of thermalization of $t\mu$ atoms proceeds), which can change not only the yield of the reaction products (9), but also the ratio between the partial probabilities for different channels of the reaction.

Below, the kinetics of the $pt\mu$ cycle is presented under the assumption that the rates of all muonic processes in the H–T mixture do not depend on energy and that thermalization of $t\mu$ atoms occurs sufficiently fast. The expected average time of thermalization of $t\mu$ atoms (according to our Monte Carlo calculations) $t_{\mathrm{therm}} \approx 10$–$30$ ns (depending on the density of the target) is considerably smaller than characteristic times of all other muonic processes in the H–T mixture.

The yields and time distributions of γ quanta with energy 19.8 MeV and the conversion muons with energy 19.2 MeV, formed in the pt reaction, can be described by the following expressions:

$$\frac{dN_\gamma}{dt} = A^\gamma_1 e^{-\lambda_1 t} + A^\gamma_2 e^{\lambda_2 t} + A^\gamma_3 e^{-\lambda_3 t} + A^\gamma_4 e^{-\lambda_4 t}, \qquad (11)$$

$$\frac{dN_\mu}{dt} = A^\mu_1 e^{-\lambda_1 t} + A^\mu_2 e^{-\lambda_2 t} + A^\mu_3 e^{-\lambda_3 t} + A^\mu_4 e^{-\lambda_4 t} + A^\mu_5 e^{-\lambda_5 t}, \qquad (12)$$

$$N_\gamma = \frac{A^\gamma_1}{\lambda_1} + \frac{A^\gamma_2}{\lambda_2} + \frac{A^\gamma_3}{\lambda_3} + \frac{A^\gamma_4}{\lambda_4}, \qquad (13)$$

Table 1. The population of $pt\mu$ molecule levels formed in the collision of a $t\mu$ atom in the parastate ($F = 0$) or orthostate ($F = 1$)[22] with a proton [$\varepsilon_{J\nu}$ is the energy of the stationary state of the $pt\mu$ molecule (Jν) in the nonrelativistic case; $\varepsilon^J_{J\nu}$ is the energy of the stationary state of the molecule $pt\mu$ (Jν) with total momentum J deduced from $\varepsilon_{J\nu}$; $a^J_{J\nu}(\uparrow\downarrow)$, $a^J_{J\nu}(\uparrow\uparrow)$ are the populations of the state (J, ν,J) of the $pt\mu$ molecule created in the collision of a $t\mu$ atom in the parastate ($F = 0$) or orthostate ($F = 1$), respectively, with a proton]

J	ν	$\varepsilon_{J\nu}$, eV	J	$\varepsilon^J_{J\nu}$, eV	$a^J_{J\nu}(\uparrow\downarrow)$	$a^J_{J\nu}(\uparrow\uparrow)$
0	0	−214.0	1/2*	0.0046	0.1120	0.2960
			1/2	−0.1344	0.8880	0.0373
			3/2	0.0649	0	0.6667
1	0	−99.0		0.0053	0.0256	0.1026
			1/2	−0.1249	0.3076	0.0086
				0.0555	0.0001	0.1111
				0.0083	0.0548	0.2039
			3/2	−0.1262	0.6119	0.0183
				0.0608	0	0.2222
			5/2	0.0594	0	0.3333

$$N_\mu = \frac{A^\mu_1}{\lambda_1} + \frac{A^\mu_2}{\lambda_2} + \frac{A^\mu_3}{\lambda_3} + \frac{A^\mu_4}{\lambda_4} + \frac{A^\mu_5}{\lambda_5}, \quad (14)$$

$$\lambda_1 = \lambda_0 + \lambda_{pp\mu}\varphi C_p + \lambda_{pt}\varphi C_t, \quad (15)$$

$$\lambda_2 = \lambda_0 + \lambda_{pt\mu}\varphi C_p + \lambda_{tt\mu}\varphi C_t + \lambda_{10}\varphi C_t, \quad (16)$$

$$\lambda_3 = \lambda_0 + \lambda_{pt\mu}\varphi C_p + \lambda_{tt\mu}\varphi C_t, \quad (17)$$

$$\lambda_4 = \lambda_0 + \lambda^{pt}_f \quad (I = 1), \quad (18)$$

$$\lambda_5 = \lambda_0 + \lambda^{pt}_f \quad (I = 0), \quad (19)$$

$$\lambda_0 = 0.455 \times 10^6\ \mathrm{s}^{-1},$$

$$C_p + C_t = 1,$$

where A^γ_1–A^γ_4, A^μ_1–A^μ_4 are the normalized coefficients given in Appendix B; N_γ and N_μ are the yields of γ quanta and conversion muons, respectively; $\lambda_0 = 0.455 \times 10^6\ \mathrm{s}^{-1}$ is the free muon decay rate; λ_{pt}, λ_{10}, $\lambda_{pt\mu}$ are the rates of the muon transition from $p\mu$ atom to triton, of the transition of $t\mu$ atom from the state with $F = 1$ to the state with $F = 0$, and of the $pt\mu$ molecule formation, respectively (the above values are reduced to liquid hydrogen density, $n_0 = 4.25 \times 10^{22}\ \mathrm{cm}^{-3}$); $\lambda_{pp\mu}$, $\lambda_{tt\mu}$ are the $pp\mu$- and $tt\mu$-molecule formation rates; $\lambda^{pt}_f(I = 0) = \lambda^{pt}_{f,\mu}(I = 0) + \lambda^{pt}_{f,ee}(I = 0)$, $\lambda^{pt}_f(I = 1) = \lambda^{pt}_{f,\gamma}(I = 1) + \lambda^{pt}_{f,\mu}(I = 1) + \lambda^{pt}_{f,ee}(I = 1)$ are the total rates of nuclear synthesis in the $pt\mu$ molecule for the total spin of proton and triton equal to 0 and 1, respectively; $\lambda^{pt}_{f,\mu}(I = 0), \lambda^{pt}_{f,\mu}(I = 1)$ are partial rates of nuclear synthesis in the $pt\mu$ molecule with muon production for the total spin of proton and triton equal to 0 and 1, respectively, and $\lambda^{pt}_{f,\gamma}(I = 1)$ is the rate of nuclear synthesis in the $pt\mu$ molecule in the state $I = 1$ with γ-quanta production; $\lambda^{pt}_{f,ee}(I = 0), \lambda^{pt}_{f,ee}(I = 1)$ are the rates of nuclear synthesis in the $pt\mu$ molecule with the formation of an electron–positron pair for the total spin of p and t equal to 0 and 1, respectively; C_p and C_t are atomic concentrations of protium and tritium in the H–T mixture; and φ is the density of the H–T mixture reduced to liquid hydrogen density.

The measurement of the synthesis rate in the $pt\mu$ molecule with the production of conversion muons, $\lambda^{pt}_{f,\mu}(I = 0)$, is very important and will allow one to verify the validity of the hypothesis of the existence of a threshold resonance in the fusion channel (and to check the charge distribution in the system with $A = 4$).

Having time distributions of γ quanta with energy 19.8 MeV [reactions (9a)–(9d)] and conversion muons with energy 19.2 MeV [reaction (9e)] or electron–positron pair [reaction (9f)] for different tritium concentration C_t, using Eqs. (11)–(19), one can derive unknown parameters: λ_{pt}, λ_{10}, $\lambda_{pt\mu}$, λ^{pt}_f $(I = 1)$, and $\lambda^{pt}_{f,\mu}$ $(I = 0)$. We assume that the values of parameters $\lambda_{pp\mu}$, $\lambda_{tt\mu}$ are known (the value $\lambda_{pp\mu}$ was taken as an average from [18, 23–27], $\lambda_{tt\mu}$ from

Table 2. The experimental and theoretical values of the parameters of the μCF process in the H–T mixture

	Experiment				Theory	
	H–T [15]	H–D–T [16]	H–T [17]	H–T [18]	[14]	[21]
$\lambda_{pt}\,[10^9\ \mathrm{s}^{-1}]$		9.3 ± 1.5	$5.86 \pm (0.10)_{\mathrm{stat}}$			
$\lambda_{10}\,[10^9\ \mathrm{s}^{-1}]$	6.0 ± 0.5	1.0 ± 0.2				
$\lambda_{pt\mu}\,[10^6\ \mathrm{s}^{-1}]$		7.5 ± 1.3		5.8 ± 0.4	0.4	
$\lambda_f^{pt}(I=1)\,[10^4\ \mathrm{s}^{-1}]$	6.5 ± 0.7	7.0 ± 1.2			≈ 1800	7
$\lambda_f^{pt}(I=0)\,[10^2\ \mathrm{s}^{-1}]$		$(15 \pm 4) \times 10^2$				8.6
$\lambda_{f,\gamma}^{pt}(I=1)\,[10^6\ \mathrm{s}^{-1}]$						0.07
$\lambda_{f,ee}^{pt}(I=1)\,[10^2\ \mathrm{s}^{-1}]$						2.4
$\lambda_{f,ee}^{pt}(I=0)\,[10^2\ \mathrm{s}^{-1}]$						3.6
$\lambda_{f,\mu}^{pt}(I=1)\,[\mathrm{s}^{-1}]$						0.35
$\lambda_{f,\mu}^{pt}(I=0)\,[10^2\ \mathrm{s}^{-1}]$					10^3–10^4	5 ± 1
$\dfrac{\lambda_{f,\mu}^{pt}(I=1)}{\lambda_f^{pt}(I=1)}$					10^{-5}	5×10^{-6}
$\dfrac{\lambda_{f,\mu}^{pt}(I=0)}{\lambda_{f,ee}^{pt}(I=0)}$					≈ 1	0.73

[28], and the remaining parameters were taken from [21, 22].

This approach is valid because the yields and time distributions of the products from different channels of the pt reaction require the same μCF parameters, which, on the one hand, can guarantee correct interpretation of the results and correct estimation of systematic errors and, on the other hand, can increase the accuracy of measured parameters.

3. OPTIMIZATION AND DESCRIPTION OF RESULTS

The existing theoretical and experimental parameters describing the $pt\mu$ cycle are presented in Table 2.

There also exist some other theoretical estimates of the above parameters not shown in the table:

$$\lambda_{pt} = 7.5 \times 10^9\ \mathrm{s}^{-1}\ [20], (7.0\text{–}8.0) \times 10^9\ \mathrm{s}^{-1}$$
$$\text{at } T = 300\text{–}30\ K\ [29], 5.8 \times 10^9\ \mathrm{s}^{-1}\ [30],$$
$$5.5 \times 10^9\ \mathrm{s}^{-1}\ [31], 5.7 \times 10^9\ \mathrm{s}^{-1}\ [32];$$
$$\lambda_{10} = 0.89 \times 10^9\ \mathrm{s}^{-1}\ [20],$$
$$0.91 \times 10^9\ \mathrm{s}^{-1}\ [33], \quad 1.3 \times 10^9\ \mathrm{s}^{-1}\ [34];$$
$$\lambda_{pt\mu} = 6.5 \times 10^6\ \mathrm{s}^{-1}\ [35], 6.38 \times 10^6\ \mathrm{s}^{-1}\ [36];$$
$$\lambda_f^{pt}(I=1) = 0.5 \times 10^6\ \mathrm{s}^{-1}\ [37],^{3)}$$
$$0.13 \times 10^6\ \mathrm{s}^{-1}\ [39]^{4)}, 0.008 \times 10^6\ \mathrm{s}^{-1}\ [42].^{4)}$$

As is shown, there is a big difference between experimental and theoretical values of some parameters like λ_{pt}, $\lambda_f^{pt}(I=1)$, and $\lambda_f^{pt}(I=0)$. Regarding the rate of $pt\mu$ molecule formation ($\lambda_{pt\mu}$), there is strong disagreement between theory and experiment.

It is shown from Table 2 that it is necessary to measure fundamental characteristics of μCF in the H–T mixture to explain the nature of the difference between theoretical and experimental values. Figure 3 shows the yield of γ quanta and conversion muons per one muon stopped in the H–T mixture [calculated according to formulas (13) and (14)] as a function of the tritium concentration C_t for a density of the H–T mixture equal to the density of liquid hydrogen, $\varphi = 1$. Comparing obtained dependences with corresponding values from papers [16], one can notice differences not only in shape but also in absolute values of the conversion muon yield for the same values of C_t. The reason for such discrepancies is not clear.

According to [16], the maximum values of the γ-quanta and conversion muon yields, calculated per one muon stopped in the H–T mixture, equal $N_\gamma^{\max} \approx$

[3)] This value was obtained according to the formula $\lambda_f^{pt}(I=1) = (4/3)K_0\rho_0$, using pt reaction constants K_0 from [37] and [38] and ρ_0 from [39].

[4)] The estimate of these values was obtained using the cross section $\sigma(n,\gamma) = 55 \pm 3$ μb of the mirror reaction $^3\mathrm{He}(n,\gamma)^4\mathrm{He}$ [40, 41].

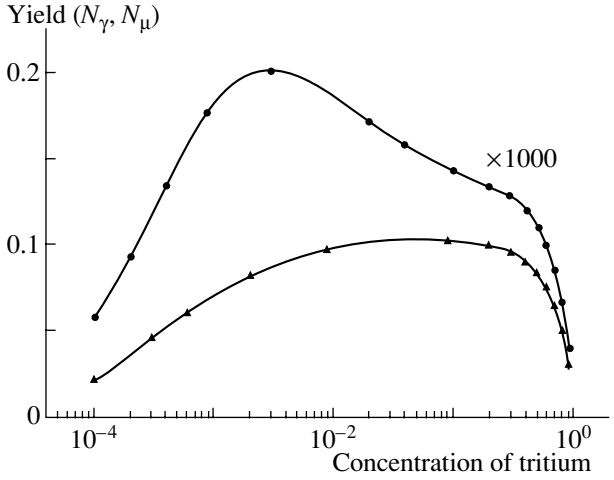

Fig. 3. The yields of γ quanta (triangles) and conversion muons (circles) from pt fusion as a function of tritium concentration.

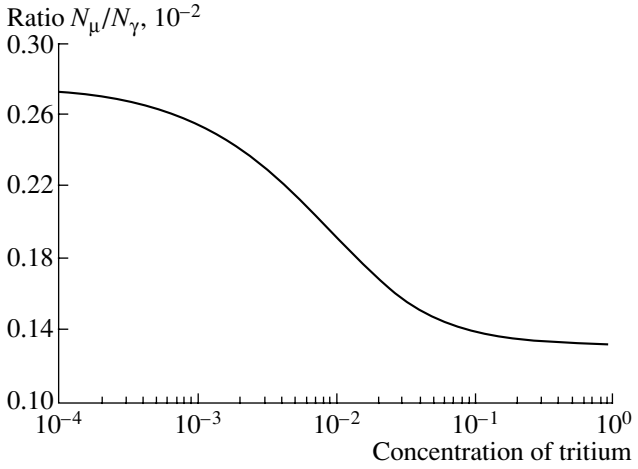

Fig. 4. Ratio between yields of conversion muons (N_μ) and γ quanta (N_γ) as a function of tritium concentration.

0.11 (for $C_t \approx 6 \times 10^{-2}$) and $N_\mu^{\max} = 0.015$ (for $C_t = 3 \times 10^{-3}$); in the present paper, $N_\gamma^{\max} \approx 0.10$ ($C_t \approx 8 \times 10^{-2}$), $N_\mu^{\max} \approx 2.0 \times 10^{-4}$ ($C_t \approx 3 \times 10^{-3}$).

The ratio between yields of the conversion muons and γ quanta as a function of tritium concentration is shown in Fig. 4. The distinguishing feature of this dependence is that the ratio N_μ/N_γ is practically constant for a tritium concentration larger than 0.2. Such behavior of the N_μ/N_γ ratio can be explained by the existence of the Gershtein–Wolfenshtein effect predicted [43] and verified before for muon-catalyzed fusion in an H–D mixture [24].

There are seven unknown parameters ε_γ, ε_μ, $\lambda_{f,\mu}^{pt}(I=0)$, $\lambda_f^{pt}(I=1)$, λ_{10}, $\lambda_{pt\mu}$, λ_{pt} in expressions (11)–(14), and to determine them with sufficient accuracy, three exposures of the muon beam in the H–T mixture for three tritium concentrations are required. Really, there are six unknown parameters, but the quantity $\lambda_f^{pt}(I=1)$ is determined from the slope of the exponent with index λ_4: $\lambda_f^{pt}(I=1) = \lambda_4 - \lambda_0$ [see expression (18)].

According to [21], the partial rates of nuclear $M1$ transition in a $pt\mu$ molecule with emission of a conversion muon ($\lambda_{f,\mu}^{pt}(I=1)$) and electron–positron pair ($\lambda_{f,ee}^{pt}(I=1)$) are negligible in comparison with $\lambda_{f,\gamma}^{pt}(I=1)$. Therefore, the following ratio is valid:

$$\lambda_{f,\gamma}^{pt}(I=1) + \lambda_{f,\mu}^{pt}(I=1) + \lambda_{f,ee}^{pt}(I=1) = \lambda_f^{pt}(I=1) \approx \lambda_{f,\gamma}^{pt}(I=1).$$

The accuracy of estimating these parameters depends on the statistics of detected events in the experiment. In principle, the rates of the processes $\lambda_{f,\gamma}^{pt}(I=1)$, λ_{10}, $\lambda_{pt\mu}$, λ_{pt} can be estimated from the slopes of exponents with indices λ_1, λ_2, λ_3, λ_4 [expressions (15)–(18)]. The value $\lambda_{f,\mu}^{pt}(I=0)$ cannot be experimentally found from the slope of the exponent with index $\lambda_5 (\lambda_5 = \lambda_f^{pt}(I=0) + \lambda_0)$ because the value $\lambda_f^{pt}(I=0)$ is very small ($\lambda_f^{pt}(I=0) = 5 \times 10^2$ s^{-1} [21]) compared to $\lambda_0 (\lambda_5 \approx \lambda_0)$. Therefore, the value $\lambda_{f,\mu}^{pt}(I=0)$ can only be found by analyzing the factor A_5^μ before the exponent with index $\lambda_5 \approx \lambda_0$ in expression (12).

Below, as an example of H–T experiment optimization, the performance of an experiment using the muon channel μE4 of the PSI meson facility (Switzerland) will be considered. As a target, it is supposed to use liquid hydrogen with tritium concentration C_t less than 10%. This value of tritium concentration is dictated by safety conditions.

The optimization of the planned experiment requires finding three tritium concentrations and corresponding times of the exposures, on the muon channel, so that the errors of the determination of unknown parameters will be minimal (this means that the sum of the squares of the relative errors of the desired parameters is minimal in the interval $C_t = 0$–0.1).

As input data, the following values were used:

$$N_{\mu\text{stop}} = 10^4 \text{ s}^{-1} \text{ [44]};$$
$$\varepsilon_\gamma = 2 \times 10^{-5}; \varepsilon_\mu = 5 \times 10^{-4};$$
$$\lambda_{pt\mu} = 7.5 \times 10^6 \text{ s}^{-1} \text{ [16]};$$
$$\lambda_{f,\gamma}^{pt}(I=1) = \lambda_f^{pt}(I=1) = 7 \times 10^4 \text{ s}^{-1} \text{ [16, 21]};$$
$$\lambda_{f,\mu}^{pt}(I=0) = 5 \times 10^2 \text{ s}^{-1} \text{ [21]};$$
$$\lambda_{tt\mu} = 1.8 \times 10^6 \text{ s}^{-1} \text{ [28]};$$

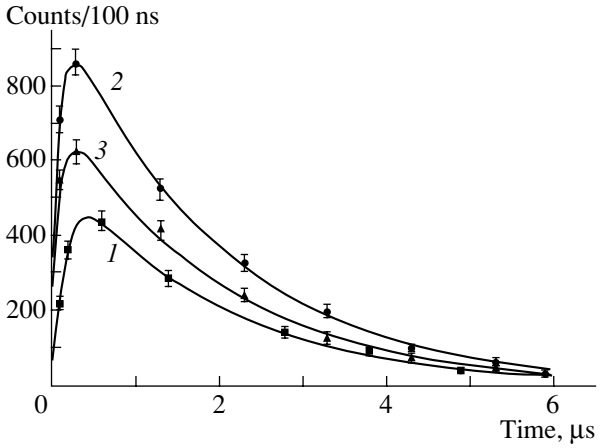

Fig. 5. The time distributions of pt fusion γ quanta for three different values of tritium concentrations: (*1*) $C_t = 5 \times 10^{-4}$, (*2*) $C_t = 6 \times 10^{-2}$, (*3*) $C_t = 1 \times 10^{-1}$. The curves are the result of fitting of the simulated time spectra; the indicated bars are the statistical errors.

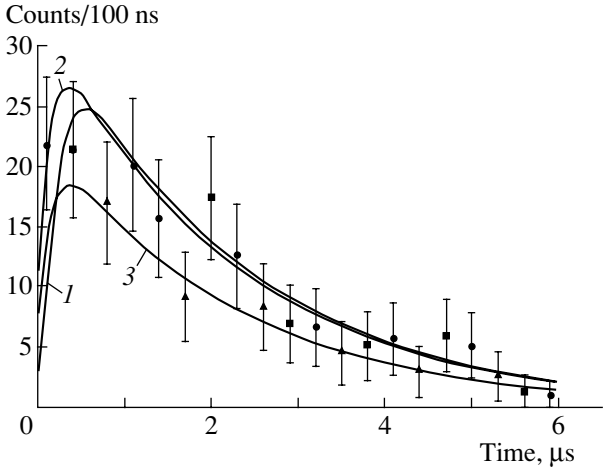

Fig. 6. Conversion muon time spectra for three chosen tritium concentrations: (*1*) $C_t = 5 \times 10^{-4}$, (*2*) $C_t = 6 \times 10^{-2}$, (*3*) $C_t = 1 \times 10^{-1}$. The curves are the result of fitting of the simulated time spectra. The indicated bars are the statistical errors.

$$\lambda_{pt} = 9.3 \times 10^9\ \mathrm{s}^{-1}\ [16];\ \lambda_{10} = 1.0 \times 10^9\ \mathrm{s}^{-1}\ [16];$$
$$\varphi = 1.0; \quad C_t = 0\text{–}0.10.$$

For the purpose of choosing optimal experimental conditions, it was assumed that the total time of exposure for three different tritium concentrations was 700 h.

The time for each of three exposures is determined as $t_1 : t_2 : t_3 = \sqrt{n_\gamma^{(3)}} : \sqrt{n_\gamma^{(2)}} : \sqrt{n_\gamma^{(1)}}$, where $n_\gamma^{(1)}$, $n_\gamma^{(2)}$, $n_\gamma^{(3)}$ are the yields of γ quanta per one second in the exposures 1, 2, 3, respectively.

As a result of the combined χ^2 analysis of the calculated six time distributions of γ quanta and conversion muons (the Monte Carlo method was used for each of the three exposures to obtain the simulated experimental time distributions of γ quanta and conversion muons), we have found three optimal values of tritium concentrations:[5)] $C_t = 5 \times 10^{-4}, 6 \times 10^{-2}, 1 \times 10^{-1}$.

Figures 5 and 6 show the calculated time distributions of the detected γ quanta with energy 19.8 MeV and conversion muons for three chosen tritium concentrations. Figure 7 shows the calculated parameter errors as functions of the statistics of detected events.

These parameter error dependences correspond to the approximation of the simulated γ-quanta and conversion muon experimental time distributions by expressions (11)–(14) with unknown parameters ε_γ, ε_μ, $\lambda_{pt\mu}$, λ_{10}, λ_{pt}, $\lambda_{f,\gamma}^{pt}(I=1)$. It should be pointed out that, in such case, the $\lambda_{f,\mu}^{pt}(I=0)$ was fixed and equal to $5 \times 10^2\ \mathrm{s}^{-1}$ [21].

As can be seen, a sufficient total time of statistics gathering for determination of parameters $\lambda_{pt\mu}$, $\lambda_{f,\gamma}^{pt}(I=1)$, λ_{pt} with accuracy of $\sim$10% is $\sim$300 h.

As for the transition rate between hyperfine levels of $t\mu$ atom λ_{10} (curve *2* in Fig. 7), the uncertainty of this magnitude is $\sim$100% for the same time gathering statistics. For the statistics gathering time of 600 h, the accuracy of λ_{10} determination is 75%.

From the proceeding, it may be seen that the result of joint analysis of γ-quanta and conversion muon time distributions obtained at three chosen tritium concentrations is weakly sensitive to the value of λ_{10}.

More precise measurement of λ_{10} is possible by substantially increasing the collection statistics and the range of variation of H–T mixture density and tritium concentration.

The next step of the μCF parameter error calculation has been done setting ε_γ and ε_μ, which are known with an accuracy of 5% from additional experiments. The results of these calculations are presented in Fig. 8. As can be seen, the possibility of determining, for the first time, information about the fusion rate $\lambda_{f,\mu}^{pt}(I=0)$ appeared. This circumstance is very important for correct description of the pt-reaction mechanism. The relative errors of other μCF parameters in the H–T mixture for optimization with known parameters ε_γ and ε_μ are less than the corresponding values from previous optimization at the same gathering times of statistics.

[5)] The minimum of χ^2 for different combinations of three tritium concentrations corresponds to the chosen set of three C_t.

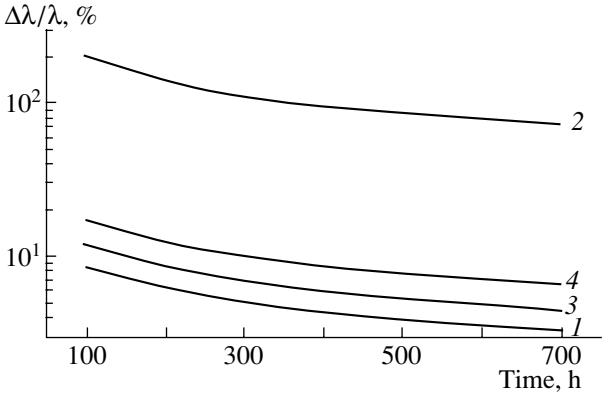

Fig. 7. Relative errors of $\lambda_{pt\mu}$, λ_{10}, $\lambda^{pt}_{f,\gamma}(I=1)$, and λ_{pt} as functions of the statistics gathering time (ε_γ, ε_μ, $\lambda_{pt\mu}$, λ_{10}, λ_{pt}, $\lambda^{pt}_{f,\gamma}(I=1)$ are the variable parameters; $\lambda^{pt}_{f,\mu}(I=0)=5\times10^2$ s^{-1}): (*1*) $\Delta\lambda_{pt}/\lambda_{pt}$, (*2*) $\Delta\lambda_{10}/\lambda_{10}$, (*3*) $\Delta\lambda_{pt\mu}/\lambda_{pt\mu}$, (*4*) $\Delta\lambda^{pt}_{f,\gamma}(I=1)/\lambda^{pt}_{f,\gamma}(I=1)$.

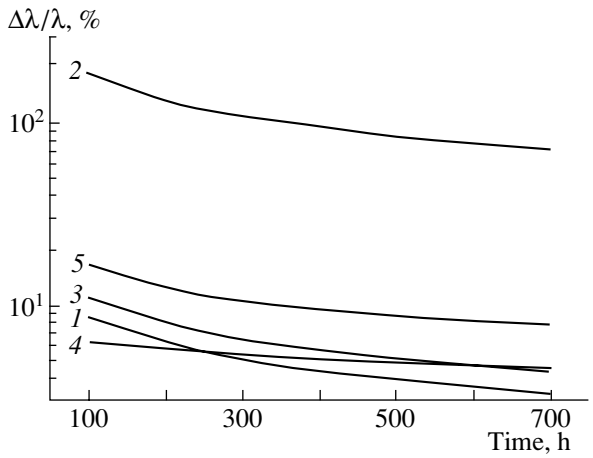

Fig. 8. The dependences of the μCF parameter relative errors on statistics gathering time (ε_γ and ε_μ are known from additional experiment). Curves *1*–*4* correspond to Fig. 7; curve *5* shows $\Delta\lambda^{pt}_{f,\mu}(I=0)/\lambda^{pt}_{f,\mu}(I=0)$.

From the presented analysis of the μCF kinetics in the H–T mixture, one can conclude that, from the experiment performed for three different tritium concentrations, the unknown parameters of μCF ($\lambda_{pt\mu}$, $\lambda^{pt}_{f,\gamma}(I=1)$, λ_{pt}) can be obtained with sufficient accuracy. Simultaneous measurement of yields and time distributions of γ quanta and conversion muons will allow one to find not only the ratio of probabilities for the radiation and nonradiation channel of the pt reaction, but also their exact values. Thus, the possibility exists to measure the fusion rate occurring in the ground state of the $pt\mu$ molecule due to $E0$ and $M1$ transitions with the conversion of muons and γ quanta, respectively.

The measurement of γ-quanta and conversion muon detection efficiencies in additional experiments will allow one to obtain the value of $\lambda^{pt}_{f,\mu}(I=0)$ and to decrease the relative errors of μCF parameters such as $\lambda_{pt\mu}$, λ_{10}, λ_{pt}, $\lambda^{pt}_{f,\gamma}(I=1)$.

In addition, the accuracy of λ_{10} can be improved due to the measurement and joint analysis of γ quanta, conversion muons, and Auger electrons emitted upon deexcitation of $pt\mu$ molecules formed in the $(J\nu)=(10)$ state.

ACKNOWLEDGMENTS

We would like to express our sincere gratitude to Dr. M. Filipowicz, E. Gula, J. Wozniak, and A. Krylov for arithmetic of H–T experiment optimization and to Dr. Mulhauser and P. Knowles for fruitful discussions.

This work was supported by the Russian Foundation for Basic Research (project no. 01-02-16483).

APPENDIX A

The Probabilities of $pt\mu$ Formation

$$W^{F=0}_{pt\mu}(J=1/2^*;I=1)$$
$$=a^{1/2^*}_{00}(\uparrow\downarrow)\cdot W^1_{1/2^*}=3.7\times10^{-3};$$

$$W^{F=0}_{pt\mu}(J=1/2;I=1)$$
$$=a^{1/2}_{00}(\uparrow\downarrow)\cdot W^1_{1/2}=8.59\times10^{-1};$$

$$W^{F=0}_{pt\mu}(J=1/2;1/2^*;I=1)$$
$$=W^{F=0}_{pt\mu}(J=1/2^*;I=1)$$
$$+W^{F=0}_{pt\mu}(J=1/2;I=1)=8.62\times10^{-1};$$

$$W^{F=1}_{pt\mu}(J=1/2;I=1)$$
$$=a^{1/2}_{00}(\uparrow\uparrow)\cdot W^1_{1/2}=3.6\times10^{-2};$$

$$W^{F=1}_{pt\mu}(J=1/2^*;I=1)$$
$$=a^{1/2}_{00}(\uparrow\uparrow)\cdot W^1_{1/2^*}=9.8\times10^{-3};$$

$$W^{F=1}_{pt\mu}(J=1/2;1/2^*;I=1)$$
$$=W^{F=1}_{pt\mu}(J=1/2;I=1)$$
$$+W^{F=1}_{pt\mu}(J=1/2^*;I=1)=4.58\times10^{-2};$$

$$W^{F=1}_{pt\mu}(J=3/2;I=1)$$
$$=a^{3/2}_{00}(\uparrow\uparrow)\cdot W^1_{3/2}=6.67\times10^{-1};$$

$$W_{pt\mu}^{F=1}(J=3/2;1/2^*;1/2;I=1)=7.13\times10^{-1};$$

$$W_{pt\mu}^{F=1}(J=1/2;I=0)=a_{00}^{1/2}(\uparrow\uparrow)\cdot W_{1/2}^{0}=1.22\times10^{-3};$$

$$W_{pt\mu}^{F=1}(J=1/2^*;I=0)=a_{00}^{1/2^*}(\uparrow\uparrow)\cdot W_{1/2^*}^{0}=0.286;$$

$$W_{pt\mu}^{F=0}(J=1/2;I=0)=a_{00}^{1/2}(\uparrow\downarrow)\cdot W_{1/2}^{0}=2.93\times10^{-2};$$

$$W_{pt\mu}^{F=0}(J=1/2^*;I=0)=a_{00}^{1/2^*}(\uparrow\downarrow)\cdot W_{1/2}^{0}=0.108,$$

where $W_{pt\mu}^{F}(J,I)$ is the probability of a $pt\mu$ formation in the state with total angular momentum J and nuclear spin I in the collisions of a $t\mu$ atom with a spin F and an H_2 molecule.

APPENDIX B

The Coefficients A_1^γ–A_4^γ and A_1^μ–A_5^μ

$$A_1^\gamma=A\left(\frac{1}{\lambda_1-\lambda_2}\frac{k+l+m}{\lambda_1-\lambda_4}+\frac{1}{\lambda_1-\lambda_3}\frac{n+p}{\lambda_1-\lambda_4}\left(\frac{1}{3}-\frac{\lambda_{10}\varphi C_t}{\lambda_1-\lambda_2}\right)\right),$$

$$A_2^\gamma=-\frac{A}{(\lambda_1-\lambda_2)(\lambda_2-\lambda_4)}\times\left((k+l+m)-\frac{\lambda_{10}\varphi C_t}{\lambda_2-\lambda_3}(n+p)\right),$$

$$A_3^\gamma=-\frac{A}{\lambda_1-\lambda_3}\frac{n+p}{\lambda_3-\lambda_4}\left(\frac{1}{3}+\frac{\lambda_{10}\varphi C_t}{\lambda_2-\lambda_3}\right),$$

$$A_4^\gamma=\frac{A}{\lambda_1-\lambda_4}\times\left(\frac{k+l+m}{\lambda_2-\lambda_4}+\frac{n+p}{\lambda_3-\lambda_4}\left(\frac{1}{3}+\frac{\lambda_{10}\varphi C_t}{\lambda_2-\lambda_4}\right)\right),$$

$$A=\frac{3}{4}N_{\mu\mathrm{stop}}\lambda_{pt}\varphi C_t\lambda_{pt\mu}\varphi C_p\lambda_{f,\gamma}^{pt}(I=1)\,\varepsilon_\gamma,$$

$$k=W_{pt\mu}^{F=1}(J=3/2;I=1)=6.67\times10^{-1},$$

$$l=W_{pt\mu}^{F=1}(J=1/2;I=1)=3.6\times10^{-2},$$

$$m=W_{pt\mu}^{F=1}(J=1/2^*;I=1)=9.8\times10^{-2},$$

$$n=W_{pt\mu}^{F=0}(J=1/2;I=1)=8.59\times10^{-1},$$

$$p=W_{pt\mu}^{F=0}(J=1/2^*;I=1)=3.7\times10^{-3},$$

$$A_1^\mu=A1\left(\frac{1}{\lambda_1-\lambda_2}\left(\frac{\lambda_{f,\mu}^{pt}(I=1)}{\lambda_1-\lambda_4}(k+l+m)+\frac{\lambda_{f,\mu}^{pt}(I=0)}{\lambda_1-\lambda_0}(r+s)\right)+\left(\frac{1}{3}-\frac{\lambda_{10}\varphi C_t}{\lambda_1-\lambda_2}\right)\frac{1}{\lambda_1-\lambda_3}\times\left(\frac{\lambda_{f,\mu}^{pt}(I=1)}{\lambda_1-\lambda_4}(n+p)+\frac{\lambda_{f,\mu}^{pt}(I=0)}{\lambda_1-\lambda_0}(t+u)\right)\right),$$

$$A_2^\mu=-\frac{A1}{\lambda_1-\lambda_2}\left(\frac{\lambda_{f,\mu}^{pt}(I=1)}{\lambda_2-\lambda_4}(k+l+m)+\frac{\lambda_{f,\mu}^{pt}(I=0)}{\lambda_2-\lambda_0}(r+s)-\frac{\lambda_{10}\varphi C_t}{\lambda_2-\lambda_3}\times\left(\frac{\lambda_{f,\mu}^{pt}(I=1)}{\lambda_2-\lambda_4}(n+p)+\frac{\lambda_{f,\mu}^{pt}(I=0)}{\lambda_2-\lambda_0}(t+u)\right)\right),$$

$$A_3^\mu=-\frac{A1}{\lambda_1-\lambda_3}\times\left(\frac{\lambda_{f,\mu}^{pt}(I=1)}{\lambda_3-\lambda_4}(n+p)+\frac{\lambda_{f,\mu}^{pt}(I=0)}{\lambda_3-\lambda_0}(t+u)\right)\times\left(\frac{1}{3}+\frac{\lambda_{10}\varphi C_t}{\lambda_2-\lambda_3}\right),$$

$$A_4^\mu=\frac{A1\lambda_{f,\mu}^{pt}(I=1)}{\lambda_1-\lambda_4}\left[\frac{1}{\lambda_2-\lambda_4}(k+l+m)+\frac{1}{\lambda_3-\lambda_4}(n+p)\left(\frac{1}{3}+\frac{\lambda_{10}\varphi C_t}{\lambda_2-\lambda_4}\right)\right],$$

$$A_5^\mu=\frac{A1\lambda_{f,\mu}^{pt}(I=0)}{\lambda_1-\lambda_0}\times\left[\frac{r+s}{\lambda_2-\lambda_0}+\frac{t+u}{\lambda_3-\lambda_0}\left(\frac{1}{3}+\frac{\lambda_{10}\varphi C_t}{\lambda_2-\lambda_0}\right)\right],$$

$$A1=\frac{3}{4}N_{\mu\mathrm{stop}}\lambda_{pt}\varphi C_t\lambda_{pt\mu}\varphi C_p\varepsilon_\mu,$$

$$r=W_{pt\mu}^{F=1}\left(J=\frac{1}{2};I=0\right)=1.22\times10^{-3},$$

$$s=W_{pt\mu}^{F=1}(J=1/2^*;I=0)=0.286,$$

$$t=W_{pt\mu}^{F=0}\left(J=\frac{1}{2};I=0\right)=2.93\times10^{-2},$$

$$u = W_{pt\mu}^{F=0}(J = 1/2^*; I = 0) = 0.108,$$

where $N_{\mu\text{stop}}$ is the number of muons stopped in the H–T mixture, and ε_γ, ε_μ are the efficiencies of the detection of γ quanta from reactions (9a)–(9d) and conversion muons from (9e), respectively.

REFERENCES

1. S. P. Merkuriev *et al.*, in *Proceedings of the International Conference on the Theory of Few-Body and Quark–Hadronic Systems, Dubna, 1987*, D4-87-692, p. 6.
2. J. L. Friar, in *Proceedings of the International Conference on the Theory of Few-Body and Quark–Hadronic Systems, Dubna, 1987*, D4-87-692, p. 70.
3. H. Paetz gen. Schieck, Few-Body Syst. **5**, 171 (1988).
4. C. Bargholz, Nucl. Phys. A **474**, 1 (1987).
5. J. L. Friar, Phys. Lett. B **251**, 11 (1990).
6. J. Torre and B. Goulard, Phys. Rev. C **28**, 529 (1983).
7. A. C. Phillips, Nucl. Phys. A **184**, 337 (1972).
8. C. Rolfs, in *Proceedings of the International School of Physics "Enrico Fermi," Course C. 3, Villa Monastero, 1987*, Ed. by P. Kienle, R. A. Ricci, and A. Rubbino (North Holland, Amsterdam, 1989), p. 417.
9. J. N. Bachcall and M. H. Pinsonneault, Rev. Mod. Phys. **64**, 885 (1992).
10. M. Arnould and M. Forestini, in *Nuclear Astrophysics Proceedings of the 3rd International Summer School, La Rabida, Huelve, Spain, 1988*, Research Reports in Physics (Springer-Verlag, 1988), p. 48.
11. W. Kolos, Phys. Rev. **165**, 165 (1968).
12. B. P. Carter, Phys. Rev. **141**, 863 (1966); **153**, 1358 (1967).
13. J. L. Friar *et al.*, Phys. Rev. Lett. **66**, 1827 (1991).
14. Ya. B. Zeldovich and S. S. Gershtein, Usp. Fiz. Nauk **71**, 581 (1960).
15. F. J. Hartmann *et al.*, Muon Catal. Fusion **2**, 53 (1988).
16. P. Baumann *et al.*, Muon Catal. Fusion **5**, 87 (1990); F. J. Hartmann *et al.*, Hyperfine Interact. **82**, 259 (1993).
17. F. Mulhauser *et al.*, Phys. Rev. A **53**, 3069 (1996); Hyperfine Interact. **101**, 229 (1996).
18. F. Mulhauser *et al.*, Hyperfine Interact. **119**, 35 (1999).
19. L. Bracci *et al.*, Muon Catal. Fusion **4**, 247 (1989).
20. A. V. Matveenko and L. I. Ponomarev, Zh. Éksp. Teor. Fiz. **58**, 1640 (1970) [Sov. Phys. JETP **31**, 880 (1970)].
21. L. Bogdanova and V. Markushin, Nucl. Phys. A **508**, 29 (1990); Muon Catal. Fusion **4**, 103 (1989); L. N. Bogdanova, Muon Catal. Fusion **3**, 359 (1988).
22. D. Bakalov, Zh. Éksp. Teor. Fiz. **79**, 1629 (1980) [Sov. Phys. JETP **52**, 581 (1980)].
23. R. Jacot-Guillarmod *et al.*, Hyperfine Interact. **101**, 239 (1996).
24. E. J. Bleser *et al.*, Phys. Rev. **132**, 2679 (1963).
25. G. Conforto *et al.*, Nuovo Cimento **33**, 1001 (1964).
26. V. M. Bystritskiĭ *et al.*, Zh. Éksp. Teor. Fiz. **70**, 1167 (1976) [Sov. Phys. JETP **43**, 606 (1976)].
27. Yu. G. Bydyashov *et al.*, Preprint No. P15-3694, JINR (Joint Institute for Nuclear Research, Dubna, 1968).
28. W. Breunlich *et al.*, Muon Catal. Fusion **1**, 121 (1987).
29. A. Adamczak *et al.*, Phys. Lett. B **285**, 319 (1992).
30. K. Kobayashi *et al.*, Muon Catal. Fusion **2**, 191 (1988).
31. J. S. Cohen and M. C. Struensee, Phys. Rev. A **43**, 3460 (1991).
32. J. S. Cohen, Hyperfine Interact. **82**, 15 (1993).
33. V. S. Melezhik, Muon Catal. Fusion **1**, 205 (1987).
34. L. Bracci *et al.*, Phys. Lett. A **134**, 435 (1989).
35. M. P. Faifman and L. I. Ponomarev, Zh. Éksp. Teor. Fiz. **71**, 1689 (1976) [Sov. Phys. JETP **44**, 886 (1976)].
36. M. Faifman, Muon Catal. Fusion **4**, 341 (1989).
37. D. J. Wagenaar *et al.*, Phys. Rev. C **39**, 352 (1989).
38. J. E. Perry and S. J. Bame, Phys. Rev. **99**, 1368 (1955).
39. S. A. Alexander *et al.*, Phys. Rev. A **41**, 2854 (1990); **43**, 2585 (1991).
40. L. H. Wolfs *et al.*, Phys. Rev. Lett. **63**, 2721 (1989).
41. R. Wervelman *et al.*, Nucl. Phys. A **526**, 265 (1991).
42. J. D. Jackson, private communication.
43. S. S. Gershtein, Zh. Éksp. Teor. Fiz. **40**, 698 (1961).
44. A. Del Rosso *et al.*, Hyperfine Interact. **118**, 177 (1999).

Physics of Atomic Nuclei, Vol. 67, No. 5, 2004, pp. 911–919. Translated from Yadernaya Fizika, Vol. 67, No. 5, 2004, pp. 935–943.

NUCLEI
Theory

Single-Particle Levels and Spin–Orbit Splitting in the Vicinity of the Doubly Magic Nucleus ^{48}Ca

V. I. Isakov*

Petersburg Nuclear Physics Institute, Russian Academy of Sciences, Gatchina, 188300 Russia

Received March 5, 2003

Abstract—On the basis of a detailed analysis of available experimental data, the spectrum of single-particle states and the isotopic dependence of spin–orbit splitting are determined for nuclei in the vicinity of the doubly magic nuclide ^{48}Ca. The spectrum of excited states of the isobaric nucleus ^{48}Sc is calculated. © *2004 MAIK "Nauka/Interperiodica".*

1. INTRODUCTION

The energy spectrum of mean-field single-particle states is among the most important features of a nucleus that underlie all microscopic descriptions of nuclear structure and which determine, among other things, the shell properties of nuclei. One of the methods for determining single-particle energies consists in calculating them within mean-field models, which may be based on either a phenomenological approach employing a mean nuclear potential of the Woods–Saxon type, or an approach relying on self-consistent calculations of the Hartree–Fock type, or the approximation of meson–nucleon phenomenology like that in the Walecka model and its further modifications. Alternatively, single-particle energies can be extracted from experimental data. Here, however, one must take into account the problem that, in actual nuclei, single-particle modes are mixed with more complex excitation modes, with the result that there occurs a redistribution of the single-particle strength (so-called configuration mixing). This effect is rather small in nuclei of the *magic nucleus* ± *nucleon* type if the single-particle energy gap between the shells is large (as is the case for "good" magic nuclei like ^{132}Sn and ^{208}Pb), but the spreading of single-particle states over levels belonging to the *quasiparticle plus phonon* type may occur here as well. In the case of a small energy gap, configuration mixing may become very strong. Here, stripping (pickup) reactions characterized by a sizable cross section excite not only single-particle states peculiar to, for example, nuclei of the *magic nucleus* ± *nucleon* type but also levels whose quantum numbers J^π correspond to single-particle levels of a shell below (above) the energy gap. In any case, an additional averaging procedure is required for extracting single-particle levels from experimental data. The energies of single-particle levels in ^{208}Pb and ^{132}Sn nuclei were found in [1] by using such a procedure, and it was shown that neutron spin–orbit splitting in those nuclides, where $N > Z$, is more pronounced than that in the analogous proton orbitals.

On the basis of a proper theoretical treatment of available experimental data on direct reactions of one-nucleon transfer, we determine here the spectrum of single-particle levels in the vicinity of the neutron-rich nucleus ^{48}Ca, where configuration-mixing effects are much stronger than in the ^{208}Pb and ^{132}Sn nuclei, but where the shells are much weaker, and confirm the conclusions drawn in [1] that concern the isospin dependence of spin–orbit splitting. The results obtained here also agree well with those from [2], where this dependence was analyzed for the charge-exchange reaction ^{48}Ca$(p,n)^{48}$Sc.

2. GENERAL RELATIONS FOR DETERMINING SINGLE-PARTICLE MEAN-FIELD ENERGIES FROM EXPERIMENTAL DATA ON DIRECT REACTIONS OF ONE-NUCLEON TRANSFER

Below, we give a consistent validation of the procedure for determining single-particle energies from experimental data on the basis of, for example, the Hamiltonian for pair forces in the second-quantization representation. We have

$$\hat{H} = \sum_{i,k} \langle i|\hat{t}|k\rangle a_i^+ a_k \qquad (1)$$

$$+ \frac{1}{4} \sum_{i,k,m,\ell} {}_a\langle ik|\hat{\vartheta}|m\ell\rangle_a a_i^+ a_k^+ a_\ell a_m,$$

*e-mail: visakov@thd.pnpi.spb.ru

1063-7788/04/6705-0911$26.00

where ${}_a\langle ik|\hat{\vartheta}|\ell m\rangle_a = \langle ik|\hat{\vartheta}|\ell m\rangle - \langle ik|\hat{\vartheta}|m\ell\rangle$ is the antisymmetric matrix element for the pair interaction $\hat{\vartheta}(x_1x_2) = \hat{\vartheta}\,(\mathbf{r}_1, \hat{\boldsymbol{\sigma}}_1, \hat{\boldsymbol{\tau}}_1, \mathbf{r}_2, \hat{\boldsymbol{\sigma}}_2, \hat{\boldsymbol{\tau}}_2)$, while $\hat{t}$ is the single-particle kinetic-energy operator. We further introduce the auxiliary quantity

$$\hat{Q}_\alpha = \{a_\alpha, [\hat{H}, a_\alpha^+]\} \equiv a_\alpha \hat{H} \cdot a_\alpha^+ - a_\alpha \cdot a_\alpha^+ H + H a_\alpha^+ \cdot a_\alpha - a_\alpha^+ H \cdot a_\alpha, \tag{2}$$

where $[\hat{G}, \hat{F}]$ and $\{\hat{G}, \hat{F}\}$ are, respectively, the commutator and anticommutator of the operators $\hat{G}$ and $\hat{F}$. On one hand, we average $\hat{Q}_\alpha$ taken in the form (2) over the ground state $|A;(0)\rangle$ of an even–even nucleus containing A particles, expanding intermediate states in a complete set of wave functions for the systems of $(A+1)$ and $(A-1)$ particles. On the other hand, we calculate directly $\hat{Q}_\alpha$ by means of (1) with a subsequent averaging. As a result, we arrive at the exact relation

$$\sum_{a\in(A+1)} [B_A(\text{gr.st.}) - B_{A+1}(\text{gr.st.}) + E_a^{\text{exc}}] s_{a\alpha}^{(+)} + \sum_{a'\in(A-1)} [B_{A-1}(\text{gr.st.}) - B_A(\text{gr.st.}) - E_{a'}^{\text{exc}}] s_{a'\alpha}^{(-)} = \langle\alpha|\hat{t}|\alpha\rangle + \langle A;(0)| \times \sum_{i,k} {}_a\langle\alpha i|\hat{\vartheta}|\alpha k\rangle_a a_i^+ a_k |A;(0)\rangle, \tag{3}$$

where

$$s_{a\alpha}^{(+)} = |\langle A+1;(a)|a_\alpha^+|A;(0)\rangle|^2, \qquad s_{a'\alpha}^{(-)} = |\langle A-1;(a')|a_\alpha|A;(0)\rangle|^2. \tag{4}$$

Here, $|A;(0)\rangle$ is the vector of the ground state of an initial even–even nucleus; $|A+1;(a)\rangle$ and $|A-1;(a')\rangle$ are, respectively, the vectors of $\{a\}$ and $\{a'\}$ states of the nuclei containing $(A+1)$ and $(A-1)$ nucleons with allowance for fragmentation effects; $E_{a,a'}^{\text{exc}}$ are the corresponding excitation energies ($E_{a,a'}^{\text{exc}} = 0$ for the ground states); and $B_{A,A\pm1}$ are the binding energies in the ground states of the corresponding nuclei. In (3) and (4), the values of J^π for the $\{a\}$ and $\{a'\}$ states are identical to those for the single-particle state $\{\alpha\}$.

The quantities $s_{a\alpha}^{(+)}$ and $s_{a'\alpha}^{(-)}$ represent the spectroscopic factors of states, specifying the fraction of the single-particle state $\{\alpha\}$ in the complex states $\{a\}$ or $\{a'\}$. They are normalized by the relation

$$\sum_{a\in(A+1)} s_{a\alpha}^{(+)} + \sum_{a'\in(A-1)} s_{a'\alpha}^{(-)} = 1, \tag{5}$$

which is exact and which follows from the anticommutation relation for the single-particle fermion operators,

$$a_\alpha^+ a_\beta + a_\beta a_\alpha^+ = \delta_{\alpha\beta}. \tag{6}$$

It should be noted that, in the literature, use is often made of the spectroscopic factors $\tilde{s}_{a(a')\alpha}^{(\pm)} = (2j_\alpha + 1) s_{a(a')\alpha}^{(\pm)}$ normalized to $(2j_\alpha + 1)$. In the present study, we everywhere employ the normalization condition (5).

We now consider the expression on the right-hand side of Eq. (3). This expression has the meaning of a single-particle energy. We will discuss this issue in more detail. We introduce the field operators $\Psi^+ = \sum_\beta \varphi_\beta^*(x) a_\beta^+$, where $\varphi_\beta(x)$ are functions of a complete single-particle set, which is considered to be arbitrary for the time being. The second term in the expression on the right-hand side of Eq. (3) can then be recast into the form

$$\int\int dx_1 dx_2 [\rho_\alpha(x_1x_1)\rho(x_2x_2) - \rho_\alpha(x_1x_2)\rho(x_2x_1)]\hat{\vartheta}(x_1x_2), \tag{7}$$

where

$$\rho_\alpha(x_1x_2) = \varphi_\alpha^*(x_1)\varphi_\alpha(x_2), \qquad \rho(x_1x_2) = \langle A;(0)|\Psi^+(x_1)\Psi(x_2)|A;(0)\rangle. \tag{8}$$

Here, the quantities ρ_α and ρ, which are diagonal in the indices x_1 and x_2, are, respectively, the density of the single-particle state $\{\alpha\}$ and the exact matter density of the core nucleus. It can easily be seen that, in terms of a diagram technique, expression (7) represents the diagonal matrix element of the "single-particle" mass operator $\hat{\Sigma}_{\text{s.p.}}$ for the single-particle Green's function G whose (x,t) representation has the form

$$G(x,t;x',t') = -i\langle A;(0)|\hat{T}\{\Psi(x,t), \Psi^+(x',t')\}|A;(0)\rangle, \tag{9}$$

where $\Psi(x,t)$ are field operators $\Psi(x)$ in the Heisenberg representation and $\hat{T}$ is the chronological-ordering operator. The mass operator corresponding to (7) can be represented as the sum of two diagrams in Fig. 1, whose form is similar to that of the mass operator in the Hartree–Fock approximation. However, the single-particle Green's function $G(\varepsilon)$, which is the Fourier transform of (9) with respect to the variable $(t-t')$ and which is depicted by a thick line in Fig. 1, is exact since the quantity $\rho(x_1x_2)$ is defined as an average over the "true" ground state of the system containing A particles. Actually, this means that the definition of $\rho(x_1x_2)$ according to (8) involves, in addition to diagrams similar to those

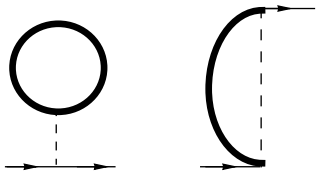

Fig. 1. Mass operator corresponding to (7).

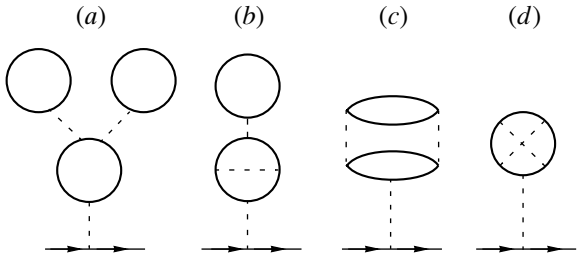

Fig. 2. Contributions to the mass operator independent of ε that are (a, b) taken into account and (c, d) disregarded in the Hartree–Fock approximation.

in Figs. 2*a* and 2*b* (appearing in the Hartree–Fock approximation), diagrams belonging to the types in Figs. 2*c* and 2*d*, corresponding to certain effects beyond the approximation in question, and reflecting the contribution of ground-state correlations. It is appropriate to mention here the study of Birbrair and Ryazanov [3], who derived relation (3) from Dyson's equation and the spectral expansion of the single-particle Green's function. Here, it is important that the single-particle energy corresponding to the mass operator independent of the input energy of the Green's function $G_\alpha(\varepsilon)$ appeared on the right-hand side of the formula analogous to (3) in [3]. It can easily be shown that the mass operator corresponding to expressions (7) and (8), which is displayed in Fig. 1, does not depend on ε, so that it does not involve fragmentation effects and corresponds to "true" single-particle states $\{\alpha\}$ diagonalizing the operator $\hat{t} + \hat{\Sigma}_{\text{s.p.}}$.

If, instead of the "true" ground state $|A;(0)\rangle$ of nucleus A, we use the ground-state vector of the Hartree–Fock approximation (that is, the Slater determinant), $|A;(0)\rangle_{\text{HF}}$—it corresponds to a Fermi step of height equal to unity in the space of occupation numbers $n_\alpha = {}_{\text{HF}}\langle A;(0)|a_\alpha^+ a_\alpha|A;(0)\rangle_{\text{HF}}$ (see Fig. 3*a*)—and if, for $\{\alpha\}$, we use the Hartree–Fock eigenfunctions, then $a_i^+|A;(0)\rangle_{\text{HF}} = 0$ for $\varepsilon_i < \varepsilon_{\text{F}}$ and $a_k|A;(0)\rangle_{\text{HF}} = 0$ for $\varepsilon_k > \varepsilon_{\text{F}}$. The right-hand side of Eq. (3) will then take the form

$$\langle\alpha|\hat{t}|\alpha\rangle + \sum_{i;\ \varepsilon_i<\varepsilon_{\text{F}}} {}_a\langle\alpha i|\hat{\vartheta}|\alpha i\rangle_a \equiv \varepsilon_\alpha(\text{HF}). \qquad (10)$$

However, the left-hand sides of (3) and (5) will involve only $s^{(+)}$ or $s^{(-)}$ components.

It should be noted that the actual ground state involves correlations; even in the absence of superfluidity, the respective particle distribution n_α, which is displayed in Fig. 3*b*, has a jump at $\varepsilon = \varepsilon_{\text{F}}$, this jump $R < 1$ being equal to the residue of the Green's function G (Migdal's theorem, [4]). As a result, $a_i^+|A;(0)\rangle \neq 0$ for $\varepsilon_i < \varepsilon_{\text{F}}$ and $a_k|A;(0)\rangle \neq 0$ for $\varepsilon_k > \varepsilon_{\text{F}}$, while expressions (3) and (5) involve both $s^{(+)}$ and $s^{(-)}$ terms.

In treating experimental data, the single-particle factors s are determined by analyzing direct reactions of single-particle stripping and pickup. We now consider this point in more detail. Suppose that the target nucleus is an even–even nucleus featuring the quantum numbers $J^\pi = 0^+$ and $T = T_z = T_0 = (N - Z)/2$. Summation in (3) and (5) covers all possible states (complete set)—in particular, all possible isospin states. By explicitly including isospin variables, we can reduce expressions (4) to the form

$$s_{a\alpha}^{(+)} = \left|\langle A+1;(a,T_f,T_{zf})|a^+_{\alpha,t=\frac{1}{2}tz}\right. \qquad (11)$$
$$\left.\times\,|A;(\text{g.s.},T_0,T_z=T_0)\rangle\right|^2$$
$$= \left[C^{T_fT_{zf}}_{\frac{1}{2}tz,T_0T_0}\right]^2 S(a,\alpha,T_f,T_0),$$

$$s_{a'\alpha}^{(-)} = \left|\langle A-1;(a',T_f,T_{zf})|a_{\alpha,t=\frac{1}{2}tz}\right. \qquad (12)$$
$$\left.\times\,|A;(\text{g.s.},T_0,T_z=T_0)\rangle\right|^2$$
$$= \left[C^{T_fT_{zf}}_{\frac{1}{2}-tz,T_0T_0}\right]^2 S(a',\alpha,T_f,T_0),$$

where the quantities S are independent of the isospin projection.

3. DETERMINATION OF THE ENERGIES OF SINGLE-PARTICLE STATES IN THE VICINITY OF THE ^{48}Ca NUCLEUS

The diagram describing the excitation of the levels of interest in the vicinity of the ^{48}Ca nucleus

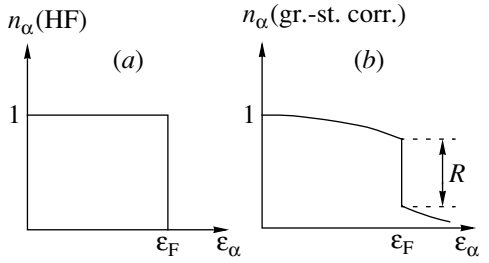

Fig. 3. Particle distribution n_α (a) in the absence and (b) in the presence of ground-state correlations.

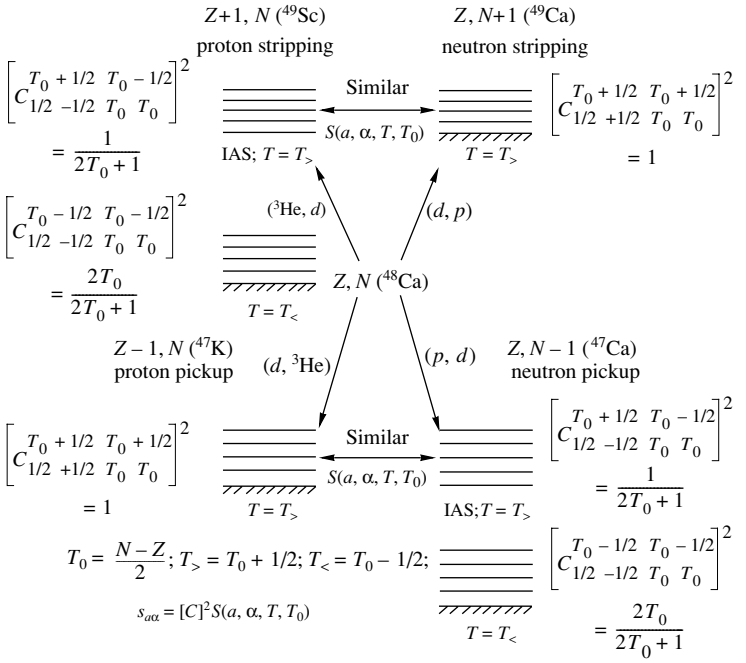

Fig. 4. Diagram of the excitation of levels in the vicinity of the ^{48}Ca nucleus in single-particle-transfer reactions.

can be represented in the form displayed in Fig. 4, where $T_< = T_0 - 1/2$ and $T_> = T_0 + 1/2$. This figure shows that, in order to determine the energies of single-particle orbitals, it is necessary, in analyzing data on reactions of proton stripping and neutron pickup, to take into account in (3) highly excited analogous states of $T = T_>$, for which experimental information is not always available. By employing isobaric symmetry, one can borrow, however, the corresponding isospin-reduced spectroscopic factors $S(a, \alpha, T_>, T_0)$ from the reactions involving neutron stripping and proton pickup and leading to low-lying states of the neighboring isobaric nuclei. At the same time, it should be borne in mind that the contribution of transitions to the analogous states of final nuclei is suppressed by the factor $1/(2T_0 + 1)$, which is equal to $1/45$ for the target nucleus ^{208}Pb, but which increases considerably for light nuclei ($1/9$ for ^{48}Ca). Another distinction of the region around $A \sim 48$ from the regions around $A \sim 208$ and $A \sim 132$ is that, in the ^{48}Ca nucleus, the shells are relatively weak, which is manifested in that direct reactions of one-nucleon transfer excite, in odd nuclei, low-lying states whose quantum numbers J^π are typical of single-particle states belonging to "alien" shells on the other side of the Fermi surface. The aforesaid indicates that both the $T_>$ states of odd nuclei and ground-state correlations must be taken into account in determining ε_α in the vicinity of the ^{48}Ca nucleus.

Since we are interested primarily in spin–orbit splitting, we will consider in detail the procedure for determining the energies of $\{1d\}$ levels, clarifying one important point in advance.

The quantities $s^{(\pm)}$ appearing in expressions (3) and (5) are determined by analyzing experimental data on direct nuclear reactions. In doing this, there arises a natural uncertainty associated both with experimental errors and with the accuracy of a theoretical description (usually, within the distorted-wave Born approximation) of stripping (pickup) processes; as a result, the right-hand side of (5) may become different from unity even in a complete experiment. In actual calculations, we therefore modified expression (3) by means of the substitution $s^{(\pm)}_{i(i')} \to s^{(\pm)}_{i(i')}/(\sum_k s^{(+)}_k + \sum_{k'} s^{(-)}_{k'})$, going over to normalized s factors. It should be noted that the electronic database from [5] and references therein (if necessary) were used as a main source of experimental data in determining the spectroscopic factors. The nuclear binding energies were borrowed from [6].

We now consider the neutron hole state $\{\nu 1d_{5/2}\}$. Figure 4 shows that a correct determination of single-particle energies here requires taking into account not only low-lying but also highly excited isobaric analogous states in ^{47}Ca at excitation energies higher than 12 MeV (in the ^{47}Ca nucleus, the lowest $T_>$ state, which is the isoanalog of the $1/2^+$ ground state of the ^{47}K nucleus, has the energy of 12.73 MeV). From experiments, it follows that the $\{\nu 1d_{5/2}\}$ state of the

^{47}Ca nucleus is strongly fragmented. Up to the excitation energy of 11 MeV, the respective (^{3}He, α) reaction exhibits 46 $5/2^+(T = T_<)$ levels characterized by $\sum_{i'} s_{i'}^{(-)} = 0.607$ and $\sum_{i'} s_{i'}^{(-)} E_{i'} = 4.798$ MeV. The lowest $5/2^+$ isoanalog of the ^{47}K nucleus has $E = 16.12$ MeV and $s^{(-)} = 0.06$ and corresponds to the $5/2^+$ level of ^{47}K at $E = 3.43$ MeV. At the same time, the reaction ^{48}Ca(d,^{3}He)^{47}K exhibits a variety of other low-lying ($E < 9$ MeV) $5/2^+$ states that are hardly seen, because of a small cross section (in particular, due to the isotopic factor of 1/9), as higher $5/2^+$ isoanalogous states of the ^{47}Ca nucleus. We can rescale the energies of low-lying $5/2^+$ states of the ^{47}K nucleus to those of the $5/2^+$ isoanalogous states in the ^{47}Ca nucleus, assuming that the relative values of $s^{(-)}$ for various isoanalogs in ^{47}Ca are identical to those for low-lying $5/2^+$ states in ^{47}K. After the normalization to the well-known experimental value of $s^{(-)}$ for the $5/2^+$ state at $E =$ 16.12 MeV, we then obtain the following values for the $T_>$ levels in the ^{47}Ca nucleus: $\sum_{k'} s_{k'}^{(-)} = 0.231$ and $\sum_{k'} s_{k'}^{(-)} E_{k'} = 4.272$ MeV. As a result, we arrive at $\varepsilon_{\nu 1d5/2} = -20.76$ MeV, with the contribution of high-lying isoanalogous states being quite significant, so that their inclusion is necessary (this shifts the level down by about 3 MeV). We will now clarify the role of ground-state correlations [terms involving $s^{(+)}$ in (3) for the case of hole nuclei]. By way of example, we indicate that the reaction ^{48}Ca$(d,p)^{49}$Ca proceeding via the excitation of a "particle" nucleus reveals three $5/2^+$ states peculiar to a neutron "hole" shell; for them, $\sum_i s_i^{(+)} = 0.129$ and $\sum_i s_i^{(+)} E_i = 0.691$ MeV. Upon the inclusion of these states, the energy of the $\{\nu 1d_{5/2}\}$ single-particle state becomes higher: $\varepsilon_{\nu 1d5/2} = -17.97$ MeV. This demonstrates that even a rather small contribution from ground-state correlations leads to a significant shift of single-particle energies, always toward the energy gap between the shells. It is worth noting that, upon the inclusion of the $T = T_>$ states and of ground-state correlations, we obtain $\sum_i s_i^{(+)} + \sum_{i'} s_{i'}^{(-)} = 0.967$, which is very close to unity. Therefore, the value of $\varepsilon_{\nu 1d5/2} = -17.97$ MeV seems quite reasonable.

We now proceed to determine the energy of the $\{\nu 1d_{3/2}\}$ neutron orbital. In contrast to the $5/2^+$ levels, the $\{\nu 1d_{3/2}\}$ state in ^{47}Ca is fragmented rather weakly. The neutron-pickup reaction exhibits only one $3/2^+$ level at $E = 2.58$ MeV in the low-lying part of the spectrum ($s^{(-)} = 0.90$) and one isoanalogous level at 13.09 MeV ($s = 0.045$); this is the isoanalog of the $3/2^+$ state at 0.36 MeV in ^{47}K. At the same time, yet another $3/2^+$ state at 3.93 MeV ($s = 0.18$) is observed among low-lying levels of ^{47}K. Upon rescaling to the ^{47}Ca nucleus with respect to isofactors and energy, this corresponds to $s = 0.02$ and $E = 16.66$ MeV. Thus, we arrive at $\sum_{i'} s_{i'}^{(-)} = 0.965$ and $\sum_{i'} s_{i'}^{(-)} E_{i'} = 3.244$ MeV. As a result, we obtain $\varepsilon_{\nu 1d3/2} = -13.31$ MeV without allowance for ground-state correlations. We now consider the contribution of these correlations. In the reaction ^{48}Ca$(p,x)^{49}$Sc, a $3/2^+$ resonance at 15.876 MeV is observed according to data reported in [5, 7, 8]; this resonance is treated as the isoanalog of the $3/2^+$ level of the ^{49}Ca nucleus. Considering that a close excited $3/2^-$ state in ^{49}Sc at $E = 11.56$ MeV is an isoanalog of the ground-state of the ^{49}Ca nucleus, we can easily determine the energy of the $3/2^+$ level in ^{49}Ca under consideration; it appears to be about 4.32 MeV, which is close to the value of $E = 4.282$ MeV obtained for the $3/2^+$ level of the ^{49}Ca nucleus (the spectroscopic factor being 0.017) in [9] from an analysis of the reaction ^{48}Ca$(\vec{d},p)^{49}$Ca. At a similar energy, this level appears in the compilation of Burrows [8], but not in [5] or in [7]. For the $\{\nu 1d_{3/2}\}$ state, we eventually obtained the values of $\sum_{i'} s_{i'}^{(-)} + \sum_i s_i^{(+)} = 0.982$ and $\varepsilon_{\nu 1d3/2} = -13.09$ MeV. Thus, the magnitude of spin–orbit splitting for the $\{1d\}$ neutron orbital in ^{48}Ca is 4.88 MeV, which is much larger than the estimate (3.6 MeV) presented in [10].

We now consider the $\{\pi 1d_{3/2}\}$ proton state. Experimental data (see, for example, [11]) indicate the excitation of only two low-lying $3/2^+$ states at $E = 0.36$ ($s = 0.97$) and 3.93 MeV ($s = 0.185$) in the proton-pickup reaction on ^{48}Ca, this corresponding to $\sum_{i'} s_{i'}^{(-)} = 1.155$ and $\sum_{i'} s_{i'}^{(-)} E_{i'} = 1.076$ MeV. At the same time, the proton-stripping reaction on ^{48}Ca results in the excitation of a set of low-lying $3/2^+$ levels among the $T_<$ states of the ^{49}Sc nucleus; for them, $\sum_i s_i^{(+)} = 0.0525$ and $\sum_i s_i^{(+)} E_i = 0.262$ MeV. Taking additionally into account the existence of the $3/2^+$ level at 4.272 MeV in the ^{49}Ca nucleus (see above), for which $s = 0.017$ in the neutron-stripping reaction, we reveal the corresponding isoanalogous level $3/2^+$ in ^{49}Sc at $E = 15.88$ MeV ($s^{(+)} = 0.017/9 = 0.0019$). Thus, the total contribution of ground-state correlations corresponds to $\sum_i s_i^{(+)} = 0.0544$ and $\sum_i s_i^{(+)} E_i = 0.292$ MeV, while the energy of the proton $\{1d_{3/2}\}$ level is -16.18 MeV (-16.73 MeV without allowance for ground-state correlations). It should be noted that, for the proton $\{1d_{3/2}\}$ orbital,

the experimental value of $\sum_i s_i^{(+)} + \sum_{i'} s_{i'}^{(-)}$ is 1.209; that is, it exceeds unity. We will discuss this issue below.

The proton $\{1d_{5/2}\}$ orbital is the last $\{1d\}$ orbital. Here, the proton-pickup reaction excites nine $T = T_<$ $5/2^+$ states for which $\sum_{i'} s_{i'}^{(-)} = 0.663$ and $\sum_{i'} s_{i'}^{(-)} E_{i'} = 3.933$ MeV (the corresponding isobaric analogs were taken into account in considering $5/2^+$ states in ^{47}Ca). The contribution of ground-state correlations is controlled by six $T = T_<$ $5/2^+$ levels in ^{49}Sc at energies lower than 12 MeV; for these levels, $\sum_i s_i^{(+)} = 0.0233$ and $\sum_i s_i^{(+)} E_i = 0.209$ MeV. In addition, it should be borne in mind that the neutron-stripping reaction excites three low-lying $5/2^+$ states of ^{49}Ca that have already been taken into account in analyzing the contribution of ground-state correlations to the energy of the $\{\nu 1d_{5/2}\}$ neutron orbital in ^{47}Ca. The counterparts of these levels in ^{49}Sc are three high-lying isoanalogous levels whose energies after rescaling are 16.03, 16.23, and 17.68 MeV, with the first and the last one being observed in the ^{49}Sc spectrum at very close energies; however, their s factors were not measured in the proton-stripping reaction on ^{48}Ca because of the smallness of the corresponding isofactor. Rescaling, according to isotopic relations, the s factors of the ^{49}Ca to those of the ^{49}Sc nucleus, we obtain $\sum_i s_i^{(+)} = 0.0143$ and $\sum_i s_i^{(+)} E_i = 0.240$ MeV for these levels. As a result, we have $\varepsilon_{\pi 1d5/2} = -20.43$ MeV, while the spin–orbit splitting of the $\{1d\}$ proton orbital is 4.25 MeV, which is considerably smaller than corresponding neutron spin–orbit splitting.

The energies of other single-particle orbitals in the vicinity of the ^{48}Ca nucleus were determined in a similar way. The corresponding values are presented in Table 1, where the results obtained by calculating the single-particle spectrum with a potential of the Woods–Saxon type are also given for the sake of comparison. The parameters of this potential are close to those in [1], and the potential itself has the form

$$\hat{U}(r,\sigma) = V_0\left(1 - 2\beta\frac{T_3\cdot t_3}{A}\right)f(r) \qquad (13)$$
$$+ V_{\ell s}\left(1 - 2\beta_{\ell s}\frac{T_3\cdot t_3}{A}\right)\frac{1}{r}\frac{df(r)}{dr}\hat{\mathbf{l}}\cdot\hat{\mathbf{s}}$$
$$+ \left(\frac{1}{2} - t_3\right)U_{\rm Coul},$$

$$f(r) = \left[1 + \exp\left(\frac{r-R}{a}\right)\right]^{-1}, \quad R = r_0 A^{1/3},$$

where $U_{\rm Coul}$ is the potential of a uniformly charged sphere of radius $R_c = r_{c0}A^{1/3}$, $t_3 = +1/2$ for the neutron, and $t_3 = -1/2$ for the proton. We note that, according to [1, 2], the parameter $\beta_{\ell s}$, which appears in (13) and which controls the isospin dependence of spin–orbit splitting, lies within the interval between about -0.6 and -1.0.

In all of the cases, with the exception of that of the $\{\pi 2p_{1/2}\}$ and $\{\pi 2p_{3/2}\}$ proton orbitals, the total experimental strength of single-particle states, which is determined by formulas (4), (11), and (12), is about unity, the spin–orbit splitting of the $1f$ proton orbital being much smaller than the neutron one. The $\{\pi 2p\}$ orbital also deserves a dedicated discussion. The compilation of experimental data concerning the proton-stripping reactions on ^{48}Ca in [5] suggests an extremely strong fragmentation of the $\{\pi 2p_{1/2}\}$ state: up to an excitation energy of about 12 MeV, there are 55 $T = T_< = 7/2$ $1/2^-$ states whose total strength is $\sum_i s_i^{(+)} = 2.04$, which is twice as great as the value following from the sum rule. In addition, three very close $T = T_> = 9/2$ $1/2^-$ levels at an energy of 13.5 MeV are observed with the total value of $\sum_i s_i^{(+)} \sim 0.1$, which correspond to the components of the energy-split isoanalog of the excited $1/2^-$ state of the ^{49}Ca nucleus at $E = 2.02$ MeV, where $s^{(+)} = 0.91$. Upon rescaling in the isofactor to the ^{49}Sc nucleus, this leads precisely to a value of about 0.1 for $s^{(+)}$. At the same time, the total strength of transitions to the $\{\pi 2p_{3/2}\}$ level—this strength receives contributions predominantly from low-lying $3/2^-$ components—is less than unity (0.682) according to [5]. Concurrently, we have $\varepsilon_{\pi 2p1/2} = -2.0$ MeV and $\varepsilon_{\pi 2p3/2} = -4.55$ MeV, while the proton spin–orbit splitting $\Delta(\pi 2p) = 2.55$ MeV is larger than that for neutrons ($\Delta(\nu 2p) = 1.78$ MeV).

It should be borne in mind, however, that, in the original study of Fortier *et al.* [12], $\{\pi 2p\}$ states were identified by the angular distribution alone, so that those authors actually determined only the value of $\ell = 1$ but not the spin of the level. It is worth noting that the $\ell = 1$ proton states in the ^{49}Sc nucleus are distributed within the interval of width about 10 MeV, which is much larger than the spin–orbit splitting of the $\{\pi 2p\}$ level. Therefore, it is reasonable to assume that $1/2^-$ and $3/2^-$ states—apart from those that are reliably identified by J^π values and which are rather low-lying and include the main components of the single-particle strength and apart from isoanalogs whose spins were determined reliably—are distributed uniformly over the spectrum. In this case, $\sum s = 1.062$ and $\varepsilon \approx -3.4$ MeV for the $\{\pi 2p_{3/2}\}$ state and $\sum s = 1.38$ and $\varepsilon \approx -2.4$ MeV

Table 1. Single-particles levels of the ^{48}Ca nucleus (ε is given in MeV)

Level	$\varepsilon^{\text{expt}}$	$\varepsilon^{\text{theor}}$(WS1)	$\varepsilon^{\text{theor}}$(WS2)	$\varepsilon^{\text{theor}}$(WS3)
		Neutrons		
$1g_{9/2}$	$\sim$0.6	0.32	0.18	0.39
$1f_{5/2}$	-1.20	-1.97	-1.84	-2.23
$2p_{1/2}$	-2.86	-2.90	-2.85	-2.77
$2p_{3/2}$	-4.64	-5.07	-5.09	-5.01
$1f_{7/2}$	-10.23	-9.22	-9.32	-9.64
$1d_{3/2}$	-13.09	-14.03	-13.94	-14.51
$2s_{1/2}$	-13.28	-14.48	-14.48	-14.68
$1d_{5/2}$	-17.97	-18.56	-18.62	-19.02
		Protons		
$1g_{7/2}$	–	9.18	9.00	9.19
$2d_{5/2}$	–	3.78	3.82	3.44
$1g_{9/2}$	–	0.52	0.66	1.05
$2p_{1/2}$	-2.4	-3.07	-3.12	-3.10
$1f_{5/2}$	-3.20	-3.58	-3.70	-2.99
$2p_{3/2}$	-3.4	-5.22	-5.19	-5.18
$1f_{7/2}$	-9.40	-10.09	-9.99	-9.35
$2s_{1/2}$	-14.92	-15.87	-15.87	-15.45
$1d_{3/2}$	-16.18	-16.32	-16.39	-15.46
$1d_{5/2}$	-20.43	-20.28	-20.22	-19.46

Note: In the calculations, we used the mean-field potential (13) at $V_0 = -51.5$ MeV, $V_{\ell s} = 33.2$ MeV fm^2, $r_0 = 1.27$ fm, $r_{c0} = 1.25$ fm, and $\beta = 1.39$. Here, WS1, WS2, and WS3 label, respectively, the case where $a = 0.6$ fm and $\beta_{\ell s} = -0.6$, the case where $a = 0.6$ fm and $\beta_{\ell s} = -1.0$, and the case where the diffuseness-parameter values are $a(\nu) = 0.55$ fm and $a(\pi) = 0.67$ fm and where $\beta_{\ell s} = -0.6$.

for the $\{\pi 2p_{1/2}\}$ level. Thus, the sum rule (3) holds to a much higher accuracy, while the proton spin–orbit splitting [$\Delta(\pi 2p) \approx 1$ MeV] is smaller than the spin–orbit splitting for neutrons.

Yet another comment is in order here. As can be seen from the above, the $\{\pi 1d_{5/2}\}$ proton orbital is characterized by $\sum_i s_i^{(+)} + \sum_{i'} s_{i'}^{(-)} = 0.701$, which is also smaller than unity. It could be assumed in this connection that the $3/2^+$ level at 3.93 MeV in the ^{47}K nucleus is in fact the $5/2^+$ state characterized by $s^{(-)} = 0.185 \cdot 4/6 = 0.122$. This would lead, on one hand, to a decrease in the total strength of the $\{\pi 1d_{3/2}\}$ state to a value of 1.024 and, on the other hand, to an increase in the strength for the $\{\pi 1d_{5/2}\}$ orbital to 0.823. Concurrently, the spin–orbit splitting of the $\{1d\}$ proton orbital would increase somewhat (up to 4.80 MeV), but it would still remain smaller than that for neutrons. However, there are no sufficiently strong experimental arguments in favor of this assumption since the level in question was identified not only by the angular distribution of the cross section but also by the angular distribution of the analyzing power [13]. Therefore, the problem of the excess of the strength for the $\{\pi 1d_{3/2}\}$ state and its deficit for $\{\pi 1d_{5/2}\}$ remains open at present. Probably, it is related to the theoretical description of nucleon-transfer reactions and the possible contribution of multistep mechanisms of such reactions [11].

Summarizing all that was said in this section, we would like to emphasize that an analysis of available experimental data concerning direct reactions furnishes compelling arguments in favor of the statement that, in the vicinity of the ^{48}Ca nucleus, the

Table 2. Experimental and calculated spectra of levels in the ^{48}Sc nucleus (E is given in MeV)

J^π	E^{expt}	E^{theor} (version 1)	E^{theor} (version 2)
6_1^+	Ground state	Ground state	Ground state
5_1^+	0.13	0.18	0.20
4_1^+	0.25	0.18	0.22
3_1^+	0.62	0.56	0.65
7_1^+	1.10	0.42	0.44
2_1^+	1.14	0.89	1.07
1_1^+	2.52	2.04	2.36
0_1^+	6.67	4.88	6.41
1_2^+	5–14	9.44	9.95

spin–orbit splitting of the $\{1f\}$, $\{1d\}$, and $\{2p\}$ neutron orbitals is larger than that of the analogous proton orbitals. However, it should be noted that this statement is fully valid only for $f_{5/2}-f_{7/2}$ splitting. In the case of the $\{1d\}$ orbital, we additionally invoked data on $T_>$ states, employing the (quite reliable) concept of isobaric symmetry, while, in determining the splitting of the $\{2p\}$ proton orbital, we assumed that the distribution of $1/2^-$ and $3/2^-$ levels over the "statistical" part of the spectrum is uniform. However, we can refer here to the result reported in [2], where the potential (13) was generalized by means of the substitution $T_3 \cdot t_3 \to \hat{\mathbf{T}} \cdot \hat{\mathbf{t}}$, with $\hat{\mathbf{T}}$ and $\hat{\mathbf{t}}$ being the isospin vector operators for the core and the nucleon, respectively. In [2], it was shown that negative values of $\beta_{\ell s}$, which, in the case of $N > Z$, correspond to larger spin–orbit splitting for neutrons than for protons, provide, for $\beta_{\ell s}$ values between about -0.6 and -1.0, a good description of polarization phenomena in the reaction $^{48}\text{Ca}(\vec{p}, n)^{48}\text{Sc}$ proceeding via the excitation of the 0^+ isoanalogous state at 6.67 MeV in ^{48}Sc. Thus, the above results agree well with those reported in [1, 2].

4. SPECTRUM OF THE ISOBARIC PARTICLE–HOLE NUCLEUS ^{48}Sc

To conclude this study, we present the results obtained by calculating the spectrum of excited states in the odd–odd nucleus ^{48}Sc, which was mentioned above. The calculations were performed on the basis of the random-phase approximation in the charged particle–hole channel. Previously, this approximation was successfully used in describing the particle–hole nuclei ^{208}Bi, ^{208}Tl, ^{132}Sb, and ^{132}In (see [14, 15], where all of the required formulas can be found). We started from pair effective interaction

$$\hat{\vartheta} = \exp\left(-\frac{r^2}{r_{00}^2}\right)\big(V + V_\sigma \boldsymbol{\sigma}_1 \cdot \boldsymbol{\sigma}_2 + V_T \hat{S}_{12} + V_\tau \boldsymbol{\tau}_1 \cdot \boldsymbol{\tau}_2 + V_{\tau\sigma}(\boldsymbol{\sigma}_1 \cdot \boldsymbol{\sigma}_2) \cdot (\boldsymbol{\tau}_1 \cdot \boldsymbol{\tau}_2) + V_{\tau T}\hat{S}_{12}\boldsymbol{\tau}_1 \cdot \boldsymbol{\tau}_2\big), \quad (14)$$

which was introduced previously. The parameters in (14) were set to $V = -9.95$, $V_\sigma = 2.88$, $V_T = -1.47$, $V_\tau = 5.90$, $V_{\tau\sigma} = 4.91$, $V_{\tau T} = 1.51$ (all of these values are given in MeV), and $r_{00} = 1.8$ fm (interaction version 1). We also used a basis consisting of 13 proton and 11 neutron orbitals closest to the Fermi surface (and involving a set of quasistationary states), with the energies of the orbitals corresponding to the WS1 parameter set in (13). The calculated energies of levels in the ^{48}Sc nucleus are given in Table 2, along with relevant experimental data. For all of the levels presented in Table 2 (with the exception of the 1_2^+ state), the leading configuration is $\pi 1f_{7/2}\overline{\nu 1f_{7/2}}$. As far as the 1_2^+ state is concerned, it corresponds to a Gamow–Teller resonance that manifests itself as a rather wide peak in the energy range 5–14 MeV, with its maximum being at about 10 MeV; its leading configuration is $0.97\,\pi 1f_{5/2}\overline{\nu 1f_{7/2}} + 0.22\,\pi 1f_{7/2}\overline{\nu 1f_{7/2}}$, with $B(\text{GT}; 0_1^+ \to 1_2^+) \sim 19$. At the same time, the 1_1^+ level is characterized by the structure $0.97\,\pi 1f_{7/2}\overline{\nu 1f_{7/2}} - 0.22\,\pi 1f_{5/2}\overline{\nu 1f_{7/2}}$ and by a value of $B(\text{GT}; 0_1^+ \to 1_1^+) \sim 5$. For the 0_1^+ state, the calculated value of the reduced probability is $B(\text{F}; 0_1^+ \to 0_1^+) \simeq 7.99$, which saturates almost completely the sum rule for a transition of the Fermi type; thus, this state is indeed the isoanalog of the ground state of the core nucleus ^{48}Ca (see preceding section). Also presented in Table 2 is the result of the calculation employing a somewhat modified interaction (version 2), where [compare with (14)] $V_\tau = 7.9$ MeV and $V_{\tau\sigma} = 5.9$ MeV. In this case, the agreement with experimental data on energies becomes better, while the values of $B(\text{F})$ and $B(\text{GT})$ undergo virtually no changes. It should be noted that, while the calculated energies of the levels are by and large in good agreement with experimental data, the energy calculated for the 7_1^+ state proves to be underestimated, but it is close to the energy 0.39 MeV of a low-lying level whose spin is not identified. It should be emphasized, however, that experimental data cast some doubt on the existence of this level, while the 7_1^+ state at 1.10 MeV was observed in a few independent studies.

It should also be noted that the calculated energies of other levels in ^{48}Sc, which are not quoted

in Table 2 and which are associated with high-lying (for example, $\pi 1f_{5/2}\overline{\nu 1f_{7/2}}$) particle–hole configurations appear to be above 3.5 MeV. In addition to the possible level at 0.39 MeV, other states manifest themselves in experiments from an energy value as low as some 1.5 MeV. Evidently, they are of more complex nature and are caused by a weak magicity of the core nucleus ^{48}Ca, as was mentioned above in discussing the spectroscopic factors of odd nuclei in the vicinity of the ^{48}Ca. These levels can be explained in terms of pairing correlations in the ground state of the ^{48}Ca nucleus. This problem will be considered in a dedicated publication.

5. CONCLUSION

On the basis of a detailed analysis of available experimental data on direct reactions of one-nucleon transfer, we have determined the spectrum of single-particle states in the vicinity of the neutron-rich nucleus ^{48}Ca and have shown that, here, the spin–orbit splitting of neutron orbitals is more pronounced than that for protons. This feature of the spin–orbit splitting is peculiar to $N > Z$ nuclei and is confirmed by the results of an analysis of polarization effects in the direct reaction $^{48}\mathrm{Ca}(\vec{p}, n)^{48}\mathrm{Sc}$ proceeding via the excitation of the isoanalogous state of the final nucleus; also, the feature in question is consistent with the isotopic dependence of spin–orbit splitting in nuclei close to ^{208}Pb and ^{132}Sn.

ACKNOWLEDGMENTS

I am grateful to V.R. Shaginyan for stimulating discussions.

This work was supported in part by the Russian Foundation for Basic Research (project nos. 0.3-0.2-1124 and 0.4-0.2-16041 in support of leading scientific schools).

REFERENCES

1. V. I. Isakov, K. I. Erokhina, H. Mach, *et al.*, Eur. Phys. J. A **14**, 29 (2002).
2. V. I. Isakov, Yad. Fiz. **66**, 1279 (2003) [Phys. At. Nucl. **66**, 1239 (2003)].
3. B. L. Birbrair and V. I. Ryazanov, Yad. Fiz. **63**, 1842 (2000) [Phys. At. Nucl. **63**, 1753 (2000)].
4. A. B. Migdal, *Theory of Finite Fermi Systems and Applications to Atomic Nuclei* (Nauka, Moscow, 1982; Interscience, New York, 1967, transl. of 1st Russ. ed.).
5. http://www-nds.iaea.or.at/.
6. G. Audi and A. H. Wapstra, Nucl. Phys. A **595**, 409 (1995).
7. T. W. Burrows, Nucl. Data Sheets **76**, 191 (1995).
8. T. W. Burrows, Nucl. Data Sheets **48**, 569 (1986).
9. R. Abegg, J. D. Hutton, and M. E. Williams-Norton, Nucl. Phys. A **303**, 121 (1978).
10. Z. Ren and H. Toki, Prog. Theor. Phys. **104**, 595 (2000).
11. C. A. Ogilvie, D. Barker, J. B. A. England, *et al.*, Nucl. Phys. A **465**, 445 (1987).
12. S. Fortier, E. Hourani, and J. M. Maison, Nucl. Phys. A **346**, 285 (1980).
13. S. M. Banks, B. M. Spicer, G. G. Schute, *et al.*, Nucl. Phys. A **437**, 381 (1985).
14. S. A. Artamonov, V. I. Isakov, S. G. Kadmenskiĭ, *et al.,* Yad. Fiz. **36**, 829 (1982) [Sov. J. Nucl. Phys. **36**, 486 (1982)].
15. K. I. Erokhina and V. I. Isakov, Yad. Fiz. **57**, 212 (1994) [Phys. At. Nucl. **57**, 198 (1994)].

Translated by O. Chernavskaya

Physics of Atomic Nuclei, Vol. 67, No. 5, 2004, pp. 920–930. Translated from Yadernaya Fizika, Vol. 67, No. 5, 2004, pp. 944–954.

NUCLEI
Theory

Semimicroscopic Description of the Gross Structure of Giant Dipole Resonances in Carbon, Nitrogen, and Oxygen Isotopes

B. S. Ishkhanov and V. N. Orlin*

Institute of Nuclear Physics, Moscow State University, Vorob'evy gory, Moscow, 119899 Russia
Received March 13, 2003; in final form, September 4, 2003

Abstract—A version of a semimicroscopic description of dipole nuclear vibrations is formulated in such a way that the deformation, the configuration, and the isospin splitting of a giant dipole resonance are taken simultaneously into account. This model is used to describe the main structural features of the cross sections for photoabsorption on ^{12,13,14}C, ^{14,15}N, and ^{16,17,18}O nuclei. © *2004 MAIK "Nauka/Interperiodica".*

1. INTRODUCTION

Recently, we proposed a semimicroscopic model of dipole nuclear vibrations that describes the deformation and the configuration splitting of a giant dipole resonance [1]. This model was successfully used to describe the gross structure of a giant dipole resonance in the light self-conjugate nuclei ^{12}C, ^{24}Mg, and ^{28}Si. In [2], this model was modified by taking into account the isospin splitting of dipole states according to formulas presented by Goulard and Fallieros [3], this making it possible to describe the gross structure of photoabsorption cross sections for a large number of spherical, deformed, and transition nuclei over the mass range $10 \lesssim A \lesssim 240$.

However, the approach formulated in [2] is not self-consistent since isospin effects are described there with the aid of the formulas derived in [3] rather than within the semimicroscopic model itself. Additionally, the degree to which these formulas are applicable in the region of light nuclei is not clear.

In view of this, we developed a self-consistent version of the model where the deformation, the configuration, and the isospin splitting of a giant dipole resonance in light nuclei ($A \lesssim 40$) are treated within a unified semimicroscopic approach. In the present study, this model is applied to analyzing the main structural features of the photoabsorption cross sections for ^{12,13,14}C, ^{14,15}N, and ^{16,17,18}O nuclei. We also consider the question of whether this model is applicable to medium-mass and heavy nuclei.

*e-mail: orlin@depni.npi.msu.su

2. FUNDAMENTALS OF THE MODEL

2.1. Semimicroscopic Description of Isovector Dipole Nuclear Vibrations without Isospin Conservation

The existence of collective dipole excitations in a nucleus can be explained [4] by the coupling of single-particle nucleon excitations to the isovector dipole field that they generate; that is,

$$F_{\mu s} = \sum_{k=1}^{A} (2t_\mu x_s)_k \qquad (1)$$
$$= \sum_{\alpha>\beta} (\langle\alpha|2t_\mu x_s|\beta\rangle a_\alpha^+ a_\beta + (-1)^\mu \langle\alpha|2t_{-\mu} x_s|\beta\rangle^* a_\beta^+ a_\alpha),$$

where x_s ($s = 1, 2, 3$) stands for the projections of the nucleon radius vector $\mathbf{r}$ onto the axes of the intrinsic coordinate frame;

$$t_\mu = \begin{cases} -(t_x + it_y)/\sqrt{2} \text{ for } \mu = +1 \\ t_z \text{ for } \mu = 0 \\ +(t_x - it_y)/\sqrt{2} \text{ at } \mu = -1 \end{cases} \qquad (2)$$

are the spherical components of the nucleon isospin; $a_\alpha^+, a_\beta^+, \ldots$ are the operators of nucleon creation in the single-particle states $|\alpha\rangle, |\beta\rangle, \ldots$ (by these, we will henceforth imply the eigenstates of the Nilsson shell Hamiltonian [5, 6]); and $a_\alpha, a_\beta, \ldots$ are the corresponding nucleon-annihilation operators.

The dipole field (1) can generate excitation quanta characterized by the isospin $\tau = 1$, the isospin z projection $\mu = 0, \pm 1$, and the direction of vibrations ($s = 1, 2, 3$). These quanta are associated with the normal modes of isovector vibrations of the nucleon system in the case where no account is taken of the

1063-7788/04/6705-0920$26.00

vector coupling between the isospin of a quantum and the isospin $T_0 = \left|\frac{N-Z}{2}\right|$ of the neutron excess in a nucleus. Vibrations for which $\mu = 0$ correspond to an ordinary photoresonance. They are generated by $\Delta T_z = 0$ dipole transitions. Modes characterized by $\mu = \pm 1$ correspond to charge-exchange vibrations of the nucleon system that involve the transformation of one proton into a neutron, or vice versa ($\Delta T_z = \pm 1$). Only for deformed nuclei, in which the degeneracy of s vibrations in energy is partly or completely removed, is it of importance to take into account the direction of vibrations. In the following, we restrict our consideration to axisymmetric nuclei, for which we must distinguish between vibrations along the nuclear symmetry axis 3 and vibrations in a direction orthogonal to it (for example, along axis 1 or 2).

In order to take into account the configuration splitting of dipole states (see the review devoted to this issue in [7]), it is necessary to double the spectrum of possible collective excitations: each of the μs modes must additionally be broken down into two parts corresponding to dipole transitions between the valence and the outer shell of a nucleus (vibrations of type 1) and dipole transitions between its inner shell and the valence shell (vibrations of type 2).

The quasiboson operators of creation and absorption ($c^{(0)+}_{\mu si}$ and $c^{(0)}_{\mu si}$, respectively) of free quanta of such excitations (the subscript i numbers configuration modes) can be introduced by means of the relations

$$F_{\mu s} = \sum_{i=1}^{2} F_{\mu si}, \tag{3}$$

$$\begin{aligned} F_{\mu si} &= \sum_{\alpha>\beta}^{(i)} (\langle\alpha|2t_\mu x_s|\beta\rangle a^+_\alpha a_\beta \\ &+ (-1)^\mu \langle\alpha|2t_{-\mu} x_s|\beta\rangle^* a^+_\beta a_\alpha) \\ &= f^{(0)}_{\mu si} c^{(0)+}_{\mu si} + (-1)^\mu f^{(0)*}_{-\mu si} c^{(0)}_{-\mu si}, \end{aligned} \tag{4}$$

where the sum $\sum_{\alpha>\beta}{}^{(i)}$ is taken over all single-particle $E1$ transitions of type i and

$$f^{(0)}_{\mu si} = \left[\sum_{\alpha>\beta}^{(i)} |\langle\alpha|2t_\mu x_s|\beta\rangle|^2\right]^{1/2} \tag{5}$$

is the amplitude of the probability for the excitation of $c^{(0)+}_{\mu si}|T_0T_0\rangle$ vibrations ($|T_0T_0\rangle \equiv |T = T_0, T_z = T_0\rangle$ is the ground state of a nucleus), their energy being [4]

$$\varepsilon^{(0)}_{\mu si} = \hbar\omega_{si} + \mu\left(V_1\frac{N-Z}{2A} - E_{\text{Coul}}\right). \tag{6}$$

Here, $\hbar\omega_{si}$ stands for the energy of free (single-particle) photovibrations in the direction along ($s = 3$) and in the direction orthogonal ($s = 1$ or 2) to the nuclear symmetry axis for dipole transitions of the type i, $V_1 \approx 94.8$ MeV is the nuclear-symmetry potential from the Weizsäcker semiempirical mass formula [8], and $E_{\text{Coul}} \approx 1.2(Ze^2/R)$ is the mean Coulomb energy of a single proton ($R \approx 1.2A^{1/3}$ fm is the equivalent radius of a nucleus).

As was shown in [1, 2], the energies $\hbar\omega_{s1}$ and $\hbar\omega_{s2}$ can be approximated by the expressions

$$\begin{aligned} \hbar\omega_{s1} &\approx 41A^{-1/3} \\ &\times \begin{cases} \sqrt{1 - \frac{4}{3}\delta'}\,[\text{MeV}] \text{ at } s = 3 \\ \sqrt{1 + \frac{2}{3}\delta'}\,[\text{MeV}] \text{ at } s = 1 \text{ or } 2, \end{cases} \\ \hbar\omega_{s2} &\approx \left(\frac{A}{A_{\text{core}}}\right)^{1/3} \hbar\omega_{s1}, \end{aligned} \tag{7}$$

where δ' is the deformation parameter in the Nilsson potential and A_{core} is the number of nucleons in the inner shells of a nucleus (that is, in the nuclear core).

Free dipole vibrations cannot be considered as normal vibrations of the nucleon system in the vicinity of the equilibrium position since, by exciting the isovector single-particle potential, they effectively interact with one another via dipole–dipole forces. Taking this into account, we write the vibrational Hamiltonian of a nucleus for vibrations along a fixed s axis in the form [1]

$$H(s) = H_1(s) + H_2(s) + H_{12}(s), \tag{8}$$

where

$$H_i(s) = \sum_\mu \varepsilon^{(0)}_{\mu si} c^{(0)+}_{\mu si} c^{(0)}_{\mu si} + \frac{1}{2}\varkappa_i(s)\sum_\mu F^+_{\mu si} F_{\mu si} \tag{9}$$

is the Hamiltonian describing normal vibrations only for dipole transitions of type $i = 1$ or 2 and

$$H_{12}(s) = \varkappa_{12}(s)\sum_\mu F^+_{\mu s1} F_{\mu s2} \tag{10}$$

is the operator taking into account the interactions of these types of dipole vibrations.

If we disregard the configuration splitting, the coupling constant $\varkappa(s)$ unified for all dipole transitions can be calculated theoretically by studying the coupling between fluctuations of the isovector component of the mean nuclear field and dipole excitations of the nucleon-density distribution. In this way, it was found in [4] that

$$\varkappa(s) \approx \frac{V_1}{4A\langle x^2_s\rangle}, \tag{11}$$

where V_1 is the aforementioned nuclear-symmetry potential [see formula (6)] and $\langle x_s^2 \rangle$ is the mean value of the square of the nucleon coordinate x_s in a nucleus.

Expression (11) takes into account the effect of the nuclear-surface deformation on dipole vibrations, since, in an axisymmetric deformed nucleus, the following relation holds [4, 5]:

$$\langle x_1^2 \rangle : \langle x_2^2 \rangle : \langle x_3^2 \rangle \approx 1 : 1 : \frac{1 + \frac{2}{3}\delta'}{1 - \frac{4}{3}\delta'}. \qquad (12)$$

From data on electron scattering, it follows that the mean value of the square of the radius vector for all nucleons is

$$\langle r^2 \rangle = \langle x_1^2 \rangle + \langle x_2^2 \rangle + \langle x_3^2 \rangle \approx \frac{3}{5}(1.2A^{1/3})^2 \,[\mathrm{fm}^2]. \qquad (13)$$

With the aid of relations (12) and (13), expression (11) can be reduced to the form

$$\varkappa(s) \approx 0.868 V_1 A^{-5/3} \theta_s(\delta') \;[\mathrm{MeV\ fm}^{-2}], \qquad (14)$$

where the factor

$$\theta_s(\delta') = \begin{cases} \dfrac{1 - \frac{2}{3}\delta'}{1 + \frac{2}{3}\delta'} \;\text{ at }\; s = 3 \\ \\ \dfrac{1 - \frac{2}{3}\delta'}{1 - \frac{4}{3}\delta'} \;\text{ at }\; s = 1 \text{ or } 2 \end{cases} \qquad (15)$$

describes the dependence of the dipole–dipole coupling constant on the nuclear deformation.

The simple calculations performed in [4] without isolating configuration and isospin modes revealed that the use of expression (14) in estimating the constant of dipole–dipole forces makes it possible to reproduce the energy of a giant dipole resonance in heavy nuclei correctly, but this leads to strongly overestimated values of this quantity in the region of light nuclei. This may be explained by the fact that the isovector dipole field specified by Eq. (1) disregards surface effects. In actual nuclei having finite dimensions, the dipole field must additionally involve the radial factor $d\rho(r)/dr$, which characterizes the rate at which the nuclear density changes at the periphery, and this weakens somewhat the mass dependence of the dipole–dipole coupling constant: $A^{-5/3} \to A^{-4/3}$ [9]. This circumstance can be taken into account by employing formula (14) with different values of the parameter V_1 in different mass regions. By way of example, we indicate that, since an ordinary value of V_1 is appropriate for heavy nuclei ($A \sim 100$–200), this value must be reduced approximately by a factor of $10^{1/3}$ for light nuclei ($A \sim 10$–20).

According to (3) and (4), the free modes $c_{\mu si}^{(0)+}|T_0 T_0\rangle$ are nothing but superpositions of particle–hole ($1p1h$) configurations of a nucleus. In the vibrational Hamiltonian specified by Eqs. (8)–(10), we used three different constants of dipole–dipole forces in describing three different versions of the interaction of $1p1h$ configurations belonging to type 1 and type 2—that is, $1 \rightleftarrows 1$, $2 \rightleftarrows 2$, and $1 \rightleftarrows 2$. The reasons for this are as follows:

(i) We can see from (14) that the dipole–dipole coupling constant is proportional to $A^{-5/3}$. Since the dipole field is determined by formula (1), this mass dependence can be used for the constants $\varkappa_1(s)$ and $\varkappa_{12}(s)$. For the $\varkappa_2(s)$, however, it is more correct to choose the $A_{\mathrm{core}}^{-5/3}$ dependence since outer (valence) nucleons have only a slight effect on dipole excitations of nucleons that belong to the filled inner shell (see the analysis of data on the quasielastic knockout of nucleons in [1]).

(ii) One can assume that intergroup interaction ($1 \rightleftarrows 2$) is weaker in general than intragroup interaction ($1 \rightleftarrows 1$ or $2 \rightleftarrows 2$) because the spatial overlap of mixed configurations is smaller (especially if transitions of type 2 lead to the formation of deep hole states). For long-range dipole–dipole forces, this effect can be taken into account by reducing the constant $\varkappa_{12}(s)$.

On the basis of the above considerations, we represent the constants $\varkappa_1(s)$, $\varkappa_2(s)$, and $\varkappa_{12}(s)$ (measured in MeV fm^{-2} units) in the form

$$\varkappa_1(s) \approx 0.868 V A^{-5/3} \theta_s(\delta'), \qquad (16)$$
$$\varkappa_2(s) \approx 0.868 V A_{\mathrm{core}}^{-5/3} \theta_s(\delta'),$$
$$\varkappa_{12}(s) \approx 0.868 V' A^{-5/3} \theta_s(\delta'),$$

where V and V' ($V' \lesssim V$) are model parameters, which are measured in MeV.

Let us diagonalize the Hamiltonian in (8) in two steps. At first, we find the eigenstates of the Hamiltonians $H_1(s)$ and $H_2(s)$; then, we take into account the interaction of these states with each other.

The first step can be realized with the aid of the linear canonical transformation

$$c_{\mu si}^{+} = X_{\mu si} c_{\mu si}^{(0)+} - Y_{\mu si} c_{-\mu si}^{(0)}, \qquad (17)$$

where the coefficients $X_{\mu si}$ and $Y_{\mu si}$ satisfy the orthogonality conditions

$$X_{\mu si} X_{\mu si}^{*} - Y_{\mu si} Y_{\mu si}^{*} = 1, \qquad (18)$$
$$X_{\mu si} Y_{-\mu si} - X_{-\mu si} Y_{\mu si} = 0.$$

The Hamiltonian in (8) then reduces to the form (see also [4])

$$H(s) = \sum_{\mu i} \varepsilon_{\mu si} c^+_{\mu si} c_{\mu si} + \varkappa_{12}(s) \sum_{\mu} F^+_{\mu s1} F_{\mu s2} + \text{const}, \quad (19)$$

where $c^+_{\mu si}$ and $c_{\mu si}$ are, respectively, the creation and annihilation operators for normal vibrations (with $\mu = 0, \pm 1$) associated with the Hamiltonian $H_i(s)$;

$$\varepsilon_{\mu si} = K + 0.5[(\varepsilon^{(0)}_{\mu si} - \varepsilon^{(0)}_{-\mu si}) + \varkappa_i(s)((f^{(0)}_{\mu si})^2 - (f^{(0)}_{-\mu si})^2)] \quad (20)$$

is the energy of these vibrations;

$$K \equiv [(\hbar\omega_{si} + \varkappa_i(s)(f^{(0)}_{0si})^2)^2 - (\varkappa_i(s) f^{(0)}_{\mu si} f^{(0)}_{-\mu si})^2]^{1/2}; \quad (21)$$

$$F_{\mu si} = f_{\mu si} c^+_{\mu si} + (-1)^\mu f^*_{-\mu si} c_{-\mu si} \quad (22)$$

is the operator in (4) in the representation of the eigenstates of the Hamiltonian $H_i(s)$; and $f_{\mu si}$ is the amplitude of the probability for the excitation of vibrations of the type $c^+_{\mu si}|T_0T_0\rangle$, this amplitude being related to the amplitude $f^{(0)}_{\mu si}$ by the equation

$$f^2_{\mu si} = 0.5((f^{(0)}_{\mu si})^2 - (f^{(0)}_{-\mu si})^2) + K^{-1}\left[\hbar\omega_{si}(f^{(0)}_{0si})^2 + \varkappa_i(s)((f^{(0)}_{0si})^4 - (f^{(0)}_{\mu si} f^{(0)}_{-\mu si})^2)\right]. \quad (23)$$

The second step in reducing the Hamiltonian in (8) to a diagonal form is realized with the aid of the transformation

$$\hat{c}^+_{\mu sa} = \sum_{i=1}^{2} (X_{\mu s}(ai) c^+_{\mu si} - Y_{\mu s}(ai) c_{-\mu si}), \quad (24)$$

where the coefficients $X_{\mu s}(ai)$ and $Y_{\mu s}(ai)$ satisfy the orthogonality conditions

$$\sum_{i=1}^{2} (X_{\mu s}(ai) X^*_{\mu s}(a'i) - Y_{\mu s}(ai) Y^*_{\mu s}(a'i)) = \delta_{aa'}, \quad (25)$$

$$\sum_{i=1}^{2} \left(X_{\mu s}(ai) Y_{-\mu s}(a'i) - Y_{\mu s}(ai) X_{-\mu s}(a'i)\right) = 0.$$

The eigenenergies $\hat{\varepsilon}_{\mu sa}$ of the Hamiltonian $H(s)$ are determined as the roots of the secular equation

$$\left(\frac{1}{\varkappa_{12}(s)}\right)^2 = \left[\frac{f^2_{\mu s1}}{\hat{\varepsilon}_{\mu sa} - \varepsilon_{\mu s1}} - \frac{f^2_{-\mu s1}}{\hat{\varepsilon}_{\mu sa} + \varepsilon_{-\mu s1}}\right] \times \left[\frac{f^2_{\mu s2}}{\hat{\varepsilon}_{\mu sa} - \varepsilon_{\mu s2}} - \frac{f^2_{-\mu s2}}{\hat{\varepsilon}_{\mu sa} + \varepsilon_{-\mu s2}}\right], \quad (26)$$

where $a = 1, 2$ and $\hat{\varepsilon}_{\mu s1} \leq \hat{\varepsilon}_{\mu s2}$.

The dipole operator (1) can be recast into the form

$$F_{\mu s} = \sum_{a=1}^{2} \left(\hat{f}_{\mu sa} \hat{c}^+_{\mu sa} + (-1)^\mu \hat{f}^*_{-\mu sa} \hat{c}_{-\mu sa}\right), \quad (27)$$

where $\hat{f}_{\mu sa}$ are the amplitudes of the probability for the excitation of the normal vibrations $\hat{c}^+_{\mu sa}|T_0T_0\rangle$. These amplitudes can be found from the relations

$$\hat{f}^2_{\mu sa} = \left|\frac{A_{\mu sa}(1) A_{\mu sa}(2)}{A_{\mu sa}(1) B_{\mu sa}(2) + A_{\mu sa}(2) B_{\mu sa}(1)}\right| \times \left[\sqrt{|A_{\mu sa}(1)|} + \sqrt{|A_{\mu sa}(2)|}\right]^2, \quad (28)$$

$$A_{\mu sa}(i) = \frac{f^2_{\mu si}}{\hat{\varepsilon}_{\mu sa} - \varepsilon_{\mu si}} - \frac{f^2_{-\mu si}}{\hat{\varepsilon}_{\mu sa} + \varepsilon_{-\mu si}} \quad (i = 1, 2), \quad (29)$$

$$B_{\mu sa}(i) = \frac{f^2_{\mu si}}{(\hat{\varepsilon}_{\mu sa} - \varepsilon_{\mu si})^2} - \frac{f^2_{-\mu si}}{(\hat{\varepsilon}_{\mu sa} + \varepsilon_{-\mu si})^2} \quad (i = 1, 2). \quad (30)$$

Finally, the expressions

$$|X_{\mu s}(a1)|^2 - |Y_{\mu s}(a1)|^2 = \frac{A_{\mu sa}(2) B_{\mu sa}(1)}{A_{\mu sa}(1) B_{\mu sa}(2) + A_{\mu sa}(2) B_{\mu sa}(1)}, \quad (31)$$

$$|X_{\mu s}(a2)|^2 - |Y_{\mu s}(a2)|^2 = \frac{A_{\mu sa}(1) B_{\mu sa}(2)}{A_{\mu sa}(1) B_{\mu sa}(2) + A_{\mu sa}(2) B_{\mu sa}(1)}$$

determine the contribution of type-1 and type-2 configurations to the dipole states $\hat{c}^+_{\mu sa}|T_0T_0\rangle$.

2.2. Inclusion of Isospin Conservation for Photoresonances in Light Nuclei

In light nuclei, proton and neutron transitions of type i ($i = 1, 2$) proceed between the same main shells. In this case, the individual terms in the isovector operator $F_{\mu s}$ that appear in the expansions in (3), (22), and (27) are also isovector quantities.

From this, it does not follow, however, that the states $\hat{c}^+_{\mu sa}|T_0T_0\rangle$ found for light nuclei are isospin eigenstates. Only the $\mu = +1$ states having the

isospin $T = T_0 + 1$ possess this property. The remaining states are not eigenfunctions of the isospin operator $\mathbf{T}$ for the nuclear system being considered. In particular, the states $\hat{c}^+_{0sa}|T_0T_0\rangle$, which describe photoresonances, involve components whose isospins are $T_< \equiv T_0$ and $T_> \equiv T_0 + 1$; that is,

$$\hat{c}^+_{0sa}|T_0T_0\rangle = \hat{f}^{-1}_{0sa}\hat{b}^+_{0sa}|T_0T_0\rangle \quad (32)$$
$$= \hat{f}^{-1}_{0sa}\left\{ -\sqrt{\frac{T_0}{T_0+1}}(\hat{b}^+_{sa}|T_0\rangle)_{T_0T_0} + \frac{1}{\sqrt{T_0+1}}(\hat{b}^+_{sa}|T_0\rangle)_{T_0+1T_0}\right\},$$

where

$$\hat{b}^+_{\mu sa} \equiv \hat{f}_{\mu sa}\hat{c}^+_{\mu sa} \quad (33)$$

is an isovector operator that creates unnormalized eigenstates of vibrations (we note that, in contrast to the operator $\hat{b}^+_{\mu sa}$, the operator $\hat{c}^+_{\mu sa}$ is not an isovector) and the symbol $(\,)_{TT_z}$ denotes the vector composition of the isospins of the operators and states enclosed by parentheses into the resulting isospin TT_z (for example, we have $(\hat{b}^+_{sa}|T_0\rangle)_{T_0T_0} = \sum_{\mu T_z}(1\mu T_0T_z|T_0T_0)\hat{b}^+_{\mu sa}|T_0T_z\rangle$).

The states $(\hat{b}^+|T_0\rangle)_{T_0T_0}$ and $(\hat{b}^+|T_0\rangle)_{T_0+1\,T_0}$ (in order to avoid encumbering the presentation, we henceforth suppress the subscripts s and a) describe the $T_<$ and $T_>$ components of the photoresonance in (32). By using the usual technique of vector composition and the commutation relations between the operator $\hat{b}^+_\mu$ and the total-isospin operator $\mathbf{T} = \{T_x, T_y, T_z\}$, we can represent the normalized wave functions for these states in the form

$$|\Psi_<\rangle = C_<^{-1/2}(\hat{b}^+|T_0\rangle)_{T_0T_0} \quad (34)$$
$$= C_<^{-1/2}\left\{ -\sqrt{\frac{T_0+1}{T_0}}\hat{b}^+_0|T_0T_0\rangle + \frac{1}{\sqrt{2T_0(T_0+1)}}T_-\hat{b}^+_{+1}|T_0T_0\rangle\right\},$$

$$|\Psi_>\rangle = C_>^{-1/2}(\hat{b}^+|T_0\rangle)_{T_0+1T_0} \quad (35)$$
$$= C_>^{-1/2}\frac{1}{\sqrt{2(T_0+1)}}T_-\hat{b}^+_{+1}|T_0T_0\rangle,$$

where $T_- = T_x - iT_y$ is the operator lowering the z projection of the isospin of states by unity and

$$C_< = \frac{T_0+1}{T_0}\hat{f}^2_0 - \frac{1}{T_0}\hat{f}^2_{+1}, \quad C_> = \hat{f}^2_{+1} \quad (36)$$

are normalization factors.

As might have been expected, the $T_>$ component of the photoresonance can be obtained from the $\mu = +1$ modes by a mere rotation in isospin space. With the aid of relations (33)–(36), one can easily calculate the energies of the states $|\Psi_<\rangle$ and $|\Psi_>\rangle$ and the probabilities of their excitation. In calculating the energies of these resonances ($E_<$ and $E_>$), it should be borne in mind that, in photovibrations, the Coulomb energy of a nucleus undergoes virtually no changes. This can be taken into account by eliminating the mean Coulomb energy E_{Coul} in formula (6). The energies ε_{+1} and $\hat{\varepsilon}_{+1}$ [see relations (20), (26)] will then accordingly increase by this quantity. The formulas given below for the energies $E_<$ and $E_>$ take into account this correction explicitly; that is,

$$E_< = \langle\Psi_<|(H - E_0)|\Psi_<\rangle \quad (37)$$
$$= \frac{\hat{\varepsilon}_0 - \frac{1}{T_0+1}\left(\frac{\hat{f}_{+1}}{\hat{f}_0}\right)^2(\hat{\varepsilon}_{+1} + E_{\mathrm{Coul}})}{1 - \frac{1}{T_0+1}\left(\frac{\hat{f}_{+1}}{\hat{f}_0}\right)^2},$$
$$E_> = \langle\Psi_>|(H - E_0)|\Psi_>\rangle = \hat{\varepsilon}_{+1} + E_{\mathrm{Coul}},$$

where E_0 is the energy of the ground state $|T_0T_0\rangle$.

The probabilities of the $E1$ excitation of the states $|\Psi_<\rangle$ and $|\Psi_>\rangle$, into which the photoresonance $\hat{c}^+_0|T_0T_0\rangle$ splits, are determined by the relations

$$M^2_< = \langle\Psi_<|F_0|T_0T_0\rangle^2 = \hat{f}^2_0 - \frac{1}{T_0+1}\hat{f}^2_{+1}, \quad (38)$$
$$M^2_> = \langle\Psi_>|F_0|T_0T_0\rangle^2 = \frac{1}{T_0+1}\hat{f}^2_{+1}.$$

From (37) and (38), we find that

$$E_<M^2_< + E_>M^2_> = \hat{\varepsilon}_0\hat{f}^2_0. \quad (39)$$

Therefore, the total oscillator strength of the states $|\Psi_<\rangle$ and $|\Psi_>\rangle$ is exactly equal to the oscillator strength of the splitting resonance $\hat{c}^+_0|T_0T_0\rangle$.

2.3. Application of the Model to Medium-Mass and Heavy Nuclei

In rather heavy nuclei, valence protons and neutrons are in different main shells of a nucleus. In this case, the individual components of the expansions in (3), (22), and (27) cannot be considered as isovector quantities, whence it follows that the procedure for separating the $T_<$ and $T_>$ components of photoresonances that was described in the preceding subsection becomes meaningless.

However, the configuration splitting plays a relatively modest role in such nuclei. Therefore, it can be disregarded for a first approximation, whereupon

the aforementioned difficulties in taking into account isospin conservation in nuclei featuring a large neutron excess are removed. To demonstrate this, we note that, if the μs modes are not separated into two configuration components, formulas (20)–(23), where the subscript i must be discarded everywhere, will determine the energies $\varepsilon_{\mu s}$ of normal μs vibrations of the nucleon system that are generated by the isovector operator $b^+_{\mu s} = f_{\mu s} c^+_{\mu s}$ and the probabilities $f^2_{\mu s}$ of their excitation [4]. At the same time, the $T_<$ and $T_>$ components of photoresonances can be separated with the aid of formulas (37) and (38), where the substitutions $\hat{\varepsilon}_0, \hat{\varepsilon}_{+1} \to \varepsilon_0, \varepsilon_{+1}$ and $\hat{f}_0, \hat{f}_{+1} \to f_0, f_{+1}$ must be made (it should be recalled that the subscript s is omitted in these formulas).

The results obtained from such calculations for the features of the isospin splitting of photoresonances ($E_> - E_<$, $M^2_>/M^2_<$) can also be used in approximately describing the isospin splitting of each of the $0si$ resonances that were calculated within the procedure described in Subsection 2.1. This procedure (which is well justified in the case of small configuration effects) makes it possible to take simultaneously into account all main kinds of giant-dipole-resonance splitting over the mass range being discussed.

For heavy nuclei, it is straightforward to obtain analytic estimates for the quantities $E_> - E_<$ and $M^2_>/M^2_<$. We will assume that the nucleus being considered is of a spherical shape and set $V = V_1$ [compare with (14) and (16)]. Upon substituting the quantities ε_0, ε_{+1}, f_0, and f_{+1} from formulas (20)–(23) into formulas (37) and (38) (in accordance with the above comments) and considering that [4]

$$\frac{1}{2}((f^{(0)}_{+1})^2 + (f^{(0)}_{-1})^2) \approx (f^{(0)})^2 \approx \frac{\hbar^2}{2M}\frac{A}{\hbar\omega_1} \approx 0.5A^{4/3}\,[\mathrm{fm}^2], \tag{40}$$

$$\frac{1}{2}((f^{(0)}_{-1})^2 - (f^{(0)}_{+1})^2) = \langle T_0 T_0|[F_{-1}, F_{+1}]|T_0 T_0\rangle = \langle T_0 T_0|\sum_{k=1}^{A}(2t_z x_1^2)_k|T_0 T_0\rangle \approx (N-Z)\langle x_1^2\rangle \approx 0.6T_0A^{2/3}\,[\mathrm{fm}^2],$$

we obtain

$$E_> - E_< \approx \frac{V_1}{2A}(T_0+1)\,[\mathrm{MeV}], \quad \frac{M^2_>}{M^2_<} = \frac{E_{\mathrm{dip}} - E_<}{E_> - E_{\mathrm{dip}}} \approx \frac{1}{T_0}\frac{1 - 2.4T_0A^{-2/3}(1-\Delta)}{1 + 2.4A^{-2/3}(1-\Delta)}, \tag{41}$$

where $\hbar\omega_1 \approx 41A^{-1/3}$ MeV is the energy of single-particle vibrations along the x_1 axis, $E_{\mathrm{dip}} = \varepsilon_0$ is the energy of a nonsplit photoresonance (energy of a giant dipole resonance), and $\Delta = (0.006\ \mathrm{MeV}^{-1})V_1 \times T_0A^{-2/3}$ is a dimensionless quantity.

For $A \gtrsim 100$ nuclei, the best fit to the giant-dipole-resonance energy is obtained at $V_1 \approx 120$ MeV for $T_0A^{-2/3}$ ranging between 0.4 and 0.6. This makes it possible to recast relations (41) into the form

$$E_> - E_< \approx \frac{60}{A}(T_0+1)\,[\mathrm{MeV}], \quad \frac{S_>}{S_<}\frac{E_<}{E_>} = \frac{E_{\mathrm{dip}} - E_<}{E_> - E_{\mathrm{dip}}} \approx \frac{1}{T_0}\frac{1 - 1.5T_0A^{-2/3}}{1 + 1.5A^{-2/3}}, \tag{42}$$

where $S_< = E_<M^2_<$ and $S_> = E_>M^2_>$ are the oscillator strengths of the $T_<$ and $T_>$ components of a giant dipole resonance.

We note that expressions (42) coincide with the formulas derived in [3].

2.4. Estimating Dipole-State Widths

This problem was considered in [2, 10]. Below, we use the main results of these considerations.

The total width of an arbitrary dipole state can be represented as the sum of the emission width $\Gamma^\uparrow$ and spreading width $\Gamma^\downarrow$:

$$\Gamma = \Gamma^\uparrow + \Gamma^\downarrow. \tag{43}$$

Following [2], we approximate the emission width by the expression

$$\Gamma^\uparrow \approx \sum_i^2 q_i\langle kP\rangle_i\left(\frac{\hbar^2\Re^2}{\mu}\right)\left\langle\frac{\varphi^2(\Re)}{\int_0^\Re \varphi^2(r)r^2dr}\right\rangle_i, \tag{44}$$

where the factor q_i specifies the fraction of configurations of type i in the dipole state being considered, $k = \sqrt{2\mu e}$ is the momentum of the emitted nucleon, $e = E - e^{-1} - B_{\mathrm{nucl}}$ is its kinetic energy, E is the energy of the dipole state, e^{-1} is the energy of the remaining hole, B_{nucl} is the nucleon-separation energy, μ is the reduced nucleon mass, P is the barrier penetrability, $\Re$ is the radius of the nucleonic reaction channel, $\varphi(r)$ is the radial function for a particle, and the symbol $\langle\,\rangle_i$ denotes averaging over configurations of type i that enter into the dipole state.

We represent the spreading width in the form [10]

$$\Gamma^\downarrow \approx GI(A)(E - \delta_{TT_>}E_{\mathrm{Coul}})^2, \tag{45}$$

where G is a constant, E is the energy of the resonance in question, T is its isospin, $E_{\rm Coul}$ is the mean Coulomb energy per proton [see Eq. (6)],

$$I(A) = \frac{1}{1+\pi^2\left(\frac{a}{R_0}\right)^2}\left[1-3\frac{a}{R_0}\frac{1+\frac{\pi^2}{3}\left(\frac{a}{R_0}\right)^2}{1+\pi^2\left(\frac{a}{R_0}\right)^2}\right] \quad (46)$$

is the factor that takes into account the effect of the diffuseness of the nuclear surface on the probability of a collision between a particle or a hole and a nonexcited nucleon, R_0 is the distance between the center of the nucleus and the locus where the nuclear-matter density ρ decreases by a factor of 2, and a is the diffuseness parameter of the nuclear surface.

As can be seen from (45), the spreading widths of the $T_>$ photoresonances are assumed to be proportional to the square of the energy $\hat{\varepsilon}_{+1}$, $\Gamma_>^{\downarrow} \propto (E_> - E_{\rm Coul})^2 = (\hat{\varepsilon}_{+1})^2$, because these resonances are the isobar analogs of the $\mu = +1$ charge-exchange resonances.

Formulas (43)–(46) involve four parameters: $\Re$, R_0, a, and G. We set the radius of the reaction channel to $\Re = 1.6A^{1/3}$ fm and choose (on the basis of data on electron scattering) the value of $R_0 = 1.07A^{1/3}$ fm. The two remaining parameters (G and a) were varied in such a way as to obtain the best fit to the experimental widths of the dipole peaks in magic and deformed nuclei over the mass range $16 \lesssim A \lesssim 240$. The resulting values are $G = 0.081$ MeV^{-1} and $a = 1.59$ fm.

3. APPLICATION TO DESCRIBING THE GROSS STRUCTURE OF GIANT DIPOLE RESONANCES IN THE MASS RANGE $12 \le A \le 18$

The model considered above was used to describe the gross structure of the cross sections for photoabsorption on ^{12,13,14}C, ^{14,15}N, and ^{16,17,18}O nuclei.

The following computational scheme was employed. First, the energies $E_<$ and $E_>$ and the oscillator strengths $S_< = E_< M_<^2$ and $S_> = E_> M_>^2$ of normal $E1$ vibrations were calculated on the basis of the formalism developed in Section 2. After that, the results obtained for the dipole states, whose number varied from four (in $N = Z$ nuclei) to eight (in $N \neq Z$ nuclei), were approximated by Lorentzian curves whose widths were estimated by formulas (43)–(46).

In order to take into account the effect of exchange forces, we introduced a scale factor that ensures a normalization of the integrated photoabsorption cross section according to the condition

$$S_{\rm int} = (1+\alpha)60\frac{NZ}{A}\ [\text{MeV mb}], \quad (47)$$

where $\alpha = 0.2$ is an exchange parameter.

In calculating single-particle states $|\alpha\rangle$ [see Eq. (1)], we employed the spheroidal Nilsson potential [6] involving the deformation parameter

$$\delta' \approx \delta \Big/ \left(1+\frac{2}{3}\delta\right), \quad (48)$$

where δ is the parameter of the quadrupole nuclear deformation,

$$\delta = \frac{3}{4}\frac{Q_0}{Z\langle r^2\rangle}. \quad (49)$$

Here, Q_0 is the intrinsic quadrupole moment and $\langle r^2\rangle$ is the mean square of the radius of the nuclear-charge distribution.

The parameters δ were estimated on the basis of data on electric quadrupole moments for the ground and excited states of nuclei [11]. From these data, it follows that, for ^{12}C, ^{14}N, ^{17}O, and ^{18}O nuclei, the parameter δ is, respectively, $\delta = +0.4(2)$, $-0.16(5)$, $-0.10(5)$, and $+0.4(2)$ (in parentheses, we give the error in the last figure of the estimate with allowance for the uncertainty in data on $\langle r^2\rangle$). In order to obtain better agreement with experimental data, these estimates were varied within the experimental errors. The ultimate values of the parameter δ that were used in the calculations are given in column 2 of the table.

We varied the free model parameters V and V'. This was done differently for nuclei belonging to the end of the $1p$ and the beginning of the $1d2s$ shell. For the ^{12,13,14}C and ^{14,15}N nuclei, we first fixed the parameter V' and then selected the value of the parameter V in such a way that the calculation reproduced the correct position of the centroid of the giant dipole resonance [10]; that is,

$$E_{\rm dip} \approx 86A^{-1/3}\sqrt{\frac{1+\pi^2\xi^2}{1+\frac{10}{3}\pi^2\xi^2+\frac{7}{3}\pi^4\xi^4}}\ [\text{MeV}], \quad (50)$$

where $\xi \equiv a_0/R_0$, $a_0 = 0.55$ fm, and $R_0 = 1.07A^{1/3}$ fm. After that, we chose a different value of the parameter V' and repeated the procedure for constructing a fit to the giant-dipole-resonance energy. This procedure for varying the parameters made it possible to find, for the parameter V' ($< V$), an optimum value that takes effectively into account the influence of the weakening of the spatial overlap

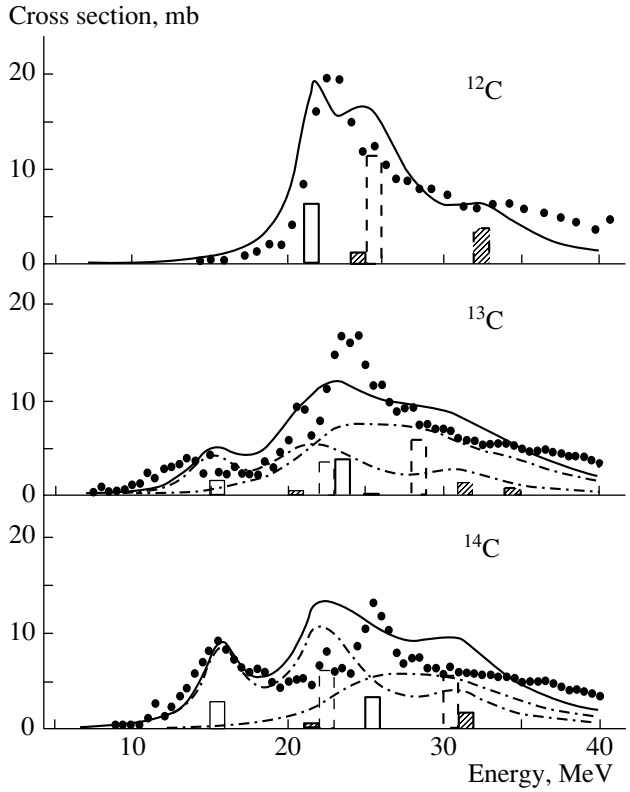

Fig. 1. Structure of a giant dipole resonance in carbon isotopes (the excitation energy of a nucleus is plotted along the abscissa): (points) experimental photoabsorption cross sections [12], (solid curves) theoretical cross section, and (dash-dotted curves) isospin components of this cross section for $N \neq Z$ nuclei. The histograms represent (in arbitrary units) the distribution of the oscillator strengths of dipole states. The solid-line and dashed-line columns correspond, respectively, to longitudinal and to transverse dipole vibrations. The thin and thick lines of the contours correspond, respectively, to $T_<$ and to $T_>$ resonances. The unshaded part of the columns represents the contribution to a dipole state from configurations of type 1, while the shaded part shows the contributions from configurations of type 2.

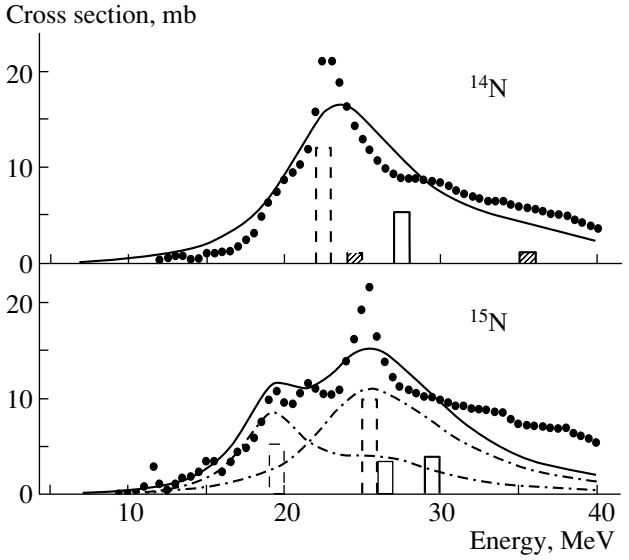

Fig. 2. Structure of a giant dipole resonance in nitrogen isotopes. The notation is identical to that in Fig. 1.

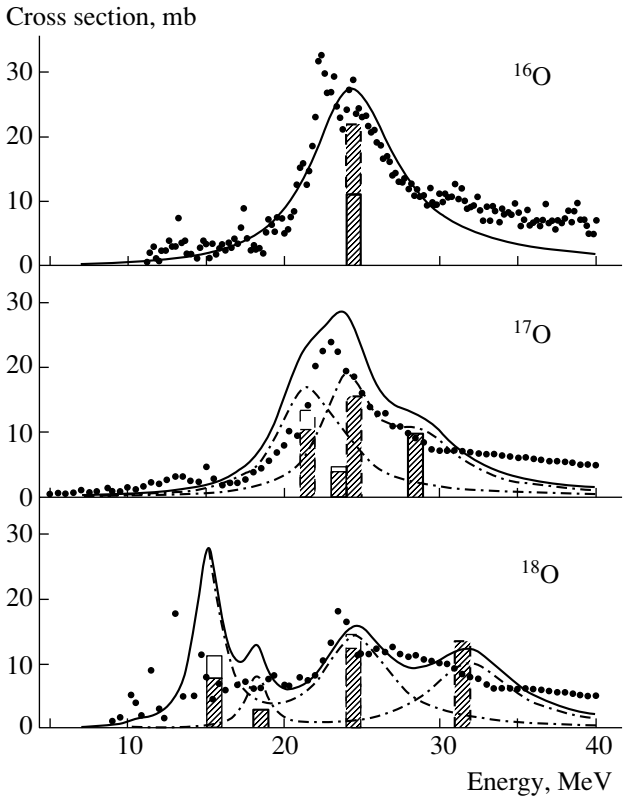

Fig. 3. Structure of a giant dipole resonance in oxygen isotopes. The notation is identical to that in Fig. 1.

of type-1 and type-2 single-particle dipole configurations for nuclei from the last one-third of the $1p$ shell. For the ^{16,17,18}O nuclei, it was assumed, in fitting the giant-dipole-resonance energy, that $V' = V$, since, when the filling of the shell begins, both types of dipole configurations are localized in the same spatial region—in the vicinity of the nuclear surface. The V and V' values used in the calculations are given in columns 3 and 4 of the table.

4. DISCUSSION OF THE RESULTS

The main results of the calculations are presented in Figs. 1–3 and in the table (columns 5–9).

Figures 1–3 give (points) experimental photoabsorption cross sections [12] along with (curves and histograms) the results of the calculations performed within the model formulated above. The solid curves correspond to the theoretical photoabsorption cross section. Two dash-dotted curves (for $N \neq Z$ nuclei)

Parameters used in the calculations and resulting features of the configuration, the deformation, and the isospin splitting of a giant dipole resonance [given in parentheses are the estimates of the giant-dipole-resonance splitting that are based on the formulas presented by Danos and Okamoto [13] (column 7) and by Goulard and Fallieros [3] (columns 8, 9)]

Nucleus	δ	V, MeV	V', MeV	$E_2 - E_1$, MeV	S_2/S_1	$E_\perp - E_{\|\|}$, MeV	$E_> - E_<$, MeV	$S_>/S_<$
^{12}C	0.2	44	20	5.8	0.31	5.3(4.3)	–	–
^{13}C	0.3	44	20	5.2	0.22	6.6(6.2)	4.8(6.9)	1.6(1.8)
^{14}C	0.3	45	20	4.0	0.14	6.0(6.1)	6.4(8.6)	0.74(0.82)
^{14}N	−0.2	51	20	5.1	0.15	−5.8(−4.8)	–	–
^{15}N	−0.2	52	20	3.3	0.08	−5.0(−4.7)	4.3(6.0)	1.6(1.8)
^{16}O	0.0	58	58	–	–	–	–	–
^{17}O	−0.15	52	52	3.0	11.6	−4.2(−3.6)	4.2(5.3)	1.4(1.8)
^{18}O	0.6	42	42	6.3	6.4	12.4(11.0)	9.2(6.7)	0.62(0.84)

represent the contribution to this cross section from the $T_<$ and $T_>$ components. The histograms show the distribution of the oscillator strengths of dipole states (in arbitrary units). The solid- and dashed-line columns correspond, respectively, to longitudinal and to transverse dipole vibrations. The thin and thick lines of the contours correspond, respectively, to $T_<$ and $T_>$ resonances. The unshaded part of the columns represents the contribution to the dipole state from configurations of type 1, while the shaded part of the columns shows contributions from configurations of type 2.

One can see from these figures that the gross structure of the cross sections for photoabsorption on the nuclei being considered is affected by all three types of giant-dipole-resonance splitting.

The configuration splitting of a giant dipole resonance manifests itself most clearly in $N = Z$ nuclei (^{12}C, ^{14}N). However, it can easily be singled out in the structure of the cross sections for photoabsorption on ^{13,14}C and ^{17,18}O nuclei. In the doubly magic nucleus ^{16}O, it is of course absent, while, in the ^{15}N nucleus, it is difficult to observe configuration splitting because of a small strength of type-2 dipole transitions there (and because of their weak interaction with type-1 transitions). In columns 5 and 6 of the table, we present the energy spacings ($E_2 - E_1$) between the centroids and the ratio (S_2/S_1) of the oscillator strengths for two configuration components of a giant dipole resonance. From these data, one can see that the role of the configuration splitting becomes more pronounced as we move away from the doubly magic nucleus ^{16}O. For the nuclei being discussed, yet another feature of the configuration splitting of a giant dipole resonance is worthy of special note: two configuration components of a giant dipole resonance mix only slightly in the ^{12,13,14}C and ^{14,15}N nuclei, which belong to the end of the $1p$ shell; on the contrary, they mix strongly in the ^{17,18}O nuclei, which belong to the beginning of the $1d2s$ shell (compare Figs. 1 and 2 with Fig. 3), where mixing occurs predominantly in the $T_<$ dipole states.

The results of our calculations also show that the set of structural features of the cross sections for photoabsorption on light nuclei arise owing to the deformation splitting of a giant dipole resonance. A static nuclear deformation leads to the splitting of the main peak corresponding to photoabsorption on a ^{12}C nucleus (it should be noted that the splitting of the type-1 configuration component plays a dominant role here) and to the emergence of two maxima associated with photoabsorption on ^{14,15}N and ^{18}O nuclei (see histograms in Figs. 2, 3). Deformation splitting strongly correlates with other types of giant-dipole-resonance splitting. For example, the aforementioned maxima of photoabsorption on a ^{15}N nucleus can be associated not only with different directions of dipole vibrations but also with different isospin modes of a giant dipole resonance. From a comparison of Figs. 1 and 4, one can see that the inclusion of configuration splitting significantly affects the results concerning the deformation splitting of the giant dipole resonance in the ^{12}C nucleus. The calculation performed in the present study gives a somewhat larger spacing $E_\perp - E_{||}$ between the centroids of the transverse and the longitudinal component of a giant dipole resonance than that which follows from formulas of the Danos–Okamoto model [13] (see column 7 in the table), although the predicted ratio of the strengths of these components has the same value in these two models: 2 : 1. The observed discrepancy between the estimates of the deformation splitting of a giant dipole resonance is explained to a considerable extent by the fact that, in the Danos–Okamoto model, the ratio

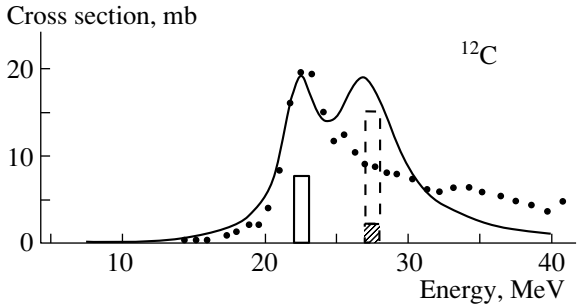

Fig. 4. Results of the calculation performed for the ^{12}C nucleus without taking into account configuration splitting. The notation is identical to that in Fig. 1.

of the energies of transverse and longitudinal dipole vibrations is given by

$$\frac{E_\perp}{E_{||}} = 0.911\frac{a}{b} + 0.089 \qquad (51)$$

$$\approx 0.911\sqrt{\frac{1+\frac{4}{3}\delta}{1-\frac{2}{3}\delta}} + 0.089,$$

where a and b are, respectively, the longitudinal and the transverse semiaxis of the nuclear spheroid of revolution. At the same time, the ratio of the corresponding energies within the present semimicroscopic model is

$$\frac{E_\perp}{E_{||}} \approx \frac{\hbar\omega_1}{\hbar\omega_3} = \sqrt{\frac{1+\frac{2}{3}\delta'}{1-\frac{4}{3}\delta'}} \approx \sqrt{\frac{1+\frac{4}{3}\delta}{1-\frac{2}{3}\delta}}, \qquad (52)$$

where ω_s are the single-particle frequencies of vibrations along the symmetry axes $s = 1, 2, 3$ of a nucleus in the Nilsson potential [5].

From the data in Figs. 1–3, it follows that, in the carbon, nitrogen, and oxygen isotopes, the increase in the giant-dipole-resonance width with increasing neutron excess can be caused by the isospin splitting of the giant resonance. This is also corroborated by the data presented in columns 8 and 9 of the table, where the present results for the energy spacings $E_> - E_<$ between the centroids of the $T_<$ and $T_>$ components of giant dipole resonances and the ratio of their intensities, $S_>/S_<$, are contrasted against their counterparts calculated by the formulas presented by Goulard and Fallieros [3] [see (42)].

As can be seen from these data, formulas (42) predict a somewhat larger contribution to the dipole sum from the $T_>$ component of a giant dipole resonance and, for all nuclei, with the exception of the ^{18}O nucleus, a greater value of the energy splitting

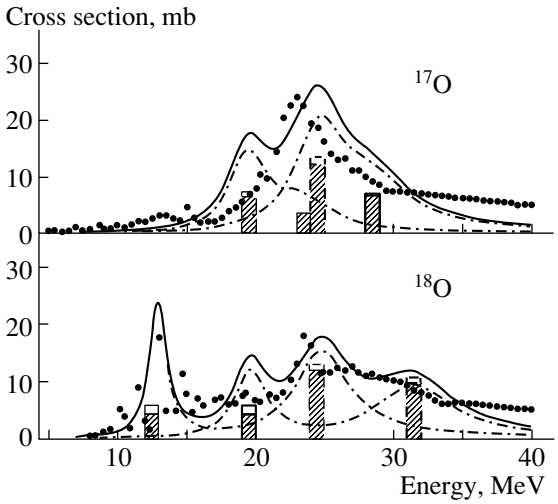

Fig. 5. Results of the calculation performed for the ^{17}O and ^{18}O nuclei, where the isospin splitting of dipole states was taken into account according to the formulas presented by Goulard and Fallieros [3]. The notation is identical to that in Fig. 1.

$E_> - E_<$ in relation to the respective results of our calculation. In [2], formulas (42) of the present article were used to take into account the isospin splitting of each state of the $\mu = 0$ mode (see Subsection 2.1). Figure 5 shows the results of such calculations for the ^{17,18}O nuclei. A comparison of this figure with Fig. 3 reveals that this method for taking into account isospin splitting is rather accurate for the ^{18}O nucleus, which has a large deformation, but that it poorly describes experimental data in the case of the weakly deformed nucleus ^{17}O—it leads to an overly strong splitting of the giant dipole resonance (this negative result cannot be compensated by any choice of the deformation parameter δ).

A comparison of experimental and theoretical data shows that, by and large, the model developed in Section 2 describes well the main features of the cross sections for photoabsorption on light nuclei. However, it is obvious that this model is unable to reproduce all nuances of giant-dipole-resonance formation, because it ignores the coupling of the introduced coherent $1p1h$ excitations to more complicated configurations and the fact that these excitations can be spread over noncollective $1p1h$ states. In particular, it seems that this explains the deficiency of the theoretical cross sections at high nuclear excitation energies (see Figs. 1–3).

To conclude the discussion, we return once again to the question concerning the choice of the parameter V'. It was mentioned in Section 3 that, for the ^{12,13,14}C and ^{14,15}N nuclei, use was made of a relatively small value of this parameter, $V' = 20$ MeV, and

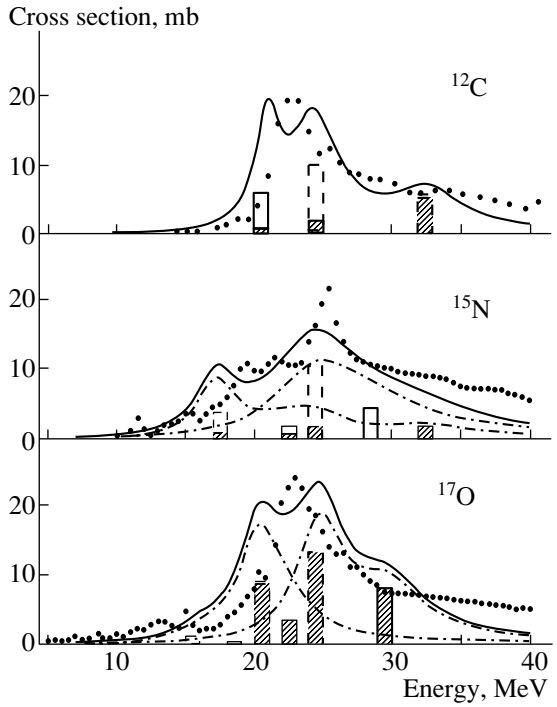

Fig. 6. Calculation performed for the ^{12}C, ^{15}N, and ^{17}O nuclei with V' values different from those used to obtain the data in Figs. 1–3: $V' = V$ for the ^{12}C and ^{15}N nuclei and $V' = 20$ MeV for the ^{17}O nucleus. The notation is identical to that in Fig. 1.

that the value of $V' = V \sim 40$–60 MeV (see table) was taken for the ^{16,17,18}O nuclei. This was justified by special features of the interaction of type-1 and type-2 dipole configurations in these nuclei. Figure 6 illustrates the results of the calculations with totally different values of the parameter V'. As can be seen from this figure, the agreement with experimental data becomes significantly poorer if we do not take correctly into account the degrees of the spatial overlap of type-1 and type-2 configurations.

5. CONCLUSIONS

The analysis performed in this study makes it possible to draw the following conclusions:

(i) The simple semimicroscopic model of isovector dipole vibrations that has been formulated in the present study takes explicitly into account the main modes of dipole excitations and enables us to explain satisfactorily the gross structure of a giant resonance over the mass range $12 \leq A \leq 18$.

(ii) For light nonmagic nuclei, the main features of the structure of photoabsorption cross sections are determined by the concerted effect of the deformation, the configuration, and the isospin splitting of giant dipole resonances.

(iii) By and large, the simple formulas presented in Subsection 2.4 describe fairly well the widths of dipole states, although they cannot explain the emergence of comparatively narrow photoabsorption peaks in such nuclei as ^{14}C and ^{15}N (see Figs. 1, 2).

ACKNOWLEDGMENTS

We are grateful to Professor I.M. Kapitonov for assistance in selecting experimental data required for the present analysis.

REFERENCES

1. B. S. Ishkhanov and V. N. Orlin, Yad. Fiz. **66**, 1269 (2003) [Phys. At. Nucl. **66**, 1229 (2003)].
2. B. S. Ishkhanov and V. N. Orlin, Yad. Fiz. **67**, 614 (2004) [Phys. At. Nucl. **67**, 595 (2004)].
3. B. Goulard and S. Falliero, Can. J. Phys. **45**, 3221 (1967).
4. A. Bohr and B. R. Mottelson, *Nuclear Structure*, Vol. 2: *Nuclear Deformations* (Benjamin, New York, 1975; Mir, Moscow, 1977).
5. S. G. Nilsson, K. Dan. Vidensk. Selsk. Mat.-Fys. Medd. **29**, 16 (1955).
6. C. Gustafson *et al.*, Ark. Fys. **36**, 613 (1967).
7. R. A. Eramzhyan, B. S. Ishkhanov, I. M. Kapitonov, *et al.*, Phys. Rep. **136**, 230 (1986).
8. S. Moshkovsky, *Structure of Atomic Nucleus* (Izd. Inostr. Lit., Moscow, 1959), p. 471.
9. E. N. Golovach, B. S. Ishkhanov, and V. N. Orlin, Yad. Fiz. **58**, 404 (1995) [Phys. At. Nucl. **58**, 354 (1995)].
10. B. S. Ishkhanov and V. N. Orlin, Yad. Fiz. **65**, 1858 (2002) [Phys. At. Nucl. **65**, 1809 (2002)].
11. N. Stone, At. Data Nucl. Data Tables **42**, 189 (1989); http://www.nndc.bnl.gov/nndc/stone-moments.
12. Nuclear Reaction Base Data, http://depni.npi.msu.su/cdfe/service/index.html.
13. M. Danos, Nucl. Phys. **5**, 23 (1958); K. Okamoto, Prog. Theor. Phys. **15**, 75 (1956).

Translated by A. Isaakyan

Physics of Atomic Nuclei, Vol. 67, No. 5, 2004, pp. 931–936. Translated from Yadernaya Fizika, Vol. 67, No. 5, 2004, pp. 955–960.

NUCLEI
Theory

Phase Transitions between Axisymmetric and Nonaxial Nuclear Shapes

R. V. Jolos*

Joint Institute for Nuclear Research, Dubna, Moscow oblast, 141980 Russia

Received May 30, 2003; in final form, August 15, 2003

Abstract—Within the interacting-boson model, phase transitions between different nuclear shapes are considered in the space of three control parameters. Depending on the values of these parameters, the equilibrium shape of a nucleus can be spherical, axially deformed, or nonaxial. It is shown that the phase transition from an axisymmetric to a nonaxial deformation is a second-order phase transition. Within the Bohr–Mottelson model, an approximate solution is found that describes a nucleus in the vicinity of the critical point of a phase transition from a spherical to nonaxially deformed shape. The results obtained for the energies and $E2$-transition probabilities are close to experimental data for the ^{134}Ba nucleus. © *2004 MAIK "Nauka/Interperiodica".*

In the Bohr–Mottelson model, the properties of low-lying collective quadrupole excitations of nuclei are associated with vibrations of the nuclear surface. The description of these properties requires numerically solving complicated differential equations or numerically diagonalizing the Hamiltonian matrix, as is done in the interacting-boson model. Only in the particular cases of a harmonic vibrator, an axial rotor, or a β-deformed γ-unstable nucleus, the respective dynamical symmetries within the interacting-boson model being $U(5)$, $SU(3)$, or $O(6)$, is it possible to obtain an analytic solution. However, the majority of the nuclei belong to a so-called transition region between the limits of dynamical symmetries. These transition regions—more precisely, the regions of phase transitions between the limiting symmetries—have always attracted considerable attention.

In recent years, considerable advances have been made in developing methods for analyzing the properties of nuclei at the critical points of relevant phase transitions. Simple analytic solutions were found for the critical points of $U(5)$–$SU(3)$ [1] and $U(5)$–$O(6)$ [2] transitions. A detailed analysis of phase transitions between nuclei of different shapes was performed within the interacting-boson model [3, 4]. An analysis of experimental data revealed that there exist nuclei whose properties are very close to those that are predicted for nuclear systems localized at the critical points [5, 6]. However, the studies in question did not address the possibility of transitions to nonaxial nuclei, but such transitions are of interest, since, in some regions of the nuclide chart, the existence of nonaxially deformed nuclei or at least nuclei that are soft with respect to a transition to nonaxial deformations cannot be ruled out, especially in view of the extension of the range of nuclei under study owing to the appearance of radioactive beams. The objective of the present study is to include nonaxial shapes in the analysis of phase transitions between different nuclear shapes. Our consideration will be performed within the interacting-boson model since this model is especially convenient in dealing with systems involving a finite number of particles.

The geometric shape of a nucleus in the ground state can be conveniently described in terms of three Euler angles specifying the orientation of a deformed nucleus in the laboratory frame and in terms of the deformation parameters β and γ. A coherent state $|N, \beta, \gamma\rangle$ can be constructed by using these parameters as [7]

$$|N, \beta, \gamma\rangle = \frac{1}{\sqrt{N!(1+\beta^2)^N}}(B^+)^N|0\rangle, \qquad (1)$$

where

$$B^+ \equiv s^+ + \beta\Big(\cos\gamma \cdot d_0^+ + \frac{1}{\sqrt{2}}\sin\gamma(d_2^+ + d_{-2}^+)\Big). \qquad (2)$$

Here, s^+ is the monopole-boson creation operator, d_μ^+ is the quadrupole-boson creation operator, N is the total number of monopole and quadrupole bosons, and $|0\rangle$ is the boson vacuum.

Averaging the Hamiltonian over the state specified in (1), we obtain the nuclear-deformation en-

*e-mail: jolos@thsun1.jinr.ru

ergy $E(N;\beta,\gamma)$,

$$E(N;\beta,\gamma) = \langle N,\beta,\gamma|\hat{H}|N,\beta,\gamma\rangle, \qquad (3)$$

where $\hat{H}$ is the nuclear Hamiltonian.

We take this Hamiltonian in the form

$$\hat{H} = \eta\hat{n}_d - \frac{1-\eta}{N}\hat{Q}_\chi\cdot\hat{Q}_\chi + \sum_r c_r((d^+d^+)_{l(r)}d^+)_r\cdot((\bar{d}\bar{d})_{l(r)}\bar{d})_r, \qquad (4)$$

where $\hat{n}_d = d^+\cdot\bar{d}$ is the operator of the number of d bosons and $\hat{Q}_\chi = (d^+s + s\bar{d})_2 + \chi(d^+\bar{d})_2$ is the quadrupole operator.

The dot symbol between the operators in (4) denotes a scalar product. The first two terms in (4) are standard. The parameter η takes values in the region $0 \le \eta \le 1$, while the parameter χ varies within the range $-\sqrt{7}/2 \le \chi \le \sqrt{7}/2$. The last term was taken from [8]. Owing to the inclusion of this term in the Hamiltonian, the deformation energy can have a minimum that corresponds to a nonaxial form. The coupling constants c_r ($r = 0, 2, 3, 4, 6$) are defined below.

Averaging the Hamiltonian in (4) over the state specified in (1) and requiring that the constants c_r obey the constraints

$$\frac{1}{5}c_2 - \frac{1}{7}c_3 + \frac{3}{49}c_4 + \frac{14}{55}c_6 = 0, \qquad (5)$$

$$\frac{2}{35}c_0 + \frac{1}{7}c_3 + \frac{3}{35}c_4 - \frac{8}{385}c_6 = \zeta(1-\eta)\frac{1}{N(N-1)}, \qquad (6)$$

we obtain the deformation energy $E(N,\eta,\chi,\zeta;\beta,\gamma)$ in the form

$$E(N,\eta,\chi,\zeta;\beta,\gamma) = -5(1-\eta) + \frac{1}{(1+\beta^2)^2}\left\{(N\eta - (1-\eta)(4N+\chi^2-8))\beta^2 + \left(N\eta + (1-\eta)\left(4 - \frac{2N+5}{7}\chi^2\right)\right)\beta^4 + 4(N-1)(1-\eta)\sqrt{\frac{2}{7}}\chi\beta^3\cos 3\gamma + \zeta(N-2)(1-\eta)\frac{\beta^6\cos^2 3\gamma}{1+\beta^2}\right\}. \qquad (7)$$

We assume that the parameter ζ is positive. In contrast to what occurred in the case considered in [4], the last term depends on three control parameters η, χ, and ζ rather than on two parameters. Therefore, a three-dimensional space of control parameters is required for considering nonaxial shapes of nuclei.

An analysis of the points of stationarity of $E(N,\eta,\chi,\zeta;\beta,\gamma)$ revealed that, at small values of η, the deformation energy $E(N,\eta,\chi,\zeta;\beta,\gamma)$ has a minimum that corresponds to a nonaxial deformed shape of a nucleus, provided that the control parameters η, χ, and ζ satisfy the following two conditions:

$$N\eta < (1-\eta)\left(4N + \chi^2 - 8 - \frac{8(N-1)^2\chi^2}{7(N-2)\zeta}\right), \qquad (8)$$

$$\frac{\left((1-\eta)\left(4N+\chi^2-8-\frac{8(N-1)^2\chi^2}{7(N-2)\zeta}\right) - N\eta\right)^{3/2}}{4(1-\eta)(N-1)\left(2-\frac{1}{7}\chi^2\right)\sqrt{N\eta + (1-\eta)\left(4N - \frac{4N+3}{7}\chi^2 + \frac{8(N-1)^2\chi^2}{7(N-2)\zeta}\right)}} > 2\frac{N-1}{N-2}\sqrt{\frac{2}{7}\chi^2}\frac{1}{\zeta}. \qquad (9)$$

The parameters η, χ, and ζ can vary within certain boundaries that determine a triangular prism. The base of this prism lies in the $\zeta = 0$ plane and is an extended Casten triangle [4] (see figure). Thus, conditions (8) and (9) determine a surface in the space of control parameters. This surface separates the parameter region where there exists a nonaxial deformed minimum from the region where there is no nonaxial deformation.

Condition (8) imposes an upper bound on η,

$$\eta < \frac{4N - 8 + \chi^2 - \frac{8(N-1)^2\chi^2}{7(N-2)\zeta}}{5N - 8 + \chi^2 - \frac{8(N-1)^2\chi^2}{7(N-2)\zeta}}, \qquad (10)$$

while condition (9) imposes a lower bound on ζ. For $N \to \infty$, the latter takes the form

$$\zeta\left(1 - \frac{2\chi^2}{7\zeta}\right) > 8\sqrt{\frac{\chi^2}{7}}. \qquad (11)$$

From (11), one can see that the lower bound on ζ is determined predominantly by the quantity χ. By way of example, we indicate that, at χ close to zero and η satisfying the condition in (10), the nonaxial deformed minimum appears at ζ values close to zero. At $|\chi| = \sqrt{7}/2$, the minimum value of ζ that ensures the emergence of a nonaxial minimum is $\zeta \approx 4.18$. Thus, nuclei featuring a nonaxial deformation or nuclei that are soft with respect to deviations from axial symmetry are most likely to appear, as might have been expected, in the region around $\chi \approx 0$. These are, for example, the isotopes of Ba, Pt, and Os.

If the conditions of the emergence of a nonaxial deformed minimum are not satisfied, then such a minimum is localized at $\gamma = 0$ ($\chi < 0$) or $\gamma = \pi/3$ ($\chi > 0$). The constraint imposed on η by the requirement that an axisymmetric minimum exist has the form

$$N\eta < (1-\eta)\left\{4N + \chi^2 - 8 - \frac{8(N-1)^2\chi^2}{7(N-2)\zeta} + 3\beta_{\min}\zeta(N-2) \times \left|\frac{\beta_{\min}^3}{1+\beta_{\min}^2} - 2\frac{(N-1)}{(N-2)}\sqrt{\frac{2}{7}\chi^2}\frac{1}{\zeta}\right| + \zeta(N-2) \times \left(\frac{\beta_{\min}^3}{1+\beta_{\min}^2} - 2\frac{(N-1)}{(N-2)}\sqrt{\frac{2}{7}\chi^2}\frac{1}{\zeta}\right)^2\right\}, \quad (12)$$

where $\beta_{\min}$ is the value of the parameter β at the minimum. Comparing (12) with the condition in (8), one can see that, as η increases from zero, the condition in (8) ceases to be valid at some value of η, but the constraint in (12) holds. This means that, with increasing η, a deformed nonaxial minimum goes over to a deformed axisymmetric minimum. As will be shown below, this is a second-order phase transition. In this case, a deformed axisymmetric and a deformed nonaxial phase do not coexist. The distinction between these two phases disappears along the transition line. As η increases further ($\chi \neq 0$), there appears a minimum at $\beta = 0$, but the minimum at nonzero β still exists. The depths of these minima become equal at $\eta = \eta_{\text{crit}}$ [4].

Let us consider in detail the transition from an axisymmetric to a nonaxial nuclear shape. Under the condition that there exists a nonaxial deformed minimum, we have

$$E(N,\eta,\chi,\zeta;\beta,\gamma_{\min}) = N\eta - (1-\eta)\left(1 + \frac{2N+5}{7}\chi^2\right) - \frac{1}{1+\beta^2} \times \left\{N\eta + (1-\eta)\left(4N - \frac{4N+3}{7}\chi^2\right) + (1-\eta)\frac{8(N-1)^2\chi^2}{7(N-2)\zeta}\right\} + \frac{1}{(1+\beta^2)^2}2(1-\eta) \times (N-1)\left(2 - \frac{1}{7}\chi^2\right). \quad (13)$$

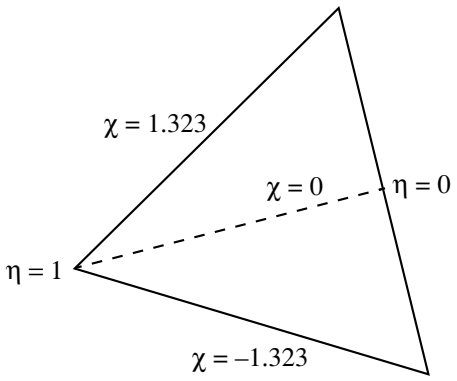

Extended Casten triangle ($\zeta = 0$).

If the deformed minimum is axisymmetric (that is, if ζ is not very large), then

$$E(N,\eta,\chi,\zeta;\beta,\gamma = 0 \text{ or } \pi/3) = N\eta - (1-\eta)\left(1 + \frac{2N+5}{7}\chi^2\right) - \frac{1}{1+\beta^2}\left\{N\eta + (1-\eta)\left(4N - \frac{4N+3}{7}\chi^2\right) + (1-\eta)\frac{8(N-1)^2\chi^2}{7(N-2)\zeta}\right\} + \frac{1}{(1+\beta^2)^2}2(1-\eta) \times (N-1)\left(2 - \frac{1}{7}\chi^2\right) + (1-\eta)\zeta(N-2) \times \left(\frac{\beta^3}{1+\beta^2} - 2\frac{(N-1)}{(N-2)}\sqrt{\frac{2}{7}\chi^2}\frac{1}{\zeta}\right)^2 \frac{1}{1+\beta^2}. \quad (14)$$

A detailed consideration revealed that, if

$$\frac{\beta^3}{1+\beta^2} < 2\frac{(N-1)}{(N-2)}\sqrt{\frac{2}{7}\chi^2}\frac{1}{\zeta}, \quad (15)$$

then there exists only an axisymmetric deformed minimum. By equating the derivative of expression (14) with respect to β to zero, one can obtain the position of this minimum with respect to β.

If

$$\frac{\beta^3}{1+\beta^2} > 2\frac{(N-1)}{(N-2)}\sqrt{\frac{2}{7}\chi^2}\frac{1}{\zeta} \quad (16)$$

[this condition is equivalent to (9)], then a nonaxial deformed minimum appears instead of an axisymmetric deformed minimum. The position of this minimum can be found by equating the derivative of expression (13) with respect to β to zero. At the point of the

phase transition from an axisymmetric deformation to a nonaxial deformation, we have

$$\frac{\beta^3}{1+\beta^2} = 2\frac{(N-1)}{(N-2)}\sqrt{\frac{2}{7}\chi^2}\frac{1}{\zeta}. \quad (17)$$

From a comparison of (13) and (14), one can see that the deformation energy at the phase-transition point is a continuous function of the control parameters. Since Eqs. (13) and (14) differ by the term that is quadratic in

$$\left(\frac{\beta^3}{1+\beta^2} - 2\frac{(N-1)}{(N-2)}\sqrt{\frac{2}{7}\chi^2}\frac{1}{\zeta}\right), \quad (18)$$

the first derivatives of the deformation energy with respect to the control parameters are also continuous at the phase-transition point. However, the second derivatives undergo a discontinuity at this point. Therefore, the transition from an axisymmetric to a nonaxial deformation is a second-order phase transition.

Let us consider the behavior of nuclei in the vicinity of the critical point in η at ζ values ensuring the appearance a nonaxial minimum. For this purpose, we use the Bohr–Mottelson equation

$$\left\{-\frac{\hbar^2}{2B}\left[\frac{1}{\beta^4}\frac{\partial}{\partial\beta}\left(\beta^4\frac{\partial}{\partial\beta}\right) + \frac{1}{\beta^2}\left(\frac{1}{\sin 3\gamma}\frac{\partial}{\partial\gamma}\left(\sin 3\gamma\frac{\partial}{\partial\gamma}\right) - \frac{1}{4}\sum_{k=1}^{3}\frac{\hat{I}_k^2}{\sin^2\left(\gamma-\frac{2\pi}{3}k\right)}\right)\right] + V(\beta,\gamma) - E\right\}\Psi(\beta,\gamma,\theta_i) = 0, \quad (19)$$

where θ_i are three Euler angles, B is the mass coefficient, $\hat{I}_k$ stands for the components of the angular-momentum operator, and the index k numbers the axes of the intrinsic coordinate frame. The potential $V(\beta,\gamma)$ has the form

$$V(\beta,\gamma) = u(\beta) + \frac{1}{2}D\beta^6\cos^2 3\gamma. \quad (20)$$

We assume that the stiffness coefficient D is so large that it is legitimate to consider only small-amplitude vibrations about the point $\gamma = \pi/6$. Equation (19) then approximately takes the form

$$\left\{-\frac{\hbar^2}{2B}\left[\frac{1}{\beta^4}\frac{\partial}{\partial\beta}\left(\beta^4\frac{\partial}{\partial\beta}\right) + \frac{1}{\beta^2}\left(\frac{\partial^2}{\partial x^2} - \frac{9DB}{\hbar^2}\beta^8x^2 - I(I+1) + \frac{3}{4}I_1^2\right)\right] + u(\beta) - E\right\}\Psi(\beta,x,\theta_i) = 0, \quad (21)$$

where $x = \gamma - \pi/6$, while I is the total angular momentum. From (21), it is clear that one can factor out the dependence on the variables x and θ_i in the total wave function; that is,

$$\Psi(\beta,x,\theta_i) = f(\beta)\exp\left(-\frac{B\omega}{2\hbar}\beta^4x^2\right) \times \frac{1}{\sqrt{\sqrt{\pi}n!2^n}}H_n\left(x\beta^2\sqrt{\frac{B\omega}{\hbar}}\right)D^I_{MK}(\theta_i), \quad (22)$$

where $\omega = 3(D/B)^{1/2}$; H_n is a Hermite polynomial, $n = 0,1,2,\ldots$; D^I_{MK} is a Wigner function; and K is the angular-momentum projection onto the intrinsic-coordinate-frame axis 1 corresponding to a minimum of the moment of inertia. From the point of view of the interacting-boson model, the assumption that the minimum with respect to γ is localized at $\gamma = \pi/6$ corresponds to $\chi = 0$. But at $\chi = 0$, a nonaxial minimum appears even at small values of ζ. An increase in ζ leads only to an increase in the energy of the 0^+_τ state.

The equation for the function $f(\beta)$ has the form

$$\left\{-\frac{\hbar^2}{2B}\frac{1}{\beta^4}\frac{\partial}{\partial\beta}\left(\beta^4\frac{\partial}{\partial\beta}\right) + \frac{1}{\beta^2}\frac{\hbar^2}{2B}\left(I(I+1) - \frac{3}{4}K^2\right) + u(\beta) + \hbar\omega\left(n+\frac{1}{2}\right)\beta^2 - E\right\}f(\beta) = 0. \quad (23)$$

Following [2], we approximate the effective potential energy as a function of β by a square-well potential; that is,

$$u(\beta) + \hbar\omega\left(n+\frac{1}{2}\right)\beta^2 = \hbar\omega\left(n+\frac{1}{2}\right)\langle\beta^2\rangle, \quad \beta \le \beta_w; \quad (24)$$

$$u(\beta) + \hbar\omega\left(n+\frac{1}{2}\right)\beta^2 \to \infty, \quad \beta > \beta_w,$$

where β_w is the maximum value of β. We then have

$$f(\beta) = \beta^{-3/2}C_{lIK}J_\nu(k_{lIK}\beta), \quad (25)$$

where $\nu = \sqrt{I(I+1) - \frac{3}{4}K^2 + \frac{9}{4}}$; $k_{lIK} = x_{lIK}/\beta_w$, x_{lIK} being the lth root of $J_\nu(z)$, $l = 1,2,3,\ldots$; and $C_{lIK} = (\sqrt{2}/\beta_w)J'_\nu(x_{lIK})$. The energy of a state characterized by the quantum numbers $lIKn$ has the form

$$E_{lIKn} = \frac{\hbar^2}{2B\beta_w^2}x^2_{lIK} + \hbar\omega n\langle lIKn|\beta^2|lIKn\rangle. \quad (26)$$

Table 1. Ratios of the energies of low-lying states according to our calculations (Th), along with the experimental data for ^{134}Ba and with the results obtained in the limit of $E(5)$ symmetry

	$E(4_1^+)/E(2_1^+)$	$E(6_1^+)/E(2_1^+)$	$E(2_2^+)/E(2_1^+)$	$E(0_\beta^+)/E(2_1^+)$
Th	2.35	3.98	1.84	3.91
^{134}Ba	2.31	3.66	1.93	3.57
$E(5)$	2.20	3.59	2.20	3.03

Table 2. Ratios of the $E2$-transition probabilities according to our calculations (Th), along with the experimental data for ^{134}Ba and with the results obtained in the limit of $E(5)$ symmetry

	$\frac{B(E2;4_1^+\to 2_1^+)}{B(E2;2_1^+\to 0_1^+)}$	$\frac{B(E2;2_2^+\to 2_1^+)}{B(E2;2_1^+\to 0_1^+)}$	$\frac{B(E2;0_\beta^+\to 2_1^+)}{B(E2;2_1^+\to 0_1^+)}$	$\frac{B(E2;0_\beta^+\to 2_2^+)}{B(E2;0_\beta^+\to 2_1^+)}$
Th	1.59	1.62	0.75	0
^{134}Ba	1.56(18)	2.2 ± 0.7	0.42(12)	0.18(8)
$E(5)$	1.68	1.68	0.86	0

The quadrupole-moment operator, which is used in calculating the probabilities of $E2$ transitions, has the form

$$Q_{2\mu} = e_2\beta\left(D^2_{\mu 0}\cos\gamma + \frac{1}{\sqrt{2}}(D^2_{\mu 2} + D^2_{\mu -2})\sin\gamma\right), \quad (27)$$

where e_2 is an effective charge. But we did not use such an effective charge because we calculated only the ratios of the $E2$-transition probabilities.

The results obtained by calculating the ratios of the energies of several low-lying states and the ratios of the $E2$-transition probabilities are given in Tables 1 and 2, respectively, along with results derived in the limit of $E(5)$ symmetry [2] and with experimental data for ^{134}Ba. The ^{134}Ba nucleus is chosen for a comparison since it is the closest to the transition region with respect to the deformation parameter β and since it is simultaneously γ-unstable [9].

One can see from Tables 1 and 2 that our results are in good agreement with the data for ^{134}Ba. At the same time, our results are similar to those obtained in the limit of $E(5)$ symmetry, although there are small distinctions. For example, the ratio $E(2_2^+)/E(2_1^+)$ in the ^{134}Ba nucleus is closer to our results, while $E(6_1^+)/E(2_1^+)$ is better described in the limit of $E(5)$ symmetry. This $E(5)$ symmetry assumes that the potential energy is independent of γ, while, in our calculations, it is assumed that the deformation energy at given β has a minimum at $\gamma = \pi/6$. Therefore, it is difficult to choose between these two assumptions on the basis of the existing data for ^{134}Ba. We note that it is of importance to take into account the finiteness of the number of valence nucleons, since the results obtained in the interacting-boson model for $N = 5$ differ slightly from those obtained in the Bohr–Mottelson model in the limit of $E(5)$ symmetry. However, our results must be compared with the limit of $E(5)$ symmetry of the Bohr–Mottelson model because both models are based on the same Hamiltonian.

In summary, we have considered phase transitions between different nuclear shapes in the space of three control parameters η, χ, and ζ, relying on the interacting-boson model. Depending on the values of these parameters, the equilibrium shape of a nucleus can be spherical, axisymmetrically deformed, or nonaxial. It has been shown that, at $\chi \approx 0$, a small increase in the parameter ζ may lead to the appearance of a nonaxial minimum. By using the Hamiltonian of the Bohr–Mottelson model, we have further considered the case where the deformation energy has a minimum at $\gamma = \pi/6$, but where the system in question is still β-unstable. In this case, the results for the energies and the probabilities of $E2$ transitions are close to those obtained in the limit of $E(5)$ symmetry (β and γ instability), although they differ slightly from the latter. At the same time, our results are close to experimental data for ^{134}Ba. Therefore, the inclusion of a nonaxial deformation in the consideration extends the possible region of various phase transitions. The inclusion of nonaxiality can also be useful in interpreting experimental data for nuclei that are considered as γ-unstable objects.

ACKNOWLEDGMENTS

This work was supported by the Russian Foundation for Basic Research (project no. 01-02-16033).

REFERENCES

1. F. Iachello, Phys. Rev. Lett. **87**, 052502 (2001).
2. F. Iachello, Phys. Rev. Lett. **85**, 3580 (2000).
3. J. Jolie, R. F. Casten, P. von Brentano, and V. Werner, Phys. Rev. Lett. **87**, 162501 (2001).
4. J. Jolie *et al.*, Phys. Rev. Lett. **89**, 182502 (2002).
5. F. Iachello, N. V. Zamfir, and R. F. Casten, Phys. Rev. Lett. **81**, 1191 (1998).
6. R. F. Casten and N. V. Zamfir, Phys. Rev. Lett. **87**, 052503 (2001).
7. J. N. Ginocchio and M. W. Kirson, Nucl. Phys. A **350**, 31 (1980).
8. P. Van Isacker and J. Q. Chen, Phys. Rev. C **24**, 684 (1981).
9. R. F. Casten and N. V. Zamfir, Phys. Rev. Lett. **85**, 3584 (2000).

Translated by S. Slabospitsky

Physics of Atomic Nuclei, Vol. 67, No. 5, 2004, pp. 937–948. Translated from Yadernaya Fizika, Vol. 67, No. 5, 2004, pp. 961–971.

NUCLEI
Theory

Relativistic Treatment of Bremsstrahlung in the Process $pp \to pp\gamma$ with Allowance for Isobar Channels and Possibility of Discriminating between Different Types of Nucleon–Nucleon Interaction

V. A. Knyr* **and N. A. Khokhlov****

Khabarovsk State Technological University, Tikhookeanskaya ul. 136, Khabarovsk, 680034 Russia

Received August 5, 2003

Abstract—A relativistic quasipotential formalism for describing electromagnetic processes involving nucleons that takes into account an explicit coupling to the $N\Delta$ (1232 MeV) and NN^* (1440 MeV) channels is developed. On one hand, this formalism is a relativistic generalization of the Lomon–Ray approach to describing nucleon–nucleon scattering within a framework explicitly including isobar degrees of freedom; on the other hand, it relies on the formalism developed by Lev [F.M. Lev, hep-ph/9403222] within relativistic quantum mechanics for constructing the electromagnetic-current operator for interacting particles. The formalism makes it possible to obtain a consistent description of a two-nucleon system in the energy region extending up to 1 GeV. It is applied to describing the reaction $pp \to pp\gamma$ over a kinematical region in which corrections associated with a virtual delta isobar are of importance. The sensitivity of this reaction to the type of the short-range component of the nucleon–nucleon potential and the possibility of discriminating between the Moscow potential and meson-exchange potentials on the basis of experimental data are confirmed. © *2004 MAIK "Nauka/Interperiodica".*

1. INTRODUCTION

Constructing the nucleon–nucleon interaction is one of the most important problems in theoretical nuclear physics. Much effort has been undertaken over the past fifty years in order to describe this interaction in terms of a relevant potential. The long-range part of the nucleon–nucleon interaction is well explained by the meson-exchange mechanism proposed long ago by Yukawa, but its short-range part is still being described phenomenologically [1]. Moreover, there are radically different approaches to describing the short-range part of the nucleon–nucleon interaction. Although the quark structure of nucleons is generally recognized, work on refining meson-exchange potentials is still being continued [2–4]. In this connection, much hope is placed on so-called effective-field theory [1]. The advocates of this theory assume that one can quite clearly single out energy regions where different mechanisms of the nucleon–nucleon interaction are operative—in particular, they believe that the use of the meson-exchange mechanism is legitimate up to an energy of 300 to 400 MeV. A repulsive core at a distance of about 0.5 fm between pointlike nucleons is a feature peculiar to meson-exchange potentials. For this reason, we classify such potentials among those that involve a repulsive core, including in this class potentials possessing this property that were obtained from quark calculations [5].

Yet, this point of view is not prevalent, since there are reasons to believe that more fundamental quark–gluon degrees of freedom must manifest themselves even in this energy region [6]. Numerical calculations of the parameters of the nucleon–nucleon potential are much more cumbersome in quark models than in meson-exchange models; for this reason, meson-exchange potentials provide a much better description of the properties of the deuteron and the scattering of two nucleons. Calculations of the parameters of the nucleon–nucleon potential within quark models yield rather contradictory results because of the unwieldiness of such calculations and the impossibility of using a reliable quark–quark interaction. In particular, the wave function for two nucleons at short distances between them may die out sharply at some parameters of gluon exchange between quarks, this corresponding to a repulsive core in meson-exchange potentials. This result confirms effective-field theory and, obviously, justifies the use of meson-exchange models at low energies.

However, there are calculations within the quark-model approach [7, 8] that predict, on the basis of the symmetry properties of a six-quark system, the existence of channels featuring a strong attraction in nucleon–nucleon systems. For example, it was

*e-mail: knyr@fizika.khstu.ru
**e-mail: khokhlov@fizika.khstu

shown that, in the case of a colormagnetic qq interaction of $\lambda\lambda\sigma\sigma$ symmetry, such an attraction is caused by the excitation of an $s^4p^2[42]_X[42]_{CS}$ quark configuration in the S and D waves. Such configurations become energetically favorable if the strength of qq interaction is sufficiently great. On the basis of these ideas, the model of the phenomenological Moscow nucleon–nucleon potential (Moscow potential) was developed in [9, 10]. The wave-function node associated with the aforementioned excited quark configurations is a feature characteristic of this potential. Thus, the Moscow potential does not have a repulsive core; on the contrary, it has a depth of about 1 to 2 GeV at internucleon distances less than 1 fm. Within the Moscow potential model, extra bound states that could arise owing to this are forbidden by the Pauli exclusion principle for the corresponding six-quark states. This approach provides a good description of the properties of the deuteron and the properties of low-energy nucleon–nucleon scattering [9–12]. Also, the differential cross sections and polarizations for nucleon–nucleon scattering in the region extending up to an energy of 5 to 6 GeV were described on its basis for the first time. Yet another spectacular piece of evidence in favor of the Moscow potential was obtained quite recently. It was shown in [13] that, by using the same central potential of the Moscow type (that is, that which has a depth about 2 GeV and which involves forbidden states), one can obtain nucleon–nucleon phase shifts for all S and P states, along with the deuteron binding energy. In doing this, the tensor component of the interaction is described by a meson-exchange potential. In this model, the number of free parameters is severalfold smaller than in the pioneering studies reported in [11, 12] and is smaller than in traditional meson-exchange models [2–4] by a factor of a few tens. Obviously, this agreement between the potentials for all S and P waves, which has never been observed for meson-exchange potentials, cannot be accidental.

Of course, the problem of experimentally discriminating between these two types of nucleon–nucleon potentials (as was indicated above, they display totally different types of behavior at short distances) is of great importance. In the momentum representation, the fact that potentials of the two types behave differently in coordinate space at short distances is reflected in the difference in the off-shell behavior of the T matrix. Upon appropriately fitting free parameters, which are present in all models of the nucleon–nucleon interaction, by no means can this difference be traced in two-nucleon systems, but it is expected to manifest itself in one way or another in any of the more complicated systems of particles. Numerous investigations revealed that distinctions between potentials involving a repulsive core are virtually immaterial and do not show up in either the properties of the triton, reactions of deuteron photo- and electrodisintegration, bremsstrahlung from proton–proton scattering, or the properties of more complex nuclei [14]. Moreover, it can be stated that these distinctions are not of fundamental importance, since, to a considerable extent, they are of a purely phenomenological origin. On the other hand, the distinction between potentials having a repulsive core and the Moscow potential is of a conceptual character, because the underlying microscopic pictures are totally different in these two cases.

Among numerous processes listed above, we chose bremsstrahlung in proton–proton scattering as a tool for studying the short-range behavior of the nucleon–nucleon potential. In relation to the others, it possesses the following properties convenient for the purposes of our investigation. First of all, it involves three particles, but only two of these interact strongly—it is sufficient to take into account the interaction with the third one (photon) in the first order of perturbation theory in electromagnetic interaction. Second, this reaction is unaffected by three-body nucleon–nucleon forces. Previously, it was assumed that effects caused by meson-exchange currents and by virtual-delta-isobar emission associated with them are also inoperative in this reaction, at least for energies below the threshold for this channel. However, this assumption was disproved by the calculations reported in [15]. According to the results of those calculations, such effects come into play from an energy of 280 MeV, effects associated with the emission of a virtual delta isobar being dominant there.

Only popular meson-exchange potentials, like the Bonn, Nijmegen, and Paris potentials, were studied in calculations performed for the reaction $pp \to pp\gamma$. All of these calculations lead to the conclusion that available experimental data on the reaction $pp \to pp\gamma$ are insufficient for discriminating between these potentials both because of large experimental uncertainties stemming from a low probability of this process in relation to proton–proton scattering and because of the dependence of the results on model assumptions for this reaction that are not fixed by a specific choice of potential [16]. The results of the calculations performed in [17–19] confirm these conclusions. At the same time, the important conclusion that, by studying hard bremsstrahlung from the reaction $pp \to pp\gamma$ at proton-beam energies in the range 350–500 MeV, one can efficiently distinguish between meson-exchange potentials and the Moscow potential was drawn from the calculations in [17–19].

In the present study, we pursue further the analysis of nucleon–nucleon potentials at short distances on the basis of the reaction $pp \to pp\gamma$, substantially

refining and extending the relativistic quasipotential formalism developed in [19] for describing the reaction $pp \to pp\gamma$ with allowance for the $N\Delta(1232\ \text{MeV})$ and $NN^*(1440\ \text{MeV})$ isobar reaction channels. The need for employing a relativistic formalism from an energy of $E_{\text{lab}} = 280$ MeV was demonstrated in [19]. The ensuing exposition is organized as follows. In Section 2, we give, among other things, a description of a two-proton system within the pointlike form of relativistic quantum mechanics, taking explicitly into account coupling to isobar reaction channels, and also obtain the electromagnetic-current operator for a two-nucleon system, explicitly including coupling to isobar channels, whereby we generalize the formalism developed by Lev in [20] for constructing the operator of an electromagnetic current for interacting particles. In Section 3, we compare the results of our calculations for the reaction $pp \to pp\gamma$ with other theoretical results and with experimental data and draw conclusions concerning the potentials under study.

2. DESCRIPTION OF THE FORMALISM USED

The relativistic quantum mechanics of systems that consist of a fixed number of particles is based on the conjecture that, at not very high energies, relativistic effects can be taken into account by assuming that the number of particles is constant, but that it is the Lorentz rather than the Galilei group that is the group of invariance for the system being considered. In [17–19], it was shown that, in just the same way as in the nonrelativistic case, the total wave function for a system of two nucleons can be represented as the product of two wave functions, that which describes the motion of the system as a discrete unit and that ($\chi(\mathbf{r})$) which describes the relative motion of the constituent nucleons.

In [19], it was shown that use can be made of a relativistic quasipotential equation for the function $\chi(\mathbf{r})$; that is,

$$[4(m^2+q^2)+V]\chi = M^2\chi \qquad (1)$$
$$\text{or}\left(\frac{q^2}{m}+\frac{V}{4m}\right)\chi = E\chi,$$

where

$$E = \frac{M^2-4m^2}{4m}. \qquad (2)$$

Here, M^2 is the operator of the square of the mass of a two-nucleon system, m is the nucleon mass, V is the nucleon–nucleon potential, and $\mathbf{q}$ is the momentum operator of one of the nucleons in the c.m. frame. Hereafter, we employ the system of units where $\hbar = c = 1$. A complete formal similarity of the present formulation to nonrelativistic theory is achieved in the representation of the relative quasicoordinate $\mathbf{r}$, which is related to the operator $\mathbf{q}$ by the conventional equation $\mathbf{q} = -i\dfrac{\partial}{\partial \mathbf{r}}$. Thus, Eq. (1) is a relativistic equation for eigenvalues and eigenfunctions of the operator of the mass squared, on one hand, and formally coincides with the nonrelativistic Schrödinger equation, on the other hand.

In order to describe isobar degrees of freedom of the nucleon–nucleon system, we generalize the relativistic quasipotential formalism developed in [19], employing the Lomon–Ray approach [21]. Here, the potential V in Eq. (1) already includes coupling to proton–isobar channels.

Upon expanding the relative-motion wave function $\chi(\mathbf{r})$ in partial waves in order to describe the nucleon–nucleon system with allowance for the $N\Delta$ and NN^* channels within the above approach, we arrive at the set of equations

$$\left[\frac{d^2}{dr^2} - \frac{l_i(l_i+1)}{r^2} - 2\mu_i V_{ii} + k_i^2\right]\chi_i = 2\mu_i \sum_{i\neq j} V_{ij}\chi_j, \qquad (3)$$

$$\left[\frac{d^2}{dr^2} - \frac{l_j(l_j+1)}{r^2} - 2\mu_j V_{jj} + k_j^2 + i\mu_j\Gamma_j\right]\chi_j = 2\mu_j \sum_{i\neq j} V_{ji}\chi_i. \qquad (4)$$

Equation (3) represents a singlet or two coupled triplet nucleon–nucleon channels. Equation (4) describes one or two isobar channels. The reduced mass in the ith channel is

$$\mu_i = \frac{m_i^{(1)} m_i^{(2)}}{m_i^{(1)} + m_i^{(2)}}, \qquad (5)$$

where m_i is the nucleon mass (938.5 MeV) or the mass of an isobar (1232 and 1440 MeV), and l_i is the orbital angular momentum in the ith channel.

As in [21], the channel wave numbers are described here by the relativistic expression

$$k_j^2 = \frac{s}{4} - \frac{\left(m_j^{(1)}\right)^2 + \left(m_j^{(2)}\right)^2}{2} + \frac{\left[\left(m_j^{(1)}\right)^2 - \left(m_j^{(2)}\right)^2\right]^2}{4s}, \qquad (6)$$

where $s = 2m_N(2m_N + E_{\text{lab}})$ is the square of the total invariant mass of the two-nucleon system. It is this relation between the wave number and the mass of the system that enables us to use Eqs. (3) and

(4) as the quasipotential Eq. (1) written for partial waves in the c.m. frame. The relativistic invariance of the description is guaranteed by expressing the generators of the Lorentz group [22] for the system in terms of the mass operator corresponding to Eq. (1).

In the nucleon–isobar channel, the asymptotic expression for the wave function has the form of a spherical Hankel function of a complex argument. For example, the asymptotic expression corresponding to the S wave is

$$\chi_{r\to\infty} = e^{-k_R r} e^{ik_I r}, \tag{7}$$

$$k_{R(I)} = \pm\frac{1}{\sqrt{2}}\left(\left[k_j^4 + (\mu_j\Gamma_j)^2\right]^{1/2} \mp k_j^2\right)^{1/2}, \tag{8}$$

where the upper and the lower sign refer to k_R and k_I, respectively, and the case of $k_R \geq 0$ and $k_I \leq 0$ corresponds to a damped diverging wave of finite radius, which is determined by the lifetime of the isobar involved and the degree of virtuality of its excitation.

The isobar widths Γ_j were borrowed from [21]. The notation V_{ij} is used for a symmetric interaction potential. For the potential in the proton–proton channel, we took here the nucleon–nucleon potentials under study (Moscow, Paris [2], and Nijmegen [3] potentials). The off-diagonal elements that describe coupling to nucleon–isobar channels and the potentials in nucleon–isobar channels were borrowed from [21].

In [19], the amplitude for the reaction $pp \to pp\gamma$ was derived in the form

$$A_{i\to f} = \sqrt{\frac{8\pi}{k}}(2\pi)^3\sqrt{M_i M_f}\,\langle\chi_f|\,\varepsilon_\mu^* j^\mu(\mathbf{h})\,|\chi_i\rangle\,, \tag{9}$$

where k is the momentum (energy) of the emitted photon in the reference frame in which the sum of the 3-velocities of the centers of mass of the initial and the final nucleon–nucleon system ($\mathbf{G}_i$ and $\mathbf{G}_f$, respectively) is equal to zero

$$\mathbf{G}_i + \mathbf{G}_f = 0. \tag{10}$$

The vector $\mathbf{h}$ is the three-dimensional vector defined as $\mathbf{h} = \mathbf{G}_i$ in this reference frame (under the Lorentz transformations, it undergoes Wigner rotations); M_i and M_f are, respectively, the initial and the final mass of the two-nucleon system; and ε_μ is the polarization 4-vector. The vector $\mathbf{j}(\mathbf{h})$ has the meaning of an electromagnetic-current operator in the same reference frame.

Using the transverse gauge

$$\varepsilon_\mu = (0,\varepsilon), \quad (\varepsilon\cdot\mathbf{k}) = 0 \tag{11}$$

and taking into account the relation

$$\mathbf{h} = \frac{2\sqrt{M_i M_f}}{(M_i+M_f)^2}\mathbf{k}, \tag{12}$$

we find that the component $j^0(\mathbf{h})$ and the terms in $\mathbf{j}(\mathbf{h})$ that are parallel to $\mathbf{h}$ do not contribute to the amplitude. For a system of noninteracting particles, the expression for the operator $\mathbf{j}(\mathbf{h})$ was obtained in [20] for the case where the initial- and final-state particles are of the same nature. Since we describe a general case where the electromagnetic-interaction operator induces $N \leftrightarrow \Delta(N^*)$ transitions, we generalize the formalism developed in [20] to the case where the electromagnetic-interaction operator changes its nature—in particular, its mass. As a result, the structure formula for the operator $\mathbf{j}(\mathbf{h})$ with allowance for electromagnetic nucleon–isobar transitions has the form

$$\mathbf{j}(\mathbf{h}) = \begin{bmatrix} \mathbf{j}_{NN\to NN}(\mathbf{h}) & \mathbf{j}_{NN\to N\Delta}(\mathbf{h}) & \mathbf{j}_{NN\to NN^*}(\mathbf{h}) \\ \mathbf{j}_{N\Delta\to NN}(\mathbf{h}) & \mathbf{j}_{N\Delta\to N\Delta}(\mathbf{h}) & \mathbf{j}_{N\Delta\to NN^*}(\mathbf{h}) \\ \mathbf{j}_{NN^*\to NN}(\mathbf{h}) & \mathbf{j}_{NN^*\to N\Delta}(\mathbf{h}) & \mathbf{j}_{NN^*\to NN^*}(\mathbf{h}) \end{bmatrix}. \tag{13}$$

The explicit expressions for the operators $\mathbf{j}_{i\to f}(\mathbf{h})$ are derived in Appendix 1.

Expression (12) makes it possible to estimate the quantity h: $h < \dfrac{k}{4m_N}$, where m_N is the proton mass and k is the photon energy in the reference frame determined by the condition in (10). At $k \approx 500$ MeV, we find that $h < 0.125$; therefore, terms of order h^2 and terms of higher orders can be disregarded under the kinematical conditions being considered. We note that the value of $k \approx 500$ MeV corresponds to a photon energy of about 1000 MeV in the laboratory frame.

The differential cross section for the reaction $pp \to pp\gamma$ in the laboratory frame can be expressed in terms of the transition amplitude $A_{i\to f}$ in a standard way [17].

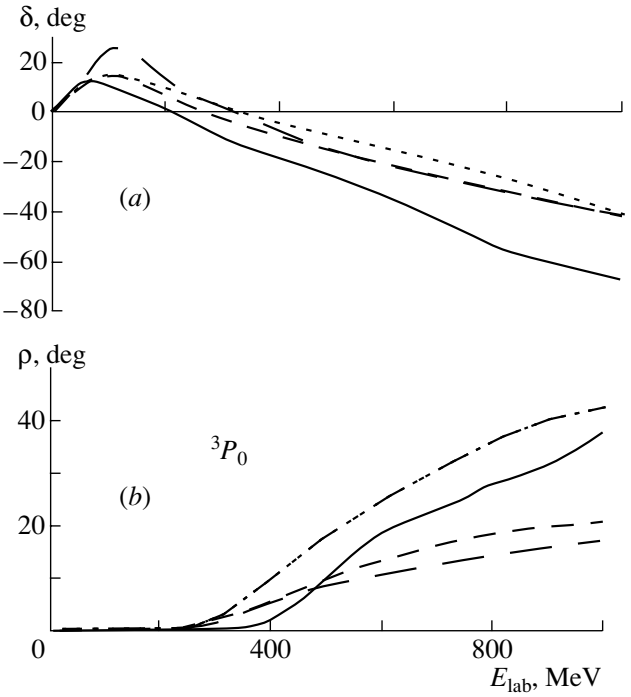

Fig. 1. (*a*) Phase shifts and (*b*) inelasticity parameters for proton–proton scattering versus the incident-proton energy in the laboratory frame: (solid curve) data of the partial-wave analysis from [24], (dash-dotted curve) results of the calculation with the Nijmegen potential, (long-dashed curve) results of the calculation with the Moscow potential [10], (short-dashed curve) results of the calculation with the Moscow potential in the MP92 version [9], and (dotted curve) results of the calculation with the Paris potential. In Fig. 1*a*, the dash-dotted and the short-dashed curve merge, while, in Fig. 1*b*, this occurs for the dash-dotted and the dotted curve.

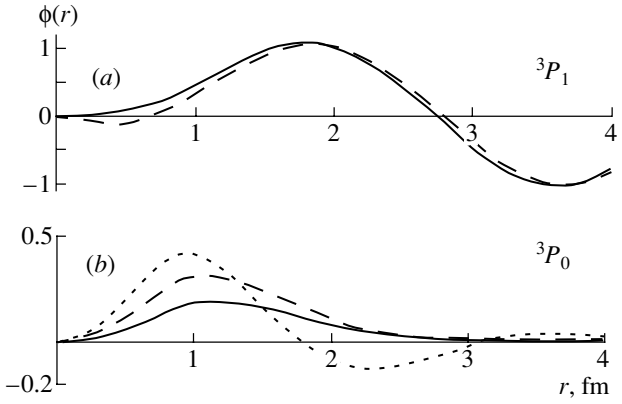

Fig. 2. (*a*) Radial parts $\phi(r)$ of the wave functions (in arbitrary units) in the $pp(^3P_1)$ channel for the Nijmegen potential (solid curve) without and (dashed curve) with allowance for coupling to the $p\Delta$ channel at the incident-proton energy of $E_{\text{lab}} = 280$ MeV. (*b*) Radial parts $\phi(r)$ of the wave functions (in arbitrary units) in the $p\Delta(^3P_0)$ channel at the incident-proton energies of $E_{\text{lab}} =$ (solid curve) 280, (dashed curve) 500, and (dotted curve) 1000 MeV. In the $pp(^3P_1)$ channel, use was made of the Nijmegen potential. The radial parts of the wave functions are normalized by the asymptotic condition $\phi(r) \to \sin(k_{pp}r - L\pi/2 + \delta_L(k_{pp}))$ in the pp channel, where L is the orbital angular momentum in this channel and $\delta_L(k_{pp})$ is the phase shift in the same channel as a function of the wave number k_{pp}.

3. RESULTS OF THE CALCULATIONS AND DISCUSSION

The present study has two objectives, that of determining the contribution of isobar channels to the cross section for the reaction $pp \to pp\gamma$ and that of clarifying the question of whether the possibility of discriminating between meson-exchange potentials and the Moscow potential by analyzing hard bremsstrahlung in the process $pp \to pp\gamma$ over a wide incident-proton-energy region (extending up to 1 GeV in the laboratory frame) survives upon taking into account isobar reaction channels.

In general, the standard parameters of the meson-exchange potentials used in the present study and of the Moscow potential were fitted to experimental data on nucleon–nucleon scattering without explicitly taking into account coupling to nucleon–isobar channels; therefore, the potential parameters must be somewhat modified upon the inclusion of isobar reaction channels in the consideration in order to avoid effects of double counting. Such a modification of the parameters of the meson-exchange potentials and of the Moscow potential was accomplished in [23] by fitting the phenomenological short-range part of these potentials to experimental data on elastic proton–proton scattering for energies up to 300 MeV in the laboratory frame. In the present study, we perform calculations for the reaction $pp \to pp\gamma$ over a broad region of incident-proton energies (which extends up to 1 GeV in the laboratory frame) without additionally fitting the potential parameters because, within available computing facilities, the time required for implementing this procedure would be overly long. Nevertheless, the calculations with the standard parameters of the meson-exchange potentials and the Moscow potential make it possible to answer the questions formulated at the beginning of this section.

At energies around and above the inelasticity threshold, the main contribution to the amplitude for the reaction $pp \to pp\gamma$ comes from transitions between ^3P_J partial waves (at least under the kinematical conditions considered here). In order to prove that, upon taking into account isobar degrees of freedom, the potentials in question nevertheless describe satis-

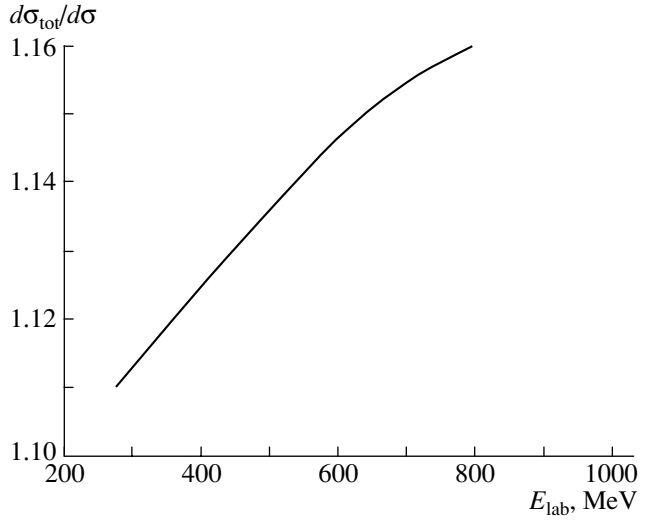

Fig. 3. Ratio $d\sigma_{tot}/d\sigma$ of the total differential cross sections for the process $pp \to pp\gamma$ to the differential cross section obtained by taking into account only transitions from the pp to the pp channel. Given in the figure are the results of the calculation with the Nijmegen potential in the pp channel at the angles of $\theta_1 = 12.4^\circ$ and $\theta_2 = 12.0^\circ$ between the momenta of scattered protons.

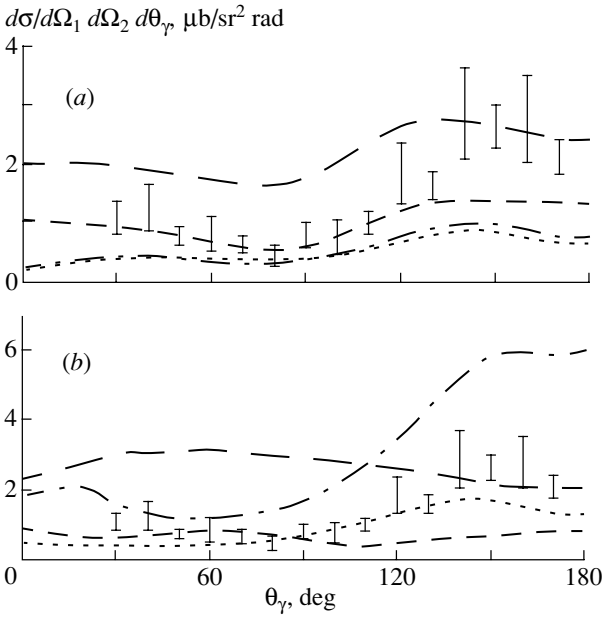

Fig. 4. Differential cross section for the reaction $pp \to pp\gamma$ as a function of the photon emission angle for the case of coplanar geometry (that is, the emitted photon travels toward the angle θ_2) at $\theta_1 = 12.4^\circ$, $\theta_2 = 12.0^\circ$, and $E_{lab} = 280$ MeV: (a) results of the calculation for the Nijmegen potential without allowance for isobar reaction channels (dash-dotted curve), results of the calculation for the Paris potential without allowance for isobar reaction channels (dotted curve), and results of the calculation for the Nijmegen potential in the pp channel with allowance for isobar reaction channels (long-dashed curve), results of the calculation for the Paris potential in the pp channel with allowance for isobar reaction channels (short-dashed curve); (b) results of the calculation for the Moscow potential with dispersion without allowance for isobar reaction channels (dash-dotted curve), results of the calculation for the Moscow potential MP92 without allowance for isobar reaction channels (dotted curve), results of the calculation for the Moscow potential with dispersion in the pp channel with allowance for isobar reaction channels (long-dashed curve), and results of the calculation for the Moscow potential MP92 in the pp channel with allowance for isobar reaction channels (short-dashed curve). The displayed experimental data (points with error bars) were borrowed from [25].

factorily waves that are of importance for the reaction being studied, we have calculated the corresponding phase shifts and inelasticity parameters for proton–proton scattering versus the incident-proton energy. From Fig. 1, where the results of our calculations for the $^3P_0$ partial wave are given along with the data from a partial-wave analysis, it can be seen that, by and large, there is qualitative agreement with these data for all of the potentials used. For the remaining partial waves, $^3P_1$ and $^3P_2$, the situation is similar.

We have investigated the effect of isobar degrees of freedom on the wave functions for the pp system. By way of example, the radial parts of the wave functions in the $pp(^3P_1)$ channel for the Nijmegen potential are given in Fig. 2a without and with allowance for coupling to the $p\Delta$ channel at the incident-proton energy of $E_{lab} = 280$ MeV. From this figure, it can be seen that the $p\Delta$ channel introduces virtually no changes in the asymptotic part of the wave function, but it changes its internal part significantly—for example, a node appears in the internal part of the wave function in the case of the Nijmegen potential. The radial parts of the wave functions in the $p\Delta(^3P_0)$ channel (in the corresponding pp channel, use is made of the Nijmegen potential) are displayed in Fig. 2b at the energies of $E_{lab} = 280$, 500, and 1000 MeV for the purpose of illustration. (For the remaining potentials and $p\Delta$ channels, the behavior of the wave functions is similar.) From this figure, one can see that, with increasing energy, the amplitude of the wave function in this channel grows, which must increase the contribution of the $p\Delta$ channel to the cross section for the process being studied. With increasing energy, there arise, however, oscillations, and this, on the contrary, may reduce the contribution of the $p\Delta$ channel to the reaction cross section (in the pp channel, the oscillations of the wave function also grow with increasing energy). This competition leads to the energy dependence of the ratio of the total differential cross section to the cross section that takes into account only transitions from the pp to the pp channel. This ratio is shown in Fig. 3 for the Nijmegen

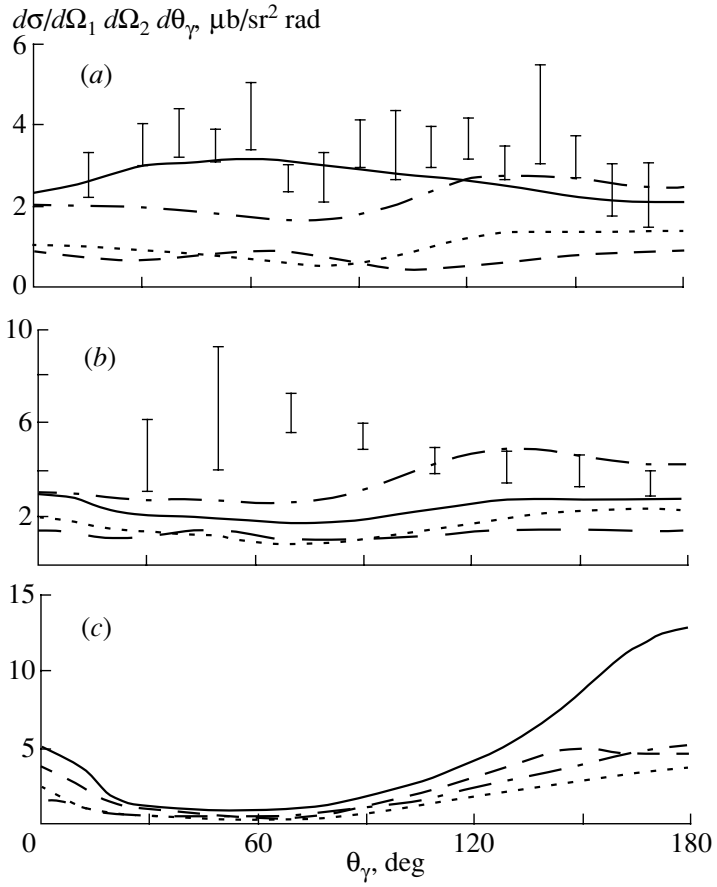

Fig. 5. Differential cross section for the process $pp \to pp\gamma$ as a function of the photon emission angle according to our calculations with allowance for isobar reaction channels for coplanar geometry (that is, the emitted photon travels toward the angle θ_2) at (*a*) $\theta_1 = 27.8^\circ$, $\theta_2 = 28.0^\circ$, and $E_{\text{lab}} = 280$ MeV; (*b*) $\theta_1 = 26^\circ$, $\theta_2 = 26^\circ$, and $E_{\text{lab}} = 389$ MeV; and (*c*) $\theta_1 = 27.8^\circ$, $\theta_2 = 28.0^\circ$, and $E_{\text{lab}} = 500$ MeV: (dash-dotted curves) results of the calculations for the Nijmegen potential in the *pp* channel, (solid curves) results of the calculations for the Moscow potential with dispersion in the *pp* channel, (long-dashed curves) results of the calculations for the Moscow potential MP92 in the *pp* channel, and (dotted curves) results of the calculations for the Paris potential [2] in the *pp* channel. The displayed experimental data (points with error bars) were borrowed from [25] (Fig. 5*a*) and [26] (Fig. 5*b*).

potential. It can be seen that, with increasing energy, the contribution of the $p\Delta$ channel grows, as might have been expected, but the rate of its growth then becomes lower.

The differential cross sections for bremsstrahlung in the process $pp \to pp\gamma$ are given in Figs. 4–6 according to calculations for five values of the incident-proton energy. In Figs. 4*a* and 4*b*, the results of the present calculations that take into account isobar channels are contrasted against the results of the previous relativistic calculations from [19], where such channels were disregarded. The first regularity that stands out here is that isobar reaction channels affect the results for the Paris and the Nijmegen potential quite differently (see Fig. 4*a*). Whereas the results for the Paris potential changed insignificantly, the differential cross section for the reaction in question for the Nijmegen potential increased quite sizably. Both potentials belong to the class of meson-exchange potentials and lead to nearly identical wave functions if coupling to isobar reaction channels is disregarded. Coupling to isobar reaction channels changed the internal part of the wave function for the Nijmegen potential substantially. As can be seen from Fig. 2*a*, this change consists in the appearance of a node at approximately $r = 0.6$ fm. This node means that, for this $^3P_1$ partial wave, the Nijmegen potential yields a wave function of the same type as the Moscow potential. For other partial waves, this effect is not observed.

A similar situation is observed for two potentials of the Moscow type (see Fig. 4*b*). While the results for the Moscow potential MP92 [9] changed quite moderately (in absolute values), the differential cross section for the Moscow potential with dispersion [10] underwent a considerable change upon the inclu-

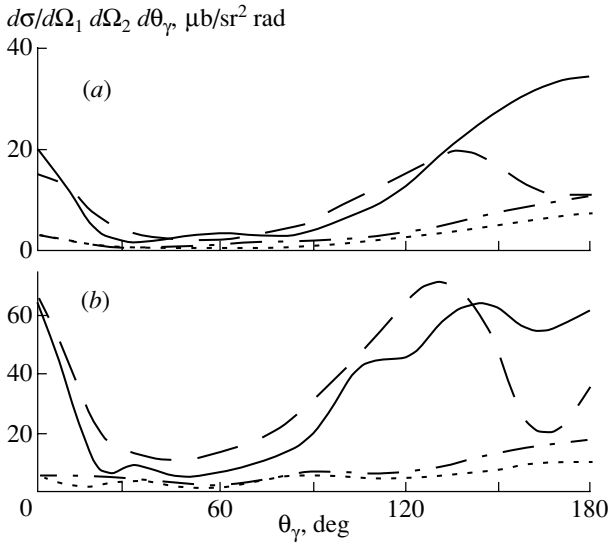

Fig. 6. As in Fig. 5*a*, but for $E_{\text{lab}} =$ (*a*) 700 and (*b*) 1000 MeV.

sion of isobar reaction channels, toward much better agreement with experimental data. It should be noted that the Moscow potential with dispersion features no tensor interaction; however, coupling between partial waves in the pp channel that are characterized by even J (total angular momentum) and odd L (orbital angular momentum) arises there owing to isobar reaction channels.

From Figs. 3 and 4, it can be seen that the contribution of isobar reaction channels to the cross section for bremsstrahlung radiation in the reaction $pp \to pp\gamma$ is significant, amounting to about 10% for all of the potentials.

In Figs. 5 and 6, the results of the calculations with allowance for isobar reaction channels are given for a broad energy region. These results demonstrate that, with increasing incident-proton energy, the results of the calculations with the different potentials differ ever more strongly, but the results for the two potentials of the Moscow type become relatively closer to each other, displaying a characteristic angular dependence of the cross section (previously, such a dependence was observed in [17]). The calculations with the Nijmegen potential yield larger values of the cross section for the reaction $pp \to pp\gamma$ than the calculations with the Paris potential. The cross sections in question appear to be highly sensitive to kinematical conditions. For all of the potentials, the contribution of isobar reaction channels to the reaction cross section is about 10% (in just the same way as for $E_{\text{lab}} =$ 280 MeV).

Thus, our calculations have led to the following important conclusions:

(i) The contribution of isobar reaction channels to the reaction $pp \to pp\gamma$ is significant, and it is necessary to take them into account in calculating this reaction from the incident-proton energy of $E_{\text{lab}} =$ 280 MeV.

(ii) The cross section for bremsstrahlung in the process $pp \to pp\gamma$ is highly sensitive to the type of potential and makes it possible to discriminate between meson-exchange potentials and the Moscow potential. In [18, 19], this statement was proven for incident-proton energies of up to 500 MeV, but, in the present study, it has been extended to incident-proton energies as high as 1 GeV in the laboratory frame.

(iii) The results of the calculations in Figs. 4 and 5 demonstrate that none of the potentials used is able to describe the entire body of available experimental data simultaneously. In order to improve this description and to refine the results of our calculations of the cross sections for the reaction $pp \to pp\gamma$, it is necessary to fit the parameters of nucleon–nucleon potentials with allowance for coupling to nucleon–isobar channels in describing data on elastic proton–proton scattering over an energy region extending at least up to 1 GeV. We are going to do this in our future studies, since, at present, the required potentials are not available in the literature.

ACKNOWLEDGMENTS

This work was supported in part by the Contest Center for Basic Research in Natural and Exact Sciences at the Ministry of Education of the Russian Federation (grant no. E00-3.3-67).

APPENDIX 1

We will derive explicit expressions for the operators $\mathbf{j}_{i\to f}(\mathbf{h})$ in (13), relying on the results reported in the review article by Lev [20] and in [19].

For a particle of 4-momentum p, we define the Lorentz transformation associated with a boost g as $p \to L(\alpha(g))p$, where [22]

$$\alpha(g) = \frac{g^0 + 1 + \boldsymbol{\sigma}\cdot\mathbf{g}}{\sqrt{2(g^0+1)}}. \qquad \text{(A.1)}$$

Here, g is the 4-velocity and $\boldsymbol{\sigma} = (\sigma_x, \sigma_y, \sigma_z)$ are the Pauli matrices. The transformation in question is realized in the following way [22]: we introduce $\sigma^0 = \begin{pmatrix} 1 & 0 \\ 0 & 1 \end{pmatrix}$ and associate the matrix $\breve{p} = \sum_{\mu=0}^{3} \sigma^\mu p_\mu$ with the 4-vector p. The components of this 4-vector are then expressed in terms of the above matrix as follows:

$$p_0 = \frac{1}{2}(\breve{p}_{11} + \breve{p}_{22}), \quad p_1 = \frac{1}{2}(\breve{p}_{12} + \breve{p}_{21}), \qquad \text{(A.2)}$$

$$p_2 = \frac{1}{2i}(-\breve{p}_{12} + \breve{p}_{21}), \quad p_3 = \frac{1}{2}(\breve{p}_{11} - \breve{p}_{22}).$$

The transformation

$$\breve{p} \to \alpha(g)\breve{p}\alpha(g)^+, \tag{A.3}$$

together with formulas (A.2), describes the action of the boost $p \to L(\alpha(g))p$.

Further, the Poincaré group transformation characterized by a 4-shift a and a 4-rotation ℓ is defined as [22]

$$U(a,\ell)\varphi(g) = \exp(i \cdot mg'a) \times D(\mathbf{s}; \alpha(g)^{-1}\ell\alpha(g'))\varphi(g'), \tag{A.4}$$

where a and ℓ are elements of the Poincaré group that correspond to a spacetime translation and a 4-rotation, respectively; $\varphi(g)$ is a normalizable spinor function; $\mathbf{s}$ is the particle spin; $g' = L(\ell)g$, $L(\ell)$ being the Lorentz transformation corresponding to ℓ; and $D(\mathbf{s}; u)$ is an operator realizing a representation of the $SU(2)$ group and corresponding to the element u of this group. In our case of spin-1/2 particles, we are dealing with the fundamental representation [22]; that is,

$$D(\mathbf{s}; \alpha(g)^{-1}\ell\alpha(g')) = \alpha(g)^{-1}\ell\alpha(g'). \tag{A.5}$$

We specify the operator ℓ by going over to a two-particle system. Here, we have the particle 4-momenta $p_i = m_i g_i (i = 1, 2)$ and the 4-velocity G of the center of mass. In the c.m. frame, the particle momenta are given by [22]

$$q_i = L[\alpha(G)]^{-1} m_i g_i, \quad \mathbf{q}_1 = \mathbf{q} = -\mathbf{q}_2. \tag{A.6}$$

Bearing in mind that the reaction $pp \to pp\gamma$ is the main subject of our analysis and choosing the coordinate frame specified by Eq. (10), we obtain a general expression for the current corresponding to the pointlike form of dynamics:

$$j^\mu(\mathbf{h}) = \sum_{i=1,2} L\left(L[\alpha(f)]\frac{q_i}{m_i^{\text{out}}}, L[\alpha(f')]\frac{d_i}{m_i^{\text{in}}}\right)^\mu_\nu \tag{A.7}$$

$$\times D\left[\mathbf{s}_k; \alpha\left(\frac{q_k}{m_k^{\text{out}}}\right)^{-1} \alpha(f)^{-1}\alpha(f')\alpha\left(\frac{d_{ki}}{m_k^{\text{in}}}\right)\right]$$

$$\times D\left[\mathbf{s}_i; \alpha\left(\frac{q_i}{m_i^{\text{out}}}\right)^{-1} \alpha(f)^{-1}\right.$$

$$\left.\times\, \alpha\left(L[\alpha(f)]\frac{q_i}{m_i^{\text{out}}}, L[\alpha(f')]\frac{d_{ki}}{m_i^{\text{in}}}\right)\alpha(f_i)\right] j_i^\nu(\mathbf{h}_i)$$

$$\times D\left[\mathbf{s}_i; \alpha(f_i')^{-1}\alpha\left(L[\alpha(f)]\frac{q_i}{m_i^{\text{out}}}, L[\alpha(f')]\frac{d_i}{m_i^{\text{in}}}\right)\right.$$

$$\left.\times\, \alpha(f')\alpha\left(\frac{d_i}{m_i^{\text{in}}}\right)\right]$$

$$\times \frac{m_i^{\text{in}} w_i(\mathbf{q})}{w_i(\mathbf{d}_i)}\left(\frac{m_i^{\text{out}} M_{\text{in}}(\mathbf{d}_i)}{m_i^{\text{in}} M_{\text{out}}(\mathbf{q})}\right)^{3/2} I_i(\mathbf{h}).$$

In this formula, $k = 2$ if $i = 1$; $k = 1$ if $i = 2$; and

$$f = L(G, G')^{-1}G, \quad f' = L(G, G')^{-1}G' \tag{A.8}$$

are the 4-velocities of the centers of mass in the initial and the final state in the reference frame specified by Eq. (10). We also have $f^2 = f'^2 = 1$, $\mathbf{f} + \mathbf{f}' = 0$, and $f_0 = f_0' = (1 + \mathbf{f}^2)^{1/2}$; $L(G, G') = L(\alpha(G, G'))$ and $\alpha(G, G') = \alpha((G + G')/|G + G'|)$; and $d_1 = (w_1(\mathbf{d}_1), \mathbf{d}_1)$, $d_2 = (w_2(\mathbf{d}_2), \mathbf{d}_2)$, $d_{12} = L[\alpha(f')^{-1}\alpha(f)]q_2 = (w_2(\mathbf{d}_1), -\mathbf{d}_1)$, and $d_{21} = L[\alpha(f')^{-1}\alpha(f)]q_1 = (w_1(\mathbf{d}_2), \mathbf{d}_2)$, where $\mathbf{d}_1$ and $\mathbf{d}_2$ are defined by the formulas

$$I_j(\mathbf{h})\chi(\mathbf{q}) = \begin{cases} \chi(\mathbf{d}_1) = \chi\left(\mathbf{q} - \dfrac{2\mathbf{h}}{1 - \mathbf{h}^2}\{w_1(\mathbf{q}) - \mathbf{h}\cdot\mathbf{q}\}\right), j = 1, \\ \chi(\mathbf{d}_2) = \chi\left(\mathbf{q} + \dfrac{2\mathbf{h}}{1 - \mathbf{h}^2}\{w_2(\mathbf{q}) - \mathbf{h}\cdot\mathbf{q}\}\right), j = 2; \end{cases}$$

f_i and f_i' are given by formulas (A.8) with the substitution of G for $L[\alpha(f)q_i/m_i^{\text{in}}]$ and of G' for $L[\alpha(f')d_i/m_i^{\text{out}}]$; $\mathbf{h}_i = \mathbf{f}_i/f_i^0$; m_i^{in} and m_i^{out} are the masses of the ith particle in, respectively, the input and the output channel; $w_i^{\text{in}}(\mathbf{q}) = \sqrt{(m_i^{\text{in}})^2 + \mathbf{q}^2}$ and $w_i^{\text{out}}(\mathbf{q}) = \sqrt{(m_i^{\text{out}})^2 + \mathbf{q}^2}$ are the energies corresponding to these masses; and $M_{\text{in}}(\mathbf{q})$ and $M_{\text{out}}(\mathbf{q})$ are the mass operators in, respectively, the input and the output channel.

Expression (A.7) differs only slightly from the corresponding expression obtained in [20] for the case where electromagnetic interaction does not change the nature of a particle (mass); since the derivation of this expression is analogous to the corresponding derivation given in [20], we do not present it here.

The diagonal elements of the matrix of currents in (13) can be obtained from the expressions for single-particle currents; that is,

$$j_i^0(\mathbf{h}_i) = eF_{e,i}, \tag{A.9}$$

$$\mathbf{j}_i(\mathbf{h}_i) = -\frac{ie}{(1 - h_i^2)^{1/2}}F_{m,i}[\mathbf{h}_i \times \mathbf{s}_i],$$

where e is an elementary charge and s_i, $F_{e,i}$, and $F_{m,i}$ are, respectively, the spin operator, the electric form factor, and the magnetic form factor of the ith particle ($i = N, \Delta, N^*$).

The off-diagonal elements were obtained from the transition currents [24]. We have

$$j^0_{N\to I}(\mathbf{h}_i) = j^0_{I\to N}(\mathbf{h}_i) = 0, \tag{A.10}$$
$$\mathbf{j}_{N\to I}(\mathbf{h}_i) = -i\frac{f_{\gamma NI}}{m_\pi}\left[\mathbf{h}_i \times \mathbf{S}_i^+\right] T_{3i}^+,$$
$$\mathbf{j}_{I\to N}(\mathbf{h}_i) = \overline{\mathbf{j}_{N\to I}(\mathbf{h}_i)},$$

where I means an isobar (Δ or N^*); $f_{\gamma NI}/m_\pi$ is the transition magnetic moment; and $\mathbf{S}_i^\pm$ and $\mathbf{T}_i^\pm$ are, respectively, the standard spin and isospin transition operators defined in the spherical basis $\hat{\mathbf{e}}_\lambda$ as

$$\left\langle \frac{3}{2} s_\Delta \left| \mathbf{S}^+ \right| \frac{1}{2} s \right\rangle = \sum_\lambda \left(\frac{3}{2} s_\Delta | 1\lambda \frac{1}{2} s \right) \hat{\mathbf{e}}^*_\lambda.$$

Here, $\left(\frac{3}{2} s_\Delta | 1\lambda \frac{1}{2} s \right)$ is a Clebsch–Gordan coefficient; an asterisk means a complex conjugation; the operator $\mathbf{S}^-$ is the Hermitian conjugate of the operator $\mathbf{S}^+$; and the operators $\mathbf{T}^\pm$ are defined analogously, but they act in isospin space. We neglect electric transitions because the smallness of the corresponding empirical amplitudes at the resonance point implies that their contribution must be small [27]. An overbar means the Hermitian conjugation of an operator.

The derivation of the expressions for the transition operators $\mathbf{j}_{NN\to NN}(\mathbf{h})$ in the first order in the quantity $h = |\mathbf{h}|$ is given in [19]. The derivation of the remaining elements of the operator $\mathbf{j}(\mathbf{h})$ in the same order of smallness is similar, a slight complication being associated with the fact that the masses of particles in channels and in the initial and the final state are now different. The inclusion of the interaction leads to the emergence of an addition $\Delta j(\mathbf{h})$ to the operator $j(\mathbf{h})$, this addition being fixed by the conditions proposed in [20], which have the form

$$\Delta j^0(\mathbf{h}) = \Delta \mathbf{j}_\perp(\mathbf{h}) = 0 \tag{A.11}$$

[$\Delta \mathbf{j}_\perp(\mathbf{h})$ is that component of the vector $\Delta\mathbf{j}(\mathbf{h})$ which is orthogonal to $\mathbf{h}$], and by the continuity equation. All this leads to the following relation for the matrix element $\Delta\mathbf{j}(\mathbf{h})$:

$$\langle \chi_f | \Delta\mathbf{j}(\mathbf{h}) | \chi_i \rangle = \frac{M_i - M_f}{M_i + M_f} \left\langle \chi_f \left| \frac{\partial j^0(\mathbf{h})}{\partial \mathbf{h}} \right|_{\mathbf{h}=0} \right| \chi_i \right\rangle; \tag{A.12}$$

that is, it is expressed in terms of the known time component of the operator $\mathbf{j}(\mathbf{h})$ for noninteracting particles.

Thus, the diagonal elements of the matrix of currents in (13) can be represented as

$$\begin{aligned}
\mathbf{j}_{NI\to NI}(\mathbf{h}) = {} & \left(\frac{F_{e,p}e}{w_p} I_1(\mathbf{h}) - \frac{F_{e,I}e}{w_I} I_2(\mathbf{h}) \right) \mathbf{q} \\
& - \left(\frac{F_{e,p}e}{m_p w_p} + \frac{F_{e,I}e}{m_I w_I} \right) (\mathbf{h}\cdot\mathbf{q})\mathbf{q} \\
& + i \left(\frac{m_p F_{m,p} e}{w_p} + \frac{m_I F_{m,I} e}{w_I} \right) [\mathbf{S}\times\mathbf{h}] \\
& + i \left(\frac{m_p F_{m,p} e}{w_p} - \frac{m_I F_{m,I} e}{w_I} \right) [\mathbf{T}\times\mathbf{h}] \\
& + i \left(\frac{F_{m,p} e}{m_p(w_p + m_p)} + \frac{F_{m,I} e}{m_I(w_I + m_I)} \right) \\
& \times [\mathbf{q}\times\mathbf{h}](\mathbf{q}\cdot\mathbf{S}) + i \left(\frac{F_{m,p} e}{m_p(w_p + m_p)} \right. \\
& \left. - \frac{F_{m,I} e}{m_I(w_I + m_I)} \right) [\mathbf{q}\times\mathbf{h}](\mathbf{q}\cdot\mathbf{T}) \\
& + i \left(\frac{F_{m,p} e}{m_p w_p} + \frac{F_{e,p} e}{w_p(w_p + m_p)} + \frac{F_{m,I} e}{m_I w_I} \right. \\
& \left. + \frac{F_{e,I} e}{w_I(w_I + m_I)} \right) (\mathbf{h}\cdot[\mathbf{q}\times\mathbf{S}])\mathbf{q} \\
& + i \left(\frac{F_{m,p} e}{m_p w_p} + \frac{F_{e,p} e}{w_p(w_p + m_p)} - \frac{F_{m,I} e}{m_I w_I} \right. \\
& \left. - \frac{F_{e,I} e}{w_I(w_I + m_I)} \right) (\mathbf{h}\cdot[\mathbf{q}\times\mathbf{T}])\mathbf{q} \\
& + \frac{M_i - M_f}{M_i + M_f} \left(\frac{F_{m,p}}{m_p} - \frac{F_{e,p}}{w_p + m_p} - \frac{F_{m,I}}{m_I} \right. \\
& \left. + \frac{F_{e,I}}{w_I + m_I} \right) [\mathbf{q}\times\mathbf{S}] \\
& + \frac{M_i - M_f}{M_i + M_f} \left(\frac{F_{m,p}}{m_p} - \frac{F_{e,p}}{w_p + m_p} \right. \\
& \left. + \frac{F_{m,I}}{m_I} - \frac{F_{e,I}}{w_I + m_I} \right) [\mathbf{q}\times\mathbf{T}],
\end{aligned} \tag{A.13}$$

where $w_i \equiv w_i(\mathbf{q})$.

For the proton–proton channel, $I = p$ and expression (A.13) reduces to the expression obtained previously in [19] for the current in the proton–proton channel.

A more complicated expression is obtained for the off-diagonal elements:

$$\begin{aligned}
\mathbf{j}_{NN\to NI}(\mathbf{h}) = {} & f^1_{NN\to NI}(q^2)[\mathbf{S}_2^+\times\mathbf{h}]T_3^+ \\
& + f^2_{NN\to NI}(q^2)(\mathbf{h}\cdot[\mathbf{q}\times\mathbf{S}_2^+])\mathbf{q}T_3^+ \\
& + f^3_{NN\to NI}(q^2)[\mathbf{q}\times\mathbf{h}](\mathbf{q}\cdot\mathbf{S}_2^+)T_3^+ \\
& + f^4_{NN\to NI}(q^2)[\mathbf{q}\times\mathbf{S}_2^+](\mathbf{h}\cdot[\mathbf{q}\times\mathbf{S}_2])T_3^+ \\
& + f^5_{NN\to NI}(q^2)(\mathbf{h}\cdot[\mathbf{q}\times\mathbf{S}_2])[\mathbf{q}\times\mathbf{S}_2^+]T_3^+ \\
& + f^6_{NN\to NI}(q^2)[\mathbf{q}\times\mathbf{S}_2^+](\mathbf{h}\cdot[\mathbf{q}\times\mathbf{S}_1])T_3^+ \\
& + f^7_{NN\to NI}(q^2)[\mathbf{q}\times\mathbf{S}_2^+]T_3^+.
\end{aligned} \tag{A.14}$$

The expression for $\mathbf{j}_{NI\to NN}(\mathbf{h})$ has a similar form (upon the replacement of $\mathbf{S}_2^+$ by $\mathbf{S}_2^-$ and of the factors $f^i_{NN\to NI}$ by the factors $f^i_{NI\to NN}$). The currents $\mathbf{j}_{NN^*\to N\Delta}(\mathbf{h})$ and $\mathbf{j}_{N\Delta\to NN^*}(\mathbf{h})$ are disregarded because it is obvious that their contribution to the cross section is small.

We note that, in the proton–isobar channels, the indices 1 and 2 correspond to the proton and the isobar, respectively; therefore, the first particle always remains a proton. Like the operator $\mathbf{S}_2^+$, the operator T_3^+ acts on the second particle; the operators $\mathbf{S}_2^+$ and $\mathbf{S}_2$ do not commute.

In this study, the factors $f^i_{NN\to NI}(q^2)$ and $f^i_{NI\to NN}(q^2)$ were obtained in an analytic form, but the expressions for them are very cumbersome and are not presented here for this reason.

APPENDIX 2

The technique for calculating matrix elements for various components of the relativistic current operator in the proton–proton channel was described previously in [19]. For the diagonal transitions ($pI\to pI$), it is similar. As for nondiagonal transitions, the most complicated operator appearing in the matrix elements can be represented in the form

$$(\mathbf{h}\cdot[\nabla\times\mathbf{S}_2])\cdot[\nabla\times\mathbf{S}_2^+]_k \qquad (A.15)$$
$$= \frac{2}{3}\left[\left[[\nabla\times\nabla]^{(0)}\times[S_2\times S_2^+]^{(0)}\right]^{(0)}\times h\right]^{(1)}_k$$
$$+\frac{\sqrt{3}}{3}\left[\left[[\nabla\times\nabla]^{(0)}\times[S_2\times S_2^+]^{(1)}\right]^{(1)}\times h\right]^{(1)}_k$$
$$-\frac{\sqrt{3}}{5}\left[\left[[\nabla\times\nabla]^{(0)}\times[S_2\times S_2^+]^{(2)}\right]^{(2)}\times h\right]^{(1)}_k$$
$$-\frac{\sqrt{5}}{3}\left[\left[[\nabla\times\nabla]^{(2)}\times[S_2\times S_2^+]^{(0)}\right]^{(2)}\times h\right]^{(1)}_k$$
$$+\frac{\sqrt{15}}{3}\left[\left[[\nabla\times\nabla]^{(2)}\times[S_2\times S_2^+]^{(1)}\right]^{(1)}\times h\right]^{(1)}_k$$
$$-\frac{\sqrt{5}}{3}\left[\left[[\nabla\times\nabla]^{(2)}\times[S_2\times S_2^+]^{(2)}\right]^{(0)}\times h\right]^{(1)}_k$$
$$+\frac{\sqrt{35}}{3}\left[\left[[\nabla\times\nabla]^{(2)}\times[S_2\times S_2^+]^{(2)}\right]^{(2)}\times h\right]^{(1)}_k.$$

The left-hand side of this equality is expressed in terms of the usual scalar and vector products of vector operators in the spherical basis. Its right-hand side involves the sum of the tensor products of tensor operators. The superscript in parentheses stands for the tensor rank of an operator. It is omitted on rank-1 tensors like ∇, S_2, S_2^+, and h on the right-hand side of the equality. The subscript k numbers components of rank-1 tensors defined in a standard way. Expression (A.15) makes it possible to expand the reduced matrix elements of the complicated operator $(\mathbf{h}\cdot[\nabla\times\mathbf{S}_2])\cdot[\nabla\times\mathbf{S}_2^+]$ in terms of the sums of the products of reduced matrix elements of the simplest operators entering into the complicated one [on the right-hand side of (A.15), the operators acting in coordinate and in spin space prove to be separated].

A similar representation was used in calculating matrix elements for the remaining vector operators.

REFERENCES

1. R. Machleidt, K. Holinde, and Ch. Elster, Phys. Rep. **149**, 1 (1987).
2. M. Lacombe, B. Loiseau, J. M. Richard, *et al.,* Phys. Rev. C **21**, 861 (1980).
3. V. G. J. Stoks, R. A. M. Klomp, C. P. F. Terheggen, and J. J. de Swart, Phys. Rev. C **49**, 2950 (1994).
4. Th. A. Rijken and V. G. J. Stoks, Phys. Rev. C **54**, 2869 (1996); Phys. Rev. C **54**, 2851 (1996); Phys. Rev. D **17**, 768 (1978); Phys. Rev. C **40**, 2226 (1989).
5. M. Oka and S. Takeuchi, Phys. Rev. Lett. **63**, 1780 (1989); Z.-Y. Zhang, A. Faessler, U. Straub, and L. Ya. Glozman, Nucl. Phys. A **578**, 573 (1994); W. Koepf, L. Wilets, S. Pepin, and F. Stancu, Phys. Rev. C **50**, 614 (1994); D. R. Entem, A. I. Machavariani, A. Valcarce, *et al.,* Nucl. Phys. A **602**, 308 (1996).
6. D. A. Liberman, Phys. Rev. D **16**, 1542 (1977).
7. V. G. Neudatchin, I. T. Obukhovsky, and Yu. F. Smirnov, Phys. Lett. B **43B**, 13 (1973); C. De Tar, Phys. Rev. D **17**, 302 (1978); V. G. Neudatchin, I. T. Obukhovsky, V. I. Kukulin, and N. F. Golovanova, Phys. Rev. C **11**, 128 (1975); Yu. F. Smirnov, R. Tamagaki, and V. G. Neudatchin, Yad. Fiz. **27**, 860 (1978) [Sov. J. Nucl. Phys. **27**, 456 (1978)]; I. T. Obukhovsky, V. G. Neudatchin, Yu. F. Smirnov, and Yu. M. Tchuvil'sky, Phys. Lett. B **88**, 231 (1979).
8. V. G. Neudatchin, N. P. Yudin, Yu. L. Dorodnykh, and I. T. Obukhovsky, Phys. Rev. C **43**, 2499 (1991).
9. V. I. Kukulin and V. N. Pomerantsev, Prog. Theor. Phys. **88**, 159 (1992).
10. S. B. Dubovichenko, Yad. Fiz. **60**, 499 (1997) [Phys. At. Nucl. **60**, 425 (1997)].
11. T.-S. H. Lee and A. Matsuyama, Phys. Rev. C **36**, 1459 (1987); M. Batinic, A. Svarc, and T.-S. H. Lee, Phys. Scr. **56**, 321 (1997).
12. V. I. Kukulin, V. N. Pomerantsev, V. M. Krasnopol'sky, and P. V. Sazonov, Phys. Lett. B **135**, 20 (1984); V. M. Krasnopol'skiĭ, V. I. Kukulin, and V. N. Pomerantsev, Izv. Akad. Nauk SSSR, Ser. Fiz. **51**, 898 (1987).
13. J.-M. Sparenberg, nucl-th/0105062.

14. V. G. Neudatchin and I. T. Obukhovsky, in *Proceedings of the XII International Seminar on Relativistic Nuclear Physics and QCD, Dubna, 1994,* Ed. by A. M. Baldin and V. V. Burov, JINR Publ. No. E1, 2-97-79 (Dubna, 1997), Vol. II, p. 3.
15. M. Jetter and H. W. Fearing, Phys. Rev. C **51**, 1666 (1995); H. W. Fearing and S. Scherer, nucl-th/9909076.
16. H. W. Fearing, Phys. Rev. Lett. **81**, 758 (1998).
17. V. G. Neudatchin, N. A. Khokhlov, A. M. Shirokov, and V. A. Knyr, Yad. Fiz. **60**, 1086 (1997) [Phys. At. Nucl. **60**, 971 (1997)]; N. A. Khokhlov, V. A. Knyr, V. G. Neudatchin, and A. M. Shirokov, Nucl. Phys. A **629**, 218c (1998).
18. N. A. Khokhlov, V. A. Knyr, V. G. Neudatchin, and A. M. Shirokov, Phys. Rev. C **62**, 054003 (2000); V. A. Knyr, V. G. Neudachin, and N. A. Khokhlov, Yad. Fiz. **63**, 1988 (2000) [Phys. At. Nucl. **63**, 1895 (2000)].
19. V. A. Knyr, N. A. Khokhlov, and V. G. Neudatchin, Izv. Akad. Nauk, Ser. Fiz. **66**, 691 (2002); N. A. Khokhlov, V. G. Neudatchin, and V. A. Knyr, Yad. Fiz. **66**, 146 (2003) [Phys. At. Nucl. **66**, 143 (2003)]; N. A. Khokhlov, V. A. Knyr, and V. G. Neudatchin, Phys. Rev. C **68**, 054002 (2003).
20. F. M. Lev, hep-ph/9403222.
21. L. Ray, Phys. Rev. C **35,** 1072 (1987); E. L. Lomon, Phys. Rev. D **26**, 576 (1982).
22. J. Werle, *Relativistic Theory of Reactions* (Polish Sci. Publ., Warsaw, 1966).
23. V. A. Knyr and N. A. Khokhlov, Izv. Akad. Nauk, Ser. Fiz. **67**, 679 (2003).
24. R. A. Arndt *et al.*, Phys. Rev. D **28**, 97 (1983).
25. K. Michaelian, P. Kitching, D. A. Hutcheon, *et al.*, Phys. Rev. D **41**, 2689 (1990).
26. K. Yasuda, H. Akiyoshi, T. Hotta, *et al.,* Phys. Rev. Lett. **82**, 4775 (1999).
27. T. Ericson and W. Weise, *Pions and Nuclei* (Clarendon Press, Oxford, 1988).

Translated by A. Isaakyan

Physics of Atomic Nuclei, Vol. 67, No. 5, 2004, pp. 949–960. Translated from Yadernaya Fizika, Vol. 67, No. 5, 2004, pp. 972–982.

ELEMENTARY PARTICLES AND FIELDS
Experiment

Polarization Parameters of Elastic *pp* Scattering in the Angular Range 22.5°–42.5° at an Energy of 1 GeV and Partial-Wave Analysis of Data

V. A. Andreev, N. A. Bazhanov, V. G. Vovchenko, A. A. Zhdanov, A. I. Kovalev, F. Lehar[1)], O. V. Miklukho, V. I. Murzin, V. V. Polyakov, A. N. Prokofiev, Yu. M. Sanjiev, V. Yu. Trautman, O. Ya. Fedorov, Yu. A. Chestnov[*], A. V. Shvedchikov, Yu. A. Scheglov, and V. A. Schedrov

Petersburg Nuclear Physics Institute, Russian Academy of Sciences, Gatchina, 188350 Russia

Received April 14, 2003

Abstract—The polarization properties of elastic scattering are studied experimentally for *pp* interaction at 1 GeV. The respective experimental results are presented for the spin-transfer parameter K_{n00n} and the polarization P_{n000} at c.m. angles of 22.5°, 27.5°, 32.5°, and 42.5° and for the analyzing power A_{000n} at c.m. angles of 22.5° and 27.5°. The experiment employed an unpolarized proton beam from the accelerator of the Petersburg Nuclear Physics Institute, a polarized proton target, and a high-resolution magnetic spectrometer. The data from this experiment are analyzed and compared with the predictions of partial-wave analyses. © *2004 MAIK "Nauka/Interperiodica".*

1. INTRODUCTION

Experiments that study proton–proton scattering at intermediate energies are aimed at reconstructing the elastic-scattering matrix **M**—that is, five complex-valued amplitudes specifying this matrix, which can be represented in the form

$$\mathbf{M}(\sigma_1,\sigma_2) = a + b\sigma_{1n}\sigma_{2n} + c(\sigma_{1n}+\sigma_{2n}) + e\sigma_{1m}\sigma_{2m} + f\sigma_{1l}\sigma_{2l}, \quad (1)$$

where σ_i are the spin operators (Pauli matrices) of the first and second protons. The amplitudes a, b, c, e, and f appearing in expression (1) for the matrix **M** are functions of the energy E and the scattering angle θ (hereafter, θ is taken in the c.m. frame).

A partial-wave analysis employing an expansion of the above amplitudes in the singlet–triplet representation in terms of Legendre polynomials is an efficient method for reconstructing the above scattering matrix. Linear combinations of the partial-wave interaction amplitudes appear as coefficients in this expansion. Different authors choose different forms for partial-wave amplitudes—that is, different parametrizations of the S matrix. The form chosen here is identical to that which was previously used, for example, in [1–3] and in which partial-wave amplitudes for states characterized by the total spin S, the total angular momentum J, and the orbital angular momentum L are described in terms of the phase shifts $\delta(^{2S+1}L_J)$, mixing parameters ε_J being additionally introduced for mixed states that differ by orbital angular momenta at the same value of the total angular momentum. The phase shifts are complex-valued quantities with positive imaginary parts, while the mixing parameters are real-valued.

Several partial-wave analyses were performed earlier at an energy of 1 GeV (see [3–6]). Differences in the parametrization of the S matrix, in the volume of the experimental data subjected to analysis and in the energy range that they cover, in the normalization conditions, etc., lead to distinctions between solutions obtained in different analyses for the parameters under comparison; however, there is qualitative agreement in the description of the main features of the interaction (see Section 6).

At the present time, an extensive program of investigations into proton scattering has been performed, which involve a complete set of orientations of the beam- and target-proton polarizations. In the energy region around 1 GeV, more than 17 independent observables (see Section 6) were measured if they are rescaled to the angular range $0° \le \theta \le 90°$ (hereafter, this is done for all experimental data). For the bulk of data, the actual angular range is $40° < \theta \le 90°$. Only the differential cross section and polarization (analyzing power) were measured for $\theta < 30°$. We can expect (disregarding correlations between the parameters in the functional to be minimized—see

[1)]DAPNIA/SPP, CEA/Saclay, F-91191 Gif-sur-Yvette, France.

[*]e-mail: chestnov@mail.pnpi.spb.ru

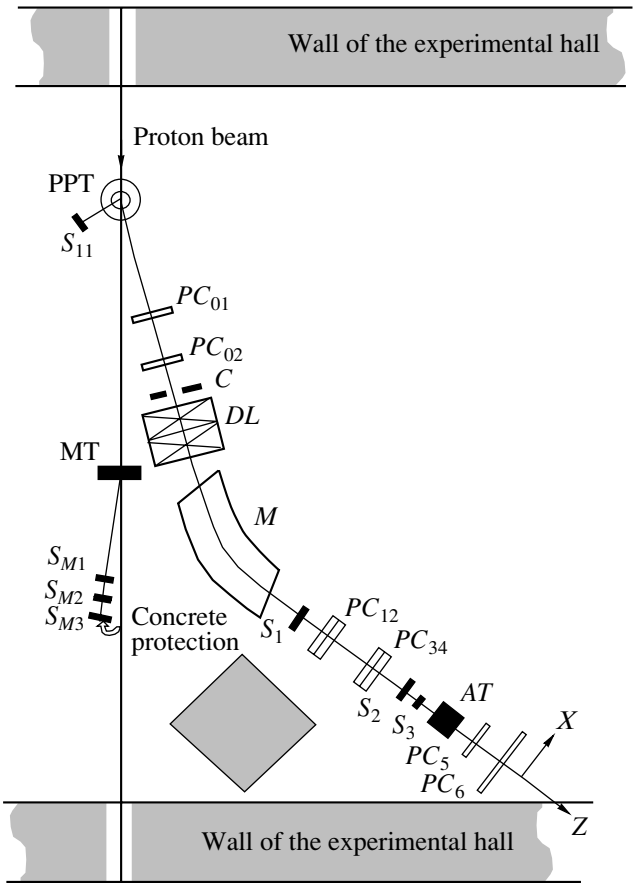

Fig. 1. Layout of the experimental setup: (PPT) polarized proton target, (C) collimator, (DL) doublet of quadrupole lenses, (M) magnet, (S) scintillation counters, (PC) proportional chambers, (AT) analyzing target, and (MT) monitor target. The coordinate axes x and z are also shown.

Section 6) that the scarcity of experimental data at small angles would lead to a significant uncertainty in the phase shifts for high angular momenta.

Previously, some polarization parameters of elastic pp scattering at energies in the vicinity of 1 GeV were measured in the angular region $\theta \geq 30°$ [2, 3, 7–11]. These included the depolarization parameter D_{n0n0} measured in a polarized proton beam from the synchrocyclotron of the Petersburg Nuclear Physics Institute (PNPI, Gatchina) and the spin-transfer parameter K_{n00n} measured in an experiment with an unpolarized beam and a polarized proton target.

Measurement of polarization parameters at small angles requires solving some additional experimental problems. First, the recoil protons have low energy in this angular region, and this generates difficulties in separating correlated pp coincidences. Second, the use of solid-state polarized proton targets, where the concentration of polarized protons is approximately 10% of the total number of nucleons, leads to the growth of the contribution to the background at small angles from accompanying channels of proton–nucleus interactions.

At energies close to 1 GeV, the depolarization and spin-transfer parameters were previously measured in the angular interval $4.8° \leq \theta \leq 23.8°$ at LAMPF [12] by using a polarized beam of energy 800 MeV and a liquid-hydrogen target. Events of elastic pp scattering at a fixed angle were separated on the basis of the scattered-proton momentum.

In the present experiment, we studied the polarization properties of elastic pp scattering for the interaction of an unpolarized beam accelerated to an energy of 1 GeV with a polarized target. Specifically, we measured the spin-transfer parameter K_{n00n} and the polarization P_{n000} at angles of 9°, 11°, 13°, and 17° in the laboratory frame (this corresponds to c.m. angles of 22.5°, 27.5°, 32.5°, and 42.5°) and the analyzing power A_{000n} at c.m. angles of 22.5° and 27.5°. The elastic-scattering channel was separated from the background produced by other channels according to the scattered-proton momentum measured by a high-resolution magnetic spectrometer (MAP) [13], proportional chambers being placed at the spectrometer inlet in order to reconstruct the interaction vertex in the target. The main difficulty in the experiment

Table 1. Experimental values of the polarization parameters

θ	A_{000n}	P_{n000}	P_{qe}	K_{n00n}
22.5°	0.335 ± 0.010	0.336 ± 0.014	0.303 ± 0.018	0.284 ± 0.054
27.5°	0.361 ± 0.008	0.367 ± 0.020	0.339 ± 0.021	0.333 ± 0.070
32.5°	–	0.410 ± 0.021	–	0.401 ± 0.033
42.5°	–	0.427 ± 0.021	–	0.552 ± 0.029

was to eliminate the effect of the background from protons scattered on the nucleons of the polarized-target nuclei. We solved this problem owing to a high momentum resolution of the spectrometer and the optimization of the data-processing algorithm.

2. EXPERIMENTAL SETUP

A detailed description of the experimental setup used and the methodology of data processing were given in [14]. Figure 1 displays the layout of the setup. A proton beam accelerated at the PNPI synchrocyclotron to 1 GeV and formed by a system of quadrupole lenses and collimators was incident on a polarized proton target (PPT) based on propanediol [15]. The target operated in the quenched-spin mode. The beam intensity of about 10^8 s^{-1} was chosen on the basis of the estimated polarization-relaxation time (200–300 h), which decreased owing to the heating of the target material as the result of the ionization losses of beam protons. The target polarization P_T in the experiment was within the range 0.6–0.8. Hereafter, we use the notation U and D for, respectively, the positive and the negative orientation of the target polarization vector with respect to the vector orthogonal to the scattering plane.

In order to determine the contribution of protons scattered by the complex nuclei of the polarized target, we performed measurements with a carbon sample that was equivalent in the stopping power—the background target (BT).

Events of elastic scattering on target protons were separated by the scattered-proton momentum measured by the magnetic spectrometer, the angular position of the spectrometer being fixed to a precision of $\pm 0.05°$. The trajectories of scattered protons that traversed the magnetic field of the polarized proton target were reconstructed from the track coordinates measured by the proportional chambers PC_{01} and PC_{02}, while the trajectories of the protons after the spectrometer magnetic field were determined from the coordinates measured in the proportional chambers PC_{12} and PC_{34}.

The coincidence signal from the scintillation counters C_1, C_2, and C_3 was a trigger for the system of information readout from the proportional chambers. For a further polarization analysis, a central part of the beam was singled out with the aid of the counter C_3. A signal from the scintillation counter C_{11}, which recorded recoil protons, participated in the formation of the trigger signal only in measurements at angles of 32.5° and 42.5°.

After an analyzing target (AT), the protons were detected by two proportional chambers (PC_5, PC_6). For the analyzing target, we used a carbon sample 17 cm thick (29 g/cm^2).

The scintillation counters C_{M1}, C_{M2}, and C_{M3}, which detected the protons scattered by a polyethylene monitor target (MT) in the vertical plane, were used to monitor the beam intensity.

3. RECONSTRUCTION OF PROTON TRAJECTORIES

The rectilinear spatial trajectories of the protons after they traversed the spectrometer magnetic field were considered in the Cartesian coordinate frame where the z axis was aligned with the proton momentum, the x frame was chosen in the horizontal plane (see Fig. 1), and the y axis was directed upward. The trajectory projections onto the horizontal and the vertical plane were reconstructed independently. The parameters of these straight lines were determined by the least-squares method on the basis of four coordinates in the planes of the chambers PC_{12} and PC_{34}. A spatial trajectory was described in terms of four parameters: α and x_0 in the xz plane and β and y_0 in the yz plane, where α and β are the slopes of the lines, while x_0 and y_0 are their coordinates at $z = 0$. The trajectories of the protons after the analyzing target were reconstructed from the coordinates measured by the chambers PC_5 and PC_6. The slopes α_{56} and β_{56} of the trajectories were calculated as the ratios of the difference of the coordinates in the chambers PC_5 and PC_6 to the distance between the corresponding planes of the chambers.

The resulting parameters of the trajectories before and after the analyzing target were then used to find the coordinates of the point of analyzing pC scattering, the minimum distance between the trajectories,

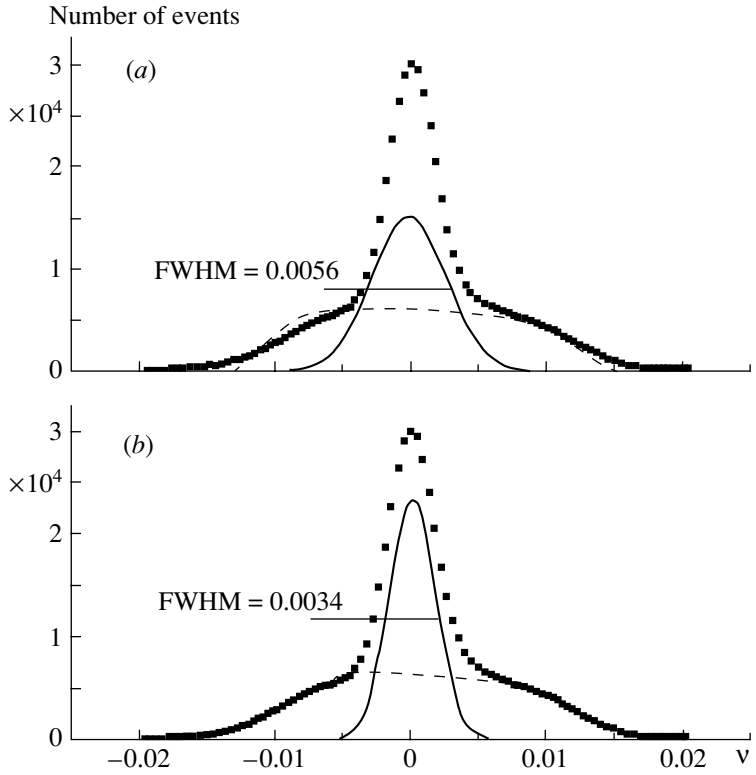

Fig. 2. Momentum spectra of protons scattered at an angle of $\theta = 22.5°$ on the polarized proton target for various versions of corrections: (*a*) the spectrum is reconstructed without allowance for the interaction coordinate in the polarized proton target; (*b*) the spectrum is reconstructed with allowance for the interaction coordinates. The points represent the measured spectrum from the polarized proton target, while the dashed curve shows the normalized spectrum from the background target; the solid curve corresponds to a normal distribution. The width of the normal distribution is given in the figure.

and the polar and azimuthal scattering angles ϑ and φ:

$$\tan^2\vartheta = \Delta\alpha^2 + \Delta\beta^2, \quad \tan\varphi = \Delta\beta/\Delta\alpha, \qquad (2)$$
$$\Delta\alpha = \alpha_{56} - \alpha, \quad \Delta\beta = \beta_{56} - \beta.$$

If a track coordinate was unknown in one of the planes of the chambers PC_5 and PC_6 (for example, in the xz plane of the coordinate frame), the scattering angles were reconstructed by using the z coordinate in the other plane (in the yz plane). From the analysis, we excluded events where (a) the chambers PC_5 and PC_6 detected more than one particle, (b) the scattering point was beyond the analyzing target (less than 5% of the total number of events), and (c) the minimum distance between the trajectories exceeded 4.5 mm (less than 5% of the total number of events).

The chambers PC_{01} and PC_{02} were used to reconstruct the x and y coordinates of the interaction point in the polarized proton target: they were taken to be equal to the values of the corresponding coordinates in the plane that contains the target center and which is orthogonal to the spectrometer axis.

4. MOMENTUM SPECTRA OF PROTONS

The propanediol target contains both free protons and carbon and oxygen nuclei. In the angular range under study, protons elastically scattered by nuclei are reliably separated in the momentum spectra (hereafter, spectra) from protons elastically scattered by hydrogen. At the same time, protons from elastic *pp* scattering (*pp* channel) and those scattered on intranuclear nucleons (quasielastic channel) fall within the same momentum interval; therefore, it is necessary to separate the contribution of the elastic channel from the quasielastic background.

This contribution was determined from an analysis of the proton spectra. Figure 2 shows the spectra at $\theta = 22.5°$ in the region around the peak of elastic *pp* scattering. Along the abscissa, we plotted the relative proton momentum $\nu = (p_0 - p)/p_0$, where p is the current value of the proton momentum, while p_0 is the momentum corresponding to the maximum of the distribution. The points represent the spectrum measured with the polarized target. The dashed curve corresponds to the spectrum measured with the background target and normalized in such a way

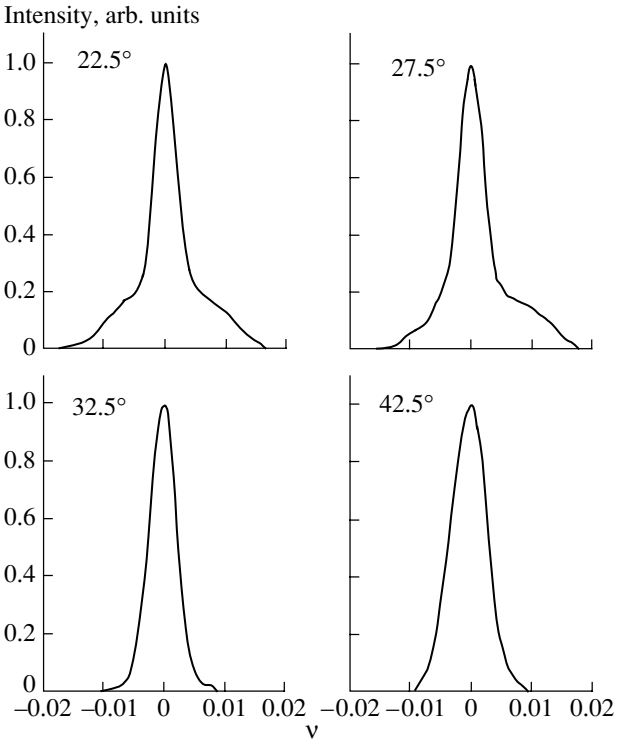

Fig. 3. Momentum spectra of protons scattered on the polarized proton target at angles of 22.5°, 27.5°, 32.5°, and 42.5° in the c.m. frame.

that, taken together with a normalized normal distribution (solid curve), it provides the best fit to the distribution for the polarized proton target. The normalization factors and the parameters of the normal distribution were found by the least-squares method, as is described in Section 5 below. Figure 2*a* displays the spectrum reconstructed without taking into account the interaction point in the polarized proton target. The spectrum in Fig. 2*b* was reconstructed with allowance for the interaction point. It is clear from Fig. 2 that, upon taking into account the interaction coordinate determined with the aid of the inlet chambers, the width of the momentum distribution (FWHM) decreases from 0.0056 to 0.0034, which, in our case, corresponds to the energy-distribution width 4.9 MeV.

Figure 3 displays the spectra measured at various scattering angles (the region of the *pp* peak, U polarization). We can see that, at angles of 22.5° and 27.5°, the quasielastic channel makes a significant contribution, but that, at angles of 32.5° and 42.5°, its contribution is negligible owing to the appearance of signals from the counter C_{11} (see Fig. 1 and Section 2).

5. RESULTS OF THE MEASUREMENTS

The analyzing power A_{000n} was determined from the proton spectra measured at different signs of the target polarization (D and U measurements) and from the spectra measured with the background target. Owing to the normalization method, the analyzing power was calculated at angles of $\theta = 22.5°$ and 27.5°, in which case the intensities of the *pp* and the quasielastic channel are commensurate.

Each spectrum was approximated by the expression

$$S(\nu) = n_{pp} \exp\left(-(\nu - \nu_0)^2/2\sigma^2\right) + n_{\mathrm{qe}} S_{\mathrm{qe}}(\nu), \quad (3)$$

where n_{pp} and n_{qe} are the normalization factors for, respectively, the elastic and the quasielastic channel; ν_0 and σ^2 are, respectively, the position of the center of the distribution and its variance; and $S_{\mathrm{qe}}(\nu)$ is the spectrum measured with the background target.

The parameters n_{pp}, ν_0, σ, and n_{qe} were determined by minimizing the functional

$$\chi^2(n_{pp}, \nu_0, \sigma, n_{\mathrm{qe}}) = \sum_i \left(\frac{N(\nu_i) - S(\nu_i)}{\Delta N(\nu_i)}\right)^2, \quad (4)$$

where $N(\nu_i)$ and $\Delta N(\nu_i)$ are, respectively, the number of measured events at the point ν_i of the spectrum and its statistical error. Summation is performed over all ν_i values in the range being considered.

We used two methods to calculate the analyzing power.

In the first case, the contributions of the scattering channels were found by minimizing the functional in (4) separately for opposite signs of target polarization. The asymmetry A_{000n} was calculated according to the expression

$$A_{000n} = \frac{1-r}{rP_{TU} + |P_{TD}|}, \tag{5}$$

$$r = I_D/I_U, \quad I_j = n_{ppj}\sigma_j/(n_{\mathrm{qe}j}S_{\mathrm{qe}}). \tag{5a}$$

Apart from an insignificant factor, I_j is the elastic-scattering-channel intensity normalized to the quasielastic-channel intensity ($j \in \{D, U\}$). For S_{qe}, we took the total number of events in the spectrum from the background target in a specific range of ν. For this normalization of the elastic channel, the error in determining the *pp* scattering angle and the error in beam monitoring in the measurements of U and D spectra did not contribute to the error in A_{000n}. The relative statistical error in the quantity S_{qe} for the collected number of events was about 0.002.

In the second approach, the analyzing power was determined from all spectra directly. In contrast to (3), the normalization factors n_{ppj} for each spectrum involved A_{000n} explicitly; that is,

$$n_{ppj} = n_{pp}(1 + A_{000n}P_{Tj}), \tag{6}$$

where j stands for the indices (numbers) of the measured spectra, which differ by the magnitude and sign of the target polarization P_T.

The analyzing power A_{000n} in (6) was determined by minimizing a functional that was similar to (4) and which involved it as a free parameter. Summation included the indices j of the measured spectra as well. The minimization code determined the value of A_{000n} and estimated its error.

Table 1 displays the values of A_{000n} for the angles of 22.5° and 27.5°. The values in the table are the averages of the results calculated by the above two methods. The displayed error is the statistical error of the second method. The systematic error in A_{000n} due to the uncertainty in taking into account the contribution of the quasielastic channel amounted to 0.01. The relative error caused by the uncertainty in the degree of the target polarization was 2%.

The polarization P_{n000} and the parameter K_{n00n} were determined from the azimuthal distribution of protons scattered on the analyzing target. Figure 4 shows the azimuthal distributions for the scattering angle of $\theta = 22.5°$. In general, this distribution has the form

$$I(\varphi) = I_0(1 + \varepsilon\cos\varphi + \delta\sin\varphi), \tag{7}$$

where I_0 is a factor that describes the intensity of unpolarized-beam scattering, ε is the left–right asymmetry, and δ is the up–down asymmetry.

The left–right asymmetry ε is defined in terms of the sought parameters as

$$\varepsilon = A_{p\mathrm{C}}\left(\frac{\alpha_1(P_{n000} + K_{n00n}P_T)}{1 + P_{n000}P_T} + \alpha_2 P_{\mathrm{qe}}\right), \tag{8}$$

where $A_{p\mathrm{C}}$ is the carbon analyzing power; α_1 and α_2 are the contributions of, respectively, the *pp* and the quasielastic channel in the chosen section of the spectrum, $\alpha_1 + \alpha_2 = 1$; and P_{qe} is the polarization of quasielastically scattered protons.

The parameters α_1 and α_2 in (8) were found from the spectra accumulated simultaneously with the distributions $I(\varphi)$: $\alpha_1 \sim n_{pp}\sigma$ and $\alpha_2 \sim n_{\mathrm{qe}}S_{\mathrm{qe}}$ [see (5a)]. Since there were no free protons in the background target, $\alpha_1 = 0$.

The carbon analyzing power $\mathrm{A}_{p\mathrm{C}}$ was determined as the weighted average value in the angular range $4° \le \vartheta_{p\mathrm{C}} \le 17°$, where the distributions with respect to φ were accumulated with the weights equal to the differential cross section for the corresponding scattering angle. In this procedure, we used data presented in [16].

In general, the parameters were found by minimizing the functional

$$\chi^2(K_{n00n}, P_{n000}, P_{qe}, \delta) = \sum_j \sum_k \left(\frac{N_j(\varphi_k) - I_j(\varphi_k)}{\Delta N_{jk}}\right)^2. \tag{9}$$

In (9), summation over j is summation over the azimuthal distributions accumulated for scattering on the polarized proton target at various P_T and for scattering on the background target; summation over k is summation over discrete values of the angle φ; and $N_j(\varphi_k)$ and ΔN_{jk} are, respectively, the number of events in the interval φ_k and its statistical error. We sought the parameters K_{n00n}, P_{n000}, P_{qe}, and δ. An investigation of the stability of the resulting solution revealed that the values of K_{n00n} depend on the width of the momentum range where the azimuthal distributions (7) were analyzed—that is, on the elastic-channel contribution α_1. Most likely, this dependence is due to the correlation between the parameters in the functional in (9).

In order to reduce the effect of the correlation between the parameters on their values, we determined P_{n000} and K_{n00n} from the azimuthal distributions obtained only with the polarized proton target in a narrow momentum interval around the *pp* peak, assuming that $P_{n000} = P_{\mathrm{qe}}$. We tested the stability of the solution with respect to variations in the width of the momentum interval: we determined the parameters P_{n000} and K_{n00n} at the angles of 22.5° and 27.5° for various widths of the momentum interval—that is, for various values of α_1. At a small contribution of the

elastic channel (for estimates, we can set $\alpha_1 < 0.5$), K_{n00n} approached the value of 0.4, while, at large α_1, it was close to 0.3. For the parameters P_{n000} and K_{n00n}, we took their values for the middle of the momentum interval and quoted them in Table 1.

The up–down asymmetry considered as a criterion of the possible instrumental asymmetry was $\delta = (0.0011-0.0030) \pm 0.0033$ for various versions. The value of χ^2 was 0.99–1.09 per point.

The parameters P_{n000} and K_{n00n} for the angles of 32.5° and 42.5° were determined under the assumption that $\alpha_1 = 1$. They are given in Table 1.

The values of P_{qe} in Table 1 were obtained from an analysis of the azimuthal distributions measured with the background target and with the polarized proton target off the pp peak, where $\alpha_1 \approx 0$.

Table 1 also presents the statistical errors in the parameters obtained by minimizing the above functional. The relative errors in K_{n00n}, P_{n000}, and P_{qe} due to the uncertainty in the analyzing power are 5%. The relative error in K_{n00n} due to the uncertainty in the target polarization is 2%. The error caused by the uncertainty in the calculated elastic-channel contribution α_1 does not exceed 0.005 for the angles of 22.5° and 27.5°. The assumption that $\alpha_1 = 0.9$ leads to the increase of 0.030 and 0.040 in K_{n00n} for the angles of $\theta = 32.5°$ and 42.5°, respectively.

The polarization P_{qe} proved to be less than the corresponding values of P_{n000} and A_{000n}. However, this difference cannot be considered to be significant in view of the systematic and statistical errors, and the hypothesis that $P_{n000} = P_{\mathrm{qe}}$, which was used to obtain the values of P_{n000} and K_{n00n}, can be considered to be justified.

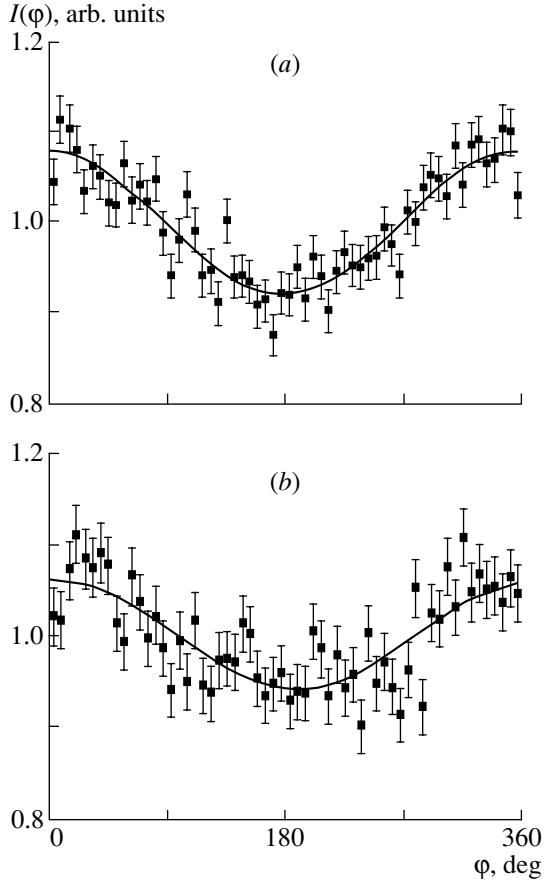

Fig. 4. Azimuthal distributions of the intensity of protons scattered on the analyzing target for various orientations of polarized-proton-target polarization: (*a*) U polarization and (*b*) D polarization. The curves represent the description in terms of the function in (7) (see main body of the text): (*a*) $I(\varphi) = 1 + 0.0795\cos\varphi + 0.0034\sin\varphi$ and (*b*) $I(\varphi) = 1 + 0.05282\cos\varphi + 0.0083\sin\varphi$.

6. DISCUSSION: PARTIAL-WAVE ANALYSIS OF THE DATA

The present data were used to refine the PNPI [3] and the Saclay–Geneva [4] solutions for phase shifts (the latter solution was obtained at the energy of 995 MeV).

In refining the PNPI solution, we employed the experimental-data set in Table 2 with references to the database in [6], the compilation from [17], and the original studies reported in [18–24]. The data set also includes the real parts of the amplitudes F_1, F_2, and F_3 from [25], these differing from the amplitudes $a(0°)$, $b(0°)$, and $f(0°)$ in the scattering matrix (1) only by kinematical factors. We calculated the kinematical variables for each experimental point at its energy. The kinetic energy averaged over all points was 990 MeV. The differential cross sections and polarization were normalized on the basis of a comparison with the predictions of the partial-wave analysis in [3], where they were normalized according to averaged values. We increased the statistical error in the differential cross sections by taking the mean square of this error and $0.01I_0$ and the statistical error in the polarization (analyzing power) by taking mean square of this error and $0.02P_{n000}$ ($0.02A_{000n}$). The statistical errors in higher rank polarization parameters (Y) were increased by taking the mean square of their error and $0.02Y$ for polarized beams or targets and the mean square of their errors and $0.04Y$ for analyzing scattering in order to take into account, respectively, the experimental uncertainties in the beam or target polarization and the carbon analyzing power.

As before, the analysis was performed for $L_{\max} = 7$. We assumed the imaginary parts of the phase shifts for $L \geq 6$ to be equal to zero and fixed them. Therefore, there were 32 free parameters for 414 experimental points. We sought solutions, starting from random initial values of the parameters in the vicinity of the

Table 2. Database of the PNPI partial-wave analysis

No	Observables	Number of points	θ, deg	Energy, MeV	References
1	$\sigma_{\rm tot}, \sigma_{\rm in}$	2	0	970	B-25, B-26 [17]
2	$\Delta\sigma_L$	2	0	995, 1012	A-164 [17]
3	$\Delta\sigma_T$	4	0	933, 1033	[18]
				1021	[19]
				1047	B-248 [17]
4	I_0	39	3.7–8.0	992	DB [6]
		24	6.5–16.7	992	[20]
		9	25.55–93.15	959	R-9 [17]
		24	43.66–89.57	960	K-70 [17]
		19	22.33–88.57	992	DB [6]
		28	35.8–89.0	991	DB [6]
		4	93	984–1002	DB [6]
		20	51–89	1003	W-7 [17]
5	P, A_{000n}	10	30–85	970	[4]
		10	41.4–81.7	985	DB [6]
		22	42.9–86.9	995	DB [6]
		14	36–88	999	DB [6]
		2	36	989	DB [6]
		6	22.5–42.5	1000	Our data
6	D_{n0n0}	13	30–135	970	[2, 3]
		6	49.9–81.1	995	DB [6]
7	K_{n00n}	6	49.2–81.2	995	[21]
		4	22.5–42.5	1000	Our data
8	D_{s0k0}	13	30–120	970	[3]
9	D_{s0s0}	10	30–120	970	[3, 8]
10	D_{0s0k}	6	50.9–81.5	995	DB [6]
		6	50.9–81.9	995	DB [6]
11	K_{0sk0}	6	50.9–81.5	995	DB [6]
12	A_{00nn}	12	35–98	970	[3, 9]
		23	42.9–86.9	995	DB [6]
13	A_{00kk}	6	66.11–82.32	995	DB [6]
		22	42.9–89.6	995	DB [6]
14	A_{00sk}	14	50.4–87.9	995	DB [6]
15	M_{s0kn}	3	70–110	970	[3, 10]
16	$N_{0nkk} + \alpha K_{0kk0}$	5	52.4–81.5	995	[22]
17	$N_{0skn} + \alpha N_{0ssn} + \beta N_{0kkn}$	3	51.5–77.5	995	[23]
18	$K_{0sk0} + \alpha K_{0ss0} + \beta K_{0kk0}$	4	53.9–77.5	995	[23]
19	$N_{0snk} + \alpha K_{0ss0}$	5	50.9–77.9	995	[24]
20	$K_{0nn0} + \alpha N_{0nsk} + \beta K_{0ks0} + \gamma N_{0knk}$	5	50.9–73.9	995	[24]

Note: DB [6] is the database presented [6]. The values of the coefficients α, β, and γ in rows 16–20 are quoted in the corresponding articles.

Table 3. Solutions of the partial-wave analyses (parameters in deg)

Parameters	PNPI solution		Saclay–Geneva solution	
	Re	Im	Re	Im
$\delta(^1S_0)$	-44.688 ± 1.670	0	-47.321 ± 1.072	0
$\delta(^3P_0)$	-47.264 ± 2.831	0.736 ± 2.751	-49.057 ± 0.827	0
$\delta(^3P_1)$	-53.530 ± 2.915	1.728 ± 1.580	-56.719 ± 1.038	6.886 ± 0.696
$\delta(^3P_2)$	9.629 ± 1.655	18.985 ± 1.978	13.374 ± 0.720	19.029 ± 0.878
ε_2	-3.832 ± 0.882	–	-4.877 ± 0.753	–
$\delta(^1D_2)$	3.166 ± 1.110	17.982 ± 1.945	-5.397 ± 0.780	16.479 ± 1.065
$\delta(^3F_2)$	-7.542 ± 1.241	2.864 ± 0.890	-6.826 ± 0.508	4.227 ± 0.478
$\delta(^3F_3)$	-12.707 ± 0.563	12.660 ± 1.058	-12.961 ± 0.403	7.873 ± 0.464
$\delta(^3F_4)$	9.110 ± 0.557	0.619 ± 0.593	9.612 ± 0.212	0
ε_4	-2.169 ± 0.309	–	-2.014 ± 0.209	–
$\delta(^1G_4)$	4.385 ± 0.363	2.805 ± 0.539	0.217 ± 0.289	2.795 ± 0.275
$\delta(^3H_4)$	-0.059 ± 0.423	2.690 ± 0.516	$-0.212 \pm 0,221$	3.148 ± 0.304
$\delta(^3H_5)$	-3.175 ± 0.547	1.148 ± 0.398	-1.559 ± 0.318	2.514 ± 0.217
$\delta(^3H_6)$	2.536 ± 0.203	0	2.543 ± 0.104	0
ε_6	-0.899 ± 0.179	–	-1.487	–
$\delta(^1I_6)$	1.081 ± 0.140	0	0.722	0.588
$\delta(^3J_6)$	0.831 ± 0.221	0	0.654	0.116
$\delta(^3J_7)$	-2.648 ± 0.398	0	-1.514	0.249
$\delta(^3J_8)$	0.356 ± 0.137	0	0.377	0
ε_8	–	–	0.763	–
$\delta(^1K_8)$	–	–	0.433	0.082
$\delta(^3L_8)$	–	–	0.287	0.018
$\delta(^3L_9)$	–	–	-0.792	0.030
$\langle\chi^2\rangle$	1.07		0.96	

required solution [3]. Upon 100 trials, we arrived at a single solution characterized by $\langle\chi^2\rangle = 1.07$ per degree of freedom. Table 3 displays this solution with the errors in the parameters.

The Saclay–Geneva solution [4] was refined by varying the phase shifts and mixing parameters for orbital angular momenta of $L \leq 5$ at fixed parameters of higher states up to $L_{\max} = 9$. The real parts were fixed at the values obtained in the one-pion-exchange (OPE) model, while the imaginary parts were calculated from the dispersion relations (see [4]).

Table 3 also shows the solution found in this way. It differs from the original one within the statistical errors in the adjustable parameters. The largest difference is observed for the real part of the phase shift $\delta(^3P_0)$. The value of $\langle\chi^2\rangle$ for this solution remained equal to the value (0.96) obtained before the inclusion of our data. The average contribution of our four points of K_{n00n} to the value of χ^2 is 1.091, and this can be considered as an indication of a satisfactory description.

This PNPI solution differs from the original one mainly within the errors of the parameter. The largest difference is observed for the real parts of the phase shifts for the $^1D_2$ and $^1G_4$ states. The phase shift $\delta(^1D_2)$ remained positive, which is at odds with the Saclay–Geneva and Arndt *et al.* [6] solutions, but is in agreement with the solution in [5]. This difference can be explained by the fact that the PNPI analysis

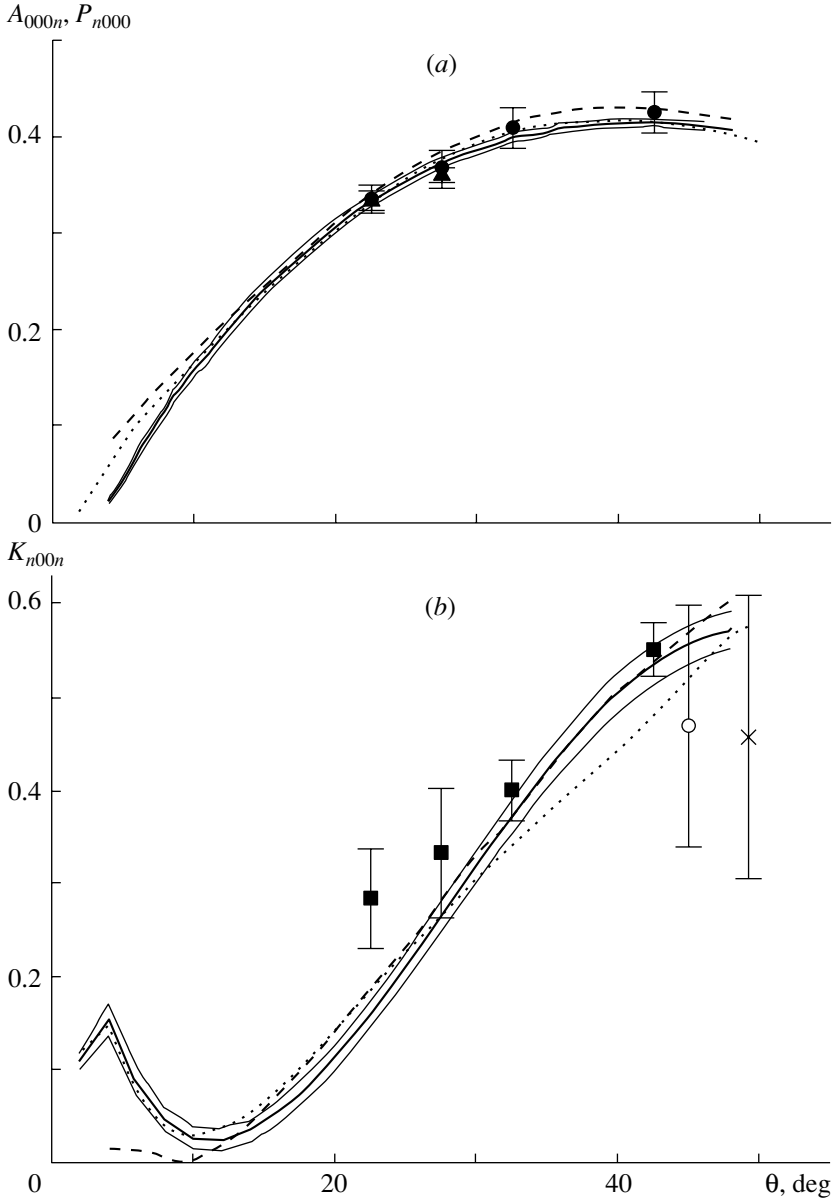

Fig. 5. (*a*) Angular dependences of the (▲) analyzing power A_{000n} and (●) polarization P_{n000} and (*b*) angular dependence of the spin-transfer parameter K_{n00n}. The curves represent the predictions of the (solid curve with the error corridor) PNPI, (dashed curve) Saclay–Geneva, and (dotted curve) SM94 solutions. The closed symbols represent our experimental data. Other displayed data were borrowed from (○) [7] and from (×) [21].

(as well as that in [5]) used the PNPI polarization data of the Leningrad period [3, 7–11], some of these data referring to the low-energy edge of the energy range covered by the experimental set.

Figure 5 displays the experimental data, along with the predictions of the PNPI (solid curve with the error corridor) and Saclay–Geneva (dashed curve) partial-wave analyses and the SM94 prediction (dotted curve), which describes our data better than other solutions [6].

In Fig. 5*a*, our data on A_{000n} and P_{n000} are contrasted against the predictions of partial-wave analyses. It is clear that our data are described well by all solutions (the contribution to χ^2 from each of six points is less than unity).

Figure 5*b* shows our data on K_{n00n}, along with data obtained in previous studies: $K_{n00n}(45°) = D_{n00n}(135°)$ from [7] and $K_{0nn0}(49.2°)$ from [6, 21]. It cannot be said that our value of $K_{n00n}(42.5°)$ contradicts the data of earlier measurements at close angles because of large statistical errors in the data. The total contribution of four newly measured points to the value of χ^2 amounts to 7.2 in the PNPI solution

(the solution from [3] predicted the contribution equal to 17.0); the main contribution (5.1) comes from the value of $K_{n00n}(22.5^\circ)$; the contribution of our points is 4.4 in the Saclay–Geneva solution (in the original solution, the functional in question is 7.2) and is 11.2 in the SM94 solution.

If the real parts of the amplitudes F_1, F_2, and F_3 are used for experimental points or if the phase shifts in higher partial waves are fixed at their model values, the predictive base of partial-wave analyses becomes narrower. It would be more interesting to compare model predictions and the results of partial-wave analyses. In order to perform such a comparison, we sought solutions in the PNPI analysis without using the real parts of the amplitudes F_1, F_2, and F_3. The solutions obtained at the level $\chi^2_{\min}$–$1.01\chi^2_{\min}$ featured a large scatter in the predictions of the real part of F_3—that is, in the real part of the amplitude $f(0^\circ)$ in the matrix **M** (1). The scatter value was as large as 50% of the calculated value of ReF_3 [25]; the analogous scatter for the other amplitudes was 15% for F_1 and 25% for F_2. This may be due to the correlation between the parameters of the minimized functional, the scarcity of experimental data at small angles, and a small relative fraction of observables (in available data) that characterize the spin components in the scattering plane.

The point $K_{n00n}(22.5^\circ)$ in the PNPI solution makes an enhanced contribution to χ^2, and this may be a consequence of the disregard of a systematic error. Such an error may stem from an instrumental asymmetry of the polarimeter. Because of different values of P_T and different contributions of the *pp* channel to proton beams that are formed by the scattering of protons on the polarized proton target having different signs of P_T (U and D polarizations) and which are analyzed by the polarimeter, the instrumental asymmetry affects not only the sought parameter P_{n000} but also K_{n00n}. At the same time, it is natural to expect that the extension of the angular range studied experimentally would require including higher harmonics in the expansion of the amplitudes in order to describe the data (for example, up to $L_{\max} = 9$, as in the Saclay–Geneva analysis and in other analyses). The PNPI solution was also obtained for the version where $L_{\max} = 9$, and this provided a better description of K_{n00n}. The total contribution to χ^2 from four K_{n00n} points is 4.0, the contribution from $K_{n00n}(22.5^\circ)$ being 3.1. However, the solution did not reduce the value of $\langle\chi^2\rangle$; moreover, the deviations of the resulting parameters [with the exception of the phase shift $\delta(^3L_9)$] from the original values were within the statistical errors in the parameters. In addition, the scatter of the predictions for the real parts of the amplitudes F_1, F_2, and F_3 proved to be substantially larger.

7. CONCLUSIONS

(i) For elastic *pp* scattering at an energy of 1 GeV, we have measured the spin-transfer parameter K_{n00n} and the polarization P_{n000} at c.m. angles of 22.5°, 27.5°, 32.5°, and 42.5° and the analyzing power A_{000n} at c.m. angles of 22.5° and 27.5°.

(ii) The existing solutions of partial-wave analyses failed to describe the parameter K_{n00n} in the angular region $\theta < 50^\circ$ satisfactorily; our data have enabled us to improve the solution.

(iii) By including our data, we have corrected the PNPI and Saclay–Geneva solutions. In the resulting solutions, the phase shifts differ from the original values mainly within the statistical errors in the parameters.

(iv) While new data do not affect the phase shifts significantly, the amplitudes in the scattering matrix may change significantly because of the correlations between the parameters. Our investigation of the PNPI solutions by means of random searches has revealed a large scatter of the predictions for the real part of the forward-scattering amplitude f. In order to obtain less ambiguous solutions in the partial-wave analysis, it is necessary to have small-angle measurements of polarization parameters that describe the spin components in the scattering plane. These may be, for example, A_{00ij} and D_{i0j0}, where $i, j = s, k\,(k, s)$.

ACKNOWLEDGMENTS

This work was supported by the Russian Foundation for Basic Research (project no. 96-02-18921a) and by the Ministry for Industry, Science, and Technologies of the Russian Federation (contract no. 40.052.1.1.1113).

REFERENCES

1. Yu. M. Kazarinov and I. N. Silin, Zh. Éksp. Teor. Fiz. **43**, 692 (1962) [Sov. Phys. JETP **16**, 491 (1963)].
2. V. G. Vovchenko *et al.*, Preprint No. 995, LIYaF (Leningrad Nuclear Physics Institute, 1984).
3. V. G. Vovchenko *et al., Pion–Nucleon and Nucleon–Nucleon Interactions, Proceedings of the 3rd International Symposium* (Leningrad–Gatchina, 1989).
4. J. Bystricky *et al.*, J. Phys. (Paris) **51**, 2747 (1990).
5. Y. Higuchi *et al.*, Prog. Theor. Phys. **88**, 1019 (1992).
6. R. A. Arndt, Phys. Rev. C **50**, 2731 (1994); http://gwdac.phys.gwu.edu
7. V. G. Vovchenko *et al.,* Pis'ma Zh. Éksp. Teor. Fiz. **29**, 95 (1979) [JETP Lett. **29**, 87 (1979)].

8. V. G. Vovchenko *et al.,* Yad. Fiz. **33**, 1551 (1981) [Sov. J. Nucl. Phys. **33**, 835 (1981)].
9. N. S. Borisov *et al.,* Pis'ma Zh. Éksp. Teor. Fiz. **34**, 137 (1981) [JETP Lett. **34**, 130 (1981)].
10. N. A. Bazhanov *et al.,* Pis'ma Zh. Éksp. Teor. Fiz. **47**, 435 (1988) [JETP Lett. **47**, 515 (1988)].
11. N. S. Borisov *et al.,* Pis'ma Zh. Éksp. Teor. Fiz. **43**, 559 (1986) [JETP Lett. **43**, 722 (1986)]; V. G. Vovchenko *et al.,* Yad. Fiz. **50**, 1005 (1989) [Sov. J. Nucl. Phys. **50**, 625 (1989)].
12. M. L. Barlett *et al.*, Phys. Rev. C **30**, 279 (1984).
13. N. P. Aleshin *et al.*, Preprint No. 1971, PIYaF (Petersburg Nuclear Physics Institute, Gatchina, 1994).
14. V. A. Andreev *et al.*, Preprint No. 2475, PIYaF (Petersburg Nuclear Physics Institute, Gatchina, 2002).
15. N. S. Borisov *et al.*, Preprint No. 13-10253, OIYaI (Joint Institute for Nuclear Research, Dubna, 1976); Preprint No. 13-10257, OIYaI (Joint Institute for Nuclear Research, Dubna, 1976).
16. O. Ya. Fedorov, Preprint No. 484, LIYaF (Leningrad Nuclear Physics Institute, Leningrad, 1979).
17. J. Bystricky and F. Lehar, *Nucleon–Nucleon Scattering Data* (Karlsrue, 1978).
18. F. Perrot *et al.*, Nucl. Phys. B **278**, 881 (1986).
19. W. P. Madigan *et al.*, Phys. Rev. D **31**, 966 (1985).
20. A. V. Dobrovolsky *et al.*, Nucl. Phys. B **214**, 1 (1983).
21. C. D. Lac *et al.*, Nucl. Phys. B **315**, 284 (1989).
22. C. D. Lac *et al.*, Nucl. Phys. B **315**, 269 (1989).
23. C. D. Lac *et al.*, Nucl. Phys. B **321**, 269 (1989).
24. C. D. Lac *et al.*, Nucl. Phys. B **321**, 284 (1989).
25. W. Grein and P. Kroll, Nucl. Phys. B **137**, 173 (1978); Nucl. Phys. A **377**, 505 (1982).

Translated by M. Kobrinsky

Physics of Atomic Nuclei, Vol. 67, No. 5, 2004, pp. 961–984. Translated from Yadernaya Fizika, Vol. 67, No. 5, 2004, pp. 983–1005.

ELEMENTARY PARTICLES AND FIELDS
Experiment

Could Primary Particles of Ultrahigh Energy Be Neutral?

A. V. Glushkov*

Institute of Cosmophysical Research and Aeronomy, Yakutsk Research Center, Siberian Division, Russian Academy of Sciences, pr. Lenina 31, Yakutsk, 677891 Russia

Received December 15, 2002; in final form, July 3, 2003

Abstract—Results are presented that were obtained from an analysis of the nuclear-physics and astrophysical features of extensive air showers of energy in the region $E_0 \geq 10^{15}$ eV that were recorded at the Yakutsk array and other arrays over the world. It is shown that, at some values of E_0, different data sets display local irregularities that are correlated in energy and which are interpreted as a manifestation of neutral particles of an extragalactic origin. The directions of their arrival point to the Supergalaxy plane (Local Supercluster of galaxies). © *2004 MAIK "Nauka/Interperiodica"*.

1. INTRODUCTION

Investigation of the composition of primary cosmic radiation of ultrahigh energy in the region $E_0 \geq 10^{15}$ eV is one of the most difficult problems in astrophysics. Since the discovery of a knee in the spectrum of extensive air showers at $E_0 \approx 3 \times 10^{15}$ eV by a group from Moscow State University more than 40 years ago [1], a great number of relevant experiments have been performed, but there is still no unambiguous understanding of this phenomenon. A clarification of its nature would greatly contribute to solving the problem of the origin of cosmic rays of ultrahigh energies up to about 10^{20} eV.

There exists the opinion that, at energies in the range $3 \times 10^{15} < E_0 \leq 10^{17}$ eV, the composition of primary cosmic radiation is significantly enriched in heavy nuclei (see, for example, [2, 3]), but that, in the range $10^{17} < E_0 \leq 10^{18}$ eV, it undergoes a sharp reverse change, toward an increase in the fraction of protons [4]. The heaviest composition is assumed to correspond to $E_0 \approx 10^{17}$ eV. This picture can be explained within the diffusion model [5], which also ensures agreement with the shape of the energy spectrum of primary cosmic radiation in the region around the aforementioned knee.

Important information about the origin of cosmic rays is contained in their anisotropy. A harmonic analysis of the distribution of the arrival directions of extensive air showers with respect to the right ascension [6] is one of the basic methods for assessing the anisotropy of the global flux of primary cosmic radiation. The application of this method at the Haverah Park array [7] resulted in discovering, at $E_0 \approx 10^{17}$ eV, a statistically significant anisotropy that was first confirmed at the Yakutsk array [8] but was then disproved [9]. The AGASA (Akeno Giant Air Shower Array) group found a significant anisotropy [the amplitude of its first harmonic being about $(4 \pm 0.06)\%$] at $E_0 \approx (8\text{–}20) \times 10^{17}$ eV [10]. This anisotropy is caused by an increased flux of primary cosmic radiation from the region in the vicinity of the Galaxy center. This result was confirmed and refined by an Australian group at the SUGAR (Sydney University Giant Air Shower Recorder) array [11].

The aforementioned (and many other) results are based on the assumption that primary cosmic radiation of ultrahigh energy consists predominantly of charged particles (protons and nuclei of various cosmic elements). They are strongly mixed by the magnetic field of the Galaxy, so that their distribution over the celestial sphere is nearly isotropic. Under such conditions, it is difficult to reveal local sources of primary cosmic radiation.

However, these ideas are not unquestionable, because there are still no direct measurements of the composition of primary cosmic radiation of ultrahigh energy and because conclusions drawn from data on extensive air showers are ambiguous and contradictory. It was previously reported in [12, 13] that, in the arrival directions of primary cosmic radiation of energy in the region $E_0 \geq 4 \times 10^{17}$ eV, there is a considerable number of groups of showers in narrow solid angles. Their distribution over the celestial sphere has a small-scale ordered structure that cannot be explained by random statistical processes. In the opinion of the present author, this may be due to a distribution of extragalactic pointlike sources of primary cosmic radiation that generate neutral particles. Recently, this hypothesis was additionally confirmed

*e-mail: a.v.glushkov@ikfia.ysn.ru

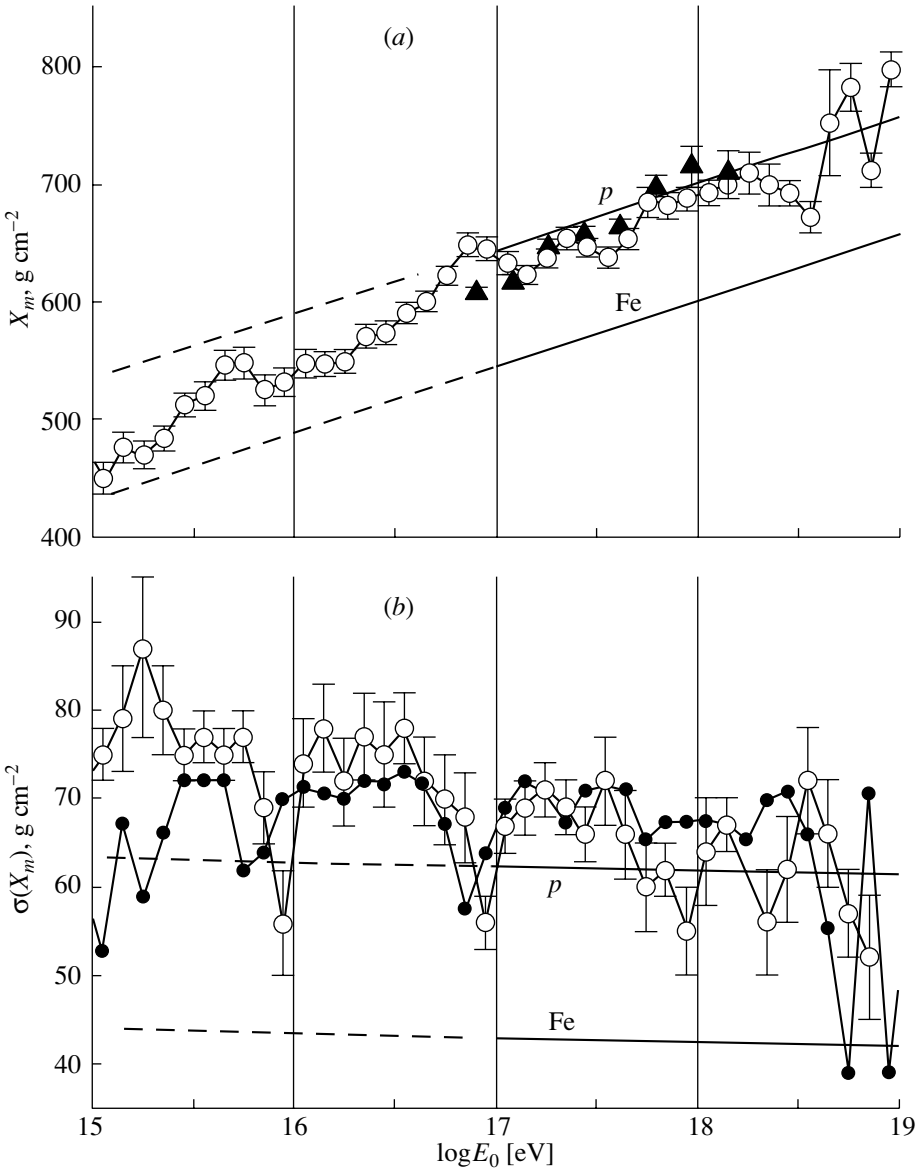

Fig. 1. (*a*) Mean depth of the shower maximum and (*b*) its fluctuations versus primary energy: (open circles) generalized experimental results from [21], (closed triangles) data from [4], (closed circles) estimates of $\sigma(X_m)$ on the basis of relation (3) for a mixed composition featuring protons and iron nuclei that is supplemented with the values obtained in this study for $\langle \ln A \rangle$ (see Fig. 2*a* below), (solid lines) results of the calculations from [23] for primary protons (p) and iron nuclei (Fe) on the basis of the QGSJET model [24], and (dashed lines) extrapolation of the results.

in [14–20]. Presented below are new experimental results favoring this point of view.

2. DEPTH X_m OF THE SHOWER MAXIMUM AND ITS FLUCTUATIONS

Let us first consider a traditional method according to which the composition of primary cosmic radiation is estimated by using the features of the spatial development of extensive air showers. The depth X_m of the shower-development maximum is one of the extensive-air-shower parameters that are the most sensitive to the composition of cosmic rays. We have

$$X_m^A \cong X_m^0 + ER(\ln E_0 - \ln A) \qquad (1)$$
$$= X_m^p - ER \ln A \ [\mathrm{g/cm^2}],$$

where A is the atomic weight of primary particles; $ER = \partial X_m / \partial \ln E_0$; X_m^A and X_m^p are the depths of the maxima of showers that are generated by primary nuclei and primary protons, respectively; and X_m^0 is a constant that depends on the model chosen for describing the development of extensive air showers.

From relation (1), one can find $\ln A$; in the case of a mixed composition, we have $\langle \ln A \rangle = \sum W_i \ln A_i$, where W_i is the fraction of nuclei whose atomic weight is A_i. Since the parameter X_m^0 is known insufficiently well, estimates of $\ln A$ on the basis of experimentally measured values of X_m are uncertain to a considerable extent. Estimates of relative changes in the composition of primary particles versus E_0 are more precise:

$$\partial \ln A / \partial \ln E_0 = 1 - (1/ER)(\partial X_m^A / \partial \ln E_0). \quad (2)$$

For a broad range of primary energies, the results obtained in [21] for the depths of the shower maxima by averaging X_m values measured at various arrays worldwide are shown by open circles in Fig. 1*a*. These data (107 values) were supplemented by 132 X_m values found in [21] by the method of model-independent parameters [22] from lateral distributions of charged particles and from the fraction of muons among the total number of charged particles (electrons and muons) according to various data obtained worldwide. The two data sets (107 and 132 values) comply with each other.

The closed triangles in Fig. 1*a* represent experimental data reported in [4], which were obtained at a hybrid facility that consisted of the High-Resolution Fly's Eye Air Fluorescence Detector (HiRes) and the Michigan Muon Array (MIA). The HiRes records the ionization fluorescence of extensive air showers in the vicinity of the cascade-curve maximum and therefore sees X_m directly. As to the MIA, it is used to improve the accuracy in determining this parameter. The data in question are consistent with those considered above, especially when E_0 is increased by a factor of 1.5 in the HiRes/MIA experiment (for the normalization with respect to E_0, see Section 3 below).

The solid lines in Fig. 1 show the dependences $X_m(E_0)$ found for primary (p) protons and iron (Fe) nuclei [23] according to the QGSJET model [24]. They correspond to the case where the rate of the shift of the shower maximum is $\partial X_m / \partial \log E_0 = 58$ g/cm^2. The dashed lines represent extrapolations of the calculations to the region of lower primary energies.

It can be seen that the experimental dependence $X_m(E_0)$ is of a rather complicated character. At individual points, there are local irregularities, which are especially pronounced at energies of $E_0 \approx 5 \times 10^{15}$ and 7×10^{16} eV and at energies above 3×10^{18} eV. By and large, the composition of primary cosmic radiation gradually becomes lighter with increasing energy. By using relation (1) for the QGSJET model and the data in Fig. 1*a*, one can estimate $\langle \ln A \rangle$. The resulting values are given in Fig. 2*a*.

Let us consider fluctuations of the depth of the shower maximum, $\sigma(X_m)$. The open circles in Fig. 1*b* represent values obtained in [21] by averaging numerous data obtained worldwide. They also include the $\sigma(X_m)$ values found additionally in [21] from fluctuations of the lateral distributions of electrons and muons by the aforementioned method of model-independent parameters on the basis of data from various facilities operating worldwide.

Near the aforementioned irregularities, the fluctuations of the depth of the shower maximum are less than in neighboring energy regions. From the relation [25]

$$\sigma^2(X_m) \cong (\sigma_p(1 - \eta\langle \ln A \rangle))^2 + (\sigma(\ln A))^2((\eta\sigma_p)^2 + ER^2), \quad (3)$$

where σ_p represents fluctuations of the depth of the maximum of showers generated by primary protons, $(\sigma(\ln A))^2 = \sum W_i (\ln A_i)^2 - \langle \ln A \rangle^2$, and $\eta = 0.1$–0.2 (its specific value depends on the choice of model for describing the development of extensive air showers), it follows that, in the case of a pure composition ($\sigma(\ln A) = 0$), small fluctuations $\sigma(X_m)$ are possible for $A \gg 1$ nuclei; at $A = 1$, they are achieved via a decrease in σ_p (for example, owing to an increase in the cross section for inelastic nuclear interactions in air).

We will make use of relation (3) and the QGSJET model in order to estimate the possible fluctuations $\sigma(X_m)$ on the basis of $\langle \ln A \rangle$ values that we obtained (see Fig. 2*a*). For the sake of simplicity, we will consider the version of a mixed composition featuring protons and iron nuclei. From the relation

$$\langle \ln A \rangle = W_1 \ln(1) + W_2 \ln(56), \quad (4)$$

we then derive the weight functions $W_1 = 1 - W_2$ (for p) and $W_2 = \langle \ln A \rangle / \ln(56)$ (for Fe) shown in Fig. 2*b* by, respectively, open and closed circles. At $\eta = 0.15$, we obtain the $\sigma(X_m)$ values represented by closed circles in Fig. 1*b*.

It can be seen that the fluctuations $\sigma(X_m)$ of the depth of the shower maximum that were obtained from the dependence $X_m(E_0)$ for the above two-component composition (p + Fe) and those that were measured directly agree within the errors. Moreover, the local irregularities at $E_0 \approx (6$–$8) \times 10^{15}$ and $(6$–$8) \times 10^{16}$ eV are also in accord in these two independent results, this being, in all probability, indicative of a nonaccidental origin of these irregularities.

The closed boxes in Fig. 2*a* represent data obtained in the KASKADE experiment [3]. These data are in a glaring contradiction with the estimates presented here and with the result reported in [4].

3. ENERGY SPECTRUM OF PRIMARY COSMIC RADIATION

The energy spectrum of cosmic rays of ultrahigh energy can shed additional light on the problem of the composition of primary cosmic radiation. In Fig. 3, the differential energy spectrum of extensive air showers that was obtained at the Yakutsk array [26] is shown by open circles. This spectrum includes only those events that are characterized by zenith angles in the region $\theta \leq 45^\circ$ and which were selected by master triangles where the spacings between the stations involved were 500 m. The crosses in this figure represent the spectrum [27] measured at the Akeno array [28], which consists of 156 scintillation detectors of area 1 m^2 that are arranged within a circle of radius 1 km. The Akeno spectrum is superimposed on our spectrum by increasing the energy corresponding to the data in [27] by a factor of 1.32, the points being concurrently shifted above by $2\log(1.32) = 0.35$. The closed triangles in Fig. 3 represent the spectrum measured in the HiRes/MIA experiment [4]; this spectrum was also rescaled to the energy region of the spectrum from [26] by increasing the energy of the data in [4] by a factor of 1.5.

Here, we can see a series of local splashes of the intensity of primary cosmic radiation that are indicated by arrows. The first of these, at $E_0 \approx (6-7) \times 10^{15}$ eV, correlates in energy with the irregularities in Figs. 1 and 2 and, in all probability, has a common origin with them. The peaks that follow this one, those at $E_0 \approx (6-7) \times 10^{17}$ and $(6-7) \times 10^{18}$ eV, are also statistically significant (not less than three standard deviations). All three peaks can be attributed to a fast change in the composition of primary cosmic radiation toward an overwhelming dominance of protons. It is difficult to explain this phenomenon within the diffusion model of cosmic-ray propagation in the Milky Way Galaxy.

4. ANISOTROPY OF PRIMARY COSMIC RADIATION

Many experiments devoted to studying the composition of primary cosmic radiation of ultrahigh energy lead to contradictory results. The problems that arise in this connection lie in the uncertainty of the very approach to solving them rather than in methodological features of one experiment or another, because the majority of the methods for determining the composition of primary cosmic radiation are indirect. They are based on a comparison of the observed features of extensive air showers with their calculated counterparts that are found by using some model concepts of the development of these showers and a specifically preassigned composition of primary cosmic radiation. Here, one encounters some kind of a vicious circle: in order to choose a correct model, it is necessary to know the composition of primary particles, but, in order to determine this composition, it is necessary to have a correct model of the development of extensive air showers.

In view of this, investigations of the anisotropy of primary cosmic radiation—in particular, searches for local sources—play a very important role here, since the arrival directions of cosmic rays do not depend on any model concepts concerning the development of extensive air showers. In [12–20], it was shown that, at $E_0 > 10^{17}$ eV, some part of primary cosmic radiation has a small-scale ordered structure associated with the distribution of extragalactic pointlike sources of primary cosmic radiation, which are likely to generate neutral particles.

4.1. Harmonic Analysis

Let us first investigate the anisotropy of the global flux of primary cosmic radiation. We consider extensive air showers that are characterized by energies in the region $E_0 \geq 10^{17}$ eV and zenith angles satisfying the condition $\cos\theta \geq 0.6$ ($\theta \leq 53^\circ$) and which were recorded at the Yakutsk array over the period between 1974 and 2002. Selected for the present analysis are only those showers for which the arrival directions were found on the basis of data from four or more stations and whose axes were within the array central circle of radius $R \leq 1000$ m. The primary-particle energy E_0 was determined from the relations

$$E_0 = (4.8 \pm 1.6) \times 10^{17} (\rho_{s,600}(0^\circ))^{1.0\pm0.02} \ \text{[eV]}, \quad (5)$$

$$\rho_{s,600}(0^\circ) = \rho_{s,600}(\theta) \exp((\sec\theta - 1) \cdot 1020/\lambda_\rho) \ [\text{m}^{-2}], \quad (6)$$

$$\lambda_\rho = (450 \pm 44) + (32 \pm 15)\log(\rho_{s,600}(0^\circ)) \ [\text{g/cm}^2], \quad (7)$$

where $\rho_{s,600}(\theta)$ is the charged-particle density measured by ground scintillation detectors at the distance of $R = 600$ m from the shower axis. The total number of showers selected in this way is 105 012.

We have used the traditional method of a harmonic analysis in terms of the equatorial coordinates [6] and examined the behavior of the first harmonic. The part of the sky viewed by the Yakutsk array was broken down into 24 sectors (with a step of $\Delta\alpha = 15^\circ$ with respect to right ascension). The harmonic-analysis method consists in choosing the best values for the amplitude A_1 and the phase φ_1 of the function

$$f(\alpha) = f_0(1 + \mathrm{A}_1 \cos(\alpha - \varphi_1)) \quad (8)$$

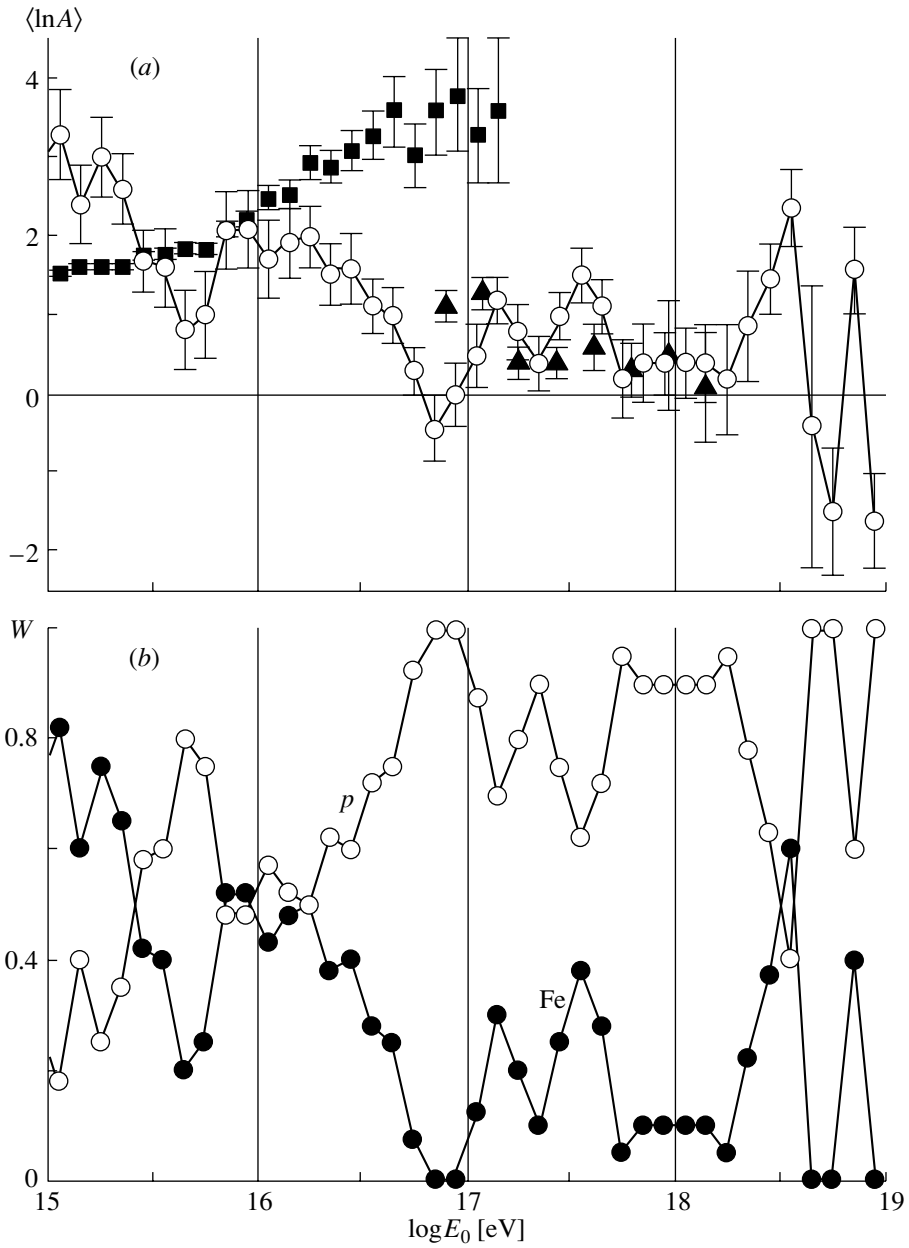

Fig. 2. (*a*) Average atomic weight for a mixed composition of primary particles as a function of their energy: (open circles) $\langle \ln A \rangle$ values obtained from the data in Fig. 1*a* and from relation (1), (closed boxes) data from [3], and (closed triangles) data from [4]; (*b*) estimates obtained for the fractions of protons (*p*) and iron nuclei (Fe) for a two-component composition of primary cosmic radiation by using the values of $\langle \ln A \rangle$ (open circles in Fig. 2*a*) and relation (4).

by minimizing the quantity

$$\chi^2 = \sum_{i=1}^{n} (f_i - N_i)^2 / f_i, \qquad (9)$$

where N_i is the number of showers in the ith spherical sector $\Delta\alpha_i$ and $f_0 = \sum_{i=1}^{n} N_i/n$.

The anisotropy was studied in the intervals $h = \Delta \log E_0 = 0.2$ (they are referred to here as bins) by consecutively shifting them along the energy scale by $0.1h$. This was done in order to perform a more detailed analysis of the behavior of the phase φ_1, since there are some indications in [21, 29–31] that, at specific values of E_0, this phase may undergo fast changes. It is the opinion of the present author (see [21]) that these changes are not accidental, reflecting the actual scenario of the propagation of primary cosmic radiation in space.

The amplitude A_1 of the first harmonic is a measure of the global anisotropy of primary cosmic radiation. If it exceeds sizably (at a level above three

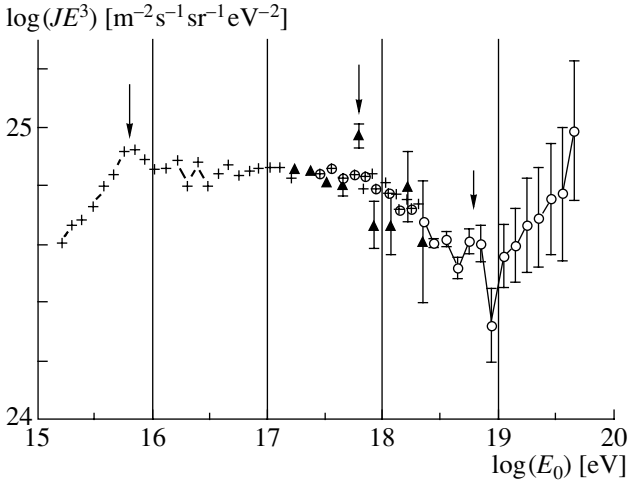

Fig. 3. Differential energy spectrum of cosmic rays: (open circles) experimental data from the Yakutsk array for studying extensive air showers [26], (closed triangles) data of the HiRes/MIA experiment [4], and (direct crosses) Akeno data [27, 28]. The arrows indicate statistically significant peaks (those at a level of three standard deviations and above that).

standard deviations) the amplitude of the adequate isotropic flux, it is assumed that the phase φ_1 reflects the actual anisotropy. We will first examine the behavior of the phase of the first harmonic, irrespective of its amplitude, postponing the analysis of A_1 as a function of E_0 to further stages of our investigation.

In Fig. 4*b*, the open circles show the dependence of φ_1 on the mean energy in a bin. It can be seen that, at some specific values of the energy, the phase of the first harmonic has stable and close values, which, at regular intervals, undergo fast variations about the dashed line, which was borrowed from the review article quoted in [21] and which characterizes the behavior of φ_1 according to world-averaged data.

The crosses in Fig. 4*b* represent the phase φ_1 as a function of energy according to the results obtained at the AGASA array [10] from an analysis of 114 000 showers having zenith angles in the region $\theta \leq 60^\circ$. Before proceeding to compare the results that come from the two arrays in question, we note that they scan different parts of the sky. This can clearly be seen from Fig. 5, where the unshaded region around the North Pole of the Earth corresponds to the sky zone viewed by the Yakutsk array (in terms of the galactic coordinates) for $\cos\theta \geq 0.6$, while the shaded region is the complementary part of the sky, that which is viewed by the AGASA array for $\cos\theta \geq 0.5$. The circles in Fig. 5 show the magnetic fields in the Milky Way Galaxy [32], the open and the closed ones corresponding to the field orientations toward and away from an observer, respectively; the diameters of the circles are proportional to the field strength. The chart is plotted in such a way that equal areas in the figure correspond to sky parts of identical area.

The AGASA data in Fig. 4*b* also indicate that there is some regularity in the behavior of the phase φ_1 (including its variations), although the authors of [10] did not pay any special attention to this. They only indicated that, for $8 \times 10^{17} < E_0 < 2 \times 10^{18}$ eV, the amplitude $A_1 \approx 0.04$ significantly exceeds the respective random value for the isotropic flux. The phase $\varphi_1 \approx 295^\circ$ of this amplitude (arrow *1* in Fig. 5) corresponds to the direction toward the outlet of the Orion arm at a galactic longitude of $l_G \approx 50^\circ$. In [10], however, this phase was associated with the Galaxy center, from which an excess flux of primary cosmic radiation originates, according to data reported there. Unfortunately, the Yakutsk array does not "see" the Galaxy center.

At first glance, the data from the Yakutsk array are poorly consistent with the AGASA data. However, this statement is true only partly. In the region $E_0 \geq 8 \times 10^{18}$ eV, the two arrays show approximately identical E_0 dependences of the phase φ_1. The discrepancy at lower energies is likely to be due to the fact that, in Fig. 4*b*, each point of the AGASA data corresponds to the anisotropy for the total flux of primary cosmic radiation for an energy value exceeding the value being considered. Under such conditions, the relevant peaks and dips can be strongly smoothed. Upon taking into account this circumstance, the distinction between the estimates of energy at the two arrays by a factor of about 1.32, and their different geographical positions (AGASA lies 27° to the south and surveys a much greater part of the sky), it becomes clear that there is some correlation between the data.

For the peaks and dips in Fig. 4*b*, we will now perform a more detailed analysis, paying special attention to the possibility of their accidental formation. We will consider the hypothesis of an isotropic distribution of showers in 24 angular spherical sectors. We will make use of the values that the functional in (9) takes in accordance with the distribution of χ^2 for $(n-3)$ degrees of freedom. For $\chi^2 > \chi^2_{1-p}$, where χ^2_{1-p} is that tabular value of χ^2 which corresponds to a specific confidence level p, this hypothesis can be rejected with the confidence probability $\beta = 1 - p$.

Figure 4*d* shows χ^2 values (for the phases φ_1 given in Fig. 4*b*) versus the mean energy in a bin. A comparison of the calculated values of χ^2 with the tabular values χ^2_{1-p} makes it possible to reject the hypothesis that the peaks and dips in Fig. 4*b* are of a random origin. Some of them have a significance level not lower than four standard deviations (with the confidence probability being $\beta \geq 0.99996$), whence it

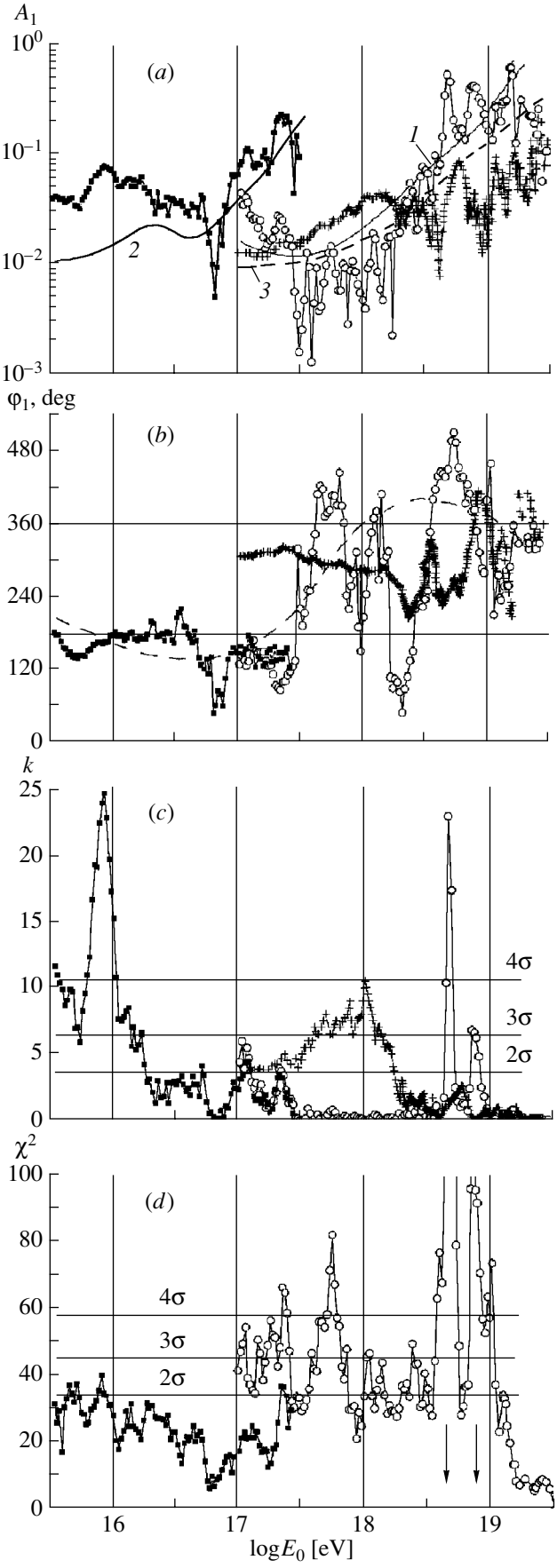

Fig. 4. (*a*) Amplitude and (*b*) phase of the first harmonic versus the energy of primary cosmic radiation; (*c*) exponent k in the formula $p(\geq A_1) = \exp(-k)$ for estimating the probability of obtaining a random value of the amplitude of the first harmonic in the region $\geq A_1$ (A_1 are measured values); and (*d*) χ^2 values calculated by formula (9) and tabular values of χ^2_{1-p} for the confidence probabilities of $\beta = 1 - p = 0.97$ (2σ), $\beta = 0.998$ (3σ), and $\beta = 0.99996$ (4σ). The closed boxes and open circles represent experimental results obtained in the present study on the basis of data from the Yakutsk array for exploring extensive air showers, while the direct crosses correspond to the AGASA data [10]. In Fig. 4*a*, curves *1* and *2* (Yakutsk array) and curve *3* (AGASA) represent the expected values of the amplitude of the first harmonic in the case where the flux of primary cosmic radiation is isotropic; in Fig. 4*b*, the dashed curve shows the behavior of the phase φ_1 according to world-averaged data [21].

follows that, at the energy values being considered, there is a strong local anisotropy, which is periodically weakened down to a nearly isotropic distribution of the arrival directions of primary cosmic radiation.

Let us now highlight some important special features of the results being discussed. For $E_0 < 5 \times 10^{17}$ eV, the phases are concentrated in the vicinity of the value of $\varphi_1 \approx 125°$, which specifies a direction lying beyond a random one at a statistical-significance level not less than three standard deviations (Fig. 4*d*) and which has no bearing on the Galaxy plane, from which one could expect an anisotropy of the flux of charged particles of primary cosmic radiation within the diffusion model of their propagation. This direction points to the outlet of one of the middle-latitude magnetic arms of the Galaxy (arrow *2* in Fig. 5) or even possibly to the plane of the Local Supercluster of galaxies (Supergalaxy plane). The dip of the phase in Fig. 4*b* at $E_0 \approx 10^{17.3-17.4}$ eV ($\varphi_1 \approx 90°$) is also indicative of the effect of the Supergalaxy plane (see Fig. 5).[1)]

In the interval $E_0 \approx 10^{17.7-17.8}$ eV, there is yet another significant peak (Fig. 4*d*). It correlates with the peak at similar energies in the energy spectrum of primary cosmic radiation (see Fig. 3). The phase $\varphi_1 \approx 40°$ in Fig. 4*b* points to the line of intersection of the Galaxy and Supergalaxy planes (arrow *3* in Fig. 5). The two planes are nearly orthogonal in space.

The dip of the phases in Fig. 4*b* in the energy range $E_0 \approx 10^{18.25-18.45}$ eV manifests itself in the data from both arrays. Of course, it must become a subject of a dedicated study. At the present stage, we may indicate once again that, according to the data from the Yakutsk array, the phase $\varphi_1 \approx 90°$ points to the Supergalaxy plane.

[1)]In the following, we use the notation $E_0 \approx 10^{17.3-17.4}$ eV.

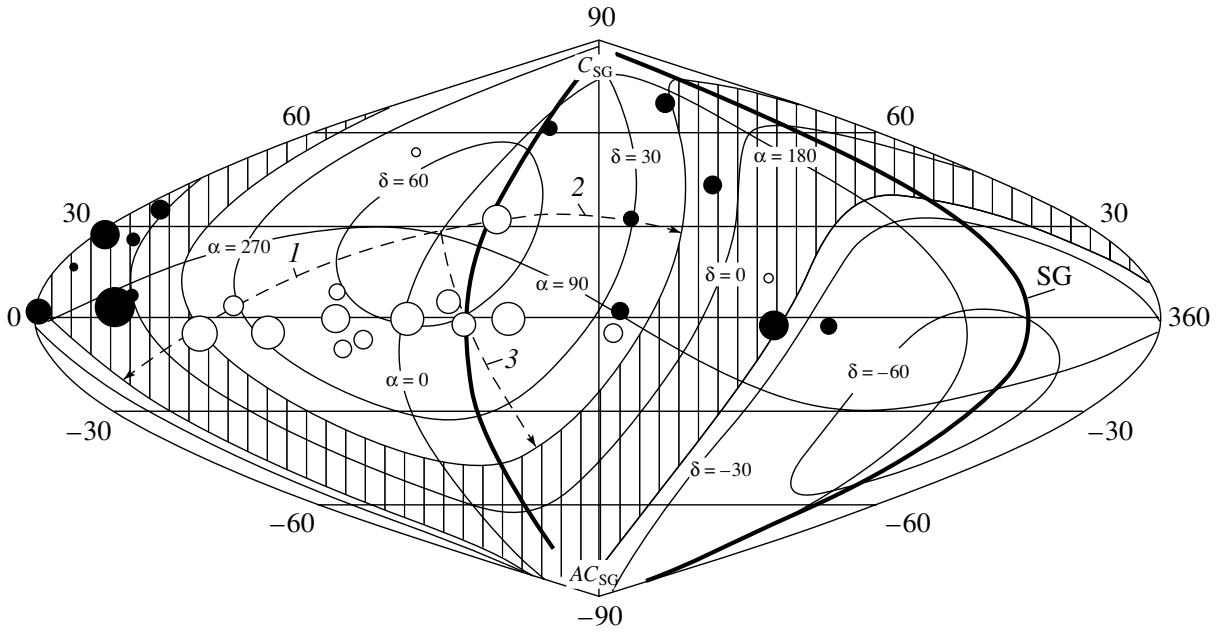

Fig. 5. Sky zones (in galactic coordinates) viewed by (unshaded region) the Yakutsk array ($\delta \approx 15^\circ - 90^\circ$) and (shaded region) AGASA ($\delta \approx -25^\circ - 90^\circ$). The closed and open circles indicate the dispositions of the magnetic arms of the Galaxy with directions, respectively, away from an observer and toward him [32], the dimensions of the circles being proportional to the field strength. The dashed arrows *1*, *2*, and *3* show the phases of the first harmonic according to the AGASA data for $E_0 \approx 10^{17.9-18.3}$ eV showers [10] and according to data from the Yakutsk array ($\varphi_1 \approx 125^\circ$ for $E_0 < 10^{17.5}$ eV and $\varphi_1 \approx 40^\circ$ for $E_0 \approx 10^{17.7-17.8}$ eV). Here, α and δ are, respectively, the right ascension and inclination (equatorial coordinates), while SG, C_{SG}, and AC_{SG}, are, respectively, the disk, the center, and the anticenter of the Supergaxy.

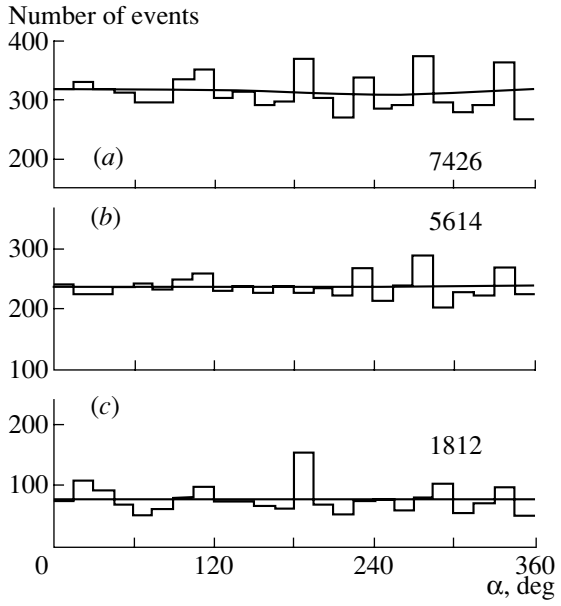

Fig. 6. Right-ascension distributions of extensive air showers of energy in the range $E_0 = 10^{17.7-17.8}$ eV (a) for the entire data set, (b) for the data set not including nodes, and (c) at nodes with angular dimensions $d \leq 3^\circ$ for $n \geq 3$ showers. The smooth curves correspond to the first harmonic in (8), while the numerals in the respective panels indicate the numbers of showers.

Finally, the energy range $E_0 \approx 10^{18.6-18.9}$ eV, where the flux of primary cosmic radiation changes global direction, possibly two times (arrows in Fig. 4*d*)—from $\varphi_1 \approx 90^\circ$ in the intervals $E_0 \approx 10^{18.6-18.7}$ and $10^{18.8-18.9}$ eV to $\varphi_1 \approx 150^\circ$ at $E_0 \approx 10^{18.7-18.8}$ eV—also deserves attention. These peaks are especially significant in Fig. 4*d*. They correlate with the peak in the differential energy spectrum in Fig. 3. It should be noted that, for $E_0 \geq 5 \times 10^{18}$ eV, the arrival directions of primary cosmic radiation correlate with the Supergalaxy plane, exceeding the isotropic flux by four to five standard deviations [15–17]. In [14, 19], it was indicated that there is a relationship between the arrival directions of primary cosmic radiation of such energies and the large-scale structure of the Universe.

Let us now consider the amplitude of the first harmonic, A_1. It is contrasted against the amplitude ΔA_1 for the isotropic flux where the number of events,

$$N = \sum_{i=1}^{n} N_i,$$

is equal to the actual number of showers. The amplitude ΔA_1 can be found from a Monte Carlo simula-

tion or analytically [6]:

$$\Delta A_1 \cong 1.25\sqrt{2/N}. \quad (10)$$

From relation (10), it follows that, even in the absence of an actual anisotropy, an experiment will inevitably exhibit nonzero amplitudes whose values would increase with decreasing number N of showers. This occurs as the energy E_0 of the showers subjected to the analysis becomes higher; that is, a random distribution can mimic the expected (on the basis of physical considerations) energy dependence of the amplitude of the first harmonic.

The question of the distribution of the parameters characterizing the observed vector of the anisotropy that arises because the data set at small N is insufficiently wide was considered by Linsley [6], who introduced the coefficient $k = N(A_1/2)^2$ and the formula

$$p(\geq A_1) = \exp(-k) \quad (11)$$

for estimating the probability that the observed value A_1 can be obtained in the case of an isotropic flux.

For the amplitude values corresponding to the phases φ_1 in Fig. 4*b*, Fig. 4*a* shows the results of measurements (circles) and the results of the calculation (curve *1*) on the basis of relation (10). The measured and calculated data of the AGASA group [10] are represented by the crosses and by curve *3*, respectively. The values of the coefficient k are given in Fig. 4*c*.

It can be seen that, in the energy range $E_0 \approx (3\text{–}20) \times 10^{17}$ eV, a sizable anisotropy was observed at the AGASA facility, its amplitude being maximal at $E_0 \approx 10^{18}$ eV. On the contrary, very small values of the amplitude A_1 were obtained at the Yakutsk array in this energy region. This situation was not due to low statistics of showers, as can clearly be seen from the example of the histogram in Fig. 6*a* for $E_0 = 10^{17.7\text{–}17.8}$ eV showers, where the measured distributions proved to be anomalously "flat" [here, the graph of the sine function (8) is virtually indistinguishable from a horizontal line]. At the same time, the data in angular sectors display many large deviations from this approximation, which lead to great values of χ^2 that are highly improbable for a random distribution (see Fig. 4*d*).

Therefore, it is natural to reject the hypothesis according to which the data from the Yakutsk array in the above energy range may be due to fluctuations of the isotropic flux of primary cosmic radiation. In all probability, the reason here is different. In my opinion, the anomalously flat distribution of the arrival directions of primary cosmic radiation arose because of a superposition of two fluxes traveling in opposite directions and having approximately equal amplitudes, as can clearly be seen in Fig. 7, where this hypothesis was simulated. There, histogram *1* represents the original distribution taken for actual showers of energy in the range $E_0 = 10^{16.8\text{–}16.9}$ eV and slightly modified in such way that the phase of the first harmonic points to the Supergalaxy plane. We will assume that this distribution for a phase of $\varphi_1 \approx 90^\circ$ reflects roughly a global anisotropy of extragalactic primary cosmic radiation. We denote by N_{SG} the total number of respective events. For this distribution, the first row of the table gives the parameters of the anisotropy vector.

Histogram *2* in Fig. 7 is obtained from histogram *1* upon a shift of 180° in the right ascension. For this distribution, the parameters of the anisotropy vector are listed in the second row of the table. They are compatible with the AGASA data; therefore, we assume that this vector gives a rough characterization a global anisotropy of galactic primary cosmic radiation. We denote by N_G the total number of events there.

The total flux of galactic and extragalactic radiation, N_Σ, is determined here by summing histograms *2* and *1* with weights satisfying the normalization condition $W_G + W_{SG} = 1$,

$$N_\Sigma = W_G N_G + (1 - W_G) N_{SG}. \quad (12)$$

More specifically, the weights W_G and W_{SG} are defined as the fractions of galactic and extragalactic primary cosmic radiation. In Fig. 7, histogram *3* illustrates the version where $W_G = 0.55$, in which case the fraction of galactic primary cosmic radiation exceeds slightly the fraction of its extragalactic counterpart. For this flux, the parameters of the anisotropy vector are given in the third row of the table. They are seen to be compatible with our experimental data given above.

Histogram *4* corresponds to the version where $W_G = 0.45$—that is, the version in which the fraction of galactic primary cosmic radiation is slightly less than the fraction of extragalactic primary cosmic radiation. In this case, the distribution is also characterized by an anomalously small value of the coefficient k, but the phase $\varphi_1 \approx 67^\circ$ points here to the Supergalaxy plane.

The last two versions of the simulations demonstrate that slight changes in the equilibrium between oppositely directed global fluxes shift the phase of the first harmonic toward the stronger flux. Concurrently, χ^2 values remain quite large (at a level of three standard deviations), and this contradicts the hypothesis that histograms *3* and *4* are of a random character.

In attempting to employ the results of the above simulation to interpret the anisotropy of data from the Yakutsk array and from AGASA for $E_0 \approx (3\text{–}20) \times 10^{17}$ eV, the following pattern may emerge. Let us

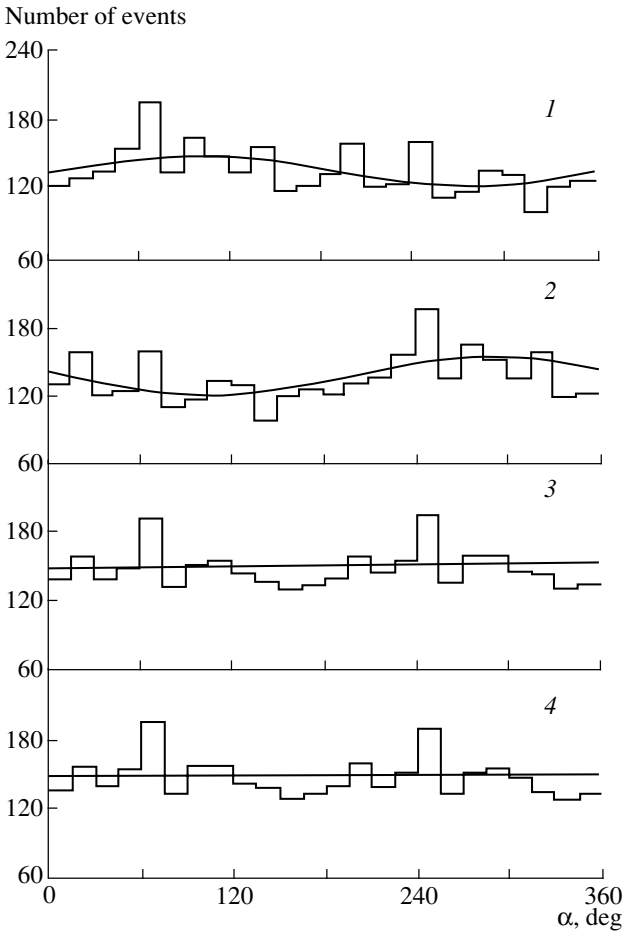

Fig. 7. Simulated distributions of showers with respect to the right ascension for the (*1*) extragalactic, (*2*) galactic, and (*3*, *4*) total fluxes (the parameters of the anisotropy vectors are given in the table). The smooth curves represent the first harmonic (8).

assume that primary cosmic radiation does indeed consist of a galactic and an extragalactic component. In this case, the AGASA facility, which has a larger angle of survey of the sky (see Fig. 5), will record predominantly the galactic component. As a matter of fact, it is "dazzled" by a direct flux of cosmic rays from the Galaxy center. The Yakutsk array, which is situated within much higher latitudes, "sees" only a slight "gleam" of this component. The anisotropy of the galactic component is neutralized by the anisotropy of extragalactic particles. At some energies, the latter outweighs the former; therefore, the phase of the first harmonic in Fig. 4*b* periodically undergoes strong variations.

Parameters of the first harmonic in simulating the anisotropy of the (*1*) extragalactic, (*2*) galactic, and (*3*, *4*) total fluxes

	W_G	A_1, %	ΔA_1, %	φ_1, deg	χ^2	k
1	0	10.6	3.1	96	58.8	9.1
2	1	12.2	3.1	285	58.1	11.7
3	0.55	2.0	3.1	302	41.2	0.3
4	0.45	1.1	3.1	67	41.3	0.1

Let us now consider the anisotropy of $E_0 \leq 3 \times 10^{17}$ eV primary cosmic radiation. We will make use of the data reported in [33], which were obtained at the Yakutsk array over the period between 1983 and 1988. The showers in question were selected by nine scintillation detectors within a central circle of radius $R \leq 250$ m (independently of the master array). In this region, the number of extensive air showers decreases fast with decreasing energy; in view of this, we took, for our analysis, only $\cos\theta \geq 0.9$ events, for the surveyed part of the sky to be invariable. The shower energy was determined from the relation

$$E_0 = 6.8 \times 10^{10} N_s(0^\circ)^{0.86}, \qquad (13)$$

where $N_s(0^\circ)$ is the total number of charged particles in vertical events.

In all, 29 235 showers were selected in this way. They were analyzed for a global anisotropy by the sliding-bin method outlined above (with a step of $h = 0.2$). The results of this harmonic analysis are represented by closed boxes in Fig. 4.

Here, a statistically significant local anisotropy at energies in the range $E_0 \approx (7{-}8) \times 10^{15}$ eV, where there is a peak in the differential energy spectrum (see Fig. 3), immediately attracts attention. This astrophysical phenomenon is accompanied by the nuclear-physics irregularity that is observed in the longitudinal development of extensive air showers (see Figs. 1, 2) and which is difficult to explain by the replacement of one group of nuclei by another within the diffusion model of the origin of primary cosmic radiation. The phase of the first harmonic, $\varphi_1 \approx 180^\circ$, turned away from the Galaxy disk, but it unambiguously points to the Supergalaxy center (see Fig. 5).

In the range $E_0 \approx (6{-}8) \times 10^{16}$ eV, there is also a local irregularity that manifests itself in a sharp decrease in the amplitude (see Fig. 4*a*) and in that the phase takes the value of $\varphi_1 \approx 90^\circ$ (see Fig. 4*b*). In all probability, some processes other than those in the range $E_0 \approx (6{-}8) \times 10^{15}$ eV occur here. We cannot rule out the possibility that they are of the same nature (superposition of fluxes traveling in opposite directions) as those in the example in Fig. 7.

Figure 4 shows that, at energies in the range $E_0 \approx (3{-}50) \times 10^{15}$ eV, there is a sizable anisotropy of the global flux of primary cosmic radiation, the phase of the first harmonic being $\varphi_1 \approx 180^\circ$. In the energy range $E_0 \approx (1{-}3) \times 10^{17}$ eV, data from the

two independent experiments in question agree with each other even in some individual details. The discrepancies between them are explained by different numbers of showers there.

4.2. Cluster Analysis

From the aforesaid, it follows that, in some intervals of the energy E_0, one can observe phases of the first harmonic that are likely to be indicative of an extragalactic origin of part of the primary cosmic radiation. Previously, it was reported in [12–20] that an analysis of the arrival directions for cosmic rays of energy in the region $E_0 \geq 10^{17}$ eV makes it possible to single out a considerable number of groups of showers in narrow solid angles. Their distribution over the celestial sphere has an ordered structure that cannot be explained by random statistical processes. We will now indicate some important special features of the small-scale anisotropy of primary cosmic radiation that seem to have some bearing on the aforementioned irregularities of the development of extensive air showers.

4.2.1. Events in the Energy Region $E_0 \geq 3 \times 10^{18}$ eV.

Let us first examine extensive air showers of energy in the region $E_0 \geq 3 \times 10^{18}$ eV that are characterized by zenith angles of $\theta \leq 45^\circ$ and which were recorded at the Yakutsk array over the period between 1974 and 2000. The present analysis deals with showers whose arrival directions were determined on the basis of data from not less than five stations and whose axes were within the array central circle of radius $R \leq 1700$ m. Here, we will consider the data sample used previously in [17].

The analysis has been performed for two data sets, that for $E_0 = (3–5) \times 10^{18}$ eV (2033 showers) and that for $E_0 > 5 \times 10^{18}$ eV (1267 showers). For each shower, all "neighbors" were found within an angular spacing of $d \leq 3^\circ$ around its arrival direction. If there were $n \geq 3$ showers within this circle, then the average of their coordinates was calculated and was further used as the coordinates of new points (they are referred to as nodes). Within this procedure, any isolated group of showers (that is, a group that is offset by a distance in excess of d from showers that do not belong to this group) forms one node.

Suppose that there is some connection between nodes and local sources of primary cosmic radiation. We will analyze the correlations of these nodes with the Galaxy and Supergalaxy planes. The deviations $n_\sigma = (N_{\rm obs} - N_{\rm ran})/\sigma$ of the observed number of nodes ($N_{\rm obs}$) involving ≥ 7 showers from the expected one ($N_{\rm ran}$) (in units of the reference quantity $\sigma = \sqrt{N_{\rm ran}}$) versus the latitude of the shower arrival are shown in Fig. 8 in galactic (G) and supergalactic (SG) coordinates (with a step of $\Delta b = 5^\circ$). The $N_{\rm ran}$ values were determined from a Monte Carlo simulation of an isotropic primary cosmic radiation. This was done by replacing, for each shower, the measured values of the arrival time and azimuth (in the horizontal reference frame associated with the array) by random values.

In galactic coordinates (Fig. 8*a*), the northern–southern asymmetry of the arrival directions is clearly seen for extensive air showers of energy in the region $E_0 > 5 \times 10^{18}$ eV (an excess comes from southern latitudes)—previously, this effect was discovered at the Yakutsk array [34]. The mean latitudes of the measured and the calculated distribution are $\langle b_{\rm obs} \rangle = 17.7^\circ \pm 2.4^\circ$ and $\langle b_{\rm ran} \rangle = 25.1^\circ$, respectively. In the vicinity of the Galaxy plane ($b_{\rm G} = -5^\circ$ to 0°), there is a significant (four standard deviations) excess of events. Statistically significant peaks are also observed at latitudes of $b_{\rm G} \approx 35^\circ$ and 65°.

On the contrary, Fig. 8*a*′ shows no asymmetry with respect to the Supergalaxy plane ($\langle b_{\rm obs} \rangle = 12.8^\circ \pm 2.4^\circ$ and $\langle b_{\rm ran} \rangle = 12.0^\circ$), but, in the vicinity of it ($b_{\rm SG} = -10^\circ$ to $+20^\circ$), there is an intense peak (shaded region), which is especially distinct against the background of the adjacent dips. A comparison shows that the areas under this peak and the aforementioned peak in the vicinity of the Galaxy plane differ by a factor of about 6. This can be interpreted as an indication that $E_0 > 5 \times 10^{18}$ eV primary cosmic radiation comes predominantly from extragalactic sources.

We note that some excess of primary cosmic radiation in the vicinity of the Galaxy plane was also found in the studies that were reported in [35, 36] and which are based on an analysis of $E_0 > 8 \times 10^{18}$ eV data from the Yakutsk array for investigating extensive air showers. Relying on these results, the author of those studies conjectured that the bulk of primary cosmic radiation having energy in the above region consists of iron nuclei generated by pulsars in the Galaxy. In my opinion, this conclusion is dubious for the following reasons. First, this conclusion is at odds with the data in Figs. 1 and 2. Second, it is in glaring contradiction with the results of a global investigation into the lateral distribution of electrons and muons in extensive air showers at the Yakutsk array [37–41]—these results rule out completely a heavy composition of primary cosmic radiation in the energy region $E_0 > 5 \times 10^{18}$ eV. Third, the peak in Fig. 8*a* in the latitude band $\Delta b_{\rm G} = -5^\circ$ to 0° is caused, to some extent, by events that also correlate with the Supergalaxy disk, from the region where the two disks intersect (see the dashed arrow *3* in Fig. 5). All of this was disregarded

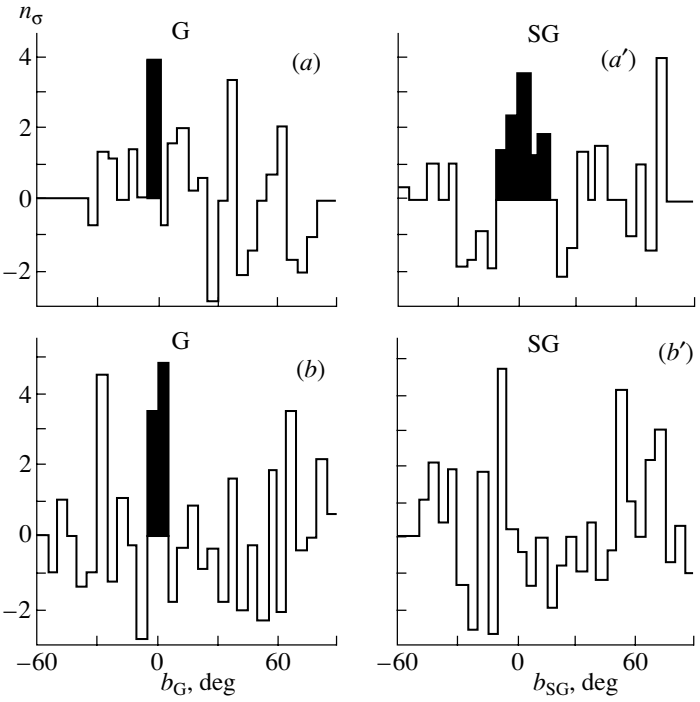

Fig. 8. Distribution of the deviations $n_\sigma = (N_{obs} - N_{ran})/\sqrt{N_{ran}}$ of the number of nodes (N_{obs}) involving $n \geq 7$ showers from the expected one (N_{ran}) in the (a, a') $E_0 > 5 \times 10^{18}$ eV and (b, b') $E_0 = (3–5) \times 10^{18}$ eV data sets versus the latitude of the shower arrival in galactic (G) and supergalactic (SG) coordinates (with a step of $\Delta b = 5^\circ$). The shaded regions correspond to significant values near the Galaxy and Supergalaxy disks.

by the author of [35, 36], so that his conclusions seem erroneous.

In the energy region $E_0 = (3–5) \times 10^{18}$ eV, the role of the Galaxy in the generation of primary cosmic radiation becomes more pronounced, which is suggested by an increased excess of events in the region of its disk ($b_G = -5^\circ$ to $+5^\circ$) in Fig. 8b in relation to what we have in Fig. 8a. Concurrently, the aforementioned northern–southern asymmetry disappears ($\langle b_{obs} \rangle = 23.2^\circ \pm 1.5^\circ$ versus $\langle b_{ran} \rangle = 24.2^\circ$). The role of the Supergalaxy seems to become much less important in this energy region, but we cannot rule it out completely at this stage; in Fig. 8b', a statistically significant, albeit weaker, excess of events survives in the vicinity of the Supergalaxy plane ($b_{SG} = -10^\circ$ to -5°).

4.2.2. Events in the Energy Range $E_0 \approx 10^{17.7–17.8}$ eV.

Let us consider showers that are characterized by energies in the range $E_0 \approx 10^{17.7–17.8}$ eV and zenith angles satisfying the condition $\cos\theta \geq 0.6$ and which were recorded at the Yakutsk array over the period between 1974 and 2001. Our analysis will be performed for extensive air showers whose arrival directions were found on the basis of data from four or more stations and whose axes are within the array central circle of radius $R \leq 1000$ m. In all, 7426 showers were selected in this way (see Fig. 6). In Fig. 4d, they form a statistically significant peak. We will now examine the small-scale anisotropy of these events.

We took seven independent data samples containing approximately the same number of events, about 1000, the only difference between these samples being that the axes of the showers entering into the different samples intersected different annular areas within the central area of the array. Each of the seven samples was analyzed individually for the presence in it of local groups of showers (nodes) over the celestial sphere. This was done in just the same way as in the preceding case.

Figure 9 shows the distributions of the deviations $n_\sigma = (N_{obs} - N_{ran})/\sigma$ (similar to those in Fig. 8) in galactic (G) and supergalactic (SG) coordinates versus the latitude of the shower arrival (with a step of $\Delta b = 3^\circ$). The upper panels display a sample that consists of 1812 showers entering into nodes, while the lower panels present the corresponding results for the remaining 5614 showers not belonging to nodes. For the showers in the nodes (in both coordinate systems), we have here the values

$$\chi^2 = \sum_{i=1}^{n} (n_{\sigma i})^2 \approx 110–150,$$

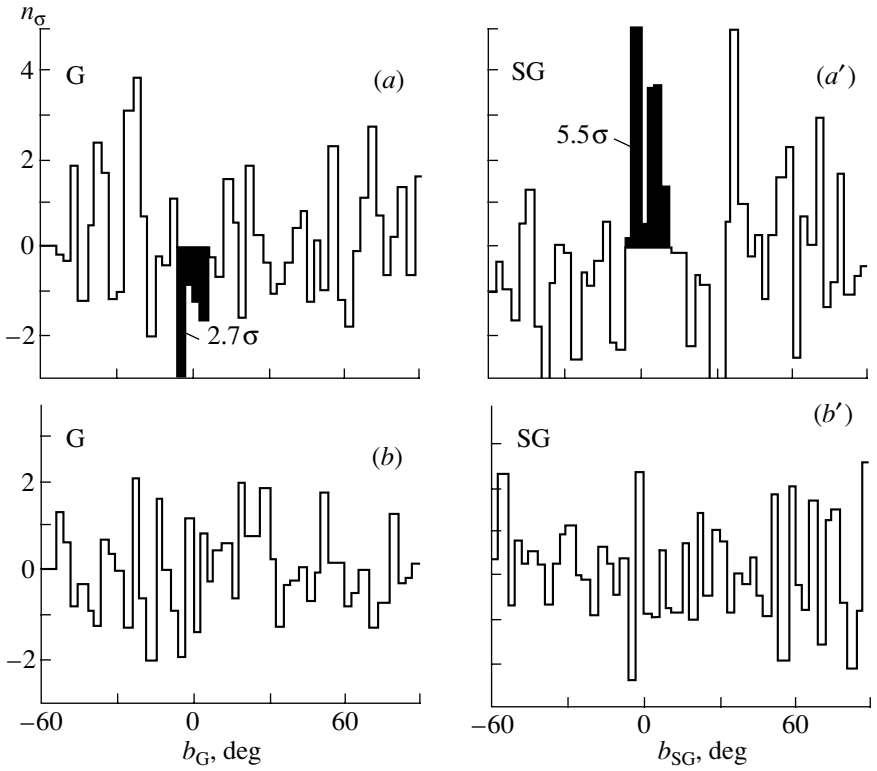

Fig. 9. Distributions of the deviations $n_\sigma = (N_{obs} - N_{ran})/\sqrt{N_{ran}}$ of the observed number of $E_0 = 10^{17.7-17.8}$ eV showers (N_{obs}) from the expected one (N_{ran}) versus the latitude of the shower arrival in galactic (G) and supergalactic (SG) coordinates (with a step of $\Delta b = 3°$): (a, a') results for 1812 showers entering into nodes (see Fig. 6c) and (b, b') results for the remaining 5614 showers not belonging to nodes (see Fig. 6b). The shaded regions correspond to significant values near the Galaxy and Supergalaxy planes.

which are enormous for $n = 50$ degrees of freedom. The probability of such random outputs is less than 10^{-5}. In the vicinity of the Supergalaxy plane, we can see a statistically significant (about five and a half standard deviations) peak, which, in many respects, is similar to the peak in Fig. 8a'. On the contrary, the Galaxy plane manifests itself in Fig. 9a only as a dip (shaded area there). We note that a similar but more significant (9.2σ, where σ is a standard deviation) peak is also observed in the Galaxy disk for $E_0 \approx 10^{17.1-7.6}$ eV [18].

These results can be interpreted as an indication of an extragalactic origin of the primary-cosmic-radiation fraction contained in the nodes. In all probability, the Galaxy only absorbs this radiation, though more intensely in the disk. Other significant peaks and dips in Figs. 9a and 9a' are likely to be indicative of a complicated and nonuniform structure of the space housing the sources of primary cosmic radiation that form nodes.

As to the showers in Figs. 9b and 9b', the pattern here changed sharply. The measured and expected distributions for random quantities are close to each other ($\chi^2 = 47-59$). This result unambiguously indicates that the primary-cosmic-radiation fraction selected in this way possesses a high degree of isotropy. The fraction of these particles in the total flux is $5614/7426 \approx 0.75$.

Within the harmonic-analysis method, we will return once again to a global anisotropy of $E_0 = 10^{17.7-17.8}$ eV primary cosmic radiation. Figure 6a shows the original distribution of all 7426 showers in 24 sectors. That part of the showers which did not enter into the nodes (Fig. 6b) form a distribution that exhibits but a slight distinction between the fluxes in different time zones ($\chi^2 \approx 37.5$); as a result, the phase $\varphi_1 \approx 211° \pm 136°$ was found for them with a large uncertainty. As before, these data are indicative of a high degree of isotropy of primary cosmic radiation. But the showers in the nodes in Fig. 6c are in strong contradiction with the hypothesis of an isotropic distribution. For example, the scatter of data around the approximating curve constructed with the aid of Eq. (8) leads to $\chi^2 \approx 154.8$ for $n = 24$ degrees of freedom, the respective probability of a random output being less than 10^{-5}.

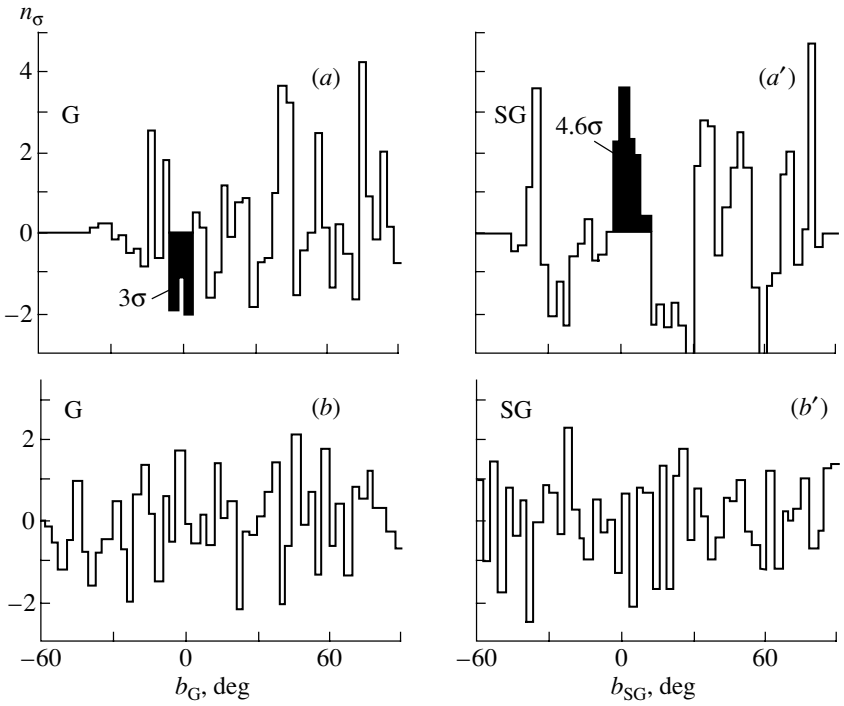

Fig. 10. Distributions of the deviations n_σ (similar to those in Fig. 9) in the $E_0 = 10^{17.2-17.3}$ eV set for (a, a') 1962 showers entering into nodes and (b, b') the remaining 5261 showers not belonging to nodes.

We would like to highlight some important details of these distributions. The peak in Fig. 6*a* at $\alpha \approx 180°-195°$ is indicative of an excess (3.4σ) radiation from the Supergalaxy disk in the vicinity of the center (C_{SG} in Fig. 5). It fully goes over to the peak in Fig. 6*c*, where the excess of events is already $(162-81)/\sqrt{81} = 9\sigma$. As to the peak in Fig. 6*a* at $\alpha \approx 270°-285°$, it goes over to the peak in Fig. 6*b*, where the excess is $(294-235)/\sqrt{235} = 3.8\sigma$, and possibly points to the Galaxy center.

4.2.3. Events in the Energy Range $E_0 \approx 10^{17.2-17.3}$ eV.

Let us consider yet another energy interval, $E_0 \approx 10^{17.2-17.3}$ eV; there, the distributions of the standard deviations n_σ (Fig. 10) are similar in many respects to the distributions in Figs. 8 and 9. Here, use is made of 7223 showers whose zenith angles satisfy the condition $\cos\theta \geq 0.6$ and whose arrival directions were determined on the basis of data from not less than four stations, their axes lying within the array central circle of radius $R \leq 1000$ m. This data sample was also broken down into seven independent subsamples featuring approximately the same number of events, about 1000, and was analyzed for the presence of correlations between the nodes and the Galaxy and Supergalaxy disks.

In Figs. 10*a* and 10*a*′, the χ^2 values for 1962 showers entering into the nodes are seen to be enormous in both coordinate frames, $\chi^2 \approx 120-150$. Here, there is, in the Supergalaxy plane, a strong excess (about 4.6σ) of events, which is especially pronounced against the background of dips on the two sides of it. As before, the Galaxy plane manifests itself only as a dip of about three standard deviations (shaded region).

For the remaining showers (their number is 5261), which do not enter into the nodes, the distributions of n_σ are shown in Figs. 10*b* and 10*b*′. The pattern here is identical to that in Figs. 9*b* and 9*b*′. The measured distributions are quite close to those that are expected for random quantities ($\chi^2 = 47-52$), this being indicative of a rather high isotropy of the primary-cosmic-radiation fraction selected in this way. The fraction of these particles in the total flux is $5261/7223 \approx 0.73$.

We will now additionally analyze the small-scale anisotropy of showers entering into the nodes (those in Figs. 10*a*, 10*a*′). We have investigated nodes for their intersection of multiplicity $m \geq 2$ in any of the seven subsamples (under the condition that their centers are within an angular distance of $d \leq 3°$). If such nodes were found, the arrival directions of all showers entering into such nodes were mutually averaged anew, and the resulting larger node (we refer to it as a cluster) was taken for a further analysis. As a matter of fact, we used here the method of multiple matching of nodes upon superimposing a few similar

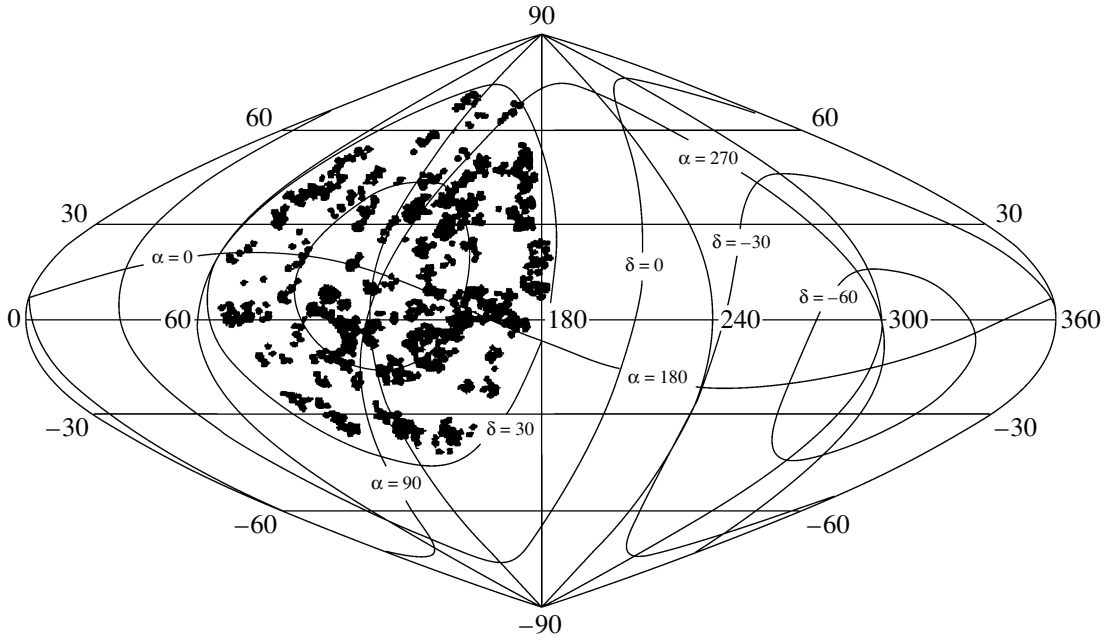

Fig. 11. Chart representing the disposition of clusters of 1156 $E_0 = 10^{17.2-17.3}$ eV showers in supergalactic coordinates (also shown are equatorial coordinates). The clusters include $m \geq 3$ nodes from any of the seven data samples under the condition that each of these nodes contains $n \geq 5$ showers, their centers lying within the $d = 3^\circ$ circle.

charts onto one another. This is an analog of the multiple-matching method, which has successfully been used in order to select ultrahigh-energy cosmic rays incident on the Earth by master detectors at arrays for studying extensive air showers.

Figure 11 shows the chart of the disposition of clusters (for events in the energy range $E_0 \approx 10^{17.2-17.3}$ eV) including $m \geq 3$ nodes from any of the seven subsamples under the condition that there are $n \geq 5$ showers in each of these nodes. The clusters are displayed in supergalactic coordinates (for the sake of convenience, equatorial coordinates are also shown there). The longitude is reckoned in the counterclockwise direction from the line pointing to the anticenter. The equatorial coordinates of the North Pole of the Supergalaxy are $\alpha = 286.2^\circ$ and $\delta = 14.1^\circ$.

It can be seen that many clusters form isolated local groups between which there are large voids. In all, clusters contain 1156 showers, the maximum number of showers in a cluster being 26. At different values of the primary-cosmic-radiation energy, one can also observe [16–20] an ordered structure of the distribution of clusters over the celestial sphere. By and large, the picture is similar to the cell-like structure of the distribution of galaxies in the Universe (see, for example, [42, 43]).

4.3. On the Structure of the Supergalaxy

The Supergalaxy is one of the elements of the cell structure of the Universe. As an individual large-scale formation, it was singled out for the first time by de Vaucouler [44]. Its disk is a flattened aggregate of field galaxies, small groups, and large clouds [45].

The structure of the Supergalaxy is clearly seen in Fig. 12, which displays, in supergalactic coordinates, the distribution of 2502 galaxies that are characterized by brightness values not exceeding 14^m and which are quoted in the catalogs in [46, 47]. The thick line represents the Galaxy disk. Presented in this figure are objects whose declination satisfies the condition $\delta \geq 30^\circ$, which makes it possible to compare the topologies of clusters and galaxies over the common part of the sky. Unfortunately, some galaxies are not seen because of light absorption in the vicinity of the Galaxy disk; therefore, the region of overlap of the data in Figs. 11 and 12 is narrowed considerably.

We would like to list once again some common structural features of the Supergalaxy and the distributions in Figs. 8–10. The distribution of the galaxies that are displayed in Fig. 12 is shown in Fig. 13*a* versus their supergalactic latitude (with a step of $\Delta b_{\mathrm{SG}} = 3^\circ$). The N_{ran} curve represents the expected distribution of the galaxies for an isotropic disposition in space with allowance for the decrease in their number in the region of the Galaxy disk (see Fig. 12). This distribution was obtained by "smearing," with the aid of the Monte Carlo method, the actual coordinates of each galaxy in the parts of the sky that are adjacent to it and which have dimensions of $\Delta\alpha = \pm 30^\circ$ and $\Delta\delta = \pm 4^\circ$.

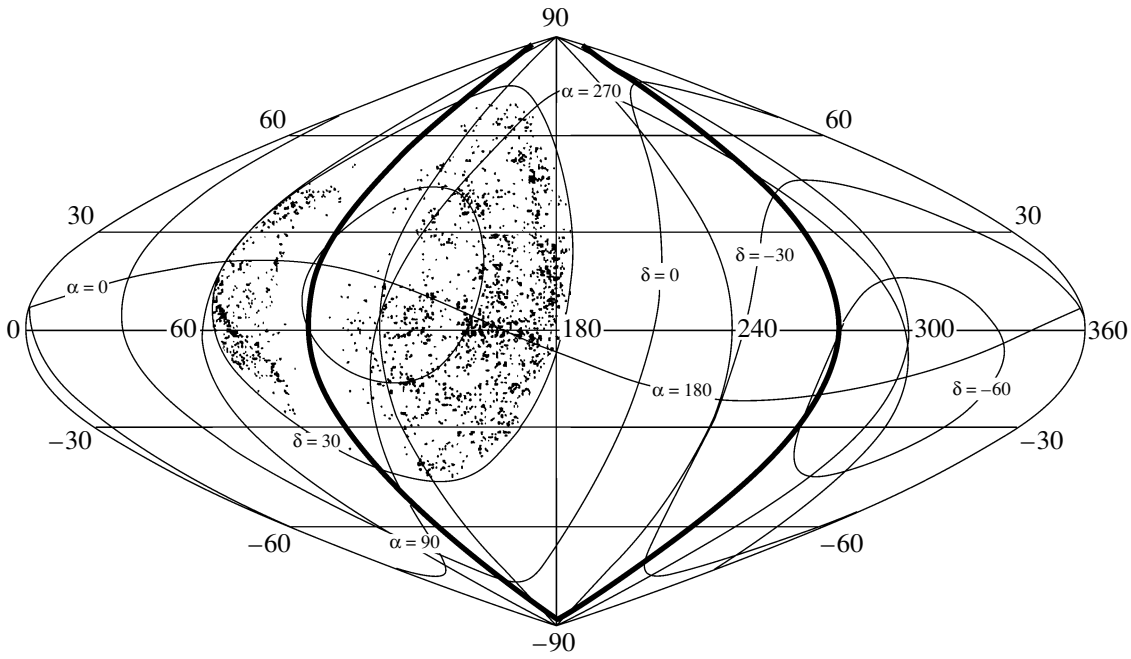

Fig. 12. Disposition of 2502 galaxies whose brightness does not exceed 14^{m} (at declinations in the region $\delta \geq 30°$) over the celestial sphere from the catalogs in [46, 47]. The thick line shows the Galaxy plane.

Figure 13*b* shows the distribution of the standard deviations $n_\sigma = (N_{\rm obs} - N_{\rm ran})/\sqrt{N_{\rm ran}}$, which bears a striking similarity to the distributions in Figs. 8–10. In addition to the peak in the Supergalaxy plane, other, finer, details are also similar. In all probability, this means that a fraction of primary cosmic radiation can indeed be formed in the Supergalaxy. At the present stage of investigations, it is hardly possible to pinpoint sources that generate this fraction of primary cosmic radiation.

4.4. Quasars as Possible Sources of Primary Cosmic Radiation

Searches for pointlike sources of primary cosmic radiation are among the most difficult problems in ultrahigh-energy astrophysics. This problem stemmed largely from the fact that it was not addressed rather than from the paucity of relevant data. The point is that the opinion a priori prevalent among researchers (see above) is that primary cosmic radiation consists predominantly of protons and nuclei of various chemical elements, these being strongly mixed by the magnetic field of the Galaxy and therefore having a nearly isotropic distribution over the celestial sphere. Under such conditions, it is difficult to find any pointlike sources of primary cosmic radiation.

But in fact, the situation may differ from that to some extent. It was indicated above that part of the primary cosmic radiation in the energy region $E_0 \geq 10^{17}$ eV may consist of neutral particles. In [18–21], it was reported that quasars may be sources of such particles. Below, we will consider this issue in greater detail.

4.4.1. Events in the Energy Range $E \geq 5 \times 10^{18}$ eV.

First, we will analyze the most powerful showers that are characterized by energies and zenith angles satisfying the conditions $E_0 \geq 5 \times 10^{18}$ eV and $\theta \leq 60°$, respectively; whose arrival directions were determined on the basis of data from not less than four stations; and whose axes intersected the array central circle of radius $R \leq 1700$ m. We will consider the correlation between their arrival directions and the nearest quasars. We took 199 quasars from the catalog in [48] that have redshifts of $z \leq 0.3$ and declinations of $\delta \geq 0°$ and which are visible from the Yakutsk array for studying extensive air showers. Because of strong light absorption, the catalog in [48] contains virtually no data concerning the equatorial region of the Galaxy ($|b_{\rm G}| \leq 30°$); for this reason, we excluded, from the analysis, all quasars and showers from this part of the sky.

In Fig. 14, the measured distribution of minimum angular spacings $d_{\rm min}$ between the arrival directions of 379 showers and 199 quasars is represented by points. The smooth curve there corresponds to the distribution expected for random events. In the angular range 0.5°–1.5° (shaded region), there is a statistically significant excess of the measured number of

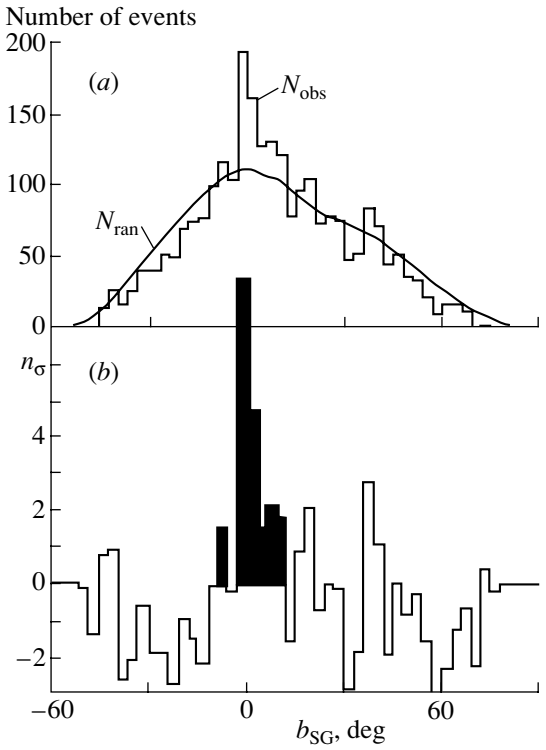

Fig. 13. (a) Distribution of galaxies having brightness values not exceeding 14^m versus the supergalactic latitude (with a step of $\Delta b_{SG} = 3°$): (N_{obs}) actual galaxies and (N_{ran}) distribution expected for the isotropic field of galaxies; (b) distribution of the deviations $n_\sigma = (N_{obs} - N_{ran})/\sqrt{N_{ran}}$.

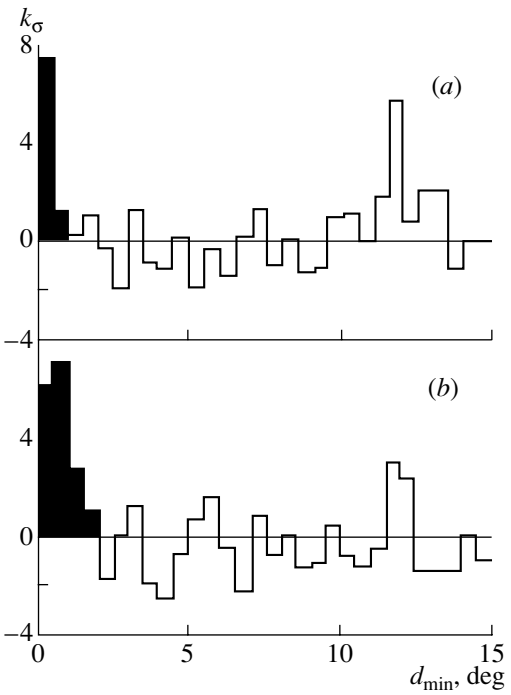

Fig. 15. Angular correlations $k_\sigma = (J_{obs} - J_{ran})/\sigma$ between the nodes of primary cosmic radiation with energies in the range $E_0 = 10^{17.7-17.8}$ eV (662 showers) and quasars with redshifts of (a) $z \leq 0.3$ and (b) $0.3 < z \leq 0.6$ [48]. Here, J_{obs} and J_{ran} are, respectively, the measured value and that which is expected for random events ($\sigma = \sqrt{J_{ran}}$).The shaded regions correspond to significant values.

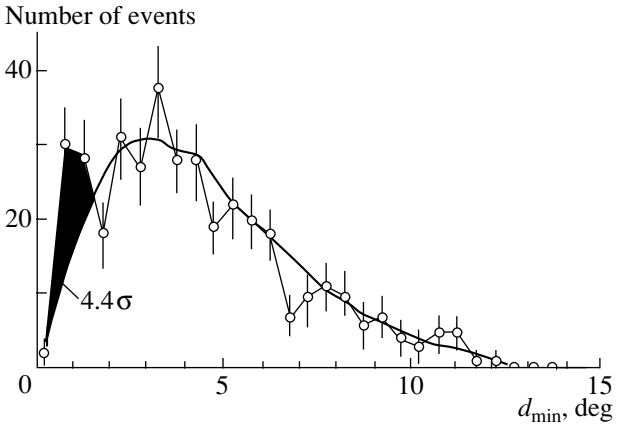

Fig. 14. Distributions of the minimum angular spacings between 379 $E_0 \geq 5 \times 10^{18}$ eV, $\theta \leq 60°$ showers and 199 $z \leq 0.3$ quasars [48]: (points) experimental data and (smooth curve) distribution expected for random shower directions obtained by means of a simulation.

events over the expected one—by $(58 - 33)/\sqrt{33} \approx 4.4\sigma$. In the angular range 0.5°–1.0°, this excess has a stable character. For example, it is observed in groups of 90–100 events in breaking down the 379 showers into four independent samples. If we consider $z \leq 0.15$ and $0.15 < z \leq 0.3$ quasars separately (92 and 107 objects, respectively), we find that, in the angular range 0.5°–1.0°, the number of observed coincidences exceeds the expected one approximately by 3.2σ in either group. In this angular range, the number of excess events constitutes $(58 - 33)/\sqrt{379} \approx 0.06$ of the total number of the showers in question.

4.4.2. Events in the Energy Range $E_0 = 10^{17.7-17.8}$ eV.

We analyze the angular correlation between the nodes of the $E_0 = 10^{17.7-17.8}$ eV showers presented in Fig. 9 and the nearest quasars. As above, we exclude, from our analysis, all quasars and showers from the part of the sky in the equatorial region of the Galaxy ($|b_G| \leq 30°$)—that is, we take only objects that have declinations of $\delta \geq 20°$ and which are visible from the Yakutsk array for studying extensive air showers. We consider all seven independent sets of showers and find the angular spacings d_{min} between the nodes and quasars. We construct the ultimate distribution (J_{obs}) as the sum of these distributions. Further, we repeat this procedure once again (from the isolation of

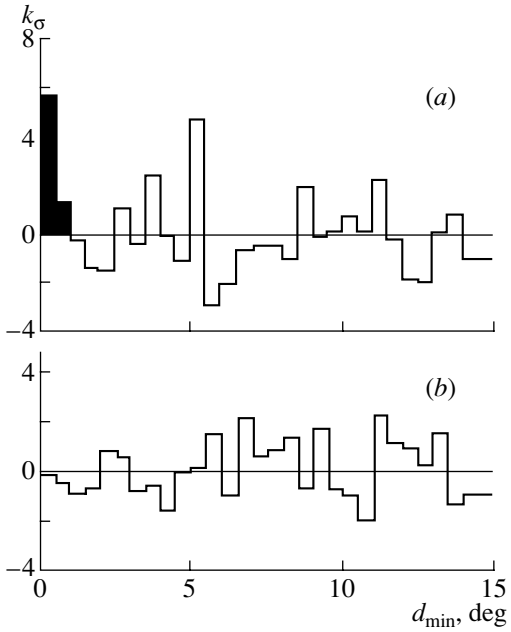

Fig. 16. Angular correlations k_σ between the nodes of primary cosmic radiation in the energy range $E_0 = 10^{16.9-17.2}$ eV and quasars with redshifts of $z \leq 03$ [48]: (a) results for showers entering into nodes and (b) results for showers not belonging to nodes.

nodes)—as was done in deriving the data presented in Fig. 9—in order to determine the distribution expected for an isotropic flux (J_{ran}). Random directions can be found on the basis of actual showers upon replacing, for them, the measured right ascension by that which was calculated by the Monte Carlo method in the angular range from 0° to 360°.

Figure 15a gives the angular correlation functions $k_\sigma = (J_{\text{obs}} - J_{\text{ran}})/\sigma\,(\sigma = \sqrt{J_{\text{ran}}})$ for 662 showers entering into nodes and 108 quasars with redshifts of $z \leq 0.3$ [48], while Fig. 15b presents the intersections of the above 662 showers and 102 quasars with redshifts of $0.3 < z \leq 0.6$. In both figures, one can see statistically significant peaks for $d_{\min} \leq 1.5°$ (shaded regions), which contain 3 and 9% of events, respectively. In all probability, these are conservative estimates of the fraction of primary cosmic radiation that has the energies specified above and which may originate from quasars. It seems that some events were not included in these estimates because of experimental errors.

4.4.3. Events in the Energy Range $E_0 = 10^{16.9-17.2}$ eV.

It was shown in [20] that, in the energy range $E_0 = 10^{16.9-17.2}$ eV, one can also observe a considerable number of nodes that partly correlate with the above quasars. We present some results of this investigation supplementing the pattern as a whole.

Figure 16 gives the angular correlation functions $k_\sigma = (J_{\text{obs}} - J_{\text{ran}})/\sigma$ similar to those displayed in Fig. 15, but for showers and quasars with declinations of $\delta \geq 30°$. The measured distributions J_{obs} and those expected for random events, J_{ran}, were derived as the sum of 18 ($= 3 \times 6$) original distributions of the minimum angular spacings $d_{\min}$ between the nodes of three groups of showers in the energy ranges $E_0 = 10^{16.9-17.0}$, $10^{17.0-17.1}$, and $10^{17.1-17.2}$ eV and 74 quasars with redshifts of $z \leq 0.3$ [48]. The nodes were obtained individually in six independent samples of showers on the basis of their distances from the axis in the same way as in the preceding case (in the energy range $E_0 = 10^{17.7-17.8}$ eV). We took only events whose zenith angles satisfied the condition $\theta \leq 45°$. Figures 16a and 16b correspond, respectively, to showers contained within nodes and to the remaining showers not belonging to these nodes.

It can be seen from Fig. 16a that a statistically significant peak is observed for $d_{\min} \leq 1°$ (shaded region), the fraction of events contained in it being $(139 - 103) \times 100\%/3130 \approx 1.2\%$. There are no significant peaks in Fig. 16b. In all probability, this indicates that some primary-cosmic-radiation fraction having energies in the region $E_0 \geq 10^{17}$ eV and forming nodes of showers can be generated by quasars.

In Fig. 16a, a significant peak (5σ) at $d_{\min} \approx 5.3°$ also deserves particular attention. The fraction of events contributing to it is $(241 - 177) \times 100\%/3130 \approx 2\%$; that is, it is twice as great as the fraction of events contributing to the peak at $d_{\min} \leq 1°$. In Fig. 15, one can also see significant peaks at $d_{\min} \approx 11.7°$. Previously, similar peaks at $d_{\min} \approx 5.5°$ and 9.5° were found in the distribution of minimum angular spacings for $E_0 \geq 10^{19}$ eV showers [17]. We cannot rule out the possibility that all of them are associated with an ordered (in one way or another) large-scale structure of the matter distribution in the Universe.

4.5. Does the Universe Have a Cubic Structure?

Let us consider yet another intriguing feature of the arrival directions of primary cosmic radiation, that which was indicated in [14,19]. In Fig. 17, the distributions of (a) the arrival directions of 583 $E_0 \geq 10^{19}$ eV showers and (b) 175 $z \leq 0.3$ quasars of brightness in the range 15.7^{m}–19.7^{m} [48] are shown versus their supergalactic latitude. All events were taken for declinations of $\delta \geq 0°$.

From Fig. 17a, it can be seen that increased fluxes of primary cosmic radiation come from the Supergalaxy disk ($|\Delta b_{\text{SG}}| \leq 2°$) and from the regions symmetrically situated at angles of $\pm b_{\text{SG}} \approx 6.5°$. In Fig. 17$b$, increased concentrations of quasars

(peaks *1* and *2*) are observed in adjacent regions. This can be considered as an additional indication that quasars may be considered as one of the sources of ultrahigh-energy primary cosmic radiation. In [49, 50], it was shown that Seifert galaxies with $z \leq 0.009$ and lacertides (BL Lac objects) with $z > 0.1$ may also be such sources. Objects of all of these three types are so-called active-core galaxies, which are among the most powerful sources in the Universe.

Observations reveal—and theoretical calculations confirm—the presence of large voids in the Universe that have dimensions of 100 to 130 Mpc and which are separated by comparatively thin (20 to 30 Mpc) layers [45, 51]. Up to 60–80% of galaxies are concentrated within these layers, showing a trend toward aggregating into prolate and oblate superclusters, including the Supergalaxy (of diameter about 50 Mpc), which is considered here. In all probability, many superclusters touch one another, forming a cell structure of the Universe [45, 51]. This may be a structure of the type of a "three-dimensional chessboard" [52] or even some kind of a giant quasicrystal [53], with the bulk of matter being concentrated in its sites. The formation of sites is logically explained within the adiabatic ("pancake") theory of Zel'dovich [54] as the last stage of the concentration of matter in the evolutionary chain of the expanding Universe: "bright surfaces"–"bright lines"–"bright drops."

Let us try to understand the origin of peaks *1* and *2* in Fig. 17 within the scenario of an ordered distribution of matter in the Universe. For the sake of simplicity, we assume that quasars are situated in the sites of a cubic lattice. We also assume that the Supergalaxy plane lies in one of the planes of this lattice. We consider in space only those sites that, in equatorial coordinates, have declinations of $\delta \geq 0°$; moreover, we exclude, from the data sample being considered, all sites that, in galactic coordinates, lie within the latitude band $b_G \leq 30°$. This is done in order to render the actually surveyed and simulated regions of the sky as close as possible.

The distances to the sites are given by

$$r = cz/H_0, \qquad (14)$$

where c is the speed of light and $H_0 = 75$ (km/s) Mpc is the Hubble constant. We will measure these distances in $x = r/L$ units, where L is the lattice constant.

Let us consider two versions, that of a steady-state universe and that of an expanding universe.

In the first case, we set $L = 120$ Mpc. Since we consider only $z \leq 0.3$ quasars, it follows from relation (14) that the farthest objects from the Earth occur at a distance of $r = 1200$ Mpc, which, in units of the number of sites, corresponds to $x = 10$. In [55], it was shown that the distribution of quasars features

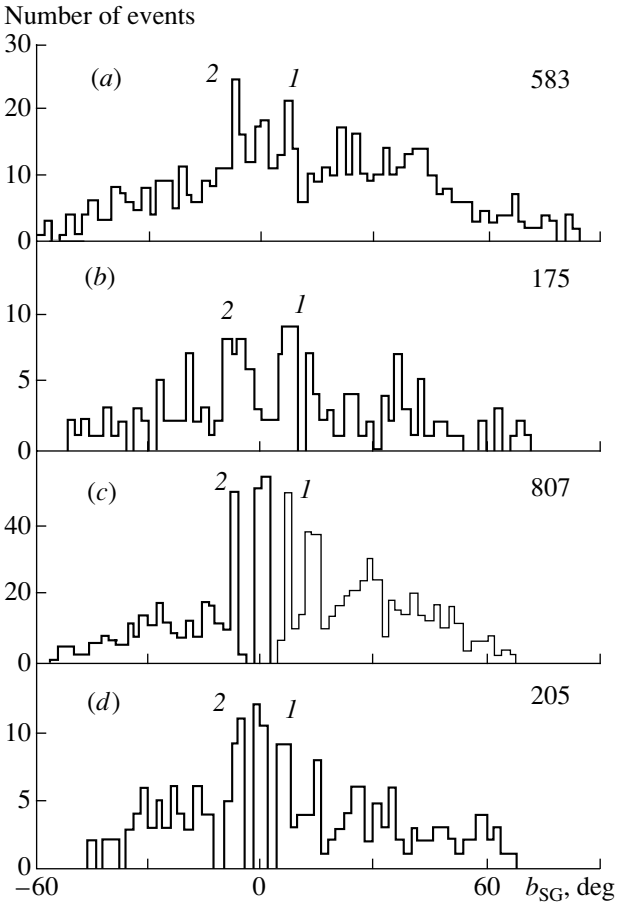

Fig. 17. Distributions of (*a*) $E_0 \geq 10^{19}$ eV showers characterized by zenith angles in the region $\theta \leq 60°$ and recorded at the Yakutsk array, (*b*) quasars with redshifts of $z \leq 0.3$ [48], and sites of a cubic lattice in the (*c*) steady-state and (*d*) expanding universe versus their supergalactic latitudes (with a step of $\Delta b_{SG} = 2°$). Numerals in plain text indicate the total number of events; *1* and *2* label peaks in the vicinity of the Supergalaxy plane.

a cosmological periodicity, which we will roughly take into account by introducing triangle functions with weights of 1, 2, and 4 for vertices at, respectively, $x = 2$, 4.5, and 7.5 and with zero weight at $x = 1$, 3, 6, and 10.

In the expanding universe, the lattice constant corresponding to the instant of photon emission by a quasar with a redshift z is [43]

$$L(z) = 120/(1 + z) \ \text{[Mpc]}. \qquad (15)$$

In our case, we have $L = 92.3$ Mpc for the farthest quasars, which occur at a distance of $r = 1200$ Mpc. As photons move from the farthest sites to an observer, the lattice constant increases gradually to 120 Mpc; although the linear coordinates of sites change, their projections onto the celestial sphere remain unchanged [43].

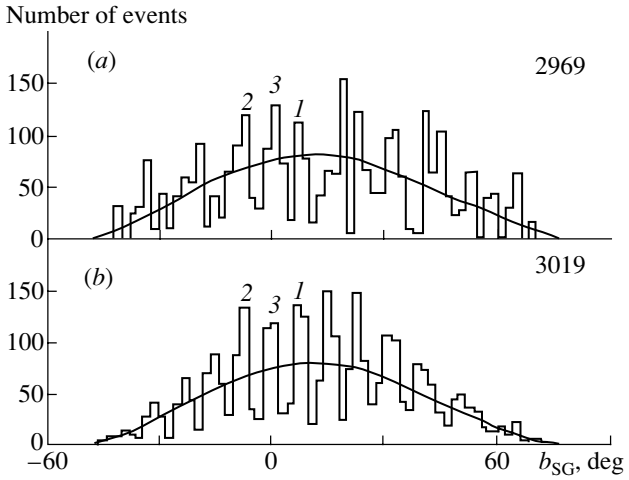

Fig. 18. Distribution of (*a*) showers in clusters (common for five groups of showers with energies in the ranges $E_0 = 10^{17.1-17.2}$, $10^{17.2-17.3}$, $10^{17.3-17.4}$, $10^{17.4-17.5}$, and $10^{17.5-17.6}$ eV [18]) and (*b*) sites of a cubic lattice in a steady-state universe versus the latitude of their arrival in supergalactic coordinates (*1–3* label peaks in the vicinity of the Supergalaxy plane). The smooth curves represent the expected distributions for random events; the figures in plain text indicate the total numbers of events.

In Fig. 17*c* (steady-state universe) and Fig. 17*d* (expanding universe), the distributions of the numbers of sites occurring at distances between 240 and 1200 Mpc are shown versus their supergalactic latitude (with a step of $\Delta b_{SG} = 2°$). In just the same way as in Figs. 17*a* and 17*b*, peaks at $\pm b_{SG} \approx 6.5°$ are also seen here. In Fig. 17*c*, they are narrower than in Fig. 17*d*, but this distinction disappears if the sites are slightly smeared around their centers in a random way. By and large, all distributions in Fig. 17 are similar.

The analogous pattern is observed for primary cosmic radiation characterized by much lower energies and concentrated largely into clusters. In Fig. 18*a*, the distribution of 2969 showers in clusters (common for five groups of showers with energies in the ranges $E_0 = 10^{17.1-17.2}$, $10^{17.2-17.3}$, $10^{17.3-17.4}$, $10^{17.4-17.5}$, and $10^{17.5-17.6}$ eV) is shown versus the latitude of their arrival in supergalactic coordinates. This distribution, which was borrowed from [18], was obtained in the case of the coincidence of the angular coordinates for 10 to 18 sites from 35 independent samples (each containing about 1000 showers), the fraction of these events in the total flux of primary cosmic radiation being $(2969/36\,825) \times 100\% \approx 8\%$. The smooth curves in Fig. 18 represent the expected distributions for random events.

It can be seen that the distribution in Fig. 18*a* is similar in many respects to the distribution in Fig. 17*a*, especially in what is concerned with peaks *1–3*. However, it has additional significant peaks situated symmetrically with respect to the Supergalaxy plane. In principle, all peaks in Fig. 18*a* are compatible with the above hypothesis of a cubic structure of the distribution of matter (more precisely, sources of primary cosmic radiation) in the Universe. This can be seen in Fig. 18*b*, which shows the distribution of the number of sites occurring at distances between 840 and 960 Mpc versus the latitude of their arrival in supergalactic coordinates.

We have considered here a steady-state universe where the cell size is $L = 120$ Mpc. The sites were smeared in a random way according to a normal law around their centers, the standard deviation being 25 Mpc (this is an approximate Supergalaxy radius, which is possibly typical of other superclusters of galaxies). Only events in which $\delta \geq 30°$ (as in actual experiments) were included in the ultimate analysis. It should be noted that this is one of the possible versions rather than the only one. All of them lead to similar results if one considers a space volume of 500 to about 1200 Mpc—what is the most important is that sites must lie within a relatively narrow (about 100 Mpc) spherical layer.

5. DISCUSSION OF THE RESULTS

Results presented in Figs. 14–18 can be interpreted as an indications that quasars with redshifts $z \leq 0.3$ are the possible sources of primary cosmic radiation with energies in the region $E_0 \geq 8 \times 10^{16}$ eV. In all probability, peaks *1* and *2* in Figs. 17 and 18—they are adjacent to the Supergalaxy plane at angles $\pm b_{SG} \approx 6.5°$—reflect the ordered structure of the matter distribution in the Universe. If this structure is similar to some extent to a cubic lattice, then the Supergalaxy plane is likely to be approximately parallel to one of the three principal planes of the present lattice.

Of course, the Supergalaxy plays some role in the origin of cosmic rays with energies in the region $E_0 \geq 8 \times 10^{16}$ eV. This is suggested by the data in Figs. 4 and 8–13. At present, it is difficult to assess its contribution to the total flux of extragalactic radiation observed on the Earth. In all probability, other clusters and superclusters of galaxies may also be local sources of primary cosmic radiation.

It should be emphasized once again that, in my opinion, primary particles entering into nodes and clusters must be electrically neutral. Because of motion in the magnetic field of the Galaxy, charged particles would lose a connection in direction with the sources of their formation and could not reveal the specific structure shown in Figs. 4–11 and 13–18.

In Figs. 9*a* and 10*a*, we have already paid attention to sizable dips (shaded regions), which we interpreted

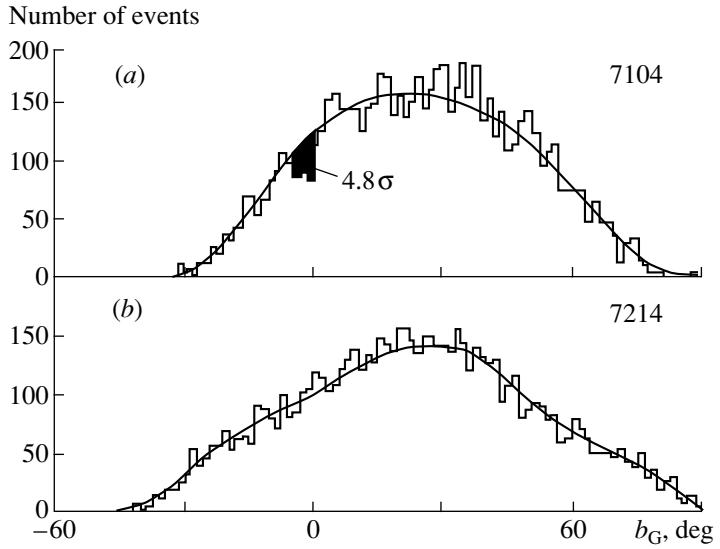

Fig. 19. Distributions of the directions of $E_0 = 10^{16.9-17.2}$ eV showers (*a*) entering into nodes and (*b*) not belonging to them versus the latitude of their arrival in galactic coordinates: (histograms) experimental data and (curves) distributions expected for an isotropic flux. Numerals indicate the numbers of showers.

as indications of the possible partial absorption of extragalactic primary cosmic radiation in the Galaxy disk. We return once again to this issue and consider the sample of $E_0 = 10^{16.9-17.2}$ eV showers (see Subsection 4.4.3). This is the energy region where there are serious contradictions in estimating the composition of primary particles (see Fig. 2*a*).

In Fig. 19, the distributions of the directions of (Fig. 19*a*) 7104 showers entering into nodes and (Fig. 19*b*) the remaining 7214 showers not belonging to them are shown versus the latitude of their arrival in galactic coordinates [20]. These distributions were obtained as the sum of 18 ($= 3 \times 6$) original distributions (with a step of $\Delta b_G = 1.5°$). As in the preceding cases (see Fig. 16), the nodes were found individually for three samples of different energies ($E_0 = 10^{16.9-17.0}$, $10^{17.0-17.1}$, and $10^{17.1-17.2}$ eV) in six independent shower samples characterized by the distances from the axis. The curves represent distributions that are expected for random events.

There are significant distinctions between the two samples presented in Fig. 19*a* and 19*b*. First, the measured distribution (histogram) in Fig. 19*a* differs strongly, according to the χ^2 criterion, from that which is expected for random events. By way of example, we indicate that, for $n = 80$ degrees of freedom, we have the value of $\chi^2 = 161$, which corresponds to a random-output probability of less than 10^{-5}. Second, a statistically significant deficit of events (shaded dip) at a level of $|259-350|/\sqrt{350} \approx 4.8\sigma$ is observed in the latitude band $-4.5°$ to $0°$. The distribution in Fig. 19*b* is totally different—in particular, it does not feature the aforementioned dip. The distribution in Fig. 19*b* leads to the value of $\chi^2 = 93$ at $n = 90$ and is indicative of an isotropic flux of primary cosmic radiation.

The result in Fig. 19*a* can be considered as yet another indication of an extragalactic origin of the primary-cosmic-radiation fraction contained in nodes. In all probability, the Galaxy only absorbs this radiation, though most strongly in the disk. The mean shift of the dip from the generally accepted Galaxy plane is $-2.1°$. This shift is likely to be due to the fact that the Sun is somewhat shifted, to the north hemisphere, with respect to the Galaxy plane considered here rather than situated strictly in the symmetry plane of the actual disk. If this is indeed so, then the primary-cosmic-radiation flux coming from southern latitudes at small angles to the disk will be absorbed more strongly in relation to the flux at the same angles from northern latitudes. This assumption is consistent with the neutral-hydrogen distribution in the Galaxy disk, where, according to data from [56], there is also a $-1.4°$ shift of the plane of the maximum hydrogen concentration from the generally accepted plane.

Suppose that the dip in Fig. 19*a* is associated with a relatively stronger absorption of extragalactic primary cosmic radiation in the Galaxy disk in relation to its high latitudes. In this case, we can roughly estimate the absorption range of unknown extragalactic particles (for the sake of brevity, we refer to them as A particles) on the basis of the relation

$$N = N_0 \exp(-\langle l \rangle / \lambda_A), \qquad (16)$$

where $N_0 \approx 350$ and $N \approx 259$ are, respectively, the expected and the measured number of events in the band of Galaxy latitudes between $-4.5°$ and $0°$ (Fig. 19*a*) and $\langle l \rangle$ is the mean thickness (in g/cm^2)of the Galaxy disk in the sector of our observations. From (16), we obtain

$$\lambda_A \approx 3.3\langle l \rangle.$$

In order to find the value of $\langle l \rangle$, we assume that neutral hydrogen plays the main role in the weakening of primary cosmic radiation, since the contribution of dust (about 1%) is negligible [56]. From Fig. 5, it can be seen that, in the Galaxy disk, primary cosmic radiation comes to us from the sector $\Delta l_G \approx 60°-180°$. Within this sector, the path r from the observer to the external boundary of the Galaxy changes from about 10 to 5 kpc ($\langle r \rangle \approx 8$ kpc). According to data from [56], the mean hydrogen concentration in the latitude band $|b_G| \leq 10°$ decreases from $\rho \approx 0.5$ cm^{-3} (at a distance of about 10 kpc from the Galaxy center) to $\rho \approx 0.1$ cm^{-3} at about 15 kpc ($\langle \rho \rangle \approx 0.25$ cm^{-3}). From here, we obtain

$$\langle l \rangle \approx \langle r \rangle \langle \rho \rangle m_p \approx 10^{-2} \text{ g/cm}^2,$$

where $m_p = 1.67 \times 10^{-24}$ g is the proton mass. The sought range is

$$\lambda_A \approx 3.3 \times 10^{-2} \text{ g/cm}^2.$$

The resulting range of unknown A particles proved to be approximately 1000 times shorter than the range of $E_0 \sim 10^{17}$ eV protons with respect to nuclear interactions; nevertheless, these particles can arrive without losses almost from the very horizon of the visible Universe. Assuming that the age of the expanding Universe is $T \approx 13$ billion years and that its mean matter density is $\rho_0 \approx 10^{-30}$ g/cm^3,we obtain

$$l_T = \rho_0 cT \approx 1.23 \times 10^{-2} \text{ g/cm}^2,$$

where c is the speed of light. From (16), the attenuation factor is $\exp(-l_T/\lambda_A) \approx 0.7$. In the Earth's atmosphere, A particles begin to interact at an altitude h_A above sea level. This altitude can be found from the barometric formula

$$\lambda_A = p_0 \exp(-h_A/h_0), \qquad (17)$$

where $p_0 = 1020$ g/cm^2 is the air pressure at sea level and $h_0 = 6.85$ km; it follows that $h_A \approx 71$ km.

These particles initiate the development of extensive air showers much earlier than particles of the usual composition of cosmic rays. If one takes, by way of example, protons of energy $E_0 \sim 10^{17}$ eV, they travel, in the Earth's atmosphere, a mean path of about 50 g/cm^2 to the first event of nuclear interaction; for iron nuclei, it is approximately two to three times shorter.

After the first interaction, mysterious A particles seem to disappear, giving way, in the development of extensive air showers, to a normal cascade of secondary particles. Otherwise, showers initiated by them would differ strongly from ordinary ones and would reveal themselves readily. Because of so short a range to the first nuclear interaction, showers from A particles are expected to cause an enhanced development of extensive air showers, with a higher maximum of the cascade curve in relation to the case of primary protons. In view of this, showers from A particles could be misinterpreted as showers from iron nuclei. We cannot rule out the possibility that one of the primary-cosmic-radiation components that is presented in Fig. 2*b* as iron reflects roughly the contribution of these particles, because, as was mentioned above, the majority of the methods for determining the composition of primary cosmic radiation are indirect: they are based on a comparison of the observed features of extensive air showers with their counterparts calculated on the basis of model concepts of the development of extensive air showers for some specifically presumed composition of primary cosmic radiation. Here, it is quite possible that the effect of any new primary particles characterized by very short ranges with respect to interactions can be erroneously treated by researchers in terms of an increase in the fraction of heavy nuclei.

6. CONCLUSION

Upon a generalization of the results presented above, there arises the following pattern. In the region of energies higher than that of the Khristiansen knee ($E_0 \geq 3 \times 10^{15}$ eV), primary cosmic radiation is likely to consist of two components, one of these being, in all probability, of an extragalactic origin. This is suggested by the data in Figs. 4–19. Of course, the Supergalaxy plays a nontrivial role in the origin of ultrahigh-energy cosmic rays (at least for $E_0 \geq 8 \times 10^{16}$ eV). Pieces of evidence for this can be found in Figs. 4 and 8–13. The results presented in Figs. 14–18 can be interpreted as an indication that quasars with redshifts of $z \leq 0.3$ may be one of the possible sources of primary cosmic radiation with energies in the region $E_0 \geq 8 \times 10^{16}$ eV. Peaks *1* and *2* in Figs. 17 and 18—they are adjacent to the Supergalaxy plane at angles of $\pm b_{SG} \approx 6.5°$—reflect, in all probability, the ordered structure of the matter distribution in the Universe.

Within $d \leq 3°$ solid angles, the extragalactic component forms many nodes and clusters. Most likely, primary particles entering into the nodes and clusters are electrically neutral; otherwise, their motion in the magnetic field of the Galaxy would lead to the disappearance of their connection with their sources in

direction, so that these particles could not disclose the aforementioned structure of the matter distribution in the Universe.

In all probability, these particles have a very short range with respect to nuclear interaction ($\lambda_a \approx 3.3 \times 10^{-2}$ g/cm^2) and cause an earlier development of extensive air showers in relation to the case of the usual composition of primary cosmic radiation. Their fraction in the total flux of primary cosmic rays at $E_0 \approx 10^{17}$ eV is $7104/14\,318 \approx 0.5$, which is about two to three times higher than in the adjacent energy range $E_0 \approx 10^{17.2-17.8}$ eV.

So fast an increase in the fraction of neutral particles at $E_0 \approx 10^{17}$ eV can be misinterpreted as a considerable change in the composition of primary cosmic radiation toward its higher weight. We cannot rule out the possibility that unknown neutral particles hypothesized here can manifest themselves sizably in the energy region $E_0 < 10^{17}$ eV as well, but further investigations are necessary in order to clarify this point conclusively.

The remaining showers, which do not belong to nodes and clusters, are distributed almost isotropically over the celestial sphere. In all probability, this part of the primary cosmic radiation consists of charged particles (protons and nuclei of various chemical elements) propagating through Galaxy via diffusion. One of their powerful sources is situated in the vicinity of the Galaxy center [10,11].

Within different energy intervals, the contributions of the components conjectured here are strongly different. It is highly probable that such a change in the composition of primary cosmic radiation is especially pronounced in the energy ranges $E_0 \approx 10^{15.7-15.9}$, $10^{16.7-16.9}$, $10^{17.7-17.9}$, and $10^{18.7-18.9}$ eV, where one observes correlated astrophysical and nuclear-physics anomalies in the development of extensive air showers.

ACKNOWLEDGMENTS

The financial support extended by the Ministry for Science of the Russian Federation to the Yakutsk multipurpose array for studying extensive air showers (grant no. 01-30) is gratefully acknowledged.

REFERENCES

1. G. V. Kulikov and G. B. Khristiansen, Zh. Éksp. Teor. Fiz. **35**, 635 (1958) [Sov. Phys. JETP **8**, 441 (1958)].
2. E. A. Vishnevskaya, N. N. Kalmykov, G. V. Kulikov, *et al.,* Yad. Fiz. **62**, 300 (1999) [Phys. At. Nucl. **62**, 265 (1999)].
3. H. Ulrich, T. Antoni, W. D. Apel, *et al.*, in *Proceedings of the 27th ICRC, Hamburg, 2001*, Vol. 2, p. 97.
4. T. Abu-Zayyad, K. Belov, D. J. Clay, *et al.*, astro-ph/0010652.
5. V. S. Ptuskin *et al.*, Astron. Astrophys. **268**, 726 (1993).
6. J. Linsley, Phys. Rev. Lett. **34**, 1530 (1975).
7. R. N. Coy, J. Lloyd-Evans, M. Patel, *et al.*, in *Proceedings of the 17th ICRC, Paris, 1981*, Vol. 9, p. 183.
8. A. A. Mikhailov and M. I. Pravdin, Pis'ma Zh. Éksp. Teor. Fiz. **66**, 289 (1997) [JETP Lett. **66**, 305 (1997)].
9. M. I. Pravdin, A. A. Ivanov, A. D. Krasil'nikov, *et al.*, Zh. Éksp. Teor. Fiz. **119**, 881 (2001) [JETP **92**, 766 (2001)].
10. N. Hayashida, M. Nagano, D. Nishikawa, *et al.,* Astropart. Phys. **10**, 303 (1999).
11. J. A. Bellido, B. W. Clay, R. B. Dawson, and M. Johnston-Hollitt, astro-ph/0009039.
12. A. V. Glushkov, Pis'ma Zh. Éksp. Teor. Fiz. **48**, 513 (1988) [JETP Lett. **48**, 555 (1988)].
13. A. V. Glushkov, Priroda, No. 5, 111 (1989).
14. A. V. Glushkov, Pis'ma Zh. Éksp. Teor. Fiz. **73**, 355 (2001) [JETP Lett. **73**, 313 (2001)].
15. A. V. Glushkov and I. E. Sleptsov, Izv. Akad. Nauk, Ser. Fiz. **65**, 437 (2001).
16. A. V. Glushkov and M. I. Pravdin, Zh. Éksp. Teor. Fiz. **119**, 1029 (2001) [JETP **92**, 887 (2001)].
17. A. V. Glushkov and M. I. Pravdin, Pis'ma Astron. Zh. **27**, 577 (2001) [Astron. Lett. **27**, 493 (2001)].
18. A. V. Glushkov, Pis'ma Zh. Éksp. Teor. Fiz. **75**, 3 (2002) [JETP Lett. **75**, 1 (2002)].
19. A. V. Glushkov, Izv. Akad. Nauk, Ser. Fiz. **66**, 1601 (2002).
20. A. V. Glushkov, Yad. Fiz. **66**, 1292 (2003) [Phys. At. Nucl. **66**, 1252 (2003)].
21. A. V. Glushkov, Preprint IKFIA (Yakutsk, 1988).
22. A. V. Glushkov, N. N. Efimov, N. N. Efremov, *et al.*, in *Proceedings of the 19th ICRC, La Jolla, 1985*, Vol. 7, p. 48.
23. A. V. Glushkov, M. I. Pravdin, I. E. Sleptsov, *et al.,* Yad. Fiz. **63**, 1557 (2000) [Phys. At. Nucl. **63**, 1477 (2000)].
24. N. N. Kalmykov, G. B. Khristiansen, S. S. Ostapenko, and A. V. Pavlov, in *Proceedings of the 24th ICRC, Rome, 1995*, Vol. 1, p. 123.
25. J. Linsley, in *Proceedings of the 18th ICRC, Bangalore, 1983*, Vol. 12, p. 135.
26. M. I. Pravdin, M. N. Dyakonov, A. V. Glushkov, *et al.*, in *Proceedings of the 26th ICRC, Salt Lake City, 1999*, Vol. 3, p. 292.
27. N. Hayashida, K. Honda, M. Honda, *et al.*, in *Proceedings of the Tokyo Workshop on Extremely High Energy Cosmic Rays: Astrophysics and Future Observatories, 1996*, Ed. by M. Nagano, p. 17.
28. M. Nagano, T. Hara, Y. Hatano, *et al.*, J. Phys. G **10**, 1295 (1984).
29. J. Linsley and A. A. Watson, Phys. Rev. Lett. **46**, 459 (1981).

30. J. Lloyd-Evans and A. A. Watson, in *Proceedings of the 8th European Cosmic Rays Symposium, Bologna, 1983*.
31. A. A. Watson, Nucl. Phys. B (Proc. Suppl.) **28**, 3 (1992).
32. A. G. Lyne and F. Graham-Smith, *Pulsar Astronomy* (Cambridge Univ. Press, 1990).
33. V. V. Prosin, private communication.
34. B. N. Afanasiev, M. N. Dyakonov, T. A. Egorov, *et al.*, in *Proceedings of the 24th ICRC, Rome, 1995*, Vol. 2, p. 756.
35. A. A. Mikhailov, Pis'ma Zh. Éksp. Teor. Fiz. **72,** 233 (2000) [JETP Lett. **72**, 160 (2000)].
36. A. A. Mikhailov, in *Proceedings of the 27th ICRC, Hamburg, 2001*, Vol. 2, p. 420.
37. A. V. Glushkov, I. T. Makarov, E. S. Nikiforova, *et al.*, Astropart. Phys. **4**, 15 (1995).
38. A. V. Glushkov, I. T. Makarov, M. I. Pravdin, and I. E. Sleptsov, Izv. Akad. Nauk, Ser. Fiz. **63**, 538 (1999).
39. A. V. Glushkov, I. T. Makarov, M. I. Pravdin, *et al.,* Pis'ma Zh. Éksp. Teor. Fiz. **71**, 145 (2000) [JETP Lett. **71**, 97 (2000)].
40. A. V. Glushkov, I. T. Makarov, M. I. Pravdin, *et al.*, in *Proceedings of the 27th ICRC, Hamburg, 2001*, Vol. 2, p. 411.
41. A. V. Glushkov, M. I. Pravdin, I. E. Sleptsov, *et al.,* Yad. Fiz. **65,** 1346 (2002) [Phys. At. Nucl. **65**, 1313 (2002)].
42. M. Seldner, B. Siebars, E. J. Groth, and E. P. J. Peebles, Astron. J. **82**, 249 (1977).
43. D. Layzer, *Constructing the Universe* (Sci. American, New York, 1984; Mir, Moscow, 1988).
44. G. de Vaucouleurs, Astron. J. **58**, 30 (1953).
45. B. A. Vorontsov-Vel'yaminov, I. D. Karachentsev, E. Turner, *et al.,* in *Large-Scale Structure of the Universe* (Mir, Moscow, 1981).
46. B. A. Vorontsov-Vel'yaminov and A. A. Krasnogorskaya, *Morphology Catalogue of Galaxies* (Izd. Mos. Gos. Univ., Moscow, 1962), Part 1.
47. B. A. Vorontsov-Vel'yaminov and V. P. Arkhipova, *Morphology Catalogue of Galaxies* (Izd. Mos. Gos. Univ., Moscow, 1964), Part 2.
48. A. Hewitt and G. Burbidge, Astrophys. J., Suppl. Ser. **63**, 1 (1987).
49. A. V. Uryson, Zh. Éksp. Teor. Fiz. **116**, 1121 (1999) [JETP **89**, 597 (1999)].
50. P. G. Tinyakov and I. I. Tkachov, Pis'ma Zh. Éksp. Teor. Fiz. **74**, 499 (2001) [JETP Lett. **74**, 445 (2001)].
51. A. V. Gurevich and K. P. Zybin, Usp. Fiz. Nauk **165**, 1 (1995).
52. J. Einasto *et al.*, Nature **385**, 139 (1997).
53. S. G. Fedoskin, *Physics and Phylosophy of Similarity from Preons to Metagalaxies* (Perm, 1999).
54. Ya. B. Zel'dovich, Pis'ma Astron. Zh. **8**, 195 (1982) [Sov. Astron. Lett. **8**, 102 (1982)].
55. M. F. Khodyachikh, Astron. Zh. **73**, 11 (1996) [Astron. Rep. **40**, 6 (1996)].
56. I. Oort, in *Handbuch der Physik*, Bd. 53, *Astrophysik IV: Sternesysteme* (West Berlin, 1959; Inostrannaya Literatura, Moscow, 1962).

Translated by A. Isaakyan

Physics of Atomic Nuclei, Vol. 67, No. 5, 2004, pp. 985–992. From Yadernaya Fizika, Vol. 67, No. 5, 2004, pp. 1006–1013.

ELEMENTARY PARTICLES AND FIELDS
Theory

Near-Threshold Radiative 3π Production in e^+e^- Annihilation*

A. I. Ahmedov[1], G. V. Fedotovich[2], E. A. Kuraev[3], and Z. K. Silagadze[2]

Received April 10, 2003

Abstract—We consider the $\pi^+\pi^-\pi_0\gamma$ final state in electron–positron annihilation at c.m.s. energies not far from the threshold. Both initial- and final-state radiations of the hard photon are considered, but without interference between them. The amplitude for the final-state radiation is obtained by using the effective Wess–Zumino–Witten Lagrangian for pion–photon interactions valid for low energies. In real experiments, energies are never so small that ρ and ω mesons would have a negligible effect. So a phenomenological Breit–Wigner factor is introduced in the final-state radiation amplitude to account for the vector mesons' influence. Using radiative 3π production amplitudes, a Monte Carlo event generator was developed which could be useful in experimental studies. © *2004 MAIK "Nauka/Interperiodica".*

1. INTRODUCTION

The new Brookhaven experimental result for the anomalous magnetic moment of the muon [1] aroused considerable interest in the physics community, because it was interpreted as indicating new physics beyond the Standard Model [2]. However, such claims, too premature in our opinion, assume that the theoretical prediction for the muon anomaly is well understood at the level of necessary precision. Hadronic uncertainties become the main concern [3]. Fortunately, the leading hadronic contribution is related to the hadronic corrections to the photon vacuum polarization function, which can be accurately calculated provided that the precise experimental data on the low-energy hadronic cross sections in e^+e^- annihilation are at our disposal.

In recent years, few high-statistics experimental data were collected in the ρ–ω region in Novosibirsk experiments at the VEPP-2M collider [4]. In this region, the hadronic cross sections are dominated by the $e^+e^- \to 2\pi$ and $e^+e^- \to 3\pi$ channels. The former is of uppermost importance for reduction of errors in evaluation of the hadronic vacuum polarization contribution to the muon g-2. Considerable progress was reported for this channel by the CMD-2 Collaboration [5]. The $e^+e^- \to 3\pi$ channel, which gives a less important but still significant contribution to the hadronic error, was also investigated in the same experiment in the ω-meson region [6]. Such high precision experiments require accurate knowledge of various backgrounds. Among them, the $e^+e^- \to 3\pi\gamma$ channel provides an important background needed to be well understood. This experimental necessity motivated our investigation of the three-pion radiative production presented here. In addition to being of interest as an important background source, this process could be of interest by itself, because a detailed experimental study of the final-state radiation will allow one to get important information about pion–photon dynamics at low energies. However, such experimental investigation will require much higher statistics than is available in VEPP-2M experiments and maybe would be feasible only at ϕ factories, where the low-energy region can be reached by the radiative return technique, as was recently demonstrated in the KLOE experiment [7].

2. INITIAL-STATE RADIATION

Let J_μ be the matrix element of the electromagnetic current between the vacuum and the $\pi^+\pi^-\pi^0$ final state. Then the initial-state-radiation (ISR) contribution to the $e^+e^- \to \pi^+\pi^-\pi^0\gamma$ process cross section is given at $O(\alpha)$ by the standard expression [8]

$$d\sigma_{\rm ISR}(e^+e^- \to 3\pi\gamma) \qquad (1)$$
$$= \frac{e^6}{4(2\pi)^8(Q^2)^2}\left\{\frac{Q^2}{4E^2}J\cdot J^*\left(\frac{p_+}{k\cdot p_+}-\frac{p_-}{k\cdot p_-}\right)^2 - \frac{Q^2}{2E^2}\frac{(p_+\cdot J)(p_+\cdot J^*)+(p_-\cdot J)(p_-\cdot J^*)}{(k\cdot p_+)(k\cdot p_-)} - \frac{J\cdot J^*}{2E^2}\left(\frac{k\cdot p_+}{k\cdot p_-}+\frac{k\cdot p_-}{k\cdot p_+}\right)+\frac{m_e^2}{E^2}\right.$$

*This article was submitted by the authors in English.

[1]Laboratory of Particle Physics, Joint Institute for Nuclear Research, Dubna, Moscow oblast, 141980 Russia.
[2]Budker Institute of Nuclear Physics, pr. Akademika Lavrent'eva 11, Novosibirsk, 630090 Russia.
[3]Laboratory of Theoretical Physics, Joint Institute for Nuclear Research, Dubna, Moscow oblast, 141980 Russia.

1063-7788/04/6705-0985$26.00

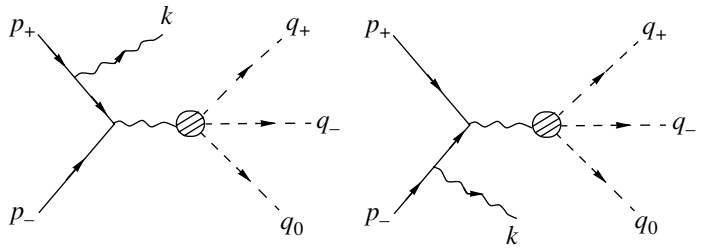

Fig. 1. Initial-state radiation diagrams and particle 4-momenta assignment.

$$\times \left(\frac{p_+\cdot J}{k\cdot p_-}-\frac{p_-\cdot J}{k\cdot p_+}\right)\left(\frac{p_+\cdot J^*}{k\cdot p_-}-\frac{p_-\cdot J^*}{k\cdot p_+}\right)\Bigg\}d\Phi$$
$$\equiv \frac{e^6}{4(2\pi)^8}|A_{\rm ISR}|^2 d\Phi,$$

where $d\Phi$ stands for the Lorentz invariant phase space

$$d\Phi = \frac{d\mathbf{k}}{2\omega}\frac{d\mathbf{q}_+}{2E_+}\frac{d\mathbf{q}_-}{2E_-}\frac{d\mathbf{q}_0}{2E_0}$$
$$\times\,\delta(p_+ + p_- - k - q_+ - q_- - q_0)$$

and $Q^2 = (q_+ + q_- + q_0)^2 = 4E(E-\omega)$ is the photon virtuality, E being the beam energy and ω being the energy of the γ quantum. Particle 4-momentum assignment can be read from the corresponding diagrams presented in Fig. 1. The current matrix element J_μ has a general form

$$J_\mu = \epsilon_{\mu\nu\sigma\tau}q_+^\nu q_-^\sigma q_0^\tau F_{3\pi}(q_+, q_-, q_0). \qquad (2)$$

For the $F_{3\pi}$ form factor, which depends only on invariants constructed from the pion 4-momenta, we will take the expression from [9]

$$F_{3\pi} = \frac{\sqrt{3}}{(2\pi)^2 f_\pi^3}\left[\sin\theta\cos\eta R_\omega(Q^2)\right. \qquad (3)$$
$$\left.-\cos\theta\sin\eta R_\phi(Q^2)\right](1-3\alpha_K-\alpha_K H).$$

Here, $\alpha_K \approx 0.5$, $f_\pi \approx 93$ MeV is the pion decay constant, $\eta = \theta - \arcsin(1/\sqrt{3}) \approx 3.4^\circ$ characterizes the departure of the $\omega-\phi$ mixing from the ideal one, and

$$H = R_\rho(Q_0^2) + R_\rho(Q_+^2) + R_\rho(Q_-^2),$$

where

$$Q_0^2 = (q_+ + q_-)^2, \quad Q_+^2 = (q_0 + q_+)^2,$$
$$Q_-^2 = (q_0 + q_-)^2.$$

The dimensionless Breit–Wigner factors have the form

$$R_V(Q^2) = \left[\frac{Q^2}{M_V^2} - 1 + i\frac{\Gamma_V}{S_V}\right]^{-1},$$
$$R_\rho(Q^2) = \left[\frac{Q^2}{M_\rho^2} - 1 + i\frac{\sqrt{Q^2}\Gamma_\rho(Q^2)}{M_\rho^2}\right]^{-1},$$

where $V = \omega, \phi$ and for the ρ meson the following energy-dependent width is used:

$$\Gamma_\rho(Q^2) = \Gamma_\rho\frac{M_\rho^2}{Q^2}\left(\frac{Q^2-4m\pi^2}{M_\rho^2-4m\pi^2}\right)^{3/2}.$$

The last term in (1) is completely irrelevant for VEPP-2M energies if the hard photon is emitted at large angle. Thus, we will neglect it in the following.

3. FINAL-STATE RADIATION

To describe final-state radiation (FSR), we use the effective low-energy Wess–Zumino–Witten Lagrangian [10]. The relevant piece of this Lagrangian is reproduced below:

$$\mathcal{L} = \frac{f_\pi^2}{4}{\rm Sp}[D_\mu U(D_\mu U)^+ + \chi U^+ + U\chi^+] \qquad (4)$$
$$-\frac{e}{16\pi^2}\epsilon^{\mu\nu\alpha\beta}A_\mu {\rm tr}[Q\{(\partial_\nu U)(\partial_\alpha U^+)(\partial_\beta U)U^+$$
$$-(\partial_\nu U^+)(\partial_\alpha U)(\partial_\beta U^+)U\}]$$
$$-\frac{ie^2}{8\pi^2}\epsilon^{\mu\nu\alpha\beta}(\partial_\mu A_\nu)A_\alpha {\rm tr}\Big[Q^2(\partial_\beta U)U^+$$
$$+Q^2U^+(\partial_\beta U)+\frac{1}{2}QUQU^+(\partial_\beta U)U^+$$
$$-\frac{1}{2}QU^+QU(\partial_\beta U^+)U\Big].$$

Here, $U = \exp(i\sqrt{2}P/f_\pi)$, $D_\mu U = \partial_\mu U + ieA_\mu[Q, U]$, $Q = {\rm diag}(2/3, -1/3, -1/3)$ is the quark charge matrix, and terms with $\chi = B{\rm diag}(m_u, m_d, m_s)$ introduce explicit chiral symmetry breaking due to nonzero quark masses. The constant B has dimension of mass and is determined through the equation $Bm_q = m_\pi^2$, $m_q = m_u \approx m_d$. The pseudoscalar meson matrix P has its standard form

$$P = \begin{pmatrix} \frac{1}{\sqrt{2}}\pi^0 + \frac{1}{\sqrt{6}}\eta & \pi^+ & K^+ \\ \pi^- & -\frac{1}{\sqrt{2}}\pi^0 + \frac{1}{\sqrt{6}}\eta & K^0 \\ K^- & \bar{K}^0 & -\frac{2}{\sqrt{6}}\eta \end{pmatrix}.$$

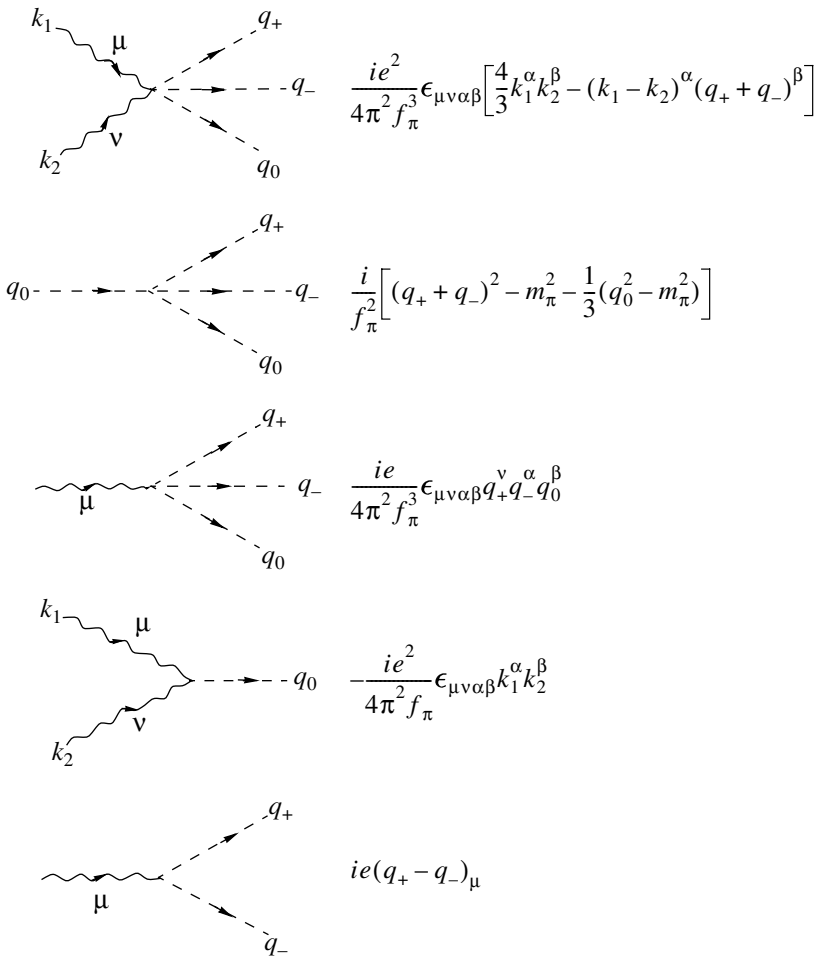

Fig. 2. Interaction vertexes relevant for final-state radiation.

It is straightforward to get from (4) the relevant interaction vertices shown in Fig. 2.

Using these Feynman rules, one can calculate the $\gamma^* \to \pi^+\pi^-\pi^0\gamma$ amplitude originating from the diagrams shown in Fig. 3. The result is

$$A_{\mu\nu}(\gamma_\mu^* \to 3\pi\gamma_\nu) = \frac{ie^2}{4\pi^2 f_\pi^3} T_{\mu\nu}, \tag{5}$$

where ($Q = q_+ + q_- + q_0 + k$ is the virtual photon 4-momentum)

$$\begin{aligned} T_{\mu\nu} = {} & \epsilon_{\mu\nu\alpha\beta} Q^\alpha k^\beta \left(1 - \frac{(q_+ + q_-)^2 - m_\pi^2}{(Q-k)^2 - m_\pi^2}\right) \\ & + \epsilon_{\mu\nu\alpha\beta}(Q+k)^\alpha q_0^\beta \\ & + \epsilon_{\mu\lambda\alpha\beta} Q^\alpha q_0^\beta \left(\frac{(2q_- + k)_\nu q_+^\lambda}{2q_- \cdot k} + \frac{(2q_+ + k)_\nu q_-^\lambda}{2q_+ \cdot k}\right) \\ & - \epsilon_{\nu\lambda\alpha\beta} k^\alpha q_0^\beta \left(\frac{(2q_- - Q)_\mu q_+^\lambda}{Q^2 - 2q_- \cdot Q} + \frac{(2q_+ - Q)_\mu q_-^\lambda}{Q^2 - 2q_+ \cdot Q}\right). \end{aligned} \tag{6}$$

The tensor $T_{\mu\nu}$ is gauge invariant,

$$Q^\mu T_{\mu\nu} = k^\nu T_{\mu\nu} = 0.$$

Note that our result for $A_{\mu\nu}(\gamma_\mu^* \to 3\pi\gamma_\nu)$ is in agreement with the known result [11, 12] for the $\gamma^*\gamma^* \to 3\pi$ amplitude (these two amplitudes are connected by crossing symmetry, of course).

If $J_\mu^{(\gamma)}$ is the amplitude of the transition $\gamma_\mu^* \to \pi^+\pi^-\pi^0\gamma$, then the FSR contribution to the $e^+e^- \to \gamma^* \to \pi^+\pi^-\pi^0\gamma$ process cross section is given by [8]

$$\begin{aligned} d\sigma_{\mathrm{FSR}} = {} & \frac{e^2}{(2\pi)^8 \cdot 64 E^4} \\ & \times \sum_\epsilon \left\{ \frac{\mathrm{Re}[(p_+ \cdot J^{(\gamma)})(p_- \cdot J^{(\gamma)*})]}{E^2} \right. \\ & \left. - J^{(\gamma)} \cdot J^{(\gamma)*} \right\} d\Phi \approx \frac{1}{(2\pi)^4 \cdot 64 E^4} \\ & \times \sum_\epsilon \left[|J_1^{(\gamma)}|^2 + |J_2^{(\gamma)}|^2 \right] d\Phi, \end{aligned}$$

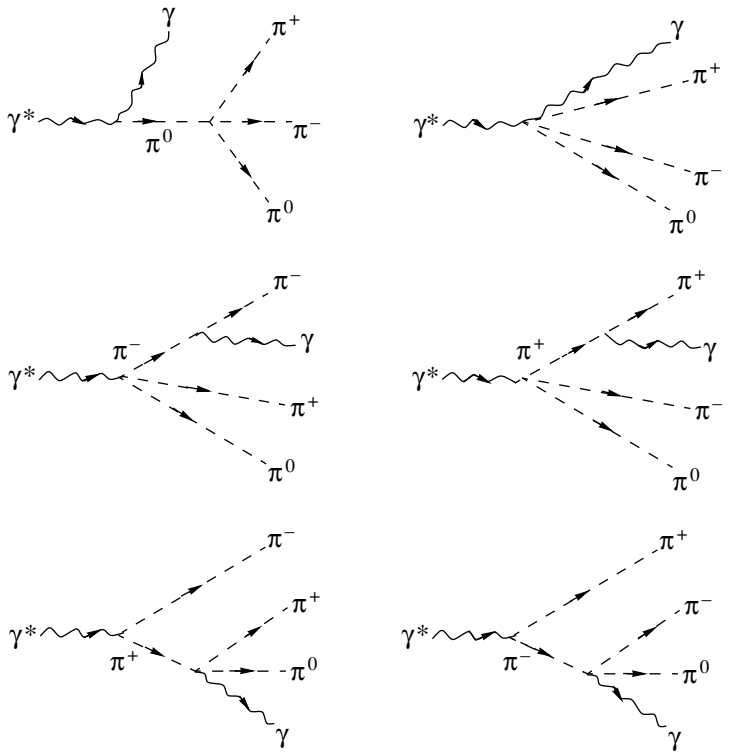

Fig. 3. $\gamma^* \to \pi^+\pi^-\pi^0\gamma$ transition diagrams.

where the sum is over the photon polarization ϵ and the z axis was assumed to be along $\mathbf{p}_-$, but $J_\mu^{(\gamma)} = \epsilon^\nu A_{\mu\nu}(\gamma^* \to 3\pi\gamma)$. Thus, we can perform the polarization sum by using $\sum_\epsilon \epsilon_\mu \epsilon_\nu^* = -g_{\mu\nu}$. By introducing gauge-invariant real 4-vectors t_1 and t_2 via $t_{1\mu} = T_{1\mu}, t_{2\mu} = T_{2\mu}$, the result can be cast in the form (note that the norm of gauge-invariant 4-vector is always negative)

$$d\sigma_{\rm FSR}(e^+e^- \to 3\pi\gamma) \tag{7}$$
$$= \frac{e^4}{(2\pi)^8 \cdot 64E^4} \frac{1}{(2\pi)^4 f_\pi^6} \left[-t_1 \cdot t_1 - t_2 \cdot t_2\right] d\Phi.$$

However, for the photon virtualities of real experimental interest, vector meson effects can no longer be neglected. Therefore, we replace (7) by

$$d\sigma_{\rm FSR}(e^+e^- \to 3\pi\gamma) \tag{8}$$
$$= \frac{e^4}{(2\pi)^8 \cdot 64E^4} \frac{1}{(2\pi)^4 f_\pi^6} [-t_1 \cdot t_1 - t_2 \cdot t_2] K_{\rm BW} d\Phi$$
$$\equiv \frac{e^6}{(2\pi)^8} |A_{\rm FSR}|^2 d\Phi,$$

where we have introduced a phenomenological Breit–Wigner factor

$$K_{\rm BW} = 3\left|\sin\theta\cos\eta R_\omega(4E^2) - \cos\theta\sin\eta R_\phi(4E^2)\right|^2.$$

This factor is similar to the one presented in ISR [see Eq. (3)] and tends to unity as $E \to 0$. It gives about an order-of-magnitude increase in $\sigma_{\rm FSR}$ for energies $2E = 0.65$–0.7 GeV.

4. MONTE CARLO EVENT GENERATOR

Although what follows can be considered as textbook material [13], we will nevertheless give a somewhat detailed description of the Monte Carlo algorithm for reasons of convenience.

An important first step is the following transformation of the Lorentz invariant phase space. Let $R_n(p^2; m_1^2, \ldots, m_n^2)$ be the n-particle phase space

$$R_n(p^2; m_1^2, \ldots, m_n^2) = \int \prod_{i=1}^n \frac{d\mathbf{q}_i}{2E_i} \delta\left(p - \sum_{i=1}^n q_i\right).$$

Inserting the identity

$$1 = \int dk_1 d\mu_1^2 \delta(p - q_1 - k_1)\delta(k_1^2 - \mu_1^2),$$

we get

$$R_4(p^2; m_1^2, m_2^2, m_3^2, m_4^2)$$
$$= \int \frac{d\mathbf{q}_1}{2E_1} R_3((p-q_1)^2; m_2^2, m_3^2, m_4^2)$$
$$= \int \frac{d\mathbf{q}_1}{2E_1} dk_1 d\mu_1^2 R_3(k_1^2; m_2^2, m_3^2, m_4^2)$$

$$\times \delta(p-q_1-k_1)\delta(k_1^2-\mu_1^2).$$

However (note that $(p-q_1)_0 = E_2+E_3+E_4 > 0$),

$$\int \frac{d\mathbf{q}_1}{2E_1} dk_1 \delta(k_1^2-\mu_1^2)\delta(p-q_1-k_1)$$
$$= \int \frac{d\mathbf{q}_1}{2E_1}\frac{d\mathbf{k}_1}{2k_{10}}\delta(p-q_1-k_1) = R_2(p^2;m_1^2,\mu_1^2).$$

Therefore,

$$R_4(p^2;m_1^2,m_2^2,m_3^2,m_4^2) \qquad (9)$$
$$= \int d\mu_1^2 R_3(\mu_1^2;m_2^2,m_3^2,m_4^2)R_2(p^2;m_1^2,\mu_1^2).$$

But [13]

$$R_2(p^2;m_1^2,\mu_1^2) = \int \frac{\lambda^{1/2}(p^2;m_1^2,\mu_1^2)}{8p^2} d\Omega_1^*,$$

where λ stands for the triangle function and Ω_1^* describes the orientation of the $\mathbf{q}_1$ vector in the p-particle rest frame.

It is more convenient to integrate over q-particle energy E^* instead of mass μ, the two being interconnected by the relation $\mu^2 = p^2+q^2-2\sqrt{p^2}E^*$ in the p-particle rest frame.

Using the relation [13]

$$\frac{\lambda^{1/2}(p^2;m^2,\mu^2)}{2\sqrt{p^2}} = \mu\sqrt{\bar\gamma^2-1},$$

where $\bar\gamma$ is the γ factor of the "particle" (subsystem) with the invariant mass μ, after repeatedly using (9),

$$R_4 = \int \frac{1}{2}\sqrt{\bar\gamma_1^2-1}\,dE_1^* d\Omega_1^* \frac{1}{2}\mu_1\sqrt{\bar\gamma_2^2-1}\,dE_2^* d\Omega_2^*$$
$$\times \frac{1}{2}|\mathbf{p}_3^*|d\Omega_3^*,$$

where $\mathbf{p}_3^*$ momentum is in the rest frame of the (3, 4) subsystem and E_2^*, Ω_2^*, $\bar\gamma_2$ are in the rest frame of the (2, 3, 4) subsystem.

Now it is straightforward to rewrite the differential cross section in the following form:

$$d\sigma(e^+e^-\to 3\pi\gamma) = \frac{\alpha^3}{2\pi^2}|A|^2 f\, d\Phi^*, \qquad (10)$$

where $|A|^2 = |A_{\rm ISR}|^5 + |A_{\rm FSR}|^2$ (we do not take into account interference between ISR and FSR; this interference integrates to zero if we do not distinguish between negative and positive π mesons),

$$f = \mu_1(\omega_{\max}-\omega_{\min})(E^*_{0\max}-E^*_{0\min}) \qquad (11)$$
$$\times \sqrt{(E_-^{*2}-m_\pi^2)(\bar\gamma_1^2-1)(\bar\gamma_2^2-1)},$$

and

$$d\Phi^* = \frac{d\omega}{(\omega_{\max}-\omega_{\min})}\frac{d\varphi}{2\pi}\frac{d\cos\theta}{2} \qquad (12)$$
$$\times \frac{dE_0^*}{(E^*_{0\max}-E^*_{0\min})}\frac{d\varphi_0^*}{2\pi}\frac{d\cos\theta_0^*}{2}\frac{d\varphi_-^*}{2\pi}\frac{d\cos\theta_-^*}{2}.$$

The upper and lower limits for energies are

$$\omega_{\max} = \frac{s-9m_\pi^2}{2\sqrt{s}}, \quad E^*_{0\max} = \frac{\mu_1^2-3m_\pi^2}{2\mu_1},$$
$$E^*_{0\min} = m_\pi.$$

The minimal photon energy $\omega_{\min}$ is an external experimental cut. Finally, $|A_{\rm ISR}|^2$ and $|A_{\rm FSR}|^2$ can be read from the corresponding expressions (1) and (8), respectively.

According to (10), we can generate $e^+e^-\to\pi^+\pi^-\pi^0\gamma$ events in the c.m.s. frame by the following algorithm:

Generate the photon energy ω as a random number uniformly distributed from $\omega_{\min}$ to $\omega_{\max}$. Calculate for the $S_1 = (\pi^+\pi^-\pi^0)$ subsystem the energy $\bar E_1 = 2E-\omega$, invariant mass $\bar\mu_1 = \sqrt{4E(E-\omega)}$, and the Lorentz factor $\bar\gamma_1 = \bar E_1/\bar\mu_1$.

Generate a random number $\bar\varphi_1$ uniformly distributed in the interval $[0,2\pi]$ and take it as the azimuthal angle of the S_1-subsystem velocity vector in the c.m.s. frame. Generate another uniform random number in the interval $[-\cos\theta_{\min},\cos\theta_{\min}]$ and take it as $\cos\bar\theta_1$, $\bar\theta_1$ being the polar angle of the S_1-subsystem velocity vector in the c.m.s. frame. This defines the unit vector $\mathbf{n}_1 = (\sin\bar\theta_1\cos\bar\varphi_1, \sin\bar\theta_1\sin\bar\varphi_1,\cos\bar\theta_1)$ along the S_1-subsystem velocity; $\theta_{\min}$ is the minimal photon radiation angle—an external experimental cut.

Construct the photon momentum in the c.m.s. frame $\mathbf{k} = -\omega\mathbf{n}_1$.

Generate the π^0-meson energy E_0^* in the S_1 rest frame as a random number uniformly distributed from $E^*_{0\min}$ to $E^*_{0\max}$. Calculate for the $S_2 = (\pi^+,\pi^-)$ subsystem the energy $\bar E_2 = \bar\mu_1 - E_0^*$, invariant mass $\bar\mu_2 = \sqrt{\bar\mu_1^2+m_\pi^2-2\bar\mu_1 E_0^*}$, and the Lorentz factor $\bar\gamma_2 = \bar E_2/\bar\mu_2$.

Generate a random number $\bar\varphi_2$ uniformly distributed in the interval $[0,2\pi]$ and take it as the azimuthal angle of the S_2-subsystem velocity vector in the S_1 rest frame. Generate another uniform random number in the interval $[-1,1]$ and take it as $\cos\bar\theta_2$, $\bar\theta_2$ being the polar angle of the S_2-subsystem velocity vector in the S_1 rest frame. This defines the unit vector along the S_2-subsystem velocity in the S_1 rest frame $\mathbf{n}_2 = (\sin\bar\theta_2\cos\bar\varphi_2, \sin\bar\theta_2\sin\bar\varphi_2,\cos\bar\theta_2)$.

Construct $\mathbf{q}_0^* = -\sqrt{E_0^{*2}-m_\pi^2}\,\mathbf{n}_2$—the π^0-meson momentum in the S_1 rest frame.

Generate φ_-^* and $\cos\theta_-^*$ in the manner analogous to what was described above for $\bar\varphi_2$ and $\cos\bar\theta_2$; construct the unit vector along the π^--meson velocity in

the S_2 rest frame $\mathbf{n}_3 = (\sin\theta^*_- \cos\varphi^*_-, \sin\theta^*_- \sin\varphi^*_-, \cos\theta^*_-)$.

Construct the π^--meson 4-momentum in the S_2 rest frame $E^*_- = \bar{\mu}_2/2$, $\mathbf{q}^*_- = \sqrt{E^{*2}_- - m^2_\pi}\mathbf{n}_3$.

Construct the π^+-meson 4-momentum in the S_2 rest frame $E^*_+ = \bar{\mu}_2/2$, $\mathbf{q}^*_+ = -\mathbf{q}^*_-$.

Transform π^0-meson 4-momentum from the S_1 rest frame back to the c.m.s. frame.

Transform π^-- and π^+-mesons' 4-momenta firstly from the S_2 rest frame to the S_1 rest frame and then back to the c.m.s. frame.

For the generated 4-momenta of the final-state particles, calculate $z = |A|^2 f$.

Generate a random number z_R uniformly distributed in the interval from 0 to $z_{\max}$, where $z_{\max}$ is some number majoring $|A|^2 f$ for all final-state 4-momenta allowed by 4-momentum conservation.

If $z \geq z_R$, accept the event, that is, the generated 4-momenta of the π^+, π^-, and π^0 mesons and the photon. Otherwise, repeat the whole procedure.

5. SOFT- AND COLLINEAR-PHOTON CORRECTIONS

We assume that the photon in the $e^+e^- \to 3\pi\gamma$ reaction is hard enough, $\omega > \omega_{\min}$, and radiated at large angle $\theta > \theta_{\min}$ so that it could be detected by experimental equipment (a detector). In any process with accelerated charged particles, soft photons are emitted without being detected because a detector has finite energy resolution. Even moderately hard photons can escape detection in some circumstances. How important are such effects? Naively, every photon emitted brings an extra factor α to the amplitude and so a small correction is expected. But this argument (as well as perturbation theory) breaks down for soft photons. When an electron (positron) emits a soft enough photon, it remains nearly on the mass shell, thus bringing a very large propagator to the amplitude. Formal application of perturbation theory gives an infinite answer to the correction due to soft-photon emission because of this pole singularity. It is well known [14] how to deal with this infrared divergence. In real experiments, very low energy photons never have enough time and space to be formed, because of the finite size of the laboratory. Thus, we have a natural low-energy cutoff. A remarkable fact, however, is that the observable cross sections do not depend on the actual form of the cutoff because singularities due to real and virtual soft photons cancel each other [15]. The net effect is that the soft photon corrections, summed to all orders of perturbation theory, factor out as some calculable, so-called Yennie–Frautschi–Suura, exponent [14].

Collinear radiation of (not necessarily soft) photons by highly relativistic initial electrons (positrons) is another source of big corrections that should also be treated nonperturbatively. Unlike soft photons, however, the matrix element for radiation of an arbitrary number of collinear photons is unknown. Nevertheless, there is a nice method (the so-called structure functions method) [16] that enables one to sum leading collinear (and soft) logarithms. The corrected cross section, when radiation of unnoticed photons with total energy less than $\Delta E \ll E$ is allowed, looks like [16]

$$\tilde{\sigma}(s) = \int_0^{\Delta E} \frac{d\omega}{\omega}\sigma(4E(E-\omega)) \qquad (13)$$
$$\times\, \beta\left(\frac{\omega}{E}\right)^\beta \left[1 + \frac{3}{4}\beta + \frac{\alpha}{\pi}\left(\frac{\pi^2}{3} - \frac{1}{2}\right)\right],$$

where $\beta = \dfrac{2\alpha}{\pi}\left(\ln(s/m_e^2) - 1\right)$ and we have omitted some higher order terms.

In our case, the hard photon is well separated (because of $\omega > \omega_{\min}, \theta > \theta_{\min}$ cuts) from the soft and collinear regions of the phase space. Thus, Eq. (13) is applicable and it indicates that the soft and collinear corrections to the cross section of the process $e^+e^- \to 3\pi\gamma$ do not exceed 20% when $\Delta E \sim \omega_{\min} = 30$ MeV, $\theta_{\min} = 20^\circ$, and $E = 0.7$ GeV. Such corrections are irrelevant for the present VEPP-2M statistics but may become important in future high-statistics experiments.

6. NUMERICAL RESULTS AND CONCLUSIONS

In Fig. 4, numerical results are shown for $\sigma(e^+e^- \to 3\pi\gamma)$ with $\omega_{\min} = 30$ MeV, $\theta_{\min} = 20^\circ$. As expected, the cross section is small, only few picobarns, for energies 0.65–0.7 GeV.

This figure shows also that FSR contributes significantly at such low energies. Thus, if future ϕ-factory experiments produce high enough statistics in this energy region, the study of FSR will become realistic. FSR and ISR give different energy and angular distributions for the photon as illustrated by Figs. 5 and 6. This fact can be used for the FSR separation from somewhat more intensive ISR.

Let us note, however, that the model considered here is not valid in the ϕ-meson region—very far from the threshold. At that, the status of uncertainties in the ISR and FSR contributions is different. We believe that the ISR amplitude remains accurate enough even in the ϕ-meson region. This belief stems from the fact that all relevant vector-meson effects are already included in the ISR amplitude (3). The

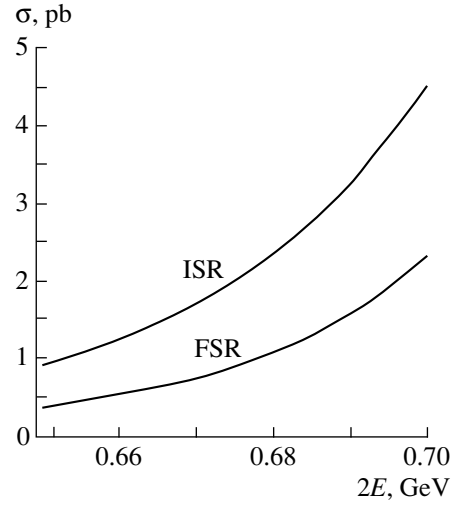

Fig. 4. ISR and FSR contributions to the $e^+e^- \to 3\pi\gamma$ cross section.

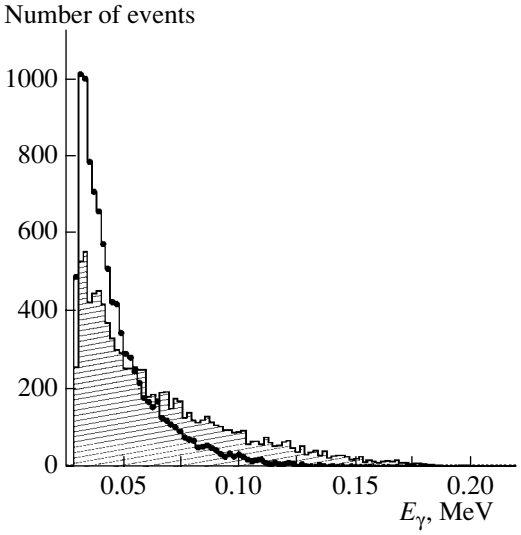

Fig. 5. The photon energy distributions for ISR and FSR (hatched histogram).

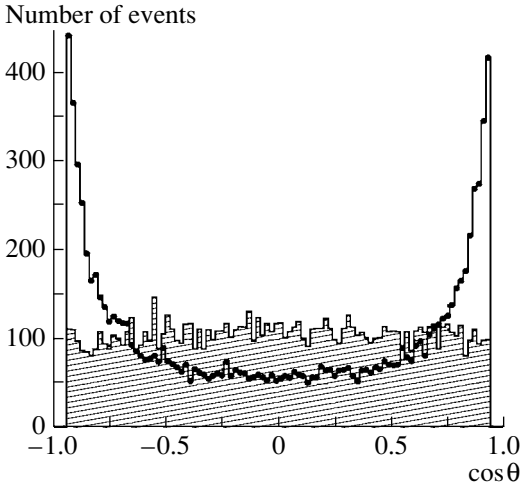

Fig. 6. The photon angular distributions for ISR and FSR (hatched histogram).

situation with the FSR amplitude is different. Our phenomenological Breit–Wigner factor mimics only some part of the vector-meson effects. To estimate the corresponding uncertainty in $\sigma_{\rm FSR}$, let us try some other choices for $K_{\rm BW}$ which also have the correct low-energy limit. If in the expression for the $K_{\rm BW}$ factor we make the change

$$R_\omega(4E^2) \to \frac{1}{2}\left[R_\omega(4E^2) + R_\rho(4E^2)\right],$$

$\sigma_{\rm FSR}$ will be lowered by $\sim 5\%$ for $2E = 0.65$ GeV and by $\sim 25\%$ for $2E = 0.7$ GeV. In the FSR amplitude, the ρ meson contributes via a number of various diagrams. For example, the $\gamma^* \to \rho \to \rho^+\rho^- \to \pi^+\pi^-\pi^0\gamma$ intermediate state, which has no counterpart in the ω-meson contribution, gives the following piece of the $T_{\mu\nu}$ tensor:

$$T^{(3\rho)}_{\mu\nu} = -\frac{\alpha_K}{2} R_\rho(4E^2)\left\{A_{1\mu\nu} - 2A_{2\mu\nu} - 2A_{3\mu\nu}\right\},$$

where

$$A_{1\mu\nu} = \epsilon_{\nu\alpha\beta\lambda}(Q - 2q_0)^\alpha \times k^\beta[(q_+ + q_0 - q_- - k)_\mu q_-^\lambda Y_- + (q_- + q_0 - q_+ - k)_\mu q_+^\lambda Y_+],$$

$$A_{2\mu\nu} = \epsilon_{\nu\alpha\beta\lambda}Q^\alpha k^\beta[(q_+ - q_0)_\mu q_-^\lambda Y_- + (q_- - q_0)_\mu q_+^\lambda Y_+],$$

$$A_{3\mu\nu} = \epsilon_{\mu\nu\beta\lambda}k^\beta[Q\cdot(q_+ - q_0)q_-^\lambda Y_- + Q\cdot(q_- - q_0)q_+^\lambda Y_+],$$

$$Y_\pm = \frac{M_\rho^2}{[(q_\mp + k)^2 - M_\rho^2][(q_\mp + q_0)^2 - M_\rho^2]}.$$

If we include this contribution and, in addition, ensure that the remaining part of the FSR amplitude (6) also takes

$$K_{\rm BW} = |R_\rho(4E^2)|^2$$

in the role of the phenomenological Breit–Wigner factor, the FSR cross section will be lowered by $\sim 10\%$ for $2E = 0.65$ GeV and by $\sim 35\%$ for $2E = 0.7$ GeV.

This uncertainty in the FSR magnitude is irrelevant for the present VEPP-2M statistics. For future high-precision experiments, a systematic inclusion of all relevant vector-meson effects in the FSR amplitude is desired.

ACKNOWLEDGMENTS

One of us (E.A.K.) is grateful to the Heisenberg–Landau Fund 2003-02 and to the Russian Foundation for Basic Research, project no. 99-02-17730.

We are grateful to G. Sandukovskaya for the help.

REFERENCES

1. H. N. Brown *et al.* (Muon g-2 Collab.), Phys. Rev. Lett. **86**, 2227 (2001).
2. For review see, for example, A. Czarnecki and W. J. Marciano, Phys. Rev. D **64**, 013014 (2001).
3. K. Melnikov, Int. J. Mod. Phys. A **16**, 4591 (2001); J. F. De Troconiz and F. J. Yndurain, hep-ph/0106025; M. Knecht and A. Nyffeler, hep-ph/0111058.
4. M. N. Achasov *et al.*, hep-ex/0010077; R. R. Akhmetshin *et al.* (CMD-2 Collab.), Nucl. Phys. A **675**, 424C (2000).
5. R. R. Akhmetshin *et al.* (CMD-2 Collab.), hep-ex/9904027.
6. R. R. Akhmetshin *et al.* (CMD-2 Collab.), Phys. Lett. B **476**, 33 (2000).
7. A. Aloisio *et al.* (KLOE Collab.), hep-ex/0107023.
8. G. Bonneau and F. Martin, Nucl. Phys. B **27**, 381 (1971).
9. E. A. Kuraev and Z. K. Silagadze, Yad. Fiz. **58**, 1687 (1995) [Phys. At. Nucl. **58**, 1589 (1995)].
10. E. Witten, Nucl. Phys. B **223**, 422 (1983); J. Wess and B. Zumino, Phys. Lett. B **37B**, 95 (1971).
11. J. W. Bos, Y. C. Lin, and H. H. Shih, Phys. Lett. B **337**, 152 (1994).
12. P. Talavera, L. Ametller, J. Bijnens, *et al.*, Phys. Lett. B **376**, 186 (1996); L. Ametller, J. Kambor, M. Knecht, and P. Talavera, Phys. Rev. D **60**, 094003 (1999).
13. E. Byckling and K. Kajantie, *Particle Kinematics* (Wiley, New York, 1973).
14. D. R. Yennie, S. C. Frautschi, and H. Suura, Ann. Phys. (N.Y.) **13**, 379 (1961).
15. F. Bloch and A. Nordsieck, Phys. Rev. **52**, 54 (1937); D. R. Yennie, in *Lectures on Strong and Electromagnetic Interactions* (Brandies Summer Institute in Theoretical Physics, Waltman, Mass., 1963), p. 166.
16. E. A. Kuraev and V. S. Fadin, Yad. Fiz. **41**, 733 (1985) [Sov. J. Nucl. Phys. **41**, 466 (1985)]; for review see M. Skrzypek, Acta Phys. Pol. B **23**, 135 (1992).

Physics of Atomic Nuclei, Vol. 67, No. 5, 2004, pp. 993–1002. Translated from Yadernaya Fizika, Vol. 67, No. 5, 2004, pp. 1014–1024.

ELEMENTARY PARTICLES AND FIELDS
Theory

Neutrinos in Electromagnetic Fields and Moving Media

A. I. Studenikin*

Moscow State University, Vorob'evy gory, Moscow, 119899 Russia

Received March 26, 2003; in final form, August 12, 2003

Abstract—The history of the development of the theory of neutrino-flavor and neutrino-spin oscillations in electromagnetic fields and in a medium is briefly surveyed. A new Lorentz-invariant approach to describing neutrino oscillations in a medium is formulated in such a way that it makes it possible to consider the motion of a medium at an arbitrary velocity, including relativistic ones. This approach permits studying neutrino-spin oscillations under the effect of an arbitrary external electromagnetic field. In particular, it is predicted that, in the field of an electromagnetic wave, new resonances may exist in neutrino oscillations. In the case of spin oscillations in various electromagnetic fields, the concept of a critical magnetic-field-component strength is introduced above which the oscillations become sizable. In considering neutrino oscillations in moving matter, it is shown within the Lorentz-invariant formalism that the relativistic motion of matter significantly affects the character of neutrino oscillations and can radically change the conditions under which the oscillations are resonantly enhanced. Possible new effects in neutrino oscillations are discussed for the case of neutrino propagation in relativistic fluxes of matter. © *2004 MAIK "Nauka/Interperiodica".*

1. DEVELOPMENT OF THEORY OF NEUTRINO OSCILLATIONS

The neutrino presents one of the most important problems in contemporary elementary-particle physics, because it possesses unique properties (having zero charge and, in all probability, a low mass, the neutrino interacts with other elementary particles very weakly) and plays a key role in the structure of weak-interaction models. So far, the experimental properties of this particle have been studied insufficiently because of difficulties in detecting neutrinos. In particular, it should be recalled that, despite considerable advances made in this field over the past few years, the range of problems that have yet to be solved is not exhausted by the problem of the neutrino mass. These include the presence of mixing and oscillations of various neutrino flavors, the possibility of a nonzero magnetic moment, and the role of neutrinos in astrophysics and cosmology (relic neutrinos, the contribution of neutrinos to dark matter in the Universe, neutrinos from supernovae and in gamma splashes, the neutrino flux from the Sun, atmospheric neutrinos, etc.). It is worth noting that a definitive answer to these open questions would make it possible to pave the way toward a further generalization of the theory of particle interactions.

Many of the aforementioned problems could be solved upon definitively proving the existence of neutrino mixing and neutrino oscillations. We would like to recall basic steps in the development of the theory of neutrino oscillations. The fundamental idea of the possibility of neutrino oscillations was put forth by Pontecorvo [1], who considered the mixing of electron-neutrino and electron-antineutrino states and transitions between them in a vacuum. Immediately after the discovery of muon neutrinos, the idea of neutrino oscillations was further developed in the studies of Sakata and his colleagues [2], who analyzed oscillations between different flavor states of the neutrino in a vacuum. In more recent studies performed by Pontecorvo, together with Gribov [3] and Bilenky [4], the idea of oscillations was reinforced by calculations of the time evolution of a neutrino beam; as a matter of fact, a formalism was developed there that is presently used in analyzing data on neutrino oscillations from numerous experiments.

A further development of the theory of neutrino oscillations is associated with the study of Wolfenstein [5], who considered the effect that neutrino interaction with matter through which neutrinos propagate exerts on neutrino oscillations. The most important result was obtained by Mikheev and Smirnov [6], who predicted the possibility of a resonance enhancement of neutrino oscillations as neutrinos propagate in matter of variable density. This phenomenon, which is referred to as the Mikheev–Smirnov–Wolfenstein effect, is presently used as a basis for providing the most probable explanation of the deficit of the solar-neutrino flux.

The next significant step in the development of the theory of neutrino oscillations was made by Voloshin,

*e-mail: studenik@srd.sinp.msu.ru

Vysotskiĭ, and Okun' [7], who investigated neutrino-spin oscillations in a transverse magnetic field (see also [8–10]) and, on this basis, analyzed the problem of solar neutrinos. Lim and Marciano [11] and, independently, Akhmedov [12] indicated that spin–flavor neutrino oscillations in matter can be resonantly enhanced (analog of the Mikheev–Smirnov–Wolfenstein effect for the case of flavor oscillations).

Below, we discuss a further development of the theory of spin and flavor neutrino oscillations for the case where neutrinos propagate in various electromagnetic fields and in media moving at arbitrary speeds, employing the results obtained at the Department of Theoretical Physics at Moscow State University over the past eight years.

2. NEUTRINO OSCILLATIONS IN A TRANSVERSE ELECTROMAGNETIC FIELD

Let us consider two neutrino flavors (for example, ν_e and ν_μ). These are superpositions of two mass eigenstates ν_1 and ν_2; that is,

$$\nu_e = \nu_1 \cos\theta + \nu_2 \sin\theta, \qquad (1)$$
$$\nu_e\mu = -\nu_1 \sin\theta + \nu_2 \cos\theta,$$

where θ is the vacuum neutrino-mixing angle. The change in the flavor composition of a neutrino beam propagating through matter consisting of electrons, protons, and neutrons and in the presence of a rotating magnetic field that is transverse with respect to the direction of neutrino motion, $\mathbf{B} = \mathbf{B}_\perp e^{i\phi(t)}$ (the angle $\phi(t)$ specifies the direction of the field in the plane orthogonal to the neutrino momentum), is described by an equation of the Schrödinger type; that is,

$$i\frac{d}{dt}\nu(t) = H\nu(t), \qquad (2)$$

where the Hamiltonian H involves four terms,

$$H = H_V + H_{\text{int}} + H_F + H_{\dot\phi}. \qquad (3)$$

Here, H_V describes vacuum oscillations, H_{int} describes the effect of neutrino–matter interactions on oscillations, the contribution H_F is responsible for spin oscillations in the transverse magnetic field, and the last term $H_{\dot\phi}$ takes into account the effect of magnetic-field rotation.

Let us consider the case of two Dirac neutrinos and introduce the basis $\nu = (\nu_{e_L}, \nu_{\mu_L}, \nu_{e_R}, \nu_{\mu_R})$. The corresponding Hamiltonian then has the form (see [13–15])

$$H^D = \begin{pmatrix} V^-_{\nu_e} & \dfrac{\Delta m^2_\nu}{4E_\nu}s & \mu_{ee}B & \mu_{e\mu}B \\ \dfrac{\Delta m^2_\nu}{4E_\nu}s & V^-_{\nu_\mu} & \mu_{\mu e}B & \mu_{\mu\mu}B \\ \mu_{ee}B & \mu_{\mu e}B & -\dfrac{\Delta m^2_\nu}{4E_\nu} + \dfrac{\dot\phi}{2} & 0 \\ \mu_{e\mu}B & \mu_{\mu\mu}B & 0 & \dfrac{\Delta m^2_\nu}{4E_\nu} + \dfrac{\dot\phi}{2} \end{pmatrix}, \qquad (4)$$

where

$$V^-_{\nu_e} = -\frac{\Delta m^2_\nu}{4E_\nu}c + V^0_{\nu_e} - \frac{\dot\phi}{2}, \qquad (5)$$
$$V^-_{\nu_\mu} = \frac{\Delta m^2_\nu}{4E_\nu}c + V^0_{\nu\mu} - \frac{\dot\phi}{2}.$$

The above Hamiltonian was derived on the basis of the Standard Model Lagrangian that additionally involves an $SU(2)$-singlet right-handed neutrino and which takes into account neutrino interaction with a magnetic field via the flavor-diagonal magnetic moments μ_{ee} and $\mu_{\mu\mu}$. Also, we assume that there can exist flavor-nonconserving electromagnetic neutrino interactions via the off-diagonal transition magnetic moments $\mu_{e\mu}$ and $\mu_{\mu e}$. The Hamiltonian in (4) corresponds to the case of the sterile and nonmixed neutrinos ν_{e_R} and ν_{μ_R}. In the case of two Majorana neutrinos, the analogous expression for the Hamiltonian in the corresponding basis $\nu = (\nu_e, \nu_\mu, \bar\nu_e, \bar\nu_\mu)$ can be found, for example, in [13].

We assume that a primary neutrino beam consists of left-handed electron neutrinos ν_{e_L} exclusively. By using the Hamiltonian in (4), we can then consider various types of neutrino transitions, $\nu_i \to \nu_j$, and the corresponding neutrino oscillations $\nu_i \leftrightarrow \nu_j$ caused by the effect of a magnetic field in the presence of a medium:

$$\nu_{e_L} \to \nu_{e_R}, \quad \nu_{e_L} \to \nu_{\mu_R}. \qquad (6)$$

The probability of finding a neutrino of the ν_j type at a distance x from the source of ν_i neutrinos is given by the general formula (see, for example, [16])

$$P(\nu_i \to \nu_j) = \sin^2(2\theta_{\text{eff}}) \sin^2 \frac{\pi x}{L_{\text{eff}}}, \quad i \neq j. \qquad (7)$$

At the same time, the probability that a neutrino preserves its initial flavor has the form

$$P(\nu_i \to \nu_i) = 1 - P(\nu_i \to \nu_j). \qquad (8)$$

From the form of the Hamiltonian in (4), it follows that the effective mixing angle θ_{eff} and the effective oscillation length L_{eff} are determined by the relations

$$\sin^2(2\theta_{\text{eff}}) = (2\tilde\mu B)^2 \Big/ \Big[\Big(\frac{\Delta m^2_\nu}{2E}A \qquad (9)$$

$$- \sqrt{2}G_{\rm F}n_{\rm eff} + \dot{\phi})^2 + (2\tilde{\mu}B\Big)^2\Big],$$

$$L_{\rm eff} = 2\pi \times \Big[\Big(\frac{\Delta m_\nu^2}{2E}A - \sqrt{2}G_{\rm F}n_{\rm eff} + \dot{\phi}\Big)^2 + (2\tilde{\mu}B)^2\Big]^{-1/2}. \quad (10)$$

We note that the effective mixing angle $\theta_{\rm eff}$ and the effective oscillation length $L_{\rm eff}$ depend on the character of magnetic-field rotation (it is specified by the quantity $\dot{\phi}$) along the direction of the neutrino trajectory (see also [17]). For the various neutrino-conversion processes (6), the quantities $\tilde{\mu}$, A, and $n_{\rm eff}$ are given by

$$\tilde{\mu} = \begin{cases} \mu, & \nu_{e_L} \to \nu_{e_R}, \\ \mu_{e\mu}, & \nu_{e_L} \to \nu_{\mu_R}, \end{cases} \quad (11)$$

$$A = \begin{cases} \dfrac{1}{2}(\cos 2\theta - 1), & \nu_{e_L} \to \nu_{e_R}, \\ \dfrac{1}{2}(\cos 2\theta + 1), & \nu_{e_L} \to \nu_{\mu_R}, \end{cases} \quad (12)$$

$$n_{\rm eff} = n_e - \frac{1}{2}n_n, \quad \nu_{e_L} \to \nu_{e_R,\mu_R}, \quad (13)$$

where μ is the electron-neutrino magnetic moment and $\mu_{e\mu}$ is the so-called transition moment.

We can now formulate a criterion that, on the basis of preset features of neutrinos, matter, and the magnetic field, makes it possible to find out whether the corresponding neutrino oscillations are significant. The probability in (7) can become a value on the order of unity if the following two conditions hold simultaneously.

(i) The amplitude of the oscillations $\sin^2(2\theta_{\rm eff})$ must be "far" from zero [or, at least, $\sin^2(2\theta_{\rm eff}) \geq 1/2$].

(ii) The neutrino-path length x in a medium must be longer than half the effective length of oscillations, $L_{\rm eff}$—that is, $x \geq L_{\rm eff}/2$.

In accordance with the above criterion, at least one of the following relations must hold:

$$\frac{\Delta m_\nu^2}{2E}A - \sqrt{2}G_{\rm F}n_{\rm eff} + \dot{\phi} = 0 \quad (\tilde{\mu}B \neq 0), \quad (14)$$

$$2\tilde{\mu}B \geq \left|\frac{\Delta m_\nu^2}{2E}A - \sqrt{2}G_{\rm F}n_{\rm eff} + \dot{\phi}\right|. \quad (15)$$

If the condition in (14) is valid, there occurs a resonance enhancement of neutrino-spin oscillations [11, 12] that is similar to the Mikheev–Smirnov–Wolfenstein effect in the case of flavor oscillations. If the "more lenient" condition (15) is valid, the enhancement of oscillations may occur in a nonresonance way. If we consider the condition in (15) and assume that a strict equality holds in it, we can obtain the critical magnetic-induction value [18]

$$B_{\rm cr} = \left|\frac{1}{2\tilde{\mu}}\Big(\frac{\Delta m_\nu^2 A}{2E} - \sqrt{2}G_{\rm F}n_{\rm eff} + \dot{\phi}\Big)\right|, \quad (16)$$

which determines the region of magnetic-induction values ($B \geq B_{\rm cr}$) at which the probability amplitude in (7) is not small—that is, $\sin^2(2\theta_{\rm eff}) \geq 1/2$. In deriving numerical estimates, it is convenient to take the critical field in a different form,

$$B_{\rm cr} \approx 43\frac{\mu_0}{\tilde{\mu}} \times \left|A\frac{\Delta m_\nu^2}{1\ {\rm eV}^2}\frac{\rm MeV}{E_\nu} - 2.5 \times 10^{-31}\frac{n_{\rm eff}}{1\ {\rm cm}^{-3}} + 2.5\frac{1\ {\rm m}}{L_{\dot{\phi}}}\right|, \quad (17)$$

where μ_0 is the Bohr magneton.

The use of the criterion specified by conditions (i) and (ii) in analyzing neutrino oscillations in the convective zone of the Sun, in the explosion of a supernova, in neutron stars, and in other astrophysical media makes it possible to obtain [13] constraints on the neutrino magnetic moment and on the magnetic-field induction (see also [7, 17, 19] and references therein). As a characteristic example of how this criterion operates, we will consider $\nu_{e_L} \leftrightarrow \nu_{e_R}$ neutrino oscillations in the magnetic field of a neutron star and assume that this process does not make a significant contribution to the evolution of the star at the given characteristics of the neutrino and the given magnetic field. For this formulation of the problem, the above criterion makes it possible to obtain information about the neutrino magnetic moment μ_ν and (or) about the induction B of the magnetic field and the dimensions of the region where it exists.

Let us consider a neutrino having a magnetic moment of $\mu_\nu \sim 10^{-18}\mu_0$ and assume that condition (i) of the criterion holds [see also formula (9)]—that is, a strong magnetic field, $B \geq B_{\rm cr}$, exists over a region of characteristic size, say, $R \approx 1$ km. It follows that, for $\nu_{e_L} \leftrightarrow \nu_{e_R}$ oscillations to be immaterial, it is necessary that condition (ii) of the criterion be violated: $x < L_{\rm eff}/2$. In other words, the characteristic range of neutrinos over the region where the strong magnetic field is operative must be shorter than half the effective length of the oscillations. Since the relation $L_{\rm eff} \approx L_B = \pi/(\mu_\nu B)$ holds in a strong magnetic field, we arrive at the conclusion that, at a length scale of $\max\{x\} = R \approx 1$ km, the magnetic field of this object must satisfy the inequality $B \leq 5 \times 10^{15}$ G.

We will now discuss the constraint that can be obtained for the neutrino magnetic moment from the requirement that $\nu_{e_L} \leftrightarrow \nu_{e_R}$ oscillations be immaterial. Suppose that, at a characteristic length scale of

$R \approx 1$ km, the magnetic-field induction is $B \approx 5 \times 10^{12}$ G [we note that this value corresponds to the critical magnetic-field induction $B_{\rm cr}$ (16) at characteristic values of the matter density of a neutron star]. It follows that, for condition (ii) of the criterion to be satisfied in just the same way as in the above case, the effective oscillation length $L_{\rm eff} \approx \pi/(\mu_\nu B)$ must be much longer than the scale of $R \approx 1$ km. Therefore, the type of neutrino oscillations that is being discussed here will not be noticeable in the presence of a magnetic field whose induction is $B \approx 5 \times 10^{12}$ G over a scale of $R \approx 1$ km, provided that the neutrino magnetic moment is constrained by a value of $\mu_\nu \sim 10^{-15}\mu_0$.

3. NEUTRINO OSCILLATIONS IN AN ARBITRARY ELECTROMAGNETIC FIELD

In studying the regularities of neutrino oscillations in strong magnetic fields, we found, approximately six years ago, that neutrino oscillations in external fields had ever been considered in the literature only for a constant magnetic field $\mathbf{B}_\perp$ transverse with respect to the direction of neutrino motion. This is because, usually, the effect of the longitudinal component of the magnetic field, $\mathbf{B}_{0\|}$, was not taken into account since, in the particle rest frame, this magnetic-field component is suppressed with respect to the transverse component in the same reference frame by the factor $\gamma = (1-\beta^2)^{-1/2}$: $\mathbf{B}_{0\perp} = \gamma\mathbf{B}_\perp$ (where β is the neutrino speed). Additionally, we note that, in all of the investigations performed to that instant for neutrino-flavor oscillations in matter, it was assumed that matter can move only at nonrelativistic speeds. It is this approximation that was used in investigating neutrino oscillations in moving media in supernova explosions [20] and on the Sun [21].

The first attempt at considering neutrino-flavor oscillations in matter moving at a relativistic velocity was undertaken in [22]. In that study, the authors tried to develop a Lorentz-invariant formalism for describing neutrino-flavor oscillations and showed that the effective neutrino potential in matter can significantly depend on the speed of matter with respect to the detector used. In the studies of our group, further investigations into neutrino oscillations within this Lorentz-invariant approach were continued only in 1999 (see [23] and references therein) by considering oscillations in an arbitrary electromagnetic field. In order to describe the evolution of the spin S_μ of a neutral particle that has a nonzero magnetic and a nonzero electric dipole moment (μ and ϵ, respectively), we choose, as a starting point, the Bargmann–Michel–Telegdi equation [24]

$$\frac{dS^\mu}{d\tau} = 2\mu\Big\{F^{\mu\nu}S_\nu - u^\mu(u_\nu F^{\nu\lambda}S_\lambda)\Big\} + 2\epsilon\Big\{\tilde{F}^{\mu\nu}S_\nu - u^\mu(u_\nu \tilde{F}^{\nu\lambda}S_\lambda)\Big\}, \quad (18)$$

which is known in QED. This equation describes the evolution of a neutral particle moving in a given electromagnetic field $F_{\mu\nu}$ at a constant velocity $\boldsymbol{\beta}(u_\mu = (\gamma, \gamma\boldsymbol{\beta}))$. The spin vector satisfies the ordinary conditions $S^2 = -1$ and $S^\mu u_\mu = 0$. Upon generalizing this equation to the case of a massive neutrino that participates in weak interactions with medium particles, we obtained an equation for the neutrino-spin 3-vector, $\mathbf{S}$; that is,

$$\frac{d\mathbf{S}}{dt} = \Big[\mathbf{S} \times \Big(\frac{2\mu}{\gamma}\mathbf{B}_0 + \frac{2\epsilon}{\gamma}\mathbf{E}_0 + \Big(V - \frac{\delta m^2 A}{2E}\Big)\mathbf{n}\Big)\Big], \quad (19)$$

where E is the neutrino energy. Although the original Eq. (18) describes the evolution of the spin of a particle having a given mass, its generalization in (19) takes into account the possibility of a change in the neutrino flavor upon the reversal of helicity, as is seen from the presence of the term that is proportional to the difference δm^2 of the squares of the neutrino masses. The time derivative on the left-hand side of (19) is calculated in the laboratory frame, while the quantities $\mathbf{B}_0$ and $\mathbf{E}_0$ are the vectors of the magnetic and electric fields in the neutrino rest frame; that is,

$$\mathbf{B}_0 = \gamma\Big(\mathbf{B}_\perp + \frac{1}{\gamma}\mathbf{B}_\| + \sqrt{1-\gamma^{-2}}\Big[\mathbf{E}_\perp \times \mathbf{n}\Big]\Big), \quad (20)$$

$$\mathbf{E}_0 = \gamma\Big(\mathbf{E}_\perp + \frac{1}{\gamma}\mathbf{E}_\| - \sqrt{1-\gamma^{-2}}\Big[\mathbf{B}_\perp \times \mathbf{n}\Big]\Big),$$

where

$$\mathbf{F}_\perp = \mathbf{F} - \mathbf{n}(\mathbf{F}\cdot\mathbf{n}), \quad \mathbf{F}_\| = \mathbf{n}(\mathbf{F}\cdot\mathbf{n}) \quad (\mathbf{F} = \mathbf{B}, \mathbf{E}) \quad (21)$$

are the transverse and longitudinal (with respect to the direction of neutrino motion) field components in the laboratory frame ($\mathbf{n} = \boldsymbol{\beta}/\beta$).

Two parameters—$A = A(\theta)$, which depends on the vacuum neutrino-mixing angle, and $V = V(n_{\rm eff})$, which depends on the difference of the effective neutrino potentials in a medium—are determined by the type of neutrino transitions. The explicit form of these parameters for specific processes of neutrino oscillations and for various compositions of matter can be found in [13, 19].

By using the equation of spin evolution, we derived an effective Hamiltonian that determines neutrino oscillations for the two-level system $\nu = (\nu_R, \nu_L)$ in the presence of electromagnetic fields that are specified by

the components $B_{\parallel,\perp}(t)$ and $E_{\parallel,\perp}(t)$ in the laboratory frame. The result is

$$H = (\boldsymbol{\sigma}\cdot\mathbf{n})\left(\frac{\delta m^2 A}{4E} - \frac{V}{2} - \frac{1}{\gamma}\Big(\mu B_\parallel + \epsilon E_\parallel\Big)\right) \tag{22}$$
$$- \mu\boldsymbol{\sigma}\cdot\Big(\mathbf{B}_\perp + \big[\mathbf{E}_\perp\times\mathbf{n}\big]\Big)$$
$$- \epsilon\boldsymbol{\sigma}\cdot\Big(\mathbf{E}_\perp - \big[\mathbf{B}_\perp\times\mathbf{n}\big]\Big).$$

Here, we neglected effects of order $1/\gamma^2$ and of higher orders. The above Hamiltonian takes into account the direct interaction of neutrinos with an electromagnetic field. We note that an indirect effect of an electromagnetic field on neutrinos (that which was considered, for example, in [25]) through polarization of matter by the longitudinal component of the field is taken into account in the neutrino potential V in matter.

The Hamiltonian in question now makes it possible to consider neutrino-spin precession in arbitrary preset configurations of electromagnetic fields, including those that involve strong longitudinal components. Below, we discuss a few specific examples and obtain the corresponding resonance conditions for neutrino oscillations.

In order to demonstrate the possibility of analyzing neutrino oscillations in new configurations of electromagnetic fields, we consider, by way of example, neutrino-spin oscillations $\nu_L \leftrightarrow \nu_R$ arising in matter under the effect of a superposition of the field of a plane electromagnetic wave and a longitudinal magnetic field. We introduce the unit vector $\mathbf{e}_3$ parallel to the neutrino-velocity vector $\boldsymbol{\beta}$. We denote by ϕ the angle between the vector $\mathbf{e}_3$ and the direction of electromagnetic-wave propagation. For the sake of simplicity, we further disregard effects associated with the electric moment ϵ of the neutrino. In this case, the effective-magnetic-field induction in the neutrino rest frame has the form

$$\mathbf{B}_0 = \gamma\Big[B_1(\cos\phi - \beta)\mathbf{e}_1 \tag{23}$$
$$+ B_2(1-\beta\cos\phi)\mathbf{e}_2 - \frac{1}{\gamma}B_1\sin\phi\mathbf{e}_3\Big],$$

where the vectors $\mathbf{e}_1$, $\mathbf{e}_2$, and $\mathbf{e}_3$ form a triplet of unit mutually orthogonal vectors. In the case of an electromagnetic wave having a circular polarization and propagating in matter, one can easily obtain

$$B_1 = B\cos\psi, \quad B_2 = B\sin\psi, \tag{24}$$

where B is the magnetic-field amplitude in the laboratory frame and the phase of the wave at the point of neutrino location at a fixed instant of time t is given by

$$\psi = g\omega t\Big(1 - \frac{\beta}{\beta_0}\cos\phi\Big), \tag{25}$$

with ω being the electromagnetic-wave frequency. This phase depends on the velocity of the wave in matter, β_0 ($\beta_0 \le 1$). The values of $g = \pm 1$ correspond to the two possible types of circular polarization of the electromagnetic wave.

In the adiabatic approximation, the probability of the transition $\nu_L \to \nu_R$ has the form

$$P_{\nu_L\to\nu_R}(x) = \sin^2(2\theta_{\text{eff}})\sin^2\frac{\pi x}{L_{\text{eff}}}, \tag{26}$$

$$\sin^2(2\theta_{\text{eff}}) = \frac{E_{\text{eff}}^2}{E_{\text{eff}}^2 + \Delta_{\text{eff}}^2}, \tag{27}$$
$$L_{\text{eff}} = \frac{2\pi}{\sqrt{E_{\text{eff}}^2 + \Delta_{\text{eff}}^2}},$$

where

$$E_{\text{eff}} = 2\mu B(1 - \beta\cos\phi) \tag{28}$$

[here, $O(\gamma^{-1})$ terms are omitted] and

$$\Delta_{\text{eff}} = V - \frac{\delta m^2 A}{2E} - g\omega\Big(1 - \frac{\beta}{\beta_0}\cos\phi\Big) + 2\frac{\mu B_\parallel}{\gamma}. \tag{29}$$

From the above formulas, one can obtain the condition for the resonance enhancement of neutrino oscillations; that is,

$$V - \frac{\delta m^2 A}{2E} - g\omega\Big(1 - \frac{\beta}{\beta_0}\cos\phi\Big) + 2\frac{\mu B_\parallel}{\gamma} = 0. \tag{30}$$

Thus, we predict the existence of a new type of resonances in $\nu_L \leftrightarrow \nu_R$ neutrino oscillations arising under the effect of a superposition of the field of an electromagnetic wave and a longitudinal magnetic field. If, in the above consideration, one discards the longitudinal magnetic field, there immediately arise the probability of neutrino oscillations in the field of a circularly polarized wave and the corresponding resonance condition for this case. We note that the case of a linearly polarized wave was considered in [26].

If the resonance condition (30) does not hold, we can, in the same way as in the case of neutrino oscillations in a transverse magnetic field, formulate a criterion that oscillations in the combined electromagnetic field being considered are significant. In particular, this means that, on the basis of the expression for the probability of oscillations in the field of an electromagnetic wave and in a longitudinal magnetic field [see Eqs. (26)–(29)], we can introduce, for the

magnetic field of an electromagnetic wave, the critical strength,

$$\tilde{B}_{\rm cr} = \frac{1}{2\mu(1-\beta\cos\phi)} \times \left| V - \frac{\delta m^2 A}{2E} - g\omega\Big(1 - \frac{\beta}{\beta_0}\cos\phi\Big) + 2\frac{\mu B_\parallel}{\gamma}\right|, \quad (31)$$

above which the corresponding oscillations will be sizable, provided that neutrinos are subjected to the effect of this field for quite a long time.

In conclusion, we would like to emphasize the circumstance that, with the aid of the formalism developed in this section for describing neutrino-spin oscillations in arbitrary electromagnetic fields, one can consider neutrino-flavor oscillations in matter in the presence of an arbitrary electromagnetic field.

4. NEUTRINO-SPIN OSCILLATIONS IN MOVING MATTER

Within the approach to neutrino-spin oscillations that was proposed above, attention was given primarily to describing the effect of various configurations of electromagnetic fields. At the same time, we restricted ourselves to considering the simplest case of immobile and unpolarized matter in simulating the effects of a medium. We now proceed [27] to extend our Lorentz-invariant approach to neutrino-spin oscillations in an arbitrary electromagnetic field to the general case, that where matter through which neutrinos propagate can move at an arbitrary speed (including a relativistic speed) and can be polarized. It should be noted that matter-polarization effects in neutrino oscillations were considered previously, for example, in [25, 28]; however, the approach used there was insufficient for obtaining correct results if matter moves at a relativistic speed. Within the approach that we present below, one can reproduce the corresponding results from [25, 28] in the case of an immobile or a slowly moving medium.

As a starting point, we will again take the Bargmann–Michel–Telegdi Eq. (18), which describes the evolution of spin in QED, and construct its generalization appropriate for describing the spin of a neutrino that participates both in electromagnetic and in weak interactions with the particles of moving and polarized matter. The Lorentz-invariant generalization of Eq. (18) can be obtained upon replacing the electromagnetic-field tensor $F_{\mu\nu} = (\mathbf{E}, \mathbf{B})$ as

$$F_{\mu\nu} \to F_{\mu\nu} + G_{\mu\nu}, \quad (32)$$

where the tensor $G_{\mu\nu}$ describes all nonelectromagnetic interactions involving neutrinos. In order to derive the explicit form of the tensor $G_{\mu\nu}$, we consider that the sought equation of neutrino-spin evolution must be linear in the neutrino spin, the electromagnetic field, and features of matter (we assume that matter consists of fermions of different types: $f = e, n, p, \ldots$) such as the fermion currents

$$j_f^\mu = (n_f, n_f\mathbf{v}_f) \quad (33)$$

and the fermion polarizations

$$\lambda_f^\mu = \left(n_f(\boldsymbol{\zeta}_f\cdot\mathbf{v}_f), n_f\boldsymbol{\zeta}_f\sqrt{1-v_f^2} + \frac{n_f\mathbf{v}_f(\boldsymbol{\zeta}_f\cdot\mathbf{v}_f)}{1+\sqrt{1-v_f^2}}\right). \quad (34)$$

Here, we have used the following notation: n_f, $\mathbf{v}_f$, and $\boldsymbol{\zeta}_f$ ($0 \le |\boldsymbol{\zeta}_f|^2 \le 1$) are, respectively, the concentration of type-f fermions, the velocity of the reference frame in which the mean momentum of f fermions is zero, and the mean value of the polarization vector of f fermions in this reference frame. The calculation of the mean value of the polarization vector $\boldsymbol{\zeta}_f$ involves the procedure of two-step averaging. First, one calculates the quantum-mechanical expectation value of the relativistic spin operator for fermion quantum states in a given electromagnetic field, whereupon one calculates the expectation value with the statistical distribution for the ensemble of type-f fermions.

In the most general case where a neutrino can interact with a medium consisting of fermions of different types f, the antisymmetric tensor $G^{\mu\nu}$ has the form

$$G^{\mu\nu} = \epsilon^{\mu\nu\rho\lambda}g_\rho^{(1)}u_\lambda - (g^{(2)\mu}u^\nu - u^\mu g^{(2)\nu}), \quad (35)$$

where

$$g^{(1)\mu} = \sum_f \rho_f^{(1)} j_f^\mu + \rho_f^{(2)}\lambda_f^\mu, \quad (36)$$
$$g^{(2)\mu} = \sum_f \xi_f^{(1)} j_f^\mu + \xi_f^{(2)}\lambda_f^\mu;$$

that is, summation is performed over the types f of fermions entering into the composition of matter. The explicit form of the coefficients $\rho_f^{(1),(2)}$ and $\xi_f^{(1),(2)}$ is fixed in specifying the model of neutrino interaction with particles of matter. In an ordinary two-component representation [where the electromagnetic-field tensor has the form $F_{\mu\nu} = (\mathbf{E}, \mathbf{B})$], the tensor $G_{\mu\nu}$ is given by

$$G_{\mu\nu} = (-\mathbf{P}, \mathbf{M}), \quad (37)$$

where

$$\mathbf{M} = \gamma\big\{(g_0^{(1)}\boldsymbol{\beta} - \mathbf{g}^{(1)}) - [\boldsymbol{\beta}\times\mathbf{g}^{(2)}]\big\}, \quad (38)$$
$$\mathbf{P} = -\gamma\big\{(g_0^{(2)}\boldsymbol{\beta} - \mathbf{g}^{(2)}) + [\boldsymbol{\beta}\times\mathbf{g}^{(1)}]\big\}.$$

The use of the two-component representation for the tensors $F_{\mu\nu}$ and $G_{\mu\nu}$ makes it possible to see from the outset that the substitution in (32) implies the corresponding shifts of the vectors $\mathbf{B}$ and $\mathbf{E}$; that is,

$$\mathbf{B} \to \mathbf{B} + \mathbf{M}, \quad \mathbf{E} \to \mathbf{E} - \mathbf{P}. \tag{39}$$

We note that these expressions are very similar in form to the relations for the vectors of the corresponding fields in electro- and magnetostatics of dielectrics.

Upon realizing the scheme outlined above, we arrive at the following equation that describes the evolution of the spin 3-vector $\mathbf{S}$ in a given electromagnetic field $F_{\mu\nu}$ and which takes into account the neutrino–matter interactions (they are specified by the tensor $G_{\mu\nu}$):

$$\frac{d\mathbf{S}}{dt} = \frac{2\mu}{\gamma}\Big[\mathbf{S} \times (\mathbf{B}_0 + \mathbf{M}_0)\Big] + \frac{2\epsilon}{\gamma}\Big[\mathbf{S} \times (\mathbf{E}_0 - \mathbf{P}_0)\Big]. \tag{40}$$

Here, the time derivative on the left-hand side is calculated in the laboratory frame and $\mathbf{B}_0$ and $\mathbf{E}_0$ are the vectors of the strengths of, respectively, the magnetic and the electric field in the neutrino rest frame. The vectors $\mathbf{M}_0$ and $\mathbf{P}_0$ take into account the effect of neutrino–matter interaction and, in the neutrino rest frame, can be expressed in terms of the quantities defined in the laboratory frame; that is,

$$\mathbf{M}_0 = \gamma\boldsymbol{\beta}\Big(g_0^{(1)} - \frac{\boldsymbol{\beta}\cdot\mathbf{g}^{(1)}}{1+\gamma^{-1}}\Big) - \mathbf{g}^{(1)}, \tag{41}$$

$$\mathbf{P}_0 = -\gamma\boldsymbol{\beta}\Big(g_0^{(2)} - \frac{\boldsymbol{\beta}\cdot\mathbf{g}^{(2)}}{1+\gamma^{-1}}\Big) + \mathbf{g}^{(2)}. \tag{42}$$

By way of example, we consider the problem of $\nu_{e_L} \leftrightarrow \nu_{e_R}$ spin oscillations in the propagation of neutrinos through moving and polarized matter consisting only of electrons (electron gas). If we assume that neutrino interactions are described by the Standard Model supplemented with an $SU(2)$-singlet right-handed neutrino ν_R, the effective Lagrangian averaged over matter electrons can be written in the form

$$L_{\text{eff}} = -f^\mu\Big(\bar\nu\gamma_\mu\frac{1+\gamma^5}{2}\nu\Big), \tag{43}$$

where

$$f^\mu = \frac{G_\text{F}}{\sqrt{2}}\Big((1+4\sin^2\theta_\text{W})j_e^\mu - \lambda_e^\mu\Big). \tag{44}$$

For the coefficients $\rho_e^{(1),(2)}$ (for the sake of simplicity, we assumed that the neutrino electric dipole moment vanishes, so that $\xi_e^{(i)} = 0$), we obtain

$$\rho_e^{(1)} = \frac{G_\text{F}}{2\mu\sqrt{2}}(1+4\sin^2\theta_\text{W}), \quad \rho_e^{(2)} = -\frac{G_\text{F}}{2\mu\sqrt{2}}. \tag{45}$$

Using formulas (36) and (41) and explicitly isolating the longitudinal (with respect to the direction of neutrino propagation) and the transverse component of the vector $\mathbf{M}_0$, we obtain

$$\mathbf{M}_0 = \mathbf{M}_{0\|} + \mathbf{M}_{0\perp}, \tag{46}$$

$$\mathbf{M}_{0\|} = \gamma\boldsymbol{\beta}\frac{n_0}{\sqrt{1-v_e^2}}\Big\{\rho^{(1)}\Big(1 - \frac{\mathbf{v}_e\cdot\boldsymbol{\beta}}{1-\gamma^{-2}}\Big) - \rho^{(2)} \tag{47}$$
$$\times\Big(\boldsymbol{\zeta}_e\cdot\boldsymbol{\beta}\sqrt{1-v_e^2} + \frac{(\boldsymbol{\zeta}_e\cdot\mathbf{v}_e)(\boldsymbol{\beta}\cdot\mathbf{v}_e)}{1+\sqrt{1-v_e^2}}\Big)\frac{1}{1-\gamma^{-2}}\Big\},$$

$$\mathbf{M}_{0\perp} = -\frac{n_0}{\sqrt{1-v_e^2}} \tag{48}$$
$$\times\Big\{\mathbf{v}_{e\perp}\Big(\rho^{(1)} + \rho^{(2)}\frac{\boldsymbol{\zeta}_e\cdot\mathbf{v}_e}{1+\sqrt{1-v_e^2}}\Big) + \boldsymbol{\zeta}_{e\perp}\rho^{(2)}\sqrt{1-v_e^2}\Big\},$$

where n_0 is the invariant electron concentration specified in the rest frame of the medium. From this expression, it follows that the effect of neutrino–matter interaction on neutrino-spin oscillations significantly depends on the neutrino velocity $\boldsymbol{\beta}$, the matter velocity $\mathbf{v}_e$, the matter polarization $\boldsymbol{\zeta}_e$, and the correlations of these three vectors. In particular, one can easily see that the effect of the medium can be annihilated owing to the relativistic motion of the matter along the direction of neutrino propagation, provided that $1 - \boldsymbol{\beta}\cdot\mathbf{v}_e \approx 0$.

5. NEUTRINO-FLAVOR OSCILLATIONS IN MOVING MATTER

Let us now proceed to consider neutrino-flavor oscillations in moving and polarized matter [29]. Within the Lorentz-invariant approach developed here, we will show that the motion of matter through which neutrinos propagate can lead to a significant change in the probability and other features (effective mixing angle and oscillation length) of neutrino-flavor oscillations in the case where matter moves at a relativistic velocity. For the sake of simplicity, we will again consider oscillations between two flavor states—for example, $\nu_e \leftrightarrow \nu_\mu$—and assume that matter consists of fermions of only one type (suppose that these are electrons: $f = e$) that can move as a discrete unit at a relativistic velocity. The possibility of a generalization to other types of flavor oscillations and to another composition of matter is obvious.

The matter effect on neutrino-flavor oscillations arises as the result of forward elastic scattering on the particles of the ambient medium. In our case, the

difference $\Delta V = V_e - V_\mu$ of the effective potentials for two flavor neutrinos arises owing to electron-neutrino interaction with electrons of the medium via charged currents (the contributions of neutral currents are significant in the case of neutrino oscillations between active and sterile states). The corresponding part of the effective neutrino Lagrangian can be represented in the form

$$\mathcal{L}_{\text{eff}} = -f^\mu \left(\bar{\nu}\gamma_\mu \frac{1+\gamma^5}{2}\nu\right), \tag{49}$$

where

$$f^\mu = \sqrt{2}G_{\text{F}}(j_e^\mu - \lambda_e^\mu). \tag{50}$$

This additional term in the Lagrangian leads to a modification of the Dirac equation for the neutrino,

$$(\gamma_0 E - \boldsymbol{\gamma}\cdot\mathbf{p} - m)\psi = (\gamma_\mu f^\mu)\psi. \tag{51}$$

It follows that the effective neutrino energy in a medium (dispersion relation) has the form

$$E_{\text{eff}} = \sqrt{(\mathbf{p}-\mathbf{F})^2 + m^2} + f_0. \tag{52}$$

In the case where the interaction is indeed weak—that is, where the condition $|\mathbf{f}| \ll t_0 = \sqrt{\mathbf{p}^2 + m^2}$ is satisfied—the effective electron-neutrino energy in moving and polarized matter takes the form

$$E_{\text{eff}} = \sqrt{\mathbf{p}^2 + m^2} \tag{53}$$
$$+ U\left\{(1-\boldsymbol{\zeta}_e\cdot\mathbf{v}_e)(1-\boldsymbol{\beta}\cdot\mathbf{v}_e) + \sqrt{1-v_e^2}\right.$$
$$\left.\times\left[\boldsymbol{\zeta}_e\cdot\boldsymbol{\beta} - \frac{(\boldsymbol{\beta}\cdot\mathbf{v}_e)(\boldsymbol{\zeta}_e\cdot\mathbf{v}_e)}{1+\sqrt{1-v_e^2}}\right]\right\} + O(\gamma^{-1}),$$

where $U = \sqrt{2}G_{\text{F}}n_0/\sqrt{1-v_e^2}$ and n_0 is the invariant medium-electron concentration (for our case of $\nu_e \leftrightarrow \nu_\mu$ oscillations and a one-component medium).

We can now solve the problem of calculating the probability of the $\nu_e \to \nu_\mu$ transition in moving and polarized matter. In the adiabatic approximation, this probability has the form

$$P_{\nu_e\to\nu_\mu}(x) = \sin^2(2\theta_{\text{eff}})\sin^2\frac{\pi x}{L_{\text{eff}}}, \tag{54}$$

where x is the distance traveled by a neutrino in matter from the point of its production to the point of its detection and L_{eff} and θ_{eff} are, respectively, the effective mixing angle and the effective oscillation length, the last two quantities being given by

$$\sin^2(2\theta_{\text{eff}}) = \frac{\Delta^2\sin^2(2\theta)}{\Big(\Delta\cos(2\theta) - A\Big)^2 + \Delta^2\sin^2(2\theta)}, \tag{55}$$

$$L_{\text{eff}} = \frac{2\pi}{\sqrt{\Big(\Delta\cos(2\theta) - A\Big)^2 + \Delta^2\sin^2(2\theta)}}. \tag{56}$$

Here, $\Delta = \delta m_\nu^2/(2|\mathbf{p}|)$, with $\mathbf{p}$ being the neutrino momentum, and θ is the vacuum mixing angle. The effect of interaction with matter on neutrino oscillations, as well as the effects of the motion and polarization of matter, is described by the quantity A,

$$A = \sqrt{2}G_{\text{F}}\frac{n_0}{\sqrt{0-v_e^2}}\left\{(1-\boldsymbol{\beta}\cdot\mathbf{v}_e)(1-\boldsymbol{\zeta}_e\cdot\mathbf{v}_e)\right. \tag{57}$$
$$\left. + \sqrt{1-v_e^2}\left[\boldsymbol{\zeta}_e\cdot\boldsymbol{\beta} - \frac{(\boldsymbol{\beta}\cdot\mathbf{v}_e)(\boldsymbol{\zeta}_e\cdot\mathbf{v}_e)}{1+\sqrt{1-v_e^2}}\right]\right\}.$$

Thus, the neutrino-oscillation probability $P_{\nu_e\to\nu_\mu}(x)$, the effective mixing angle θ_{eff}, and the effective oscillation length L_{eff} significantly depend on the velocity $\mathbf{v}_e$ of the medium (electrons in our case) and its polarization, as well as on the correlations between the three vectors $\boldsymbol{\beta}$, $\mathbf{v}_e$, and $\boldsymbol{\zeta}_e$. Therefore, the condition

$$\frac{\delta m_\nu^2}{2|\mathbf{p}|}\cos(2\theta) = A \tag{58}$$

of the resonance enhancement of neutrino oscillations will also significantly depend on the motion and polarization of matter and on the neutrino speed.

It is obvious that, for immobile (or slowly moving) matter, the resonance condition (58) becomes coincident with the Mikheev–Smirnov–Wolfenstein condition upon taking into account the limiting value of A for $\mathbf{v}_e \ll 1$. A more detailed analysis of the effective neutrino potentials in various moving and polarized media is given in [29].

The general conclusion that must be particularly emphasized is as follows: In the case of a relativistic motion of matter, the condition of the resonance enhancement of neutrino oscillations can be satisfied even if, for the specific features of the neutrino (vacuum mixing angle θ, difference δm_ν^2 of the masses squared, and energy $|\mathbf{p}|$) and the invariant matter concentration n_0, the resonance is impossible in immobile matter. On the contrary, the condition of the resonance enhancement of oscillations can be violated upon taking into account the relativistic motion of matter (as well as upon taking into account the effects of matter polarization).

6. CONCLUSION

We have considered neutrino-spin oscillations in matter and in a transverse magnetic field and introduced the concept of the critical magnetic-field strength above which the corresponding oscillations

become sizeable even if the condition of their resonance enhancement does not hold. We have proposed a Lorentz-invariant approach to neutrino-spin and neutrino-flavor oscillations in matter and in electromagnetic fields. This approach makes it possible to describe oscillations under the effect of arbitrary electromagnetic fields. In particular, we have predicted the existence of new types of neutrino-spin oscillations (and obtained the corresponding resonance conditions) in the field of an electromagnetic wave and for a superposition of the field of an electromagnetic wave and a longitudinal magnetic field. For the example of spin oscillations in this electromagnetic-field configuration, which is rather complicated, we have also determined the critical field-strength value above which the oscillations become sizeable.

Our Lorentz-invariant approach to describing neutrino oscillations makes it possible to take into account the effects of the motion and polarization of matter in neutrino-spin and neutrino-flavor oscillations for arbitrary (including relativistic) speeds of motion of matter. In particular, it has been shown that, irrespective of the type of neutrino transitions, the effects of matter in the resonance condition for oscillations are suppressed in the case of a relativistic motion of matter along the direction of neutrino propagation. In the case of a relativistic motion of matter antiparallel to the neutrino momentum, the effects of matter are enhanced. These new regularities of neutrino oscillations in the presence of matter must manifest themselves under actual astrophysical conditions where neutrinos propagate through relativistic jets of matter.

The possibly strong dependence of the features of neutrino-spin oscillations on the speed of motion of matter must be taken into account in determining the critical magnetic-field strength (16). By way of example, we indicate that, if one considers $\nu_{eL} \leftrightarrow \nu_{eR}$ neutrino oscillations in moving matter and in a transverse magnetic field $B_\perp$ that is constant along the neutrino trajectory, the critical magnetic-field strength determined with allowance for the motion of matter has the form

$$B_{\rm cr} = \frac{1}{\sqrt{2}} \frac{G_{\rm F} n_0 (1 - \boldsymbol{\beta} \cdot \mathbf{v}_e)}{\mu \sqrt{1 - v_e^2}}. \qquad (59)$$

For the sake of simplicity, we assumed here that matter consists of electrons exclusively, their invariant concentration being n_0, and also neglected the possible effects of the polarization of particles of matter. It is obvious that, in the case of a relativistic motion of matter along the direction of neutrino propagation, we have $B_{\rm cr} \approx 0$. Therefore, the probability amplitude for neutrino-spin oscillations will tend to unity, in which case the oscillations can be significant even in a rather weak transverse magnetic field.

The possible emergence of neutrino-spin oscillations (for example, $\nu_{e_L} \leftrightarrow \nu_{e_R}$) owing to neutrino interaction with matter under the condition that there exists a nonzero transverse current component or polarization of matter (that is, $\mathbf{M}_{0\perp} \neq 0$) is the most important new effect that follows from the investigation of neutrino-spin oscillations in Section 4. So far, it has been assumed that neutrino-spin oscillations may arise only in the case where there exists a nonzero transverse magnetic field in the neutrino rest frame. It should be noted here that, in [30], it was also shown that neutrino-spin oscillations in matter will always arise (even without an external electromagnetic field and in the case of unpolarized and immobile matter), provided that the primary neutrino state is not fully polarized along (parallel or antiparallel) the direction of neutrino motion.

Let us estimate numerically parameters that are determined by the neutrino properties, the strength and the structure of a magnetic-field, and the features of the ambient medium and at which $\nu_{e_L} \leftrightarrow \nu_{e_R}$ neutrino-spin oscillations may arise owing precisely to neutrino interaction with particles of the medium. In the general case of an arbitrary motion of matter and an arbitrarily oriented constant magnetic field, the probability of oscillations is determined by formula (7), where [see Eq. (27)]

$$\sin^2(2\theta_{\rm eff}) = \frac{E_{\rm eff}^2}{E_{\rm eff}^2 + \Delta_{\rm eff}^2},$$

$$L_{\rm eff} = \frac{2\pi}{\sqrt{E_{\rm eff}^2 + \Delta_{\rm eff}^2}}$$

with

$$E_{\rm eff} = \mu \left| \mathbf{B}_\perp + \frac{1}{\gamma_\nu} \mathbf{M}_{0\perp} \right|, \qquad (60)$$

$$\Delta_{\rm eff}^2 = \frac{\mu}{\gamma_\nu} \left| \mathbf{M}_{0\|} + \mathbf{B}_{0\|} \right|. \qquad (61)$$

From the analysis performed in Section 2 for the probability of oscillations in a transverse magnetic field, it follows that the situation of interest is that in which the quantity $\Delta_{\rm eff}$ is much smaller than $E_{\rm eff}$, which, in turn, is so great that the effective oscillation length $L_{\rm eff}$ takes a value compatible with characteristic dimensions of astrophysical objects and media where one can expect the occurrence of the processes being considered. An analysis of the longitudinal and the transverse component of the vector $\mathbf{M}_0$ shows that, under the condition $\gamma_\nu \gg \gamma_e$ (neutrino is a more relativistic particle than electrons of the medium), the desired relation between $\Delta_{\rm eff}$ and $E_{\rm eff}$ cannot be attained without taking into account the effects of a magnetic field. In this connection, the possibility of an additional compensation of the contribution of $\mathbf{M}_{0\|}$

owing to a sufficiently strong longitudinal magnetic field $\mathbf{B}_\parallel$ is of interest. We consider the case where the main contribution to E_{eff} comes from the $\mathbf{v}_{e\perp}$-dependent term in $\mathbf{M}_{0\perp}$. For E_{eff} and Δ_{eff}, we then have the estimates

$$E_{\text{eff}} \approx \frac{n_0 G_{\text{F}}}{2\sqrt{2}\gamma_\nu}, \quad \Delta_{\text{eff}} \approx \left|\frac{n_0 G_{\text{F}}}{2\sqrt{2}\gamma_e} - \frac{\mu}{\gamma_\nu} B_\parallel\right|. \quad (62)$$

From the requirement $E_{\text{eff}} > \Delta_{\text{eff}}$, it follows that the amplitude of neutrino oscillations will be large (in excess of $1/2$) if the longitudinal magnetic field is

$$B_\parallel \approx \frac{\gamma_\nu}{\gamma_e}\frac{n_0 G_{\text{F}}}{2\sqrt{2}\mu}. \quad (63)$$

At a characteristic medium-particle concentration of $n_0 \sim 10^{23}$ cm^{-3} and a neutrino magnetic moment of $\mu \sim 10^{-10}\mu_0$ (on the order of magnitude, this value corresponds to modern experimental accelerator constraints on the magnetic moments of the electron and the muon neutrino [31]), this estimate for the longitudinal magnetic field leads to a value of $B_\parallel \sim 10^8$ G. It follows that, under the above conditions, neutrino-spin oscillations become significant owing to neutrino interaction with moving matter.

To conclude this article, we would like to indicate yet another new effect recently predicted in [30] within the development of our Lorentz-invariant approach to describing neutrino-spin oscillations. A neutrino moving in matter and (or) in an electromagnetic field can emit electromagnetic radiation owing to spin precession. This radiation, which is referred to as neutrino spin light, leads to the self-polarization of the neutrino spin (analog of the Sokolov–Ternov effect for electrons in a magnetic field [32]): in the process of radiation in matter or in an external field, active left-handed neutrinos ν_L are converted into right-handed neutrinos ν_R. Neutrino spin light may efficiently arise in the dense matter of various astrophysical objects or the early Universe.

ACKNOWLEDGMENTS

I am grateful to L.B. Okun for his interest in the results presented in this article and for enlightening comments.

REFERENCES

1. B. M. Pontekorvo, Zh. Éksp. Teor. Fiz. **33**, 549 (1957) [Sov. Phys. JETP **6**, 426 (1957)]; **34**, 247 (1958) [**7**, 172 (1958)].
2. Z. Maki, M. Nakagava, and S. Sakata, Prog. Theor. Phys. **28**, 870 (1962).
3. V. Gribov and B. Pontecorvo, Phys. Lett. B **28B**, 493 (1969).
4. S. Bilenky and B. Pontecorvo, Phys. Lett. B **61**, 248 (1976).
5. L. Wolfenstein, Phys. Rev. D **17**, 2369 (1978).
6. S. P. Mikheev and A. Yu. Smirnov, Yad. Fiz. **42**, 1441 (1985) [Sov. J. Nucl. Phys. **42**, 913 (1985)].
7. M. B. Voloshin and M. I. Vysotskiĭ, Yad. Fiz. **44**, 845 (1986) [Sov. J. Nucl. Phys. **44**, 544 (1986)]; L. B. Okun', Yad. Fiz. **44**, 847 (1986) [Sov. J. Nucl. Phys. **44**, 546 (1986)]; M. B. Voloshin, M. I. Vysotskiĭ, and L. B. Okun', Yad. Fiz. **44**, 677 (1986) [Sov. J. Nucl. Phys. **44**, 440 (1986)]; Zh. Éksp. Teor. Fiz. **91**, 754 (1986) [Sov. Phys. JETP **64**, 446 (1986)].
8. A. Cisneros, Astrophys. Space Sci. **10**, 87 (1971).
9. K. Fujikawa and R. Shrock, Phys. Rev. Lett. **45**, 963 (1980).
10. J. Schechter and J. W. F. Valle, Phys. Rev. D **24**, 1883 (1981).
11. C.-S. Lim and W. Marciano, Phys. Rev. D **37**, 1368 (1988).
12. E. Akhmedov, Phys. Lett. B **213**, 64 (1988).
13. G. G. Likhachev and A. I. Studenikin, Zh. Éksp. Teor. Fiz. **108**, 769 (1995) [JETP **81**, 419 (1995)].
14. L. Smirnov, Phys. Lett. B **260**, 161 (1991).
15. J. Vidal and J. Wudka, Phys. Lett. B **249**, 473 (1990).
16. P. Pal, Int. J. Mod. Phys. A **7**, 5387 (1992).
17. E. Akhmedov, S. Petcov, and A. Smirnov, Phys. Rev. D **48**, 2167 (1993).
18. G. Likhachev and A. Studenikin, in *Phenomenology of Unification from Present to Future*, Ed. by G. Diambrini-Palazzi, L. Zanello, and G. Martinelli (World Sci., Singapore, 1994), p. 67.
19. E. Akhmedov, A. Lanza, and D. Sciama, Phys. Rev. D **56**, 6117 (1997).
20. G. Fuller, R. Mayle, and J. Wilson, Astrophys. J. **322**, 795 (1987).
21. W. Haxton and W.-M. Zhang, Phys. Rev. D **43**, 2484 (1991).
22. G. Likhachev and A. Studenikin, 1995 (unpublished).
23. A. Egorov, A. Lobanov, and A. Studenikin, Phys. Lett. B **491**, 137 (2000).
24. V. Bargmann, L. Michel, and V. Telegdi, Phys. Rev. Lett. **2**, 453 (1959).
25. H. Nunokawa, V. Semikoz, A. Smirnov, and J. Valle, Nucl. Phys. B **501**, 17 (1997).
26. M. S. Dvornikov and A. I. Studenikin, Yad. Fiz. **64**, 1705 (2001) [Phys. At. Nucl. **64**, 1624 (2001)].
27. A. Lobanov and A. Studenikin, Phys. Lett. B **515**, 94 (2001).
28. S. Bergmann, Y. Grossman, and E. Nardi, Phys. Rev. D **60**, 093008 (1999).
29. A. Grigoriev, A. Lobanov, and A. Studenikin, Phys. Lett. B **535**, 187 (2002).
30. A. Lobanov and A. Studenikin, Phys. Lett. B **564**, 27 (2003).
31. Particle Data Group, Phys. Rev. D **66**, 010001 (2002).
32. A. A. Sokolov and I. M. Ternov, Dokl. Akad. Nauk SSSR **153**, 1052 (1963).

Translated by A. Isaakyan